ORNL/TM-12428

ornl

OAK RIDGE NATIONAL LABORATORY

MARTIN MARIETTA

Ceramic Technology Project Semiannual Progress Report for October 1992 Through March 1993

Prepared for
U.S. Department of Energy
Assistant Secretary for
Energy Efficiency and Renewable Energy
Office of Transportation Technologies
Materials Development Program

CERAMIC TECHNOLOGY PROJECT

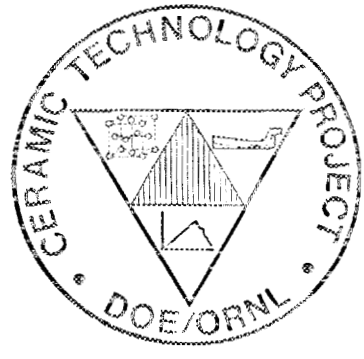

MANAGED BY
MARTIN MARIETTA ENERGY SYSTEMS, INC.
FOR THE UNITED STATES
DEPARTMENT OF ENERGY

ORNL/TM-12428

Metals and Ceramics Division

CERAMIC TECHNOLOGY PROJECT SEMIANNUAL PROGRESS REPORT FOR OCTOBER 1992 THROUGH MARCH 1993

D. R. Johnson
Project Manager

Date Published: September 1993

NOTICE: This document contains information of a preliminary nature. It is subject to revision or correction and therefore does not represent a final report.

Prepared for
U.S. Department of Energy
Assistant Secretary for Energy Efficiency and Renewable Energy
Office of Transportation Technologies
Materials Development Program
EE 51 01 00 0

Prepared by the
OAK RIDGE NATIONAL LABORATORY
Oak Ridge, Tennessee 37831-6285
managed by
MARTIN MARIETTA ENERGY SYSTEMS, INC.
for the
U.S. DEPARTMENT OF ENERGY
under Contract DE-AC05-840R21400

REPORTS PREVIOUSLY ISSUED

ORNL/TM-9325	Period March 1983-September 1983
ORNL/TM-9466	Period October 1983-March 1984
ORNL/TM-9497	Period April 1984-September 1984
ORNL/TM-9673	Period October 1984-March 1985
ORNL/TM-9947	Period April 1985-September 1985
ORNL/TM-10079	Period October 1985-March 1986
ORNL/TM-10308	Period April 1986-September 1986
ORNL/TM-10469	Period October 1986-March 1987
ORNL/TM-10705	Period April 1987-September 1987
ORNL/TM-10838	Period October 1987-March 1988
ORNL/TM-11116	Period April 1988-September 1988
ORNL/TM-11239	Period October 1988-March 1989
ORNL/TM-11489	Period April 1989-September 1989
ORNL/TM-11586	Period October 1989-March 1990
ORNL/TM-11719	Period April 1990-September 1990
ORNL/TM-11859	Period October 1990-March 1991
ORNL/TM-11984	Period April 1991-September 1991
ORNL/TM-12133	Period October 1991-March 1992
ORNL/TM-12363	Period April 1992-September 1992

Research sponsored by the U.S. Department of Energy, Assistant Secretary for Energy Efficiency and Renewable Energy, Office of Transportation Technologies, as part of the Ceramic Technology Project of the Materials Development Program, under contract DE-AC05-84OR21400 with Martin Marietta Energy Systems, Inc.

CONTENTS

CERAMIC TECHNOLOGY PROJECT SEMIANNUAL PROGRESS REPORT FOR OCTOBER 1992 THROUGH MARCH 1993

SUMMARY

The Ceramic Technology Project was originally developed by the Department of Energy's Office of Transportation Systems (OTS) in Conservation and Renewable Energy. This project, part of the OTS's Materials Development Program, was developed to meet the ceramic technology requirements of the OTS's automotive technology programs.

Significant accomplishments in fabricating ceramic components for the Department of Energy (DOE), National Aeronautics and Space Administration (NASA), and Department of Defense (DoD) advanced heat engine programs have provided evidence that the operation of ceramic parts in high-temperature engine environments is feasible. However, these programs have also demonstrated that additional research is needed in materials and processing development, design methodology, and data base and life prediction before industry will have a sufficient technology base from which to produce reliable cost-effective ceramic engine components commercially.

An assessment of needs was completed, and a five-year project plan was developed with extensive input from private industry. In July 1990, the original plan was updated through the estimated completion of development in 1993. The original objective of the project was to develop the industrial technology base required for reliable ceramics for application in advanced automotive heat engines.

During the course of the Ceramic Technology Project, remarkable progress has been made in the development of reliable structural ceramics. However, further work is needed to reduce the cost of ceramics to facilitate their commercial introduction, especially in the highly cost-sensitive automotive market. To this end, the direction of the Ceramic Technology Project is now shifting toward reducing the cost of ceramics to facilitate commercial introduction of ceramic components for near-term engine applications. In response to extensive input from industry, the plan is to extend the engine types which were previously supported (advanced gas turbine and low-heat-rejection diesel engines) to include near-term (5-10 years) applications in conventional automobile and diesel truck engines. To facilitate the rapid transfer of this technology to U.S. industry, the major portion of the work is being done in the ceramic industry, with technological support from government laboratories, other industrial laboratories, and universities.

A systematic approach to reducing the cost of components is envisioned. the work elements are as follows: economic cost modeling, ceramic machining, powder synthesis, alternative forming and densification processes, yield improvement, system design studies, standards development, low-expansion ceramics, and testing and data base development.

This project is managed by ORNL for the Office of Transportation Technologies, Office of Transportation Materials, and is closely coordinated with complementary ceramics tasks funded by other DOE offices, NASA, DoD, and industry. A joint DOE and NASA technical plan has been established, with DOE focus on automotive applications and NASA focus on aerospace applications. A common work breakdown structure (WBS) was developed to facilitate coordination. The work described in this report is organized according to the following WBS project elements:

0.0 Project Management and Coordination

1.0 Materials and Processing

- 1.1 Monolithics
- 1.2 Ceramic Composites
- 1.3 Thermal and Wear Coatings
- 1.4 Joining
- 1.5 Cost Effective Ceramic Machining

2.0 Materials Design Methodology

- 2.2 Contact Interfaces
- 2.3 New Concepts

3.0 Data Base and Life Prediction

- 3.1 Structural Qualification
- 3.2 Time-Dependent Behavior
- 3.3 Environmental Effects
- 3.4 Fracture Mechanics
- 3.5 Nondestructive Evaluation Development

4.0 Technology Transfer

- 4.1 Technology Transfer

This report includes contributions from all currently active project participants. The contributions are arranged according to the work breakdown structure outline.

0.0 PROJECT MANAGEMENT AND COORDINATION

D. R. Johnson
Oak Ridge National Laboratory

Objective/scope

This task includes the technical management of the project in accordance with the project plans and management plan approved by the Department of Energy (DOE) Oak Ridge Operations Office, and the Office of Transportation Technologies. This task includes preparation of annual field work proposals, initiation and management of subcontracts and interagency agreements, and management of ORNL technical tasks. Monthly management reports and bimonthly reports are provided to DOE; highlights and semiannual technical reports are provided to DOE and program participants. In addition, the program is coordinated with interfacing programs sponsored by other DOE offices and federal agencies, including the National Aeronautics and Space Administration (NASA) and the Department of Defense (DoD). This coordination is accomplished by participation in DOE and NASA joint management meetings, annual interagency heat engine ceramics coordination meetings, DOE contractor coordination meetings, and DOE Energy Materials Coordinating Committee (EMaCC) meetings, as well as special coordination meetings.

1.0 MATERIALS AND PROCESSING

INTRODUCTION

This portion of the project is identified as project element 1.0 within the work breakdown structure (WBS). It contains four subelements: (1) Monolithics, (2) Ceramic Composites, (3) Thermal and Wear Coatings, and (4) Joining. Ceramic research conducted within the Monolithics subelement currently includes work activities on low cost Si_3N_4 powder, green state ceramic fabrication, characterization, and densification, and on structural, mechanical, and physical properties of these ceramics. Research conducted within the Ceramic Composites subelement currently includes silicon carbide, silicon nitride, and oxide-based composites. Research conducted in the Thermal and Wear Coatings subelement is currently limited to oxide-base coatings and involves coating synthesis, characterization, and determination of the mechanical and physical properties of the coatings. Research conducted in the Joining subelement currently includes studies of processes to produce strong, stable joints between zirconia ceramics and iron-base alloys. As part of an expanded effort to reduce the cost of ceramic components, a new initiative in cost effective machining has been started.

A major objective of the research in the Materials and Processing project element is to systematically advance the understanding of the relationships between ceramic raw materials such as powders and reactant gases, the processing variables involved in producing the ceramic materials, and the resultant microstructures and physical and mechanical properties of the ceramic materials. Success in meeting this objective will provide U.S. companies with new or improved ways for producing economical, highly reliable ceramic components for advanced heat engines.

1.1 MONOLITHICS

1.1.1 Silicon Carbide

High Temperature Hexoloy SX Silicon Carbide

S. K. Lau and G. V. Srinivasan (The Carborundum Company)

- **Introduction:**

  HEXOLOY®[1] SX SiC has been demonstrated to possess higher toughness and strength than HEXOLOY SA SiC. Its toughness is about 50% to 100% higher than that of HEXOLOY SA SiC and its typical room temperature MOR value ranges between 620-915 MPa (90-133 ksi). Moreover, these are only preliminary data, and it is believed that the mechanical properties can be further improved via proper optimization of composition, powder selection and processing conditions.

- **Scope and Objective:**

  The approach taken for this work was to first establish a complete mechanical property database and conduct a detailed microstructural characterization on the first generation SX material. The emphasis would then be focused on the selection of a best SiC powder source and the optimization of processing conditions for this first generation material via a systematic designed experimental method. In parallel, a Carborundum in-house sponsored program with the objective of identifying a second generation additive composition with improved high temperature properties was also to be conducted. Once this second generation composition was identified, the information would be fed into the current program. Further experiments would then be conducted to optimize the properties of this second generation SX material. Finally, the complete property database would then be established for the second generation composition.

  The three major objectives for the current program are as follows: (1) to establish the property database and conduct a detailed characterization of the best SX material at program startup, (2) to improve the processing conditions of that material via a designed experimental method, and (3) to develop a second generation SX material with improved properties.

- **Task 1 Objective:** Complete Characterization of Generation I SX-SiC Material.

  Completed, details reported in previous semi-annual report.

- **Task 2 Objective:** SiC Powder Selection.

  Completed, details reported in previous semi-annual report.

- **Task 3 Objective:** Property Optimization for Generation I SX-SiC

  Status: Completed.

  Repeated sintering runs were conducted to fabricate samples for deliverables. The last batch sintered at the optimum conditions yielded an average room temperature MOR of 122 ksi. While this was lower than the 140 ksi from the earlier design experiments, it represented the closest value obtained using a different batch of starting SiC powder. Twenty MOR bars from this batch were sent to ORNL to fulfill the contract deliverable requirement.

- **Task 4 Objective:** Complete Characterization of Generation II Material.

  Status: Completed.

  The original objective of Task 4 was to optimize a second generation SX material. However, based on experimental findings reported and detailed in the last semi-annual report, the program plan was modified to conduct a second series of design experiments to further improve the SX-G1 composition. This approach was approved by ORNL.

---

[1] HEXOLOY is a registered trademark of The Carborundum Company

Densification runs for the Task 4 design experiments were then conducted. The experimental conditions were:

Powder Processing Technique:	Modified Turbomilling
Sinter Temperature:	ST3 (-1) to ST4 (+1)
Post-Treat Temperature:	PT3 (-1) to PT4 (+1)
Post-Treat Pressure:	P3 (-1) to P4 (+1)

Near theoretical densities were obtained for sintering temperature levels (0) and (+1), when followed by any of the post-sinter treatment conditions used. However, for the lowest sintering temperature level (-1), only 90 to 97% T.D. was obtained after various post-sinter treatments. Mechanical property evaluated included MOR at room temperature and high temperature (1232°C for selected samples), Chevron Notch toughness at room temperature and 1232°C, and dynamic fatigue at 1232°C. The results are listed in the attached Table 1. Low MOR values were observed for the lowest sintering temperature as expected. The highest average room temperature MOR obtained was 128 ksi corresponding to the sintering condition of (+1) and post-treat temperature of (-1) and post-treat pressure of (+1).

When comparing two relatively similar densification conditions between this set of design experiments and that of Task 3, the current design yielded an average room temperature MOR of 118 ksi compared to 140 ksi from the previous design. This difference again highlights the reproducibility difficulties in the SX-G1 furnacing process.

After the completion of Task 4 matrix experiments, about 20 plates had been sintered under the optimum conditions for a more detailed mechanical characterization.

Fabrication of tensile rods was also conducted. Previous experience in sintering rods for tensile samples suggested that the densification conditions would be different from those for the smaller plates for MOR bars. Experimental rods of shorter lengths were first sintered at various conditions. The optimum densification conditions were identified. Finer adjustments were then conducted for the longer actual size rods. More than 20 fully dense rods were successfully fabricated.

Mechanical characterization, including MOR, tensile and dynamic fatigue testing of all these Task 4 specimens densified at the optimum conditions was then completed using both Carborundum and HTML/ORNL facilities. The MOR values determined at various temperatures with strength limiting defects are listed in Table 2.

The strength limiting defects were again identified to be "Si rich pools" and machining induced surface defects up to a temperature of 1232°C. The mechanism of formation of "Si rich pools" as a reaction product was explained in earlier reports. In this task, about 30% of the failures were due to "Si pools" compared to 70% in Task 1. The use of the optimum sintering conditions identified appears to have reduced the frequency of formation of "Si pools" and increased the strength as shown in Figure 1. At 1370°C, surface glass formation was again identified as the strength limiting defect.

As described earlier, different sintering conditions were needed to densify the larger tensile rods. It was found that the Task 4 conditions identified were in fact very similar to those employed in Task 1. As a result, no significant change in tensile strength was observed as shown in Figure 1. Figure 2 shows the dynamic fatigue data obtained for both Tasks 1 and 4. No slow crack growth was observed up to a minimum temperature of 1232°C as expected.

All the technical work for this contract has been completed. The 20 MOR bar deliverables to ORNL have also been fabricated and delivered.

- **Task 5 Objective:** Development of an Improved Dispersion Process.

  Completed, details reported in previous semi-annual report.

- **Communications/Visits/Travel:**

  Dr. G.V. Srinivasan conducted tensile tests at HTML/ORNL during the month of December 1992. Drs. S.K. Lau, G.V. Srinivasan and R.S. Storm presented the final program review at ORNL on February 4, 1993.

Table 1

Task 4 Matrix Experiment Characterization Results

Sin. Temp.	Post Temp.	Post Press.	Sint. Density %	Post Density %	MOR in ksi		Toughness MPa. m		SCG Parameter at 1232°C
					RT	1232°C	RT	1232°C	
−1	−1	−1	85	91.5	57		3.1	2.5	No SCG
−1	−1	1	85	89.9	56		3.1	2.7	No SCG
−1	1	−1	85	93.7	79		4	2.7	No SCG
−1	1	1	85	97.4	75		4	2.8	No SCG
0	0	0	95.6	99.9	119	78	4.5	3.3	No SCG
0	0	0	94.8	99.8	114	71	4.5	3.1	No SCG
1	−1	−1	97	99.7	95		4.3	3	No SCG
1	−1	1	97	99.9	128	69	4.9	3.2	No SCG
1	1	−1	97.8	99.7	104	56	5	3.7	No SCG
1	1	1	97.8	99.8	100	55	5.2	4	No SCG

Table 2

Task 4 MOR As Function of Temperature

MOR in MPa (ksi)	Temperature, °C	Strength Limiting Defect
896 (130)	25	Volume: "pool" Surface: Machining
620 (90)	1000	,,
527 (77)	1232	,,
389 (56)	1370	Surface: Glass phase formation

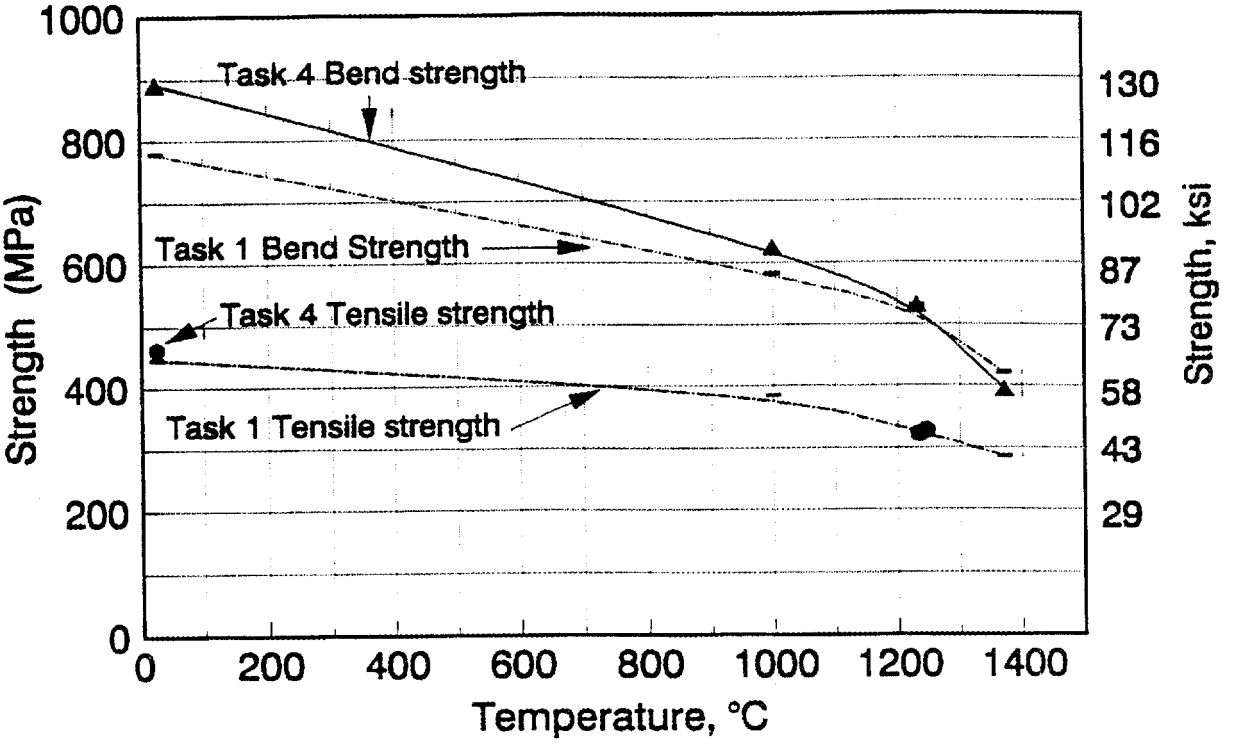

Figure 1. Strength characteristics of SX-G1

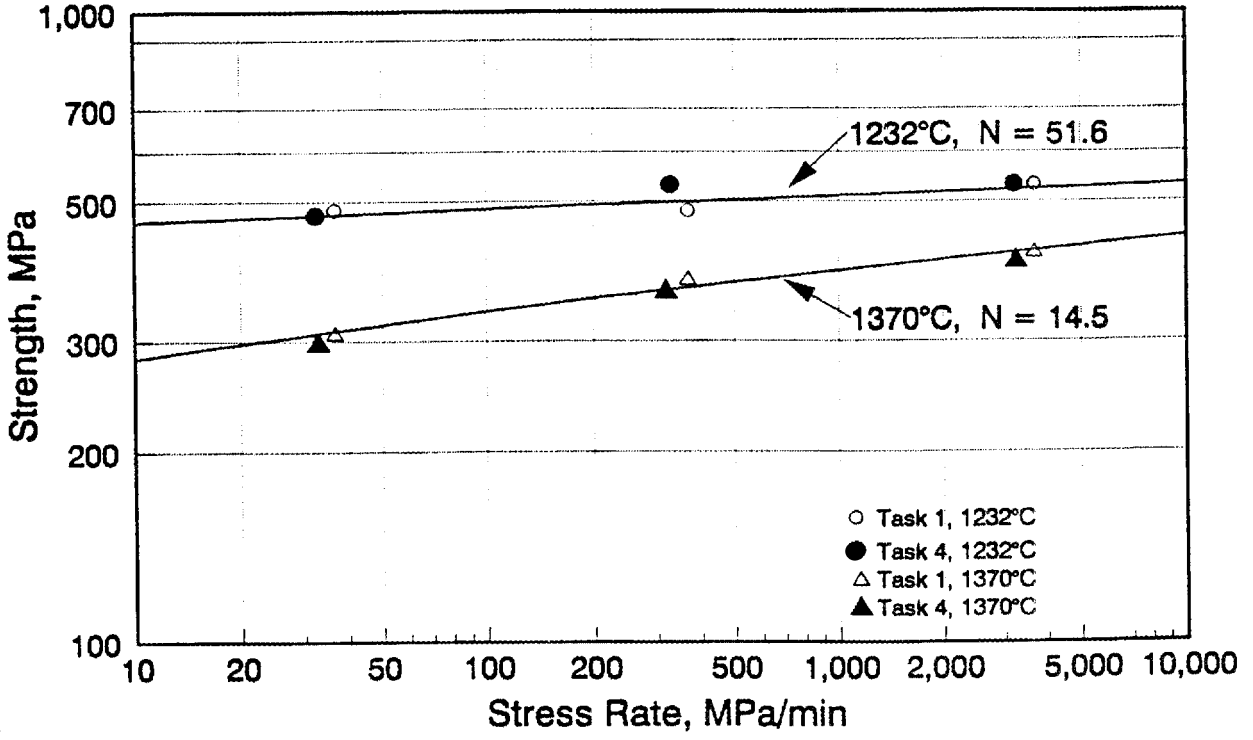

Figure 2. Dynamic fatigue characteristics of SX-G1.

- **Problems Encountered:**

  Difficulties in reproducing the strength levels obtained from different densification runs have been regularly encountered. It is suspected that the reaction between SiC and the Y-Al-O second phases forming strength limiting pools of varying sizes and shapes is the main reason for this variability. Carborundum needs to assess the severity of this problem before going further with the development and commercialization of SX materials.

- **Publications**

  1. Srinivasan, G.V., S.K. Lau, and R.S.Storm, "Recent Advances in Development of High Temperature HEXOLOY SX-SiC," to appear in the Proceedings of the Annual Automotive Technology Development Contractor's Coordination Meeting, Detroit, November 2-5, 1992, SAE, Warrendale, PA.
  2. Srinivasan, G.V., S.K. Lau, R.S. Storm, M.K. Ferber, and M.J. Jenkins, "Process Optimization of HEXOLOY SX-SiC Towards Improved Mechanical Properties," to appear in the Proceedings of the International Gas Turbine Meeting, Cincinnati, OH, June 1993.

- **Plan**

  At this time all the experimental work under this contract has been completed. The final program report is in preparation.

1.1.2 Silicon Nitride

Characterization of Attrition Milled Silicon Nitride Powder

S. G. Malghan, P. T. Pei and D. B. Minor
(National Institute of Standards and Technology)

Objective/Scope

Currently, the starting materials in the manufacture of silicon nitride ceramic components are fine powders. These fine sized powders tend to form agglomerates due to the van der Waals attractive forces. For improved reliability in the manufacture of ceramic components, the agglomerates in the powders should be eliminated since they form defects. In addition, the powders should have an appropriate range of size distribution and specific surface area for achieving a near-theoretical density of the ceramic after densification. These factors necessitate the use of powder milling as one of the major powder processing unit operations. Therefore, milling of powders is an integral unit operation in the manufacture of silicon nitride components for advanced energy applications. The production and use of these powders require the use of efficient milling techniques and understanding of characteristics of the milled powders in a given environment. High energy attrition milling appears to offer significant advantages over conventional tumbling and vibratory mills.

The major objectives of this project are: 1. establish repeatability of particle size distribution and other relevant characteristics of slurries milled in a high energy agitation mill (HEAM); 2. determine processing and densification characteristics of powders milled in HEAM; and 3. compare properties of powder, and resulting ceramic obtained by milling in the HEAM vs. vibratory ball mill in a collaborative project with Norton Company.

Technical Progress

During this reporting period, we completed the analysis of first stage experiments on repeatability, and developed a modified procedure for follow-up milling experiments. Briefly described, these experiments consisted of milling of a mixture of SNE-10, 5 and 3 powders in a high energy agitation mill, and sampling at 0, 20, 32, 50 and 80 min. milling periods. Yttrium oxide was added at the 20th min. after all the silicon nitride powder was added. The specific surface area data were obtained using the BET method. The particle size distribution data was obtained using a standard procedure for Horiba LA-900, a light scattering device. Three samples from each milling time were analyzed; and the 10th, 25th, 50th, 75th and 90th percentiles of that distribution were recorded for further analysis. One of the conclusions of review of repeatability data on milling of silicon nitride powders is that the observed spread of repeatability is due to both variability in the milling system and measurement procedure. The following are some data on variability due to the specific surface area measurement procedure.

Figure 1 shows data on specific surface area of 80 min. milled samples. For each of the five tests, three samples were analyzed by using the procedure recommended by IEA Subtask 6, which included 200°C degassing prior to the measurement. All these measurements were obtained within 48 hrs. after the milling test. These samples were dried in a convection oven at 40°C. The data for tests 40, 41, 42, 43 and 44 are represented by circles as (Set #1). The data represented by triangles were obtained from these samples after approximately six weeks of the completion of milling tests (Set #2). The same procedure was used for surface area measurement for Set #1 and 2. During this period, the samples were stored in a closed bottle under the normal laboratory environment. Figure 2 shows the same data, but presented in randomized order under which Set #2 surface area data were obtained. These data in Figure 1 and 2 show several trends:

- Surface area of six weeks delay samples (Set #2) was mostly lower than those obtained within 48 hrs. of the milling test (Set #1).

- Average of all 30 data points was 10.57 m^2/g. Most of the data fell within + or - one σ (standard deviation).

- Surface area of 80 min. milled powder decreased as milling proceeded from tests 41 to 44, as shown by the trend-line.

- Randomized data presentation showed no trend with respect to the order in which the tests were conducted (Figure 2).

These data demonstrated that variation in repeatability with respect to surface area measurement is due to both milling and measurement procedure.

A measurement factor responsible for this type of wide variation in the surface area data could be moisture in the milled powder. To examine this aspect, the milled samples from all five tests were heated to 550°C and cooled samples were analyzed for surface area. These data demonstrated a drastic improvement in the range of variability. The average surface area decreased from 10.5 to 9.0 m^2/g and standard deviation was also less than 1 m^2/g which is of the order of measurement error. From these data we find that the component related to variation in repeatability due to surface area measurement can be controlled by treatment of the samples. However, this raises a question on possibility of agglomerates formation at 550°C.

Next the particle size distribution data were analyzed. The data of five tests in Figure 3 show, as expected, a log-linear decrease in the median diameter as a function of natural log of time. Except for time 0 data, the results show statistically significant differences between the data of milling tests for all percentiles of the distribution. Results of the five tests represented by different symbols in Figure 4 are clearly separated for longer milling times, demonstrating the statistical significance between tests data.

The within-mill run (test) standard deviation and between mill run (test) standard deviations have been estimated for each of the five

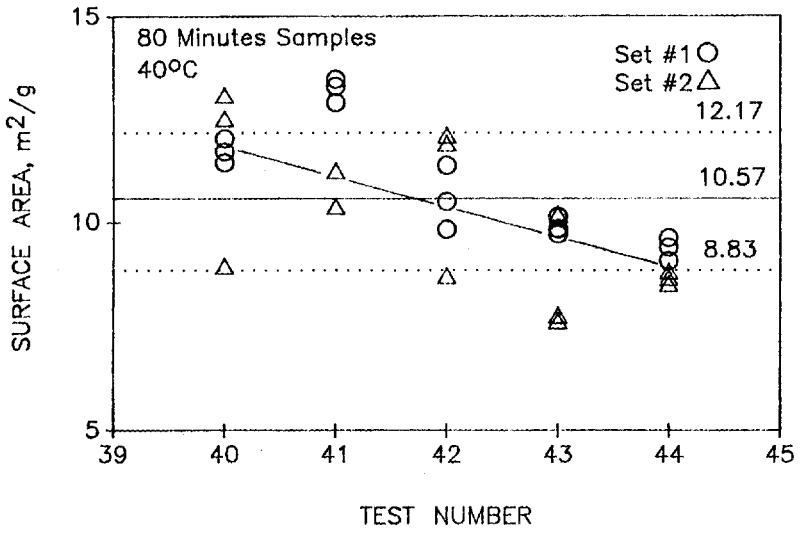

Figure 1. Specific surface area of powder samples milled for 80 min. in tests 40 to 44. Set #1 refers to data collected within 48 hrs. of the milling test. Set #2 refers to data collected after 6 weeks delay. All three samples in each test were dried at 40°C. Trend-line is shown by an arrow.

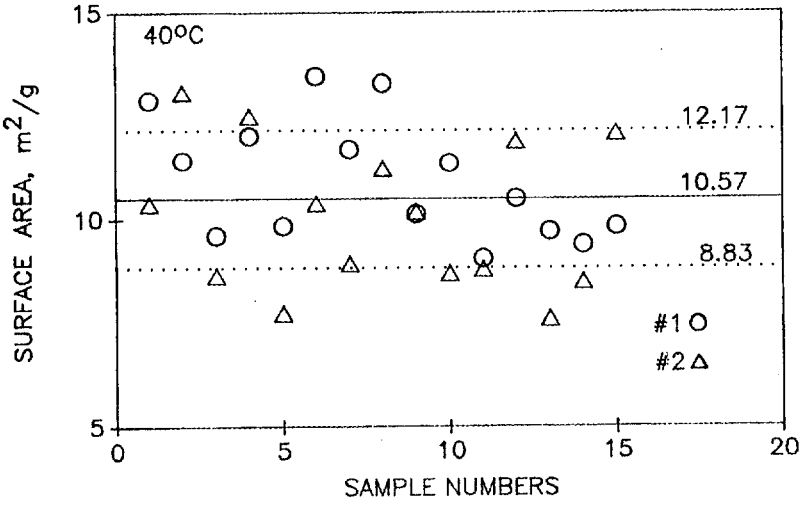

Figure 2. The same data as in Figure 1, but represented in random order of analysis, rather than successive order to samples analysis from test 41 to 44.

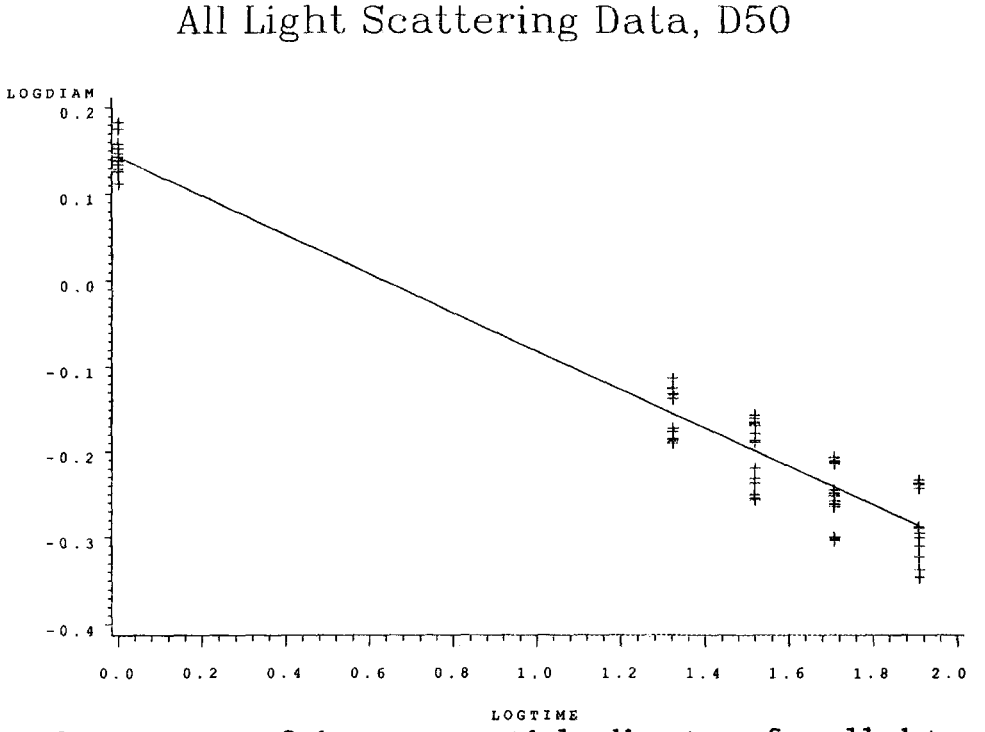

Figure 3. Response of d_{50}, mean particle diameter, for all data as a function of milling time, plotted on log scale.

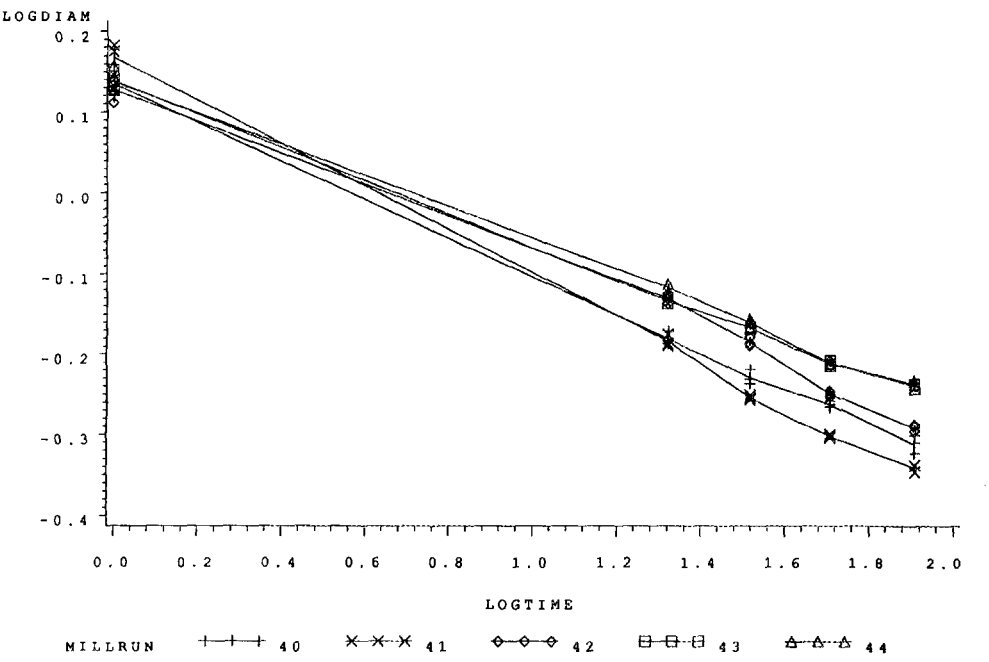

Figure 4. The same data as in Figure 3, but data from each test are presented discretely so that the differences can be observed.

percentiles, at each of the five milling times. Plots of their relative sizes (in percent) are shown in Figure 5 and 6. The relative within-run standard deviation is approximately constant for all percentiles for milling times 20 and above. The reason for a single apparent outlier in one of the mill runs is not known. With the four "outlying" exceptions, 95% confidence intervals for these estimates range from 0.6 to 3%. The relative between-run standard deviation is also about constant for all percentiles and times 20 min. and above. The approximate 95% confidence intervals ranging from 3% to 25% are also fairly wide.

The standard deviation of a single measurement at 95% confidence interval is an useful measurement since it includes both within-run measurement error variability as well as between-run variability. The 95% confidence intervals for the standard deviation of a single measurement were determined. Since all measurements on milled samples were made shortly after the sample was milled, the confidence intervals from these data are sufficient to characterize day-to-day variability in the measurement process. However, this does not answer the question of how much of the variability between mill runs is due to the effect of milling or due to the measurement process.

The second series of tests to evaluate the repeatability were initiated in February using a modified procedure based on the results of the first series. The primary modifications from the first series included the following: (1) completion of powder addition in the first twenty minutes of milling to promote uniformity in milling data; (2) addition of yttria in the form of suspension dispersed in the presence of Daxad 34 dispersant to enhance dispersability of yttria; (3) The measurement of particle size distribution at all five sampling times in triplicate of three samples to evaluate measurement error; (4) decrease of the number of electrokinetic sonic amplitude (ESA) measurements to three at 32, 50, and 80 min only. The milling is carried out at 53-55% volume loading of powder in the slurry. Initial observations of settling and casting data of these slurries show that the dispersion of particles has improved.

The casting of these slurries has shown that consistently we have been able to achieve 2.11 to 2.18 g/cm^3 green density, depending on the slurry conditions. Our casting procedure has not been optimized and we have found that it can be improved. Improvements such as porosity of gypsum block and pressure application may further improve the green density to 2.3 g/cm^3. The concentration of Daxad 34 polyelectrolyte in the dispersion of these powders has been evaluated and found to be not very critical as long as the concentration is in the range of 1500 ppm based on the powder weight. The increase of Daxad 34 concentration by four-fold resulted in an increase of viscosity of this slurry which was accompanied by faster settling rate and low green density. At higher Daxad 34 concentrations, the size of agglomerates appears to be slightly larger which could not be detected by the particle size measurement. The pH of dispersion preparation appears to be an important parameter though the pH does not change drastically provided the initial mixing of the powder is carried out at pH 9.5 to 10.0.

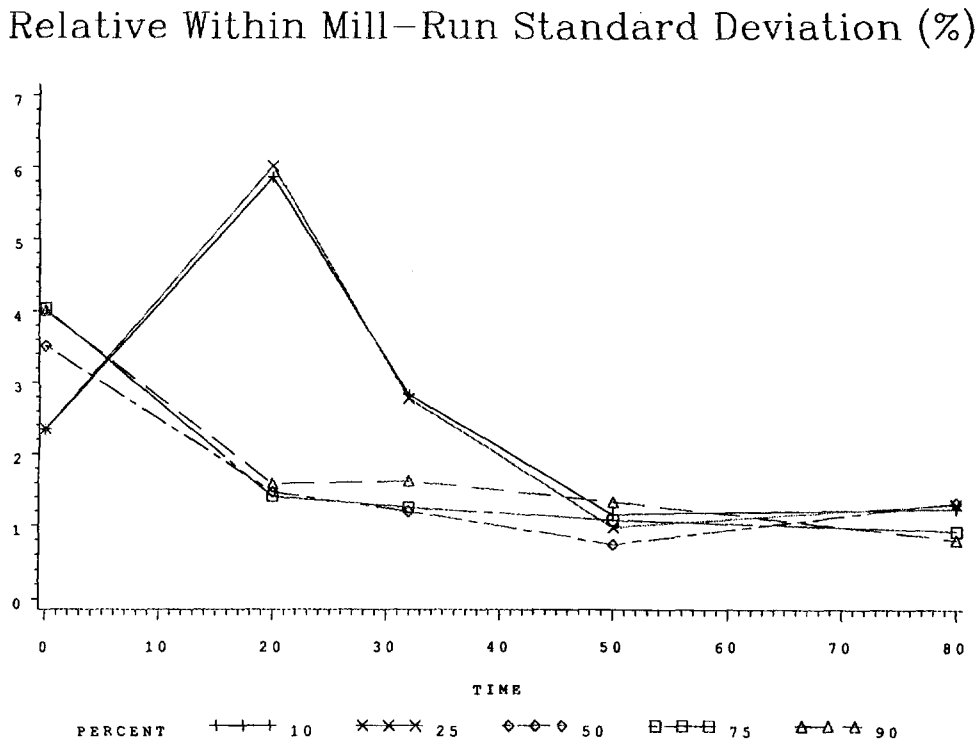

Figure 5. Response of relative within mill (run) standard deviation as a function of milling time for data of five percentiles.

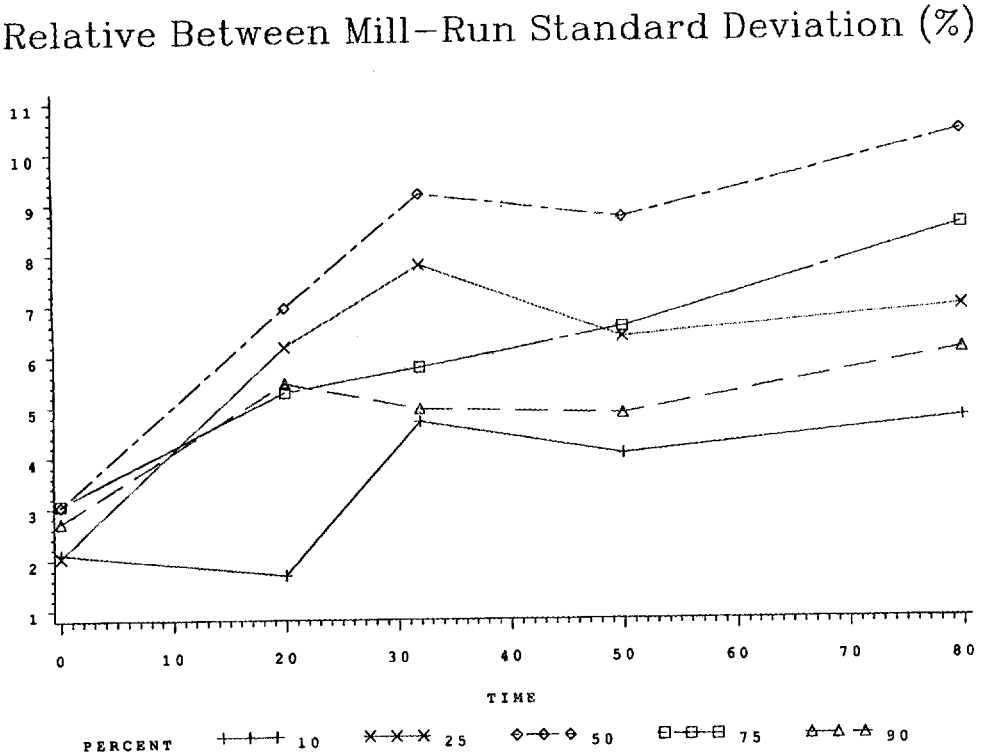

Figure 6. Response of relative between mill (run) standard deviation as a function of milling time for data of five percentiles.

Status of Milestones

On target.

Communications/Visits

S. J. Lombardo, St. Gobain-Norton Company visited to discuss milling collaboration.

Publications

Hackley, V. A. and Malghan, S. G., "Application of Electroacoustic Analysis to Colloidal Processing of Silicon Nitride Powders," Proc. NIST Workshop on Electroacoustics for Particulates Characterization, May 1993.

Wang, P., Minor, D. B., and Malghan, S. G., "Binder Distribution in Silicon Nitride Green Body by Stray-Field NMR Imaging," accepted for publ. in J. Materials Research, May 1992.

Malghan, S. G. and Minor, D. B., "Silicon Nitride Powders Processing in High Energy Agitation Mill," Annual Automotive Technology Development Contractors Coordination Meeting, October 1992.

Microwave Sintering of Silicon Nitride

T. N. Tiegs, J. O. Kiggans, K. L. Ploetz, H. D. Kimrey, and P. A. Menchhofer
(Oak Ridge National Laboratory)

Objective/scope

The objective of this research element is to identify those aspects of microwave processing of silicon nitride that might (1) accelerate densification, (2) permit sintering to high density with much lower levels of sintering aids, (3) lower the sintering temperature, or (4) produce unique microstructures. The investigation of microstructure development is being done on dense silicon nitride materials annealed in the microwave furnace. The sintering of silicon nitride involves two approaches. The first approach comprises heating of silicon nitride and sialon powder compositions in the 2.45- or 28-GHz units. The second approach deals with using reaction-bonded silicon nitride as the starting material and is done entirely in the 2.45-GHz microwave furnace.

Technical highlights

Sintered Reaction-Bonded Silicon Nitride (SRBSN) - In previous reports, we have shown that the mechanical properties of the MW-SRBSN are not equal to ceramics made from the higher-cost powders but are appropriate for a number of applications at lower temperatures and stress levels.[1] It would be desirable to improve both the strength and toughness of the materials. Consequently, additional samples were fabricated using different processing procedures and materials to improve these properties. For example, isopropyl alcohol (IPA) was substituted for the water in the milling step. This reduced the oxygen pickup and improved nitridation of the silicon at lower temperatures, thereby increasing the α-Si_3N_4 content of the compacts prior to high-temperature sintering.[2] The current samples are also nitrided with approximately 5 vol % He in the N_2-H_2 atmosphere to further increase the α-Si_3N_4 content in the compacts.[3] Analysis indicated an increase in α-Si_3N_4 content after nitridation as shown in Table 1. The increase in α-content is believed to increase the aspect ratio of the ß-Si_3N_4 grains and improve the fracture toughness of these materials.

Table 1. Summary of results on a α-Si_3N_4 content of samples after irradiation. Final compositions of samples were Si_3N_4-11.5% La_2O_3-3% Al_2O_3

Sample ID	Milling medium	Nitridation time (h)	Nitridation atmosphere	α-Si_3N_4 content (%)
TM-137F	Water	20	N_2-4% H_2	27
TM-137J	Water	25	N_2-4% H_2	52
TM-140H	Water	28	N_2-4% H_2-5% He	57
TM-150A	Isopropanol	27	N_2-4% H_2-5% He	88

A comparison of the costs for the different sample types of silicon nitride is shown in Table 2. The cost advantage of the SRBSN materials is readily evident. It should be emphasized that these costs are based on purchases made by the present authors on quantities of 20 lb (10 kg). Purchases of large quantities of these materials would be expected to decrease the costs by 40% from those presented here. Thus, a commercial-scale operation for either SRBSN composition, assuming a 40% reduction, would be expected to have raw materials costs on the order of $6/lb or less. Comparison of the raw material costs reveals that all of the SRBSN compositions in the present study are <27% those for either of the sintered silicon nitride (SSN) materials.

Table 2. Composition of sintered reaction-bonded silicon nitride (SRBSN) materials

Sample No.	Sample type	Silicon impurity (wt %)	SiO_2 Additive (wt %)	Sintering aid content* (wt %)	Initial α-Si_3N_4 content (wt %)	Milling liquid/ forming method#	Material Cost - ($/lb) as-sintered†
TM-137	SRBSN	<0.05[a]	None	11.5 % La_2O_3 3% Al_2O_3[f,g]	10[c]	Water/slip-cast	6.42
TM-139	SRBSN	<0.05[a]	None	11.5 % La_2O_3 3% Al_2O_3[f,g]	5[d]	Water/slip-cast	5.17
TM-141	SRBSN	<0.05[a]	1.6	11.5 % La_2O_3 3% Al_2O_3[f,g]	10[c]	Water/CIP‡	6.42
TM-142	SRBSN	<0.05[a]	1.6	9 % Y_2O_3 3% AL_2O_3[g,j]	10[c]	IPA**/CIP‡	9.89
TM-145	SRBSN	<0.05[a]	None	11.5 % La_2O_3 3% Al_2O_3[g,j]	10[c]	IPA**/CIP‡	9.30
TM-150	SRBSN	<0.05[a]	1.6	11.5 % La_2O_3 3% Al_2O_3[f,g]	10[c]	IPA**/CIP‡	6.19
TM-152	SRBSN	<0.05[a]	None	11.5 % La_2O_3 3% Al_2O_3[f,g]	10[c]	IPA**/CIP‡	6.19
TM-133	SSN††	N.A.††	None	11.5 % La_2O_3 3% Al_2O_3[h,i]	>98[e]	Water/slip-cast	37.26
TM-132	SSN††	N.A.††	None	9 % Y_2O_3 3% AL_2O_3[i,j]	>98[e]	Water/slip-case	41.76

*All compositions contain the same molar content of sintering additives.
#Material cost based on purchase price in 10-kg lots. Cost will decrease at larger quantities.
†Assumes a yield from nitridation of silicon of 58% for water milled and 62% for IPA milled materials.
‡Cold isostatic pressing.
**Isoprophyl alcohol.
[a]Elkem Metals, Co., Buffalo, N.Y.; Grade Si-HQ; 4.2-μm mean particle size.
[b]Elkem Metals, Co., Buffalo, N.Y.; Grade Metallurgical Si; 3.4-μm mean particle size.
[c]Starck, Berlin, Germany; Grade LC-10N Si_3N_4.
[d]Starck, Berlin, Germany, Grade Sl Si_3N_4.
[e]Ube Industries, Japan; Grade E-10 Si_3N_4.
[f]La_2O_3-Molycorp, White Plains, N.Y.; Grade 5205, >99.9%.
[g]Al_2O_3-Reynolds, Malakoff, Tex.; Grade RC-HP DBM.
[h]La_2O_3-Molycorp, White Plains, N.Y.; Grade 5200, >99.99%.
[i]Al_2O_3-Ceralox, Tucson, Ariz.; Grade P (0.5 μm).
[g]Y_2O_3 Molycorp, White Plains, N.Y.; Grade 5600, >99.99%.

Densification behavior of the SRBSN and SSN materials is summarized in Table 3. As shown, high densities were obtained with samples fired at temperatures of 1800°C for 1 to 4 h. Microwave sintering of the SRBSN was more effective than conventional sintering for similar conditions as indicated by the results from samples TM-137 and -139. This behavior has been observed in previous comparisons of microwave and conventional sintering of Si_3N_4 powder compacts and SRBSN.[1,4,5] As a result, comparative sintering runs were not made for all of the sample types, and the microwave sintering was emphasized. The specimens fabricated with the high-purity powders (TM-133 and -132) sintered to densities >98% at temperatures of 1700°C with microwave heating.

Table 3. Summary of results of the densifcation and strength of the sintered reaction-bonded silicon nitride (SRBSN) materials

Sample	Heating type	Sintering conditions (°C/h)	Sintered density (g/cm^3, % T.D.)	Flexural strength at 25°C (MPa)
TM-137 (SRBSN)	Conventional	1800/1	3.09, 91.3	N. D.
TM-137 (SRBSN	Microwave	1800/1	3.37, 99.9	480 ± 86
TM-139 (SRBSN)	Conventional	1800/4	3.20, 95.4	N. D.
TM-139 (SRBSN)	Microwave	1800/2	3.23, 96.4	415 ± 54
TM-141 (SRBSN)	Microwave	1800/1	3.35, 99.4	310 ± 54
TM-142 (SRBSN)	Microwave	1800/2	3.25, 97.7	677 ± 45
TM-145 (SRBSN)	Microwave	1800/1	3.12, 93.7	N. D.
TM-145 (SRBSN)	Microwave	1800/2	3.23, 97.0	785 ± 98
TM-150 (SRBSN)	Microwave	1800/1	3.16, 93.6	N. D.
TM-152 (SRBSN)	Microwave	1800/2	3.34, 99.1	526 ± 17
TM-133 (SSN)	Microwave	1700/1	3.32, 98.3	654 ± 16
TM-132 (SSN)	Microwave	1700/1	3.27, 98.5	N. D.

Densification was also dependent on the powder processing conditions and the initial α-Si_3N_4 content. The materials milled in water generally sintered to high densities easily as exhibited by TM-137 and -141. It is a well known fact that significant oxidation of the Si occurs during milling in water, and it is this additional SiO_2 in these samples that improved densification. When the same composition was processed in IPA (TM-150), the SiO_2 content was diminished and densification was lower. To compensate for the low SiO_2 content, a small amount was added to the same composition (TM-152), and high densities were again easily obtained. Consequently, for the other compositions processed in IPA (TM-142 and -145), additional SiO_2 was added at a level to simulate the SiO_2 content in a typical Si_3N_4 powder. The effect of the initial α-Si_3N_4 content is shown in a comparison of TM-137 and -139, where a lower α-Si_3N_4 level resulted in lower densities. The cause for this behavior is presently being examined in more detail to

further understand the processes involved. From an economic standpoint, it would be desirable to lower the α-Si_3N_4 content since it represents a significant portion of the total cost of these materials.

Mechanical testing was performed on selected materials that achieved high density as shown in Table 2, and observed strength variations were attributed to several factors. Processing in water was detrimental to the strength of the SRBSN materials. This is illustrated by the cold isostatically pressed (CIPed) samples, where the strength was significantly improved by using IPA during the milling step (TM-141 vs -152). Other research has shown agglomeration of the Si during water processing, and this is evidently affecting the strength in the water-milled materials.[2] By far the most important factor affecting the strength was the rare earth additive. By substituting Y_2O_3 for La_2O_3 (TM-142 vs -152), the strength increased from ~525 to ~675 MPa even though the density was lower.

The highest mean ambient temperature strength was 785 MPa. This strength is higher than for similar SRBSN materials processed at temperatures ≤1800°C by conventional heating.[6] The highest strength materials contained Y_2O_3-Al_2O_3 and used the lower purity silicon. It is known that the lower purity results in a higher α-Si_3N_4 content in the samples after nitridation but before the sintering step. Generally, the samples with the low-purity silicon had ~70% α-phase content after nitridation as compared to <50% for the nitridation product from the high-purity silicon. It is believed this higher α-content results in more acicular grain growth during the α-to-ß transformation and improved properties. However, the lower purity powders are expected to have lower-high temperature properties due to the less refractory nature of the intergranular phases. Flexural testing at elevated temperatures showed appreciable strength decrease at temperatures above 1000°C (see Fig. 1). The sample containing Y_2O_3-Al_2O_3 and using the high-purity Si (TM-142) showed good strength retention up to 1000°C.

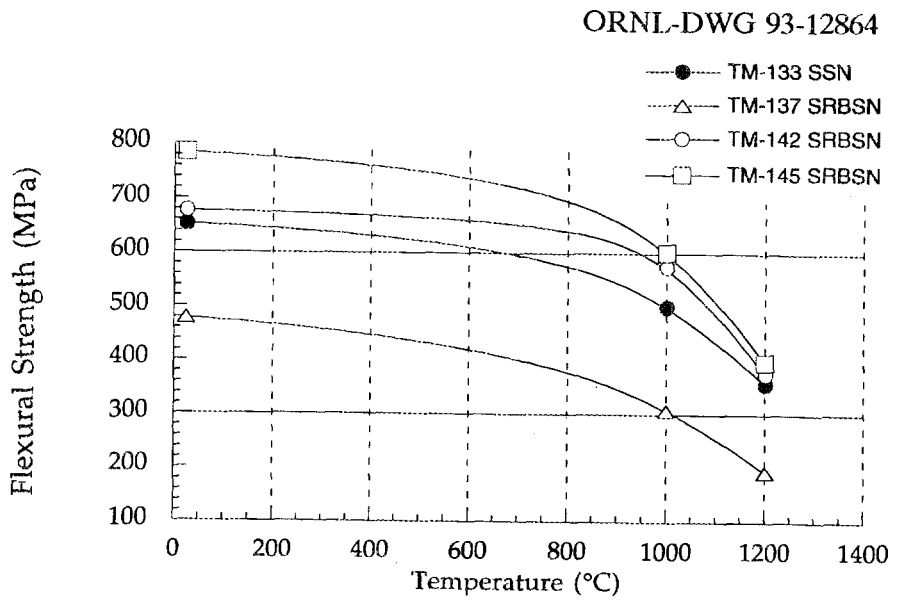

Fig. 1. Flexural strength of sintered reaction-bonded silicon nitride and sintered silicon nitride material as a function of temperature. Samples TM-133 and -137 were nominally Si_3N_4-11.5% La_2O_3-3% Al_2O_3. Samples TM-142 and -145 were nominally Si_3N_4-9% Y_2O_3-3% Al_2O_3. TM-137, -142, and -145 were reaction-bonded and sintered at 1800°C for 1 to 2 h. TM-133 were fabricated from high-purity materials and sintered at 1700°C for 1 h. All samples were heated in the microwave.

Along with fabricating test samples, parts were fabricated for demonstration of reaction-bonding and sintering of complex shapes in the microwave. Several parts were produced having both thick and thin cross sections. Comparisons of the microstructures and the properties of the materials from the various locations can then be made.

In addition to complex shape fabrication, it is also planned to demonstrate the microwave reaction-bonding and sintering of a large number of parts. At the current time, two samples are heated at the same time, and parts as large as 1 kg in mass have been successfully nitrided. Scaling the process up to significantly higher values will require significant effort in fabricating green parts. The possibility of purchasing unnitrided parts from an outside vendor is being explored.

The starting materials for the SRBSN consisted of appropriate amounts of silicon, α-Si_3N_4, Al_2O_3, and Y_2O_3, to give a final composition for the TM-145 samples after nitriding and sintering of Si_3N_4 - 9 wt % Y_2O_3- 3 wt % Al_2O_3. The powders were first turbomilled in IPA, then the slurry was dried and sieved through a 40-mesh screen. Pellets of approximately 100 g were formed by uniaxial pressing in a 76-mm-diam die, followed by isostatic pressing at 5 kg/cm^2 to give green densities of 1.59 to 1.62 g/cm^3. The SRBSN discs, which were approximately 70 mm diam by 15 mm thick, were pre-sintered in argon at 1200°C for 1 h and then bisque-machined to produce either complex parts or thin rectangular pieces (4.5 mm thick × 16.5 mm wide × 45 to 74 mm long), used in experiments in which multiple SRBSN samples were processed by microwave or conventional heating.

Figure 1 shows the typical sample arrangement and insulation scheme that was used for two multi-sample experiments. In setup 1 [see Fig 2(*a*)] bisque-fired samples, stacked on boron nitride (BN) plates, were surrounded by dense Si_3N_4 milling media. Eight bisque-fired samples were equally spaced in a vertical orientation against the inner surface of the BN crucible. This is called the picket-fence (PF) arrangement, similar to the arrangement described by Kimrey et al.[7] In setup 2 [see Fig. 2(*b*)], the close-pack-mixed (CPM) arrangement, the pickets were not used. Instead, dense (~ 99% TD) previously processed SRBSN samples with the same composition were placed along the outer edges of each BN plate surrounding an inner group of four bisque-fired TM-145 samples. Microwave processing of complex SRBSN pieces was done without the aid of any picket or CPM. In these experiments, two to three bisque-fired machined pieces were stacked on alternating layers of BN plates and surrounded by dense Si_3N_4 milling media. In both the multisample configurations and the complex piece configuration, samples were enclosed in a BN crucible, which was packed in Si_3N_4 powder. As indicated in the figure, a molybdenum-sheathed thermocouple with a BN sleeve was inserted between the sample layers to measure the temperature.

Nitridation was performed in a static atmosphere containing N_2-4% H_2-5% He at ~0.1 MPa (16 psia) with additional N_2 added as the reaction proceeded. After nitridation, the temperature was increased to the sintering temperature and maintained for the appropriate time. An entire heating cycle to 1800°C required approximately 25 h. The conventional processing for the SRBSN samples was carried out in a graphite-resistance heated furnace in a two-step process. In step one, the pre-sintered test pieces were stacked on BN plates inside a graphite crucible and heated to 1450°C in flowing nitrogen in 34 h. The samples were then cooled and covered with Si_3N_4 packing powder and heated in flowing nitrogen at 5°C/min to 1800°C. Note that, in this conventional process, two steps were required, because earlier studies showed that parts completely packed in powder in step 1 experienced partial melting during the exothermic nitridation reaction stage.[8]

Samples were measured and weighed before and after experiments. Locations of samples within insulation setups were recorded for later analysis of heating uniformity between different areas of the packages. Densities of all test samples were determined by

ORNL-DWG 93-12865

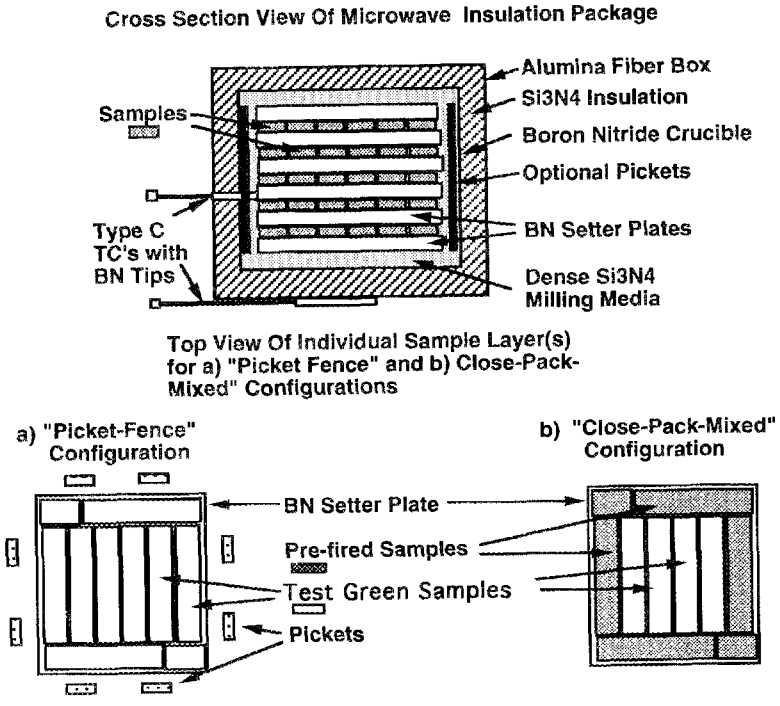

Fig. 2. Typical sample arrangement and insulation scheme used in multi-sample SRBSN sintering: (*a*) picket-fence arrangement (PF) and (*b*) close-packed-mixed (CPM) arrangement.

the Archimedes method. Samples from various experiments were machined into bend bar specimens with nominal dimensions of $3 \times 4 \times 50$ mm. Flexural strength testing was done in four-point bending with inner and outer spans of 20 and 40 mm, respectively. Diamond machining was used to remove 1.25 mm of the surface layer of the six rectangular projections on complex SRBSN parts that were processed by either conventional or microwave heating. Fracture toughness and hardness of these parts were determined by indentation using a 10-kg load. Two indentations were made on each specimen and the results averaged.

The first attempt at processing of multiple SRBSN samples by microwave heating involved the PF arrangement. Inspection of samples from the different areas of this heating arrangement indicated unequal heating. The "picket" samples of the insulation arrangement showed extreme warping and slumping. Samples around the edges of each BN plate (edge samples) exhibited slight amounts of unequal sintering with one of the dimensions more fully sintered than the other. Samples completely surrounded by other samples (interior samples) were uniformly sintered. A com-parison of the densities obtained for these groups of samples is shown in Table 4. The average density of the picket samples was significantly lower than the average for all samples. The average density of the edge samples was higher than the picket group but lower than the interior group of samples, which had the highest densities overall. It appears that there was a temperature gradient from the center (high) to the outer edge of the crucible (low). Thus

Table 4. Densities of sintered reaction-based silicon nitride samples processed by microwave heating using the "picket fence" arrangement

Sample group	Density (g/cm^3)	Density (% T.D.)	Standarrd deviation
Picket samples	3.14	94.0	0.021
Edge samples	3.17	95.0	0.017
Interior samples	3.18	95.2	0.021
Average	3.17	94.9	0.024

the PF arrangement did not adequately supply enough heat to the outer samples in the package for equal processing. The highest density achieved was only 95.2% TD, which was lower than desired.

The second attempt at processing multiple SRBSN samples by microwave heating involved the CPM arrangement. Since dense SRBSN samples were placed completely around the perimeter of the untreated samples and no pickets were used, there was one sample type, interior. However, in this experiment, data for the five sample layers were also compared. All the samples from all five sample layers were uniform in appearance. The average densities for the samples of individual layers were calculated and the standard deviations of the densities within each layer determined (Table 5). In general, the average densities of individual layers increased slightly from the top layer to the bottom layer with higher densities on the bottom. Flexural strengths were then obtained from each sample, and the average strengths for each layer were determined (Table 5). The average flexural strengths followed the trend of the densities and also increased from the top to bottom of the package. Both the densities and strengths of all the samples were comparatively high for this type of SRBSN. However, there appeared to be a temperature gradient from the top of the sample package to the bottom.

To evaluate more fully the results of the CPM microwave heating setup, a conventional processing experiment was performed. As indicated in the experimental procedure, two separate furnace cycles with different sample packing were necessary; therefore, an exact comparison to the microwave results was difficult to make. The sintered SRBSN samples were uniform in appearance; however, both the densities and strengths of all five sample layers were lower than the CPM microwave samples (see Table 5). It was interesting that the densities and strengths were also higher for the bottom layer in this conventional treatment as was the case with the microwave processing. However, the standard deviation for both the densities and the strengths for the five layers, as well as the average of all samples was lower for the conventional processing than the microwave processing. Thus, overall, the CPM microwave arrangement worked quite well and resulted in SRBSN material of high quality. However, work needs to be done to further improve the heating uniformity.

The next question addressed in this study was whether microwave heating could be used to process complex shapes, especially parts with multiple sharp edges (possible low absorption), close gaps between sections of a part (possible arcing), and both thick and thin sections (non-uniform properties). A non-functional part having areas of six

Table 5. Density and flexural strength values for sintered reaction-bonded silicon nitride samples processed in the close-pack-mixed arrangement using microwave heating or conventional heating

	Microwave		Conventional	
Sample group	Density (g/cm^3)	Strength (MPa)	Density (g/cm^3)	Strength (MPa)
Layer 1	3.128 ± 0.001	660 ± 39	3.188 ± 0.005	509 ± 66
Layer 2	3.227 ± 0.006	619 ± 53	3.188 ± 0.001	446 ± 74
Layer 3	3.226 ± 0.005	638 ± 64	3.187 ± 0.002	502 ± 37
Layer 4	3.245 ± 0.004	724 ± 54	3.188 ± 0.004	463 ± 32
Layer 5	3.243 ± 0.006	714 ± 87	3.197 ± 0.006	534 ± 32
Average	3.232 ± 0.012	671 ± 72	3.19 ± 0.005	487 ± 60

*Each layer consisted of four samples. Two flexure bars were machined per sample.

different thicknesses with varying gaps between the raised areas was made from bisque-fired material (see Fig. 3). The surface layer was removed and the sections polished prior to testing for hardness and indent toughness.

The microwave- and conventionally fired complex SRBSN parts reached densities of 97.14 and 96.78% TD, respectively. The conventional piece had a small amount of molten silicon on its surface despite doubling the time at nitridation temperatures. A summary of the hardness and toughness values for each section of the complex piece is given in Table 6. There does not appear to be a correlation between thickness of the sections and the hardness and toughness values obtained for either sample. All sections of the microwave-processed part exhibited significantly higher hardness and toughness values than for the part processed by conventional process, although there was only a small difference in the final densities of the two parts. More importantly, the standard deviations of the hardness and toughness from different sections of the parts were comparable for the microwave- and conventionally processed parts. Thus, it appears that microwave heating can be used to process complex parts having areas of varying thicknesses without significant variations in the properties. Other complex shapes have been produced to further verify these observations (see Fig. 4).

In conjunction with the effort on upscaling the process, a study was conducted to map the heating uniformity of the present microwave cavity, since this will influence our ability to heat large numbers of parts in a controlled fashion. The initial data revealed some non-uniform heating across the area occupied by the samples. Consequently, some modifications are being made to the furnace. These include adding another microwave port into the cavity, incorporating a deflector plate into the system to direct more of the incoming energy at the mode stirrer, and modifying the table in the cavity to allow microwaves to pass through it. Changes to heating uniformity will be reported later.

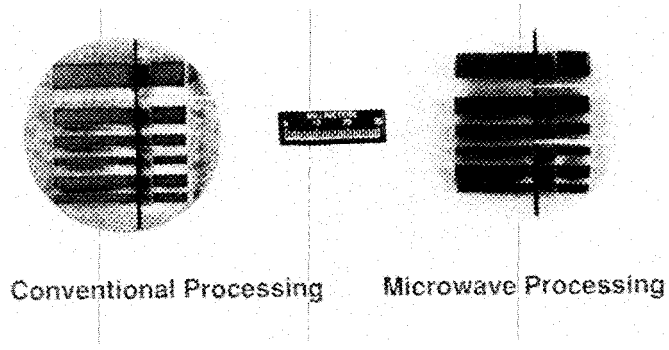

Fig. 3. Complex sintered reaction-bonded silicon nitride parts processed by microwave and conventional heating.

Table 6. Summary of results on hardness and fracture toughness for sintered reaction-bonded silicon nitride material processed by microwave and conventional heating

		Microwave processing		Conventional processing	
Sample section	Section thickness (cm)	Vickers hardness (GPa)	Indent toughness (MPa$\sqrt{m}$)	Vickers hardness (GPa)	Indent toughness (MPa$\sqrt{m}$)
A	0.825	13.90	6.56	12.30	5.59
B	0.585	14.40	6.39	12.30	5.17
C	0.410	14.10	6.23	12.80	5.80
D	0.355	13.80	6.19	12.80	5.55
E	0.315	14.60	6.29	12.60	5.48
F	0.280	14.10	6.30	12.80	5.43
Average		14.13	6.32	12.58	5.50
Std. Dev.		0.38	0.21	0.31	0.23

Final processing conditions 1800°C for 1.5 h.

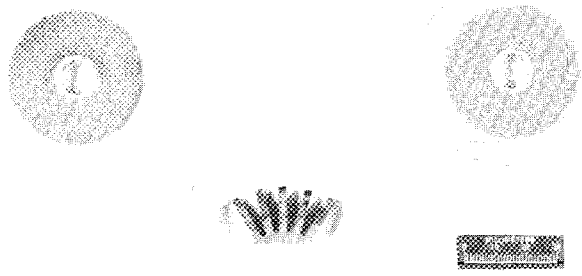

Fig. 4. Variety of complex shapes of sintered reaction-bonded silicon nitride produced with microwave heating.

Cooperative Research and Development Agreements (CRADAs) - Three CRADAs are being performed in the area of microwave processing of silicon nitride. The first CRADA is with Garrett Ceramic Components/Allied-Signal and involves annealing of specimens of silicon nitride with high additive contents (>5%). Compositions include AS-44, GN-10, and AS-700. A second CRADA with Norton also involves annealing of silicon nitride in the microwave but with additive contents less than 5%. Most of the work was involved with NT-154 with a range of α-phase contents. Norton was also involved in the third CRADA where reaction-bonded silicon nitride was fabricated in the microwave. The results were directly compared to materials fabricated by conventional heating.

Annealing of Norton Silicon Nitride - Analyses of the annealing studies with Norton have been completed. The materials used were encapsulated hot-isostatically-pressed silicon nitride containing 4 wt % Y_2O_3 as the sintering additive. The formulation is commercially known as NT-154 and was fabricated by St. Gobain/Norton Industrial Ceramics. The as-fabricated materials contained either about 25 or 12% residual α-Si_3N_4 phase and were >99% dense. The samples were in the form of tiles approximately 10 × 55 × 100 mm.

After annealing, the specimens were machined into bars nominally 3 × 4 × 50 mm. Flexural strength testing was performed at ambient temperature and 1370°C in four-point bending with inner and outer spans of 20 and 40 mm, respectively. Dynamic fatigue testing was done in flexure with the same dimensional parameters as for the strength measurements. However, stressing rates varied from 0.001 to 37 MPa/s, and the samples were tested until failure occurred. This type of testing is an indicator of resistance to slow crack growth.

Heating of the specimens in the microwave cavity revealed poor coupling of the Si_3N_4-4% Y_2O_3 at temperatures below ~1200°C. At ~1550°C, a decrease in power requirements is indicative of a dielectric relaxation of the materials. This temperature corresponds to the eutectic temperature of the intergranular glass phase and the formation of liquid. Similar observations have been made previously for other silicon nitride materials.[8-11] A second thermocouple placed in the insulation powder indicates the

surrounding powder bed did not heat significantly, and most of the power was used in heating the samples.

Crystallization of Si_3N_4-Y_2O_3 materials results in the formation of a $Y_2Si_2O_7$ grain boundary phase that has several polymorphs stable at different temperatures as shown below.[12] Volume changes accompany these phase changes.

$$\alpha \xrightarrow{1225^\circ C} \beta \xrightarrow{1445^\circ C} \gamma \xrightarrow{1535^\circ C} \delta$$

A few consistent trends were observed for grain boundary phase crystallization during microwave annealing. As shown in Table 7, no β- or δ-$Y_2Si_2O_7$ were observed in any of the samples. At temperatures >1650°C, α-$Y_2Si_2O_7$ was predominantly present indicating that crystallization occurred during cooldown. These samples also had generally low α-Si_3N_4 contents indicating α-to-ß Si_3N_4 transformation took place during annealing. For temperatures between 1400 and 1560°C, the γ-$Y_2Si_2O_7$ was predominantly present, and generally high α-Si_3N_4 contents were observed. Crystallization, in these cases, probably took place during microwave annealing with no further α-to-ß Si_3N_4 transformation taking place.

As indicated in Table 7, continued α-to-ß Si_3N_4 transformation was observed as low as 1650°C, especially when it was coupled with long anneal times (10 h). At higher temperatures, α/ß transformations occurred in much shorter times. Only minor grain coarsening was observed for the high-temperature anneals (>1700°C), but no enhanced elongation of the ß-Si_3N_4 grains was found.

The high-temperature fast fracture strength did not show an obvious dependence on anneal conditions (see Fig. 5). However, the high-temperature strength did appear to be dependent on the residual α-Si_3N_4 content in the specimens (see Fig. 6). The residual α-Si_3N_4 may be indicative of a finer average grain size for these specimens and not an inherent higher strength for the alpha-phase materials.

The effect of microwave annealing on fracture toughness is shown in Fig. 7. Compared to conventional annealing at 1400°C, with a baseline K_{Ic}=5.1 MPa$\sqrt{m}$, increases in fracture toughness were observed for microwave annealing between temp temperatures of 1200 and 1650°C. The decrease in fracture toughness for the highest temperature anneal is believed due to the minor amount of grain coarsening that took place in this sample.

The dynamic fatigue testing at 1370°C showed increased failure stress (and hence longer times to failure) at the lowest stressing rates (0.001 MPa/s) as indicated in Fig. 8. The conventional annealed materials have a dynamic fatigue failure stress of ~340 MPa. The present results indicate that improvements in the failure stress can be obtained by annealing between 1400 to 1550°C for >5 h. These temperatures are just below the eutectic temperature for the intergranular glass phase where optimum crystallization should take place.

While there were some observed property improvements, they were not so dramatic to justify abandoning conventional over microwave heating. The Si_3N_4-4% Y_2O_3 materials used in the study were developed for elevated temperature use and already possess excellent high-temperature strength, fatigue resistance, and creep properties. This is due to the very refractory nature of the grain boundary phases and the small quantity of secondary phase present. However, microwave annealing of these materials may be necessary in applications where the maximum in fracture toughness and fatigue resistance is required and thus justifies its use.

Norton SRBSN - Additional samples of Norton reaction-bonded silicon nitride have been processed. This involved four combined reaction-bonding and sintering runs and one reaction-bonding only. The samples were sent to Norton for evaluation.

Table 7. Summary of results of phase analyses of microwave-annealed silicon nitride

Sample	Anneal temperature (°C)	Anneal time (h)	Residual α-Si3N4 content (%)	Y_2Si_2O7 phase
MW-1[a]	1738	0.5	0	alpha
MW-2[a]	1507	6.7	25	gamma
MW-3[a]	1650	5.3	21	alpha
MW-4[a]	1738	1.4	7	alpha
MW-5[a]	1650	10	0	alpha
MW-6[a]	1773	6.7	0	gamma
MW-7[a]	1562	1.4	21	gamma
MW-8[a]	1400	5	3	gamma
MW-9[a]	1738/1507	0.5/5	3	alpha
MW-10[a]	1650	5.3	23	---
MW-11a[a]	1500	5.3	19	gamma
MW-11b[b]	1500	5.3	6	gamma
MW-12[b]	1400	5	12	gamma
MW-13[b]	1200	5	12	gamma

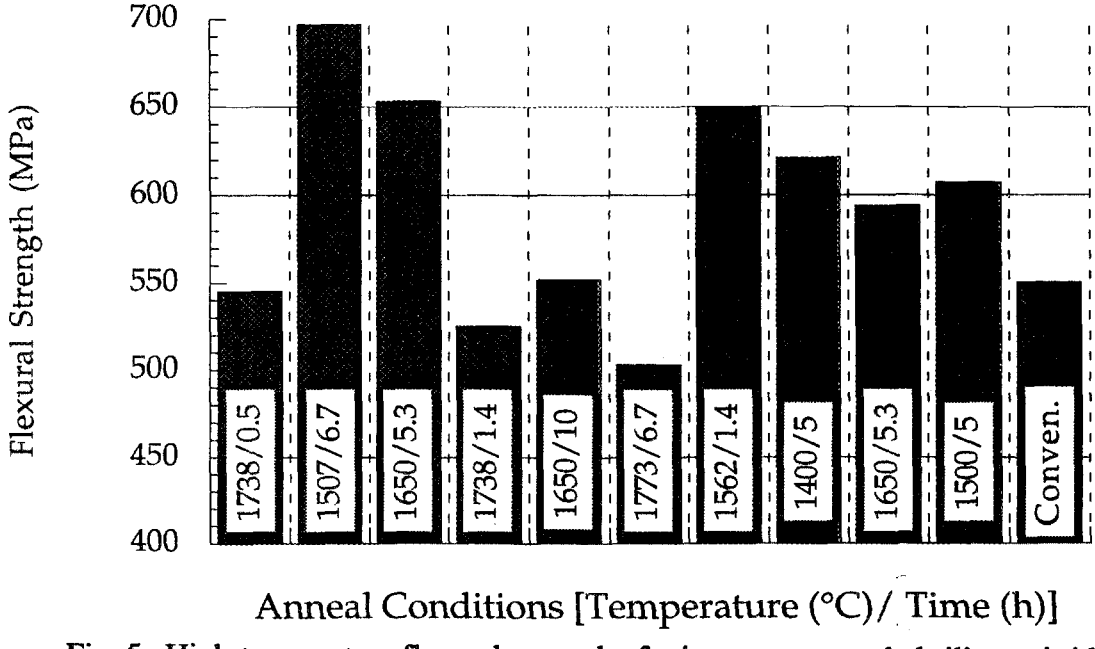

Fig. 5. High-temperature flexural strength of microwave-annealed silicon nitride.

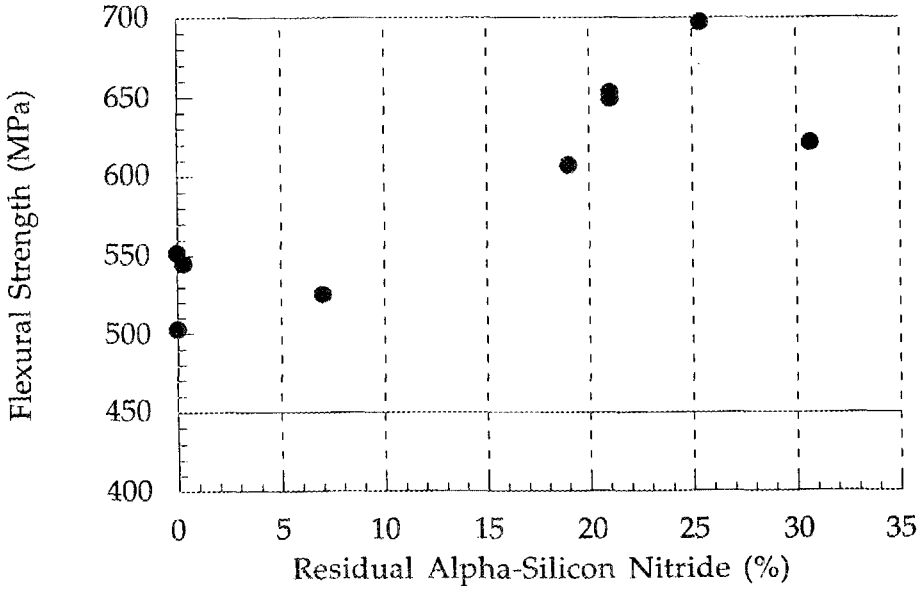

Fig. 6. High-temperature flexural strength of microwave-annealed silicon nitride as a function of residual alpha-silicon nitride content.

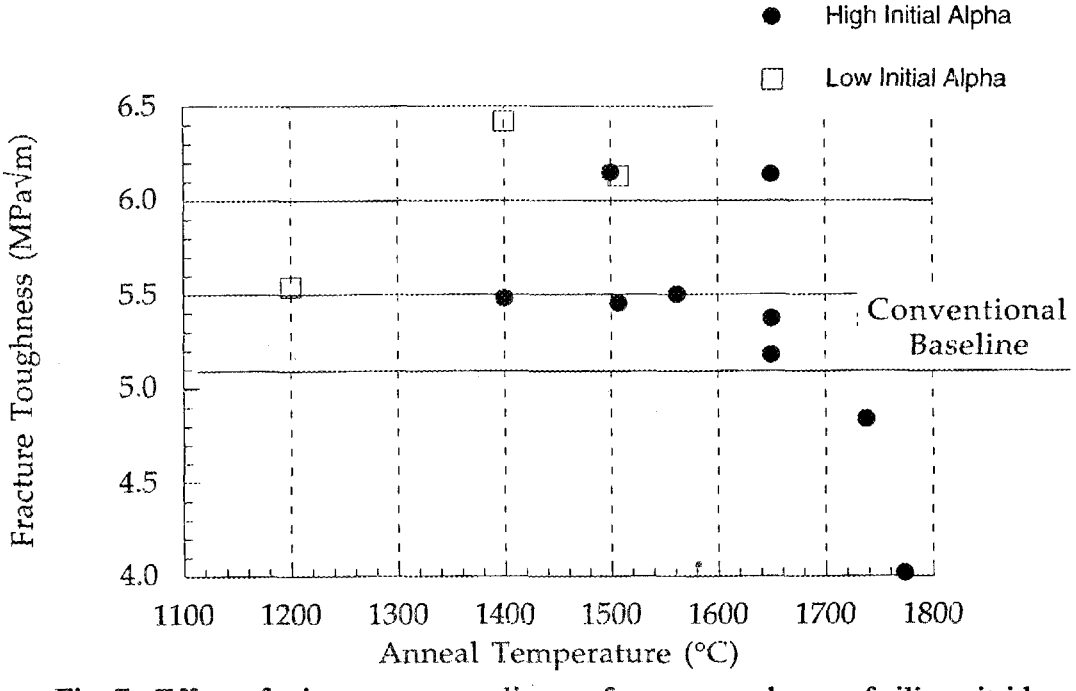

Fig. 7. Effect of microwave annealing on fracture toughness of silico nitride.

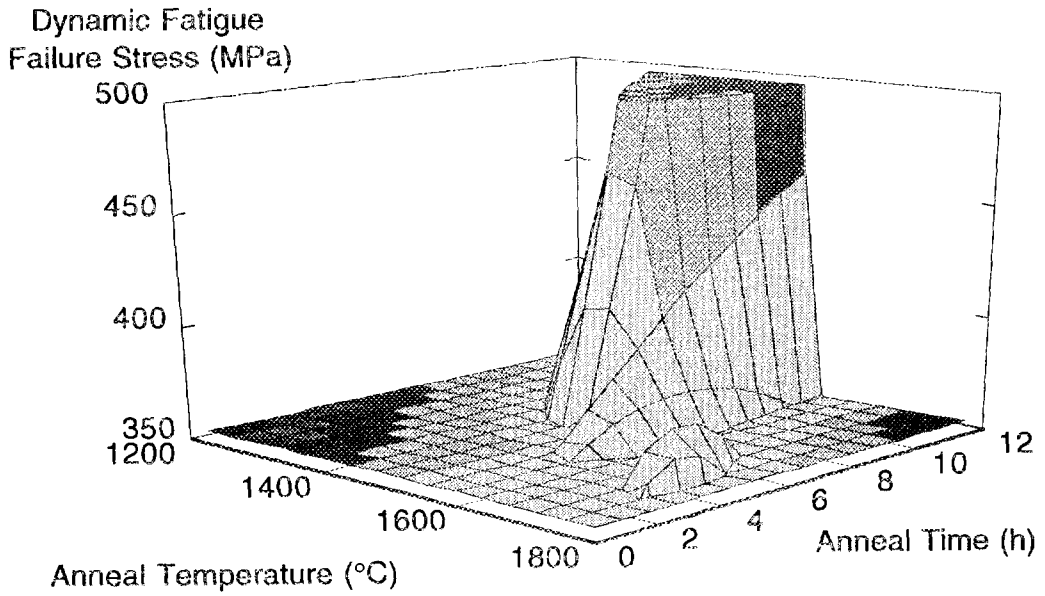

Fig. 8. Dynamic fatigue failure stress at 1370°C as function of anneal time and temperature. Stressing rate was 0.01 MPa/s. Baseline conventional materials have failure stress of ~370 MPa.

References

1. T. N. Tiegs, J. O. Kiggans, and K. L. Ploetz, "Cost-Effective Sintered Reaction-Bonded Silicon Nitride for Structural Ceramics" to be published in Ceram. Eng. Sci. Pro., American Ceramic Society.

2. R. G. Stephen and F. L. Riley, "The Influence of Pre-Oxidation on the Processing of Silicon Powder," pp. 307-14 in *Proceedings of 4th International Symposium on Ceramic Material Components for Engines*, ed. R. Carlsson, T. Johansson, and L. Kahlman, Elsevier Applied Science, New York 1992.

3. B. Q. Lei, D. Ashkin, T. Johansson, and T. Lindbäck, "Optimization of the Silicon Nitridation Process," pp. 633-40 in *Proceedings of the 4th International Symposium on Ceramic Material Components for Engines*, ed. by R. Carlsson, T. Johansson, and L. Kahlman, Elsevier Applied Science, New York 1992.

4. T. N. Tiegs, and J. O. Kiggans, "Fabrication of Silicon Nitride Ceramics by Microwave Heating," pp. 665-71 in *Proc. 4th International Symp. Ceram. Mater. & Compon for Engines*, ed. by R. Carlsson, T. Johansson, and L. Kahlman, Elsevier Applied Science, New York, 1992.

5. T. N. Tiegs, J. O. Kiggans, and H. D. Kimrey, "Microwave Sintering of Silicon Nitride," *Ceram. Eng. Sci. Proc.* 12[9-10], 1981-92 (1991).

6. J. A. Mangels, "Sintered Reaction-Bonded Silicon Nitride," *Ceram. Eng. Sci. Proc.* 2[7-8], 589-603 (1981).

7. H. D. Kimrey, J. O. Kiggans, M. A. Janney, and R. L. Beatty, "Microwave Sintering of Zirconia-Toughened Alumina Composites," pp. 243-55 in *Microwave Processing of Materials II*, Vol. 189, ed. W. B. Snyder, W. H. Sutton, D. L. Johnson, and M. F. Iskander, Materials Research Society, Pittsburgh, 1991.

8. J. O. Kiggans and T. N. Tiegs, "Characterization of Sintered Reaction Bonded Silicon Nitride Processed By Microwave Heating," pp. 285-90 in *Microwave Processing of Materials III*, ed. R. L. Beatty, W. H. Sutton, and M. F. Iskander, Material Research Society, Pittsburgh, 1992.

9. D. R. Clarke and W. W. Ho, "Effect of Intergranular Phases on the High-Frequency Dielectric Losses of Silicon Nitride Ceramics." pp. 246-52 in *Additives and Interfaces in Electronic Ceramics, Advances in Ceramics* , Vol. 7, American Ceramic Society, Westerville, Ohio, 1983.

10. H. Ohno and Y. Katano, "Electrical Properties of Silicon Nitride," Mater. Sci. Forum, 47, 215-27 (1989).

11. T. N. Tiegs, J. O. Kiggans, and H. D. Kimrey, "Microwave Sintering of Silicon Nitride," *Ceram. Eng. Proc.*, **12** [9-10], 1981-92 (1991).

12. R. L. Yeckley and K. N. Siebein, "High Temperature Cavitation of HIP Silicon Nitride," pp. 751-65 in *Proceedings of the 3rd International Symposium on Ceramic Materials and Components for Engines*, American Ceramic Society, Westerville, Ohio, 1989.

Status of Milestones

Milestone 112405 has been completed. The results are shown in this report.

Communications/Visits/Travel

Travel by T. N. Tiegs from November 1-4, 1992, to San Francisco, Calif. to attend the 45th Pacific Coast Regional Meeting of the American Ceramic Society and present a paper entitled "Silicon Nitride from MARS."

Travel by T. N. Tiegs from November 30 - December 3, 1992, to Boston, Mass. to attend the Fall Meeting of the Materials Research Society and present a paper entitled "Sintered Reaction-Bonded Silicon Nitride by Microwave Heating."

Travel by T. N. Tiegs from January 11-15, 1993, to Cocoa Beach, Fla., to attend the 17th Annual Conference on Composites and Advanced Ceramics of the American Ceramic Society and present a paper entitled "Microwave Processing of Silicon Nitride Ceramics."

Problems Encountered

The microwave furnace was not in operation for approximately 5 weeks due to computer malfunctions in the control system.

Publications

T. N. Tiegs, J. O. Kiggans, and K. L. Ploetz, , "Sintered Reaction-Bonded Silicon Nitride by Microwave Heating" to be published in *Mater. Res. Soc. Proc.*

T. N. Tiegs, J. O. Kiggans, and K. L. Ploetz, "Application of Microwave Heating for Fabrication of Silicon Nitride Ceramics" to be published in *Ceram. and Eng. Sci. Proc.*

T. N. Tiegs and J. O. Kiggans, "Microwave Processing of Silicon Nitride for Advanced Gas Turbine Applications" to be published in the Proceedings of the ASME Gas Turbine Conference to be held in Cincinnati, Ohio on May 24-27, 1993.

J. O. Kiggans, T. N. Tiegs, H. D. Kimrey, and C. E. Holcombe, "Processing of Complex Sintered Reaction Bonded Silicon Nitride Parts by Microwave Heating," to be published in *Ceramic Transactions, Microwaves: Theory and Application in Materials Processing II, American Ceramic Society*, Westerville, Ohio.

T. N. Tiegs, K. L. Ploetz, J. O. Kiggans, and R. L. Yeckley, "Crystallization of Grain Boundary Phases in Silicon Nitride with Low Additive Contents by Microwave Annealing" to be published in *Ceramic Transactions, Microwaves: Theory and Application in Materials Processing II, American Ceramic Society*, Westerville, Ohio.

Development of Microwave Processing of Silicon Nitride Components for Advanced Heat Engine Applications Reaction Bonded and Sintered Reaction Bonded Silicon Nitride
C. A. Willkens (Norton)

Objective/Scope

Microwave processing offers potential advantages, such as decreased nitriding and sintering times, nitriding of larger cross-sections and unique microstructures, as compared to traditional sintering techniques. This CRADA project will apply Microwave processing technology developed at ORNL to unfired reaction bonded silicon nitride (RBSN) and sintered reaction bonded silicon nitride (SRBSN) materials processed at NRDC. Powder compacts produced at NRDC will be brought to ORNL for microwave nitriding and sintering studies. The properties of microwave nitrided and/or sintered silicon nitride will be directly compared against same lot materials traditionally "fired" at NRDC.

Technical Progress

RBSN

Significant differences in as-nitrided microstructure between microwave and traditionally nitrided samples have been observed. In order to better understand these differences, cast and CIP'd test bars and tiles of a two different size distributions have been fabricated, presintered for strength and sent to ORNL for microwave nitriding. A same lot set was nitrided traditionally and sent to ORNL for comparison testing with the Microwave nitrided samples. Properties are being determined on the as-nitrided surfaces of the test bars.

SRBSN

SRBSN precursor tiles of two different compositions (9032, 9033) were traditionally sintered and sent to ORNL for comparison testing with companion precursor tiles that were nitrided and sintered in a single cycle at ORNL. Companion silicon nitride powder tiles (7054, 7059) were also sintered and sent for comparison testing with microwave sintered tiles of the same powder lot. Modifications to the traditional sintering cycle to achieve higher density, strength and toughness were implemented and transferred to the microwave cycle.

Status of Milestones

On schedule.

Publications

None

Cost Effective Sintering of Silicon Nitride Ceramics (SIU-C)

D. E. Wittmer (Associate Professor, Southern Illinois University at Carbondale, Carbondale, IL 62901

Objective/Scope

The purpose of this work is to investigate the potential of cost effective sintering of Si_3N_4 through the development of continuous sintering techniques and the use of lower cost Si_3N_4 powders and sintering aids.

Technical Highlights

The project research goals for Phase I are divided into 3 major tasks:

Task 1. Refine Economic Model and Design for Chosen Furnace Configuration.

In the most recent work, economic comparisons were made for batch and continuous sintering of small and large cam-roller followers as functions of furnace size, capacity, production volume, yield, and type of hot zone (tungsten or graphite). The results are currently scheduled for publication in the June 1993 issue of the Ceramic Bulletin. Figures 1 and 2 are typical of the results obtained in this modelling. The belt furnaces are labelled 840 and 880 while the batch furnaces are labelled 242436 and 242448. In all cases, it was predicted that sintering of small or large cam-roller followers in belt furnaces is more cost effective than in batch furnaces, and sintering in furnaces with graphite heating elements and shielding is more economical than in furnaces with tungsten heating elements and molybdenum shielding.

Task 2. Continue Evaluation of Sintering Parameters on Properties of Selected Si_3N_4 Compositions.

Work has continued on determining the physical property data for the compositions previously sintered in the belt furnace, in addition to more recent compositions containing reduced amounts of sintering aids. All of the compositions successfully sintered in the belt furnace have had four-point flexural strength and fracture toughness measured (given in Table I). An image analyzer with digital imaging was used to measure the crack lengths for indented test bars. Because of the improved resolution and contrast of the crack geometry, more precise crack length measurements are possible, resulting in more accurate fracture toughness determination. A system similar

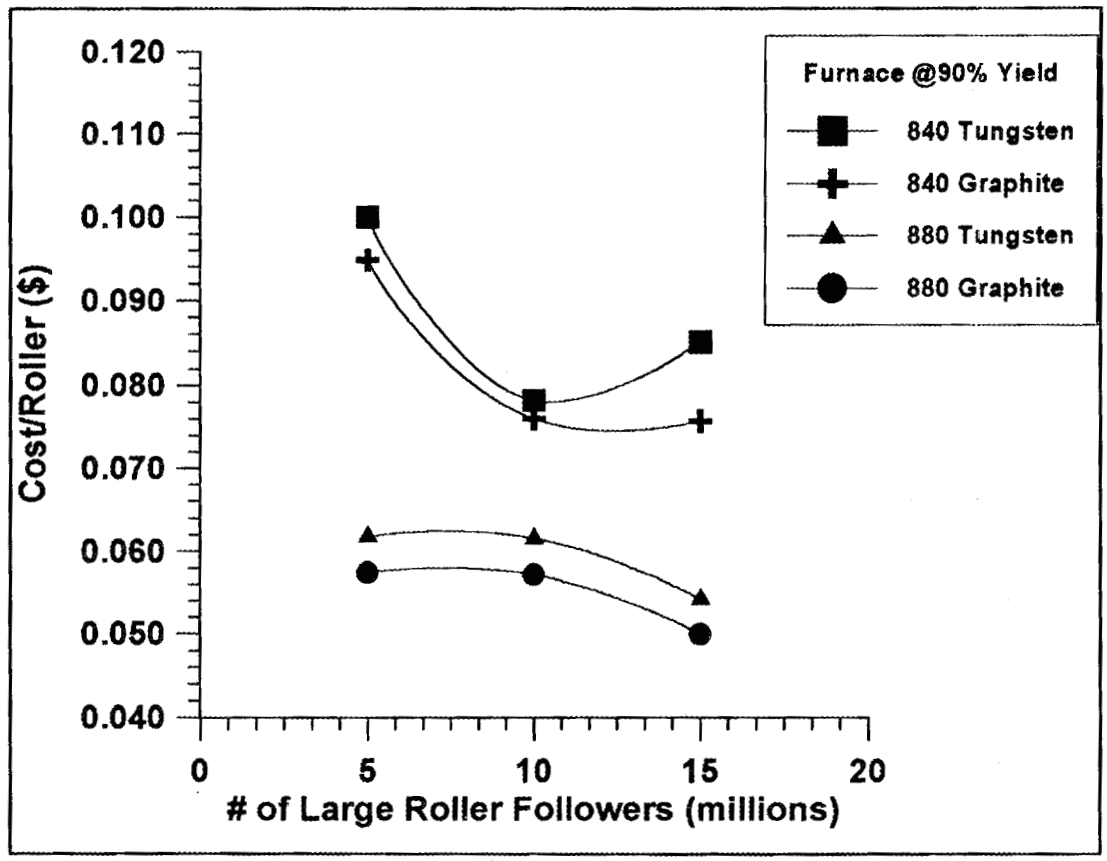

Figure 1. Projected cost for sintering large cam-roller followers in graphite and tungsten belt furnaces as a function of production volume.

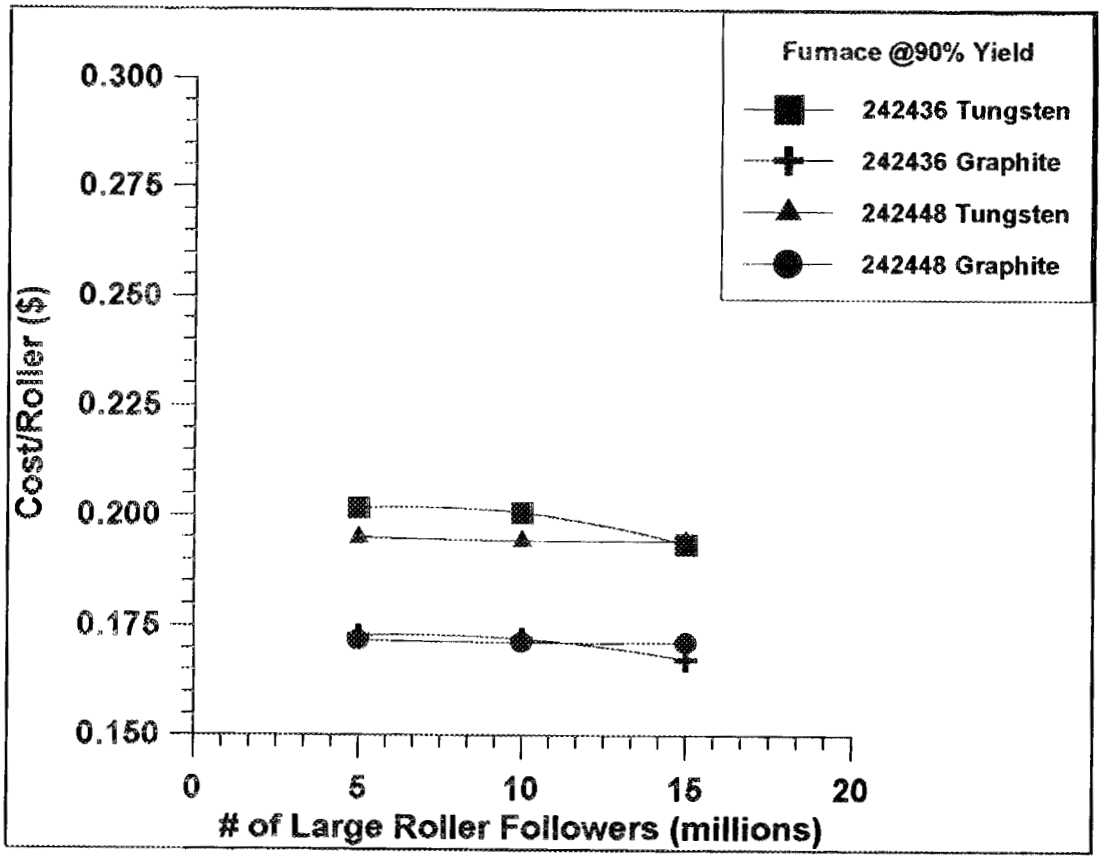

Figure 2. Projected cost for sintering large cam-roller followers in graphite and tungsten batch fumaces as a function of production volume.

to the one used will be procured for use in all future measurements.

During this reporting period additional Si_3N_4 formulations, using UBE E-10 Si_3N_4 powder were processed by turbomilling and pressure casting techniques described previously. The formulations were A2Y6, A2Y8 with 5 wt.% β-Si_3N_4 seed, and A4Y6 with 5 wt.% β-Si_3N_4 seed. Due to the previously successful belt sintering of the A2Y8 compositions, the A2Y6 formulation was added to the composition matrix, in order to determine the feasibility of continuously sintering a Si_3N_4 formulation with only 8% sintering additives. The A2Y8 and A4Y6 formulations with 5 wt.% β-Si_3N_4 seed added were included to complete the data set for seeded vs. unseeded compositions. The data generated will be used in comparing compositions sintered in the overpressure furnace with those pressureless sintering in the Centorr Model 6-BF belt furnace.

Also, during this reporting period, work was initiated to determine the effect of using graphite and/or SiC setters with BN coatings as suitable materials for the sintering some selected Si_3N_4 compositions in the belt furnace. The SiC setter plates cracked down the middle during a break-in run, while parts sintered in the graphite boat with BN setter plate warped and discolored. The surface discoloration is thought due to a reaction with the C vapor present in the boat, while the warpage may be due to this reaction or differences in emissivity between graphite and the previous Mo boats. Additional sintering runs are planned in graphite boats at lower temperatures to try to minimize reactions.

Task 3. Continue Evaluation of Low Cost Si_3N_4 Powders.

This task was initiated through the use of 3 commercially available Si_3N_4 powders as part of Task 2. These 3 Si_3N_4 powders have a range of purity and cost, with the LC-10 being the lower cost and purity and Ube E-10 being the higher in cost and purity. Another source of low purity and cost Si_3N_4 (ASN-34) from Performance Ceramics, Peninsula, OH was evaluated. The results for these various powders are shown in Table I. Some of the highest room temperature flexural strengths were obtained from these lower cost powders. During the next phase of this subcontract, evaluation will continue and will include powders when they become available from Dow Chemical Company.

Table I. Sintering Conditions and Physical Property Results for Compositions Sintered in the Centorr Model 6-BF Belt Furnace

Comp.	Sintering Conditions		% TD	MOR (MPa)	K_{IC} (MPa-$m^{½}$) Cook & Lawn	K_{IC} (MPa-$m^{½}$) Chan-tikul et al.
	Temp (°C)	Time (min)				
A4Y6 E-10	1700	60	99.9	870-926	5.5	6.5
A4Y6 LC-10	1700	60	96	917-1021	7.9	6.7
A4Y6 LC-12	1725	90	98.8	778-938	5.7	6.2
A2Y8 E-10	1750 1700 1625	90 90 30 90	100 99.0 94.4 93.7	926-1036 1004-1118 850-1051 880	10.3 9.6 7.1 7.4	7.3 7.1 6.2 6.5
A2La8 E-10	1750 1725	90 90	98.5 99.0	683-866 896-995	7.9 8.0	6.7 6.8
A4Y6La7 E-10	1725 1700 1625	90 90 90	98.1 99.0 98.3	755-965 962-982 907-1041	6.5 8.3 8.0	6.0 6.9 6.6

Table I. Sintering Conditions and Physical Property Results for Compositions Sintered in the Centorr Model 6-BF Belt Furnace (Continued)

Comp.	Sintering Conditions		% TD	MOR (MPa)	K_{Ic} (MPa-$m^{½}$) Cook & Lawn	K_{Ic} (MPa-$m^{½}$) Chan-tikul et al.
	Temp (°C)	Time (min)				
A4Y13 LC-10	1625	90	99.5	969	7.2	6.5
A4Y13 ASN-34	1700 1675	90 90	99.8 100	879-1059 980-1166	8.1 7.2	6.5 5.8
A4Y13 E-10	1725 1700 1625	90 30 90	99.8 99.6 99.6	784-1121 1016-1042 896-942	12.9 8.1 12.5	6.5 6.3 6.1
A4Y13 E-10 5%β Seed	1725 1700 1675 1625	90 30 90 90	99.5 99.3 99.7 99.3	870-954 870-1042 894-1121 894-1017	13.3 7.2 ---- 12.7	6.4 7.0 ---- 6.5

- LC-10 and LC-12 Si_3N_4 powders were purchased from Hermann C. Starck, W. Germany
- E-10 Si_3N_4 powder was purchased from UBE Industries America, NY, NY
- ASN-34 Si_3N_4 powder was a gratis sample from Performance Ceramics, Peninsula, OH
- Y_2O_3 and La_2O_3 (high purity grades) powders were gratis samples from Molycorp, Inc.,White Plains, NY
- Al_2O_3 (HPA-0.5 AF grade) powder was a gratis sample from Ceralox Corp., Tuscon, AZ

Status of Milestones

1.	Refine Economic Model and Design for Chosen Furnace Configuration	Completed
2.	Continue Evaluation of Sintering Parameters on Properties of Selected Si_3N_4 Compositions	On Schedule
3.	Continue Evaluation of Low Cost Si_3N_4 Powders	On Schedule

Communications/Visits/Travel

D.E. Wittmer to Annual Cocoa Beach Conference to present paper based on work performed as part of this contract.

D.E. Wittmer, J.J. Conover, and V.A. Knapp to Annual ACS Meeting in Cincinnati to present results of research performed as part of this contract.

Problems Encountered

Faulty isopress pump delayed processing.

Publications

D.E. Wittmer, J.J. Conover, V.A. Knapp, and C.W. Miller, Jr., "Economic Comparison of Continuous and Batch Sintering of Si_3N_4," accepted for Publication as feature in the June 1993 issue of the American Ceramic Society Bulletin.

Presentations

D.E. Wittmer, J.J. Conover, V.A. Knapp, and C.W. Miller, Jr., "Economic Comparison of Continuous and Batch Sintering of Si_3N_4", presented at the Annual ACS Meeting April 18-23, 1993 in Cincinnati, OH.

D.E. Wittmer, J.J. Conover, T. Paulson and C.W. Miller, Jr., "Self-Reinforced Si_3N_4 Sintered in a Controlled Atmosphere Belt Furnace," presented at the 17th CCAC, Cocoa Beach, FL Jan. 10-15, 1993.

Development of a High Quality, Low Cost Silicon Nitride Powder

G.A. Eisman, D.F. Carroll, A.W. Weimer, C.L. Conner, G.C. Cochran, S.D. Dunmead, and J. Hwang. (The Dow Chemical Company)

OBJECTIVE/SCOPE

The objective of this program is to scale a carbothermal nitridation process to the pilot plant level for the production of a high quality, low cost silicon nitride powder. The initial tasks of this program are designed to 1) determine the relationships between raw material precursors, reactor conditions, and post-processing on the characteristics of carbothermal powder using an intermediate scale reactor and 2) identify those characteristics which yield a sinterable powder that can be pressure-less sintered into dense, high strength components. This information will provide a basis for the ensuing pilot plant facility scale-up of carbothermal silicon nitride powders. The program's target goals are to produce a high quality, low cost silicon nitride powder that can be pressureless sintered into components with a density greater than 98% theoretical, an average room temperature strength greater than 800 MPa, a Weibull modulus greater than 15 and a fracture toughness greater than 5 MPa-$m^{1}/_{2}$.

The intent of the program is to facilitate a domestic supply of powder produced by a process which, at market maturity, sells for approximately $10/lb (1992 dollars).

TECHNICAL PROGRESS

TASK I Reference Process Flowsheet and Cost Estimate

The objectives of Task I are: synthesis of 3 kg of powder in a pre-pilot plant reactor, a process flow sheet of non-proprietary elements of the process, and a preliminary cost analysis of the current process.

Task 1.1 Process Flow Sheet

The process flow sheet currently being assembled and to be delivered in May, incorporates the unit operations which are utilized in the silicon nitride process. Pre-processing unit operations involving feed preparation and post-processing unit operations which are in place to handle the powder after the reaction stage are depicted. In addition, the steps involved in the reaction stage are outlined. Below is an outline of the general stages of the process.

Overall, the process to prepare the feeds, synthesize the product, and handle the "crude" product is quite simple and therefore lends itself to potentially low cost operations. In the first block of operations detailing the feed preparation, raw materials are added at various stages and then mixed. In addition to the reactants, any additives utilized in the process are added and blended into a final precursor "mix". The feed preparation involves additional proprietary steps to

prepare the precursor complex for the reaction stage. The reaction stage is simply a reactor with simple feed and feed take-off porting. Once reacted, the "crude" powder is removed and the excess carbon utilized in the reaction is removed via a controlled oxidation step in a calciner. The silicon nitride is then put through a mild milling stage to break up weak agglomerates. The material is then packaged and stored until ready for shipment.

Task 1.2 Preliminary Economics

The estimate, based on current experience, is a price/volume relationship for powder manufactured in various sized facilities. At high volumes, the price is expected to be in the $10-15/lb. (1992 dollars). The estimate of the powder costs in the existing facility which is representative of low volume, unoptimized unit operations, is typical of research-like costs for a newly developed process.

TECHNICAL PROGRESS

Task 1.3 Powder Synthesis

The powder synthesis work conducted in Task 1.3 has been conducted at an intermediate scale (0.5 to 1.0 kg lots) using Reactor Configuration #2. Using this approach, the characteristics of the powder were varied in a controlled manner. Sufficient quantities for part fabrication and mechanical property evaluations were produced. Initial efforts in Task 1.3 concerned optimizing the characteristics of the carbothermal powder with respect to sinterability. In the first two months the feed composition, reaction temperature, and reaction time were varied to determine their effect on product quality. After the optimal synthesis conditions were determined using an iterative set of statistically designed experiments; subsequent experimentation focused on making 6 kg (3 kg for MMES, 2 kg for Task 3, and 1 kg retainer) of powder for the May 93 deliverables.

Through the first 6 months of the contract, 83 reactor runs were completed using a total of 58 kg of raw material feed. Of the material produced, 8 lots averaging 1.0 kg were selected and supplied to Task 3 characterization and evaluation. The production of the 6 kg of powder for the May 1993 deliverable has been completed and the powder is now being evaluated. A preliminary characterization of this powder is summarized in Table 1. Future efforts will be geared towards optimization of yield, phase chemistry, morphology, and carbon removal conditions.

TASK III

The objectives of this task are: the development of a characterization plan for both powder and parts, the analysis of all synthesized powder, the development of powder processing (greenware) and sintering procedures and lastly, the fabrication of MOR bars for mechanical testing.

Table 1. Approximate characteristics of the Si_3N_4 powder made in Task 1.3 to meet the May 93 deliverables.

	6.0 kg for May 93	Contract Goals
Oxygen Content (wt%)	2.2	<2.5
Carbon Content (wt%)	0.4	<0.6
Al (ppm)	<50	<1300
Fe (ppm)	20	<2000
Ca (ppm)	70	<1000
Surface Area (m2/g)	11	5 to 20
d10 (μm)	0.3	-
d50 (μm)	0.7	0.1-0.8
d90 (μm)	2.1	-

Task 3.1 Powder Characterization

The carbothermal silicon nitride powders synthesized in Task 1.3 are currently being characterized to determine their physical properties. Table 2 is a summary of results obtained on powders produced in the intermediate reactor during the first six months of the contract. As indicated in Table 2, a broad range of powder characteristics could be obtained with our carbothermal process. The residual oxygen and carbon contents in these powders varied from 1.40 to 2.46 wt.% and 0.30 to 0.71 wt.%, respectively. The impurity level in the carbothermal powder is low and well within specifications. An improvement to increase the quality of the powder can be seen by comparing the iron and aluminum concentrations in earlier powders A-D to later powders E-F. The levels of iron and aluminum have been significantly reduced by improving our raw materials handling procedures. This continuous process improvement dramatically improved the mechanical properties of our materials (see Task 3.7). The surface areas[a] of the powders have ranged from 5.6 to 11.6 m^2/g. In all cases, the powders have had an alpha silicon nitride phase content greater than 95 wt.%. Figure 1 is an SEM micrograph showing the morphology of carbothermal powder B. This powder is sub-micron in size and has an equiaxed particle morphology.

Task 3.2 Powder Sinterability

Sinterability studies were conducted according to an experimental design to identify which powder characteristics, reactor conditions, and raw material precursors produced a high quality sinterable powder. In these experiments, carbothermal powders were mixed with a proprietary sintering additive formulation, which had a total glass content of 7.5 volume%. The sintering additive formulations took into account the oxygen contents of each carbothermal powder. The formulations were uniaxially pressed into greenware and *partially* sintered at elevated temperatures. This partial sintering technique facilitated comparisons between powder characteristics and relative rates of densification. The sintering formulations were also systematically varied to determine the effects of sintering composition. Figure 2 summarizes the effect of the residual carbon content on the sinterability of carbothermal powders. The error bars in

---

[a] prior to the mild milling post-processing step.

Table 2
Characteristics of five different lots of carbothermal silicon nitride powder produced in Task 1.3 using reactor configuration #2.

Property	A	B	C	D	E	F	Program Goals
Oxygen (wt.%)-Leco	2.11	1.78	1.94	2.07	2.44	2.46	<2.5
Carbon (wt.%)-Leco	0.71	0.30	0.53	0.48	0.40	0.43	<0.6
Al (ppm)-XRF	176	230	125	nm	<20	<50	<1300
Fe (ppm)	123	98	145	"	31	18	<2000
Ca (ppm)	90	87	66	"	70	67	<1000
Na (ppm)	nm	nm	nm	"	nm	nm	<10
Mg (ppm)	"	"	"	"	"	"	<50
K (ppm)	"	"	"	"	"	<5	<10
Cl (ppm)	11	19	<10	"	"	<10	<100
S (ppm)	nm	nm	<10	"	"	<20	<100
Surface Area (m2/g)	8.7	8.0	11.6	11.5	10.1	10.9	5-20
wt.% Alpha Si_3N_4	>95	>95	>95	>95	>95	>95	>90
Ave. Part. Size (μm)	nm	nm	nm	nm	nm	0.78	0.1-0.8

nm - not measured. Analyses in progress.

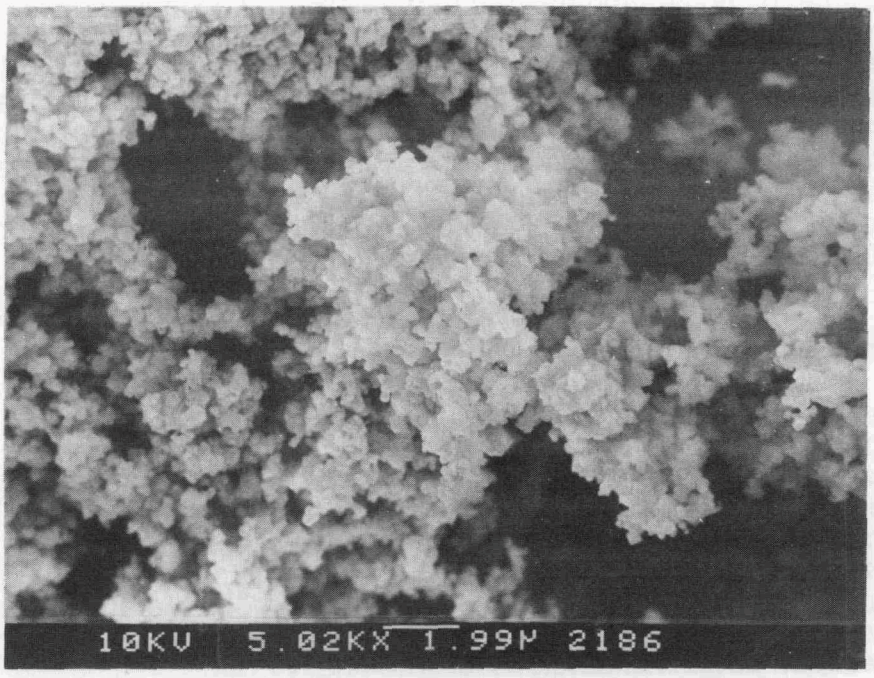

Figure 1. Scanning electron micrograph of carbothermal powder B.

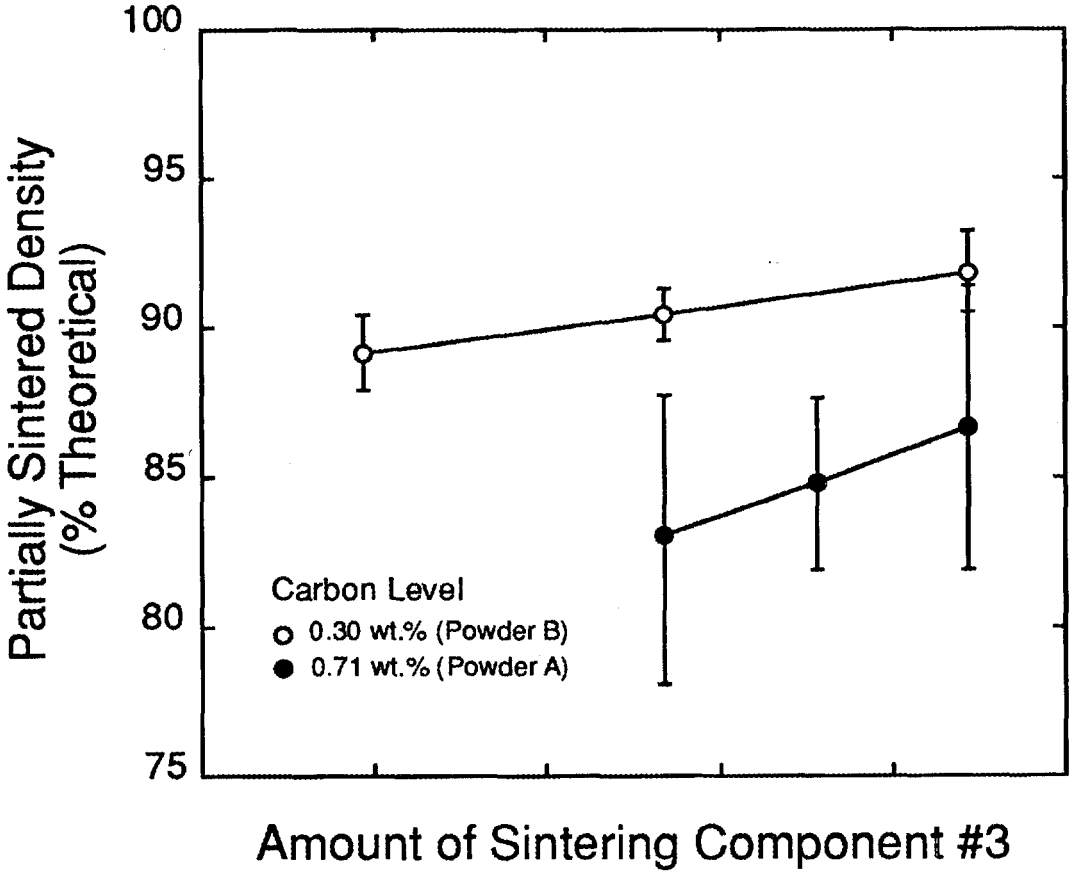

Figure 2. The effect of residual carbon on the sinterability of carbothermal powder. Specimens were partially sintered at elevated temperatures to examine the relative rates of densification.

Figure 2 represent a 95% confidence interval derived from an analysis of the experimental design data. As the amount of sintering additive #3 is increased, the partial-sintered density for the low carbon powder (powder B) remains greater than the density of the high carbon powder (powder A). Based upon these results and other evaluations, the best sinterability is generally obtained in carbothermal powders with residual carbon contents less than 0.6 wt.%.

The effect of surface area on sinterability of carbothermal powders is shown in Figure 3 for two carbothermal powders with a residual carbon content less than 0.6 wt.%. As the surface area increases from 8.0 m^2/g (Powder B) to 11.6 m^2/g (Powder C), an increase in the partial sintered density is observed. The increase in densification is attributed to a finer particle size of the higher surface area powder. In order to compare the sinterability of the carbothermal powders with respect to commercially available silicon nitride powders, the densification behaviors of a di-imide[b] and direct metal[c] powder are also shown in Figure 3.[1] The results show that Powder C, which has a residual carbon content less than

[b] Ube Industries, SNE10.

[c] Denka, P21C

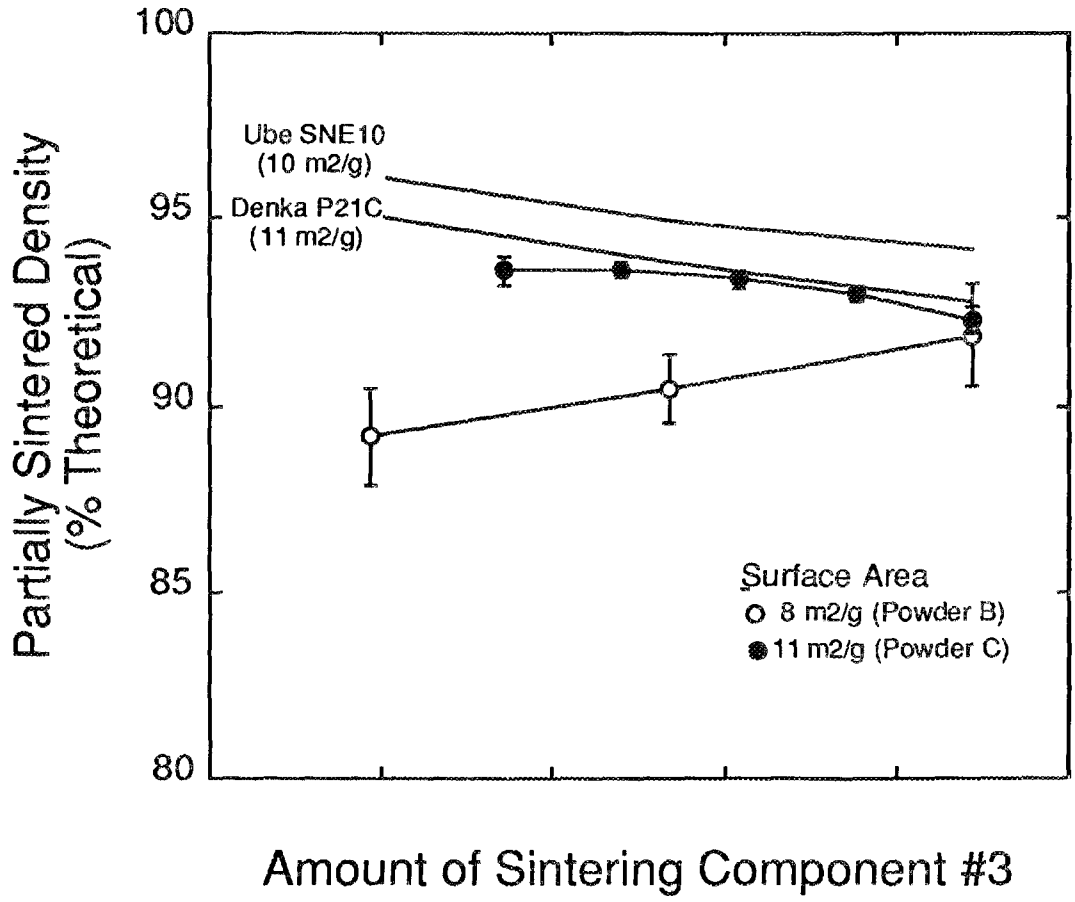

Figure 3. The effect of surface area on the sinterability of carbothermal silicon nitride powders. Specimens were partially sintered at elevated temperature to examine the relative rates of densification.

0.6 wt.% and a surface area of 11.6 m^2/g, exhibited a sinterability similar to the direct metal powder and slightly less than the di-imide powder. It is anticipated that further optimization of the carbothermal powder, such as the particle size distributions should increase the sinterability to a level comparable to the di-imide powder.

Task 3.3 Sintering Aid Optimization

Statistically designed experiments are currently underway to develop an optimum sintering formulation that can pressureless sinter the carbothermal silicon nitride powder to greater than 98% of theoretical density. Two sintering formulations are currently being evaluated: a Dow proprietary sintering formulation (total glass content 7.5 volume%) and a generic Y_2O_3-Al_2O_3 sintering formulation (total glass content 11.5 volume %). Table 3 summarizes preliminary densification results using near optimum compositions for the proprietary and generic formulations. Using sintering cycles that were developed primarily for a commercial di-imide powder[b], powders A, B, C and E were sintered to densities of 97.1%, 98.9%, 98.6% and 96.5%, respectively with the proprietary sintering formulation. Powders B and C were sintered to 98.1% and 97.6% of theoretical density using a 5 wt.% Y_2O_3-5 wt.% Al_2O_3 formulation. These preliminary results indicate that

Table 3.
Densification results for carbothermal silicon nitride powders sintered with a proprietary sintering aid formulation and a generic Y_2O_3-Al_2O_3 formulation.

Powder	Dow Proprietary Formulation	5 wt.% Y_2O_3 5 wt.% Al_2O_3 Formulation
A	97.1	nm
B	98.9	98.1
C	98.6	97.6
E	96.5	nm

nm - not measured.

the carbothermal powders have the characteristics necessary to be pressureless sinter into dense components. With optimization of the sintering schedule, it is anticipated that the sintered densities will be well above the goal of the contract (>98% density).

Task 3.4 Suspension Development

To understand the stability of carbothermal powders in water, slips of 1 volume% solids were prepared from powders B-E. The pH, conductivity and sedimentation behavior of these slips were continuously monitored over a 24 hour period. A fifth carbothermal powder, which was mildly milled after burn-out, was also evaluated. The results indicate that all powders reached a constant pH and conductivity after a 15-minute exposure to water. Powders B-E exhibited a constant pH of 4.6 to 4.8 while the mildly milled powder exhibited a higher pH of 8.1. The higher natural pH exhibited by the mildly milled carbothermal powder may be the result of fresh silicon nitride surfaces exposed during milling. For comparison, the natural pH of a commercially available di-imide[b] and direct metal[c] powder have been evaluated to be 8.9 and 4.0, respectively.[1] The conductivity measurements of the carbothermal powders ranged from 7 to 15 µs/cm with no apparent difference between the milled and unmilled powders. These values were lower than those obtained for a commercially available di-imide[b] (26 µm/cm) and direct metal[c] (95 µm/cm) powders.[1] All suspensions were stable over the 24 hour period with no apparent sedimentation.

The zeta potential of a carbothermal powder was also measured to characterized the powder surface. Figure 4 is an example of the zeta potential as a function of pH for our carbothermal powder. The isoelectric point for this powder was observed at a pH of 2.3. This behavior is characteristic of an oxygen enriched surface layer on the Si_3N_4 powder. The carbothermal powder was also found to exhibit a large, negative zeta potential at pH values >6. This extended region of a highly negative zeta potential over a broad range of pH values is desirable especially when preparing stable suspensions of silicon nitride/sintering aid formulations. The zeta potential of a di-imide produced powder[b] is also shown in Figure 4 for comparison.[1] The di-imide powder had an isoelectric point at a pH of 6 and a large negative zeta potential at pH values greater than 8-9.

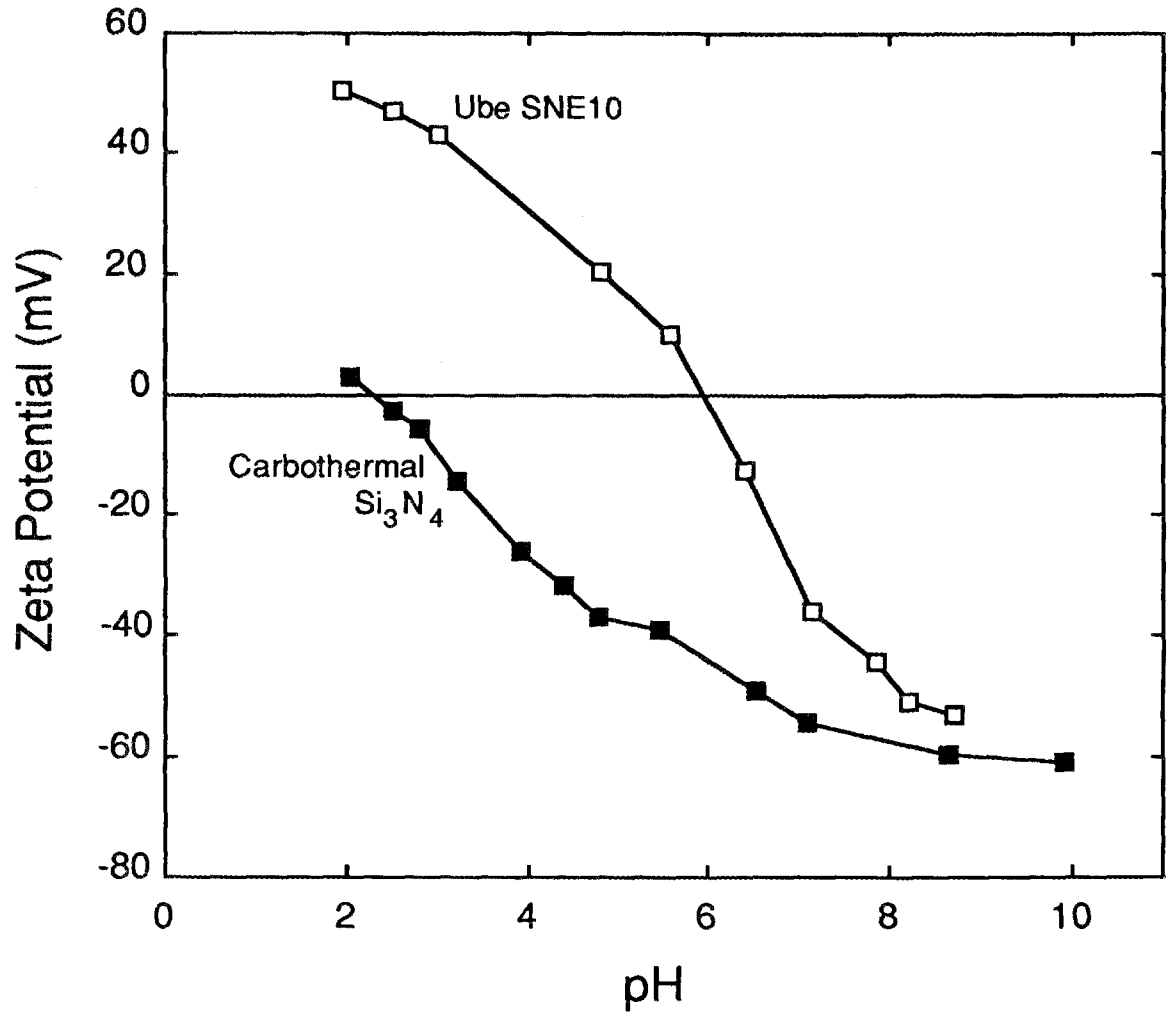

Figure 4. Zeta potential of a carbothermal silicon nitride powder as a function of pH. The zeta potential for a di-imide based powder is also shown for comparison.

Task 3.5 Greenware Formation and Part Densification

Examination of several kinds of dispersants for the carbothermal powders are under way using powders produced in Task 1.3. At least two dispersants have been identified which produce slips with viscosities less than 100 cps at high solid loadings. Pressure casting and slip-casting results have shown that high quality, crack-free greenware with densities ranging from 53 to 58% can be made with the carbothermal powders. Further improvements in green densities are expected with an optimization of the carbothermal powders' particle size distributions. An examination of greenware homogeneity has also revealed an uniform distribution of sintering additives can be obtained in a 1.5 inch thick part.

In order to produce sintered blanks for mechanical property evaluation in Task 3.7, greenware from powders A, B and E and Dow's proprietary sintering formulation were fabricated using a slip-casting technique. This greenware was sintered, using our standard conditions, to a density of 97.2%, 98.9% and 96.5% for powders A, B and E, respectively.

Task 3.7 Part Characterization

The sintered blanks produced from powders A, B and E in Task 3.5 were machined into mechanical test specimens. In order to evaluate the quality of the carbothermal powder, the average room temperature strength, Weibull modulus and fracture toughness were measured. The results of this evaluation are summarized in Table 4, in comparison to the contract goals. The average room temperature strengths of the specimens made from powders A and B were 600 ± 115 MPa and 510 ± 145 MPa, respectively. Fracture surface analysis revealed that the modest strengths of these specimens were due to small metallic inclusions in the material. The source of these inclusions was identified and corrective actions were taken to remove these defects from the carbothermal powder (see Task 3.1). Powder E is an example of the improvement in mechanical properties after the metal inclusions were eliminated. The average room temperature strength increased to 795 ± 45 MPa. The Weibull modulus for this material was 18. Even though these strength results are near the contract goals, further improvements in strength are expected after the greenware, sintering formulation and sintering conditions are optimized for the carbothermal powder. The average fracture toughness for each material was determined using the chevron-notched bend beam technique. Powders A, B and E had fracture toughnesses of 7.4 ± 0.2, 6.8 ± 0.2 and 7.3 ± 0.2 MPa-$m^{1/2}$, respectively.

STATUS OF MILESTONES

All milestones on schedule.

Table 4
Mechanical property summary for three carbothermal silicon nitride lots.

	Powder A	Powder B	Powder C	Contract Goals
Strength (MPa)	600	510	795 ± 45	> 800
Weibull Modulus	-	-	18*	> 15
K_{IC} (MPa-m1/2)	7.4 ± 0.2	6.8 ± 0.2	7.3 ± 0.2	> 5.0

* based upon 27 specimens.

PUBLICATIONS

1. Carroll, D.F., Cochran, G.C., Conner, C.L., Dunmead, S.D., Eisman, G.A., Hwang, J., Weimer, A.W., and Mossner, D., "Characteristics of a Carbothermal Silicon Nitride Powder," Presented at the 1993 American Ceramics Society Meeting, Cincinati, Ohio, April 19, 1993.

REFERENCES

1. D. Carroll and J. Hwang, unpublished data.

COMMUNICATIONS/VISITS/TRAVEL

Ray Johnson, Susan Winslow, and Sonny Rogers, of the Ceramic Technology Program at the Oak Ridge National Laboratory, and Bob Schulz of the Department of Energy (Washington, D.C.), visited the Dow Chemical Company in December, 1992 to attend the kick-off meeting.

C.L. Conner visited Garrett Ceramics (El Sugundo, CA) to begin assessing the forthcoming interaction and collaboration on Dow generated powder. April, 1993.

D.F. Carroll traveled to Cincinati, Ohio to attend and present a paper at the 1993 American Ceramic Society meeting. April 19, 1993.

PROBLEMS ENCOUNTERED

None to-date.

Cost Effective Process Silicon Nitride Engine Components

Garry Garvey (Golden Technologies Company, Inc.)

Objective/Scope:

The objective of this work is to develop a low-cost process for the manufacture of high quality ceramic engine components based on sintered reaction bonded silicon nitride technology. The work shall comprise three technical tasks including materials selection, process development, and property evaluation. The material property goal for this work phase is a mean RT 4-point flexure strength of 525 MPa with Weibull modulus of 15.

Background:

The commercialization of silicon nitride engine components requires that reliable, high strength silicon nitride material be available at a cost effective price. Today, many suppliers offer high strength and reliable silicon nitride. However, this material is very costly to produce due to high raw material and high processing costs. Typical silicon nitride powders range in price from $15 to $70 per pound. Sintering aids for silicon nitride are equally expensive. Yttria ranges from $20 to $60 per pound. The use of silicon as a raw material for sintered reaction bonded silicon nitride (SRBSN) can produce raw material savings, however, the current commercial practice of non-aqueous milling adds substantially to the processing costs.

In terms of the cost of thermal processing, the current practice of over-pressure sintering of silicon nitride requires substantial capitalization compared to ambient pressure sintering. It also requires a batch type approach to sintering. Both aspects of sintering add to the product costs.

Ideally, silicon nitride should be sintered at a minimum temperature at ambient pressure in a continuous mode.

Coors Ceramics Company/Golden Technologies Company has an executed License and Commercialization Agreement to license patents related to silicon nitride technology from Eaton Corporation. This technology is based on the aqueous processing of silicon metal to produce high quality SRBSN and promises to result in reducing the cost of silicon nitride parts.

Approach:

The experimental plan is based on an iterative design in which silicon metal powder and other raw materials are characterized (task 1), subjected to cost effective processing (task 2) and the silicon nitride parts thus produced are evaluated (task 3). The emphasis being on identifying low cost processes capable of producing high strength, reliable parts. The program is also designed to identify low cost, reliable domestic suppliers of the requisite raw materials that can be used to produce high quality parts.

Task I: "Raw material selection and characterization" will be conducted by sampling up to five different manufacturers for each component. Ceramic raw material lots will be characterized with respect to particle size distribution, surface area, LOI, heterogeneous and homogeneous compositions. Organic batch components will be analyzed for consistency of manufacturer specified parameters.

In addition to evaluation of raw materials as received from manufacturers, task 1 will also focus on the selection of organic additives as binders, dispersants, lubricants and electrolytes and levels required to facilitate milling, spray drying, forming and the achievement of reliable product properties.

Task II: "Material processing". The point of departure of this task will be to replicate the technology licensed form Eaton Corporation. Once this facet has been completed, Coors/GTC will endeavor to develop novel proprietary and patentable technology to simultaneously improve properties, reduced costs and limit environmental risks. Each operation in the process flow path will be investigated for opportunities for improvement. Unit operations to be examined include: milling, spray drying, forming, debindering, nitriding, sintering and machining.

Task III: "Property testing". Property testing will be used in an iterative manner to evaluate the effects of process modifications. The primary characterizations will include quantitative microstructural analysis, strength (MOR) and Weibull analysis. In addition, hardness, phase analysis (XRD) and toughness will be determined for selected batches. All testing will be designed to obtain statistically significant results.

Milestone Schedule:

- We have successfully exceeded the goals of this program for strength and reliability. GTC-530-71A-81 exceeds the strength goal by 16% and the reliability goal by 5%. The following table is a report of three completely separate and consecutive batches of SRBSN including: strength, reliability and batch size: (WBS-3.1.2) (03/31/93)

SAMPLE	STRENGTH (MOR, kpsi)	WEIBULL MODULUS	BATCH SIZE
Target Properties	75	15	
UPB	94.1	14.5	1 kg
UPC	87.2	14.6	1 kg
GTC-530-71A-81	87.0	15.7	100 kg

- Three full scale attrition mill runs were completed. The milled powder was characterized and processed into sintered parts. Quantitative microstructural analysis indicated similar results to bench scale experiments confirming the scalability of the process. Batch sizes were 210# of slip producing 130# of dry body per run. (WBS-2.1.1) (03/31/93)

- The fast fracture strength of SRBSN has been evaluated at temperature up to 1125°C. SRBSN sample retained 90% of their strength up to 950°C. (WBS-3.1.2) (03/31/93)

- A seven component dry pressing binder system has been developed. Bench top pressing yields have been improved from 40 to 95%. Debindering and sintered properties have been proven to be satisfactory with this new composition. Final compositional adjustments will be made once the automatic press is operational. (WBS-2.1.3) (03/31/93)

- We have implemented a program to characterize property gradients in sintered parts. While many samples are homogenous due to a combination of processing parameters, many exhibit anisotropy. Anisotropy generally results from non-optimal thermal processing. Several experiments have been performed by perturbing preferred operating conditions resulting in low density products and/or thermo-decomposition of silicon nitride resulting in increased silicon and porosity. Optimal thermal processing parameters have been identified which produce homogeneously low silicon and porosity levels. (WBS-3.1.2) (02/15/93)

- Detailed TEM and electron diffraction studies of Coors/GTC SRBSN was performed at Case-Western Reserve University. Results indicated that no residual amorphous intergranular phase exists. The silicon nitride phase was determined to be beta phase with a large fraction of grains exhibiting acicular morphology. Typical aspect ratios of 8:1 were found. (WBS-3.1.2) (02/01/93)

- The effects of refractories on the sintering characteristic of silicon nitride were studied. Both refractory metals and ceramics were studied including molybdenum, graphite, alumina, silicon carbide, boron nitride and silicon nitride. A standard refractory material was selected. (WBS-2.1.5) (02/01/93)

- A series of experiments were performed to correlate powder properties, process parameters, and product properties. Particle size, surface are and oxygen content were varied. The microstructural and mechanical properties of parts produced from these powders were evaluated. Optimal particle size, surface area and oxygen content were determined. (WBS-1.2) (02/01/93)

- A series of experiments consisting of fifteen continuous sintering runs have been performed. Maximum temperatures, time at temperature and thermal profiles of the three zone furnace were varied. These experiments indicated that silicon nitride can be rapidly sintered in a continuous furnace to 99% density. (WBS-2.1.4) (01/15/93)

- An experiment was performed to evaluate the effectiveness of different milling and mixing techniques at producing high quality silicon nitride parts. High shear mixing was eliminated as a substitute for mill due to economic considerations. Attrition milling was found to be more efficient than ball milling and eliminated the explosion hazard inherent in aqueous milling of silicon in ball mills. Six different milling medias were evaluated for their milling rates and ability to produce high quality silicon nitride. (WBS-2.1.1) (01/01/93)

- An extensive Rheological Matrix Experiment has been performed. The effects of thirty-two different additives on Rheology have been evaluated. Each dispersant, binder, lubricant and electrolyte were evaluated at least four different levels and six different shear rates. Matrix effects of binary combinations were also evaluated. From these experiments, a standard dispersant-binder-lubricant-electrolyte combination was selected as a standard composition. (WBS-1.1) (12/01/92)

- The Eaton Process has been reproduced. Results are consistent with those reported by Eaton. These results are given below: (12/01/92)

Density (Archimedes) (g/cc)	3.27
Absorption (%)	0.1
True porosity (%)	3.0
Hardness (Vickers @ 1 kg) (kg/mm2)	1450
Toughness (15B)	6.0
MOR (ksi) (MPa)	449

1.1.4 Processing of Monolithics

Improved Processing

V. K. Pujari, D. M. Tracey, M. R. Foley, A. K. Garg, N.I. Paille, P. J. Pelletier, L.C. Sales, C. A. Willkens, R. L. Yeckley (Norton Company)

Objective/scope

The goals of the program are to develop and demonstrate significant improvements in processing methods, process controls, and nondestructive evaluation (NDE) which can be commercially implemented to produce high-reliability silicon nitride components for advanced heat engine applications at temperatures to 1370°C. Achievement of this goal shall be sought by:

- The use of silicon nitride - 4% yttria composition which is consolidated by glass encapsulated HIP'ing.
- The generation of baseline data from an initial process route involving injection molding.
- Fabrication of tensile test bars by colloidal techniques - injection molding and colloidal consolidation.
- Identification of (critical) flaw populations through NDE and fractographic analysis.
- Correlation of measured tensile strength with flaw populations and process parameters.
- Minimization of these flaws through innovative improvements in process methods and controls.

The quantitative program goals are: 1) mean RT tensile strength of 900 MPa and Weibull modulus of 20, 2) mean 1370°C fast fracture tensile strength of 500 MPa, and 3) mean 1230°C tensile stress rupture life of 100 hours at 350 MPa.

Technical highlights

During the reporting period, the focus was on analysis of data generated during the Stage III process demonstration, which was conducted from May 1 to November 30, 1992. The demonstration involved the fabrication and testing of several hundred NCX-5102 tensile rods. The fabrication followed the standard operating procedure (SOP) of the aqueous based, pressure casting process optimized during the 15 month Stage II portion of the program.

Stage I involved the establishment of baseline forming data using injection molding and colloidal consolidation processes for fabrication of near net shape formed (NSF) tensile rods. Pressure casting was found to offer the best potential for achieving the program's mechanical property targets and for cost-effective manufacturability. The progress from these baseline process iterations to the current is summarized in Figure 1a. Mean tensile strength has been effectively doubled, with the current level of NCX-5102 mean strength at 1 GPa. Tensile strengths at the 1 GPa level have rarely been reported in the past. This current result is the mean for over 300 samples, as discussed in detail below. In general,

flexure mean strength levels have not been this high, as indicated by competitive material data plotted in Figure 1a. The enhancement in strength realized in this program has been achieved by affecting a fivefold reduction in average flaw size (from 250 to 50μm) and significantly reducing flaw frequency, as summarized in radiography data, Figure 1b.

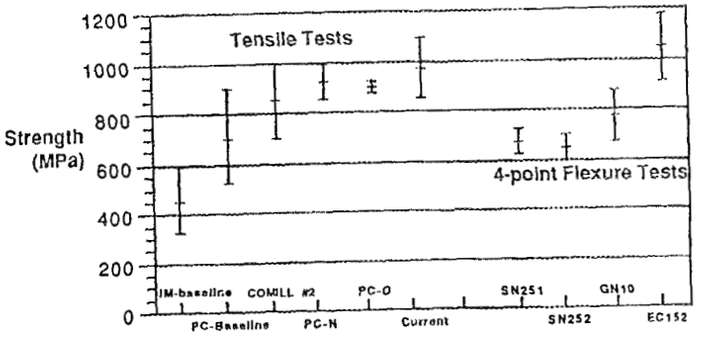

a) Tensile Strength Improvement - NCX5102

(Flaw-pores, inclusions, agglomerates)

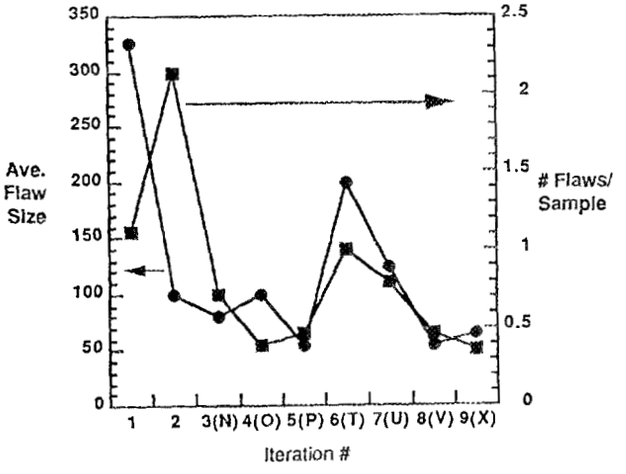

b) Flaw Reduction

Figure 1: Chronology of Process Improvement

Stage III Room Temperature Tensile Strength Database

The tensile test database from the Stage III demonstration set includes fractography results on location, type and size of the failure origins obtained using optical and scanning electron microscopy. The majority of the room temperature specimens had failure origins at the

surface within the uniformly stressed 6 mm diameter gage length. Two types of surface failure origins were identified; namely, machining flaws and amorphous areas that developed during a post-machining treatment step. A typical machining flaw which includes a grinding groove and associated radial cracks as depicted by liquid dye penetrant technique is shown in Figure 2. Also, two distinct types of volume flaws were observed. One was a microstructural flaw characterized by a zone of microporosity. The other involved inclusions from contamination subsequently traced to a piece of processing equipment.

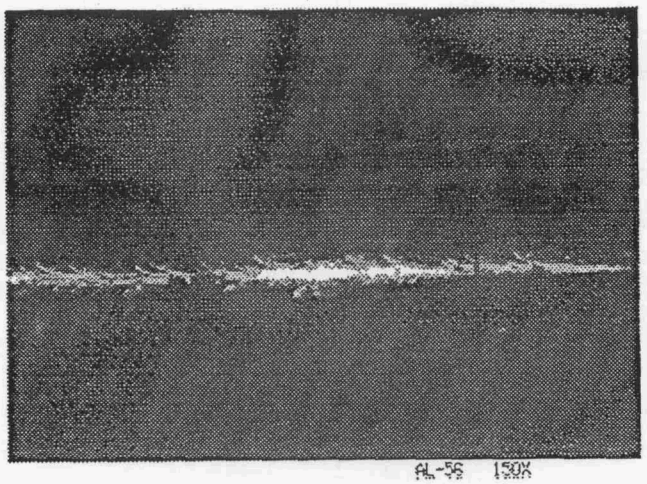

Machining groove (13μm) in HIP'ed/machined NCX-5102 revealing crack branching and material fracture.

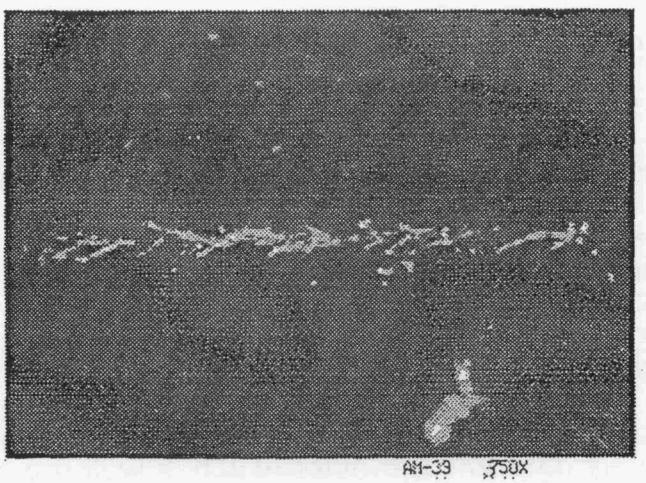

A grinding groove, 6 μm wide, which produces 8-35 μm radial cracks (350X)

Figure 2: LDP Detection of Machining Related Cracks

In the statistical analysis discussed below, the surface amorphous flaws and the volume microstructural flaws were considered to comprise a set of intrinsic flaws, since they randomly occur within the standard processing cycle. On the other hand, the machining damage and inclusion flaws were classified as being extrinsic flaws, since they are subject to control by means unrelated to the silicon nitride process per se.

The database includes a total of 320 valid tensile tests. The 320 strength data are presented in a cumulative probability of failure plot using standard Weibull coordinates in Figure 3. The data range from 540 to 1237 MPa and have a mean value of 997 MPa. The nonlinear character of the distribution with multiple inflections suggests that a 2-parameter Weibull fit of this data (σ_o=1038 MPa, m=10.4) would be inappropriate and that the multimodal nature of the data should be represented using competing risk analysis.

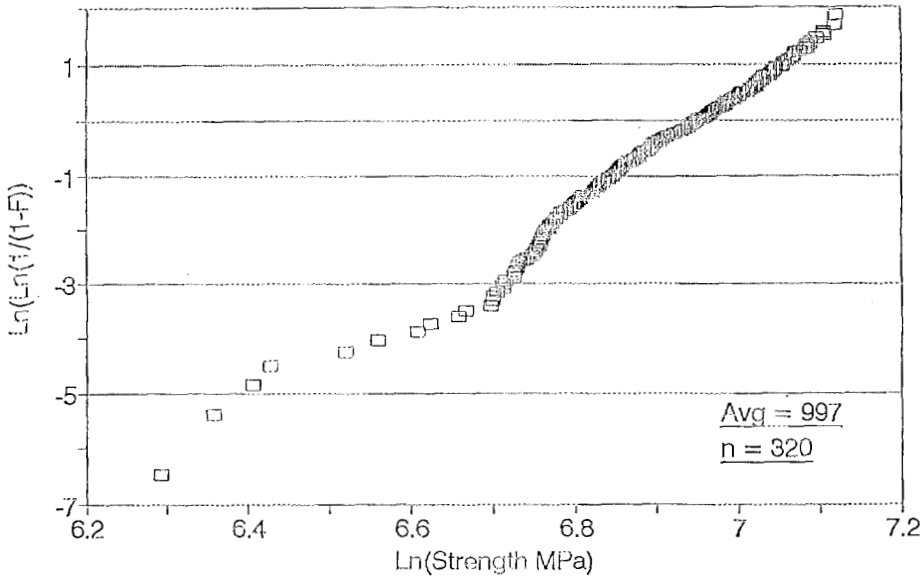

Figure 3: Cummulative Probability of Failure Plot of Stage III Data

The multimodal analysis was pursued by considering the group of 320 strength data as being composed of two sets, with one set (n=170) representing strengths of intrinsic defects and the other (n=150) representing strengths of extrinsic defects, Figure 4. Competing risk analysis reveals that the extrinsic strength data dominate the nonlinear low strength tail of the overall distribution, Figure 4. A plot of their distribution is similar to that of Figure 3. The intrinsic strength data on the other hand has a distinctly different character which is well represented by a 3-parameter Weibull model with a threshold stress of 665 MPa, a scale value of 444 MPa and a shape value of 3.92. The intrinsic strength data are plotted in Figure 5 along with this 3-parameter model and also with a 2-parameter fit which clearly is a poor representation of the data. The line

to the left of the data represents the program target material having a mean tensile strength of 900 MPa and a 2-parameter Weibull modulus of 20.

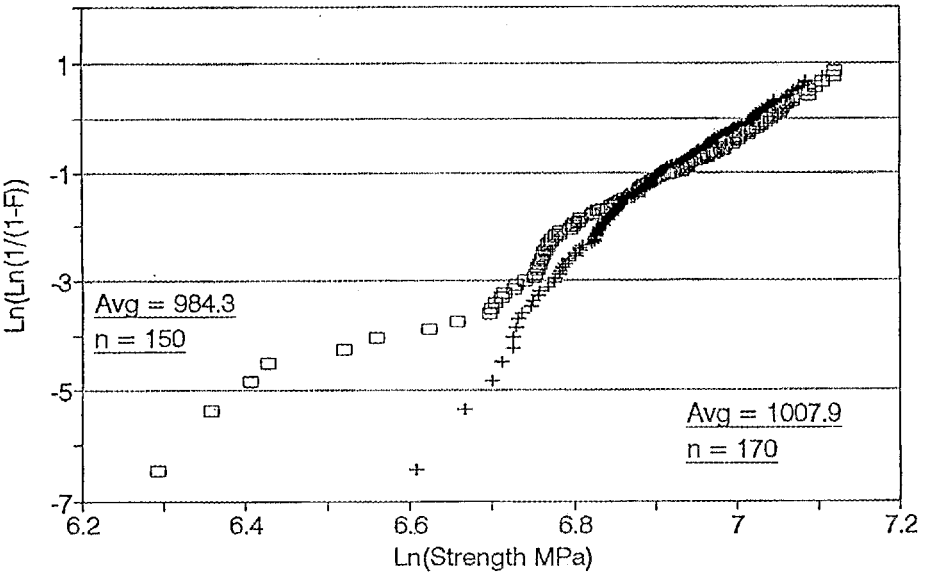

Figure 4: Competing Risk Weibull Plot: Intrinsic vs. Extrinsic Failure Origins

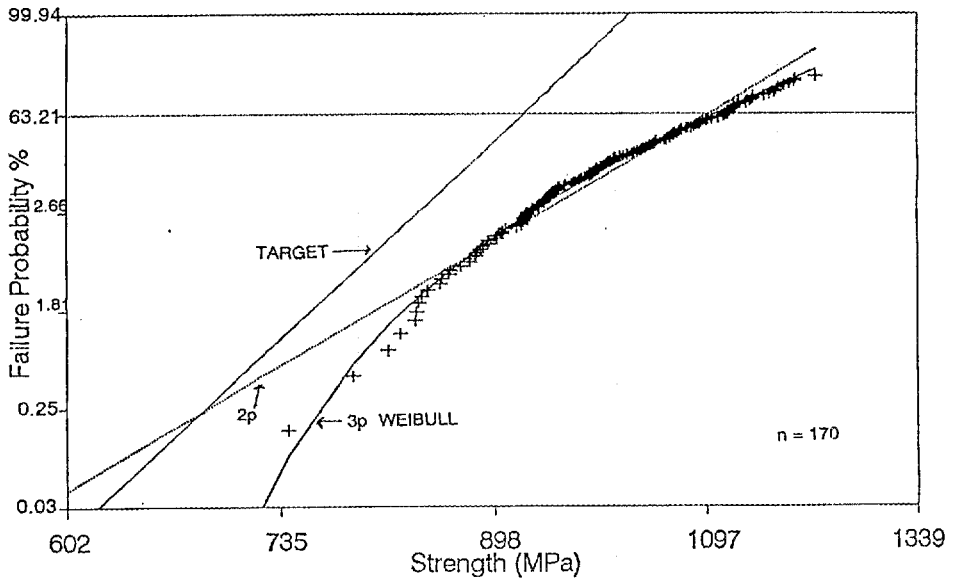

Figure 5: Cummulative Probability of Failure Plot of Intrinsic Strength Data

From a reliability perspective, the important feature of the 3 parameter Weibull distribution is the existence of a threshold stress below which there is zero probability of failure. Physically this corresponds to a processing methodology which has succeeded in truncating the upper tails of the critical flaw size distributions. A threshold at the level indicated clearly has direct impact on design systems used in fielding reliable ceramic components. For instance, NCX-5102 with the 3 parameter distribution of Figure 5 would provide higher reliability at all stress levels when compared to the program target material, as indicated in Table 1.

Table 1: Probability of Survival at Given Stresses (MPa)

	Target	Weibull 2 parameter	Weibull 3 Parameter
R99	735	766	802
R999	655	639	741
R9999	583	533	707
R99999	520	444	689
R999999	463	370	678

Elevated Temperature Tensile Test Data

The potential of reaching the program's elevated temperature mechanical property targets was demonstrated during Stage II using a specialized SOP. Fast fracture strengths at 1370°C were found to range from 425 to 520 MPa with a mean of 477 MPa in 5 tests. Stress rupture lives at 1230°C equaled or exceeded 100 hours at 250, 300 and 350 MPa in separate tests, although not all tests at 350 MPa survived 100 hours.

It was found that processing conditions for optimum room temperature properties differed from the above SOP. The primary focus in the program was to establish strength and reliability improvements through flaw control using room temperature strength data as the measure of improvement. On this basis, the Stage III optimization focused on SOP which favored room temperature characterization of NCX-5102.

Fifteen Stage III samples were tested to fast fracture at 1370°C. The mean strength was 396 MPa, with a range 344-452 MPa. Ten Stage III stress rupture tests were conducted at 1230°C. The target 100 hour lifetime was achieved at 250 MPa, but not at higher stress levels. The data from the Stage II and Stage III tests are shown in Figure 6 in a plot of applied stress vs. failure time.

Large Cross Section Specimen Strength Data

The general applicability of the optimized process beyond NSF tensile rods was demonstrated by fabricating and testing 50 mm diameter,

150 mm long specimens. These have been referred to as MLP (machined from large piece) specimens, in that the specimens were machined into many flexure bars (3x5x50mm) for assessment of the properties across the 50 mm section. Excellent fast fracture strength results were obtained both at room and elevated (1370°C) temperatures. The data were found to fit a 3 parameter Weibull form in each case, Figure 7a,b, with threshold stress values of 653 and 517 MPa for room temperature and 1370°C, respectively.

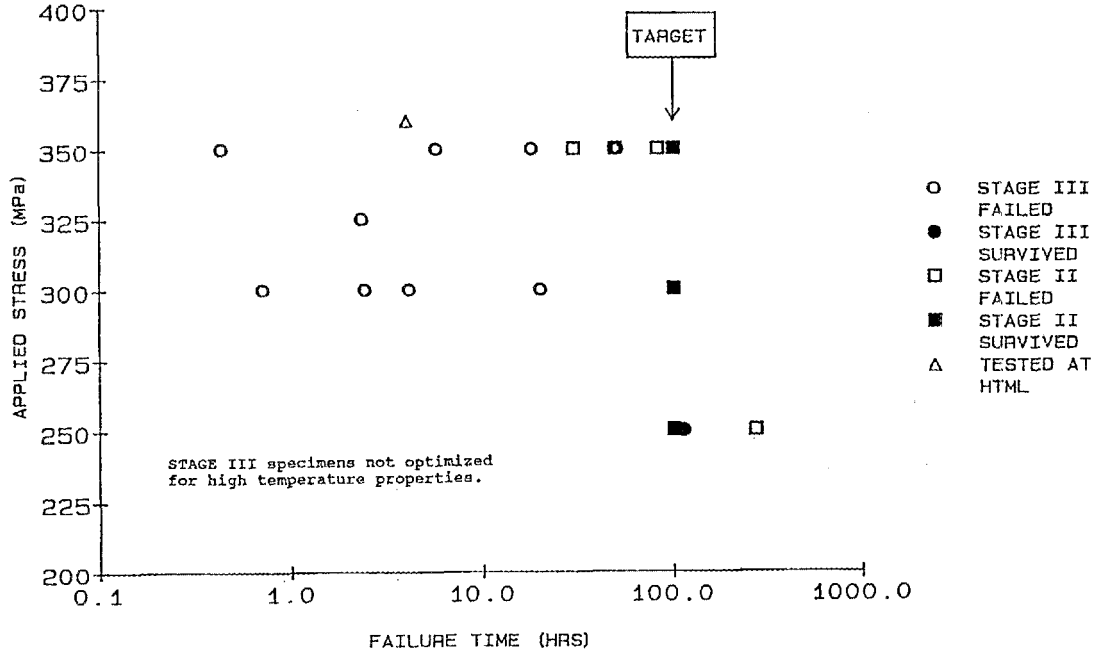

Figure 6: Tensile Stress Rupture Data at 1230°C in Air for Stage II and Stage III Specimens

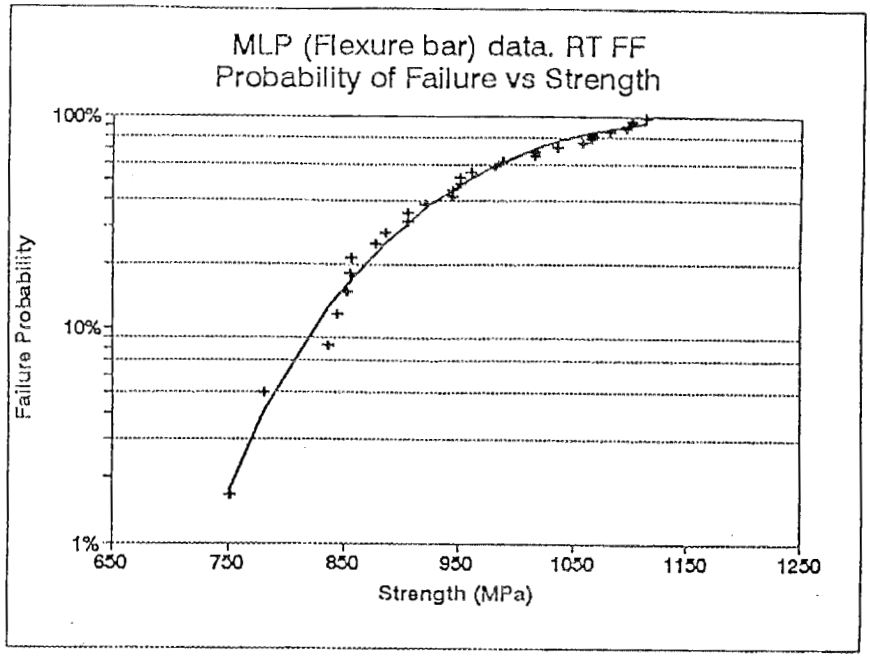

(a)

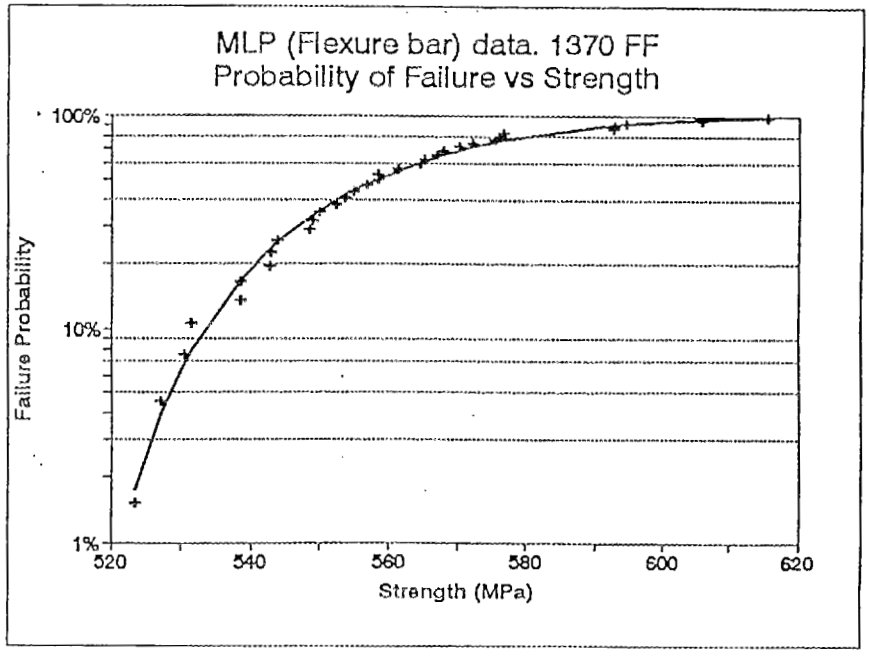

(b)

Figure 7: Flexure Strength Data from Large Cross Section (MLP) Specimen

Status of milestones

Milestone #114110 - Submit camera ready final report - rescheduled to June 30, 1993. Submission of final report draft to MMES scheduled for April 30, 1993.

Publications/presentations

1. "Development of Improved Processing and Evaluation Methods for High Reliability Structural Ceramics" was presented by V.K. Pujari at the Ceramic, Power Metal and Composite Manufacturing Symposium, Worcester Polytechnic Institute, Worcester, MA, October 21, 1992.

2. "Processing Methodology for the Production of Reliable High Strength Silicon Nitride" was presented by V.K. Pujari at the Automotive Technology CCM, Dearborn, MI, November 4, 1992.

3. "Process Control Methods in the Consolidation of Highly Concentrated Suspensions" by V.K. Pujari, L.C. Sales and N.I. Paille was presented by L.C. Sales as a poster paper at the MRS Fall Meeting, Boston, MA, November 30, 1992.

4. "High Strength Silicon Nitride Production Through Advanced Processing", by D.M. Tracey et.al, presented at the MRS Fall Meeting, Silicon Nitride Ceramics Symposium, Boston, MA, December 2, 1992.

5. "Silicon Nitride Tensile Strength Database from CTP Processing for Reliability Project," by M.R. Foley et.al; presented at ASTM Symposium on Life Prediction Methodologies and Data for Ceramic Materials in Advanced Technology Application - A Basis for Standards, Cocoa Beach, FL, January 12, 1993, to appear ASTM STP 1201.

6. "Ceramic Process Monitoring and Control by NDE Techniques", presented by V.K. Pujari at the ASNT's 1993 Spring Conference and Second Annual Research Symposium, Nashville, TN, March 31, 1993.

7. "Processing Methods for High Reliability Silicon Nitride Heat Engine Components", by V.K. Pujari and D.M. Tracey to be presented at ASME Turbo Expo - Land, Sea & Air, Cincinnati, Ohio, May 24-27, 1993, manuscript submitted for Proceedings, January 6, 1993.

Problems encountered

None.

Improved Processing

S. D. Nunn, O. O. Omatete, C. A. Walls, N. Bell,
and K. L. Ploetz (Oak Ridge National Laboratory)

Objective/scope

The objective of this task is to determine and develop the reliability of selected advanced ceramic processing methods. This program is to be conducted on a scale that will permit the potential for manufacturing use of candidate processes to be evaluated. The emphasis is on silicon nitride. Issues of practicality; safety, hygiene, and environmental issues; and in-process testing methods are to be addressed in addition to technical feasibility. The methodology includes selection of candidate processes and evaluation of their range of applicability to various kinds of commercially available ceramic powders.

Technical highlights

I. Silicon Nitride Gelcasting

Work is continuing on silicon nitride compositions prepared using two of the new gelcasting systems that are being evaluated as lower-toxicity replacements for acrylamide. The two systems are: methacrylamide monomer (MAM) with polyethylene glycol dimethacrylate (PEG DMA) crosslinking agent and MAM with methylene bisacrylamide (MBAM) crosslinker. The compositions are being evaluated for maximum solids loading, viscosity, and deairing characteristics. The gel system monomer-to-crosslinker ratio, catalyst addition, and accelerator level are being studied to determine the effect on slurry and gel properties.

A new casting method is being evaluated to reduce the possibility of trapping air in the mold and causing either surface defects or non-filled regions in thin mold sections. The method involves designing the mold to have the capability of being partially evacuated before being filled with the gelcasting slurry. Two vacuum gelcasting molds have been designed and fabricated. One of the molds will produce a simple flat plate that will be used to make modulus of rupture bars for 4-point bend test strength measurements. The other mold will be used to cast button-head tensile test rods.

Another processing approach that is being evaluated is low-pressure injection molding. An injection molder and flat plate mold have been received and are presently being prepared for use in gelcasting. Some modification of the equipment will be required to allow chilling of the slurry supply tank (to prevent premature gelation) and to provide mold heating capability to allow gelling in place. It is believed that this system may demonstrate gelcasting in a production-type environment.

Samples of gelcast silicon nitride containing 6 wt. % Y_2O_3 and 2 wt. % Al_2O_3, which were gas-pressure sintered for 2 h at 1850°C and 100 psi nitrogen pressure followed by 1 h at 1900°C and 300 psi, had a density of 99%. The gelcasting formulation

used to prepare the batch was MAM/MBAM in a 9:1 ratio. The average room-temperature 4-point bend strength of this material was 673 ± 76 MPa. The fracture toughness was about 7 MPa$\sqrt{m}$. Scanning electron microscopy (SEM) examination of the fracture surfaces revealed a relatively fine-grained microstructure (grain diameter 0.5 to 1.0 μm) with the grains having a high aspect ratio. An example of the microstructure is shown in Fig. 1.

Several gelcasting batches were prepared using various chemical formulations. All of the batches were made with UBE E-10 silicon nitride powder and contained 45 vol % solids:

A 6 Y_2O_3/2 Al_2O_3 batch was made using the old standard premix "C" formulation (acrylamide/MBAM 23:1). This batch was used to cast the first button-head tensile rod specimen. The mold is designed to allow evacuation before casting and bottom filling, both of which should minimize the possibility of trapping or entraining air bubbles during the casting procedure. A photograph of the mold and examples of parts that were successfully cast in the mold are shown in Fig. 2. Some distortion of the tensile rods occurred during drying because the gelled rods were not strong enough to be self-supporting.

To increase the rigidity of the gelled body, a batch was prepared using the MAM/MBAM formulation with a ratio of 6:1. The viscosity of the turbomilled slurry was

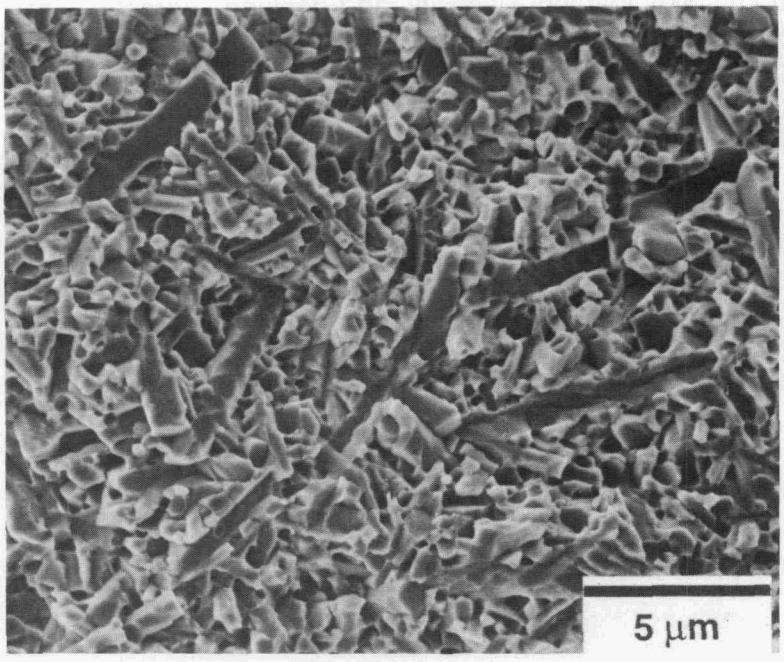

Fig. 1. Fracture surface of gelcast UBE E-10 silicon nitride containing 6 wt % Y_2O_3 and 2 wt % Al_2O_3 fired in a two-step gas-pressure sintering process for 2 h at 1850°C and 100 psi nitrogen followed by 1 h at 1900°C and 300 psi pressure.

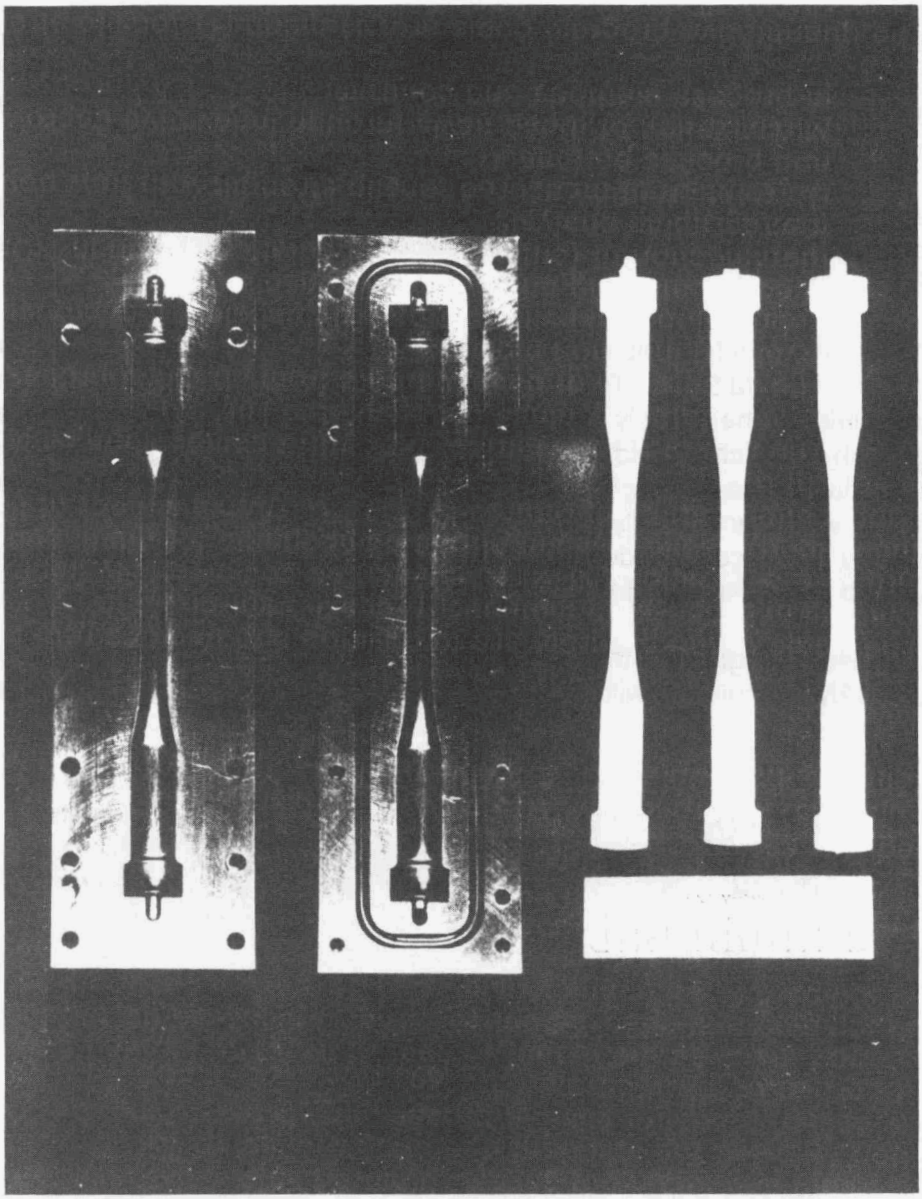

Fig. 2. Button-head tensile rod specimen mold with gelcast parts of silicon nitride and alumina.

measured at various shear rates. As shown in Fig. 3, the slurry exhibited pseudoplastic behavior with the viscosity dropping rapidly to a relatively constant level of 100 to 200 mPa•s (cP) when the shear rate was increased to more than about 150 s^{-1}. The slurry was very fluid and was deaired and cast easily. The increased amount of cross-linking agent in this batch produced a much stronger gelled tensile rod, but further improvement will be required both in gel strength and in fixturing to support the tensile rods during drying to completely eliminate distortion.

To evaluate the consistency of strength values that may be obtained using the gelcasting process, another 6 Y_2O_3/2 Al_2O_3 silicon nitride batch was prepared using the MAM/PEG 3:1 ratio, which has been described in previous reports. The batch was mixed and carefully vacuum deaired before being cast in flat plate molds. The cast samples were dried and fired at 1850°C for 4 h under a 50 psi nitrogen atmosphere. The samples had a density of 99%. Twenty 4-point bend test bars were fabricated and broken at room temperature. The average strength was 622 ± 49 MPa. The Weibull modulus was about 15, indicating excellent uniformity in the strength.

II. Sintered Reaction Bonded Silicon Nitride (SRBSN) Gelcasting

Gelcasting of Si for forming SRBSN parts was evaluated in the MAM/MBAM gelcasting system. Attempts at preparing gelcast batches were unsuccessful due to the reactivity of Si metal in the aqueous slurry. Pretreatment of the Si powder by aging in water at room and at elevated temperatures, oxidizing in air at 600°C, and partially nitriding the powder at 1200°C were methods that were tried to passivate the powder surface and reduce reactivity. However, the new surface created during milling of the powder for batch preparation negated these surface treatments and resulted in gas evolution in the slurry.

Additional batches were prepared using isopropyl alcohol or a mixture of alcohol and water to reduce gas evolution at the Si surface. While this method helped during the milling process, gas formation was observed when the catalyst and the accelerator were added to the batch prior to casting.

A study was then undertaken to determine the effect of solution pH on gas evolution. It was found that gas formation was eliminated at low-solution pH levels (~pH 4). This indicated that Si gelcasting may be possible in an acidic system. One such system that is being considered utilizes acrylic acid (H_2C = CHCOOH) as the monomer and the lanthanum salt of acrylic acid as the crosslinker. The salt is prepared by dissolving La_2O_3 powder in acrylic acid, forming a trifunctional organometallic compound $[H_2C{=}CHCOO]_3La$. Aqueous 15% solutions of the monomer and crosslinker were prepared. The optimum monomer/crosslinker ratio, initiator level, and accelerator level were determined in a series of trials. It was found that good gels could be obtained at 80°C using a 7:1 ratio of monomer to crosslinker with 0.42% ammonium persulfate (AP) initiator and 0.21% TEMED accelerator. This system will now be evaluated with Si to see whether the outgassing problem can be eliminated.

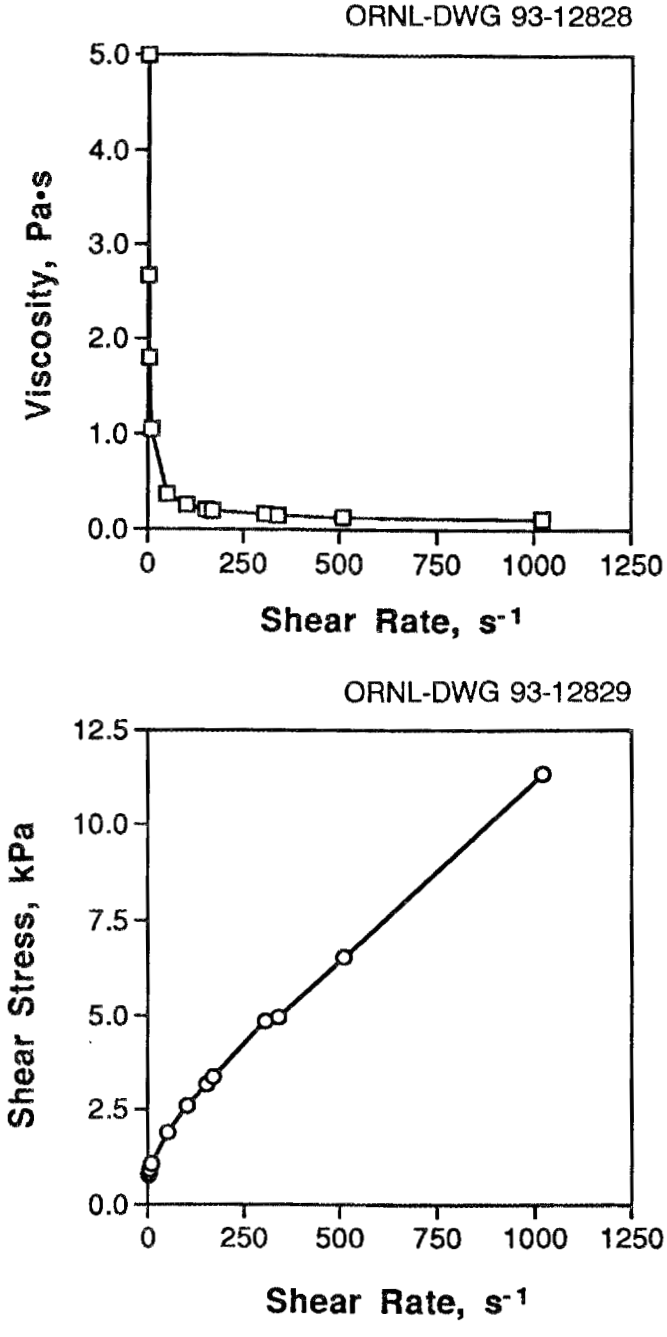

Fig. 3. The measured viscosity versus shear rate and shear stress versus shear rate relationships for a turbomilled methacrylamide monomer/methylene bisacrylamide 6:1 gel-casting slurry of 6 Y_2O_3/2 Al_2O_3 silicon nitride containing 45 vol % solids.

III. Alumina Gelcasting

The fracture surfaces of 4-pt. bend test bars described in an earlier report were examined using SEM. The examination revealed a uniform microstructure consisting of equiaxed grains approximately 2 μm in diameter. The fracture surface of a typical sample is shown in Fig. 4. The examination also showed a mixed fracture mode, with about 25% transgranular fracture.

An alumina batch was prepared using a MAM/MBAM mixture (9:1 ratio). The batch contained 55 vol % Reynolds RC-HP DBM alumina, a fine-particle-size, sinterable alumina containing 0.05 wt. % MgO. The gelcasting slurry was cast in thin plate molds, and the dried and debindered plates were fired at 1500° C for 4 h in air. The fired plates had a measured density of 99%. Four-point bend test bars were cut from the samples and had an average fracture strength of 451 ± 81 MPa. This is an excellent strength for sintered alumina, but the standard deviation needs to be improved.

A portion of this batch was also cast in the tensile rod mold and produced an excellent gelled casting as shown in Fig. 2.

IV. Alternate Gelcasting Systems - Gel Characterization

As was discussed in the last progress report, three gels (acrylamide, MAMPEG, and MAM-MBAM), were characterized by three rheometer vendors. Based on their experimental reports, a purchase specification for an automated rheometer was prepared. Since the rheology of gels filled with ceramic powders will also be investigated, a high torque (200 mN•m) was specified. The specification has been approved and sent to the three vendors to bid on supplying the rheometer.

A large controlled-temperature/humidity chamber has been delivered and installed. It provides a large workspace 0.5 m^3 (~19 ft^3) for drying gelcast parts and should have an approximate controllable combined temperature and humidity range of 25 to 95° C and relative humidity of 25 to 95%. The chamber is undergoing trial runs preparatory to further studies of the drying of gelcast ceramic parts.

Dried MAM-PEG gel was examined using thermogravimetric analysis (TGA) at a slightly lower heating rate of 4° C/min compared to 6° C/min reported earlier. Figure 5 shows the comparison of the data. The shape of the curves is similar. However, the curve at the slower rate gives sharper inflection points, which are better suited for determining the binder burnout schedule.

Pure gels were prepared from the three gelcasting systems: acrylamide, MAM-PEG, and MAM-MBAM. Similarly, 50 vol % alumina cylinders were gelcast in the three systems. Both the pure gels and the alumina green parts were dried at controlled relative humidity and room temperature. The dried gels and the alumina green parts were pyrolyzed in a Mettler TGA Model T-60, specially modified to serve as a temperature program reactor, from room temperature to 800° C at 4° C/min. The flue gas was passed into a UTI-100 quadrapole mass spectrometer for gas analysis.

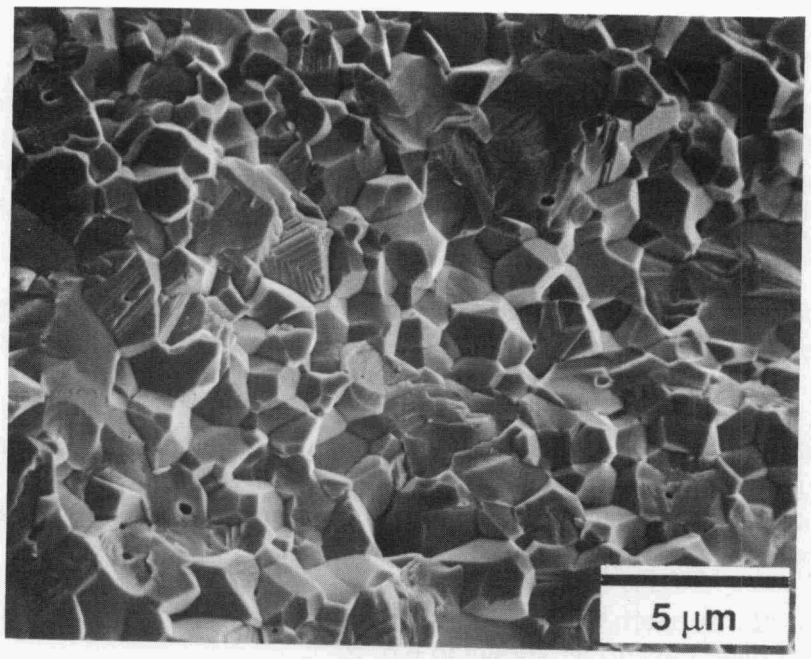

Fig. 4. Fracture surface of 4-point bend test specimen of gelcast RC-HP DBM Al_2O_3 fired at 1500° C for 4 h showing uniform grain structure and mixed-mode fracture.

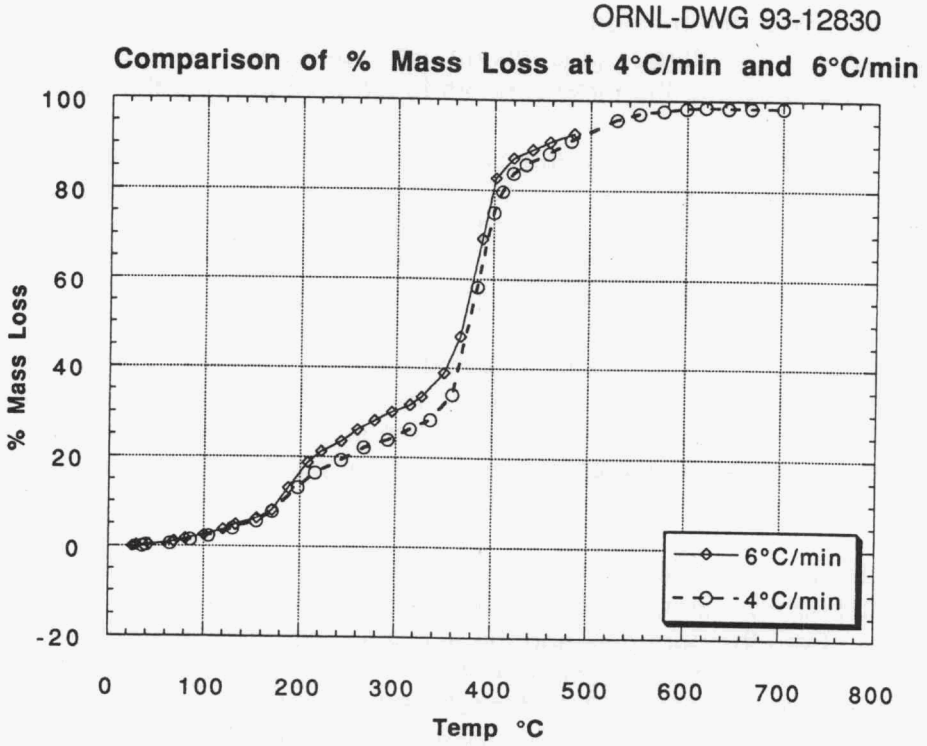

Fig. 5. A comparison of the mass loss of two samples of methacrylamide monomer/polyethylene glycol dimethacrylate gel during thermogravimetric analysis. One sample was heated at a rate of 6° C/min and one sample at 4° C/min.

The TGA data for the pure gel and the green part for each gelcasting system were compared by plotting them on the same graph. In all three systems, the green parts lost only 4 to 5 % of their weight, the dried gel serving as binder; the gels were completely pyrolyzed. The green bodies commenced weight loss just above room temperature and lost all the weight at about 500° C. The weight loss for the pure gels commenced around 100° C and was not complete until temperatures above 600° C. Figure 6 shows the burnoff for the MAM-MBAM system, which typifies the trend discussed above.

The data from the mass spectrometer showed that the pure gels eluted similar mass species at about the same temperatures. The same species at much lower concentrations also came off the green parts but at slightly lower temperatures than the pure gel. Figures 7 and 8 show, respectively, the mass species eluted for pure MAM-PEG gel and the green part in the same system. As Figure 7 shows, the graph for pure gels can be divided into three regions: room temperature to about 250° C, 250 to 450° C, and above 450° C. Below 250° C, only bound water is eluted with two peaks both above 100° C. In the intermediate region, the gel decomposes and small

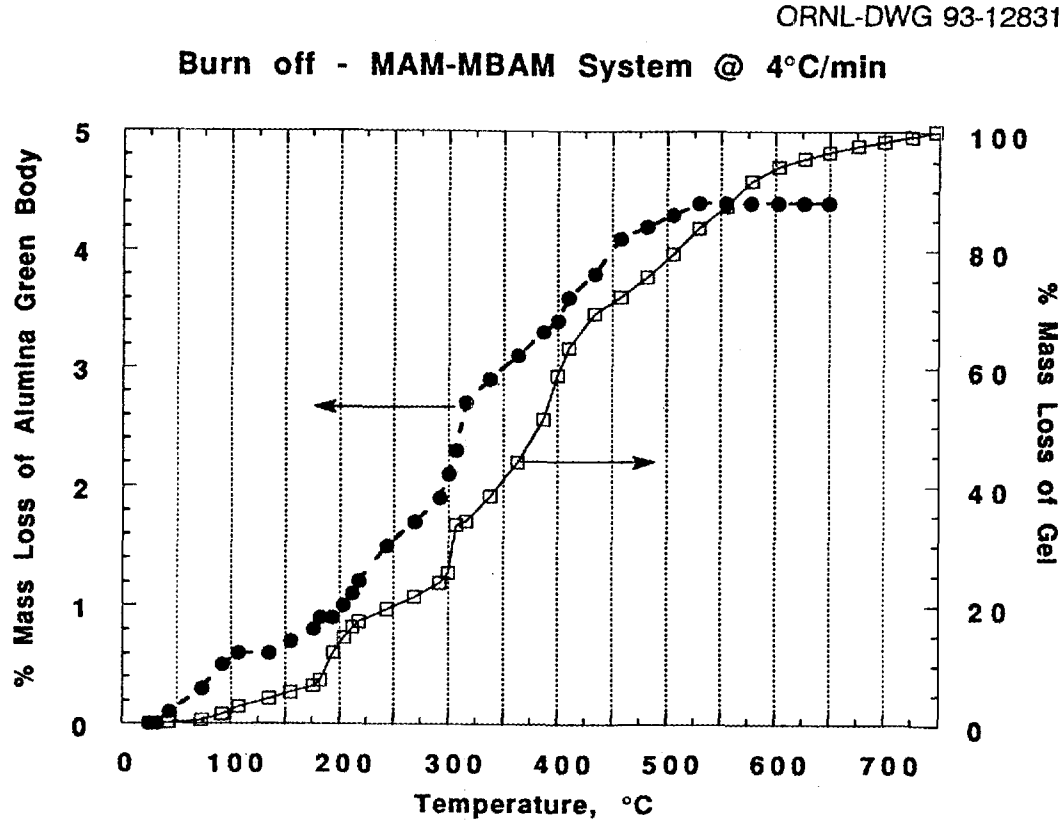

Fig. 6. A comparison of the mass loss during thermogravimetric analysis of two samples: pure methacrylamide monomer/methylene bisacrylamide gel and an alumina green body gelcast in the methacrylamide monomer/methylene bisacrylamide system.

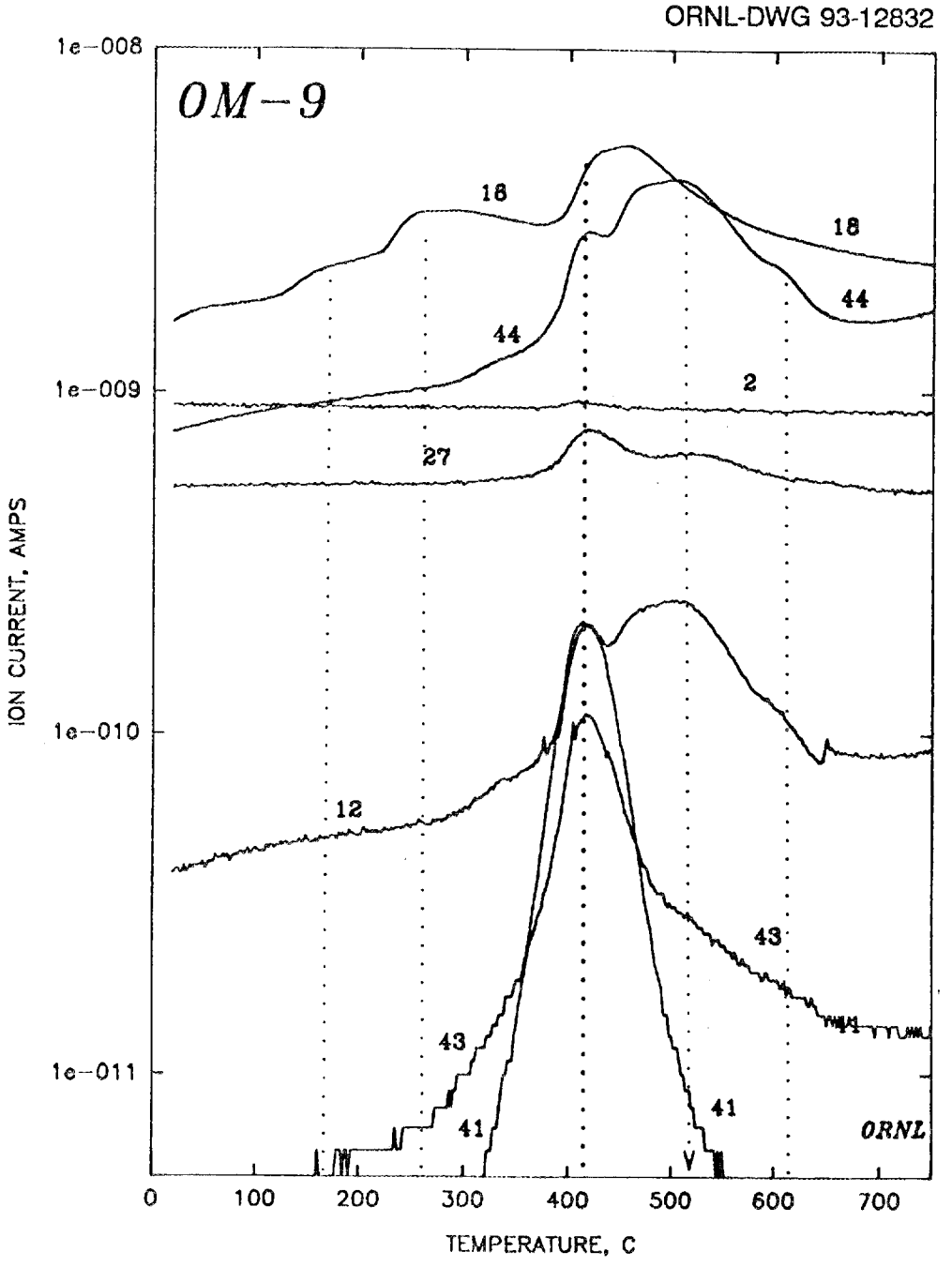

Fig. 7. Pyrolysis products of the pure methacrylamide monomer/ polyethylene glycol dimethacrylate gel sample. Digits on curves indicate the mass of the detected species.

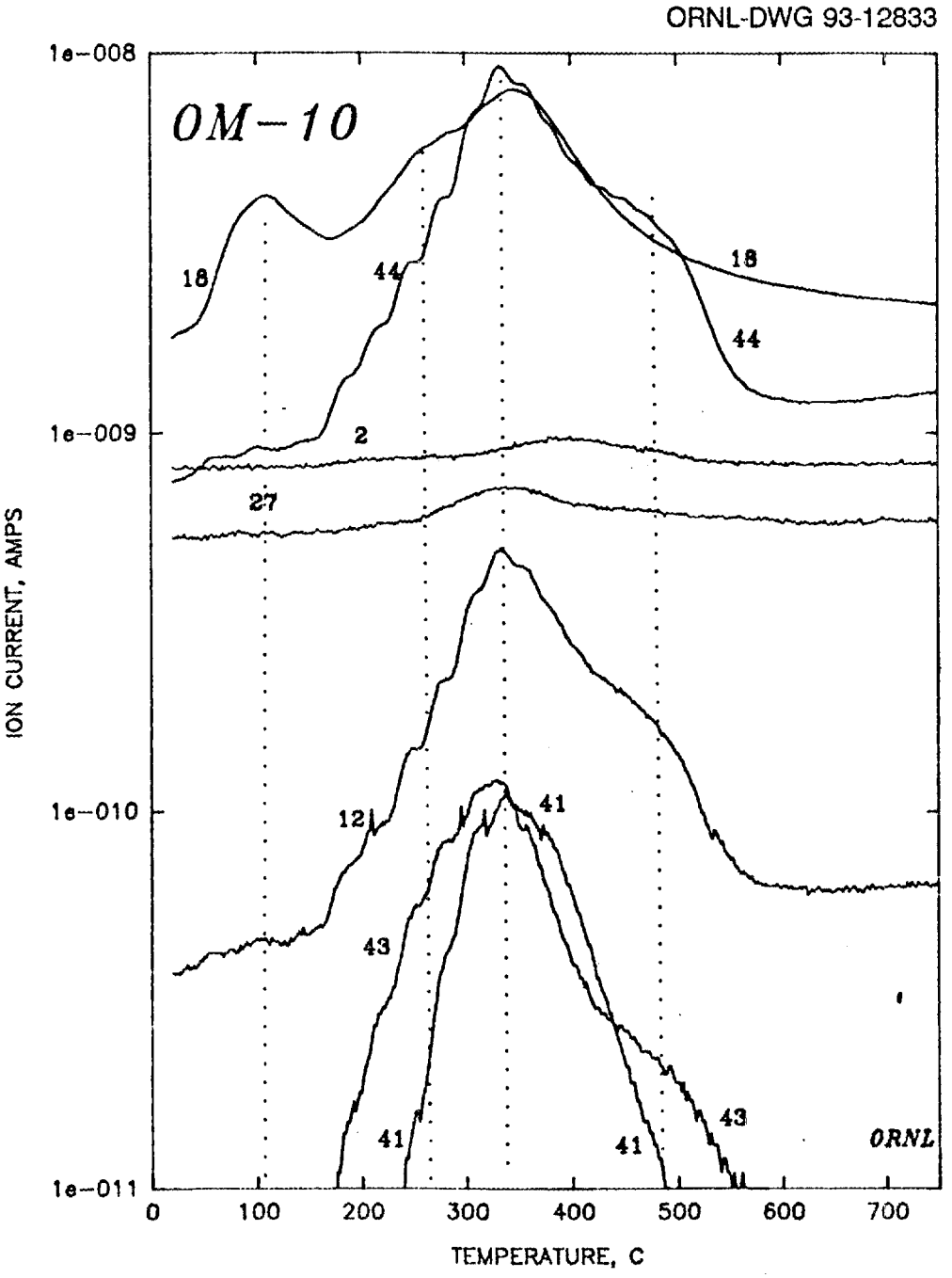

Fig. 8. Pyrolysis products of the alumina green body which was gelcast in the methacrylamide monomer/polyethylene glycol dimethacrylate system. Digits on curves indicate the mass of the detected species.

hydrocarbon species are eluted. In the region above 450°C, there is combustion in addition to decomposition as both water and carbon dioxide are eluted and show peaks, in addition to the hydrocarbon species peaks.

Figure 8, which typifies the data for the green parts, falls into two parts, below and above 150°C. Below 150°C, only water which was retained in the incompletely dried green body is eluted, and the peak is at 100°C. Above 150°C, the multiple decomposition peak temperatures were nearly the same for all of the species (with the major decomposition peak at ~340°C) indicating that decomposition and combustion occur concurrently. There is usually a sharp, large species-12 peak. This is not pure carbon but a measure of other hydrocarbons (and even carbon monoxide) that contain carbon and were not specifically being monitored.

V. Garrett Cooperative Research and Development Agreement (CRADA)

As a follow-on to the previous CRADA between ORNL and Garrett Ceramic Components (GCC), work on the gelcasting of silicon nitride components is continuing under an extension of the CRADA. Research under the previous agreement demonstrated the feasibility of using gelcasting to produce complex-shaped components (automotive turbocharger rotors) using GCC's GN-10 Si_3N_4 composition. Mechanical property testing showed that gelcast Si_3N_4 could be produced that had mechanical properties comparable to GCC's slipcast Si_3N_4. Under the new agreement, ORNL is incorporating one of the new gelcasting chemical systems that has improved environmental, safety, and health ratings. (Previous work was done in the acrylamide system. The acrylamide monomer has a high toxicity rating.) Work focuses on achieving low-viscosity slips containing high volume fractions of Si_3N_4 powder and on complete removal of the organic materials during binder burnout. GCC is firing gelcast samples using glass-encapsulation hot-isostatic pressing and measuring the mechanical properties.

Two gelcasting trial batches were prepared using the GCC GN-10 silicon nitride formulation. The batches were to compare two of the new gelcasting systems and to determine the best initiator and accelerator levels to obtain acceptable gels. The two systems were the MAM/MBAM and the MAM/PEG systems, which have been described in some detail in earlier reports. Both of these systems appear to be good alternatives to the acrylamide system.

The 200-ml batches were prepared with approximately 45 vol % solids loading. Mixing was done by hand and on the KS-500 shaker table. Daxad 30 and pH control using ammonium hydroxide were used to improve particle dispersion. The AP initiator level was varied from 0.02 to 0.36 vol %, and the TEMED accelerator level was varied from 0.04 to 0.36 vol %. The samples were placed in an oven at 45°C to gel. A qualitative evaluation of the gels that were formed indicated that the best gel was the MAM/PEG composition with 0.09 vol % AP and 0.09 vol % TEMED.

A large gelcasting batch (1500 ml) was prepared using the previously determined composition. To obtain complete dispersion of the ceramic powders in the solution, the batch was mixed using a turbomill. The resulting slurry was very fluid and deaired

well under vacuum. Addition of the AP and TEMED to the deaired slurry resulted in spot gelation (the formation of gelled lumps) in the slurry. This is an undesirable characteristic and has been shown in the past to result in inhomogeneities in the fired material. This difference in response to the level of initiator and accelerator additions between the test batches and the large batch appears to be due to a difference in the extent of powder dispersion. The small, hand-mixed batches were dilatant (shear thickening), while the turbomilled batch was thixotropic (shear thinning). These differences in the rheology of the slurries indicate a clear difference in the dispersion.

A second 1500-ml batch of GN-10 in MAM/PEG was prepared to reevaluate the initiator and accelerator levels that would be required in the turbomilled batches. From a series of samples tested at 45°C, it was found that 0.02 vol % AP and 0.01 vol % TEMED additions resulted in the best gel.

Having determined the additions needed to obtain a good gel with the turbomilled batch, a new batch was prepared for gelcasting based on these findings. Again, the batch consisted of 45 vol % GN-10 in a MAM/PEG solution. The batch was deaired under vacuum, and the initiator and accelerator were added. A portion of the batch was cast in a flat-plate mold using our normal procedure of pouring the slurry into the open top of the mold. Another portion of the slurry was cast into a new mold, which is capable of being evacuated and then filled from the bottom. The vacuum molding procedure can eliminate trapped air in the mold and also eliminates the possibility of entrapping air in the turbulent stream of a poured slurry, as in the conventional casting method. The vacuum casting mold produces a simple thick plate. The cast samples were dried and are being examined to determine whether or not the vacuum casting was beneficial in eliminating flaws from the cast part.

An additional gelcasting batch consisting of 45 vol % GN-10 composition in a MAM/PEG (3:1) solution was prepared. The batch was deaired under vacuum, and the initiator and accelerator were added. This batch was cast in the new tensile rod mold to evaluate the ease of filling and gelling in an evacuated mold. The cast parts showed excellent molding characteristics but suffered from the same distortion problems observed with other materials (see Sects. I and III) during drying due to inadequate stiffness of the gelled part. A GN-10 tensile rod specimen is shown in Fig. 2. Modifications to improve the process are being evaluated.

The remaining T-25 turbocharger rotor molds (provided by GCC) are being prepared for casting. A special casting setup has been designed to allow the molds to be bottom filled inside an evacuated chamber. This procedure should help to minimize the possibility of forming surface defects and non-filled areas in the thin sections of the rotor fins.

Status of milestones

On schedule.

Publications and presentations

None.

Processing Science for Reliable Structural Ceramics Based on Silicon Nitride

F. F. Lange and D. S. Pearson (University of California)

Objective/scope.

We are trying to increase the understanding of the role of interparticle forces in the processing of ceramics. The effects of electrolyte addition and pH changes on the rheological properties of dispersions, the kinetics of pressure filtration, and the mechanical properties and microstructure of the resulting bodies will be compared to each other and to existing models of interparticle forces (*i.e.* , DLVO theory).

Technical Progress.

Two approaches were taken to improve the processability of silicon nitride slurries. Both methods attempt to produce short range repulsive potentials between particles, i.e., make coagulated slurries. It has been demonstrated for alumina slurries that this type of repulsion produces suspensions which can be consolidated to high relative densities and do not mass segregate. Coagulated alumina slurries are produced by adding salt to dispersed slurries. Bodies consolidated from these slurries are plastically deformable and thus will not crack due to the removal of the forming stress and may be reformed after consolidation (while wet) to complex shapes.

The first approach is to change the surface chemistry of the silicon nitride to mimic alumina which is known to coagulate. Silicon nitride powder can be coated in two methods. The first relies on precipitation of an aluminum salt onto the particle surface. The reaction involves heating a suspension of the powder, an aluminum salt (e.g. aluminum nitrate) and urea. Urea decomposes at approximately 80 C raising the pH of the slurry and forcing the aluminum to precipitate. The second method reacts aluminum alkoxide (e.g. aluminum sec-butoxide) directly to the silanol groups of the silicon nitride surface. The reaction occurs spontaneously at room temperature. By slowly adding water to the nonaqueous slurry, a thicker layer of alumina is built up because the water reacts with the alkoxide bound to the surface which is then capable of reacting with more alkoxide.

We have pursued both procedures in the past and found that uniform coatings of the surface are not obtained. We had hoped that by building up thicker layers of alumina we would improve the behavior of the powder. Although we can change the isoelectric point of the coated silicon nitride from pH 5.5 to pH 9, i.e. the same as alumina (see figure 1), the powder packs to the same relative density as the as-received powder. Measurements of the slurry viscosity as a function of shear rate indicate that the addition of salt does coagulate dispersed slurries, very similar to the effect seen on alumina slurries. Figure 2 shows that slurries with added salt at ph 4 have lower viscosities than slurries that have been flocced at pH 9. This is contrary to the prediction of DLVO theory and a primary indication of the presence of a short range repulsive potential. The consolidated bodies are elastic whether the powder is alumina coated or as-received.

Figure 1 Shows the zeta potential of two batches of alumina coated silicon nitride which display an iso-electric point identical to that of alumina.

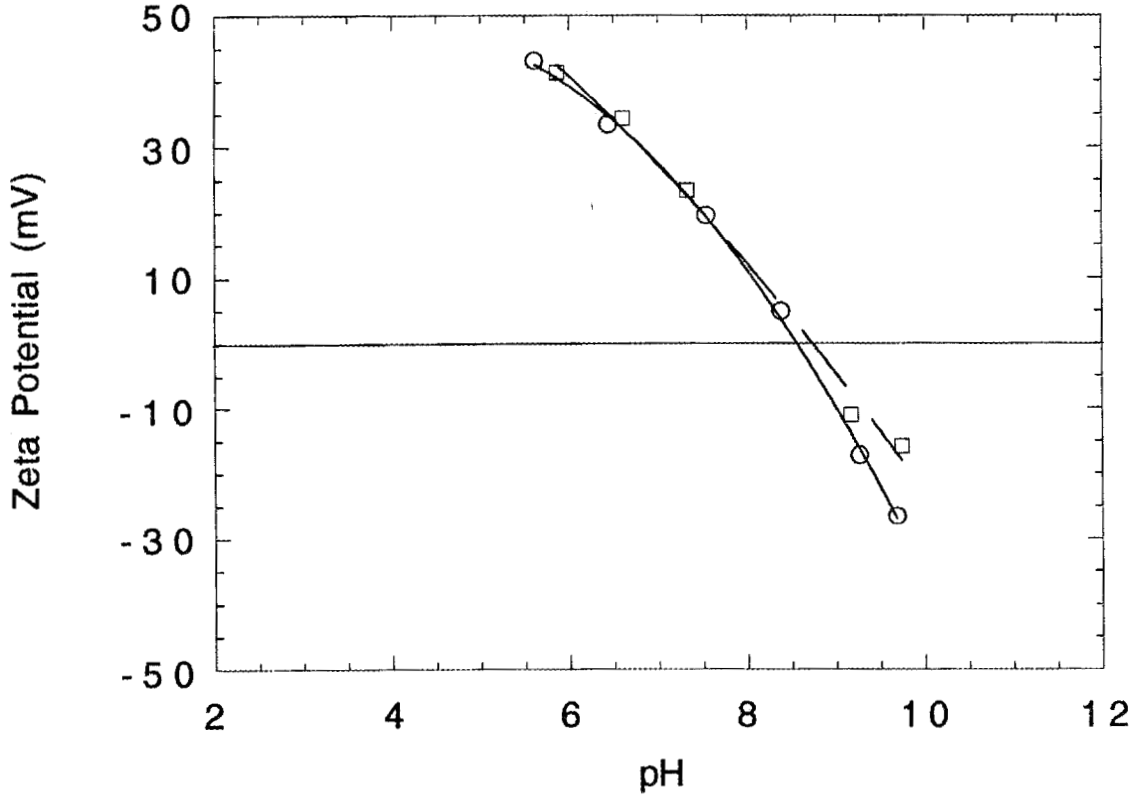

Figure 2 Viscosity of precipitated powder slurries at pH 4 unless noted.

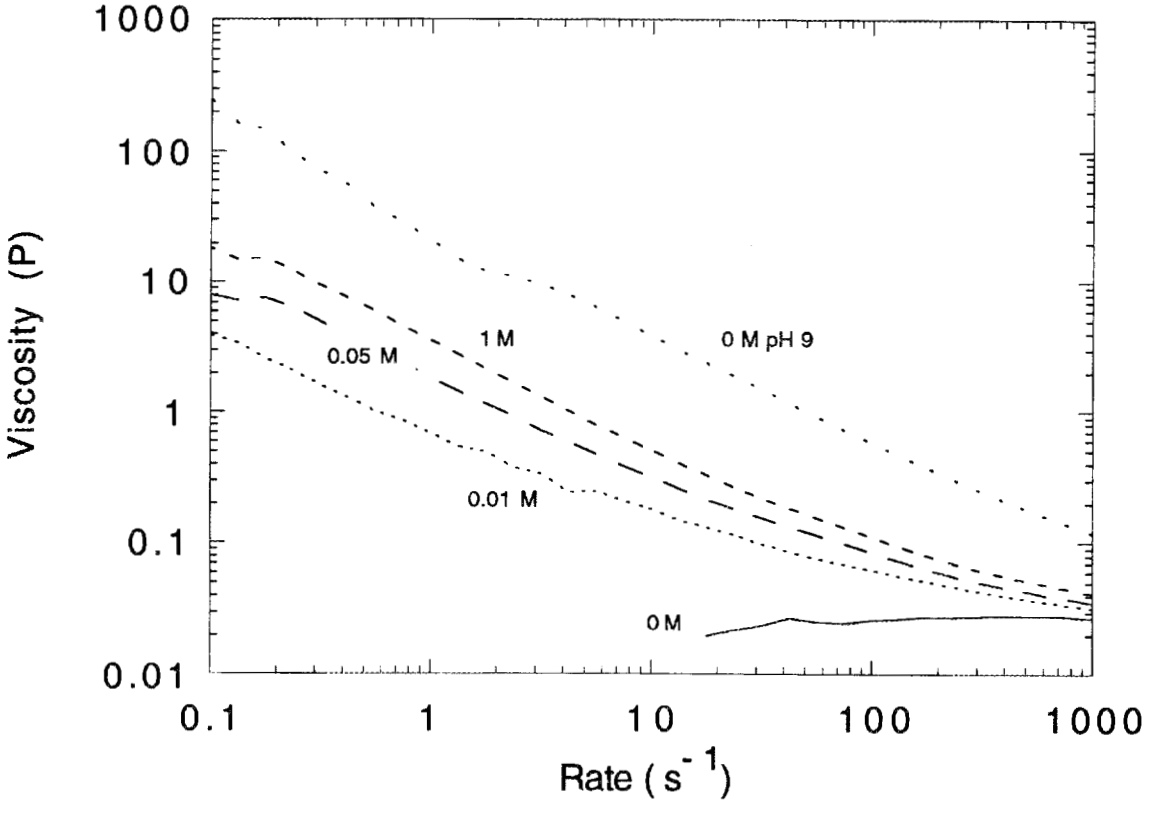

The second approach to producing short range repulsive potentials in silicon nitride is to use different electrolytes. Indifferent electrolytes such as NH_4Cl used to coagulate alumina slurries are believed to surround the particle surface and therefore prevent particle-particle contact. The addition of indifferent electrolytes to silicon nitride slurries produces short range repulsive potentials (as seen by packing density and viscosity measurements) however the consolidated bodies are elastic. We conjectured that the ions surrounding the particles are pushed off during slurry consolidation, that is, the short range repulsion does not persist in the consolidated body. Following this reasoning, potential determining ions were added to slurries because they are more strongly bonded to the particle surface. The first such electrolyte added was ammonium citrate tri-basic. The citrate ion changes the isoelectric point of alumina from pH 9 to pH 3. The iep of silicon nitride is slightly changed from pH 5.5 to 4.5 as seen in figure 3. Dispersed alumina slurries with ammonium citrate are coagulated and behave similarly to slurries with ammonium chloride added. Besides the obvious changes in processing pH (namely coagulated slurries are processed at pH 8 when ammonium citrate is present), the yield stress of alumina slurries is lower when ammonium citrate is added. This is true of slurries in both the flocced and coagulated states. It appears that the much larger citrate ion produces a larger short range repulsion than the chloride ion.

The addition of ammonium citrate to silicon nitride slurries coagulates the slurries as expected. No yield stress measurements have been done to show if there is a difference between the strength of the repulsion due to citrate versus chloride ions because the hoped for effect does not occur, namely, the short range repulsion does not persist during packing. Consolidated bodies are elastic regardless of the presence of the citrate ion. Since the positive site charge density of silicon nitride is less than for alumina at the pH where the slurries were coagulated, we thought that the number of citrate ions bonding to the silicon nitride was probably less than for the alumina. The silicon nitride surface can be highly negatively charged at high pH. Consequently, large potential determining cations were found for the silicon nitride slurries.

Tetraethylamine and tris (2-aminoethyl) amine are large potential determining cations. TEA changes the isoelectric point of silicon nitride from pH 5.5 to pH 6.5 while TAEA changes the iep from pH 5.5 to pH 9.5. Viscosity measurements indicate that both ions produce short range repulsive potentials in silicon nitride slurries. Figure 4 shows the effect with TEA. Neither ion produces consolidated bodies that are plastically deformable, i.e., the short range repulsive potentials developed do not persist during packing.

As alluded to earlier, yield stress measurements seem to be the most sensitive method of measuring the strength of the short range repulsion. We have found significant differences in yield stress in alumina slurries with added ammonium citrate that might appear insignificant in simple viscosity measurements. This allows us to investigate the effect of ion size on the strength of the interparticle repulsion. We have already observed that

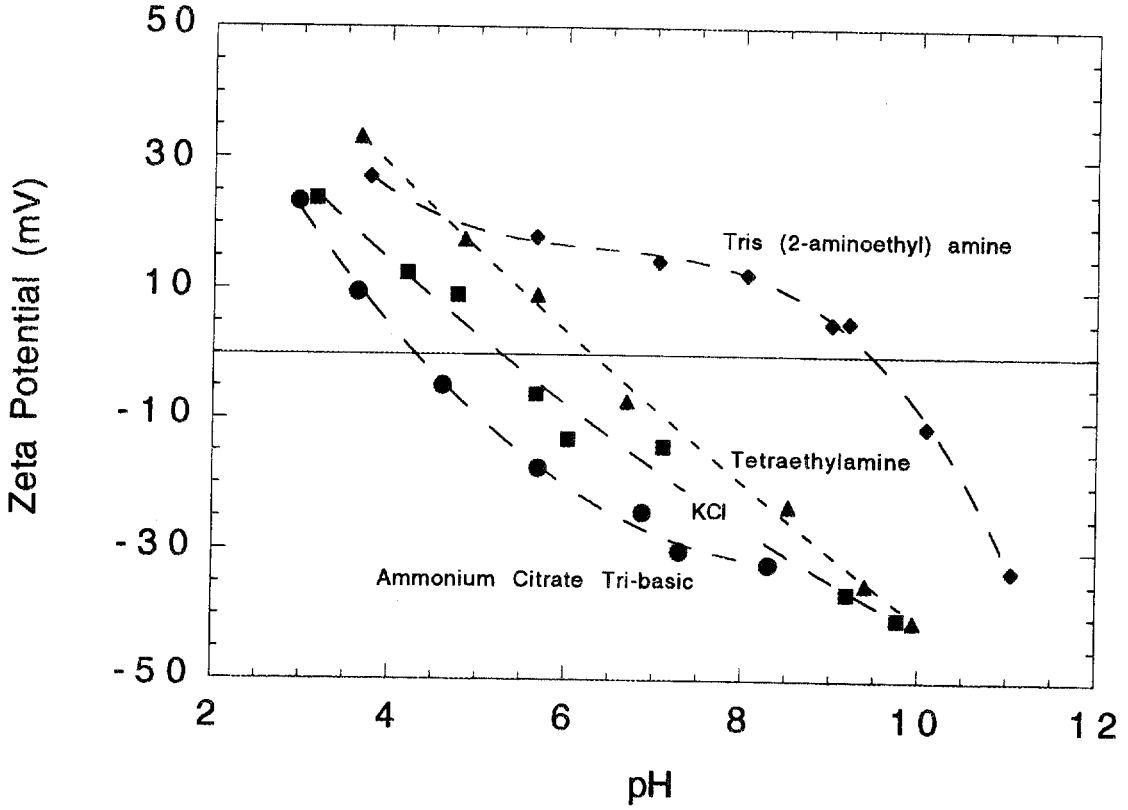

Figure 3 The effect of ion type on the isoelectric point.

Figure 4 Silicon nitride slurries at pH 10 (unless otherwise noted) with tetraethylamine showing that adding salt produces a short range repulsion between particles.

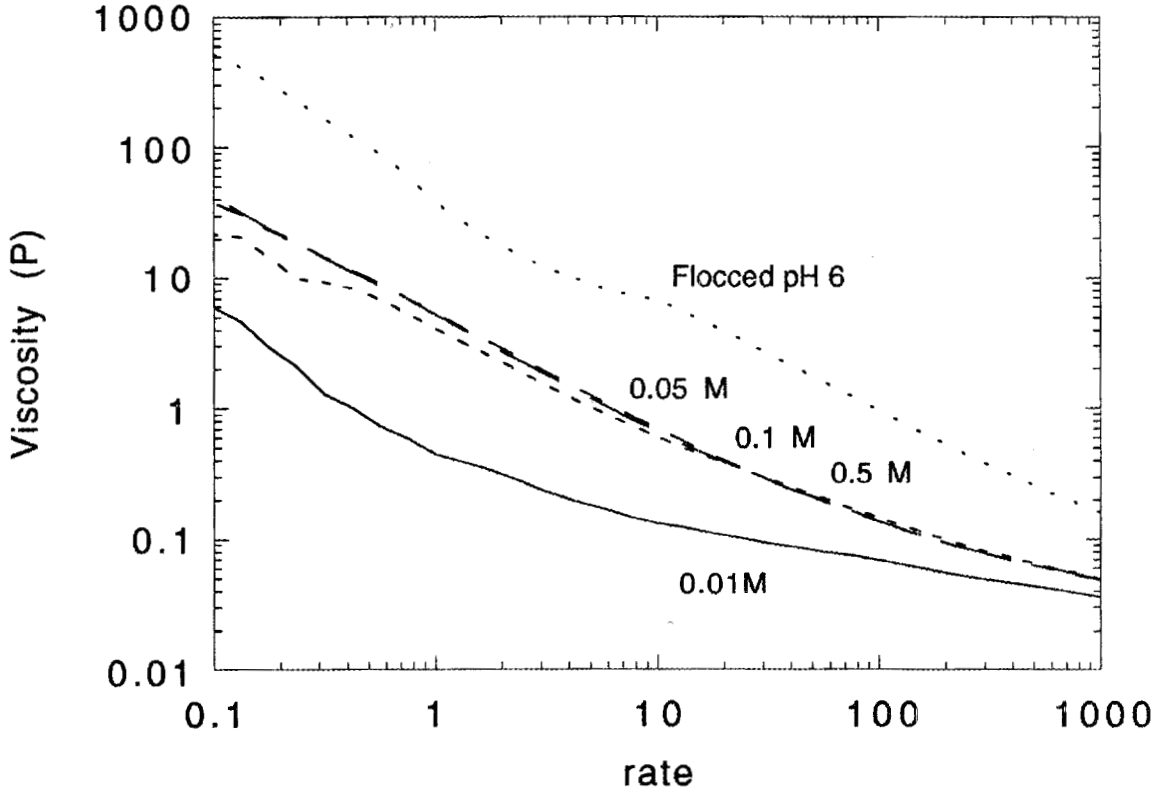

alumina slurries with 0.3 M ammonium citrate appear flocced at pH 3 (the new isoelectric point) as seen in figure 5. This amount of ammonium citrate is approximately enough to cover the particle surface with a monolayer. It is about equal to the critical coagulation concentration. When more ammonium citrate is added, the yield stress decreases indicating that several layers of citrate ions are building up to lower the yield stress. The yield stress measurement technique enables us to measure the strength of the short range repulsion giving us insight as to the function of the salt in the process of coagulation.

Communications/Visits/Travel

None.

Problems Encountered

None.

Publications.

None.

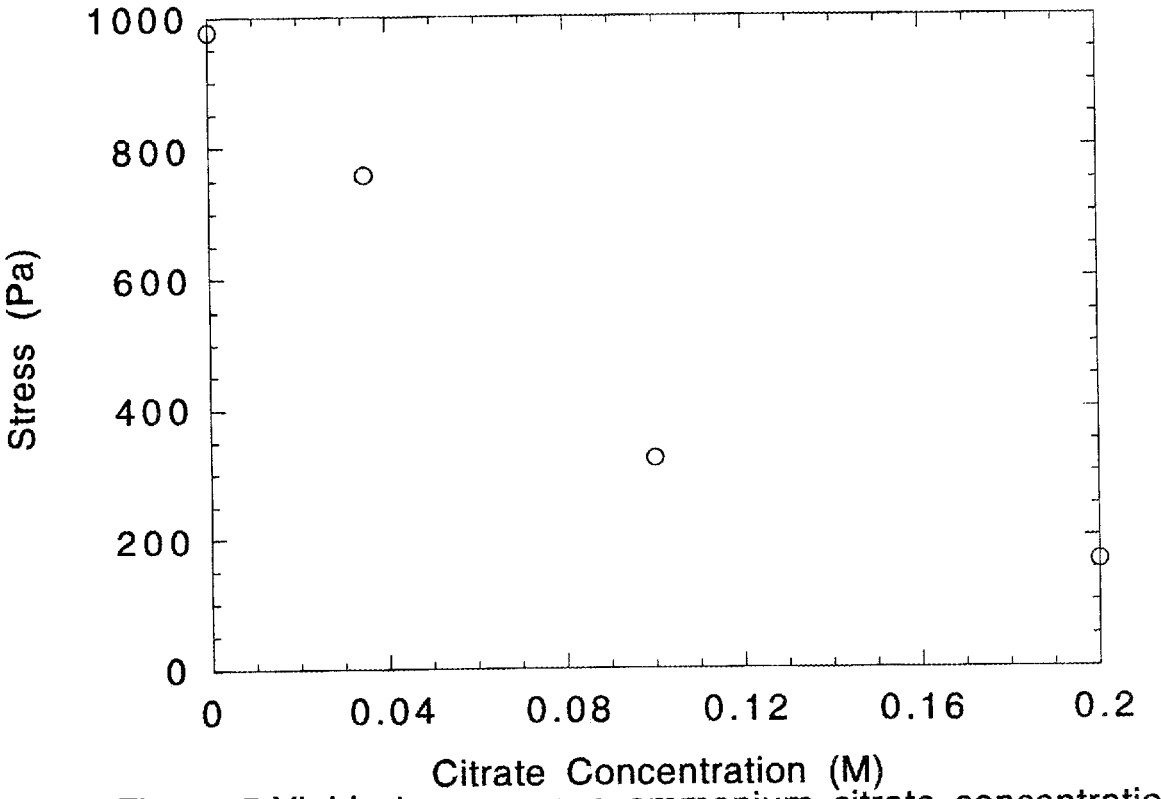

Figure 5 Yield stress versus ammonium citrate concentration showing a decrease in yield stress with increasing salt. All slurries are at pH 3 except 0M at pH 9.

1.2 CERAMIC COMPOSITES

1.2.2 Silicon Nitride Matrix

Optimization of Silicon Nitride Ceramics

K. J. Lee, W. W. Yao and T. Y. Tien (The University of Michigan)

Objective/Scope

To develop processing methods to optimize strength, toughness and creep resistance of monolithic silicon nitride ceramics. Silicon nitride ceramics with fiber-like β-Si_3N_4 grains will have higher fracture strength and toughness and better creep resistance. The fiber-like structure can be obtained by sintering the silicon nitride ceramics at high temperature under a nitrogen over-pressure. The mechanical properties can further be improved by controlling the size and the aspect ratio of the fiber like β-Si_3N_4 grains and the composition and nature of the grain boundary phase(s). The major goal of this project is to develop monolithic silicon nitride ceramics with optimum mechanical properties.

Technical Progress:

Previous results indicated that strength and toughness depend on the size and aspect ratio of the β-Si_3N_4 grains. This investigation contains two part: 1) Effect of chemistry of the sintering aid used on the morphology of the β-Si_3N_4 grains and 2) The effect of starting powder on the morphology of the β-Si_3N_4 grains.

Sintering additives selected for this study was MgO, CaO and Y_2O_3 and any combination of these compounds. Compositions were prepared and sintered. Grain size measurement will be performed in the next period.

Three different silicon nitride powders from Ube were selected for this study. These three different powders have the same β-Si_3N_4 content (5%) but with different particle sizes. Compositions were prepared and sintered. Grain size measurement will be performed in the next period.

Status of Milestones

On schedule

Communications/Visit/Travel

None

Problems Encountered

None

Characterization of Grain Boundary Phases in Silicon Nitride Ceramics

I. M. Peterson and T. Y. Tien (University of Michigan)

Objective/Scope

The objective of this investigation is to develop silicon nitride ceramics with high flexural strength, high fracture toughness and superior creep resistance. The fiber-like structure of the β-Si_3N_4 grains can be obtained by sintering the silicon nitride ceramics at high temperature under high nitrogen pressure. The composition of the sintering additives will affect the microstructural development, grain boundary characteristics, and hence the mechanical properties. The grain boundary phases have never been synthesized separately and their properties have never been studied. The goal of this project is to synthesize and characterize the grain boundary phase and to understand the relationships between the nature of the grain boundary phase and the properties of silicon nitride ceramics. It is believed that with a thorough understanding of these relationships, ceramics with optimum mechanical properties can be obtained.

Glass forming compositions in the system Y,Si,Al,Mg/N,O were selected for this study. Compositions investigated for previous reports were in the compatibility triangle Si_3N_4, cordierite, N-phase. N phase has a composition $2Si_2N_2O{:}MgAl_2O_4$. Both cordierite and N-phase have thermal expansion coefficients lower than that of silicon nitride. In this report, thermal expansion coefficients of glass compositions in the YAG/cordierite/ Si_3N_4 region are reported.

Technical Highlights

The glasses were synthesized from the starting powders, Al_2O_3, Si_3N_4, SiO_2, Y_2O_3 and MgO. They were mixed by hand with isopropyl alcohol with an agate mortar and pestle, dried, and cold pressed into pellets. The pellets were melted at 1650°C, for two hours under 10 atmospheres of N2. The samples were quenched by turning off the power to the furnace, and cooled to room temperature in approximately 3 hours. . The presence of crystalline phases was determined by x-ray diffraction. Only samples which did not show any crystalline peaks were used to determine the thermal expansion coefficient and Tg of the glass .

The thermal expansion coefficient was measured from room temperature to 1200°C using an alumina single rod dilatometer calibrated with a fused silica standard. The value of the thermal expansion coefficient form room temperature to 515°C was calculated. The Tg was determined from the dilatometer trace.

The thermal expansion coefficient of the glass can be calculated from the weighted sum of the thermal expansion coefficients of the constituents of the glass, as expressed in equation 1:

$$\alpha = \sum \alpha_i X_i \qquad 1$$

where X_i is the mole fraction of the constituent and α_i is the empirically determined thermal expansion coefficient.

Using previously reported αi values for MgO, Al_2O_3 and SiO_2, αi values for Si_3N_4 and Y_2O_3 and AlN were determined. The αi values are listed in Table I. Figure 1 shows the calculated and measured values for a wide range of Y-Mg-Si-Al-O-N glasses.

Figure 2 shows the glass transition temperature as a function of silicon nitride content for cordierite-based glasses. The glass transition temperature can be expressed in equation 2:

$$Tg\ (°C) = 826 + 9.07\ (Wt\ \%\ Si_3N_4) \qquad 2$$

Status of Milestones
On schedule

Communications/Visits/Travel
None

Problems Encountered
None

Publications
None

TABLE I

	This study	Takahashi[1]	Appen[2]
SiO_2	3.8		3.8
Al_2O_3	3.1	3.1	
Y_2O_3	16.0	**	
MgO	6.0	6.0	6.0
Si_3N_4	- 5.0		
AlN	- 1.5		

** **Takahashi SrO 16**
CaO 14.5

1) Takahashi, K: J. Soc. Glass Technol. 37, 3N (1953)
2) Appen, A.A.: Silikattechn. 3 , 113 (1953)

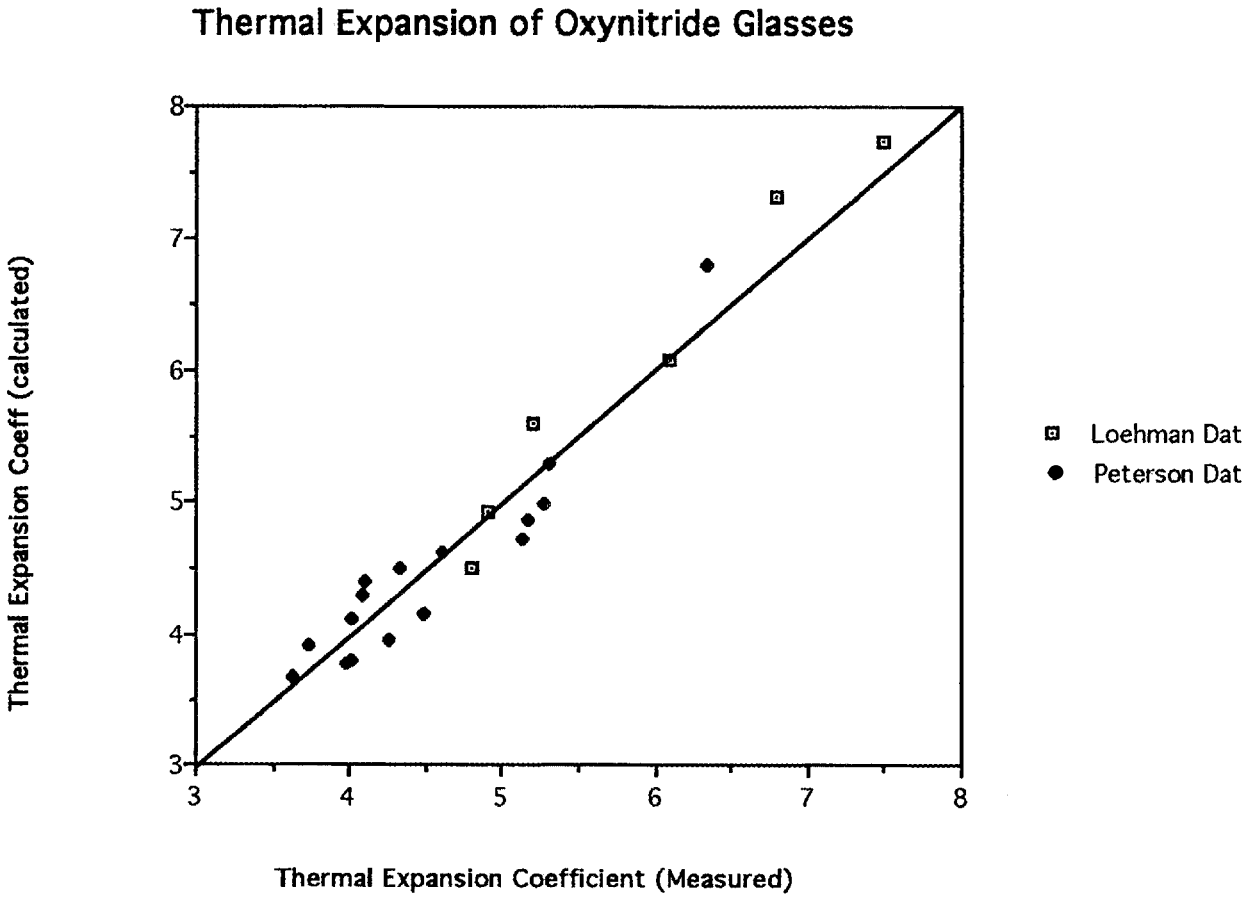

Loehmann data after Loehmann, R.E. J. Am. Cer. Soc 62 491-4 1974
Figure 1

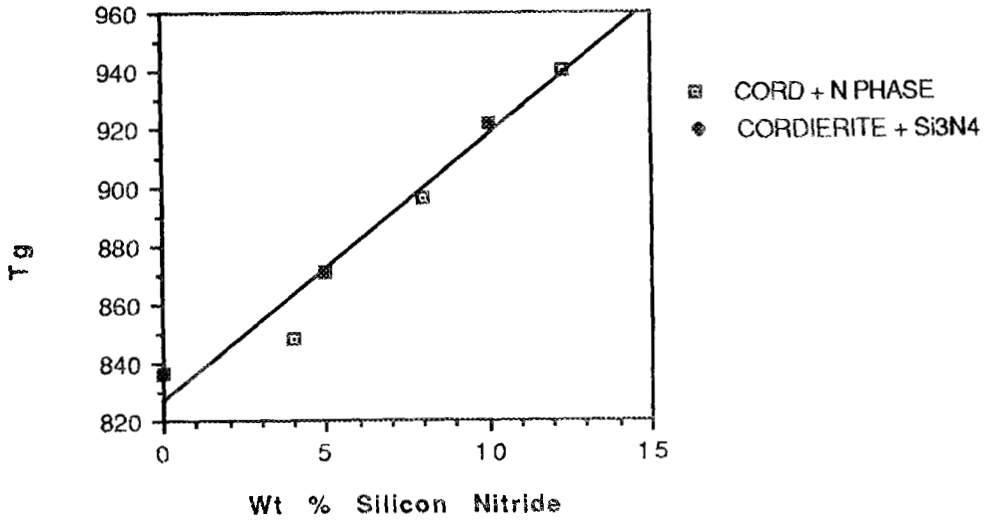
960
940
920
900
880
860
840
820
Tg
0
5
10
15
Wt % Silicon Nitride
CORD + N PHASE
CORDIERITE + Si3N4

Figure 2

Reaction Sintering of α'/β' SiAlON Ceramics

K. Houser and T. Y. Tien (University of Michigan)

Objective/Scope

The objective of this project is to develop processing techniques to obtain silicon nitride ceramics with a controlled grain morphology for optimum mechanical properties at room temperature as well as at high temperatures. Silicon nitride ceramics exhibit high fracture strengths and high fracture toughness when the microstructure contains fiber-like β'-SiAlON grains. Obtaining these fiber-like β'-SiAlON grains depends upon the temperature, nitrogen pressure and the grains' interaction with other phases present. Ideally, if the equilibrium conditions between the phases present are understood as well as the kinetics controlling the growth of these fiber-like grains, one could ultimately tailor a silicon nitride ceramic's microstructure for certain mechanical properties. This project will focus on these structure-property relationships for one composition in the Si,Al,Y/N,O system.

Background:

This project will be working with compositions from the α' + β' SiAlON region on the α'-SiAlON plane in the Si, Al, Y/N, O system. The α' plane is defined by the equation $Y_{m/3}Si_{12-(m+n)}Al_{m+n}O_nN_{16-n}$ and is illustrated in Figure 1. The β' phase is a subtituional solid solution where the (Si-N) is replaced by (Al-O). The α' phase is a stuffed derivative of the α-Si_3N_4 phase that can incorporate some of the yttrium atoms into the unit cell as interstitials. The formation of these solid solutions reduces the amount of residual glass at the grain boundaries, which in turn allows for better high temperature mechanical properties.

There are two competing processes occurring during the sintering of these compositions; the transformation of the initial α-Si_3N_4 to β'-SiAlON and α'-SiAlON and the densification of the ceramic. Both of these processes depend upon the presence of a transitional liquid phase. If the transformation rate is faster than the densification process, the transitional liquid will be consumed by the solution/re-precipitation mechanism of transformation, and densification by liquid phase sintering will stop. Therefore understanding the kinetics of these two processes is necessary to obtain fully dense two phase Si_3N_4 ceramics. Once fully dense ceramics have been obtained, a controlled study of the effect of temperature and time on the growth of the fiber-like β'-SiAlON grains and the α'-SiAlON grains will be performed.

Representation of the Y-SiAlON system

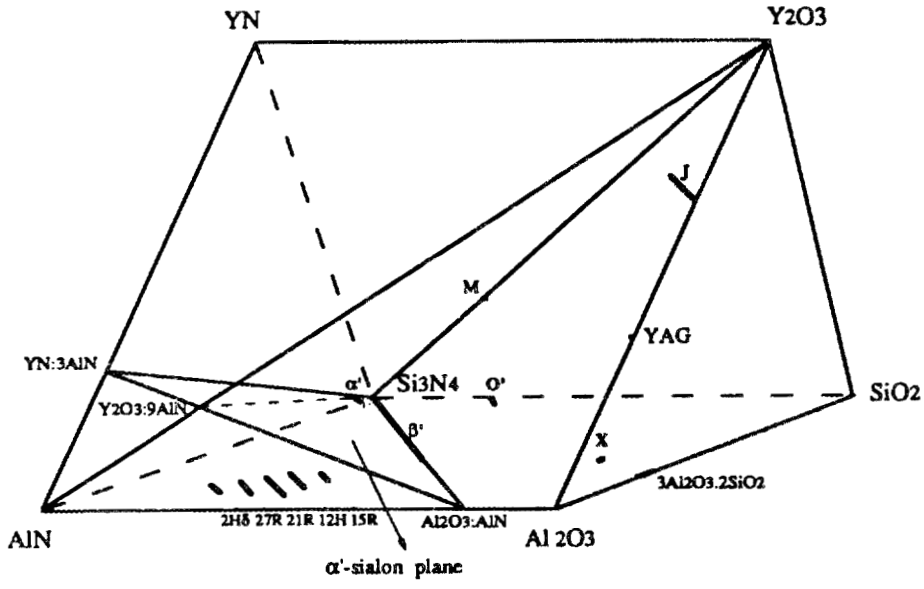

(a)

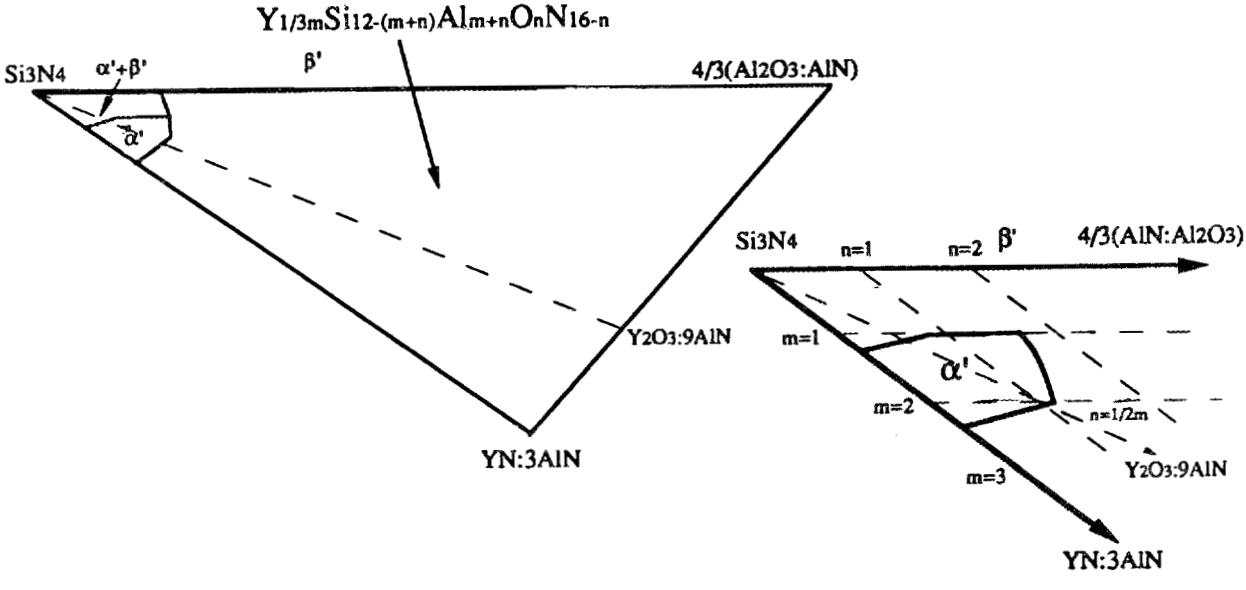

Figure 1: The α'-SiAlON plane

Technical Highlights:

The initial compositions used in this study followed the Si_3N_4-Y_2O_3:9AlN join in the Si,Al,Y/N,O system. (See Figure 2) In order to obtain the composition $Y_{m/3}Si_{12-(m+n)}Al_{m+n}O_nN_{16-n}$ where m=0.3, n=0.15, amounts of Si_3N_4, Al_2O_3, AlN, and Y_2O_3 were mixed in the proper ratios. These compositions were sintered in 10 atm N_2 at 1900°C for 2 hours. Results of x-ray diffraction (XRD) showed two phases present--both α' and β' SiAlON. However the densities of the samples were under 3.00 g/cm^3, which is less than 90% of the theoretical density. In order to improve the density of these samples it was determined that the percentage of oxides must be increased.

Further compositions were made following the m=0.3 tie line, varying n from values of 0.5 to 1.75. As the value of n increased, the percentage of AlN and Al2O3 increased. (See Figure 2.) The compositions were gas pressure sintered under the same conditions as listed above. XRD results showed that both α' + β' SiAlON were formed. The densities of the samples however, were still less than 3.00 g/cm^3.

The composition m=0.3, n=1.75 was chosen for a more thorough investigation of its sintering characteristics at various temperatures and times. Samples were sintered at 1600, 1700, 1800, and 1900°C in 10 atm of N_2 for 2 hours and at 1700 and 1800°C for 1, 2 and 4 hours. Density measurements revealed that lower temperatures yielded denser samples and that this density was relatively constant over time at a given temperature. Scanning electron microscope (SEM) pictures of the polished surface of the samples shows this density difference by the increasing amount of porosity with increasing temperature. (See Figure 3.)

XRD established that both α' and β' phases were present. The sample fired at 1600°C for 2 hours also showed traces of α-Si_3N_4. This signifies that the α to β transformation was not complete in the 2 hour sintering run and that possibly at longer times further transformation and densification would occur.

Y-SiAlON Compositions

$$Y_{m/3}Si_{12-(m+n)}Al_{m+n}O_nN_{16-n}$$

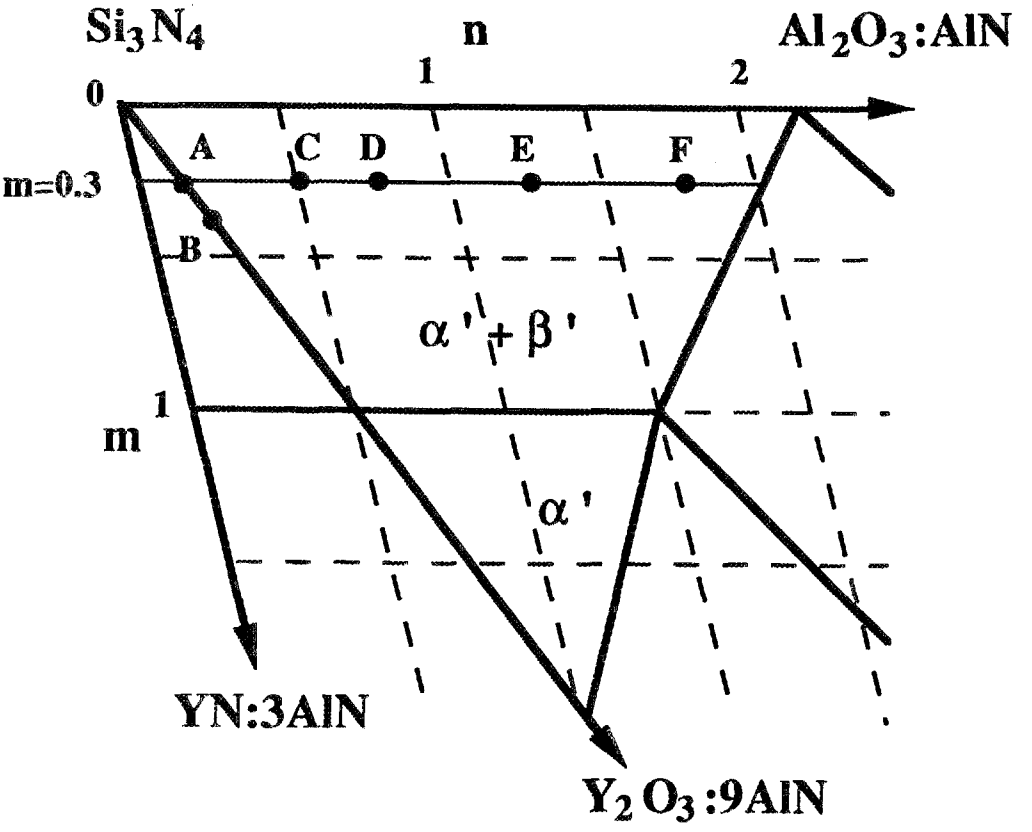

Sintering Conditions: 1900°C/2hrs/10atm N2

	Composition	*Phases*	*Density, g/cm3*
A	m=0.30, n=0.15	α′+β′	< 3.00
B	m=0.40, n=0.20	α′+β′	< 3.00
C	m=0.30, n=0.50	α′+β′	< 3.00
D	m=0.30, n=0.75	α′+β′	< 3.00
E	m=0.30, n=1.25	α′+β′	< 3.00
F	m=0.30, n=1.75	α′+β′	< 3.00

Figure 2

Influence of Temperature on Porosity in m=0.30, n=1.75 Y-SiAlON

$$Y_{m/3}Si_{12-(m+n)}Al_{m+n}O_nN_{16-n}$$

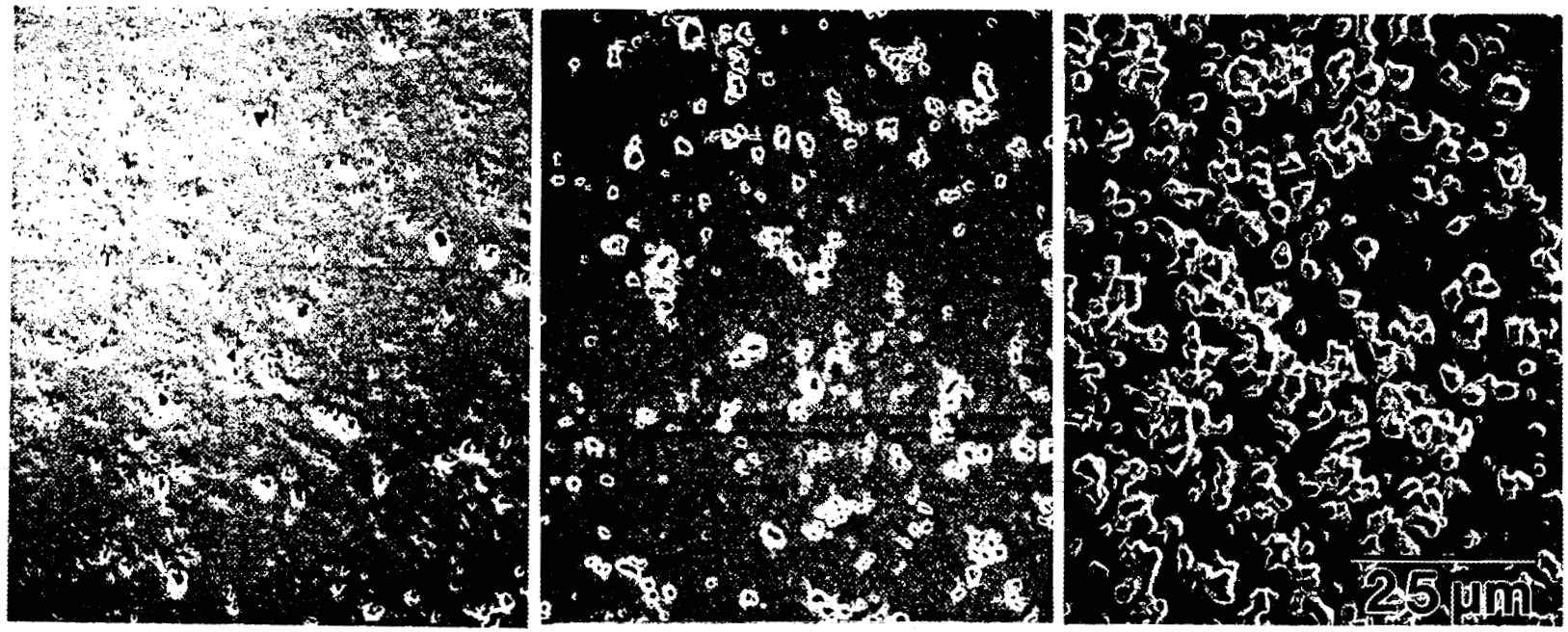

1700°C/2hrs **1800°C/2hrs** **1900°C/2hrs**

Figure 3

In-Situ Reinforced Silicon Nitride

H. Yea and J. Pollinger (Garrett Ceramic Components)
J. Yamanis and C-W. Li (Allied-Signal Research and Technology)

Objective/Scope

The objective of this program is to develop compositions and processes to obtain high fracture toughness and strength for silicon nitride (Si_3N_4) based ceramic materials through microstructure control. Resulting microstructures would have elongated grains that would promote crack bridging and deflection toughening mechanisms. These types of materials known as *in situ* reinforced (ISR) Si_3N_4, are intended for application in advanced heat engine components. A significant amount of the improved mechanical properties must be retained to elevated temperatures. The properties should not substantially degrade over time and would thus allow the material to survive stress under extended exposures at high and moderate temperatures in oxidizing environments. The mechanical property goals of the program are listed below:

Modulus of Rupture at 25°C*	900 MPa (130 ksi)
Modulus of Rupture at 1200°C*	630 MPa (90 ksi)
Modulus of Rupture at 1400°C*	490 MPa (70 ksi)
Stress Rupture at 1000°C#	630 MPa (90 ksi)
Stress Rupture at 1200°C##	490 MPa (70 ksi)
Weibull Modulus+	20
Fracture Toughness, K_{Ic} at room temperature**	10 MPa.$m^{1/2}$
Maximum Use Temperature	1400°C

The technical effort is divided into two stages. The first stage shall be a refinement stage (Tasks 1 and 2) and shall focus on the effects and interactions of the chemical composition and thermal processing variables on microstructure, mechanical behavior, and oxidation resistance. In parallel, the effects of green processing on the required amount of sintering aids, room temperature strength, Weibull statistics, and critical flaws shall be assessed. The goal for this stage shall be to identify conditions which improve the baseline

---

* Four point flexure using Department of Defense MIL-STD-1942 (size B) test specification

\# Stress at which sample shall survive 100 h at 1000°C.

** Measured by Chevron notch method.

\+ As determined by maximum likelihood method.

material and to map composition-processing-property relationships. The second stage shall be an optimization stage (Tasks 3, 4 and 5) and shall focus on the development of ISR Si_3N_4 with optimized microstructure and properties which meet or exceed the property goals and on the establishment of composition-processing-property correlation. In addition, a simulated engine component shall be fabricated in order to demonstrate process feasibility.

The technical effort was initiated in February 1992. In accordance with the program schedule, Task 1 - Composition and Process Development was completed end of September 1992 (Milestone 122601); Task 2 - Material Property Characterization was completed end of January 1993; Task 3 -- Composition and Process Optimization was initiated beginning of January 1993 and shall be continued through August 1993. Discussed below are the work performed in this semi-annual reporting period which included the completed Task 2 effort and on-going Task 3 effort.

Technical Highlights

TASK 1 - Composition and Process Development

Completed.

TASK 2 - Material Property Characterization

This task requires the selection of at least four compositions, based on Task 1 results, for a more comprehensive characterization, which included strength, toughness, oxidation, post-oxidation strength, and crystallization behavior. In selected cases, the stress-rupture life at 1000°C and creep resistance at high temperatures were also evaluated. The results will be used to guide the final optimization of the material to be conducted under Task 3 - Composition and Property Optimization.

All required property characterization of the four selected compositions has been completed. Fast fracture strength, indentation strength, and the fast fracture strength of materials after a grain boundary cryatsllization treatment, are summarized in Table 1, while the oxidation weight gain and post-oxidation strength for three of the four compositions (Composition 3 was not included due to its significantly inferior properties shown in Table 1) are shown in Tables 2 and 3. The 1000°C/1000h oxidation data (Table 2) confirm that Composition 1 has the poorest oxidation resistance at 1000°C (usually referred as intermediate temperature) among the three compositions. It is very encouraging to note that Compositions 2 and 4 show a very low weight gain (~0.05 mg/cm^2) and a very small strength loss (<~10%) after the 1000°C/1000 hour treatment. These data confirm that Compositions 2 and 4 do not have the intermediate temperature oxidation problem. The strength loss for these two compositions is about 20% after a 1400°C/100 h oxidation. Composition 4 shows better surface quality and less weight gain after the 1400°C/100 hour oxidation.

Table 1. Property Data for Task 2 Compositions

Composition No.		Fast Fracture Strength (MPa)			Residual Strength (MPa) / Indentation Load (kg)	Toughness ($MPa \cdot m^{1/2}$)
		RT	1000°C	1400°C		
1	$0.67W_3$** $0.33W_m$** M_0	847 ±39 (17)	702 ±6 (3)	612 ±21 (3)	650/ 1 386/10 310/30	8.5
ditto, Crystallized		870 ±35 (10)				
2	$0.80W_3$ $0.33W_m$ M_0	847 ±47 (30)	751 ±34 (2)	578 ±13 (5)	651 / 1 381 / 10 312 / 30	8.6# 8.5*
ditto, Crystallized		830 ±44 (15)		585 ±37 (4)		
3	$0.80W_3$ $0.0W_m$ M_0	702±46 (17)	500±36 (2)	477±31 (3)	410 / 10 314 / 30	8.7*
4	$0.80W_3$ $0.33W_m$ $4M_0$	841 ±48 (10)	683 (1)	534 ±51 (3)	750 / 1 394 / 10 304 / 30	8.5*
ditto, Crystallized		778±38 (10)		602 ±15 (3)		

#Chevron-notch value; *Indentation-strength-in-bending using 50 kg load. Numerals in parentheses denote number of specimens tested.
**W_3:wt% of sintering aid 3; M_0: mol ratio of sintering aid 2 to sintering aid 1; W_m:wt% grain growth modifier.

Table 2
Oxidation Weight Gain (mg/cm^2)

Temp.	1000°C				1315°C		1400°C
Time	100 h		1000 h		150 h		100 h
Comp.	Sintered	Cryst.	Sintered	Cryst.	Sintered	Cryst.	Sintered
1	0.15± 0.05	0.12± 0.02	-	0.19± 0.01	-	0.14	0.40± 0.03
2	0.04± 0.03	0.06± 0.03	0.13± 0.03	0.05± 0.02	0.15± 0.01	0.15± 0.01	0.49± 0.14
4	0.14± 0.02	0.06± 0.01	-	0.05± 0.02	0.13	0.09	0.36± 0.06

Table 3
Post-Oxidation Strength (MPa)

Temp./Time	1000°C/1000 h	1315°C/150 h	1400°C/100 h
Comp.	Crystallized	Crystallized	As-Sintered
1	688±27 (3)	767 (1)	579±61(3)
2	764±65 (3)	670±19 (3)	643±69 (7)
4	758±25 (3)	689±41 (3)	647±53 (6)

Fractography results showed that the fracture origins for Composition 2 are oxidation pits, while for Composition 4 the fracture origins are still large grains.

In summary, Compositions 2 and 4 exhibit better overall properties and thus have been selected for further optimization under Task 3. The major reasons for eliminating the other two compositions are: Composition 1 has poorer oxidation resistance at 1000°C (intermediate temperature), and Composition 3, which does not have the grain growth modifier, has low strength. The high temperature strengths of compositions 2 and 4, either in the as-sintered or crystallized states, meet the program goals, while the room temperature strengths for the as-sintered materials are only ~50 MPa below the program goal. Furthermore, it has been found that the crystallization treatment tends to lower the room temperature strength. Both Compositions 2 and 4 exhibit excellent intermediate temperature oxidation resistance, especially after the crystallization treatment, with composition 4 having a better oxidation resistance in the temperature range of ~1300-1400°C.

TASK 3 - Composition and Process Optimization

The objective of this task is to further improve the material properties, based on results from Tasks 1 and 2, to meet the program goals. The approaches include optimization of the selected compositions through modification of thermal processing, green forming, and composition. The optimized material will then be characterized in-depth under Task 4.

Based on Tasks 1 and 2 results, Compositions 2 and 4 were selected for optimization. In addition to these two compositions, a third composition, designated Composition 5, was formulated during this reporting period for inclusion in the optimization effort. Composition 5 was selected for its potential of higher elevated temperature strength based on the trends observed in Tasks 1 and 2. These three compositions were slip cast into standard green samples using the established procedures, and then densified in an modified sintering cycle, Cycle A-1. This cycle featured lower temperatures at the last two stages, relative to the cycle used in Task 2, in the three stage sintering cycle, in an attempt to improve the properties as well as lowering the thermal processing cost. All three compositions achieved >99% theoretical density; however Composition 4 exhibited a less dense thin surface layer. The strengths of these three materials were measured and the results are listed in Table 4.

Comparing to Task 2 strength results, these results show that Cycle A-1 did not affect the strength of Composition 2 but lowered the strength of Composition 4. (Composition 5 is a new composition, no previous strength data available for comparison). As predicated that Composition 5 did exhibit the highest 1400°C temperature strength. Oxidation and recrystallization behavior of this material was also evaluated. Its weight gain after 1350° C/100 h oxidation was 0.3 mg/cm^2, which is lower than that of Composition 2 (0.4 mg/cm^2) but higher than that of Composition 4 (0.2 mg/cm^2). A crystallized Composition 5 sample loaded under a 483 MPa bend stress at 1000°C survived more than 150 h. However the weigh gain was higher than those of Compositions 2 and 4 tested under the same condition. This is attributed to the lower SA_3 concentration in Composition 5.

Table 4 Four-Point Bend Strength (MPa)

	RT	1200°C	1400°C
Composition 2	846±46 (15 bars)	696±50 (3)	601±43 (3)
Composition 4	818±49 (5)	605±15 (2)	527±69 (3)
Composition 5	832± (10)	651±19 (2)	632±2 (2)

Additional sintering cycles were also investigated in this reporting period, including lower first stage temperature and time. Results of these experimental runs are still being compiled. However, preliminary results indicated that grain and flaw size becomes smaller and the trend of strength improvement becomes more apparent. For example, one run generated a

Composition 2 sample having a room-temperature strength of 895±48 MPa (49 bars) and a Weibull of 22.8.

Status of Milestones

Milestone 122601 (Refinement of baseline composition) was completed on schedule (Oct. 10, 1992). The progress of all other milestone are on schedule.

Communications/Visits/Travel

J. Pollinger, J. Yamanis and H. Yeh attended the Annual Automotive Contractors Coordination Meeting, Nov. 2-5, Dearborn, MI. and presented the progress report.

Problems Encountered

None

Publications

None

1.2.3 Oxide Matrix

Dispersion-Toughened Ceramic Composite

T. N. Tiegs, S. D. Nunn, P. J. Jones, K. L. Ploetz, D. Barker, C. Davisson, and C. A. Walls (Oak Ridge National Laboratory)

Objective/scope

Initially, this work involved development and characterization of SiC whisker-reinforced ceramic composites for improved mechanical performance. To date, most of the efforts involving SiC whisker-reinforced alumina, mullite, silicon nitride, and sialon have been completed. In addition, studies of whisker-growth processes were initiated to improve the mechanical properties of SiC whiskers by reducing their flaw sizes and, thereby, improving the mechanical properties of the composites. Currently, in situ acicular grain growth is being investigated to improve fracture toughness of silicon nitride materials.

Technical highlights

In Situ Toughening of Silicon Nitride by Microstructure Development

Microstructure Development During Gas-Pressure-Sintering (GPS)-is one technique used to grow elongated grain structures and obtain high-toughness silicon nitrides with refractory grain boundary phases. Samples have been fabricated at ORNL and initial results reported previously. The refractory grain boundary phases fall into two general classifications: (1) rare-earth silicates, based on $M_2Si_2O_7$ as the crystalline intergranular phase, where M = Y, Yb, La, or Nd; and (2) grain boundary phases based on the rare-earth oxide and nitride apatites, such as $Sr_2Y_8(SiO_4)_6O_2$, $Ba_2Y_8(SiO_4)_6O_2$, $Mg_2Y_8(SiO_4)_6O_2$, $Sr_2Nd_8(SiO_4)_6O_2$, and $Sr_2La_8(SiO_4)_6O_2$.

As reported previously, samples have been fabricated by turbomilling 1 to 12% rare-earth oxide (Y_2O_3, La_2O_3, or Nd_2O_3) and 1 to 8% SiO_2 additives. The apatite materials also have SrO, MgO, or BaO added to the mixtures. Both slip-casting and cold-isostatic-pressing have been used as the green forming method. The densification of the initial series of silicon nitrides with refractory grain boundary phases has been reported previously.[1] Specimens were sintered both at 1 atm pressure and with gas overpressure. The materials that achieved >95% T. D. were machined into bend bars for mechanical property tests, which were summarized in earlier reports.[1]

Rare-earth silicates as grain boundary phases - The 1000°C oxidation resistance of the GPS samples containing 4.4 equiv % oxygen is shown in Fig. 1. After a total exposure time of 800 h, the samples containing yttrium and lanthanum show a weight gain of only about 1 g/m^2. This is a very low weight gain for silicon nitride at this temperature[2] and shows the highly refractory nature of the intergranular phase formed by the sintering aids. The samples containing neodymium show less resistance to oxidation, especially the sample fired at the higher temperature. This may be due to the formation of less refractory oxynitride phases. The secondary phases that were formed could not be identified from the X-ray diffraction peaks for the neodymium samples. The patterns did not correspond to any JCPDS file patterns.

Examination of the fracture surfaces of the samples showed that the materials developed highly acicular grains and appeared to have a bimodal grain size distribution. The microstructures consist of mostly fine grains (<1 μm in diameter) intermixed with numerous large grains (2 to 4 μm in diameter). Both the large and small grains have a high aspect ratio. Such a microstructure should result in a material with high fracture toughness.[3-6] However, the measured fracture toughness values were in the range of

ORNL-DWG 93-12842

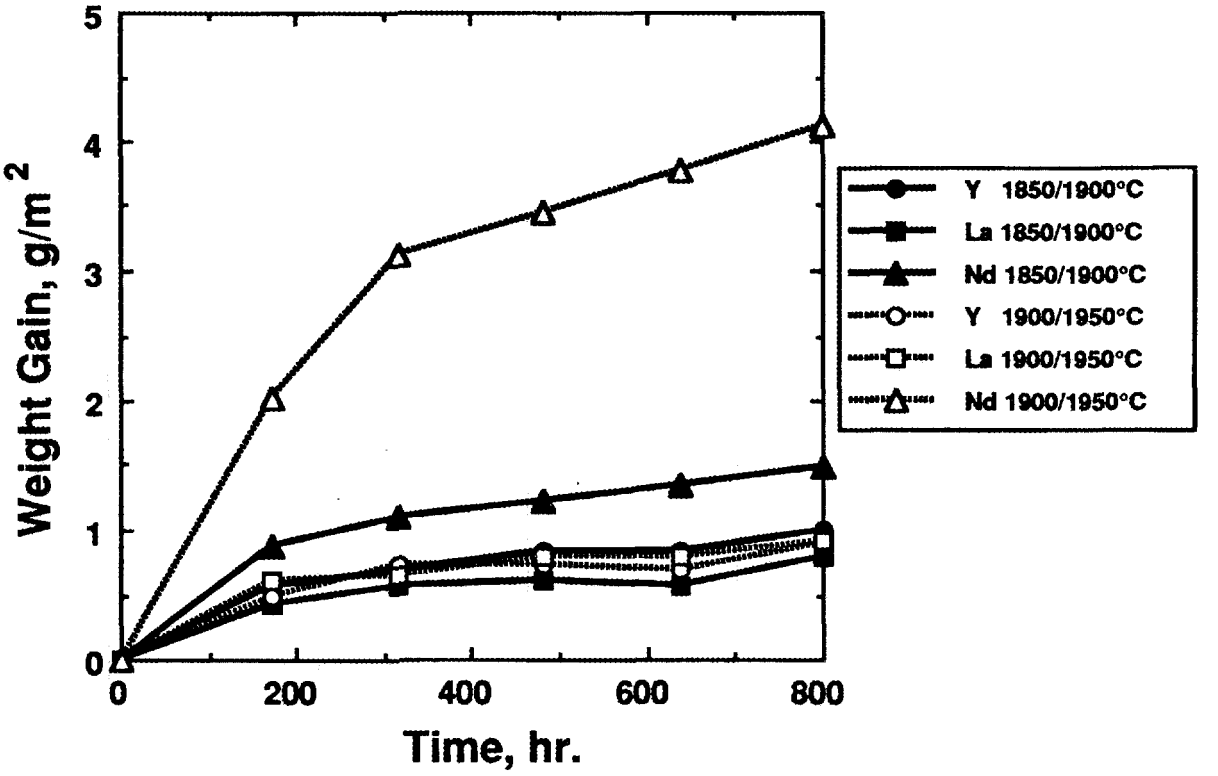

Fig. 1. A plot of the weight gain of the gas-pressure sintered samples with rare-earth silicate grain boundary phases and containing 4.4 eq. % oxygen after long-term exposure to oxidizing conditions at 1000°C.

3 to 6 MPa$\sqrt{m}$, which are low to moderate toughness for silicon nitride. The reason for the relatively low toughness is not completely understood at this time, but may be due to the development of strong interfacial bonding between the ß-Si_3N_4 grains and the grain boundary phases, which would limit the extent of crack deflection, debonding, and pull-out toughening mechanisms.

Rare-earth oxygen and nitrogen apatites as grain boundary phases - A summary of the results on the fracture toughness (K_{Ic}) is shown in Fig. 2. Measurements were made by two different methods which showed only rough agreement between them.[7,8] Generally, the highest toughnesses were observed with the Y_2O_3-SrO-containing materials (TRSN-3) while the lowest toughnesses were associated with the samples containing Nd_2O_3 (TRSN-4). The highest fracture toughnesses were for the Y_2O_3-SrO-containing sample sintered at 1850°C/2 h-1900°C/2 h (TRSN-3-1), which had values from 8.6 to 10.1 MPa$\sqrt{m}$. These values are comparable to toughnesses obtained in previous studies.[3-6]

One of the advantages mentioned for the nitrogen apatites in silicon nitride was that they do not experience volume increases upon oxidation. In the past, volume expansion during intermediate temperature oxidation, especially for melilite phases, has been observed to cause severe degradation of the materials.[9] Weight gain measurements

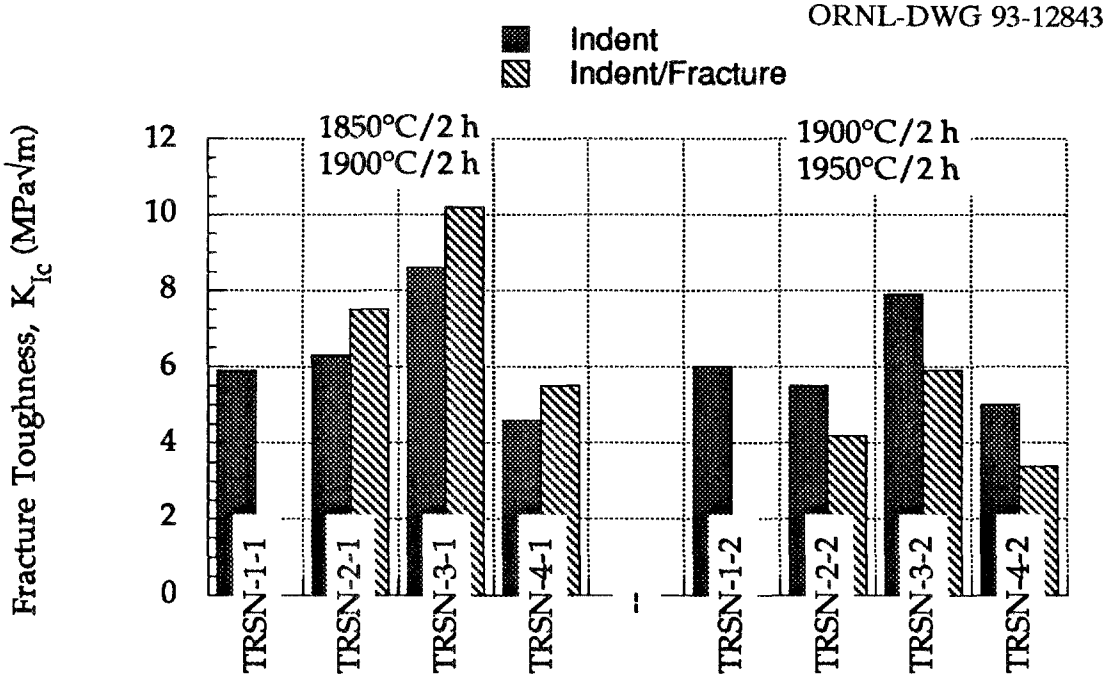

Fig. 2. Summary of results on fracture toughness of Gas-pressure-sintered silicon nitride compositions with rare-earth apatite grain boundary phases by indentation and indentation/fracture techniques.

at 1000°C showed parabolic kinetics, for most of the compositions (Fig. 3). This indicates the formation of a protective layer and little to no volume expansion of the reaction product during oxidation. However, the samples containing Nd_2O_3 (TRSN-4) exhibited nearly linear weight gain kinetics indicating the formation of a non-protective layer.

Effect of Si_3N_4 Powder Characteristics on GPS - Currently, the effects of Si_3N_4 powder characteristics on the densification and mechanical properties are being examined. Cost of the powders is also a consideration. Numerous studies have shown that the silicon nitride powder used in fabrication is an extremely important variable in the microstructural development and final properties of the materials.[10-21] Several powders were selected that comprise a wide variety of characteristics, such as surface area, particle size, purity, oxygen content, and cost (see Table 1).

To assess the effects of silicon nitride powder, two compositions were chosen that had shown good densification, mechanical properties, and oxidation resistance in the previous study.[1] The intergranular phases chosen are $Y_2Si_2O_7$ (at 5 equiv % oxygen) and $Sr_2La_4Yb_4(SiO_4)_6O_2$ (at 8 equiv.% oxygen). The compositions are given in Tables 2 and 3. The oxygen content of the silicon nitride powders was taken into account in the calculation of the silica addition, and milling was done in isopropanol to minimize any oxygen pickup during processing. These samples are currently being fabricated.

GPS of these compositions has been completed. Sintering was performed at two sets of conditions: (1) 1850°C for 2 h and 0.3 MPa followed by 1900°C for 2 h and 2 MPa, or (2) 1900°C for 2 h and 0.6 MPa followed by 1950°C for 2 h and 2 MPa. The densities achieved for the Si_3N_4-$Sr_2La_4Yb_4(SiO_4)_6O_2$ and Si_3N_4-$Y_2Si_2O_7$ compositions

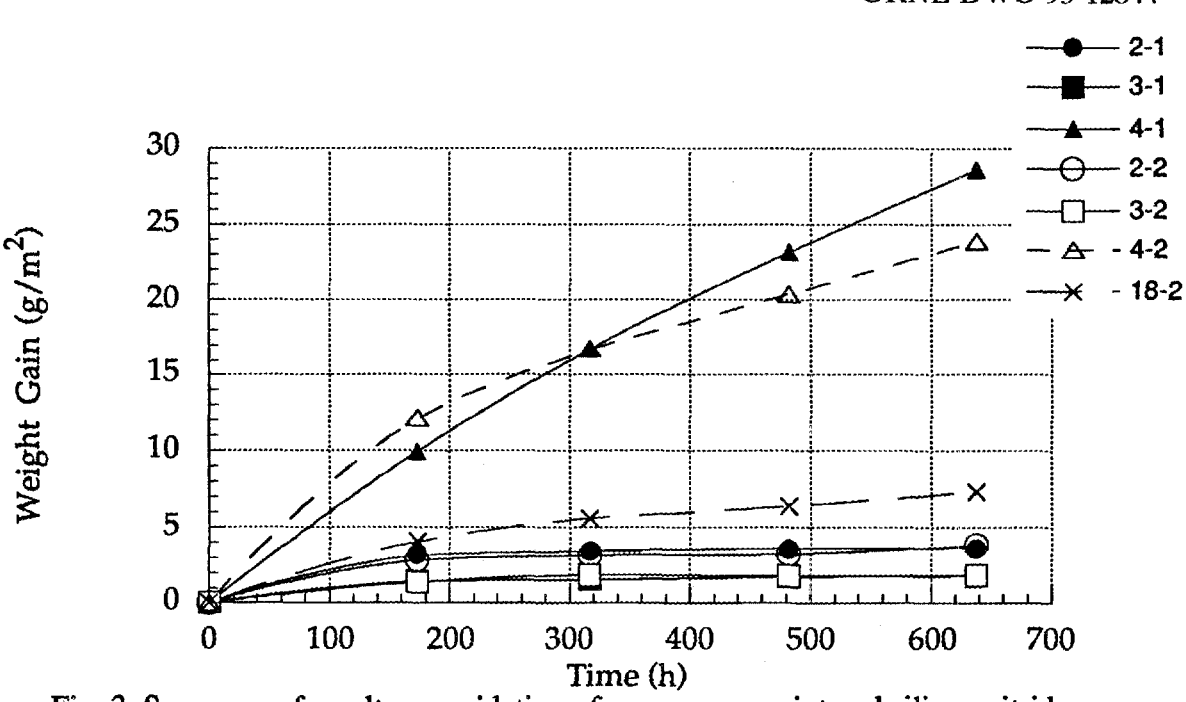

Fig. 3. Summary of results on oxidation of gas-pressure-sintered silicon nitride compositions with rare-earth apatite grain boundary phases at 1000°C.

Table 1. Characteristics of silicon nitride powders (Manufacturers' reported values)

Manufacturer	Grade	Fabrication route	Cost ($/kg)*	Mean particle size (μm)	Surface area (m^2/g)	α-phase content (%)	Oxygen content (wt %)	Total impurity content (ppm)
Ube	E-10	Diimide	99	---	11.7	<95%	1.40	<300
Starck	LC-12SX	Si Nit.[a]	75	0.41	19.1	97.5	2.06	<200
Denka	9FW	Si Nit.[a]	110	0.80	10.9	92.1	0.98	<0.5[b]
Starck	LC-10N	Si Nit.[a]	61	0.50	13.2	96	1.59	<1000
Starck	GP	Gas Phase	90	0.55	10.9	95	1.12	<200
Starck	S 1	Si Nit.[a]	52	0.68	7.4	94.7	1.96	<1000

*Based on purchases of 10 kg.
[a]Silicon nitradation.
[b]Values in wt %.

Table 2. Compositions of samples for assessing effect of silicon nitride powder characteristics on properties of silicon nitrides with $Y_2Si_2O_7$ as the intergranular phase

Batch	Si_3N_4 Type	Si_3N_4	SiO_2*	Y_2O_3	Si†
TRSN-37	Ube E-10	92.49	0.99	6.52	
TRSN-38	Starch LC-10N	92.78	0.70	6.52	
TRSN-39	Starck LC-12SX	93.63	0.00	6.52	
TRSN-40	Starck GP	91.94	1.54	6.52	
TRSN-41	Starck S1	93.45	0.03	6.52	
TRSN-42	Denka 9FW	91.70	1.78	6.52	
TRSN-43	Starck LC-10N	13.00	5.44‡	6.52	72.18

*Cabosil
†Elkem Si HQ.
‡U.S. silica 5 μm.

Table 3. Compositions of samples for assessing effect of silicon nitride powder characteristics on properties of silicon nitrides with $Sr_2La_dYb_4(SiO_4)_6O_2$ as the intergranular phase

		Weight %					
Batch	Si_3N_4 Type	Si_3N_4	SiO_2*	La_2O_3	Yb_2O_3	$SrCO_3$	Si†
TRSN-30	UBE E-10	79.08	1.85	7.28	8.55	3.24	
TRSN-31	Starck LC-10N	79.33	1.60	7.28	8.55	3.24	
TRSN-32	Starck LC-12SX	80.06	0.87	7.28	8.55	3.24	
TRSN-33	Starck GP	78.62	2.32	7.28	8.55	3.24	
TRSN-34	Starck S1	79.90	1.03	7.28	8.55	3.24	
TRSN-35	Denka	78.41	2.53	7.28	8.55	3.24	
TRSN-36	Starck LC-10N	10.48	5.39‡	9.89	11.61	3.24	58.24

are shown in Figs. 4 and 5, respectively. As indicated, the nitrided powders showed the lowest densities while the diimide and gas-phase powders had the highest densities.

To improve the densification of the samples, an oxidation treatment of 1 h at 1000°C was performed to increase the oxygen content in the samples. As shown in Fig. 6 for the Si_3N_4-$Sr_2La_4Yb_4(SiO_4)_6O_2$ composition, increases in the densities were observed for most of the powder types. The effect of the oxidation treatment on fracture toughness is shown in Fig. 7. As shown, the oxidation treatment had a significant effect on the fracture toughness for the Ube E-10 and Starck GPS powders. However, as shown in Fig. 8 for the Ube E-10 powder, while the toughness and room-temperature flexural strength are improved by increasing the oxygen content, more severe degradation of high- temperature strength is evident.

References

1. T. N. Tiegs et al., "Dispersion Toughened Ceramic Composite," to be published in Ceramic Technology Project Semiannual Progress Report April-Sep. '92, ORNL/TM.

2. D. M. Mieskowski and W. A. Sanders, "Oxidation of Silicon Nitride Sintered With Rare-Earth Oxide Additions," *J. Am. Ceram. Soc.*, **68** [7] C160-C163 (1985).

3. E. Tani, S. Umebayashi, K. Kishi, K. Kobayashi, and M. Nishijima, "Gas-Pressure Sintering of Si_3N_4 With Concurrent Addition of Al_2O_3 and 5 wt % Rare Earth Oxide: High Fracture Toughness with Fiber-Like Structure," *Am. Ceram. Soc. Bull.* **65**[9], 1311-15 1986.

4. C. Li and J. Yamanis, "Super-Tough Silicon Nitride With R-Curve Behavior," *Ceram. Eng. Sci. Proc.* **10**[7-8], 632-45 1989.

5. K. Matsuhiro and T. Takahashi, "The Effect of Grain Size on the Toughness of Sintered Si_3N_4," *Ceram. Eng. Sci. Proc.* **10**[7-8], 807-16 1989.

6. T. Kawashima, H. Okamoto, H. Yamamoto, and A. Kitamura, "Grain Size Dependence of the Fracture Toughness of Silicon Nitride Ceramics," *J. Ceram. Soc. Jpn* (1991).

7. G. R. Anstis, et al, "A Critical Evaluation of Indentation Techniques for Measuring Fracture Toughness: I, Direct Crack Measurements," *J. Am. Ceram. Soc.* **64**[9], 533-38 (1981).

8. P. Chantikul, et al, "A Critical Evaluation of Indentation Techniques for Measuring Fracture Toughness: II, Strength Method," *J. Am. Ceram. Soc.* **64**[9], 539-43 (1981).

9. F. F. Lange, S. C. Singhal, and R. C. Kuznicki, "Phase Relationships and Stability Studies in the Si_3N_4-SiO_2-Y_2O_3 Pseudoternary," J. *Amer. Ceram. Soc.* **60** [5-6], 249-52 (1977).

10. F. F. Lange, "Fracture Toughness of Si_3N_4 as a Function of the Initial a-Phase Content," *J. Am. Ceram. Soc.* **62**[7-8], 428-30 (1979).

11. G. Wötting and G. Ziegler, "Powder Characteristics and Sintering Behavior of Si_3N_4-Powders," *Powder Met. Internat.* **18**[1], 25-32 (1986).

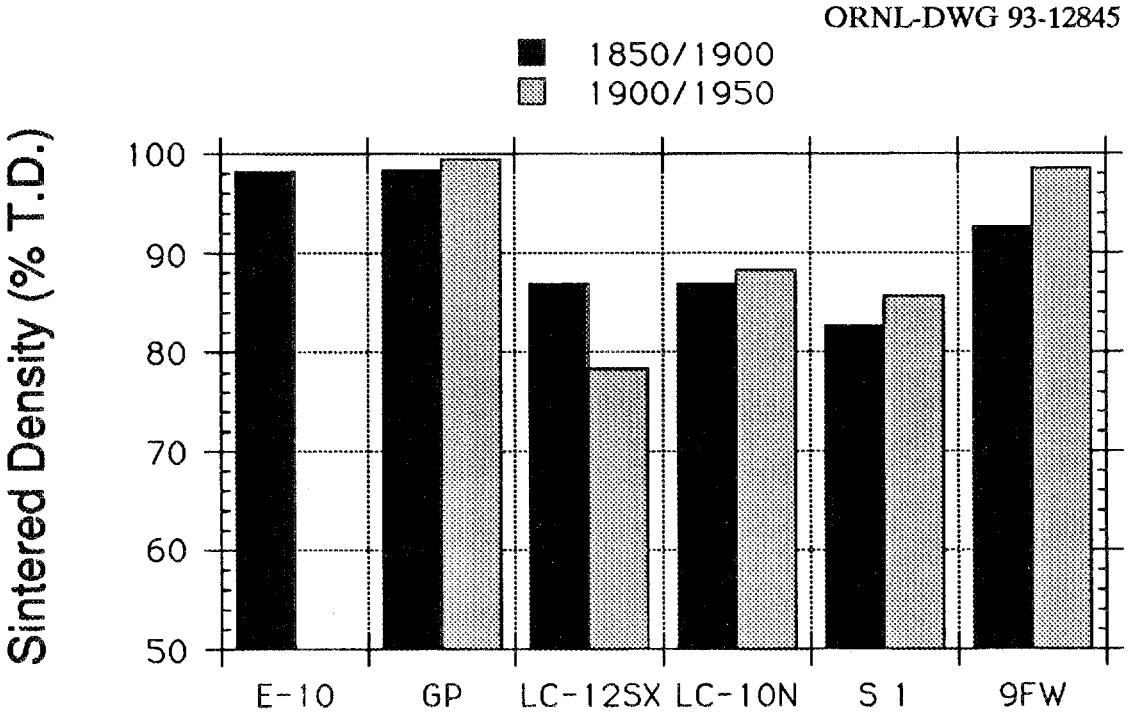

Fig. 4. Densification of Si_3N_4-$Sr_2La_4Yb_4(SiO_4)_6O_2$ during gas-pressure sintering.

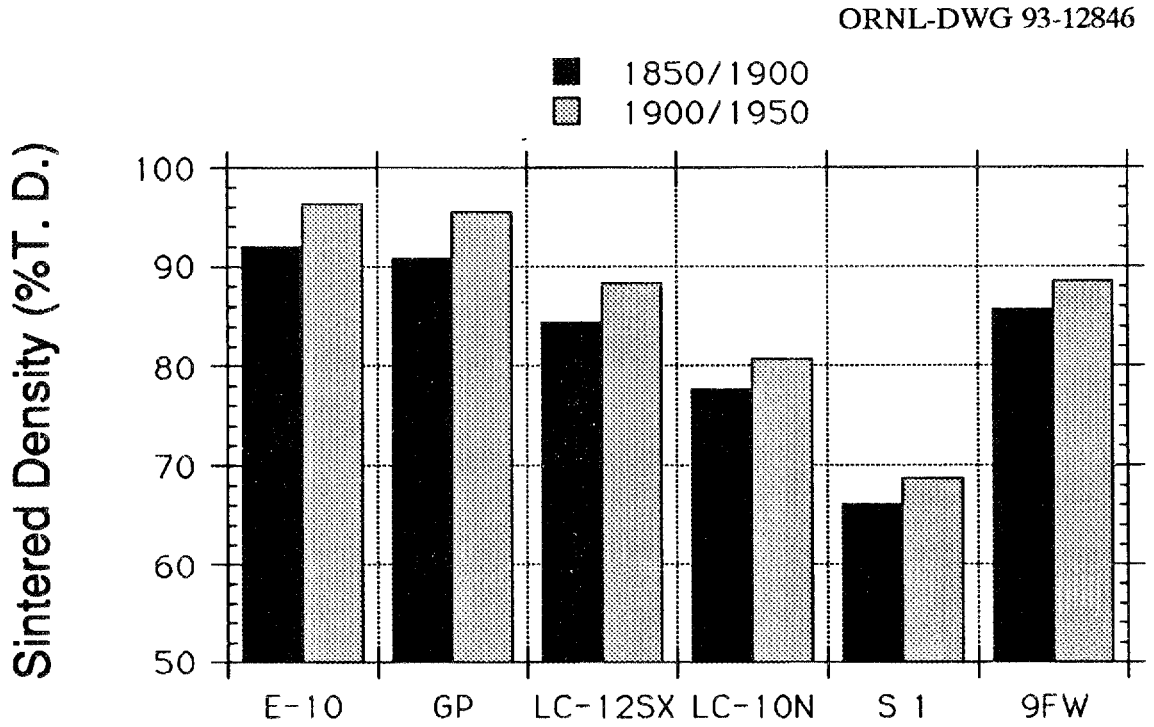

Fig. 5. Densification of Si_3N_4-$Y_2Si_2O_7$ during gas-pressure sintering.

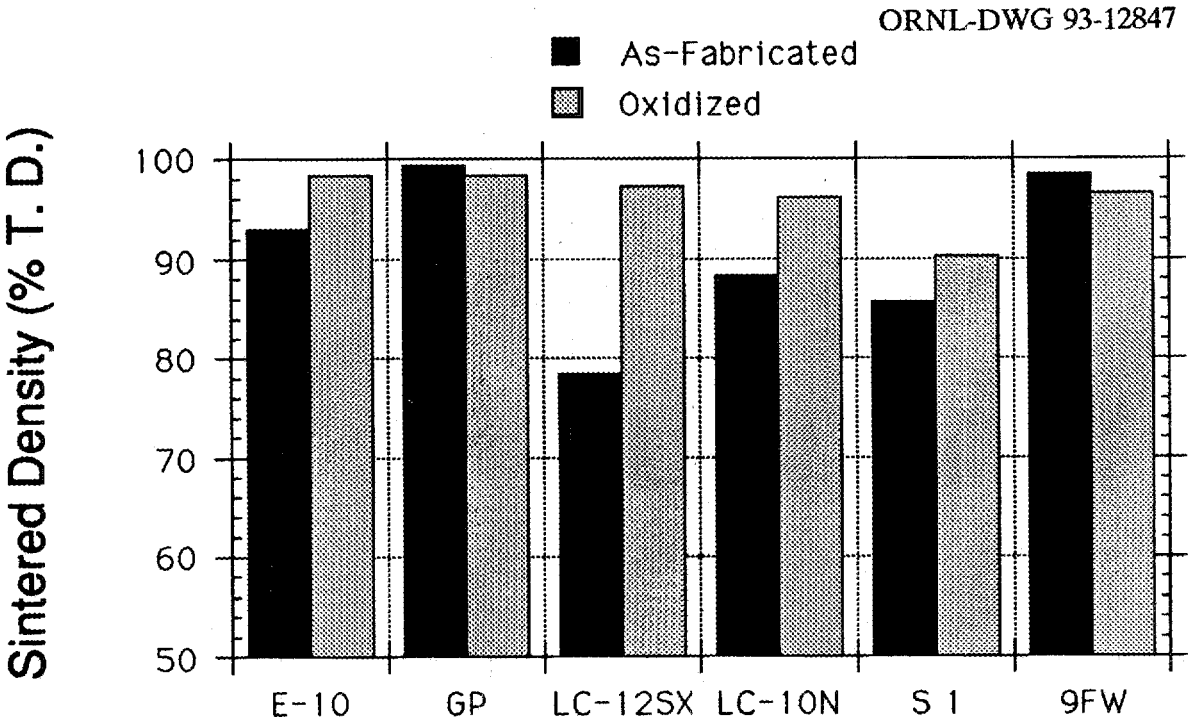

Fig. 6. Densification of gas-pressure sintered Si_3N_4-$Sr_2La_4Yb_4(SiO_4)_6O_2$ as-fabricated and after a one hour oxidation treatment at 1000°C. Sintering conditions were 1900°C/2h/0.3 MPa-1950°C/2 h/2 MPa.

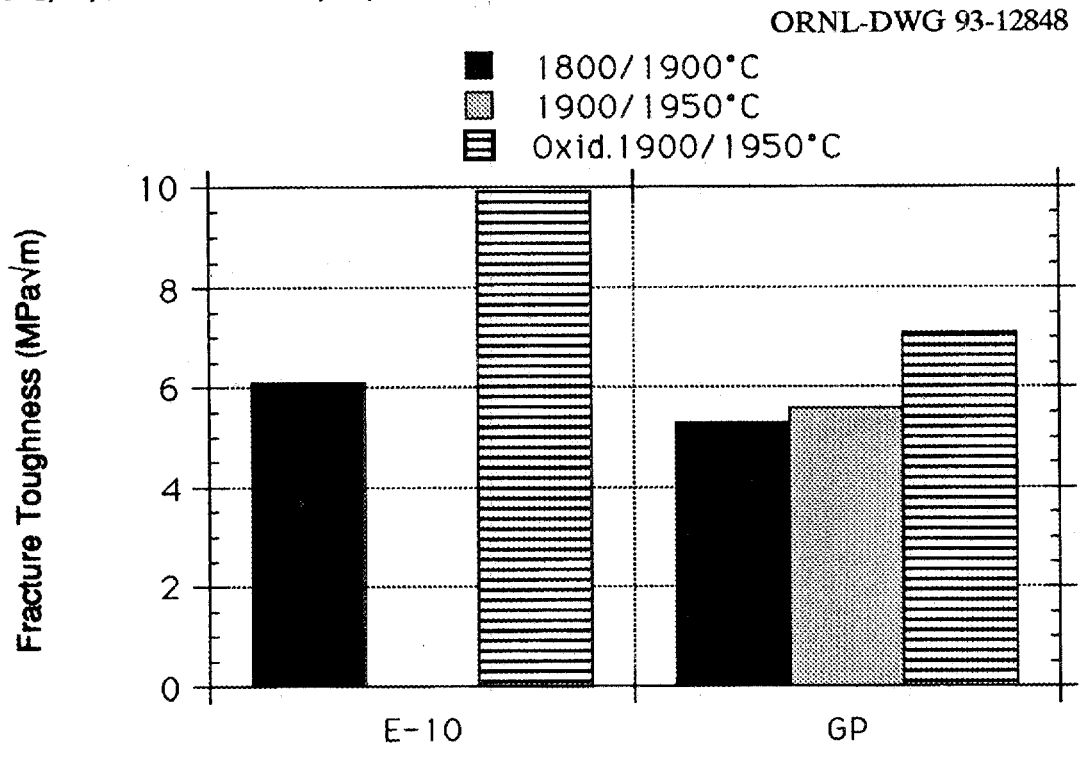

Fig. 7. Fracture toughness of gas-pressure sintered Si_3N_4-$Sr_2La_4Yb_4(SiO_4)_6O_2$ as-fabricated and after one hour oxidation treatment at 1000°C.

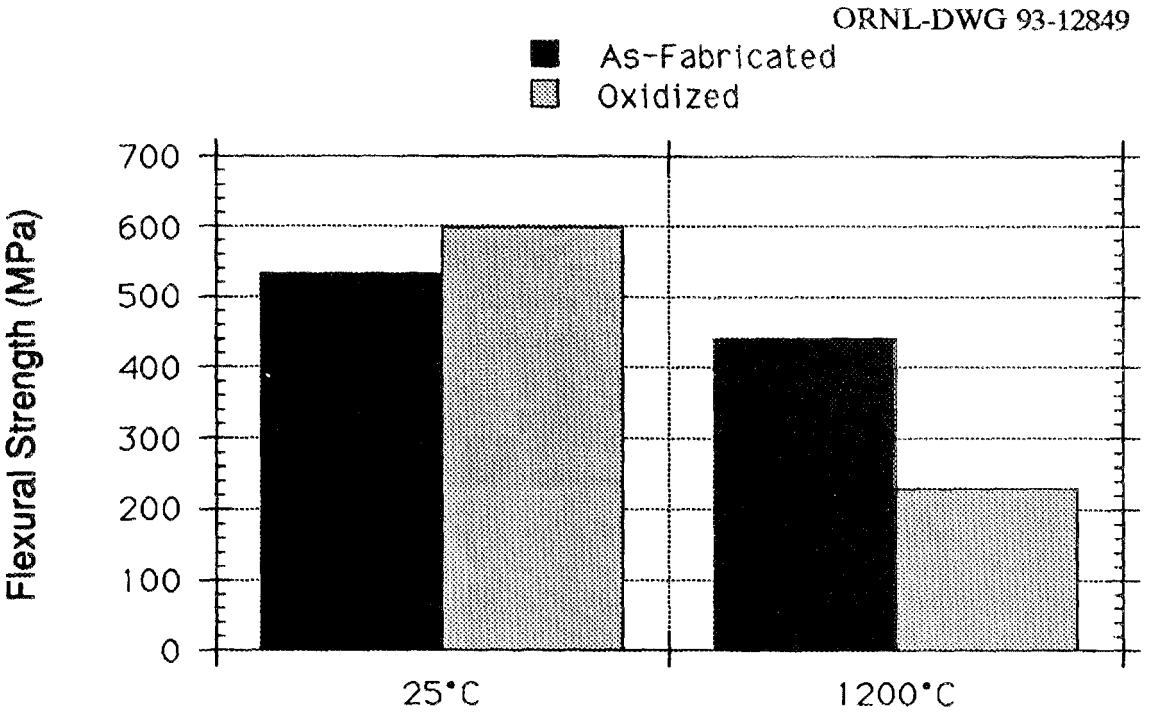

Fig. 8. Effect of increasing oxygen content on flexural strength of Si_3N_4-$Sr_2La_4Yb_4(SiO_4)_6O_2$ gas-pressure sintered at 1900°C/2h/0.3 MPa-1950°C/2 h/2 MPa.

12. T. Ekstrom, N. Ingelstrom, R. Brage, M. Hatcher, and T. Johansson, "a-ß Sialon Ceramics Made from Different Silicon Nitride Powders," *J. Am. Ceram. Soc.* **71**[12], 1164-70 (1988).

13. T. Shimamori, H. Matsuzaki, T. Kato, Y. Tajima, and Y. Matsuo, "High Temperature Properties of Post Sintered Silicon Nitride," pp. 737-44 in *Proceedings 2nd InternationaSymposium on Ceramic Materials and Components for Engines*, ed.W. Bunk and H. Hausner, Verlag Deutsche Keramische Gesellschaft, Bad Honnef, Germany, 1986.

14. D. D. Lee, S. L. Kang, G. Petzow, and D. N. Yoon, "Effect of a to ß(ß') Phase Transition on the Sintering of Silicon Nitride Ceramics," *J. Am. Ceram. Soc.* **73**[3], 767-69 (1990).

15. W. Braue, G. Wötting, and G. Ziegler, "Influence of Impurities in Different Si_3N_4-Powders on High-Temperature Properties of Sintered Materials," Br. Ceram. Proc. **8** 71-80 (1986).

16. G Wötting, E. Gugel, G. Schwier, and H. Lange, "Processing for Improved Fracture Toughness of Dense Silicon Nitride," pp. 647-61 in *Ceramic Trans., Ceramic Powder Sci.* IV, Vol. 22, American Ceramic Society, Westerville, Ohio (1990).

17. K. Ichikawa, "The Influence of Si_3N_4 Powder Characteristics on Sintering Behavior," pp. 107-16 in *Silicon Nitride-1*, Elsevier Applied Science, New York, 1989.

18. G. Franz, B. Laubach, U. Wickel, G. Wötting, and E. Gugel, "Optimization of a High Purity Silicon Nitride Powder Concerning Sintering and Mechanical Properties," pp. 1-12 in *Proceedings 3rd International Symposium on Ceramic Materials and Components for Engines*, ed. V. J. Tennery, American Ceramic Society, Westerville, Ohio, 1989.

19. V. Vandeneede, A. Leriche, F. Cambier, H. Pickup, and R. J. Brook, "Sinterability of Silicon Nitride Powders and Characterization of Sintered Materials," pp. 53-68 in *Non-Oxide Technical and Engineering Ceramics*, ed.S. Hampshire, Elsevier Applied Science, New York, 1986.

20. N. Itoh, T. Sasamoto, T. Sata, K. Komeya, and A. Tsuge, "Impurities in Silicon Nitride Raw Materials and Correlation with Mechanical Strength of the Hot-Pressed Body," *Yogyo-Kyokai-Shi*, 90, 209-213 (1979)

21. W. Braue, G. Wötting, and G. Ziegler, "Impact of Compositional Variations and Processing Conditions on Secondary Phase Characteristics in Sintered Silicon Nitride Materials," pp. 883-96 in *Ceramic Microstructures '86: Role of Interfaces*, Vol. 21, ed. J. A. Pask and A. G. Evans, Materials Science Res., Plenum Press, New York 1987.

22. G. Wötting and G. Ziegler, "Influence of Powder Properties and Processing Conditions on Microstructure of Sintered Si_3N_4," pp. 951-62 in Ceramic Powders, ed. P. Vincenzini, Elsevier Sci. Pub., Amsterdam, 1983.

Status of milestones

Milestone 123111, "Fabricate high-toughness silicon nitride materials with elongated grain microstructures," was completed.

Communications/visits/travel

Travel by T. N. Tiegs on November 10-12, 1992, to Anaheim, Calif. to present a paper at the ASME Winter Meeting entitled "Whisker Reinforced Ceramic Composites."

Travel by T. N. Tiegs from November 30 - December 3, 1992, to Boston, Mass. to attend the Fall Meeting of the Materials Research Society and present a paper entitled "Fabrication and Properties of Si_3N_4 With Rare Earth Apatite Grain Boundary Phases."

Travel by S. D. Nunn from November 30 - December 3, 1992, to Boston, Mass. to attend the Fall Meeting of the Materials Research Society and present a paper entitled "Silicon Nitride Containing Rare Earth Silicate Intergranular Phases."

Travel by T. N. Tiegs on December 2, 1992, to Nashua, N. H. to Centorr Furnaces to observe the belt furnace for sintering of silicon nitride.

Problems encountered

None.

Publications

T. N. Tiegs, S. D. Nunn, K. L. Ploetz, P. A. Menchhofer and C. A. Walls, "Fabrication and Properties of Si_3N_4 With Rare Earth Apatite Grain Boundary Phases" to be published in Materials Research Society Proceedings.

S. D. Nunn, T. N. Tiegs, K. L. Ploetz, C. A. Walls and N. Bell, "Silicon Nitride Containing Rare Earth Silicate Intergranular Phases" to be published in Materials Research Society Proceedings.

1.2.4 Silicate Matrix

Characterization and Testing of Low-Expansion Ceramic Materials

D. P. Stinton and S. Subramaniam (Oak Ridge National Laboratory)

Objective/scope

Insulated exhaust port liners are needed in advanced diesel engines to increase engine fuel efficiencies by increasing the combustion temperatures and reducing the combustion heat that is lost through the head and into the water cooling system. Low-expansion materials have potential for this application because of their very low thermal conductivity, extraordinary thermal-shock resistance, and potential to reduce attachment stresses. Thermal-shock resistance is critical because the shape of the port liners requires that they be cast into the metallic cylinder head. Because functioning exhaust port liners are inaccessible after being cast into cylinder heads, they must not require maintenance for the life of the head (~1 million miles). Contracts are being placed with Coors Ceramics Co. and Low Thermal Expansion Ceramics, Inc. (LoTEC) to develop cost-effective processes for the fabrication of port liners. Coors is investigating Al_2TiO_5 and $Ca_{1-X}Mg_XZr_4P_6O_{24}$ while LoTEC is investigating $Ca_{1-X}Sr_XZr_4P_6O_{24}$ and $Ba_{1+X}Zr_4P_{6-2X}Si_{2X}O_{24}$ (BaZPS). A program has been initiated at ORNL to assist Coors and LoTEC with the characterization and evaluation of low-expansion materials.

Technical highlights

A new family of very low thermal expansion ceramic materials was discovered by Rustum Roy and co-workers at Penn State in the early 1980s. The interesting properties (very low thermal expansion and thermal conductivity) exhibited by the $NaZr_2P_3O_{12}$ (NZP) family of materials are attributed to its unique crystal structure, which is capable of accommodating numerous ionic substitutions at various lattice positions. The extensive substitutions led to hundreds of new compounds with varying thermal expansions. In fact, the thermal conductivities in the a and c directions of the hexagonal structure can be tailored by varying the ions substituted into different lattice positions. Barium zirconium phosphate silicate ($Ba_{1+X}Zr_4P_{6-2X}Si_{2X}O_{24}$ or BaZPS) is one such crystalline system that was developed by researchers at Ceramatec, Inc., and is currently being fabricated at LoTEC, Inc. The thermal and mechanical properties of BaZPS materials will be systematically investigated as a function of grain size in this project.

A systematic investigation of the mechanical and thermal properties of BaZPS ceramics as a function of composition and grain size has been initiated. Materials for evaluation (X = 0, 0.175, 0.250, 0.375, and 0.500) were fabricated using solid state processing techniques. Stoichiometric quantities of $BaZrO_3$, ZrP_2O_7, and SiO_2 were ball milled to produce homogeneous batches and calcined to produce single-phase compositions. The calcined powders were then mixed with binder and water to form a slurry and slip cast into 6-mm-thick plates and sintered. Materials with X = 0, 0.175, and 0.500 were sintered for 30, 300, and 3000 min to produce materials with varying grain sizes (see Table 1). Materials with X = 0.250 and 0.375 were sintered only for 3000 min.

Densities of the sintered samples (measured using the Archimedes method) were found to vary from about 84 to 98% of the theoretical values. As expected, the density of the sintered materials increased with increasing sintering time and decreased with increasing Si content (see Fig. 1). The high density obtained for the BS37 composition produced stronger and harder specimens than the other four compositions.

Table 1. BaZPS materials for testing and evaluation

Composition	Grain size[a] (μm)	Grain size[b] (μm)	Grain size[c] (μm)	Si (at. %)
$Ba_{1.0}Zr_4P_6O_{24}$	1 to 2	3 to 4	4 to 6	0.000
$Ba_{1.175}Zr_4P_{5.65}Si_{.35}O_{24}$	1 to 2	3 to 4	4 to 6	0.995
$Ba_{1.25}Zr_4P_{5.5}Si_{0.5}O_{24}$			4 to 6	1.418
$Ba_{1.375}Zr_4P_{5.25}Si_{0.75}O_{24}$			4 to 6	2.121
$Ba_{1.5}Zr_4P_{5.0}SiO_{24}$	1 to 2	3 to 4	4 to 6	2.817

[a]Batches sintered for 30 min.

[b]Batches sintered for 300 min.

[c]Batches sintered for 3000 min.

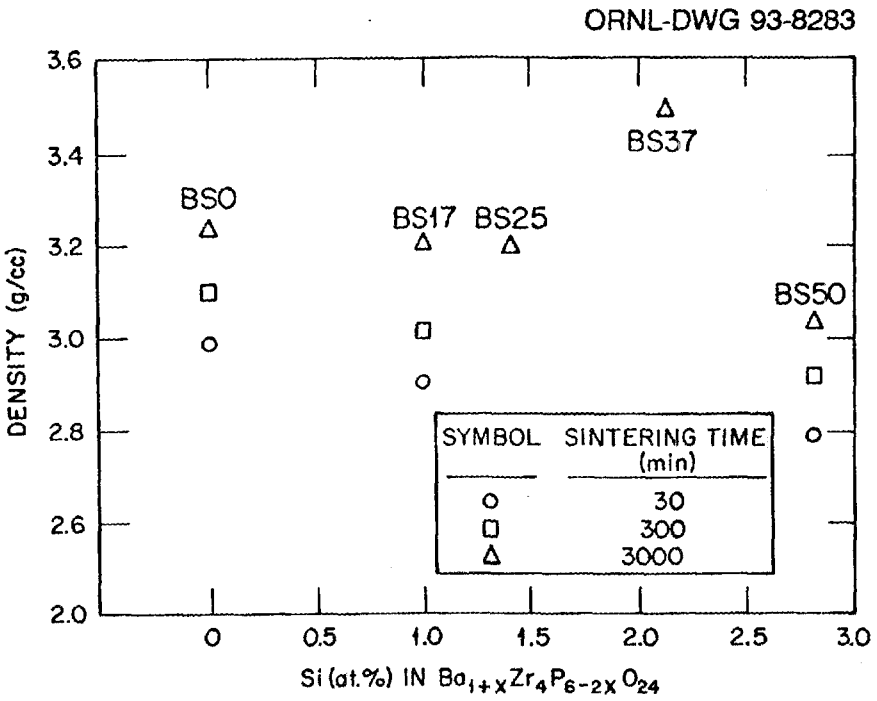

Fig. 1. Final bulk densities increase with sintering time and Si content.

The bulk thermal expansion of BaZPS compositions was determined using a computer-controlled dual-push-rod-type dilatometer. The thermal expansion measurement was carried out between 50 and 900°C using a single-crystal sapphire rod as the reference material. Specimens 3 x 4 x 25.4 mm in dimensions were heated at 10°C/min to the peak temperature, held for 10 min, and cooled at 10°C/min to 300°C. Below 300°C, natural cooling was employed by switching off the furnace. The bulk thermal expansion coefficients varied from $+2.0 \times 10^{-6\circ} C^{-1}$ to $-0.6 \times 10^{-6\circ} C^{-1}$ as the percent Si increased from 0 to 2.817 (see Fig. 2).

The room- and elevated-temperature flexural strengths were measured following MIL-STD-1942(MR). Flexural test specimens were 3 x 4 x 50 mm with all surfaces ground to a 16 -μin. finish, again according to the standard. To minimize edge failures, the long edges of the tensile surface were beveled. Flexural strength was measured using four-point-bend test fixtures with 40 and 20 mm as outer and inner spans, respectively. The test specimens were loaded at the rate of 5.08 mm/min. The flexural strengths for materials sintered for 3000 min increased with increasing Si content for compositions between BS0 and BS37. However, a further increase in Si content drasically reduced the flexural strength. The same behavior was observed at 200°C (see Fig. 3).

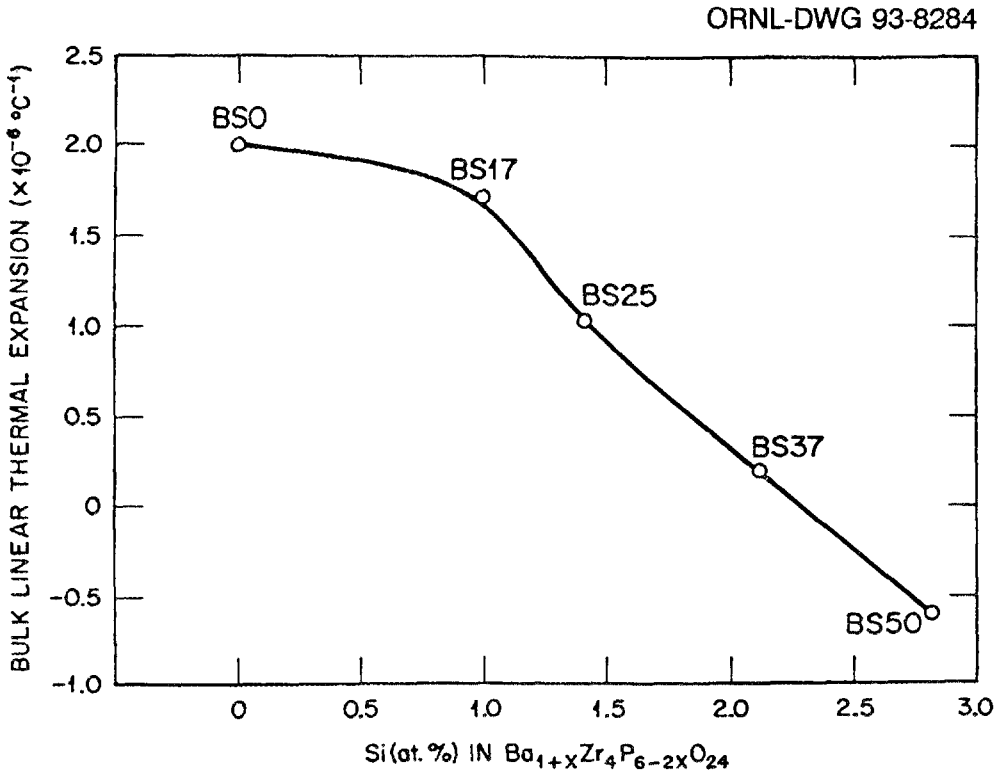

Fig. 2. The bulk thermal expansion coefficients of specimens sintered for 3000 min were controlled by the specimen composition.

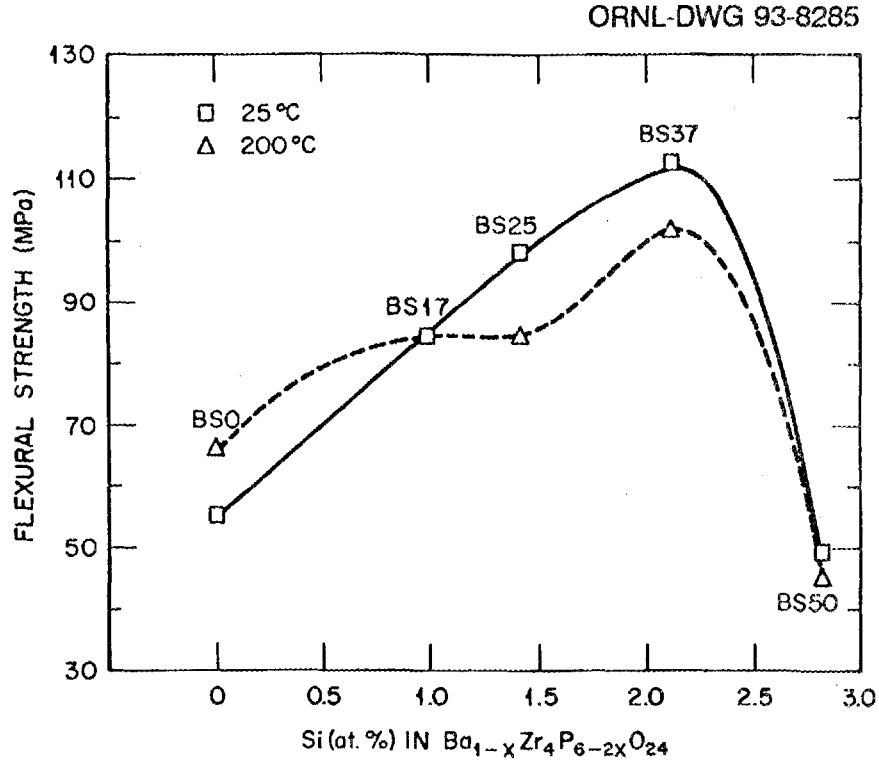

Fig. 3. Flexural strengths of specimens sintered for 3000 min increase as the Si content increases from BS0 to BS37 but decrease drastically for the specimen with the highest Si content (BS50).

The mechanical properties of the NZP family of low-expansion ceramics are degraded by microcracking that occurs due to the anisotropy in thermal expansion. The thermal expansion along the a axis is initially positive (~4 x 10^{-6}/°C) for X = 0 and decreases to ~-2 x 10^{-6}/°C as X increases to 0.5. The thermal expansion along the c axis is initially negative (~-1 x 10^{-6}/°C) and increases to ~4 x 10^{-6}/°C as X increases to 0.5. The anisotropy is a minimum at X = ~0.175. In order to investigate the microcracking of these materials, a novel dual-push-rod-type dilatometer has been assembled. This dilatometer enables one to measure the bulk thermal expansion while simultaneously determining any acoustic activity or microcracking. Several investigators have recognized that microcracking is common in polycrystalline materials which exhibit thermal expansion anisotropy. Further, when microcracking occurs, acoustic emissions (AEs) are generated and can be detected by piezoelectric sensors attached directly to the surface of the material or through a wave guide.

The dilatometer uses two alumina push rods to measure the difference of thermal expansion between a sample and a reference of known thermal expansion (fused sapphire). The alumina push rod touching the sample serves as the contact between the sample and stainless steel rod to which the piezoelectric transducer is bonded. The temperature and AE information is recorded as the material is heated or cooled between

room temperature and 1000°C. Thus, the temperature at which microcracking occurs is identified by plotting the acoustic activity versus temperature, and the extent of microcracking can be qualitatively determined. Preliminary testing indicated that $Ba_{1.5}Zr_4P_{5.0}SiO_{24}$ exhibits the greatest acoustic activity while $Ba_{1.175}Zr_4P_{5.65}Si_{0.35}O_{24}$ exhibits the least activity.

The microstructure and chemistry of the BaZPS ceramics were studied. Polished cross sections of each of the five compositions were prepared, etched, and viewed by optical and scanning electron microscopy (SEM). Fracture surfaces of the sintered samples were also studied by SEM. Observation of the SEM micrographs of the BaZPS ceramics reveals that the average grain size was 1 to 2 μm for samples sintered 30 min, 3 to 4 μm for samples sintered 300 min, and 4 to 6 μm for samples sintered 3000 min (see Table 1). Second-phase particles that were incompatible with the matrix were observed for several compositions. Electron diffraction identified the matrix to be the desired BaZPS composition and the second-phase particles to be a zirconium phosphate of unidentified composition. Fracture surfaces revealed predominantly transgranular fracture, suggesting that the grains were strongly interconnected.

Low Expansion Ceramics for Diesel Engine Applications
D. A. Hirschfeld and J. J. Brown (VPI)

Objective/Scope

Optimize the chemistry, properties, and processing of selected low thermal expansion compositions based on the zircon (NZP) and the β-eucryptite-$AlPO_4$ systems. These materials also exhibit stable properties above 1200°C. The major objective is to demonstrate fabricability and to promote commercialization of these ceramics.

Technical Highlights

Zircon (NZP) System

The effect of thermal cycling on the thermal expansion of $(Ca_{0.6},Mg_{0.4})Zr_4(PO_4)_6$, (CMZP), was examined. Samples of CMZP hot pressed by Dr. M. Haselkorn, Caterpillar, Inc., were cycled from room temperature to 1000°C six times. No significant change in expansion after cycling and no significant hysteresis were observed as shown in Figure 1. The average coefficient of thermal expansion on heating from room temperature to 1000°C was 3.20 x 10^{-6}/°C and on cooling was 3.71 x 10^{-6}/°C.

To optimize the densification of CMZP using cold pressing/sintering, the effect of ZnO (a sintering aid) on the bulk density of CMZP was examined. ZnO was added to sol-gel derived CMZP powder in two different manners. In method one, CMZP powder is first calcined at 600°C for 6 h then 5 wt% ZnO was added. Alternatively, CMZP powder was calcined at 350°C then 5 wt% ZnO added and the mixture calcined at 600°C for 6 h (method two). After calcining, pellets approximately 12mm in diameter and 9mm high were cold pressed and sintered (1000°C for 6 h, then 1200°C for 24 h). Four pellets were made using each method. The sintered pellets exhibited average densities of 89% and 98% of theoretical for methods one and two, respectively.

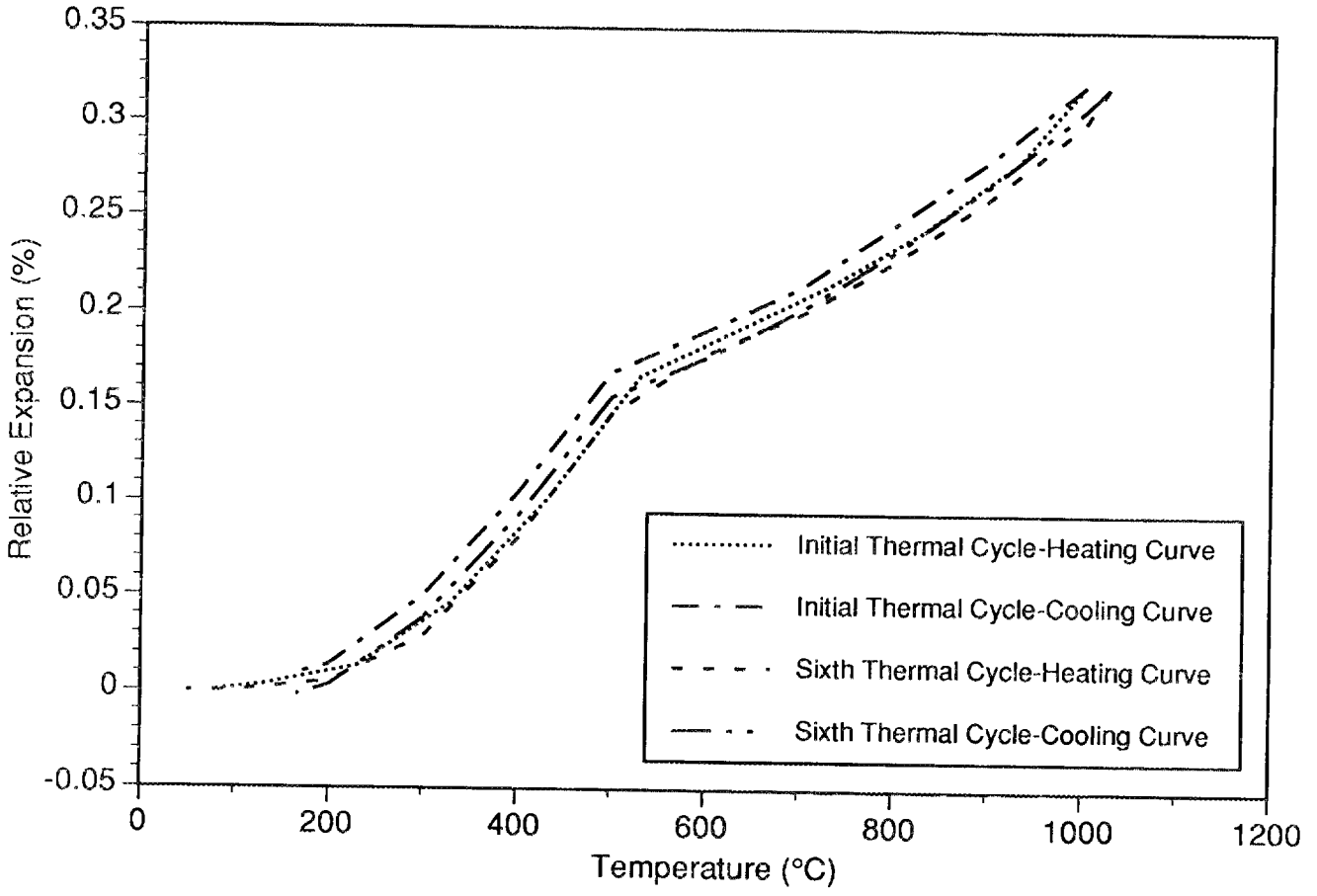

Figure 1. Effect of thermal cycling on relative expansion of CMZP hot pressed at 1280°C for 2 hours with 5600psi.

The density of CMZP as a function of ZnO content was examined to clarify the effect of ZnO on densification and presence of second phases which have been linked to expansion hysteresis. The relative density tends to increase with ZnO content for both processing methods. X-ray diffraction analyses of ground pellets show that as ZnO content increases the $(ZrO)_2P_2O_7$ peaks increase in intensity. Because ZnO forms a liquid phase at 1000°C, it is believed that Ca and Mg readily diffuse into the liquid phase allowing the formation of $(ZrO)_2P_2O_7$.

To improve the alkali corrosion resistance of ceramics such as Si_3N_4 and SiC, CMZP coatings derived by both organic and inorganic sol-gel techniques have been investigated. Films of CMZP were put on Si_3N_4 substrates which were then covered with an aqueous solution of $NaCO_3$ at room temperature then heated to 1000°C and held for 40 h. The room temperature flexural strength of as-received, coated, and corroded Si_3N_4 was measured according to Military Specification 1942 B. The flexural strengths reported are an average of five specimens. Before alkali exposure, both the coated and uncoated Si_3N_4 exhibited an average flexural strength of 595 MPa. After exposure, the average strength of the coated samples increased to 669 MPa while the uncoated samples exhibited an average strength of 573 MPa. It is believed that CMZP reacts with the protective SiO_2 film on Si_3N_4 to form a continuous reaction layer that minimizes corrosion. A scanning electron micrograph of the dense protective layer is shown in Figure 2.

Ceramic Composites

The effects of hot isostatic pressing (HIP) parameters on the flexural strength of SiC whisker (SiC_w) reinforced CMZP was examined using a series of designed experiments based on Taguchi methods to determine the HIP temperature, time, and pressure as well as whisker content to maximize the room temperature flexural strength of the composites. CMZP composites containing up to 30 vol% of SiC whiskers were made by mixing sol-gel derived CMZP powder with SiC whiskers cold-pressing CMZP-SiC whisker mixture into bars then air-sintering the bars at 1000°C for 6 hours. The sintered bars were encapsulated in glass then HIPed. Based on densification studies, HIP temperatures from 1030 to 1070°C at pressures from 10,000 to 15,000 psi for 0.25 to 0.5 h were used to produce composite samples exhibiting densities greater than 99% of theoretical. Two to four bars from each HIP sample were machined and tested according to Military Standard Specification 1942 B.

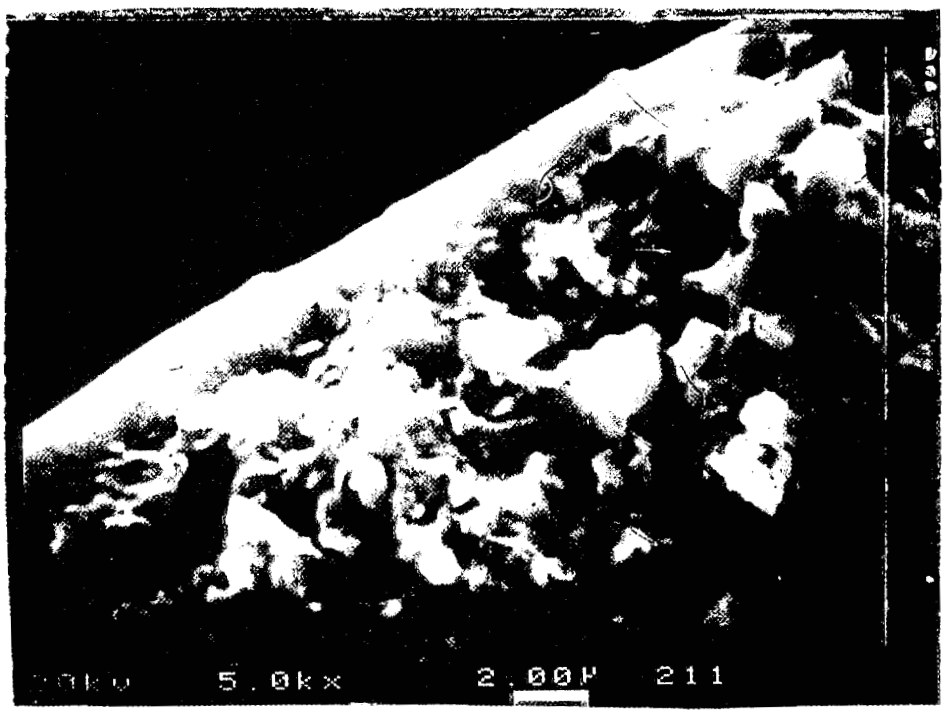

Fig. 2. CMZP coating on Si_3N_4 after alkali exposure at 1000°C for 40 h.

The flexural strength of SiC_w/CMZP composites was shown to increase with whisker contents up to 30 vol% which exhibited the highest flexural strengths as shown in Figure 3. It was noted that some of the HIP samples containing 5 or 10 vol% whiskers broke while being machined into flexure bars and that all of the 20 vol% samples survived under the same machining conditions.

To understand the effects of the whiskers on the strength and the fracture process, the fracture surfaces of SiC_w/CMZP composites were examined using scanning electron microscopy. As anticipated, flexure bars containing more whiskers exhibited a rougher fracture surface indicative of higher fracture resistance. Micrographs of 10 and 20 vol% SiC_w/CMZP bars hot isostatically pressed at 1070°C, 10000 psi for 0.25 h indicate that failure originated from defects on the tensile surfaces (Figures 4 and 5, respectively). The flexural strength of the 20 vol% bar was 113 MPa versus 86.5 MPa for the 10 vol% sample even though the surface defects appear more severe. This result suggests that the CMZP matrix is reinforced by the SiC whiskers.

The nature of the whisker-matrix interaction was examined on the fracture surfaces using SEM and a combination of whisker pull out and mechanical bonding was observed. As indicated in Figure 6, whiskers can have a smooth surface and partially debond from the matrix likely due to thermal expansion mismatch. Whiskers which have either rough surfaces or irregular shapes are mechanically locked during the fracture process requiring more energy to be consumed.

The flexural strength of chopped NICALON™ SiC fiber reinforced CMZP composites (SiC_f/CMZP) produced by hot isostatic pressing (HIPing) was studied. SiC_f/CMZP composites containing 10 and 20 vol% of fibers were made by mixing sol-gel derived CMZP powders with SiC whiskers, cold-pressing CMZP-SiC whisker mixture into bars and air-firing the bars at 1000°C for 6 hours, encapsulating the fired bars into glass tubes under vacuum, then HIPing the glass-encapsulated bars at 1150°C at 103 MPa (15 ksi) for 0.25 and 0.5 hours, respectively. These HIPing conditions had been determined in previous experiments to yield the highest densities for SiC_f/CMZP composites containing up to 20 vol% of fibers. HIPed samples were machined into MOR specimens and tested according to Military Specification 1942 A. The reason for using type A MOR bars was that SiC_f/CMZP samples were commonly curved after HIPing possibly due to the low green strength of the bars prior to HIPing and a temperature gradient inside the HIPing

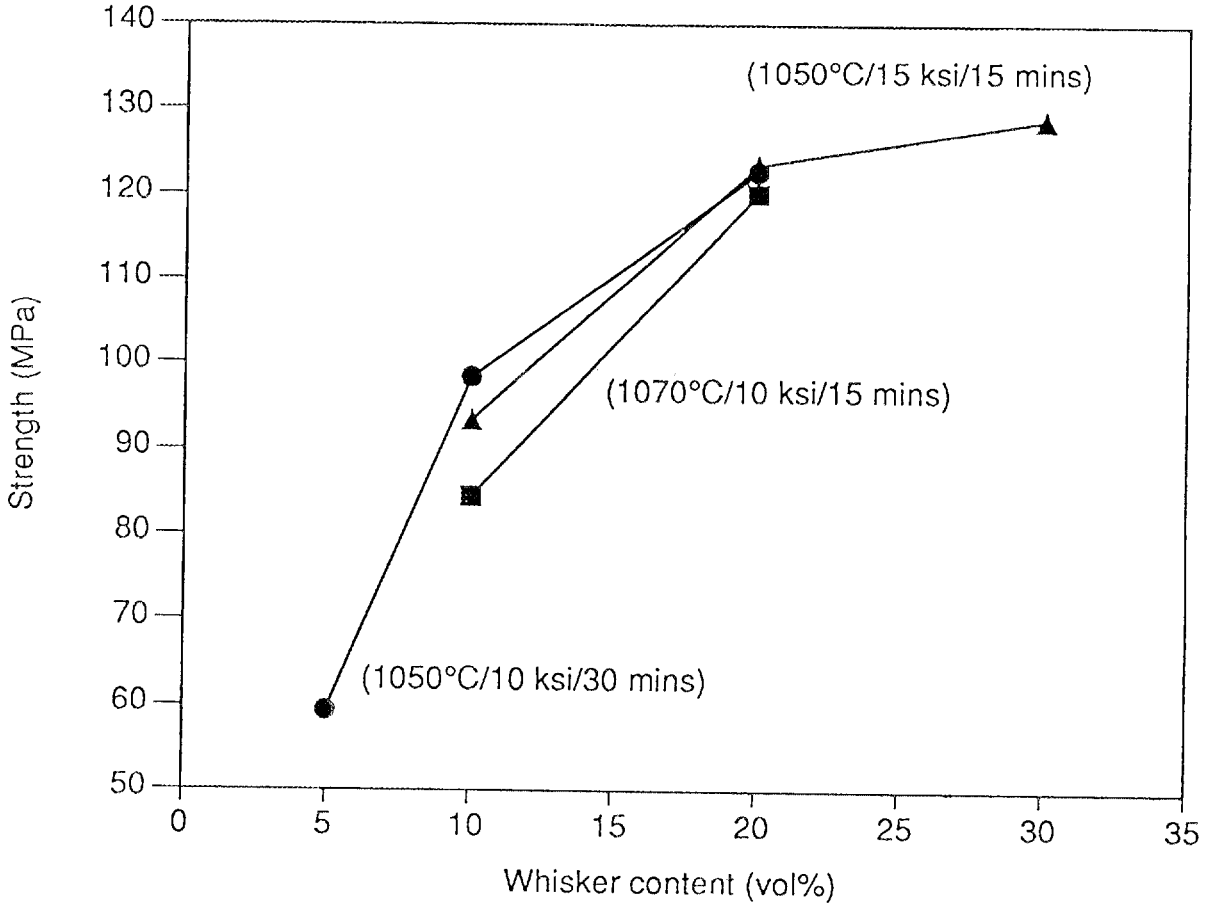

Figure 3. Effect of whisker content on flexural strength of SiC whisker reinforced CMZP

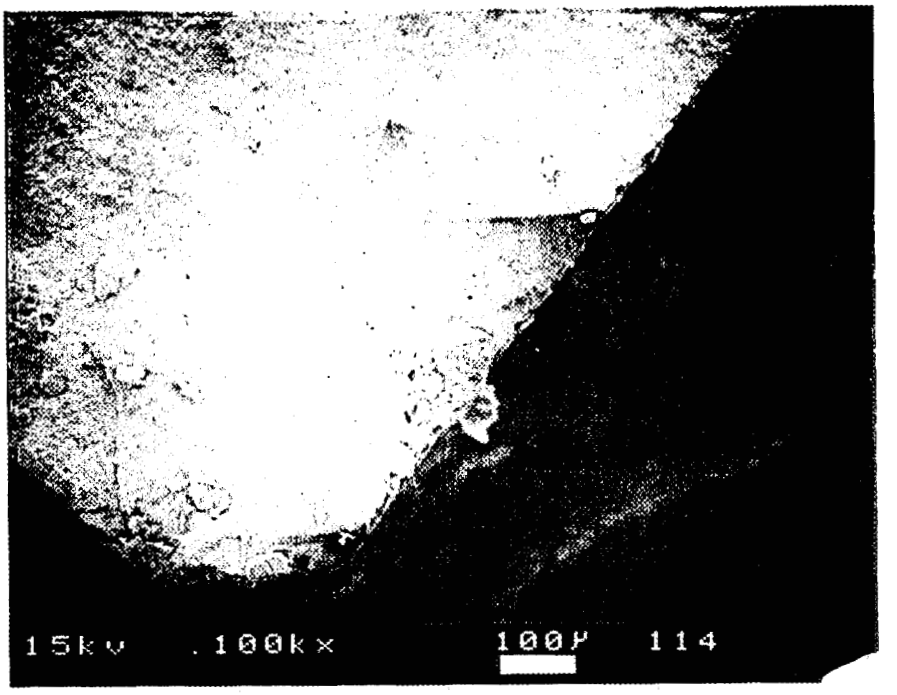

Figure 4. Fracture surface of CMZP composite with 10 vol% SiC whisker, HIP at 1070°C, 10000 psi for 0.25 h

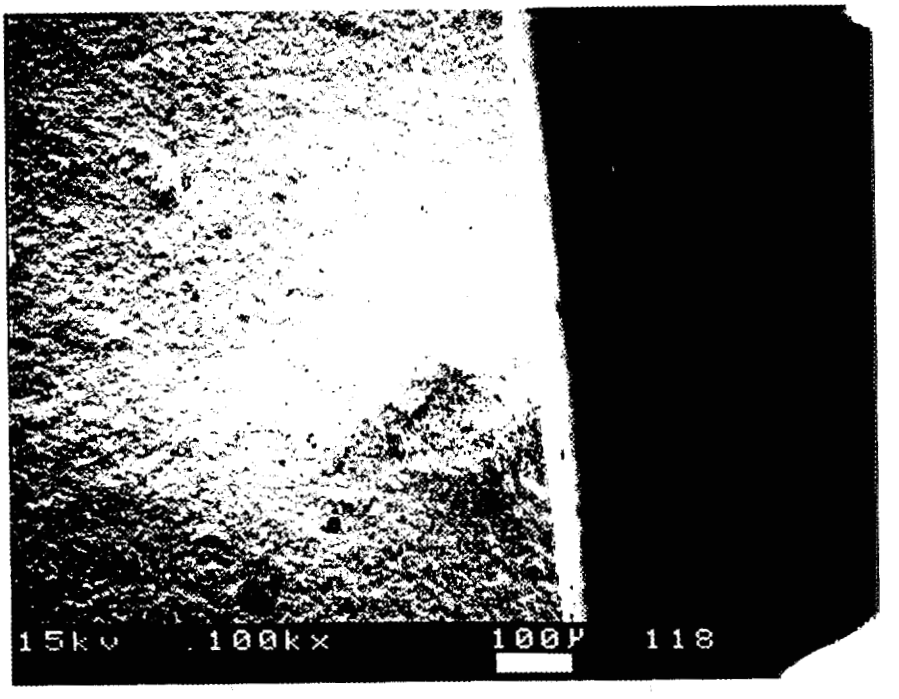

Figure 5. Fracture surface of CMZP composite with 20 vol% SiC HIP at 1070°C, 10000 psi for 0.25 h

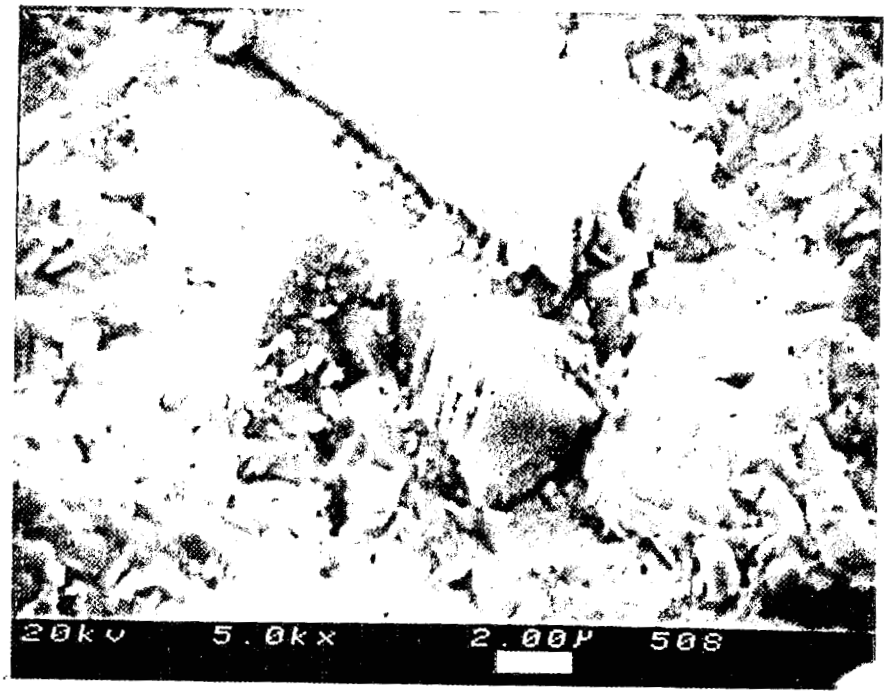

Figure 6. Fracture surface of CMZP composite exhibiting both whisker pull-out and bonding

chamber, and hence only the type A MOR bars could be machined from the HIPed samples. The room temperature flexural strength, S_f, is summarized in Table 1.

SiC_f/CMZP composites prepared by HIPing exhibit a higher strength than the ones made by hot pressing as previously reported (52 MPa on 10 vol% fibers and 91 MPa for 20 vol% fibers with densities varying from 93 to 99 percent of theoretical). The improved strength is attributed to the fact that the HIPed composites are more dense and have improved fiber-matrix bonding, as shown in Figure 7.

Table 1. Room temperature flexural strength of HIPed SiC_f/CMZP composites

Fiber content (vol%)	HIPing condition (°C/MPa/hour)	Density (%)	S_f (MPa)
10	1150/103/0.5	98.5	87
20	1150/103/0.5	98.5	97.3
10	1150/103/0.25	98.3	79
20	1150/103/0.25	98.4	91

Testing conditions: 4-point bending, type A.

Modified β-eucryptite

The fracture toughness of in situ TiO_2 reinforced $AlPO_4$ modified β-eucryptite was examined using the indentation-strength method(1). Flexure bars were machined from samples according to Military Standard Specification 1942 B. One side of each bar was polished then annealed at 750°C for 2 h to remove any residual stresses from either machining or polishing. Three Vickers indents were made 5 mm apart in the center of the polished surfaces using loads of either 2.94, 4.9 or 9.8 N. The flexural strengths of at least seven bars for each indentation load were then determined again according to Military Standard Specification 1942 B. The fracture strength decreases with increased indentation load as shown in Figure 8. The resulting fracture resistance varies from 1.89 to 2.5 MPa $m^{1/2}$. as indicated in Figure 9.

Figure 7. Fracture surface of HIPed SiC_f/CMZP composite containing 20 vol% chopped fibers

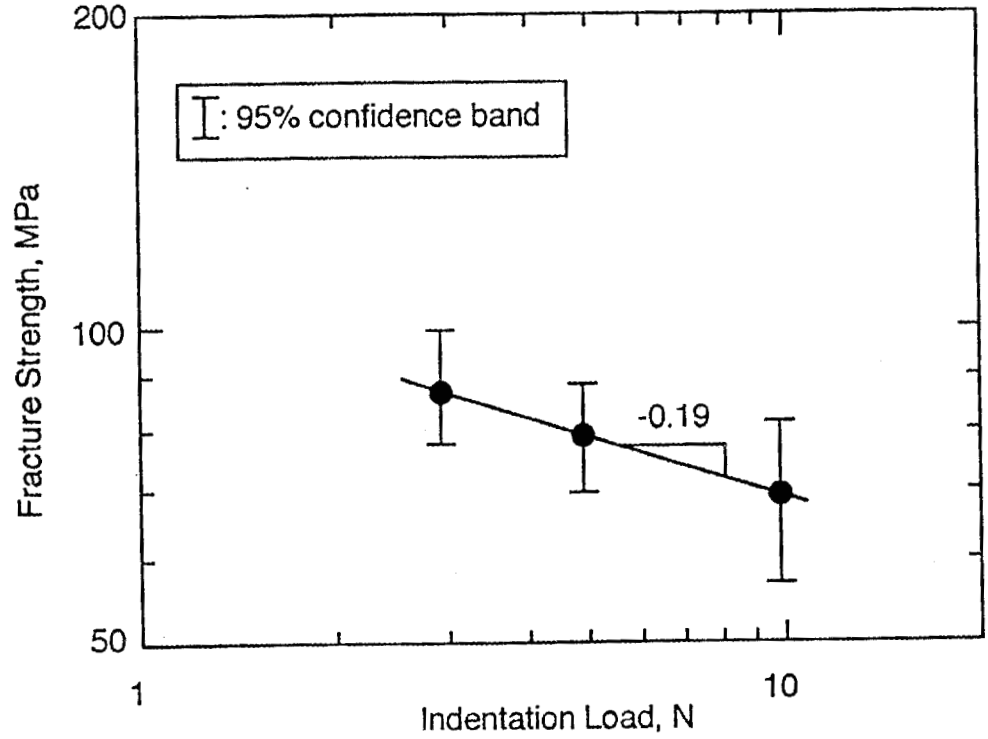

Figure 8. Flexural strength as a function of indentation load

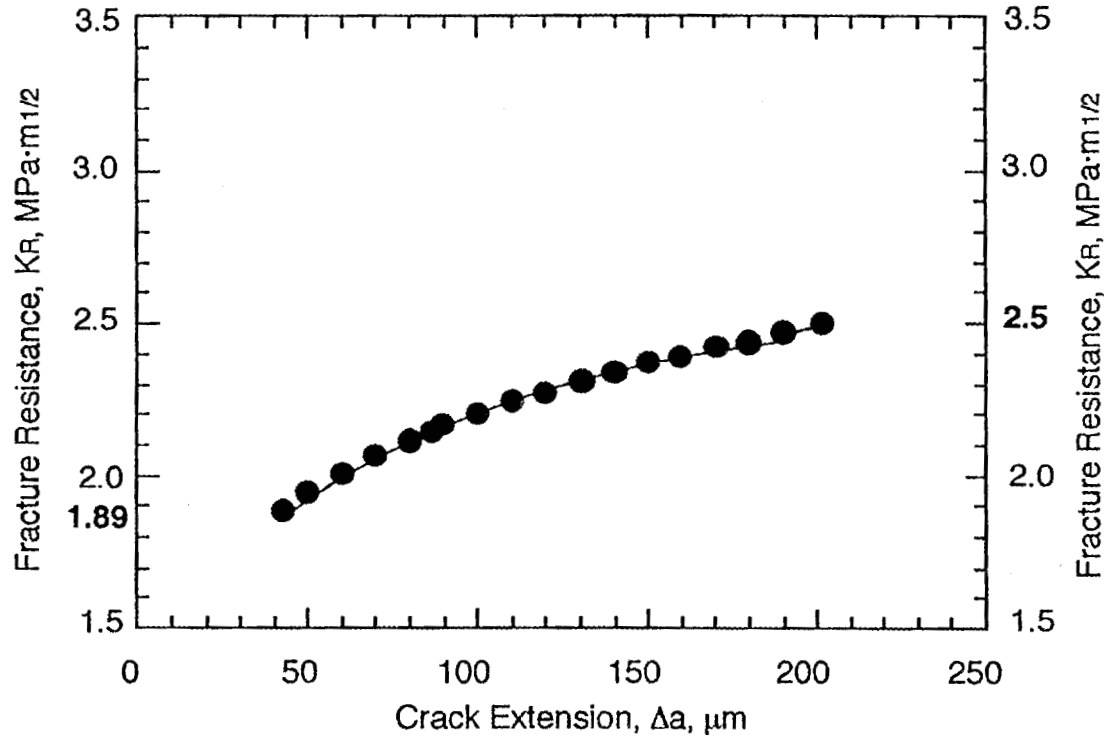

Figure 9. Fracture resistance as a function of crack extension

References

1. R.F. Krause, "Rising Fracture Toughness from the Bending Strength of Indented Alumina Beams," J. Am. Ceram. Soc. 71[5], 338-43(1988).

Status of Milestones

A nine month no cost extension was granted to allow completion of the evaluation of mechanical properties of the ceramics and composites.

Additional CMZP powder has been provided to Dr. Michael Haselkorn, Caterpillar, Inc., for hot pressing to make samples for mechanical property determination (Milestone VPI 2.4.1, Table 2).

The high temperature mechanical properties of NZP Ceramics is underway and will be completed in the near future. (Milestone VPI 2.4.3b, Table 2).

The characterization of in-situ NZP whisker reinforced composites (Milestone VPI 2.4.6b, Table 2) is underway and slightly behind schedule.

The fracture toughness and R-curve behavior of CMZP and CMZP composites will be evaluated at the High Temperature Materials Laboratory, Oak Ridge National Labs.

Communications/Visits/Travel

Dr. T. K. Li presented an invited paper entitled "Thin Film Coatings of $(Ca_{0.6},Mg_{0.6})Zr_4(PO_4)_6$" at the 1992 AIChE annual meeting in Miami, Florida on November 1-6, 1992.

Dr. J. J. Brown, Jr. presented a paper entitled "Alkali Corrosion Resistant Coatings for Si_3N_4 Ceramics" at the 1992 Fall Meeting of the Materials Research Society in Boston, Massachusetts on December 2-3, 1992.

Two presentations were made at the Fourth Annual Program Review and Steering Committee Meeting of the Center for Advanced Ceramic Materials, Feb. 18 and 19, 1993,

Table 2. KEY TO MAJOR MILESTONES (WBS ELEMENTS)

		Completion Date
VPI 2.4.1	Property Optimization by Hot Pressing	July 31, 1992
VPI 2.4.2	Optimization of Compositions	Mar. 31, 1991
VPI 2.4.3	Mechanical Properties of NZP Ceramics	
	a. Characterization at Room Temperature	Dec. 31, 1991
	b. Characterization at High Temperature	July 31, 1992
VPI 2.4.4	Fiber Reinforced Composites	
	a. Synthesis of SiC/NZP Composites	July 31, 1991
	b. Characterization of Mechanical Properties	July 31, 1992
VPI 2.4.5	Lightweight Insulation	Sept. 30, 1991
VPI 2.4.6	Characterization of In-Situ Toughened Composites	
	a. Modified β-eucryptite Composites	July 31, 1992
	b. NZP Whisker Reinforced Composites	July 31, 1992
VPI 2.4.7	Submit Technical Paper on Research Results for Publication	July 31, 1991
VPI 2.4.8	Final Report	Sept. 30, 1992

Figure 10 Status of milestones

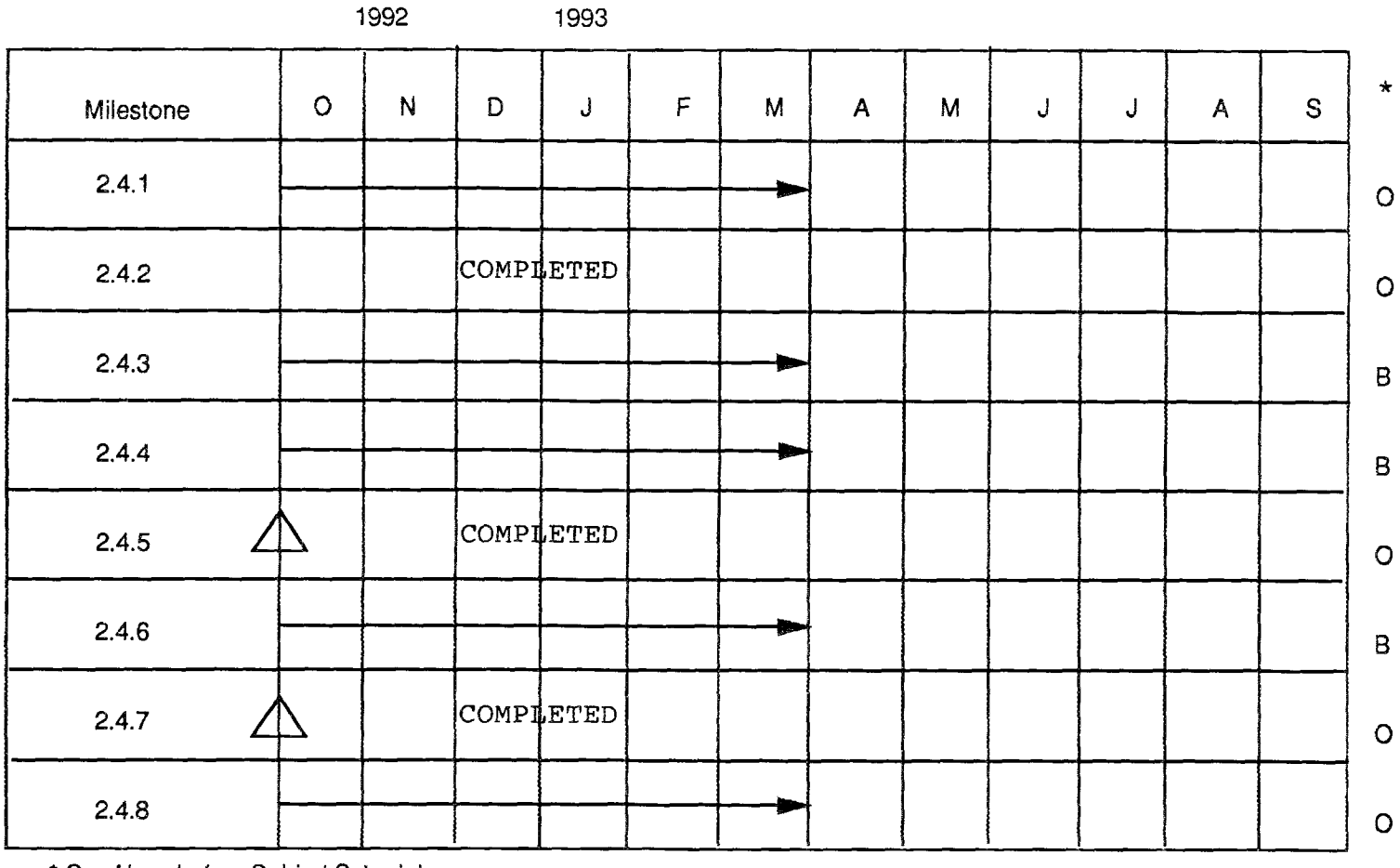

* On, Ahead of, or Behind Schedule

Blacksburg, VA:

1) T.K. Li and D. A. Hirschfeld, "CMZP Coatings on SiC and Si_3N_4."

2) K. H. Lee, "In Situ Reinforced Glass Ceramic in the Lithia-Alumina-Silica System."

Problems Encountered

None

Publications

U.S. Patent #5,186,729 issued on Feb. 16, 1993, to K.H.Lee, D.A.Hirschfeld, and J.J.Brown entitled "An In-Situ Whisker Reinforced Glass-Ceramic."

Development of NZP Ceramic Based "Cast-in-Place" Diesel Engine Port Liners

Santosh Y. Limaye, (LoTEC, Inc.)

Objective/Scope

The overall objective of this research program is to develop sodium-zirconium-phosphate (NZP) ceramic based "cast-in-place" diesel engine port liners. Specific objectives are: (1) Materials requirement analysis, (2) successful demonstration of metal casting around the ceramic, (3) Cost-effective process development, and (4) Develop high temperature database (stability, thermal cycling, thermal shock). This effort is comprised of seven major tasks.

Technical Progress

Task 1: Materials Requirements Analysis: A preliminary finite element analysis (FEA) has been carried out to evaluate the stresses involved in metal casting process. A set of properties based on prior information was chosen for the NZP ceramic, metal and the sand used in metal casting process. Table I shows the properties that were chosen for this finite element stress analysis. Two different casting configurations are being considered for this finite element analysis; a straight tube and an L-shaped tube as shown in Figure 1. Instead of using commercially available FEA software packages such as ANSYS, a set of public domain software packages called INGRID (for grid generation), TOPAZ2D (for thermal analysis) and NIKE2D (for stress analysis) were used. These software packages are less expensive and provide similar results. In order to verify the functionality of these software packages, a standard "high confidence" problem was analyzed using these software packages and the solutions were found to be satisfactory. The results of the preliminary FEA are shown in Figure 2 and Table II. These results show that the NZP ceramic is subjected to large compressive hoop stresses along the radial directions.

A series of tubes have been fabricated for metal casting trials to verify the results of the analytical model. Figure 3 shows the configuration for metal casting trials. A series of thermocouples will be buried at various locations to compare with the thermal gradient patterns generated by the FEA (as shown in Figure 2). Once the first metal casting trials are completed, further modifications to the FEA model will be made as a result of this testing. As the work on this task progresses, the data generated will be utilized to further refine this FEA model. Eventually, this model will be refined to perform a parametric study of the effects of various materials' properties on thermal stresses.

TABLE I: Preliminary data used for developing the thermal analysis model.

Material Properties and Model Inputs (Presented in the MKS, cgs units system)	**NZP**	**Gray Cast Iron**	**Sand**
General Properties			
Length (cm)	15	15	15
Thickness (cm)	0.3	1	30
Density (kg/m^^3)	3200-3650	7000	1450
Mechanical Properties			
Flexural Strength (MOR) (MPa)	***	***	***
25 C	70	***	***
1000 C	70	***	***
1500 C	65	***	***
Young's Modulus 25 C to 1000 C (GPa)	70	***	***
Fracture Toughness (MPa)	1.5-2.0	***	***
Ultimate Strength (MPa)	***	***	***
Tension	30-90	370	***
Compression	90-300	830	***
Shear	***	330	***
Yield Strength (MPa)	***	***	***
Tension	30-90	250	***
Shear	***	165	***
Allowable Stresses (kPa)	***	***	***
Tension or Compression	***	165475	***
Shear	***	99975	***
Elastic Moduli (GPa)	***	***	***
Tension or Compression	35-100	172	***
Shear	***	83	***
Poisson Ratio	0.24	0.28	
Thermal Properties			
Thermal Conductivity (W/m K)	1	41.9	1.26
Thermal Conductivity as a f(Temp) (W/m K) (Sand) 0.6606-2.084E-4 T+7.741E-7 T^^2			
Specific Heat (J/kg K)	***	***	***
Ambient	460	628	838
473 K	***	***	975.7
673 K	***	***	1092.9
873 K	***	***	1151.5
1073 K	***	***	1159.9
1273 K	***	***	1176.7
Thermal Diffusivity (m^^2/sec)	6.00E-07	9.50E-06	9.10E-07
Coef. of Thermal Expansion (1/C) (NZP range 0.5E-6 to 2.5E-6)	1.00E-06	1.21E-05	***
Heat Transfer Coefficient at Interface (W/m^^2 K) mold/outside air = 83.8	***	***	***
Ambient Temperature K	293	293	293
Liquidus Temperature K	2173	1573	***
Solidus Temperature K	2073	1275	***
Initial Temperature K	293	1273	293

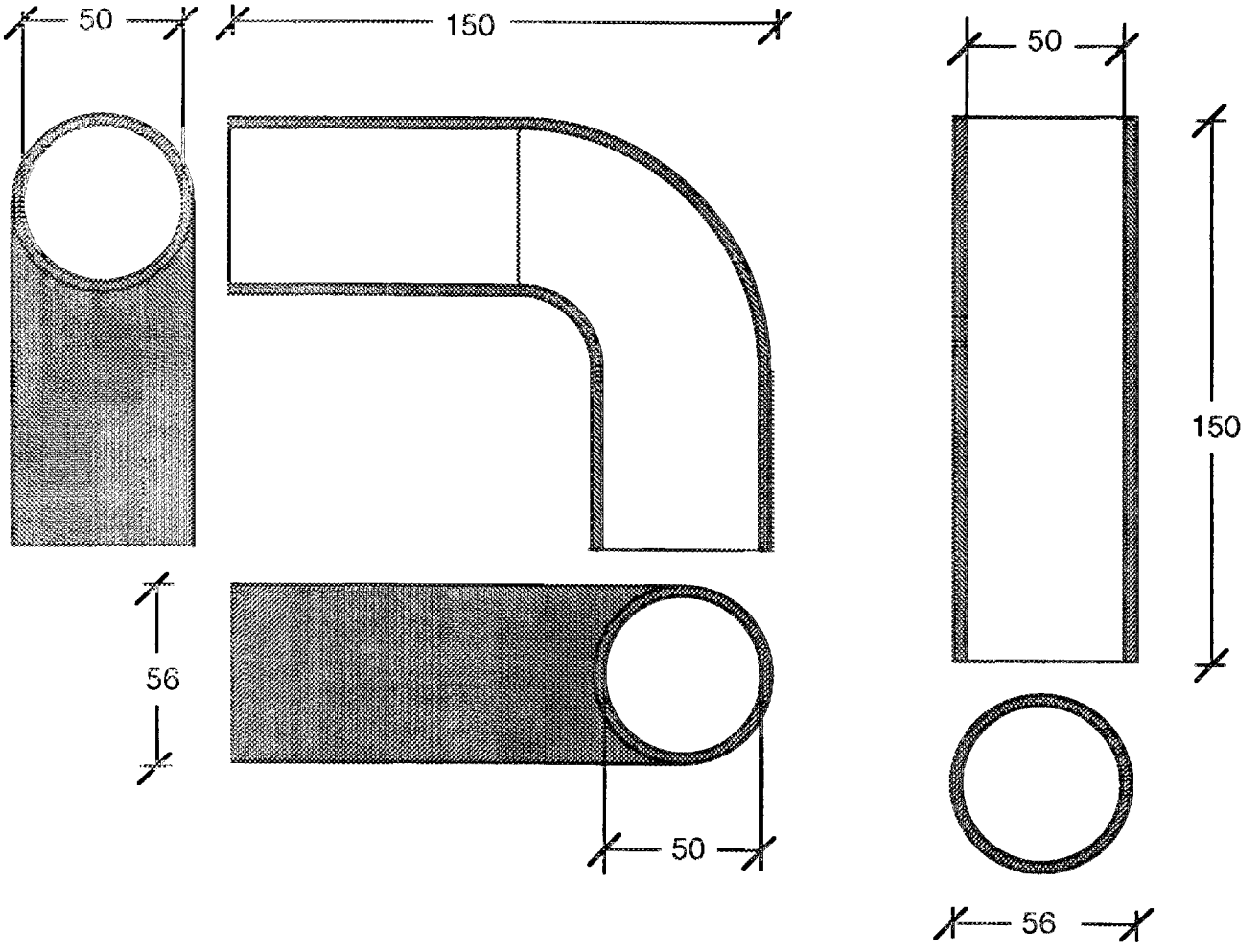

ALL DIMENSIONS ARE IN MILLIMETERS

Figure 1: Dimensions of ceramic tubes for molten metal casting trials. Initial efforts will be focused on straight tubes and as the work progresses, L-shaped tubes will be tested.

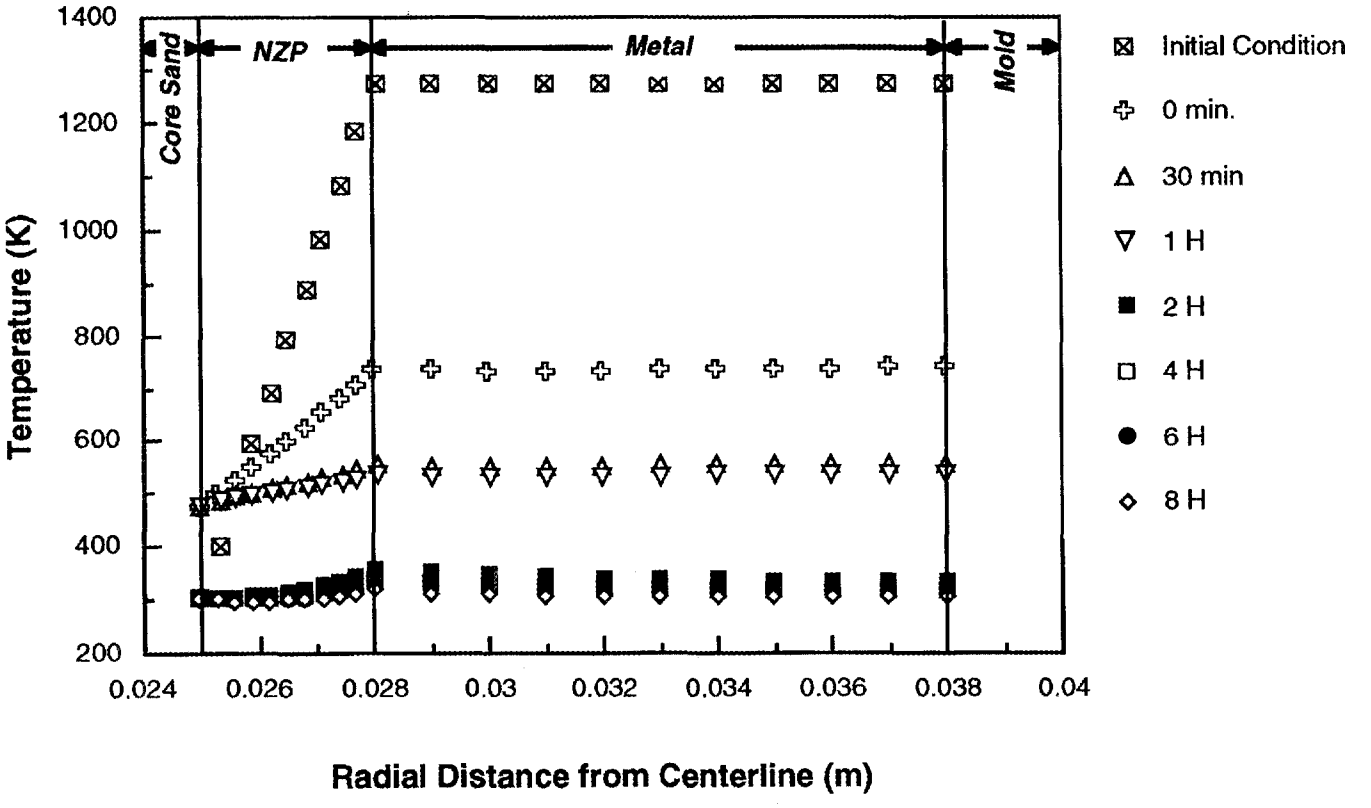

Figure 2: Temperature distribution as a function of time during molten metal casting process. These results were obtained from TOPAZ2D.

Table II: Mechanical Stresses: Results from NIKE2D Software Package

Material	Radial Dist. (m)	Tangential Stresses (MPa)			Type
		30 Min.	2 H	4 H	
NZP	0.025	-718.9	-578.3	-344.1	Compressive
NZP	0.028	-646.0	-519.6	-309.2	Compressive
Cast Iron	0.028	246.1	198.0	117.8	Tensile
Cast Iron	0.038	173.2	139.3	82.9	Tensile

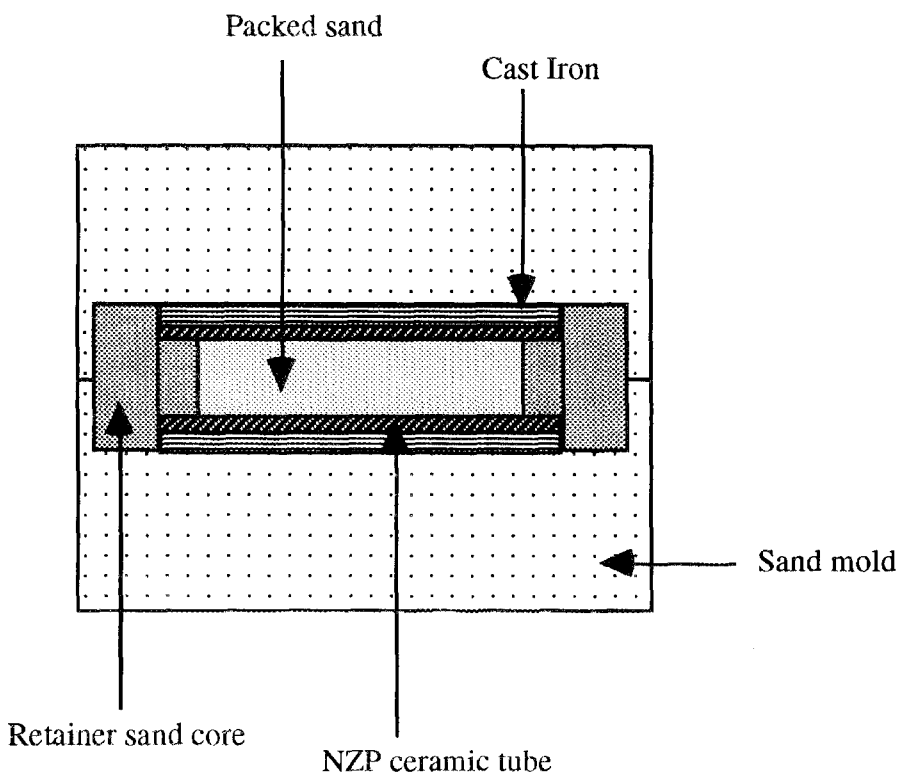

Figure 3: Set-up for molten metal casting trials

Task 2: Fabrication of Test Specimens: BS-25 ($Ba_{1.25}Zr_4P_{5.5}Si_{0.5}O_{24}$) and CS-25 ($Ca_{0.75}Sr_{0.25}Zr_4P_6O_{24}$) are the two NZP compositions chosen to establish the baseline properties. Large (20 kg) batches of BS-25 and CS-25 were synthesized using routine oxide batch mixing process. The size of these batches should insure enough material to perform all the required testing and evaluation on a single batch. Batching consists of milling the raw materials together, screening the milled powder, calcining each composition at its required calcination temperature to produce the single phase NZP structure and post calcination screening. Routine characterization such as powder X-ray diffraction, particle size measurement and surface area analysis was carried out to ensure that the powders had appropriate set of properties.

After the calcination, ceramic slurry was prepared for slip casting by using the standard method of adding an appropriate dispersant, binder, weight percent distilled water and grinding media. A series of tiles of size 2" x 2" x 0.25" were slip cast. These tiles were machined (ground) into specimens to determine mechanical properties (flexural strength, Weibull modulus, Young's modulus), thermal properties (thermal conductivity, thermal expansion, heat capacity) and microstructure.

Task 3: Fabrication of Test Specimens for Metal Casting Trials: As described earlier, a series of cylindrical specimens have been fabricated for the casting trials. The specimen geometry is as described in Figure 1. The metal casting testing was scheduled for the end of May 1993; however, due to the delays in samples preparation, these casting trials have been postponed till the third week of June. The results of these metal casting trials and refined finite element analysis work will be utilized and to fabricate the next iterations of samples for metal casting trials.

Task 4: Process Development: Synthesis of NZP materials and fabrication of specific components are highly crucial to the success this program. Thus a detailed process development task is underway to yield NZP ceramics with appropriate set of properties. The initial process development consist of a study to determine if increases in green density, lower firing shrinkage, and higher sintered density, can be achieved through the use of bi-modal and tri-modal particle size distributions. A detailed work plan has been established to improve the green density by controlling the particle size distribution. Also, a series of experiments have been planned to evaluate various binders, dispersants, and other additives. The effect of these additives on various variables such as slurry rheology, casting rate (during slip casting), binder strength, green density, etc. will be characterized.

Task 5: Materials and Process Modifications: No work has been performed under this task. As the iterative process of metal casting and finite element analysis provides additional guidelines, a set of test matrices will be developed to attain those specific properties.

Task 6: Characterization: Measurement of flexural strength and Weibull modulus on the baseline compositions, BS-25 and CS-25 was carried out during this reporting period. Bar shaped specimens were prepared (approx. 5.5 mm x 6.5 mm x 50 mm), by grinding and slicing 2" x 2" x 0.4" slip cast tiles. The sliced bars had their edges chamfered. The bars were strained to failure using a 4-point bend strength fixture mounted on an Instron Universal Testing Machine. The cross head speed was 0.5 mm/min. and the load at failure was recorded. From the load at failure and the cross-sectional dimensions of the test specimens the flexural strength was calculated. Table III summarizes the results. There were 60 BS-25 specimens and 100 CS-25 specimens.

The sintered density and open porosity of the two compositions are a function of the processing. The average particle size (mass percent) and particle size range for BS-25 was 2.1 μm and 6 to 0.7 μm respectively, and the surface area was 3.20 m^2/g.. The average particle size (mass percent) and particle size range for BS-25 was 5.3 μm and 18 to 0.9 μm respectively, and the surface area was 5.3 m^2/g. The differences in sintered density, etc. between BS-25 and CS-25 is due to the typical sintering temperatures and times. As the process is further refined, it is expected that the mechanical properties will improve substantially for both BS-25 and CS-25.

Task 7: High Temperature Testing: No work has been performed under this task.

Table III: Summary results of Flexural Strength Measurements of BS-25 and CS-25

Composition	Average Density	Average Open Porosity	Average Flexural Strength	Standard Deviation	Weibull Modulus
BS-25 (60 samples)	2.52 g/cm^3	27.5%	38.4 MPa	3.46	12.9
CS-25 (100 samples)	2.51 g/cm^3	21.0%	28.4 MPa	3.22	10.1

Status of milestones

Milestone 1 Disseminate characterization data for baseline compositions to all program participants: partially complete

Milestone 2 Disseminate results of thermal stress modeling to all program participants: partially complete

Publications

None

References

None

1.3 THERMAL AND WEAR COATINGS

Fabrication and Testing of Corrosion-Resistant Coatings

W. Y. Lee, D. P. Stinton, and D. W. Graham (Oak Ridge National Laboratory)

Objective/scope

Sodium corrosion of SiC and Si_3N_4 components in gas turbine engines is a potentially serious problem. The outer surfaces of SiC and Si_3N_4 parts oxidize at high temperatures to form an SiO_2 layer that inhibits further oxidation. However, sodium that is present in high-temperature combustion atmospheres reacts with the SiO_2 layer, such that it is no longer protective. The objective of this program is to develop a coating that will protect the underlying SiC or Si_3N_4 from sodium corrosion and provide simultaneous oxidation protection. To evaluate the behavior of potential materials such as stabilized ZrO_2 or HfO_2, TiO_2, $Al_2O_3 \bullet TiO_2$, and Ta_2O_5 in sodium-containing atmospheres, the corrosion resistance of hot-pressed samples of these materials will first be evaluated. A chemical vapor deposition (CVD) process will be developed for the application of the most promising coatings. The effect of the combustion environment upon coating characteristics such as microstructure, strength, adherence, and other properties will then be evaluated.

Technical progress

(1) Ta_2O_5 CVD Process Development

It was previously reported that most of the well-adherent Ta_2O_5 coatings deposited on SiC and Si_3N_4 substrates tended to grow as highly faceted columnar grains or whiskers. In general, the columnar grains did not readily coalesce during growth, resulting in the formation of undesirable open voids and pin-holes in the coating structure. In this reporting period, 12 deposition experiments were conducted to better understand the influences of process parameters on growth kinetics and coating morphology. In these experiments, deposition temperature, O_2 flow rate, and Cl_2 flow rate (used for Ta chlorination) were systematically varied as summarized in Table 1. The microstructure of Ta_2O_5 coatings deposited on Si_3N_4 (G10) substrates was characterized using scanning electron microscopy (SEM) and X-ray diffraction (XRD).

The growth rate of Ta_2O_5 could not be correlated in any consistent manner with respect to the changes in temperature or O_2 concentration. In general, the variations in growth rate were random and unpredictable. One consistent trend identified from the deposition data was that the growth rate tended to increase with an increase in Cl_2 partial pressure at 1200°C, providing that the total flow rate in the reactor remained relatively constant as shown in Fig. 1. A similar behavior was observed at 1100°C as shown in Fig. 2. It was also evident from these figures that the total flow rate appeared to have a somewhat strong, non-linear influence on the deposition process.

The SEM study indicated that the coating morphology was strongly affected by the changes in process conditions but not in any predictable manner. In general, the coatings tended to be columnar or fibrous, sparsely nucleated, and loosely coalesced as summarized in Table 1. As an example, Fig. 3 shows a micrograph of such morphology. Ta_2O_5 deposited from run #1(142) was the only coating that looked fairly dense as shown in Fig. 4. Some coatings were not uniform in thickness and morphology, particularly in the direction perpendicular to flow (i.e., radial direction), although the Si_3N_4 substrates

Table 1. Summary of Ta_2O_5 CVD experiments conducted using Si_3N_4 (G10) substrates (1 × 0.45 × 0.3 cm). Prior to deposition, the substrates were treated in O_2 at 1200°C for 75 min to improve coating adhesion

Run No.	T(°C)	Flow Rate (cm^3/min at STP)			P (torr)	Weight gain (mg/h)	Surface morphology
		Cl_2	O_2	Ar			
1(142)	1200	2	30	40	50	0.67	Densely nucleated
2(143)	1100	1	30	40	50	0.03	Columnar/fibrous
3(144)	1200	1	10	40	50	0.17	Columnar
4(145)	1200	1	30	40	50	0.30	Fibrous
5(146)	1100	2	20	40	50	3.77	Columnar/fibrous
6(147)	1200	1	20	40	50	0.13	Sparsely nucleated
7(148)	1100	2	10	40	50	2.80	Columnar
8(149)	1200	2	20	40	50	1.43	Sparsely nucleated
9(150)	1100	1	10	40	50	0.40	Columnar/fibrous
10(151)	1100	2	30	40	50	5.50	Columnar
11(152)	1100	1	20	40	50	1.80	--
12(153)	1200	2	10	40	50	1.23	Fibrous

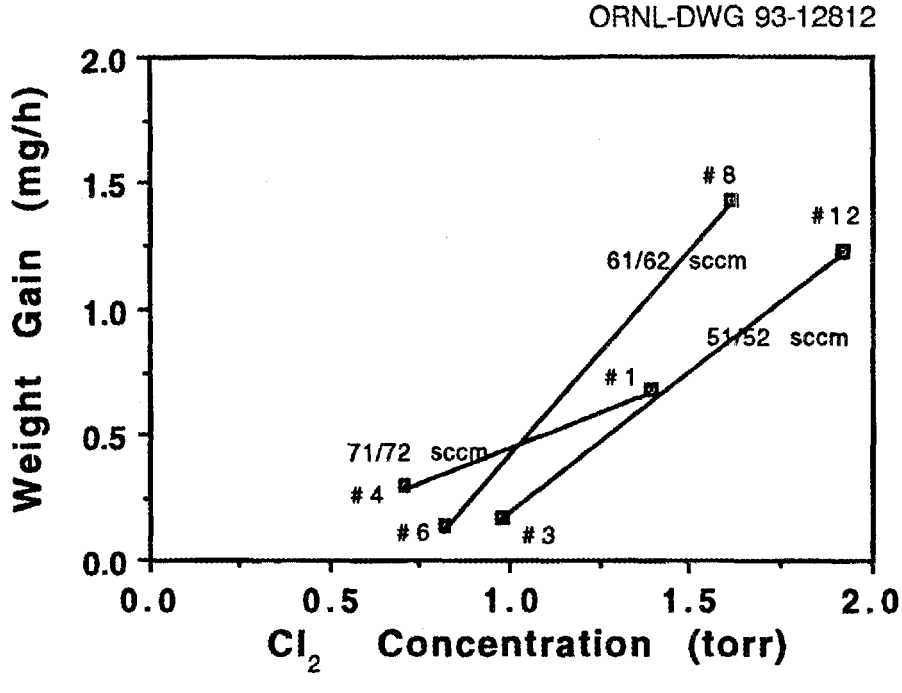

Fig. 1. Weight gain per deposition time plotted as a function of inlet Cl_2 partial pressure at 1200°C. The weight gain increased with increased Cl_2 partial pressure when the total flow rate remained relatively constant.

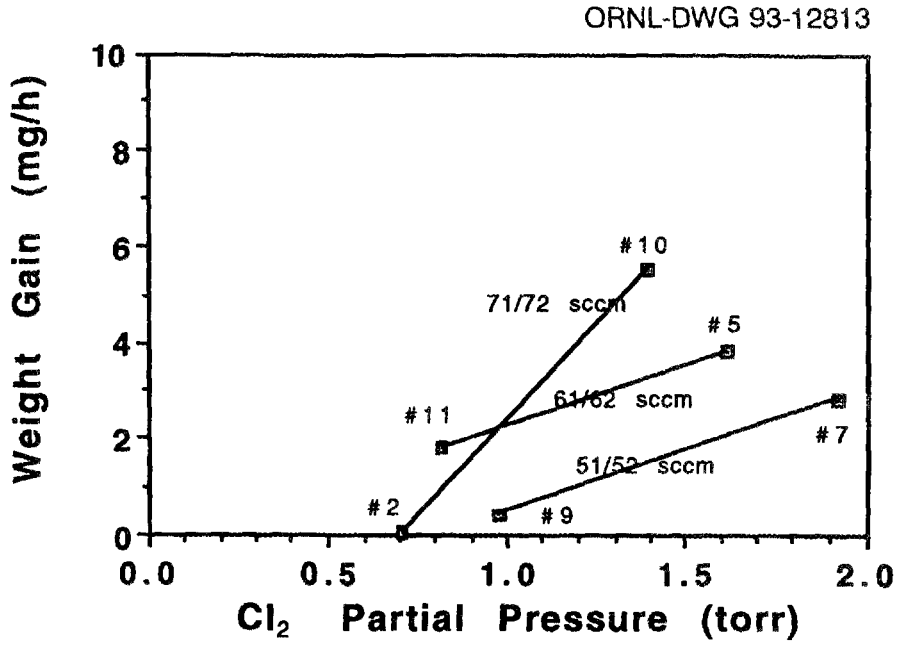

Fig. 2. Weight gain per deposition time plotted as a function of inlet Cl_2 partial pressure at 1100°C. The weight gain increased with increased Cl_2 partial pressure when the total flow rate remained relatively constant.

used in this study were thought to be geometrically too small (1 × 0.45 × 0.3 cm) to cause such behavior.

In order to comprehend these observations, the flow characteristics in the reactor were considered. For the above deposition experiments, a total flow rate of 50 to 70 cm^3/min at STP (mixture of Ar and O_2) was typically injected into the reactor using a small stainless steel tube having a diameter of 0.3 cm while Ta was chlorinated in another larger tube. Under this situation, the gas velocity coming out of the 0.3-cm tube was extremely high and almost supersonic (i.e., several hundred m/s). This gas velocity was probably too high for reagents to radially diffuse and mix with $TaCl_5$ in the deposition zone. Near the tip region of the injector, the Peclet (Pe) number, which could be interpreted as a ratio of the rate of convective mass transfer in the axial direction versus the rate of diffusive mass transfer in the radial direction, was estimated to be in the range of about 1000. The Pe number is defined as $Pe = vd/D_{O2\text{-}TaCl5}$, where v is the total fluid velocity at the tip of the 0.3-cm injector, d is the diameter of the reactor tube, and $D_{O2\text{-}TaCl5}$ is the binary diffusion coefficient between O_2 and $TaCl_5$. $D_{O2\text{-}TaCl5}$ was calculated using the Chapman-Enskog relationship.[1] The large Pe number indicated that the deposition experiments were performed in a highly convection-dominant region, which would most likely cause inadequate reagent mixing as well as the development of strongly convergent and unstable flow patterns in the reactor tube. The deposition of nonuniform coatings observed in our experiments was probably as a result of these undesired flow characteristics. More importantly, since the influence of flow rate on the deposition process was too overwhelming, the role of other process parameters, such as temperature and O_2 concentration, could not be easily identified from the deposition data.

149

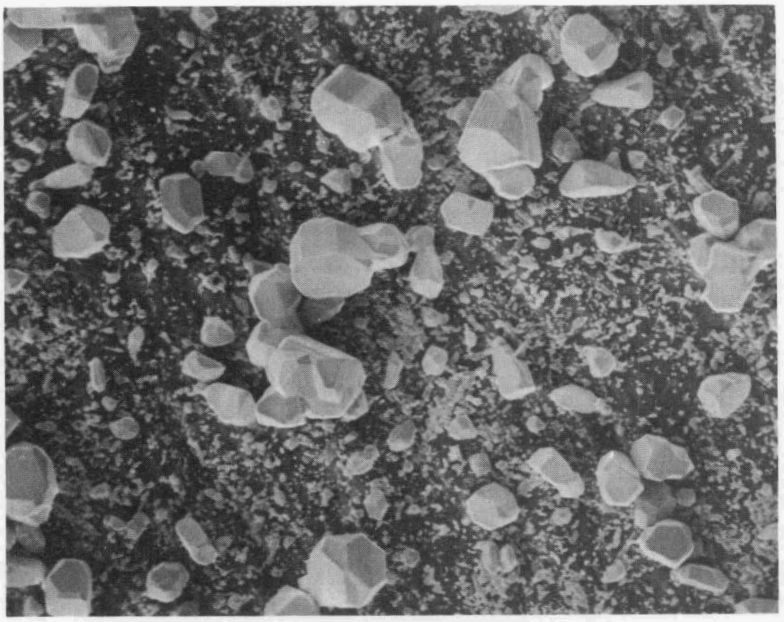

Fig. 3. Scanning electron microscopy micrograph of columnar Ta_2O_5 coating from run #3(149); scale: 1cm = 5μm.

142

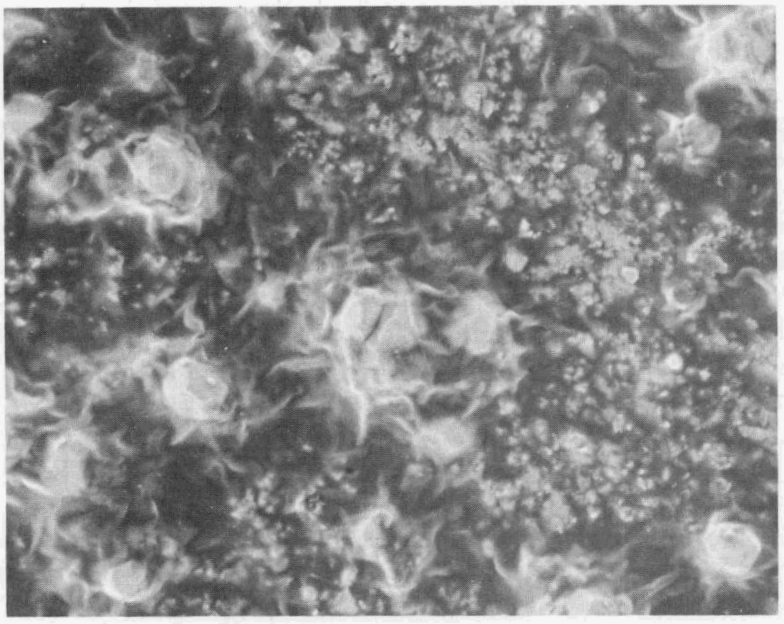

Fig. 4. Scanning electron microscopy micrograph of Ta_2O_5 coating with relatively dense surface morphology: run #1(142); scale: 1cm = 5μm.

The results from the fluid mechanical analysis clearly suggested that a new gas injection system was needed to perform deposition experiments in a more diffusive and kinetically controllable environment. A new dual-path, co-axial injector, which has relatively large cross-sectional areas for gas introduction, was designed and fabricated. The inner path (1.27 cm diam) will be used for the chlorination of Ta, and the outer one (1.91 cm diam) will be used for injecting CO_2 and H_2.

Our recent literature review on the CVD of oxide materials indicated that the use of CO_2 and H_2 as an oxygen precursor might provide superior coating morphology. It is generally viewed that H_2O may be too reactive for the CVD of oxides. For example, when H_2O is directly fed into a reaction chamber, the formation of oxide powder is typically observed.[1] On the other hand, O_2 is kinetically stable so that the formation of oxides tends to be limited by the supply of oxygen and atoms on the deposition surface. Under this type of low supersaturation conditions, highly crystalline, faceted oxide grains are expected to grow. It appears that the reactivity of the CO_2+H_2 mixture is somewhere between that of H_2O and O_2 and, therefore, is probably more suitable for the CVD of dense, pin-hole-free Ta_2O_5 coatings. Prior work on the CVD of Ta_2O_5 by researchers at Ultramet also indicates that the use of CO_2 and H_2 is found to be most effective in preparing coatings used for oxidation protection of carbon-carbon composites.[2]

We are planning to perform deposition experiments using CO_2 and H_2. Necessary gas line modifications have been completed, and the apparatus is currently being checked for air leaks. With the newly designed injector and the use of CO_2 and H_2, it is expected that the kinetics of the Ta_2O_5 CVD process can be better analyzed, and the coating microstructure can be appropriately tailored.

(2) Thermodynamic Feasibility of $ZrTiO_4$

The CVD of $ZrTiO_4$ by reaction of O_2 with titanium chloride and zirconium chloride was considered from a thermodynamic standpoint. With the lack of any prior work on the CVD of $ZrTiO_4$, equilibrium calculations were used to determine the thermodynamic feasibility of the $ZrTiO_4$ deposition process and also to identify suitable deposition conditions for experimentation. A computer program, ChemSage,[3] and a thermodynamic data base developed by Scientific Group Thermodata Europe (SGTE)[4] were used to simulate the chemical equilibria for the Zr-Ti-O-Cl system.

The thermochemical data for $ZrTiO_4$, which have not been reported in the literature, were estimated using the following method. Heat-capacity (C_p) data for $ZrTiO_4$ were obtained using Kopp's rule: the heat capacity of a solid or liquid compound is equal to the sum of the heat capacity of its constituent elements in the solid or liquid states.[5] As a consequence of Kopp's rule, the entropy ($\Delta S°_{298.15K}$) of solid and liquid compounds can be estimated from the addition of the entropy of their constituent components in the solid or liquid states.[6] Also, a good estimate of the enthalpy of formation of a compound may be obtained by similarly adding the enthalpy of the components.[7,8] The enthalpy of formation ($\Delta H°_f$) for $ZrTiO_4$ was initially estimated by adding together the existing data for ZrO_2 and TiO_2 in the SGTE data base. This value was then used as a starting point from which the value of $\Delta H°_f$ could be modified to obtain agreement with the observed incongruent melting of $ZrTiO_4$ at ~2123K.[9]

As shown in Fig. 5, a CVD phase diagram of the Zr-Ti-O-Cl system was constructed as a function of $ZrCl_4$, $TiCl_4$, and O_2 concentrations at 1373 K and 1.33 kPa. This phase diagram showed that $ZrTiO_4$ was predicted to be deposited as a single phase in only a

ORNL-DWG 93-12814

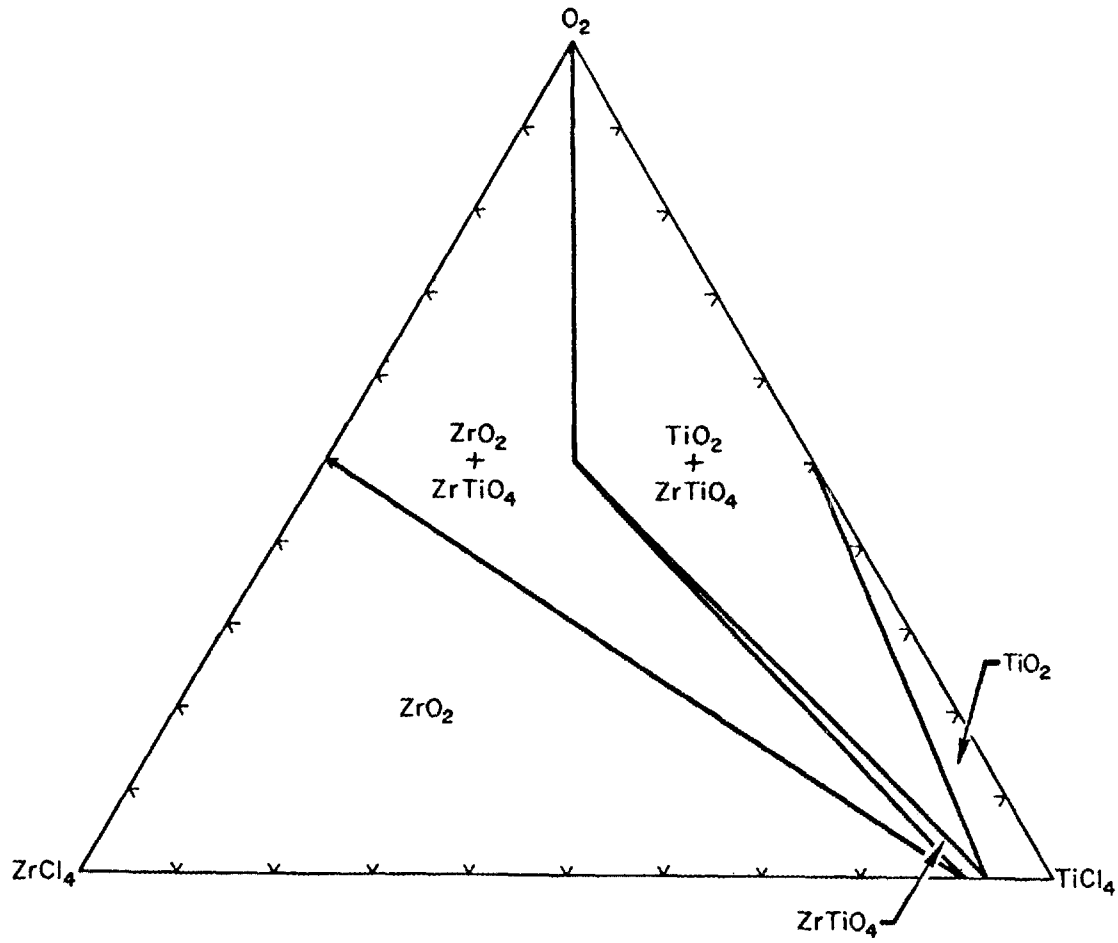

Fig. 5. Chemical vapor deposition phase diagram of the Zr-Ti-O-Cl system at 1373 K and 1.33 kPa.

narrow region of the diagram. Figure 5 also illustrated that, with increased mole fraction of O_2, the codeposition of either ZrO_2 or TiO_2 with $ZrTiO_4$ was expected to occur. ZrO_2 was predicted to be deposited as a single phase over a large portion of the $ZrCl_4$-rich region of the diagram. The deposition of TiO_2 as a single phase was predicted in the region of high $TiCl_4$ concentrations. The effect of temperature on the stability of the $ZrTiO_4$ phase was found to be relatively insignificant in the range of 1173 and 1500 K.

In summary, the results of the thermodynamic calculations indicated that the CVD of $ZrTiO_4$ from O_2, $ZrCl_4$, and $TiCl_4$ would be feasible over a relatively narrow range of deposition conditions. Therefore, from a thermodynamic point of view, it could be suspected that the deposition of pure $ZrTiO_4$ would be experimentally difficult to achieve and/or control. However, kinetic experiments should be performed to address the ultimate feasibility of the $ZrTiO_4$-CVD process.

References

1. R. C. Reid, J. M. Prausnitz, and T. K. Sherwood, "The Properties of Gases and Liquids," 3d ed., McGraw Hill Book Company, New York, 1977.

2. A. J. Sherman, Ultramet, private communication.

3. G. Eriksson and K. Hack, "ChemSage - A Computer Program for the Calculation of Complex Chemical Equilibria," *Metall. Trans. B* **21B**, 1013 (1990).

4. SGTE Solution and Pure Substances Data Base was supplied by the developers of the ChemSage program; GTT Gesellschaft fur Technische, Thermochemie und -physik mbH, Kaiserstrabe 100, 5120 Herzogenrath 3.

5. H. Kopp, *Ann. Chem. Pharm. Suppl.* **3**, 289 (1964).

6. C.H.P. Lupis, *Chemical Thermodynamics of Materials*, North-Holland, New York, 1983.

7. T.M. Besmann, Oak Ridge National Laboratory, private communication.

8. B. Gallois, Stevens Institute of Technology, private communication.

9. E.M. Levin and H.F. McMurdie, p. 169 in *Phase Diagrams for Ceramists, 1975 Supplement*, American Ceramic Society, Westerville, Ohio, 1975.

Development of Adherent Coatings to Reduce Contact Stress Damage of Ceramics

V. K. Sarin (Boston University)

Objective/Scope

The development of oxidation/corrosion resistant, high toughness, adherent coating configurations for silicon based ceramic substrates for use in advanced gas turbine engines.

Technical Progress

Al_2O_3 coatings have been successfully grown on Si_3N_4 substrates in a reactor geometry that is also suitable for depositing SiO_2. As was previously reported, SiO_2 coatings had been deposited on Si_3N_4 using Tetraethoxysilane ($Si[OC_2H_5]_4$) as the source at 800°C and 50 torr pressure. Successful deposition of Al_2O_3 has enabled us to co-deposit SiO_2 and Al_2O_3. Process parameters used for depositing Al_2O_3 were varied within the range established for SiO_2. The reactor geometry and process parameters had to be adjusted so as to accommodate both SiO_2 and Al_2O_3 coatings.

Thermodynamic calculations(using the Solgasmix program[1]) were used to determine limiting criteria for the co-deposition of SiO_2 and Al_2O_3 and aid in establishing rate-limiting gaseous species. Additionally, this information was used to help determine the range of input conditions which would produce SiO_2 and Al_2O_3 at equilibrium. Relative proportions in concentrations of the reactants necessary ($Si[OC_2H_5]_4$, and $AlCl_3$) to deposit SiO_2 and Al_2O_3 were varied over a set of temperatures (800 and 900 °C) and pressures (50 and 100 torr). CVD phase diagrams were constructed by varying the concentration of $AlCl_3$ over a range of 0.1 to 1.5 moles and that of $Si[OC_2H_5]_4$ over a range of 0.1 to 0.4 moles. Figures 1,2,and 3 show CVD phase diagrams generated using these set of conditions. These diagrams have been generated with a limited number of calculations (approximately 500) and therefore only reflect general trends.

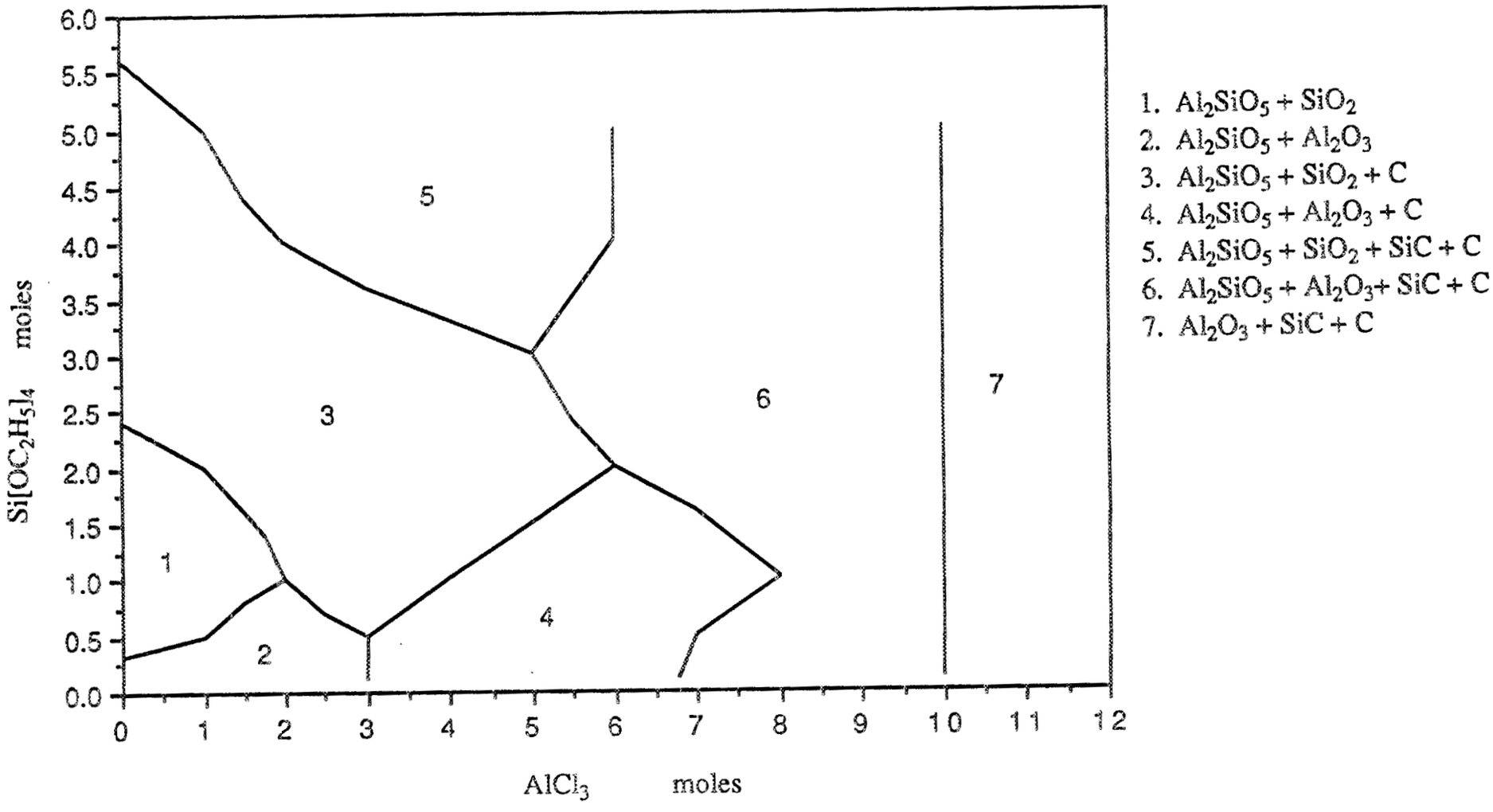

Figure 1: CVD phase plot of the $Si[OC_2H_5]_4$ / $AlCl_3$ system T=800 ^{0}C, Pressure = 50 torr

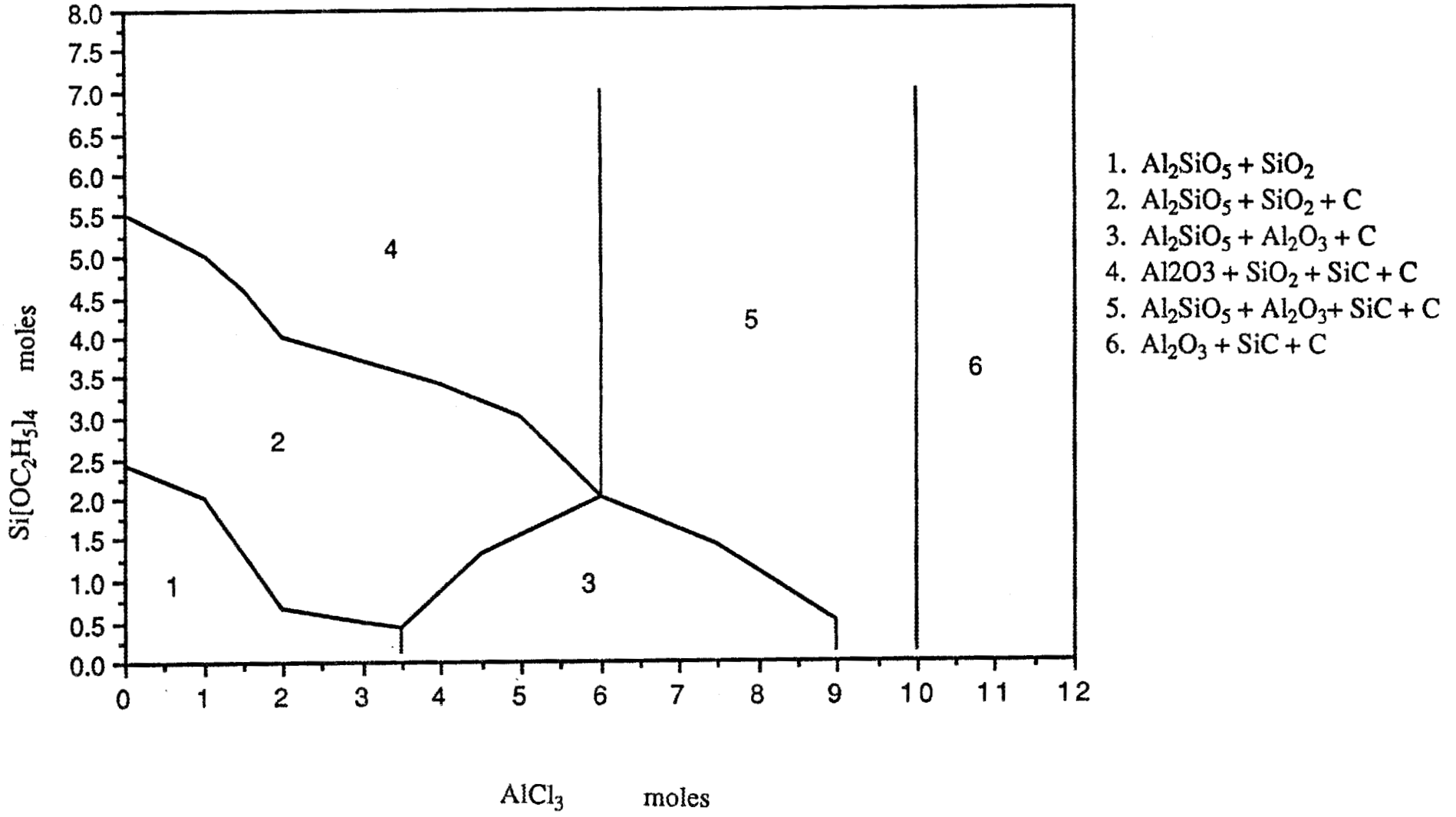

Figure 2: CVD phase plot of the $Si[OC_2H_5]_4$ / $AlCl_3$ system T=800 ^{0}C, Pressure = 100 torr

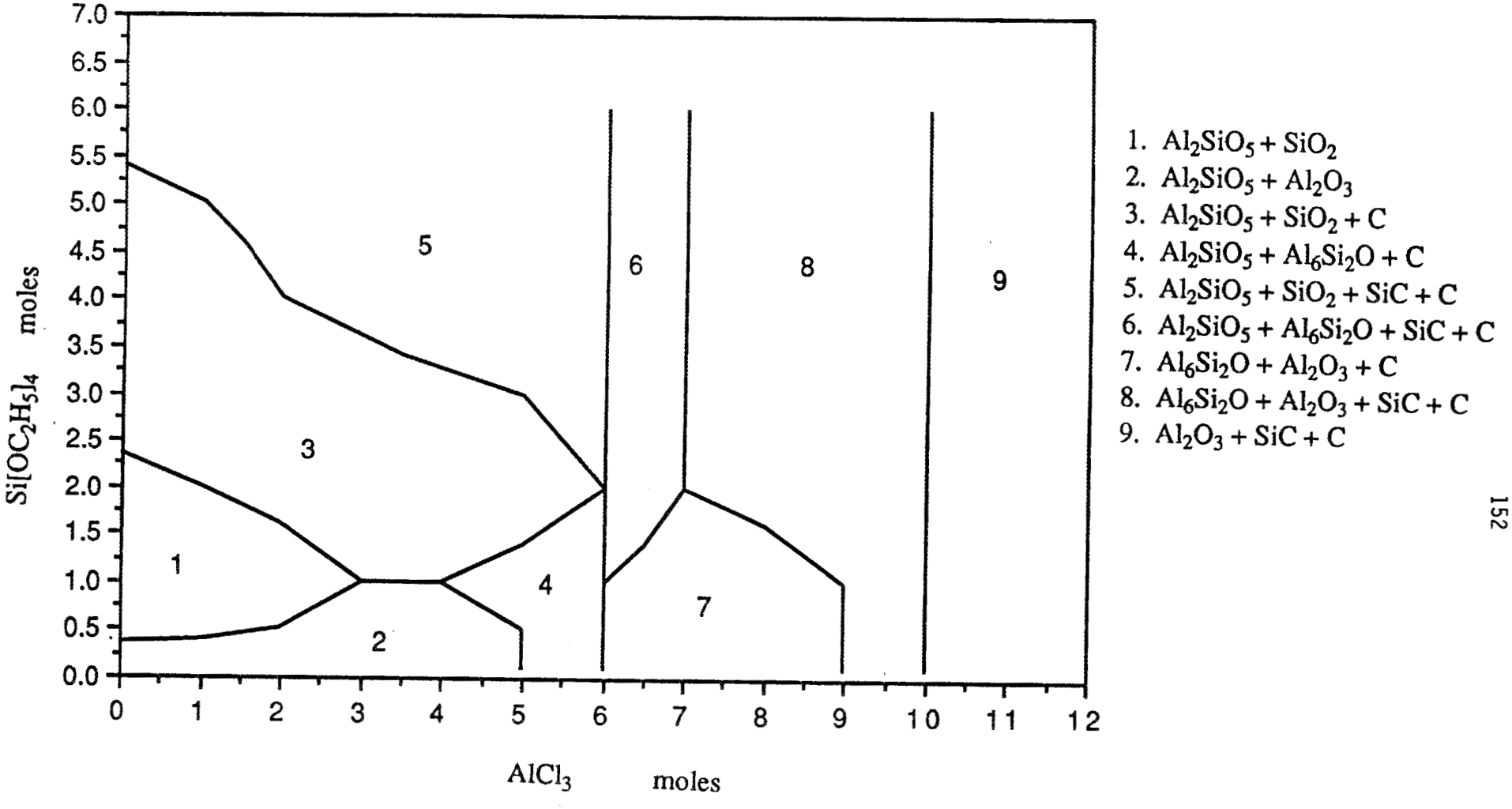

Figure 3: CVD phase plot of the $Si[OC_2H_5]_4$ / $AlCl_3$ system T=900 ^{0}C, Pressure = 50 torr

Thermodynamic calculations indicate that SiO_2 and Al_2O_3 can never form simultaneously for any of the input conditions. However, compounds such as Al_2SiO_5 are formed along with Al_2O_3 and SiO_2 at different conditions. It was also found that Al_2O_3 and SiC may be formed simultaneously over a range of input conditions and reactant concentrations. These phases may be used as an intermediate layer in the cases when SiC is used as a substrate.

These calculations suggest that multi-layers of aluminosilicate compound (Al_2SiO_5) with either Al_2O_3 or SiO_2 can be deposited with the same input conditions by simply varying the concentration of the reactant species. Thickness of these layers will be adjusted to obtain the overall relative proportions of Al_2O_3 and SiO_2. These multi-layered coatings may then be post-treated to ensure diffusion between layers and thus form stoichiometric Mullite.

In order to accurately control the concentration of the reactants and reactor pressures, a computer driven process controller manufactured by MKS Instruments has been incorporated into the system. The controller sets process parameters and times from a preset recipe thus providing repeatability, allowing for precise control of the phases generated in the multi-layered/composite coating.

Al_2O_3/SiO_2 composite coatings have been grown on Si_3N_4 and SiC substrates. Three different configurations were considered.

i) Codeposition of Al_2O_3 and SiO_2

ii) SiO_2/Al_2O_3 multi-layers

iii) composite coating with SiO_2 interlayers.

Configuration I: Codeposition of Al_2O_3 and SiO_2 lead to a compositionally graded undefined interface. It is hypothesized that the absence of a sharp interface and the gradual change in the thermal expansion coefficient would decrease the residual stresses and improve adherence by avoiding interfacial cracking. The composition of the composite coating was varied by varying the proportions of the individual reactants necessary for grow monolithic Al_2O_3 and SiO_2 coatings. It has been observed from preliminary EDS analysis on the scanning microscope that, as the reaction progresses, Al_2O_3 tends to be the dominant growth species. Further investigations need to be made to understand the kinetics of this growth predominance so that it can be controlled to yield the desired composition. Figure 4 shows a typical SEM micrograph of a Al_2O_3/SiO_2 composite coating on SiC.

Configuration II: Alternate layers of SiO_2 and Al_2O_3 were grown on SiC and Si_3N_4. SiO_2 was chosen as the first layer to best match the naturally present SiO_2 layer on the silicon based substrates. The multi-layered coating starts with sharp interfaces, and can then be heat treated to achieve a concentration gradient perpendicular to the interface. The reaction between pressed alumina and silica pellets at 1600°C have shown the formation of mullite crystals with their c-axis parallel to the direction of diffusion of silica into alumina. This would lead to crystallites of mullite being oriented perpendicular to the interface. These crystallites could act as pegs between the layers, thus improving the mechanical properties. The overall composition of the coating can be adjusted by varying the relative proportion of the reaction time for individual deposition of each layer.

Configuration III: To control the dominance of Al_2O_3 as observed in Configuration I, an SiO_2 inter-layer was introduced intermittently. This layer has been chosen because of its compatibility with the composite coating, and its adhesion characteristics. This should act as an interruption thus providing control over the surface concentration of the coating. The purpose of the inter-layer is to arrest the uncontrolled growth of Al_2O_3. Figure 5 shows a typical SEM micrograph of a layered coating of SiO_2 and Al_2O_3/SiO_2 composite on SiC.

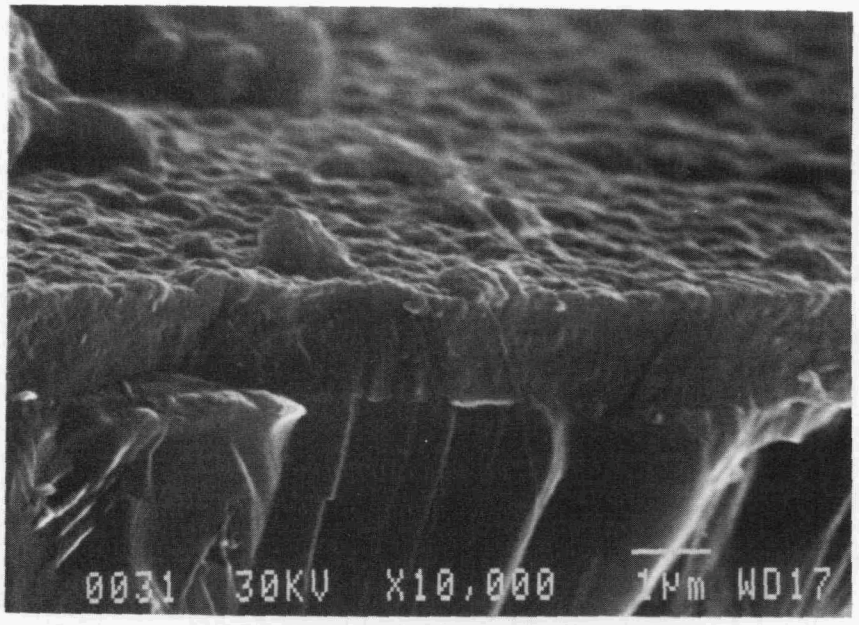

Figure 4: SEM micrograph of a Al_2O_3/SiO_2 composite coating on SiC.

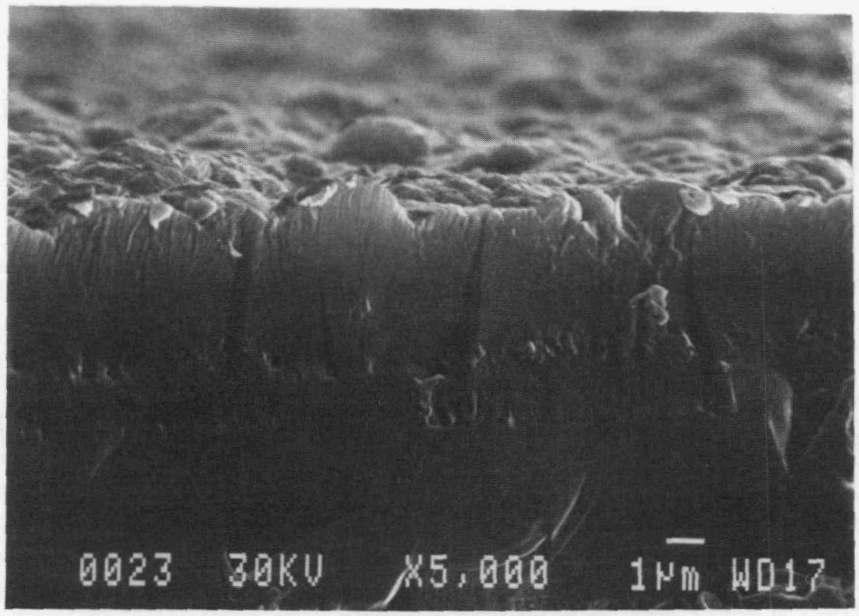

Figure 5: SEM micrograph of a layered coating of SiO_2 and Al_2O_3/SiO_2 composite on SiC.

Scratch Testing with a Rockwell C indentor was used to measure the adhesion of these coatings. The test was performed with continuously increasing normal load until the onset of coating removal from the substrate. This value is used as a measure of the work energy or shear stress required to debond the coating, and therefore an indication of its adherence. The thickness of the range of coatings tested was in the order of 1-4 µm. Initial testing shows that all the three configurations yielded at a critical load of 35-40 N for Si_3N_4 substrates, and 25-30 N for SiC substrates. Table 1 lists the results of the scratch test. Further experiments and investigations need to be made to study the effect of thickness and composition on the adhesion of these coatings.

Configuration	Coating Thickness	Critical Load
I	4µm	38 N
II	2µm	35 N
III	1-2µm*	33 N

Table 1: Scratch Test Results for the three different configurations on Si_3N_4 substrates.

*The accuracy and reliability of these results is not established since this test has not been standardized for coatings of this thickness.

Status of Milestones

	Schedule	Status
Task 1: Development of Al_2O_3/SiO_2 coatings.	5/94	On Schedule
Task 2: Coating Characterization for selection of best technique from Task 1.	7/94	On Schedule
Task 3: Development of the complete coating configuration for contact stress, oxidation and corrosion resistance evaluation.	9/94	On Schedule

References

1. "Solgas-Mix-PV for the PC", Theodore M. Bessman, Oakridge National Laboratories.

Wear-Resistant Coatings

M. H. Haselkorn (Caterpillar Inc.)

Objective/Scope

The goal of this technical program is to develop wear-resistant coatings for piston ring and cylinder liner components for low heat-loss diesel engines.

Friction and wear screening in Phase I identified plasma sprayed high carbon iron-molybdenum and chromia-silica coatings as candidate piston ring wear coatings. Plasma sprayed chromia-silica and high carbon iron-molybdenum coatings, as well as, a low temperature arc vapor deposited (LTAVD) chrome nitride coating were identified as candidate cylinder liner wear coatings. The cast iron porcelain enamel coatings exhibited unsatisfactory wear rates because of porosity in the coating.

The three main technical tasks for Phase II are further optimization of the LTAVD chrome nitride and of the cast iron porcelain enamel wear coatings and the process scale-up of wear-resistant plasma coatings for cylinder liners.

The optimization of the LTAVD chrome nitride coating involves the development of an adherent 15 micron thick coating which meets the friction and wear goals of this program. The cast iron porcelain enamel process optimization centers on developing a CIPE composition with a minimum of porosity. The process scale-up of the plasma coatings will first develop I.D. plasma spray parameters for coating cylinder liners. Next, simulated cylinder liner specimens will be coated and the friction and wear properties of these coatings will be determined using reciprocating friction and wear testing using both new and "used" engine oil.

Technical Progress

Phase II Task 1 Optimization of LTAVD Chrome Nitride Coating

In Phase I, a 3-5 micron thick, low temperature arc vapor deposited (LTAVD) chrome nitride coating was applied to cast iron substrates which met the friction and wear goals of the contract. However, wear curves generated showed that even with wear coefficients of less than 10-8 mm3/N-m, a 5-micron thick coating will not meet commercial diesel engine durability requirements. The wear curves showed a 15-micron thick LTAVD chrome nitride coating is needed to meet these durability requirements. For this reason, the overall goal of this task is the development of a 15 micron thick, adherent chrome nitride coating which can be applied to the inner diameter of cast iron cylinder liners. This task was divided into four subtasks:

1. Optimization of LTAVD chrome nitride coating parameters,
2. Development of a 15-micron thick LTAVD chrome nitride coating containing an intermediate layer,
3. Determination of the effect of single vs. multiple alternative layers on the adherence of 15-micron thick LTAVD chrome nitride coatings, and
4. Friction and wear characterization of selected 15-micron thick LTAVD chrome nitride coating systems.

The LTAVD chrome nitride coating development has been completed. Only nitrogen partial pressure and substrate cleaning procedures had any significant effect on the LTAVD chrome nitride coating adherence or microhardness. Incorporating a chromium or a layered titanium/titanium nitride intermediate coating in combination with either a 15-micron thick chromium nitride or a 15-micron thick "layered" coating (consisting of alternating layers of chromium and chromium nitride) resulted in LTAVD chrome nitride coating systems which had excellent physical appearances, hardnesses and adherence to a cast iron substrate. In addition, these coating systems were able to withstand both up- and down-cycle thermal shock testing from room temperature and 650 C.

Upon completion of the thermal shock and adherence testing, three LTAVD chrome nitride coating systems were selected and applied to cast iron Hohman A-6 rub shoes. These shoes were evaluated for friction and wear by running against a plasma-sprayed, high carbon iron-molybdenum coated disk. The three LTAVD chrome nitride coating systems selected were:

1. 15-micron thick chrome nitride top coat over a chromium intermediate layer (System 1),
2. 15-micron thick top coat consisting of alternating chrome nitride and chromium layers over a chromium intermediate layer, (System 2), and
3. 15-micron thick top coat consisting of alternating chrome nitride and chromium layers over a layered titanium and titanium nitride intermediate layer (System 3).

Table 1 lists the results of the friction and wear characterization of the three LTAVD chrome nitride coating systems.

TABLE 1
Friction and Wear Test Results — After 1000 Minutes of Testing at 350 C, Lubricated

LTAVD Chrome Nitride Coating System	Average Shoe Wear Rate (mm3/N-m)	Average Disk Wear Rate (mm3/N-m)
System 1	3.0xE-8	1.6xE-5
System 2	No measurable wear	7.6xE-6
System 3	No measurable wear	4.2xE-6

Using the thermal shock tests, friction and wear characterization, and an estimate of the production costs for application for each chrome nitride coating system as a guide, chrome nitride coating Systems 1 and 2 were selected for further optimization.

The overall objective of Task 8, Process Scale-up of Wear-Resistant Plasma Coatings for Cylinder Liners, is the optimization of inner diameter (I.D.) plasma spray gun parameters for both the chromia-silica composite and high carbon iron-molybdenum blend powders.

Statistical experiments were designed and run to determine the effect of primary gas flow, current, voltage, spray distance and carrier gas flow on coating microstructure and hardness, as well as, deposition efficiency.

The results of these experiments were then used to build a predictive equation to select three sets of I.D. plasma spray gun coating parameters for both the chromia-silica and high carbon iron-molybdenum powders. The coating parameters selected by the model will produce the optimum plasma spray coating microstructures and hardnesses along with the highest coating deposition efficiencies.

Three sets of Hohman A-6 conforming rub shoes were plasma sprayed with each powder using an I.D. plasma spray gun and the spray parameters selected by the model. The counterfaces run against these shoes were disks plasma sprayed with the opposite powder; i.e., high carbon iron-molybdenum shoes run against chromia-silica disks.

The friction and wear results showed that varying the plasma spray parameters for the chromia-silica powder has little influence on the friction and wear properties of this coating running against the high carbon iron-molybdenum. For this reason, the plasma spray parameters which resulted in the highest deposition efficiency were selected for the application of the chromia-silica powder to the inner diameter of simulated diesel engine cylinder liners.

The friction and wear properties of the high carbon iron-molybdenum were influenced by plasma spray parameters. Thus, for this powder, the plasma spray parameters which produced the coating with the best friction and wear properties were selected for the application of this powder to the inner diameter of the simulated diesel engine cylinder liners.

Norton's Ceramic Machining Technology Center was selected to do the machining studies of the Cost Effective Machining task. A fully programmable Huffman HS-75R 5-axis CNC grinder was used by Norton for the machining. Norton rotated the machine head 90 degrees and built a special chuck to enable the Huffman to do surface grinding.

The high carbon iron-molybdenum blend and chromia-silica composite plasma sprayed coatings were evaluated at Caterpillar after Norton completed themachining. The results of this evaluation illustrated that, irrespective of the coating composition being machined or grinding wheel bond type, the optimum surface finish was obtained using the finest (15-micron) diamond grit. Material removal rates could be increased by increasing either the depth of cut or diamond grit size. However, increasing material removal rates by either of these methods produced a rougher surface finish. Reducing surface feed rates improved surface finish with both vitreous orresinoid bonded wheels. In summary, the best combination of material removal rates and surface finish was obtained with the reduced surface feed rates and large depth of cut using a 15-micron diamond grit in a vitreous bonded wheel.

The friction and wear properties of each machined surface were characterized using a Falex pin-on-disk friction and wear test machine, running against a ceramic counterface. The machining parameters which produced the surface with the lowest coefficient of friction values for the high carbon iron-molybdenum powder were low surface feed rates and large depth of cuts, using a 15-micron diamond grit in a resin bonded wheel. Slightly higher coefficient of friction values (0.04 vs. 0.08) were obtained with the medium feed rates and large depth of cuts, using a 15-micron diamond grit in a vitreous bonded wheel. However, the second set of machining conditions (vitreous bond, medium feed rate) produced twice the material removal rates as the first set of machining conditions (resin bond, small depth of cut).

The machining parameters for the plasma sprayed chromia-silica coatings which produced the surfaces which had the lowest coefficient of friction values were:

1. 90-micron diamond grit, vitreous bond, slow feed rate, andsmall depth of cut, and
2. 52-micron diamond grit, vitreous bond, slow feed rate, and large depth of cut.

However, incorporating the 52-micron diamond grit along with large depth of cut had ten-fold greater material removal rate compared to the 90-micron diamond grit and small depth of cut.

The finish machining parameters for both the chromia-silica and high carbon iron-molybdenum powders were selected using the following criteria---material removal rates, surface finish, and the pin-on-disk friction and wear properties of the machined surface. Two finish machining procedures were selected for each powder. One procedure selected results in a high material removal rate while the second procedure results in a lower material removal rate, but produces a slightly better surface finish.

Cylinder liners and piston rings have been procured and are currently being machined to the proper I.D. (cylinder liners) and O.D. (piston rings) prior to the application of the plasma spray powders. Each powder will be applied to the I.D. of at least six cylinder liners using the parameters previously selected. Three of the plasma sprayed liners will be machined at Caterpillar using the machining parameters which produce the highest material removal rates. The remaining plasma spray liners will be machined using the parameters which produce a surface finish with the best friction and wear properties.

In addition, piston rings will be plasma sprayed with the high carbon iron-molybdenum and chromia-silica powders and machined at Caterpillar. These plasma sprayed piston rings will be evaluated in reciprocating friction and wear tests running against the plasma sprayed cylinder liners at both Caterpillar and Battelle Columbus Labs.

Thick Thermal Barrier Coating (TTBC) Systems for Low Heat Rejection Diesel Engines

M. B. Beardsley (Caterpillar Inc.)

Objective/Scope

The objective of this program is to advance the fundamental understanding of thick thermal barrier coating systems for application to low heat rejection diesel engine combustion chambers. Areas of TTBC technology that will be examined include powder characteristics and chemistry; bond coat composition; coating design, microstructure, and thickness as they affect properties; durability, and reliability; and TTBC "aging" effects (microstructural and property changes) under diesel engine operating conditions.

Technical Progress

TTBC POWDERS

Determination of thermal conductivity and density of the sprayed coatings for the initial 36 parameters is near completion. Optimization runs for the baseline 8% yttria-zirconia material have been sprayed with mixed results. The predicted densities and conductivities were achieved, but the deposition efficiencies were lower than anticipated. At the same time that these specimens were sprayed, problems occurred with the spray system. The voltage measuring circuit of the spray system failed and was replaced. After replacing the board, the voltage/hydrogen relationship of the system changed. Recalibration of the mass flow meter controlling hydrogen flow and the voltage measuring circuit did not resolve this problem. Comparison of replicate data points indicates that the original voltage and currently measured voltage do a good job of predicting the resulting thermal conductivities and deposition efficiencies. Therefore, to resolve the problems with the change in the voltage/hydrogen relationship, the model being used for prediction of the resulting coating properties was changed to include voltage rather than hydrogen flow.

Comparisons of the deposition efficiencies (DEs) of the materials are shown in Table 1. The DEs of the zirconia materials are nearly equal with a difference of 14 being the largest. This indicates that the differences in the powders do not greatly affect the resulting DE, at least for the average of the 36 parameters.

Comparison of the thermal conductivities of the baseline 8% yttria-zirconia sprayed using the 36 parameters and the other materials is shown in Table 2. The conductivities of the HOSP (baseline), sol gel, spray dried, and spray dried-sinter-crushed 8% yttria-zirconias were determined to be equal for equivalent spray parameters. The fused and crushed zirconia has a higher thermal conductivity than the baseline, which is probably due to the lower surface area per weight for the fused and crushed powder resulting in lower amount of melting of the powder during spraying. The thermal conductivity of the

Table 1. Comparison of the deposition efficiencies of the 15 ceramic powders for the 36 sets of spray parameters.

Material	Mfg. Method	Lot #	Average Difference from Baseline	Significance (95% confidence)
8% YSZ	HOSP	34547	Baseline	N/A
20% YSZ	S/D	34108	- 2.4	equal
24% CSZ	HOSP	34209	-10.4	less than
8% YSZ	S/D	32678	-11.6	less than
8% YSZ	S/D-S	34850	0.5	equal
8% YSZ	F/C	281	13.8	greater than
8% YSZ	Sol gel	34440	- 0.8	equal
8% YSZ	S/C/S	39073	5.9	greater than
8% YSZ	S/D-S	1081	1.0	equal
8% YSZ	HOSP	34143	1.0	equal
8% YSZ	HOSP	34302	2.0	equal
8% YSZ	S/D-S	34992	5.0	greater than
8% YSZ	S/D-S	34993	-3.0	less than

Table 2. Comparison of the thermal conductivities of several zirconia powders for the 36 sets of spray parameters.

Material	Mfg. Method	Lot #	Average Difference from Baseline	Significance (95% confidence)
8% YSZ	HOSP	34547	Baseline	N/A
20% YSZ	S/D	34108	0.16	less than
24% CSZ	HOSP	34209	0.03	equal
8% YSZ	S/D	32678	0.15	less than
8% YSZ	F/C	281	-0.25	greater than
8% YSZ	S/C/S	39073	0.03	equal

24% ceria-zirconia is also the same as the baseline 8% yttria-zirconia; while the 20% yttria-zirconia has a lower conductivity due to the higher yttria content. The mullite and calcium titanate both have higher thermal conductivities compared to the baseline zirconia.

DESIGN, DEPOSITION, AND CHARACTERIZATION

Parameters for the baseline 8% yttria-zirconia and other 8% yttria-zirconias have been chosen for making tensile and compressive strength samples.

Determinations of residual stresses by X-ray diffraction techniques have been made using the facilities at the X-ray Residual Stress User Center of the High Temperature Materials Laboratory at ORNL. Axial compressive samples of the 24% ceria-zirconia were used in an attempt to determine the correct elastic modulus of the material to be used in the X-ray diffraction calculation of stress. Previous attempts to do this using Caterpillar's X-ray equipment were hampered by problems in the Japanese software used for peak location. At the User Center a low angle peak was used to compensate for the poor signal at higher angles. A baseline residual stress was found in the samples, which were then loaded in a small load cell and X-rayed under stress. The modulus found at various stress levels is shown in Table 3 and appear to compare well with the bulk modulus numbers for the plane used in the X-ray analysis. This confirms that the pores and microcracks of the plasma sprayed materials do not influence the resulting measured residual stress. Further work and the X-ray Residual Stress User Center is planned to confirm this initial finding and to investigate other materials.

DURABILITY/RELIABILITY

The durability testing of coatings at the University of Illinois has produced interesting results. The compressive fatigue strength of the TTBC has been shown to increase at 800 C compared to room temperature measurements. This increase in strength is currently under investigation. An increase in the elastic modulus occurred with the increase in strength;therefore, comparison of the effects of temperature and static loads on the observed increase in the elastic modulus have been done. This assumes that a change in the elastic modulus is synonymous with the increase in observed fatigue resistance. The mechanism of the fatigue strength increase is thought to be due to a sintering/hot pressing effect due to the synergistic effect of compressive load and temperature that the fatigue test is run under.

The initial test conditions for 10 specimens are shown in Table 4. Both the temperature and load are being investigated. The resulting changes in the room temperature elastic moduli are shown in Figures 1 and 2. This indicates that there is a variation in the strength increase dependent on the temperature/stress combination. Further investigation into this effect is underway using three additional materials; the 24% ceria stabilized

Table 3. Modulus of a 24% ceria-zirconia determined from a compressive specimen under stress and X-rayed.

Stress, MPa	Elastic Modulus, GPa	Possion Ratio
-70.8	123	0.34
-70.8	118	0.37
-73.5	148	0.25
-126.0	151	0.45
-201.0	195	0.43

Table 4. The test conditions for the 10 samples is shown. The elastic modulus of each was than measured at room temperature and is shown in Figures 1 and 2. The static load for the samples was 75% of the ultimate strength in compres sion.

Tests 1 to 5, Constant Static Load, Variable Temperature

Specimen#	Time	Temp. C	Stress, MPa
1	1 hr.	800	200
2	1 hr.	600	200
3	1 hr.	400	200
4	1 hr.	200	200
5	1 hr.	20	200

Tests 6 to 10, Constant Temperature, Variable Static Load

Specimen#	Time	Temp. C	Stress, MPa
6	1 hr.	800	0
7	1 hr.	800	50
8	1 hr.	800	100
9	1 hr.	800	200
10	1 hr.	800	300

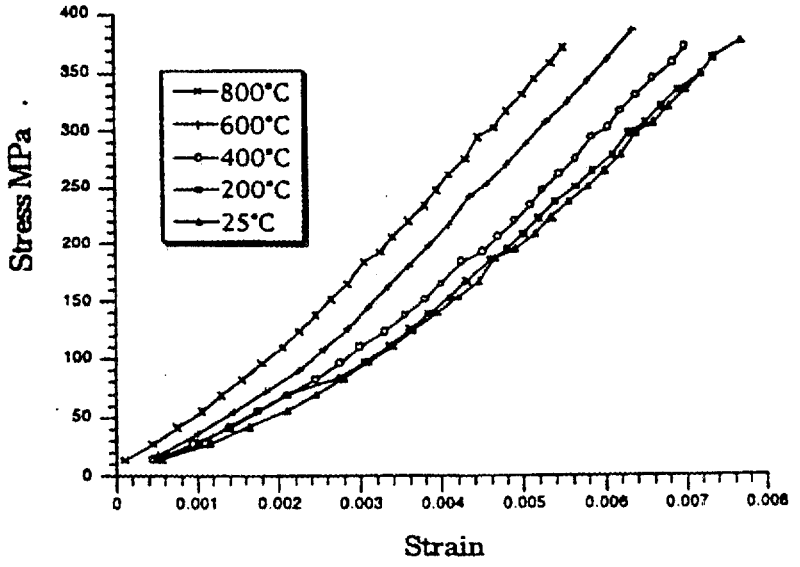

Figure 1. Room temperature elastic modulus after an applied static load of 200 MPa at different temperatures for 1 hour.

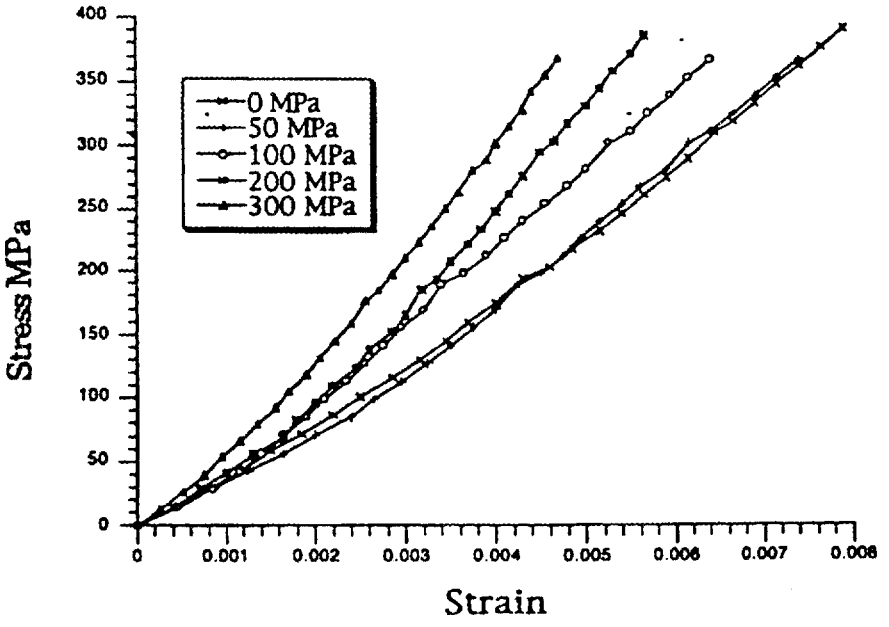

Figure 2. Room temperature elastic modulus after different static loads at 805 C for 1 hour.

zirconia, calcium titanate, and a composite coating of 90% zirconia and 10% NiCrAlY bond coat.

The new design for the tensile/compressive, coating fatigue test machine at the University of Illinois has been set up and is in the process of being checked out. This machine will allow the coating specimens to be tested in tension as well as compression, allowing for a fatigue R ratio of -1 to be used if desired. The unusual fatigue response of the TTBC materials previously reported will be further investigated by testing the 26% ceria-zirconia and calcium titanate materials for the fatigue response and aging effect previously shown by the 8% yttria-zirconia tests. Specimens of these materials will be supplied to the University of Illinois in May.

Status of Milestones

Milestones 134203 and 134204 have been completed.

All milestones are on schedule.

Publications

1. An article describing the fatigue testing of the ceramic coatings at the University of Illinois has been submitted to E. L. Long of ORNL for publication in the Ceramic Technology Newsletter.

2. A paper on the same subject titled "Cyclic Compression of Thick Thermal Barrier Coatings" by K. F. Wesling and D. F. Socie of University of Illinois and M. B. Beardsley of Caterpillar Inc. will be submitted to the American Ceramic Society for publication.

1.4 JOINING

1.4.1 Ceramic-Metal Joints

Joining of Ceramics for Heat Engine Applications
M. L. Santella (Oak Ridge National Laboratory)

Objective/scope

The objective of this task is to develop strong reliable joints containing ceramic components for applications in advanced heat engines. The overall emphasis of this task is on studying the brazing characteristics of silicon nitride and silicon carbide. The techniques of direct brazing, as well as vapor coating ceramics to circumvent wetting problems, are being applied to these materials. The planned activities during FY 1993 will include continuing the study of both the high-temperature brazing of silicon nitride and the mechanical behavior of braze joints. The work will encompass creep testing of silicon nitride braze joints, further evaluation of a materials system and analysis package developed specifically for silicon nitride-to-metal braze joints, and evaluating nonmetallic bonding materials for joining silicon nitride.

Technical highlights

Si_3N_4-to-metal brazing: Preliminary experiments were done to evaluate the brazing characteristics of the SK-1 and -2 braze filler metals developed by GTE Laboratories for producing braze joints of PY6 to PY6, PY6 to Incoloy, and Incoloy to Incoloy. The experiments were done in vacuum at either 1100 or 1200°C, and selected specimens were prepared for metallographic analysis. Based on previous wetting experiments, it was expected that acceptable joints of PY-6 to PY-6 would be obtained but that joints of PY-6 to Incoloy 909 and Incoloy 909 to Incoloy 909 would be more difficult to achieve. This was not the case. Joints of PY-6 to PY-6 bonded reasonably well and had very good exterior appearance, but they contained large unbonded regions after brazing at both 1100 and 1200°C. No bonding could be obtained in joints of PY-6 to Incoloy 909. In these joints, the filler metals adhered to the Incoloy 909 but not to the Ti-vapor-coated PY-6. Acceptable joints of Incoloy 909 to Incoloy 909 were obtained at both brazing temperatures even though the wetting experiments indicated that melting was incomplete in both cases. The results of the brazing experiments suggest that there is no inherent difficulty in the bonding of these filler metals to Incoloy 909. On the other hand, they also suggest that reactions between the filler metals and the Ti-vapor-coated PY-6 occur which are detrimental to forming an acceptable bond.

Si_3N_4 brazing: Fast fracture tests were done on specimens from joints of Ti-vapor-coated SN220 Si_3N_4 made by vacuum brazing at 1130°C with Au-25Ni-25Pd wt % filler metal. Specimens of monolithic SN220 were also tested for comparision. The tests were done at 500 and 600°C at loading rates of 10 and 0.01 lb/min. Three specimens were tested at each loading condition, and the results are shown in Table 1 and Fig. 1.

The average fracture strength of the joint specimens was lower than that of the monolithic specimens at both test temperatures. At 500°C, neither specimen type showed a dependance of fracture strength on loading rate. In contrast, the strength of the joint specimens decreased significantly at the 10 lb/min loading rate at 600°C. In previous

Table 1. Loading rate dependance of fracture strength for Si_3N_4 braze joints

Si_3N_4 specimen type	Test temp. (°C)	Loading rate (lb/min)	Av. fracture strength, MPa
Joint	500	0.01	459
Joint	500	10	420
Monolithic	500	0.01	556
Monolithic	500	10	622
Joint	600	0.01	459
Joint	600	10	260
Monolithic	600	0.01	575
Monolithic	600	10	541

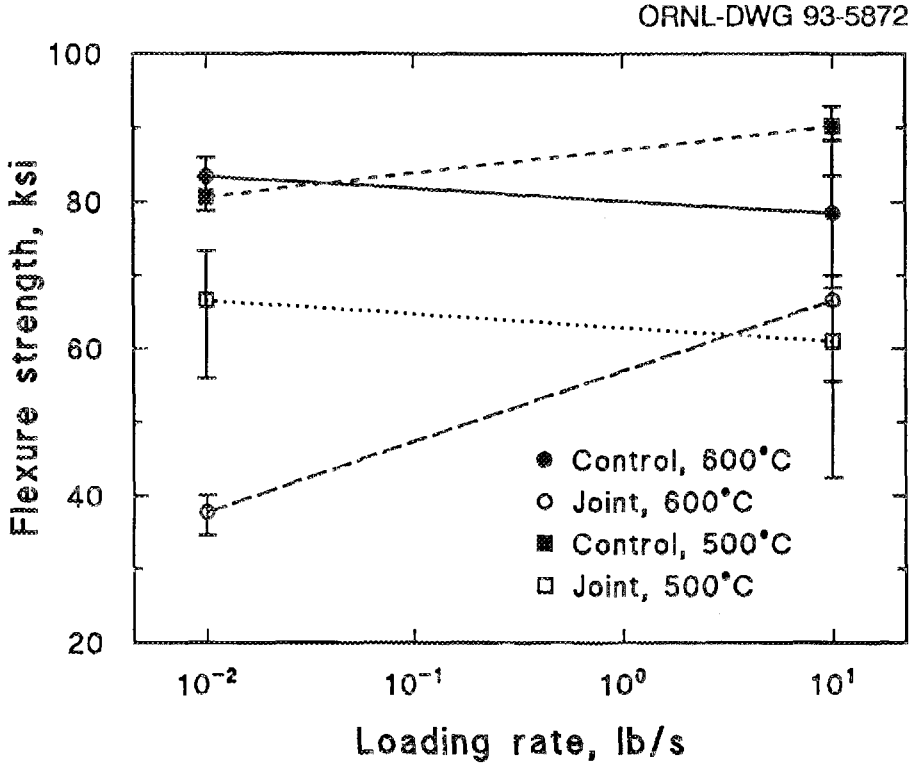

Fig. 1. Effect of loading rate and temperature on the strength of monolithic Si_3N_4 (control) and Ti-vapor-coated Si_3N_4 brazed with Au-25Ni-25Pd, wt % filler metal (joint).

testing, the failure of joint specimens often occurred in the Si_3N_4 away from the brazed interfaces. However, all of the present specimens failed near a brazed surface. Further examination of the tested bars and additional testing are planned.

Si_3N_4 glass bonding: The glass mixtures listed below were formulated to serve as a basis for investigating the bonding of dense Si_3N_4 with nonmetallic materials:

1. 62 SiO_2 - 18 Al_2O_3 - 20 MgO wt %,
2. 55 SiO_2 - 10 Al_2O_3 - 35 MgO wt %,
3. 52 SiO_2 - 22 Al_2O_3 - 26 MgO wt %,
4. 46 SiO_2 - 21 Al_2O_3 - 33 Y_2O_3 wt %,
5. 34 SiO_2 - 20 Al_2O_3 - 46 Y_2O_3 wt %,
6. 28 SiO_2 - 28 Al_2O_3 - 44 Y_2O_3 wt %,

All of the compositions were selected using melting temperature as the main criterion; equilibrium phase diagrams indicate they all melt below 1500°C. The first compositions formulated were Nos. 1 and 4, and their selection was based entirely on their melting temperatures: ~ 1350°C for No. 1 and ~ 1400°C for No. 4. The compositions of Nos. 2 and 5 were taken from published reports of similar work. The compositions of Nos. 3 and 6 were selected to further reduce the SiO_2 content of the mixtures without compromising their melting temperatures too much.

Initial evaluation of these materials consisted of depositing the blended powders of Nos. 1 and 4 on specimens of Si_3N_4 and holding them at temperatures of 1350 to 1500°C for 30 min under nitrogen at a pressure just below 0.1 MPa (1 atm). The monolithic Si_3N_4 materials used for substrates were SN220 (Kyocera), NC132 (Norton), and PY6 (GTE). The MgO-based mixture became molten at 1400°C and showed increased spreading at 1450°C. The molten glass also appeared to react with each of the Si_3N_4 substrates, and the higher temperature promoted this also. The PY6 material showed more extensive reaction than the SN220 or NC132 at both temperatures. The Y_2O_3-based mixture also became molten at 1400°C, but it decomposed at 1500°C. At 1400°C, it produced a relatively clear glaze on all three Si_3N_4 materials, but it also appeared to react more extensively with the PY6 Si_3N_4.

Also, Si_3N_4 powder (UBE, SN-E10) was then incorporated into the Nos. 1 and 4 oxide mixtures in separate milling operations to levels: 20, 60, and 80 vol %. The mixtures with 60 and 80% Si_3N_4 did not melt at temperatures up to 1650°C. Both oxide mixtures containing 25% Si_3N_4 melted in the range of 1400 to 1450°C, and both flowed over the substrate surfaces. However, both of these mixtures started frothing immediately upon melting.

In another experiment, 5 wt % of Si metal powder was added to the No. 4 mixture. This powder mixture melted and formed a relatively stable droplet on an Si_3N_4 surface and showed no signs of frothing. The edge of the droplet and its general features are shown in Fig. 2. Its wetting angle on the Si_3N_4 is about 23°, which is well within the range of acceptability for joining operations. A closer view of the interface between the Si_3N_4 and the droplet is shown in Fig. 3. The light, circular features are metallic Si, and these particles range up to about 8 μm in size. Also, there is no evidence of excess reaction between the glass and the Si_3N_4. These experiments are consistent with published reports on the formation of Si-oxynitride glasses and their reactions with dense Si_3N_4. Future work will continue to address the suppression of frothing reactions.

YP17717

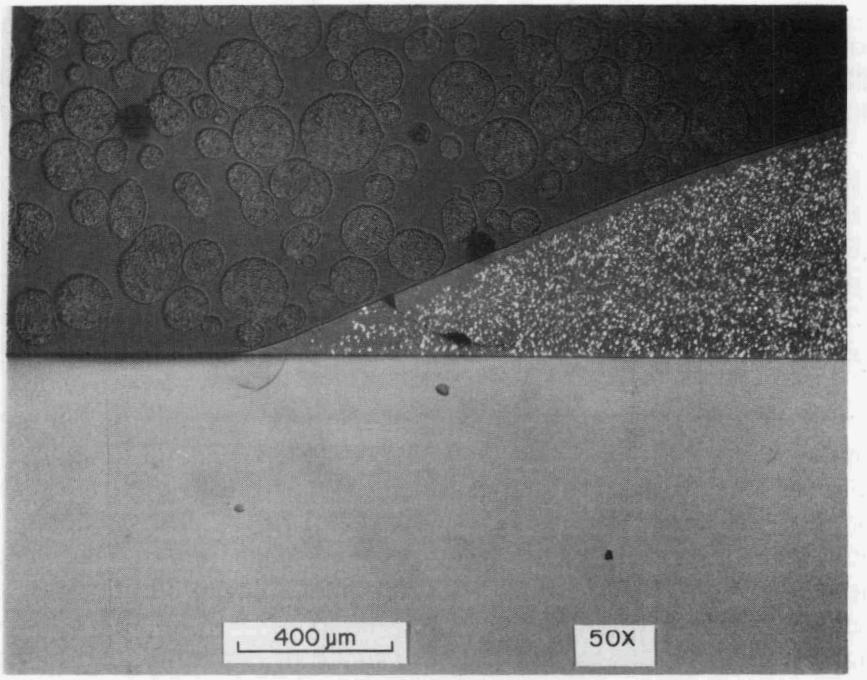

Fig. 2. Optical micrograph of a cross-sectional view of (oxide + Si_3N_4 + Si metal) powder mixture after melting on Si_3N_4 substrate under 1 atm of nitrogen.

YP17716

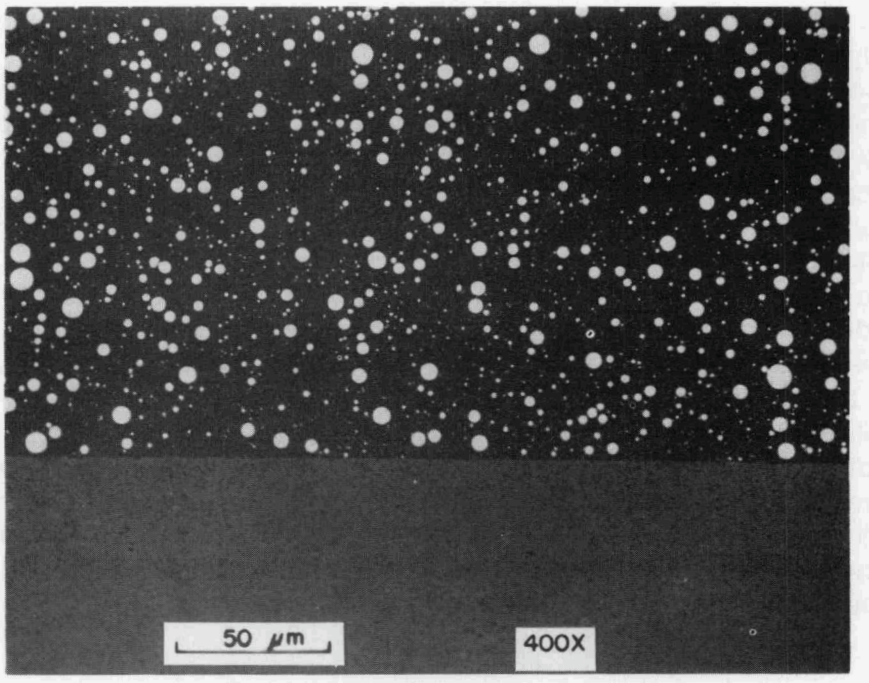

Fig. 3. Optical micrograph at interface between Si_3N_4 and (oxide + Si_3N_4 + Si metal) powder.

Status of milestones

141111 Complete metallographic analysis of reactions of high-temperature braze filler metals with silicon nitride: Dec-31-1992. Completed; report is attached as an appendix to this report.

Publications

The paper entitled, "Brazing Ti-Vapor-Coated Zirconia," by M. L. Santella and J. J. Pak appeared in *Weld. J.* 72(4), 165-s-172-s (1993).

Unpublished work

None

APPENDIX

Report on reactions of high-temperature braze filler metals with Si_3N_4

Introduction: Of the many techniques available for joining ceramics,[1-4] brazing was selected for the present study. Brazing is a liquid-phase bonding process with characteristics that: (1) only the filler material, but not the parts being joined, is melted during bonding; and (2) the filler material must wet the base materials and be drawn into or held in the joint by capillary forces. Traditionally, the term "brazing" is used for processes where the filler material is metallic, but, in general, non-metallic materials such as glasses can also be used as filler materials. Ideally, the process is accomplished by assembling the component and filler materials and then uniformly raising the temperature of the assembly to a point where the filler material becomes molten. If wetting conditions are favorable, the liquid filler material will be drawn into an intentionally made gap (i.e., the joint gap) between the parts being bonded, or it will remain in the joint gap if preplaced. Generally, some chemical reaction or mass transport occurs between the liquid filler material and the base materials, and, upon cooling, the filler material solidifies to produce a bonded part.

The brazing process has some significant advantages compared to other joining techniques. For instance, because melting of the base materials is avoided, joining can be accomplished over a wide temperature range depending on filler material composition. This characteristic also makes it possible to join ceramics by brazing. Also, the use of a liquid bonding phase means that minor variations in surface flatness, surface topology, and part fit-up tolerances can be accommodated with relative ease. Other desirable features of the process are that thermally induced stresses can be minimized by heating components uniformly in a furnace, and close assembly and finish tolerances can be maintained which can reduce the need for costly secondary finishing operations. Lastly, the equipment and processing requirements for brazing are usually simple and straightforward, e.g., furnace heating in vacuum or controlled atmosphere.

Of course, brazing ceramics with metallic filler materials has drawbacks. One is that the full high-temperature and strength capabilities of some ceramic components may by compromised by the presence of metallic braze layers. Another is that many ceramics are wetted only with difficulty by liquid metals including most commercially produced braze filler metals. This means that identifying or developing filler metals suitable for particular ceramics and their expected service conditions can often be problematic.

This report summarizes work on the reaction of high-temperature brazing alloys with sintered Si_3N_4. Wetting of the Si_3N_4 was accomplished by vapor coating its joint surfaces with Ti prior to brazing. Titanium was selected for a coating material because it was previously found to be effective for producing zirconia braze joints. Details of preliminary Si_3N_4 brazing studies are reported elsewhere.[5,6]

Materials and experimental details: The sintered Si_3N_4 used for this work was procured from Kyocera Corporation, and its commercial designation is SN-220. Selected properties of SN-220, as quoted by the manufacturer, are given in Table A1. The chemical composition of the SN-220 was not available from the manufacturer and was not determined, but it reportedly[7] relies on sintering aids of Al and Y and also contains particles of WC. This material was selected because it was judged to be representative of sintered silicon nitrides being evaluated for various heat engine applications and because it was readily

Table A1. Selected properties of SN-220 Si_3N_4. Room-temperature (RT) values are given unless otherwise noted

Bulk density (g/cm^3)	Flexure strength, MPa					Weibull modulus (RT)
	RT	800°C	1000°C	1200°C	1300°C	
3.2	588	598	510	323	118	7-15

Fracture toughness (MPa-√m)	Hardness (GPa)	α_l, μm/m/°C 40 to 800°C	Thermal conductivity, W/m-K	Thermal shock resistance, ΔT°C
6.2	14.7	3.2	20.9	500-600

Young's modulus (GPa)	Poisson's ratio	Oxidation resistance, mg/cm^2 in 24 h			
		1200°C	1250°C	1300°C	1400°C
294	0.28	0.2	0.6	0.8	1.9

available and relatively inexpensive. The SN-220 material was supplied in billets with dimensions of 150 x 10 x 5 mm, which were cut into 10-by 10-mm coupons for brazing trials and metallographic specimens.

Prior to brazing, all Si_3N_4 joint surfaces were coated with a 1 to 2-μm-thick layer of Ti by vacuum evaporation. The Ti vapor was produced by melting a pure Ti source held in a water-cooled Cu crucible with an electron beam melting system operating at 7 kV and 100 mA. Typically, the pressure inside the evaporation chamber was 400 μPa at the time melting of the Ti commenced, and it eventually dropped to near 50 μPa during evaporation. The Si_3N_4 specimens were shielded from the Ti vapor until the pressure inside the chamber stabilized at the lower level. A standard quartz oscillation technique was used to monitor coating thickness during evaporation, and thickness was verified by reference weighing tabs. A typical time to produce a 1-μm-thick coating was 30 min. The Si_3N_4 specimens also were heated with quartz lamps to the range of 250 to 300°C prior to initiating the coating process. The Si_3N_4 specimens were rinsed with acetone followed by ethyl alcohol and then air dried before being placed in the evaporation chamber.

All brazing was done in vacuum. Joint assemblies were placed in an alumina tube that was subsequently sealed and evacuated to a pressure of about 130 μPa. Afterwards, the tube was inserted into an air muffle furnace preset and equilibrated at the brazing temperature. A thermocouple positioned near each joint assembly was used to continuously monitor temperature during the brazing thermal cycle. The holding time at the

brazing temperature was normally 20 min, after which the alumina tube was withdrawn from the furnace and cooled to room temperature. Joint assemblies for metallographic examination were secured together with Mo wire, but no additional load was applied across the joints during brazing.

Intermediate temperature brazing: The filler metal used for the intermediate temperature brazing experiments has a nominal composition of Au-25Ni-25Pd wt %. This alloy is commercially available in a variety of forms [American Welding Society (AWS) standard designation: BVAu-7 Gr1]. A 25-μm-thick foil was used for brazing the Ti-vapor-coated Si_3N_4 coupons. Typically, a piece of filler metal foil was cut to match the interfacial area of the braze joint and preplaced between the Si_3N_4 coupons before heating to the brazing temperature. The liquidus temperature of the filler metal is near 1120° C, and a brazing temperature of 1130° C was used for all experiments. This alloy was selected for study for two reasons: (1) it is a relatively common commercially available alloy and (2) it represented a significant increase in brazing temperature (~300° C) compared to the alloys used in initial brazing experiments.

The overall appearance of the Si_3N_4 braze joints made with the Au-Ni-Pd filler metal is typified by the cross-sectional view shown in Fig. A1(*a*). Generally, the joint gaps were uniformly filled by the filler metal, there were no indications of cracking in the Si_3N_4 near the joints, and there was very little porosity in the braze layers. Microstructural details at the Ti-vapor-coated Si_3N_4 surface are shown in Fig. A1(*b*). After brazing, the filler metal layer contained two major phases: an Au-rich matrix and irregularly shaped Ni-rich particles. The presence of the Au- and Ni-rich phases is consistent with the solid-state phase separation observed for both the Au-Ni and Au-Pd binary systems.[8] The overall composition of the filler metal layer and those of the individual phases are given in Table A2. The overall composition is reasonably close to the nominal composition of Au-25Ni-25Pd wt %, but the presence of Si in the filler metal layer after brazing indicates that some reaction with the Si_3N_4 occurred. A Vickers indenter under a 100-g load was used to measure the hardness of the filler metal layer at 2.52 GPa, and based on these measurements, the yield strength of the braze filler metal was estimated to be 265 MPa at room temperature.

The interface region between the filler metal and the Ti-vapor-coated Si_3N_4 is shown in Fig. A1(*b*). After brazing, the layer at the Si_3N_4 surface was still about 1 μm thick and Ti-rich, but reaction of the Ti-vapor coating was evident, and Ti was detected throughout the braze layer. The Ti-rich layer was studied in more detail by dissolving away the filler metal in an acid solution and examining the exposed, reacted surface in the scanning electron microscope (SEM) and by X-ray diffraction (XRD). The surface revealed by this approach was composed of fine cuboidal grains and occasional larger, smooth regions as shown in Fig. A2. Microchemical analysis indicated that the cuboidal grains contained Ti with trace amounts of Al, Au, Ni, Pd, and Si, while the smooth regions were Au rich, indicating they were filler metal fragments. Analysis by XRD showed that the only phase present besides Si_3N_4 was TiN. These observations show that the Ti-vapor coating reacted with the Si_3N_4 during brazing to form a TiN layer.

The metallographic examination showed that the Au-25Ni-25Pd wt % filler metal was effective for producing sound, defect-free braze joints of Ti-vapor-coated Si_3N_4. A Ti-rich layer was found at the Si_3N_4 surfaces after brazing, but Ti was also detected throughout the braze layers, indicating that some dissolution in the filler metal occurred. Microchemical analysis also detected small concentrations of Si in the braze layer

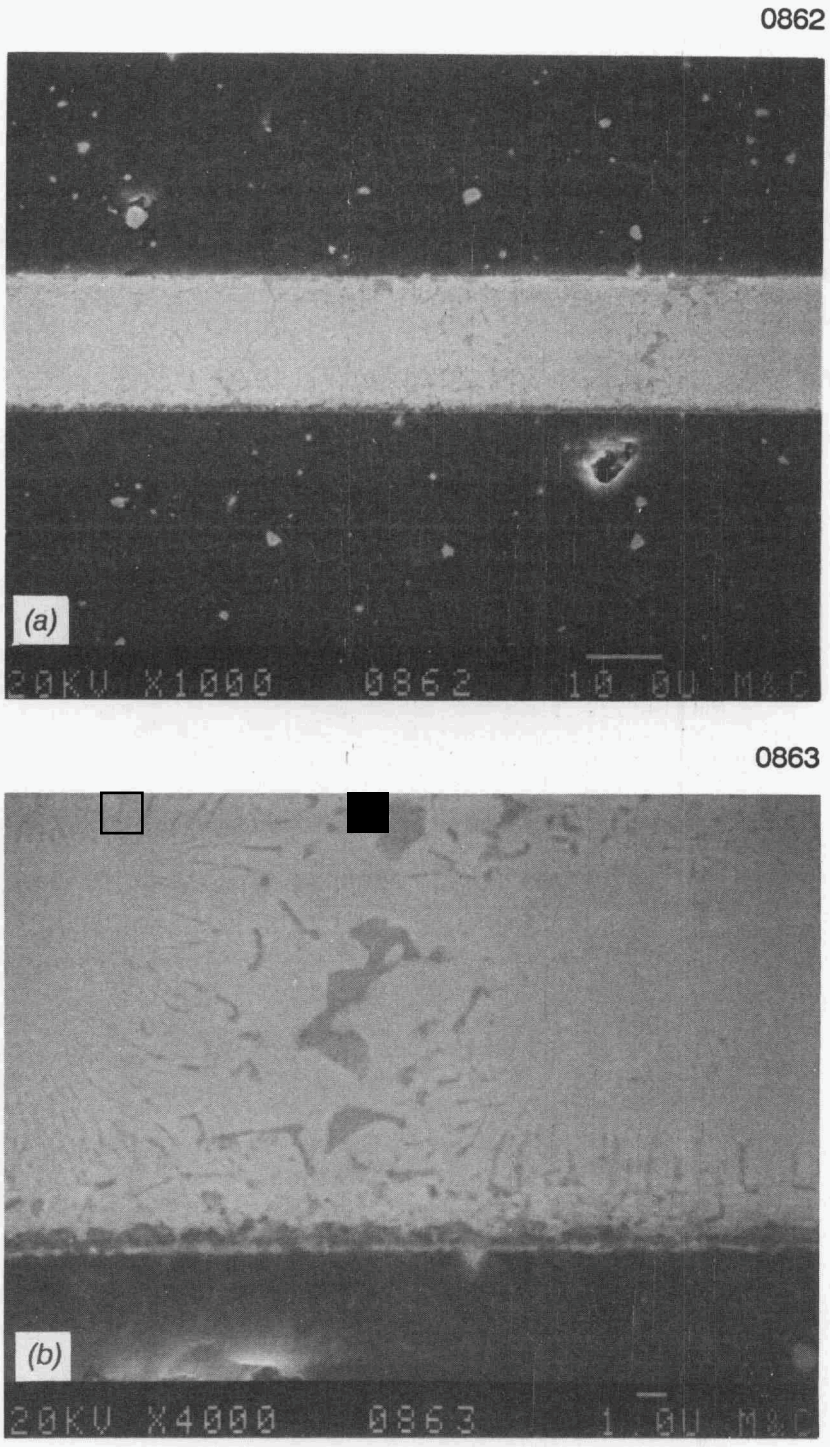

Fig. A1. Scanning electron microscope micrograph from a cross-sectioned joint showing the overall appearance of: (*a*) the Au-Ni-Pd filler metal layer between coupons of Ti-vapor-coated Si_3N_4 and (*b*) the microstructure at a Ti-vapor-coated Si_3N_4 surface after brazing.

Table A2. Compositions from braze filler metal layer after brazing at 1130° C

Braze layer analysis location	Composition in wt %				
	Au	Ni	Pd	Ti	Si
Overall	50.43	23.60	23.51	2.07	0.41
Au-rich matrix	51.20	23.43	23.10	1.91	0.36
Ni-rich particles	34.77	43.01	19.20	1.73	1.29

8881

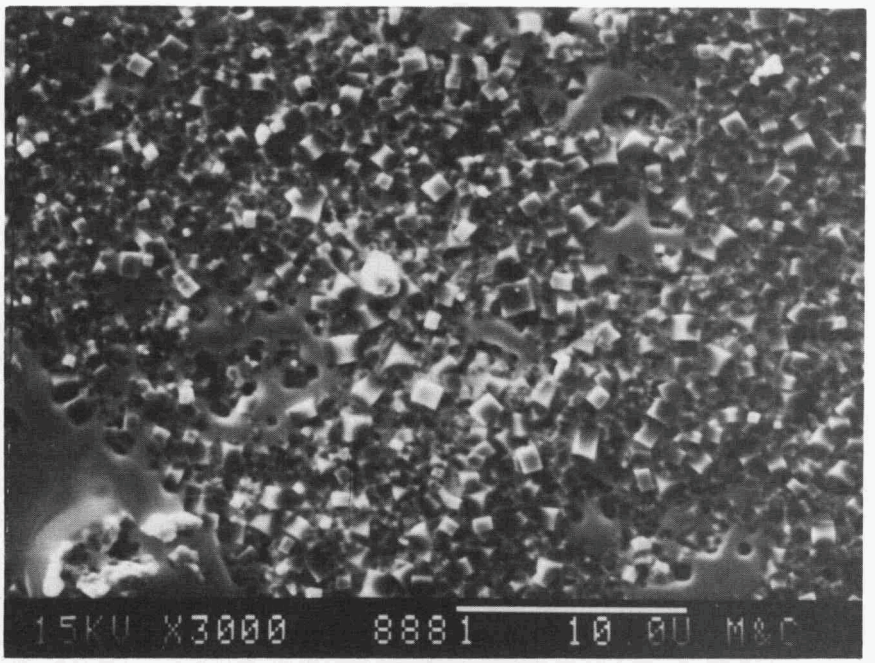

Fig. A2. Scanning electron microscope micrograph on an Si_3N_4 surface after brazing and removal of the braze filler metal by acid dissolution showing grains of TiN.

suggesting that reduction of the Si_3N_4 occurred during the brazing operation. Titanium forms a stable nitride and silicides, and because the Ti was in direct contact with Si_3N_4, reaction between them was likely. The possible reactions for which thermodynamic data are available[9,10] are:

$$1/5Si_3N_4 + Ti = 1/5Ti_5Si_3 + 2/5(N_2)\Delta G^0_T = -14.7 \text{ kcal/mole} \quad (1)$$

$$1/3Si_3N_4 + Ti = 1/3TiSi + 2/3(N_2)\Delta G^0_T = -16.9 \text{ kcal/mole} \quad (2)$$

$$2/3Si_3N_4 + Ti = TiSi_2 + 4/3(N_2)\Delta G^0_T = +13.5 \text{ kcal/mole} \quad (3)$$

$$1/4Si_3N_4 + Ti = TiN + 3/4Si\Delta G^0_T = -32.1 \text{ kcal/mole} \quad (4)$$

These data show that TiN, Ti_5Si_3, and TiSi can all form by reaction of titanium with Si_3N_4 at 1130°C but that TiN is considerably more stable than the titanium silicides. The XRD data confirmed that a layer of TiN formed preferentially at the Si_3N_4 surfaces during brazing. The lack of porosity in the braze layers also offers indirect evidence for the preferential formation of TiN. If silicide reactions were preferred, they would have released N_2, which would have formed pores in the liquid filler metal.

Other phases such as Ni, Pd, or Ti silicides or Ni_xTi compounds were not directly observed by SEM or XRD. However, their presence cannot be precluded. Quantities of these compounds too small to be detected may have formed in the braze layer microstructures. It is also possible that low-melting compounds incorporated into the reaction layer at the Si_3N_4 surfaces were dissolved by the acid solution used to reveal the TiN.

Microchemical analysis further showed that Si partitioned preferentially to Ni-rich particles found in the braze layer. The unmelted filler metal is ductile, and the absence of cracking in the reacted filler metal layers indicates that the dissolution of the Si and Ti did not seriously compromise braze layer ductility. The lack of cracks around hardness indentations also suggests that ductility was maintained in the braze layers.

High-temperature brazing: Several Ti-vapor-coated Si_3N_4 joints were also made at 1250°C with a 60Pd-40Ni wt % commercial foil (25 μm thick), and these joints contained considerable porosity. In a separate experiment, braze joints were made with the 50Au-25Ni-25Pd wt % and the 60Pd-40Ni wt % alloys at 1250°C (about 120°C above the normal brazing temperature for the Au-Ni-Pd alloy). The result was that an acceptable porosity-free joint was obtained only with the Au-Ni-Pd alloy. Standardless microchemical analysis of the joints in an SEM showed that both braze layers had become enriched to some extent with Si: 2.4 wt % for the Au-Ni-Pd alloy and 9.7 wt % for the Pd-Ni alloy. A cross-sectional view of the microstructure of the Au-Ni-Pd joint, taken in the SEM, is shown in Fig. A3(*a*). The light regions in this braze layer are an Au-rich matrix containing second-phase particles. The darker regions in this braze layer are comprised of grains of an Ni-rich phase and some grains with a composition of $(Pd,Ni)_3Si$. The Ti in this joint remained localized at the Si_3N_4 surfaces. The microstructure of the Pd-Ni joint is shown in Fig. A3(*b*). In this case, the braze layer appears to be primarily a $(Pd,Ni)_3Si$ phase containing small Ni-rich particles. Several cracks, such as the one shown in Fig. A3(*b*), were also found in this braze layer, and these are an indication that the $(Pd,Ni)_3Si$ phase is brittle. Based on composition, it is also likely that the M_3Si-phases found in both braze

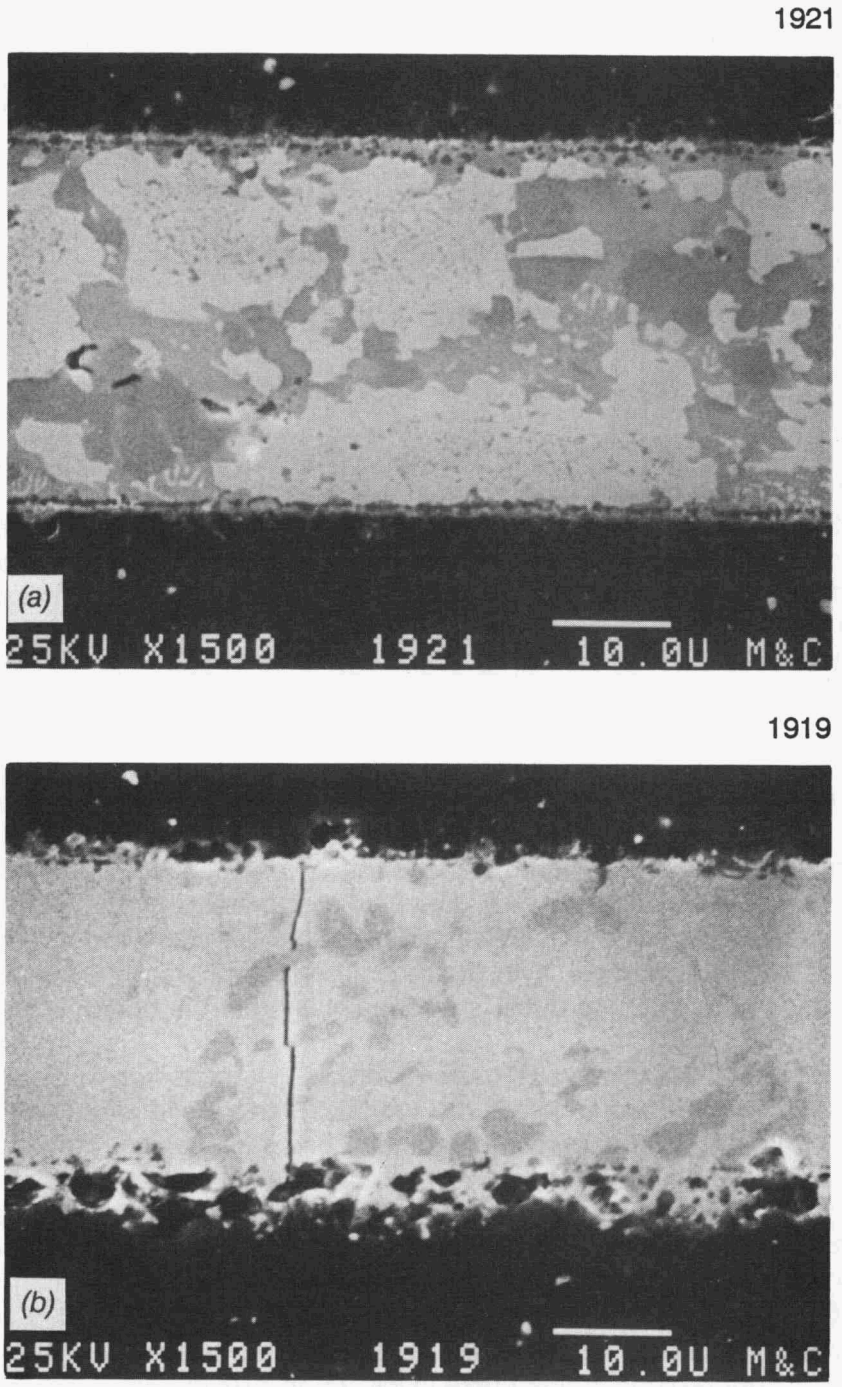

Fig. A3. Cross-sectional view of Ti-vapor-coated Si_3N_4 brazed at 1250°C with: (*a*) Au-25Ni-25Pd wt % filler metal and (*b*) Pd-40Ni wt % filler metal.

layers have relatively low melting temperatures since for Ni_3Si, T_M = 1170°C and for Pd_3Si, T_M = 960°C. This experiment also shows that the 50Au-25Ni-25Pd wt % braze filler metal is particularly well suited for brazing Ti-vapor-coated Si_3N_4 and suggests that consideration of high-Au-containing filler metals might permit brazing temperatures to be used.

Based on the above results, a commercially available Au-25Pd wt % alloy was also used to make several joints with Si_3N_4, which was vapor coated with a 2-μm layer of either Ti or Mo. The brazing trials were done at 1425 and 1375°C, which are, respectively, 15°C over and 35°C under the nominal melting temperature (1410°C) of this filler metal. Melting of the filler metal was achieved at both temperatures. Joints were formed for each experimental condition, and those made at 1375°C had good external appearance, but sectioning revealed that all of the joints contained large void areas. The microstructure, as viewed in the SEM, of a joint made at 1375°C using Ti-vapor-coated Si_3N_4 is shown in Fig. A4. In this case, microchemical analysis indicated that the major phase in the braze layer had a composition of 13.6 wt % (36.6 at. %) Si, which suggests that it may be a two-phase mixture of Pd_2Si and PdSi. The high Si level indicates extensive reaction between Pd and the Si_3N_4 occurred. The minor phase in the braze layer appeared to be Au rich. Figure 4 also shows a large number of particles near the Si_3N_4 surfaces. These particles could not be identified, but some of them were Ti rich and could have been TiN or Ti-silicides. It is also clear that the Ti layer did not remain intact and continuous on the Si_3N_4 surfaces and did not inhibit reaction of the braze filler metal with the Si_3N_4. The reaction with Pd undoubtedly is responsible for depression of the filler metal melting

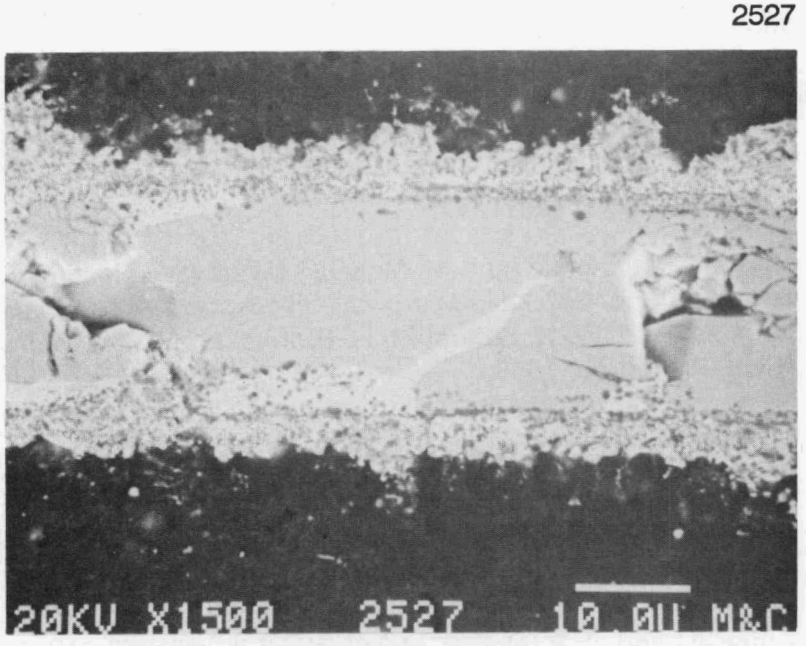

Fig. A4. Microstructure of Ti-vapor-coated Si_3N_4 brazed at 1375°C with an Au-25Pd wt % filler metal.

temperature and appears to be a significant problem in identifying filler metal compositions which may permit brazing at temperatures above 1130°C.

These experiments indicate that the conditions during the brazing of Si_3N_4 with Ni-and Pd-containing filler metals are favorable for the formation of silicide phases. They also indicate that the formation of large quantities of silicide phases in these joints is undesirable because silicides have relatively poor mechanical properties and possibly low melting points. Also, the formation of silicides in the braze layers involves decomposition of the Si_3N_4 and evolution of nitrogen gas, which then leads to expulsion of filler metal from the joint gaps and the formation of large void regions.

References

1. H. E. Pattee, "Joining Ceramics to Metals and Other Materials," *Weld. Res. Counc. Bull.* **178** (November 1972).

2. M. G. Nicholas and D. A. Mortimer, "Ceramic/metal joining for structural applications," *Mater. Sci. Technol.* 1(9), 657-65 (1985).

3. R. E. Loehman and A. P. Tomsia, "Joining of Ceramics," *Ceram. Bull.* **67**(2), 375-80 (1988).

4. M. M. Schwartz, *Ceramic Joining*, ASM International, Materials Park, Ohio, 1990.

5. M. L. Santella, "Brazing of Titanium-Vapor-Coated Silicon Nitride," *Adv. Ceram. Mater.* **3**, 457-62 (1988).

6. M. L. Santella and L. C. Manley, "Strength and Microstructure of Titanium-Vapor-Coated Silicon Nitride Braze Joints," accepted for publication in *Proceedings of the 3rd International Symposium, Ceramic Materials and Components for Engines*, American Ceramic Society, Westerville, Ohio, 1989.

7. H. Fukushima, T. Yamanaka, and M. Matsui, " Microwave Heating of Ceramics and Its Application to Joining," pp. 267-72 in *Microwave Processing of Materials, Symposium Proceedings, Vol. 124*, ed. W. H. Sutton, M. H. Brooks, and I. J. Chabinsky, Materials Research Society, Pittsburgh, 1988.

8. T. B. Massalski, *Binary Alloy Phase Diagrams*, American Society for Metals, Materials Park, Ohio, 1986.

9. I. Barin, O. Knacke, and O. Kubaschewski, *Thermochemical Properties of Inorganic Substances*, Springer-Verlag, Düsseldorf, Germany, 1977.

10. O. Kubaschewski and C. B. Alcock, *Metallurgical Thermochemistry*, 5th ed., ed. G. V. Raynor, Pergamon Press, New York, 1979.

1.4.2 Ceramic-Ceramic Joints

Analytical and Experimental Evaluation of Joining Silicon Carbide to Silicon Carbide and Silicon Nitride to Silicon Nitride for Advanced Heat Engine Applications

G. J. Sundberg, J. A. Wade, and C. S. White (Norton)

OBJECTIVE/SCOPE

Joins of hot isostatically pressed (HIP'ed) Si_3N_4-4wt% Y_2O_3 (NCX-5100 family) and sintered Beta-SiC (NCX-4500) were developed during Phase I of the contract and were demonstrated to have mechanical properties attractive for advanced heat engine applications.[1] An experimental database was developed for both materials based upon limited MOR and buttonhead tensile tests. Within the limitations of this database, analytical/numerical models were developed for prediction of join reliability. The purpose of this program is to develop joining technologies for HIP'ed Si_3N_4 with 4wt% Y_2O_3 and for a siliconized SiC (NT-230) for various geometries including: butt joins, curved joins and shaft to disk joins. In addition, more extensive mechanical characterization of silicon nitride joins to enhance the predictive capabilities of the analytical/numerical models for structural components in advanced heat engines will be provided. Mechanical evaluation will be performed by: MOR at 22°C and 1370°C, stress rupture at 1370°C, high temperature creep, 22°C tensile testing and spin tests.

TECHNICAL/HIGHLIGHTS

Si_3N_4 Butt Joints - Creep Resistance (Task 1.1)

Model Development

The development of material models are useful only insofar as they can be used to predict the performance of structural components. The finite element method is the most popular and, arguably, the most flexible numerical method for application of advanced material laws to actual components. In conjunction with the development of material models to describe the joins and parent material, is an investigation to use these models in the prediction of the response of complex members.

In previous reports, we have detailed the experimental results, to date, for the creep of Si_3N_4-Si_3N_4 joins and parent material.[2] These experimental results have been modeled in two ways: theta projection model, and Norton's law. The preliminary modeling results have been presented in previous reports. Current work is underway to extend the Norton's law modeling of the apparent steady state creep to include modeling the primary creep response. This is an important component that needs to be included in a useful material model for the NCX-5100 Si_3N_4 which we have tested.

The first results being reported here involve incorporating the Norton's law modeling into a finite element code and demonstrating how it can be used to predict the mechanical response of a structure. Then, the steady state model is extended to include primary creep behavior.

The ANSYS code is a well known and widely used lagrangian, nonlinear, finite element code. It is commercially available and in use worldwide. Nonlinearity is important for creep modeling. Since the strain rates evolve with time and temperature the solution must be tracked in an incremental manner. ANSYS also has thermal stress and heat transfer capabilities so it can be used in nonuniform temperature fields and also to predict residual stress.

Research sponsored by the U.S. Department of Energy, Assistant Secretary for Conservation and Renewable Energy, Office of Transportation Technologies, as part of the Ceramic Technology Project of the Materials Development Program, under contract DE-AC05-84OR21400 with Martin Marietta Energy Systems, Inc.

The one-dimensional Norton's law can be expressed in multicomponent form such as:

$$\dot{\epsilon}_{ij}^{cr} = A\sigma_e^n e^{-Q/RT} \frac{3}{2} \frac{\sigma'_{ij}}{\sigma_e}, \qquad (1)$$

where σ'_{ij} is the stress deviator tensor, and σ_e is the equivalent stress ($\sigma_e = (3/2\ \sigma'_{ij} \cdot \sigma'_{ij})1/2$). The total strain rate is given as the sum of the elastic strain rate and the creep strain rate as given above.

Several criteria were used to select a component to apply the finite element method. The component was required to have: (1) a nonuniform stress and strain distribution, primarily tensile loading since the material constants were determined from tensile loading; (2) a fairly simple geometry; and (3) amenability to being tested experimentally. Guided by the above considerations, a notched, cylindrical tensile member was selected (see Figure 1). The geometry is fairly simple to represent due to the two planes of symmetry. The specimen has a semicircular notch at the center of the gauge section. The notch radius was chosen to be one-half of the gauge radius. The notch serves as a universal stress and strain concentrator. The geometry was meshed with several different refinements to ensure that sufficient elements were used. The mesh shown in Figure 1 has 529, eight node, axisymmetric elements. The preliminary results for this analysis was presented at the Symposium on Life Prediction Methodologies at Cocoa Beach, January 1993. The main concern expressed by the audience was whether a fine enough mesh had been used. A mesh convergence study has been done and the results for a mesh having four times as many elements verifies the results presented at Cocoa Beach. The mesh is loaded by applying a 10 MPa tensile stress to the top of the specimen and setting the temperature to 1368°C everywhere in the mesh. This simulation was conducted assuming isothermal conditions, but that is not a necessary requirement. The load was applied, then the specimen was allowed to creep for 500 hours in 150 equal time increments. This was a much shorter time division than required by the convergence criterion specified in ANSYS.

Model Results

The results are presented for two different times in the analysis. In Figure 2 the vertical normal stress, σ_y, is plotted at ten hours and 500 hours of deformation. Note that at short times the vertical normal stress has its maximum at the notch root as would be expected from linear elastic analysis. As the creep deformation continues the creep strain builds up at the notch root and redistributes the stress more evenly across the section. Figure 2b shows the vertical normal stress after 500 hours of deformation. It is shown that the stress is more uniform and that the maximum now occurs at the center of the specimen, not at the notch root. This is a consequence of the creep strain being driven by the deviatoric stresses. The accumulated creep strain at 500 hours, has its maximum at the notch root, as shown in Figure 3. The creep strain accumulates monotonically with time.

This simulation is given as an example of the type of analysis that can apply advanced material models to engineering structures. The failure prediction from such simulations is currently restricted to being based upon reaching a critical creep strain. That is consistent with the Monkman-Grant relationship if the exponent is unity. Otherwise, the evolution of a damage variable could be tracked and used as in the failure criterion.

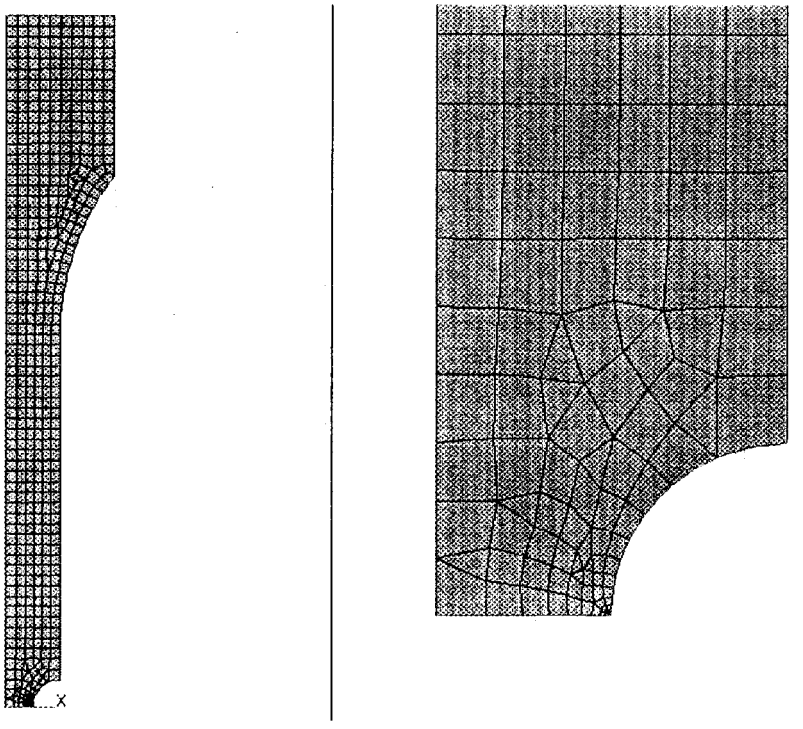

Figure 1: Notched Tensile Member Geometry And Coarse Mesh

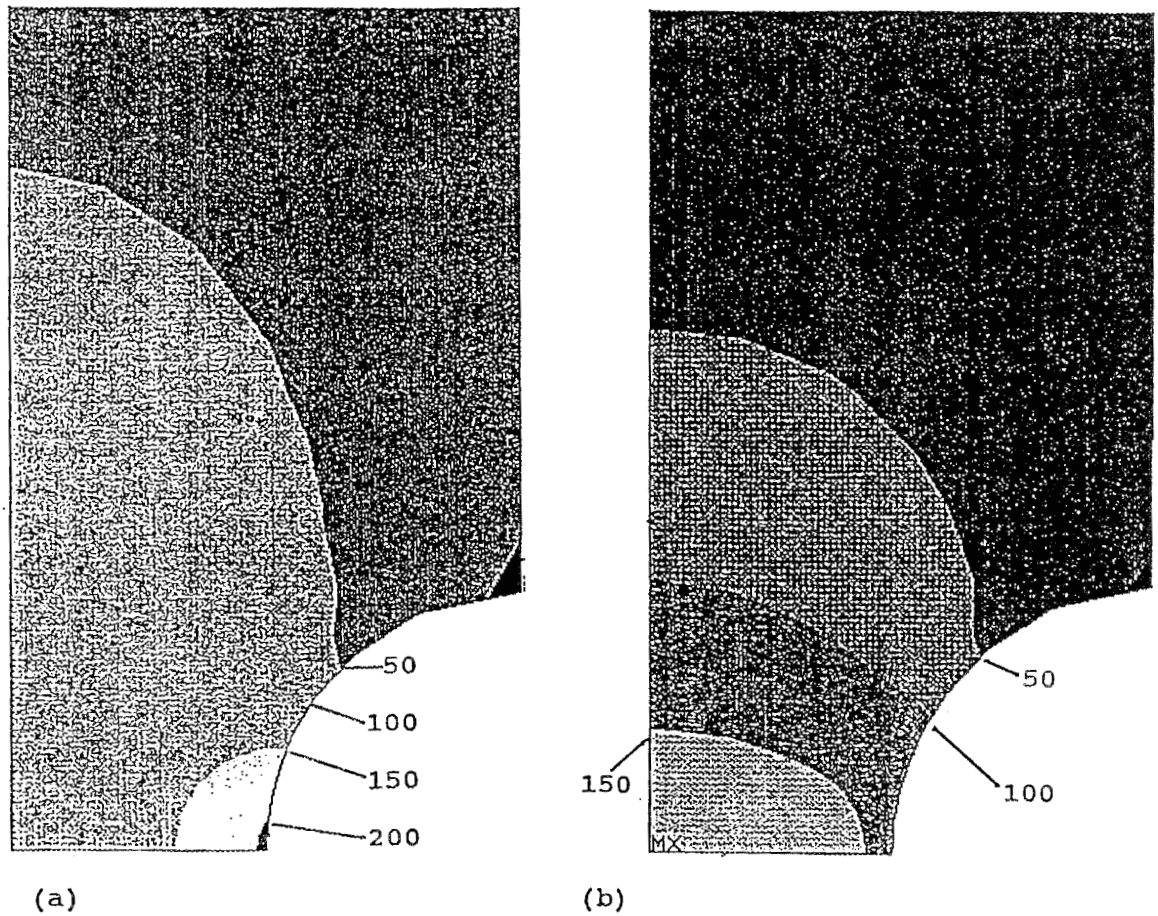

Figure 2: Vertical Normal Stress After (a) Ten And (b) Five Hundred Hours (MPa)

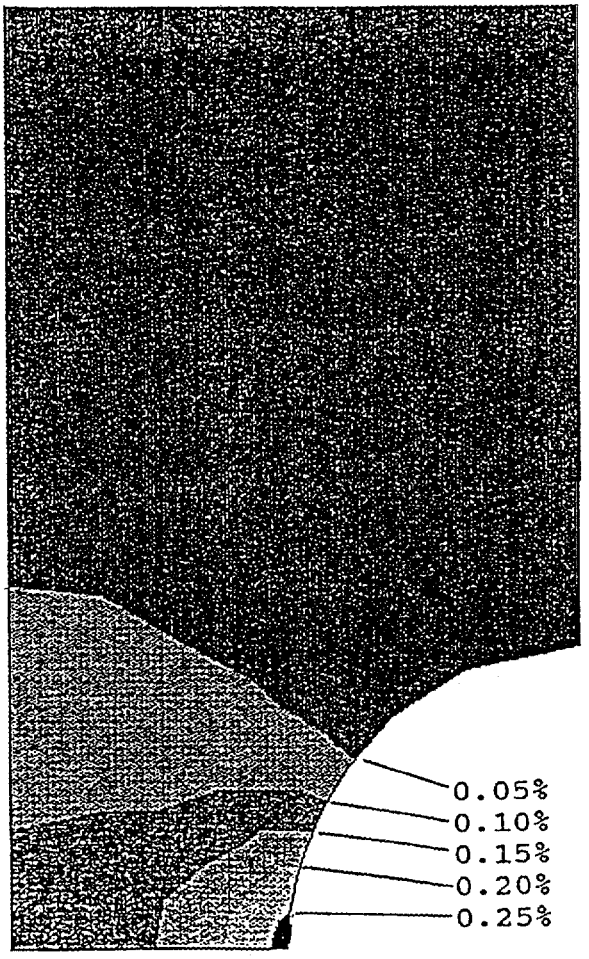

Figure 3: Accumulated Creep Strain After 500 Hours

Arrhenius Model of Steady State Creep Rate

Additional creep data has supported former findings that the apparent activation energy for creep was dependent upon applied stress. The simple Arrhenius form of Norton's equation was applied:

$$\dot{\varepsilon}_s = A\sigma^n e^{-Q/RT} \qquad (2)$$

where $\dot{\varepsilon}_s$ is the steady state strain rate, A and n are material constants, σ is the applied stress, Q is the apparent activation energy for creep, R is the universal gas constant, and T is the absolute temperature. This equation has received wide acceptance for high temperature creep behavior in the literature for both ceramics and metals. Consider the natural logarithm of Norton's equation:

$$\ln\dot{\varepsilon}_s = \ln A + n\ln\sigma - \frac{Q}{RT} \qquad (3)$$

The values of Q, n, and A can be determined from plotting the natural logarithm of the steady state creep strain rate against various parameters. The value of Q was determined from plotting $\ln(\dot{\varepsilon}_s)$ versus 1/T at constant stress (Figure 4). The value of Q is the negative of the slope of that curve multiplied by the universal gas constant (R). In Figure 4 we see that the calculated value of the apparent activation energy Q varies with the value of the applied stress. The data is summarized in Figure 5. There is an approximately linear increase in Q with stress. The range of measured values in Q going from 627 KJ/mole to 1425 KJ/mole is consistent with other values from the literature. This phenomenon of increasing Q with stress is currently being investigated. There is evidence from the literature of the creep of metals for Q to decrease with stress but not to increase.

The value of n was determined by taking the slope of $\ln(\dot{\varepsilon}_s)$ as a function of $\ln(\sigma)$ at constant temperature (Figure 6). The values of n were 0.703, 5.241, 7.095, and 5.781 for temperatures of 1400, 1370, 1300, and 1250°C, respectively. There was a trend of increasing n with decreasing temperature except for a temperature of 1250°C where a limited amount of data was available.

Failure Modeling

The time to failure for each minimum strain rate is plotted in Figure 7. This correlation follows the Monkman-Grant relationship given below.

$$\dot{\varepsilon}_s^{\beta} t_f = C \qquad (4)$$

where t_f is the time to failure and the Monkman-Grant parameters β and C are 1.271 and 1.892e-4 $hr^{-0.271}$. Since β is nearly equal to unity, the creep strain to failure is a constant. This was used as the criterion for failure in the finite element code.

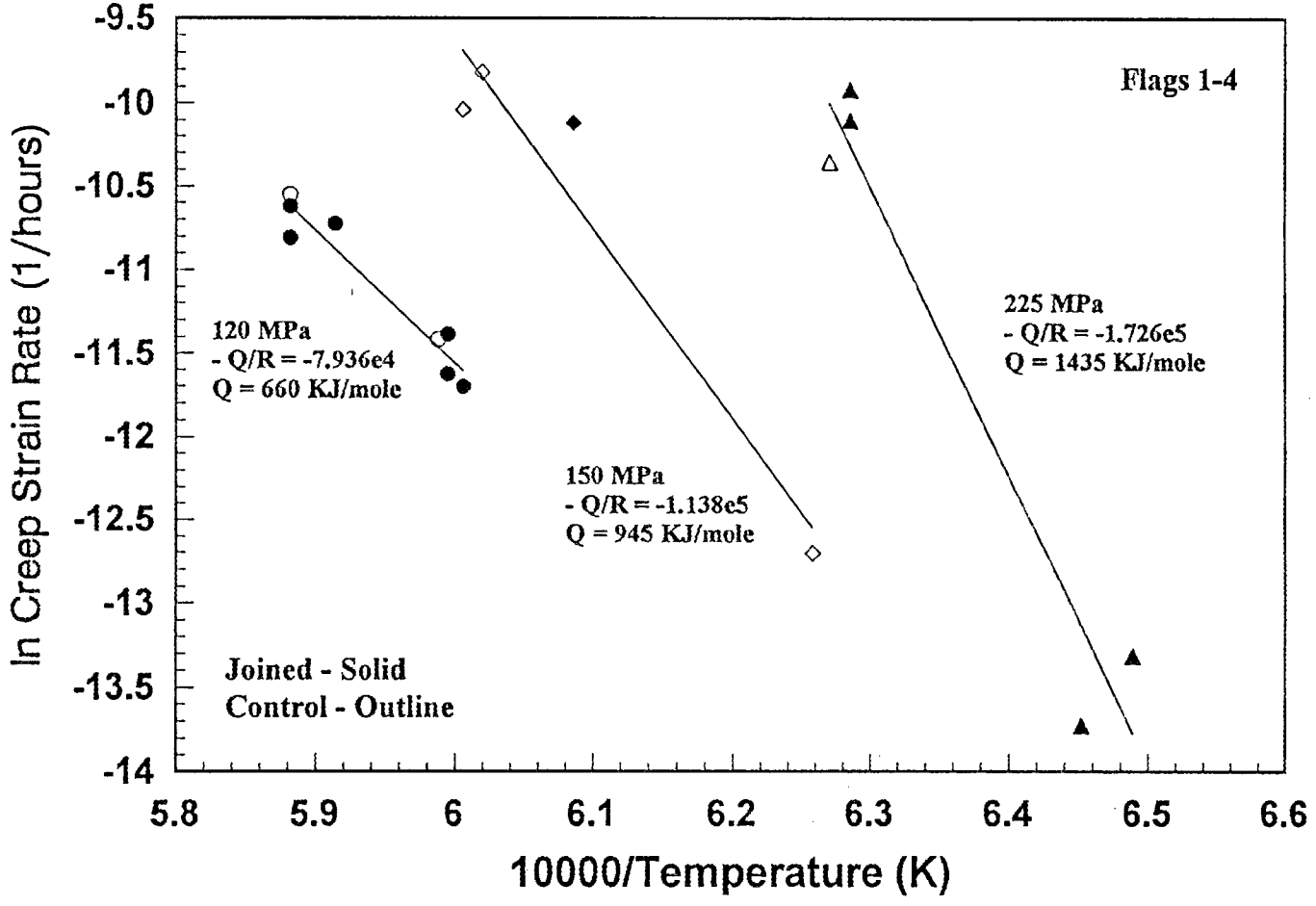

Figure 4: Determination Of The Activation Energy (Q) - NCX-5100

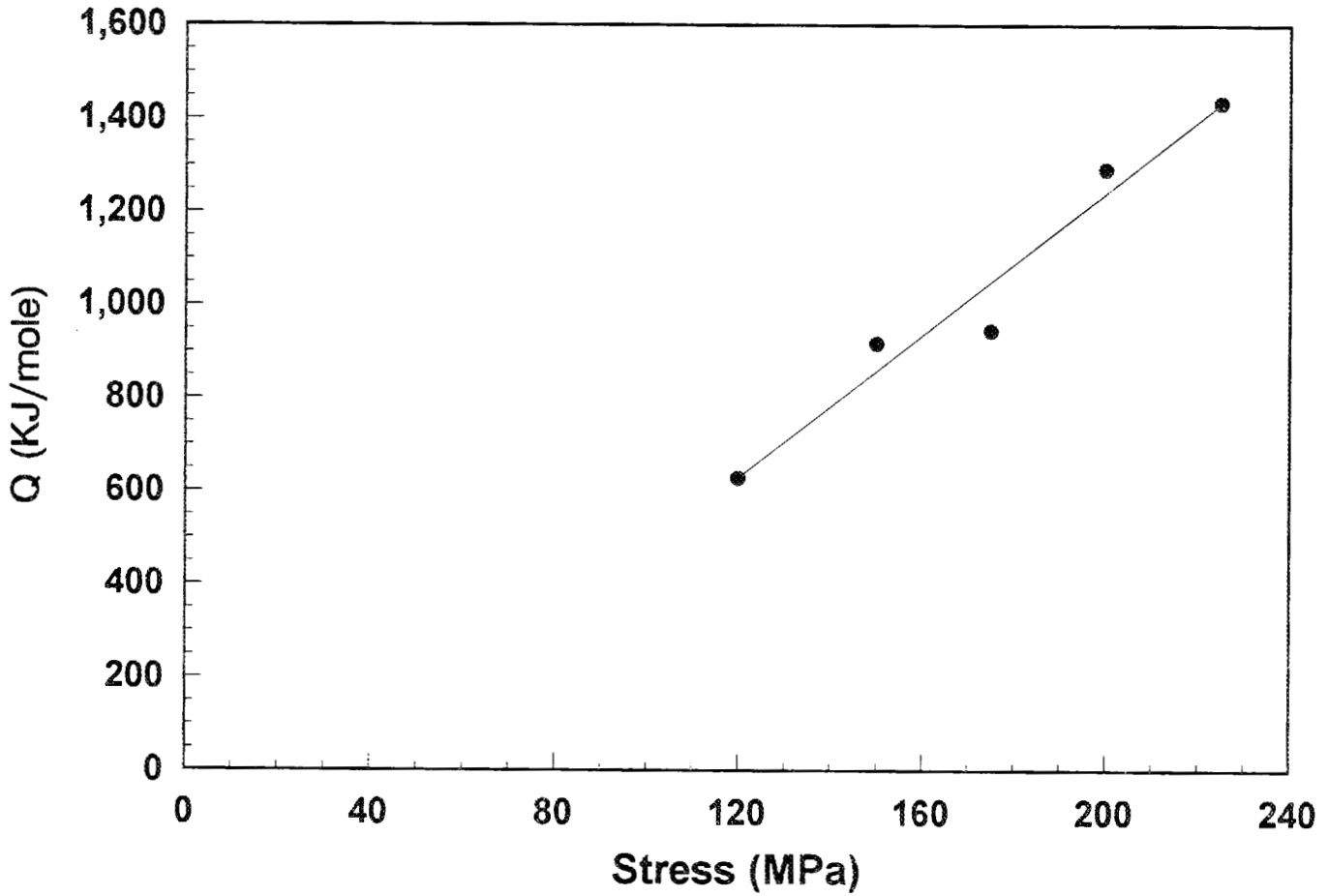

Figure 5: Apparent Activation Energy Of The Minimum Creep Rate As A Function Of The Applied Stress For NCX-5100

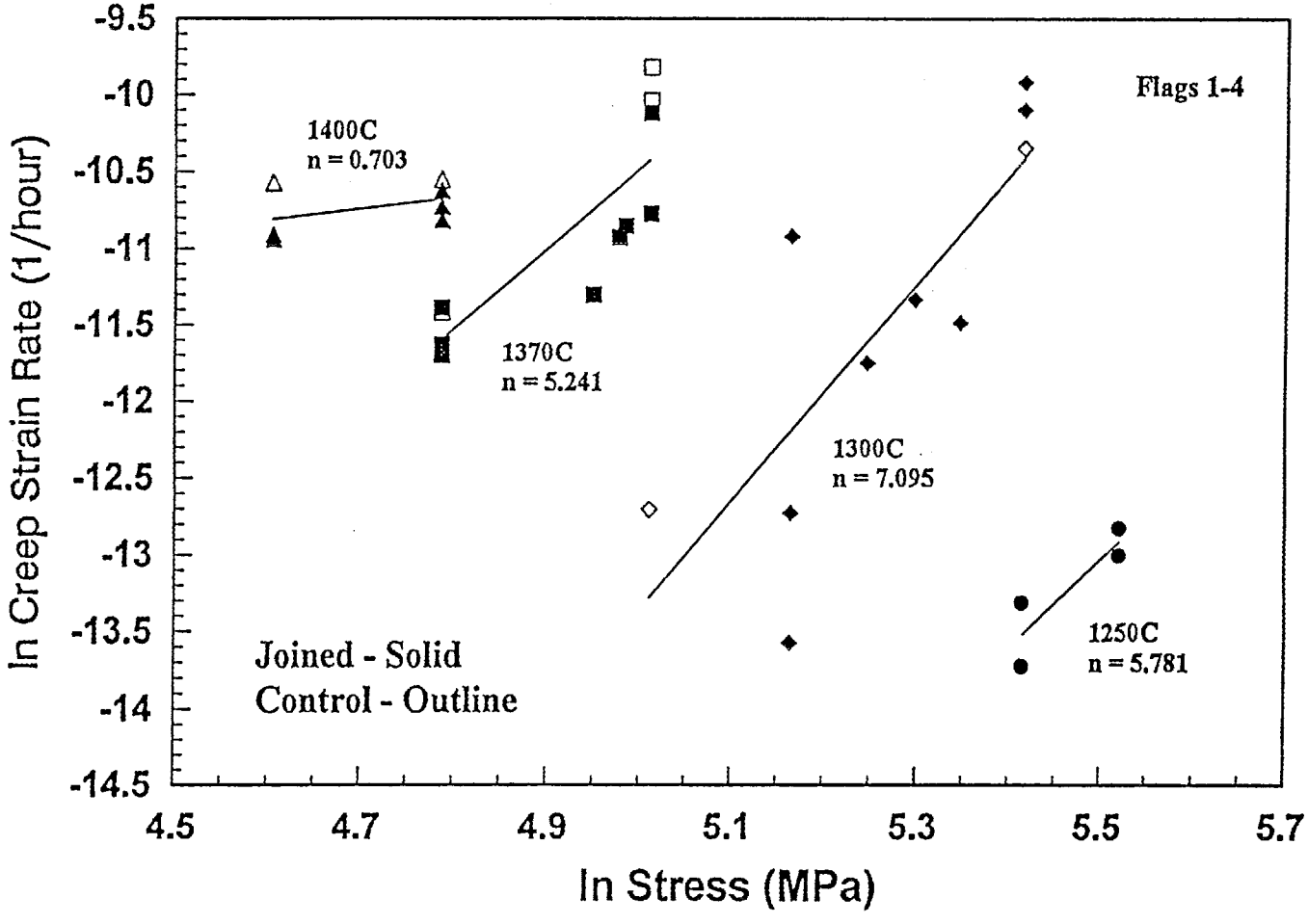

Figure 6: Determination Of The Stress Exponent (n) - NCX-5100

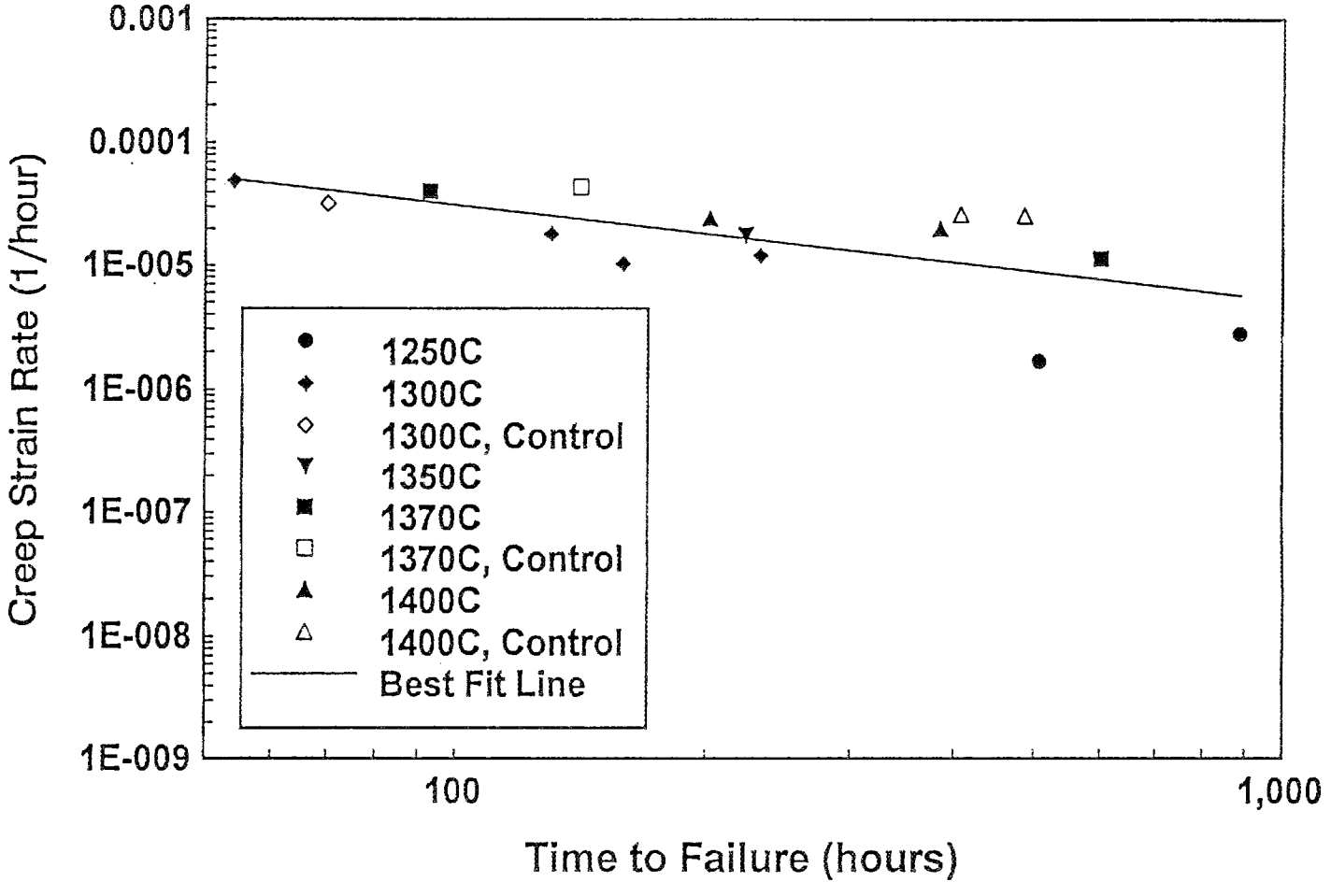

Figure 7: Monkman-Grant Relationship For Flags 1-4 - NCX-5100

Since the creep strain rate for this material does not show a tertiary regime we observe that the strain rate continuously decreases until failure. Thus the minimum creep rate is the strain rate observed just prior to failure.

Having the minimum creep rate characterized is not sufficient as input for predicting the creep of structural components. The entire creep curve should be represented. The following approach was evaluated as an effective way to extend the minimum creep rate model (Equation 2) to the primary regime as well.

If we start with the assumption that the effect of stress and temperature on the minimum creep rate is representative of their effects on the entire creep curve then we can use an internal variable model which involves the dimensionless variable, s, and a material parameter, h. The change in structure will be represented by s, while h, is a measure of how quickly the material hardens. During creep, s evolves from its initial to final values. Here we will assume that we can normalize s such that its final value is unity. As s goes from s_o to 1 the creep rate will continuously decrease from its initial value until it reaches the temperature and stress dependent minimum value. This can be represented by the equations below.

$$\dot{\varepsilon}_{cr} = \frac{A}{s}\sigma^n e^{-Q/RT} \tag{5}$$

$$\dot{s} = h(1-s)\dot{\varepsilon}_{cr}. \tag{6}$$

Equations 5 and 6 represent a system of two, coupled first order differential equations that can be solved for $\varepsilon(t)$ to compare with experiments. The approach of using internal state variables is also being considered by Ding et al.[3] and has been used extensively in metals[4] to capture nonlinear material behavior.

In order to evaluate this new model, the creep tests of nine NCX-5100 joins that were tested until failure were used. The minimum creep rate parameters A, n and Q were determined from a least squares fit of the experimentally measured minimum creep rates. The determined values were:

$n = 2.987$
$Q = 609$ KJ/mole
$A = 8.85 \times 10^7$ $(\text{hour}*\text{MPa}^n)^{-1}$.

Using these values, the creep curves that were used in determining the parameters were simulated using Equations 5 and 6. The results are shown in Figure 8. The solid curves represent the experimental data and the dashed curves are the model predictions. The two parameters, s_o and h, were judiciously chosen to provide a good fit to the data.

The results in Figure 8 show good agreement with the experiment. The shape and total strain are predicted reasonably well. In testing it was noticed that there is significant scatter in the measured creep response curves even for identical testing conditions. The model would not be able to capture this kind of experimental variability. In future constitutive modeling efforts, the model will be applied to the control specimens using the parameters determined for the joins. This will provide one way on viewing whether there is significant, systematic difference between the joined specimens and the base material.

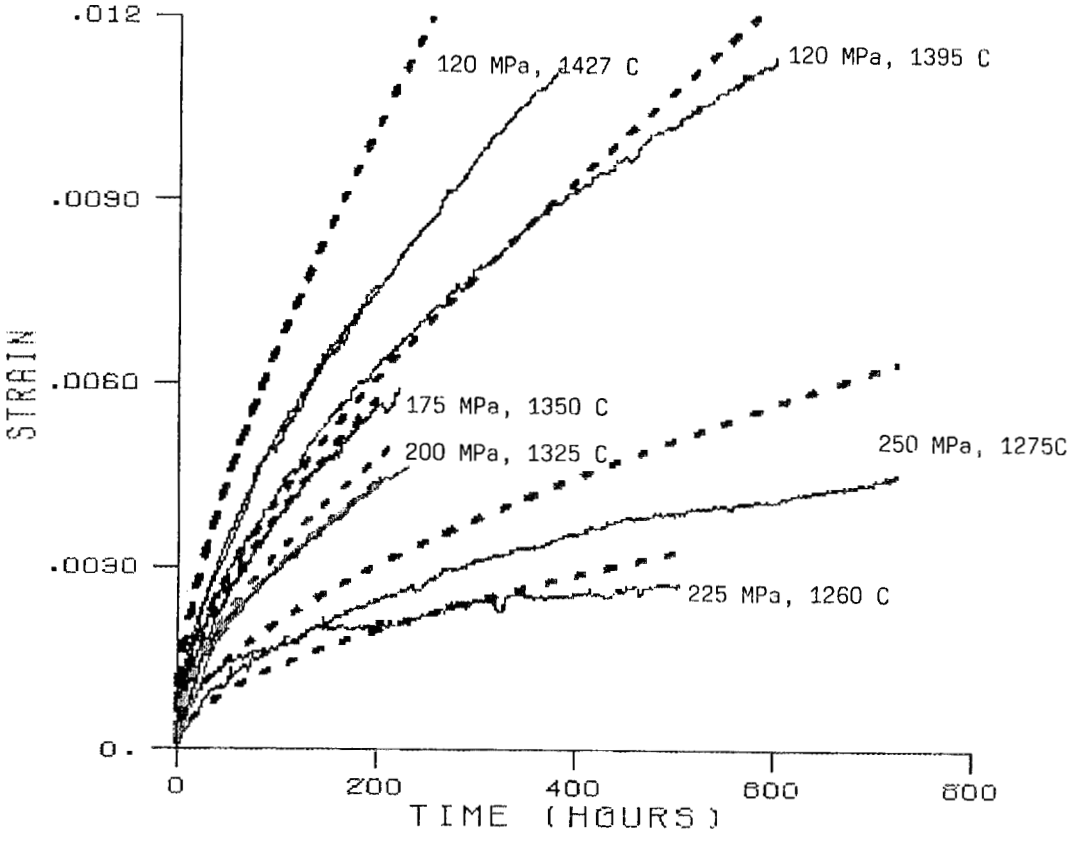

Figure 8: Comparison Of Model With Experiment For NCX-5100 Joined Specimens. Solid Curve Is Experiment, Dashed Curve Is Model.

Silicon Nitride Curved Joint - Joint Development (Task 1.2)

Mechanical Testing

Room Temperature Fast Fracture: Densified curved join disks made from slip type D were sectioned according to Figure 9 and ground into ASTM C-1161 (derived from MIL-STD-1942MR) "A" flexure specimens. Results of flexure tests on a 5mm x 20mm span are summarized in Table 1. A statistical comparison of the outer layers (A,D) to the inner layers (B,C) using a robust non-parametric paired analysis found no difference at the 95% confidence interval within each joined disk. A similar analysis was run for all layers of a disk with each of the other disks. The result indicated a lower strength in joins 20 and 24. The reduced strength in join 20 may be due to the lower density, however, the cause of the lower strength of join 24 is not apparent. Optical fractography showed failure origins to be located primarily at the surface and in most cases near a chamfer. The Weibull modulus for all outer layers (A,D) and all inner layers (B,C) were essentially identical at 16.4 and 16.5 respectively (Figure 10). The Weibull modulus for the combined groups is 16.4. The combined average strength is 886.3 +/- 56 MPa.

1370°C Fast Fracture: Results from 1370°C ASTM C-11161 specimen "A" type bars are summarized in Table 2. As with the room temperature tests there were no significant differences between join layers. The average strength for all specimens tested was 516 MPa +/- 47 MPa. The Weibull modulus was 16 (Figure 11).

Shear Testing: Two densified silicon nitride joined disks were sliced perpendicular to the axis to make three test specimens 2.50 mm thick by 70 mm diameter from each disk for a total of six specimens. Five specimens were shear tested at 25°C and one at 1370°C. The loading configuration is shown in Figures 12 and 13. Two different load/support ring diameter ratios were used. The results are summarized in Table 3.

Table 3: Shear Test Results

Sample	Temp.	R Loading Ring/ R Support	Load (kg)	Biaxial Flexural Stress (MPa)	Max. Shear Stress (MPa)	Ave. Shear Stress (MPa)	Flaw Origin	Join Failure
1	Room	0.802	1684	407.0	173.0	55.0	Surface	No
2	Room	0.802	1838	447.4	188.8	60.1	Surface	No
3	Room	0.802	1830	444.8	188.0	59.8	Surface	No
4	1370°C	0.918	3240	329.6	324.0	105.9	?	?
5	Room	0.918	2000	203.5	200.0	65.4	Surface	No
6	Room	0.918	1853	188.5	185.3	60.6	Surface	No

It was decided that by increasing the ratio the maximum bending stress would decrease while maintaining a constant average shear stress at the join. Increasing the radius of the inner load ring resulted in a ratio of 0.918. Upon loading a uniform biaxial tensile stress is

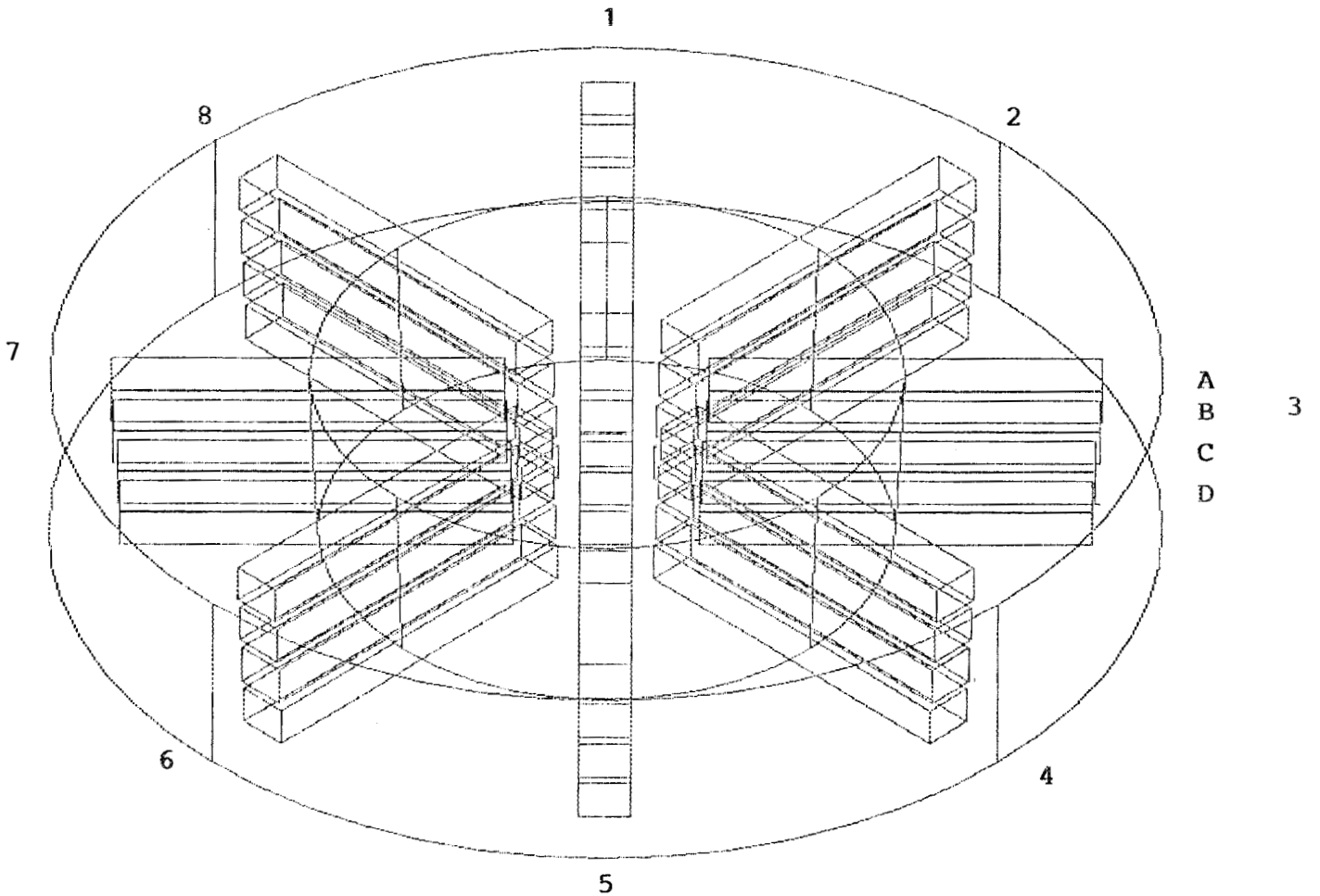

Figure 9: Configuration Of Join Sectioning For Flexure Test Specimen Preparation (Task 1.2 - Final Iteration)

Table 1: Curved Join Development

Room Temperature Fast Fracture Data (Task 1.2)							
Disk Number	Slice	Specimens Tested	Mean Strength (Mpa)	Std. Dev. (Mpa)	Join Failures	Join Non Closure	Density gms/cc
19	A-D	16	925.3	38.6	0	0	3.229
19	B-C	16	914.3	75.2	0	0	
20	A-D	16	840.5	55.2	2	0	3.208
20	B-C	16	843.2	42.1	0	0	
21	A-D	16	906.1	69	0	0	3.229
21	B-C	15	926	60.7	0	0	
23	A-D	14	885.3	61.4	0	0	3.226
23	B-C	16	885.3	51.7	0	0	
24	A-D	15	867.4	49	0	0	3.229
24	B-C	16	869.4	64.1	0	0	

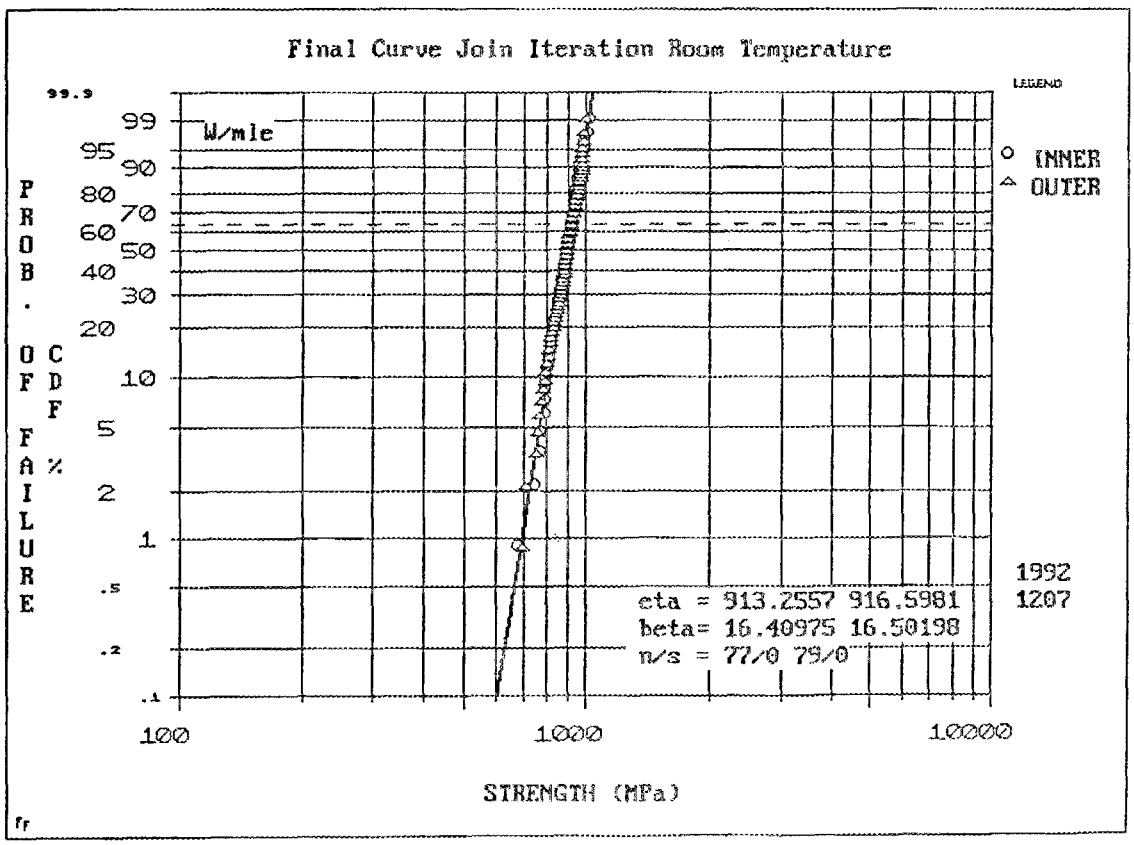

Figure 10: Weibull Probability Plot For Room Temperature Flexure Strength Evaluation (Task 1.2 - Final Iteration)

Table 2: Curved Join Development

1370 Celsius Fast Fracture Data (Task 1.2)							
Disk Number	Interlayer	Specimens Tested	Mean Strength (Mpa)	Std. Dev. (Mpa)	Join Failures	Join Non-closure	Density gms/cc
26	A,D	14	506.8	35	1	0	3.228
26	B,C	16	490.2	74.5	2	1	
28	A,D	15	523.3	32.1	0	0	3.232
28	B,C	14	544	45.5	0	0	

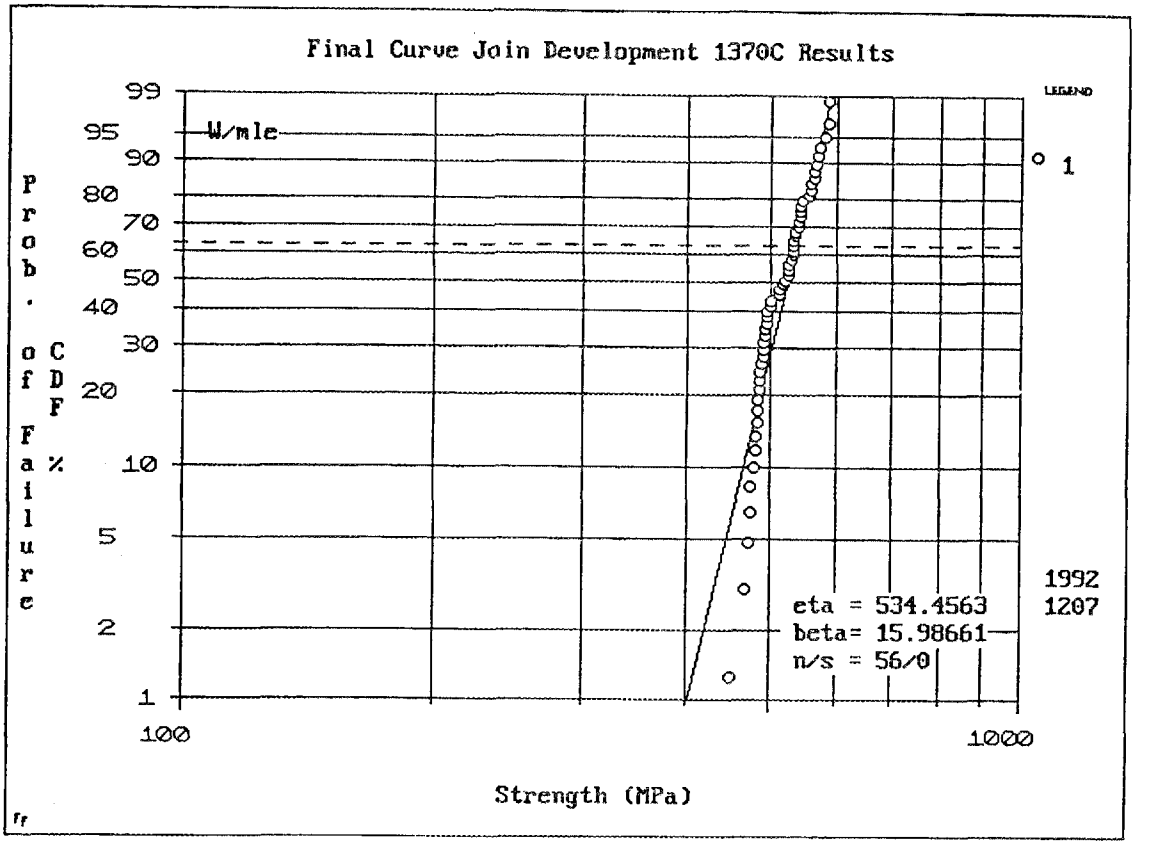

Figure 11: Weibull Probability Plot For 1370° Flexure Strength Evaluation (Task 1.2 - Final Iteration)

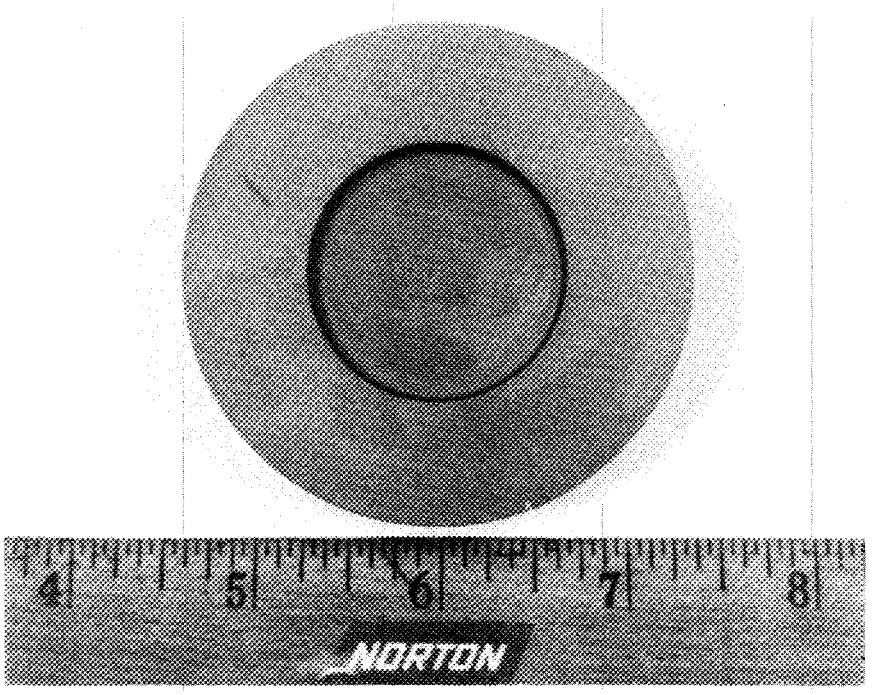

Figure 12: NCX-5101 Silicon Nitride Curved Join

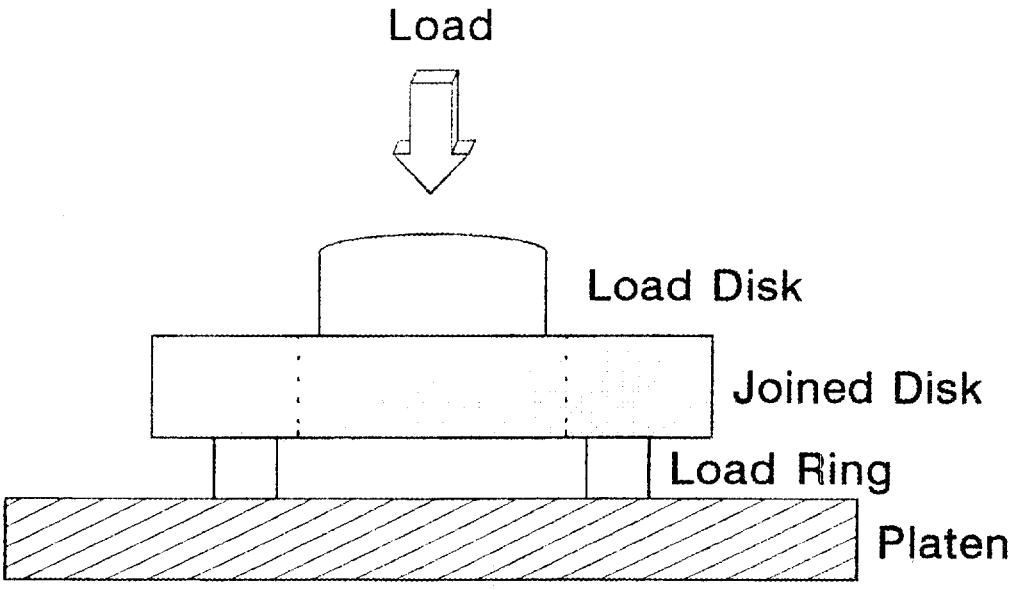

Figure 13: Shear Test Configuration

achieved over the area of the loading ring. This stress is calculated by the following equation by T.R. Wilshaw[5]:

$$\sigma = \frac{3P}{2\pi t^2}\left[(1-\nu)\frac{a^2-r^2}{2b^2}+(1+\nu)\ln\frac{a}{r}\right] \qquad (7)$$

where a = radius of support, b = radius of specimen, r = radius of loading ring, t = thickness of specimen, and P = applied load.

The shear stress was determined from an axisymmetric finite element model. Figures 14 and 15 show contour plots for the maximum principal stress and the shear stress for each load ring configuration. Notice the reduction in the maximum principal stress as the load ring ratio is increased from 0.802 to 0.918. The shear stress is dependent on the applied load at failure and is similar for the two cases since the failure loads are similar.

Fractographic analysis of failed disks revealed surface failure origins in the principal region under the inner load ring for all room temperature tests, consistent with biaxial flexure testing of a monolithic ceramic disc. At room temperature, none of the failures were attributed to the join. The failure origin at 1370°C requires further fractography to identify. Figure 16 shows a reconstructed sample. The failure origin is located within the dotted area.

The probability of failure was calculated from ANSYS results using Weibull normal stress averaging for volume flaws with material constants determined from flexure tests. Note the lack of agreement between experimental results in Table 3 and predicted failure loads in Figure 17. While there is some agreement for the test data at 1370°C, the predominance of observed surface failures lends us to believe that in all testing configurations bending is controlling the failure.

Siliconized SiC Butt Joint - Joint Development (Task 2.1A)

Additional silicon carbide joins were made to minimize the excessive silicon enrichment and porosity at the join interlayer reported earlier.[2] Six interlayer types, termed A through F, were used for joining both siliconized and unsiliconized parent materials. Interlayer A was a replication of the earlier work which resulted in silicon enrichment and porosity of the join interlayer. Join interlayers were applied as aqueous dispersions of silicon carbide and other additives and used to join silicon carbide billets of 51 x 51 x 38 mm dimensions. Attempts were made to sinter and siliconize twelve joins, six with siliconized parent materials and six with unsiliconized parent materials. One join made from the siliconized parent materials and five joins of the unsiliconized parent materials separated during presinter, siliconization or grinding of the mechanical test specimens. Flexure specimens were ground from the remainder of the joins to evaluate join strength.

ASTM C-1161 (MIL-STD-1942MR) B geometry flexure specimens were ground from the joins with the join interlayer plane located at the center of the flexure specimens perpendicular to the length. Room temperature strengths of the joins were not improved with the different join interlayer treatments (Table 4). Failure originated predominantly within the join interlayer at regions of porosity and/or silicon enrichment. The join strengths are low by comparison to the strength of the unjoined NT-230 silicon carbide parent material of similar cross sectional thickness, 38mm. The NT-230 parent material of 38mm cross-sectional thickness demonstrated significantly lower strength than was typical for NT-230 of thinner cross-section (410MPa for 10mm thick cross-section). Characterization is underway to

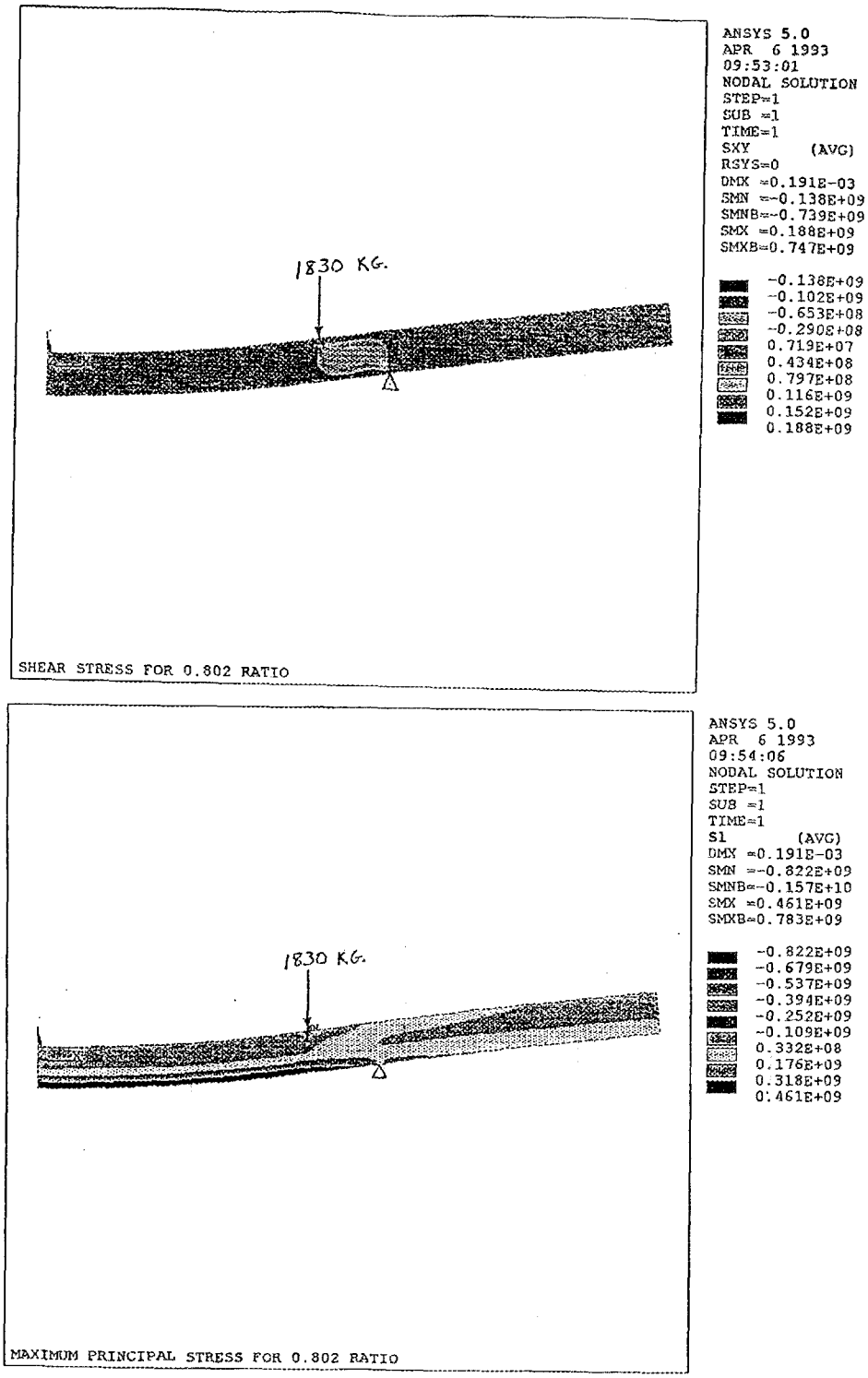

Figure 14: Contour Plots For 0.802 Load Ring Diameter Ratio

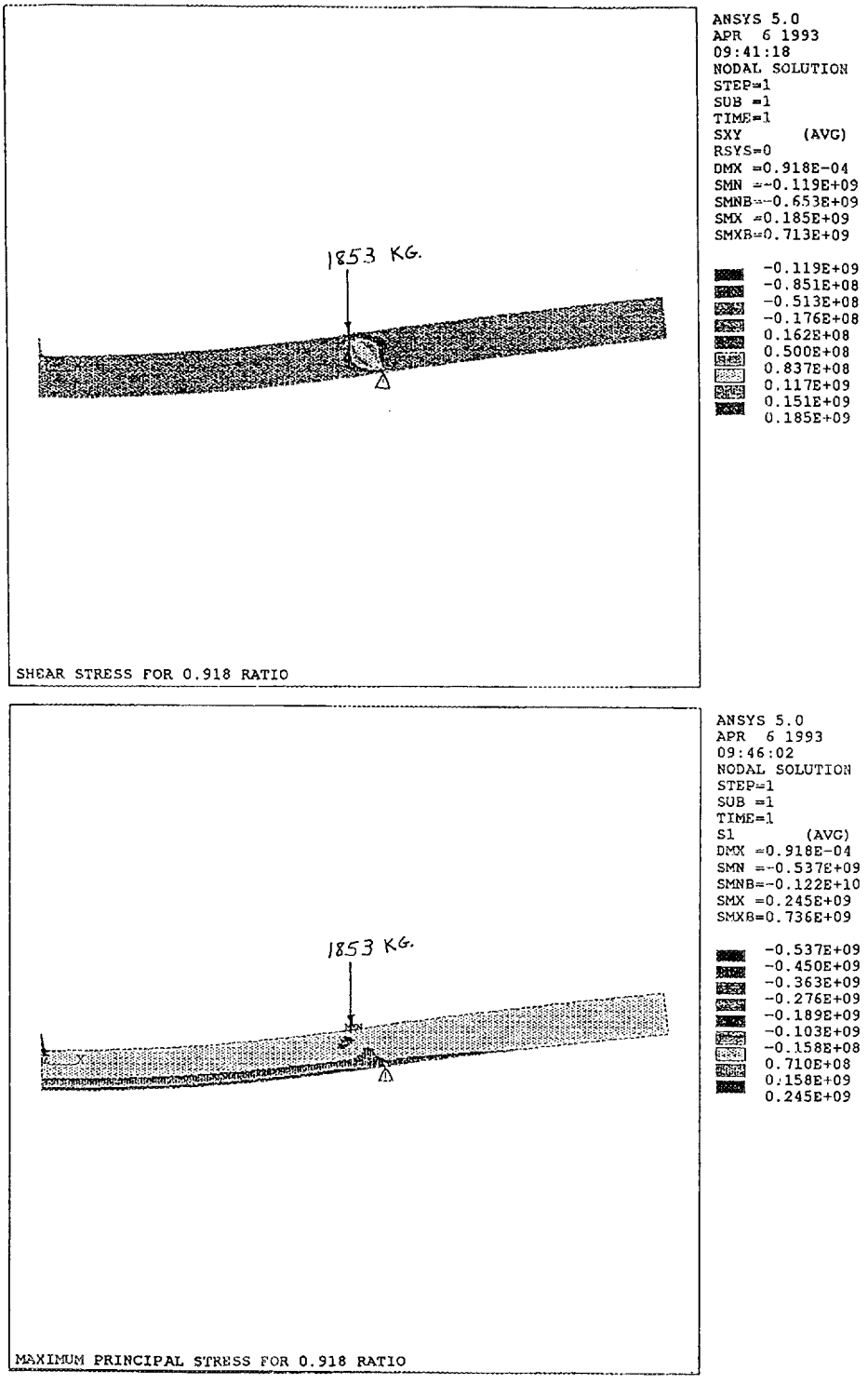

Figure 15: Contour Plots For .918 Load Ring Diameter Ratio

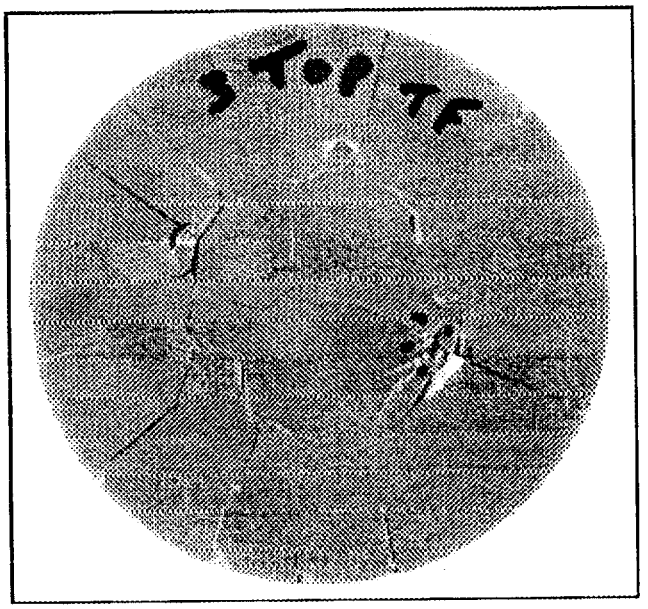

Figure 16: Failed Joined Disk

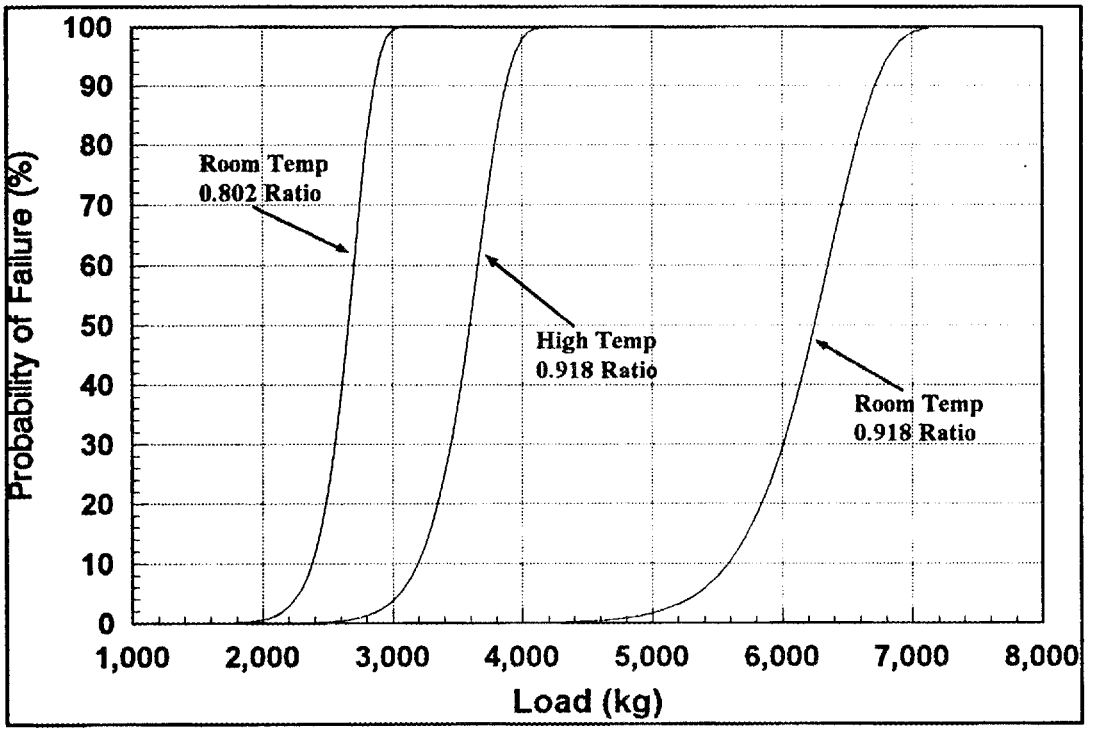

Figure 17: Probability Of Failure For Volume Flaws

Table 4: Silicon Carbide Join Summary

Billet	Interlayer	Flexure Strength (MPa)	Std. Dev. (MPa)	Number Tested	Number of Failed Joins
Siliconized	A	221.8	40.5	10	10
Siliconized	B	101.11	39.6	14	14
Siliconized	C	141.76	49.7	14	12
Siliconized	D	171.06	39.2	14	14
Siliconized	E	122.87	33.7	15	15
Siliconized	F	127.02	41.0	15	15
Unsiliconized	D	179.53	51.2	15	12
Unjoined Control 38mm Thickness		232.9	70.5	27	

confirm the suspected cause of strength dependence upon cross-sectional thickness.

Polished sections available to date of the joined interlayers are exhibited in Figures 18 to 23. Joins are identified for ease of discussion by the type of parent material (siliconized=S or unsiliconized=U) and join interlayer (A through F). For example, a join S-D was made with the initially siliconized parent materials and joined with interlayer D. The appearance of the joins vary widely with S-B exhibiting the most uniform microstructure and the lowest silicon content (Figure 18). The join S-C and U-D demonstrate extreme silicon enrichment (lighter phase) in the center of the join interlayer with segregation of the silicon carbide (darker phase) at the edges of the interlayer adjacent to the parent materials (Figures 19 and 23). Although, the joins S-B, S-D and S-F exhibit a more homogeneous distribution of silicon carbide and silicon, all of the joins lack a contiguous network of silicon carbide that extends into the parent material. All of the join methods resulted in join interlayers that were discrete relative to the parent materials and of higher silicon concentration. The distinct interface between the join interlayer and parent material consisted largely of silicon within the join and silicon carbide within the parent material with an absence of interpenetration across the interface. In addition, voids within the join interlayer are strength limiting and undesirable (Figures 20, 21 and 22).

Additional silicon carbide joining work is required to improve silicon carbide join quality.

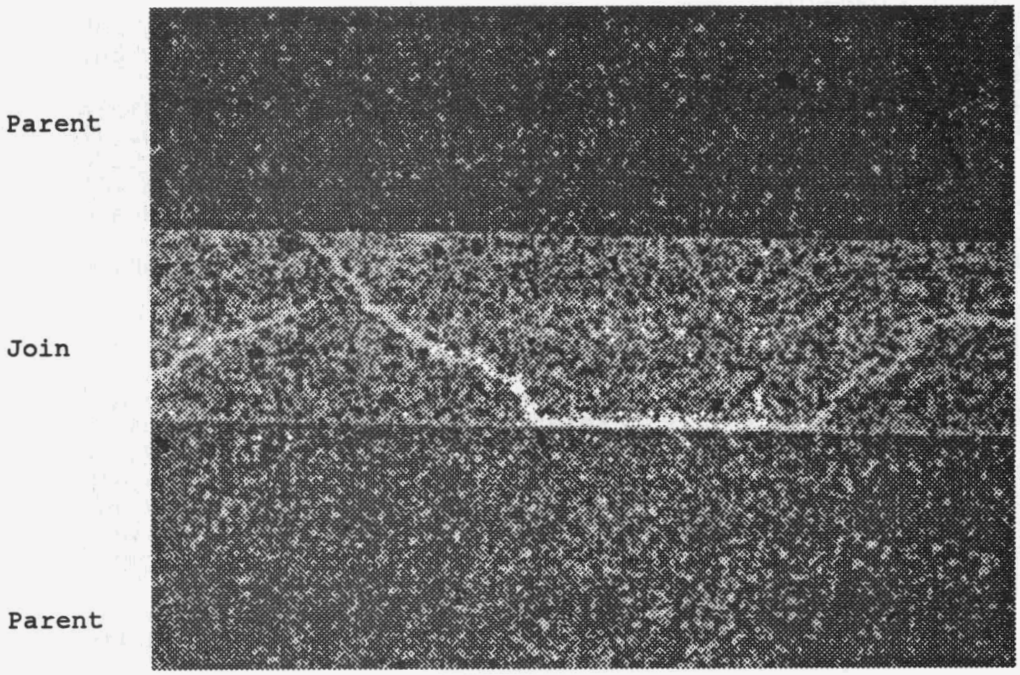

A) 200X

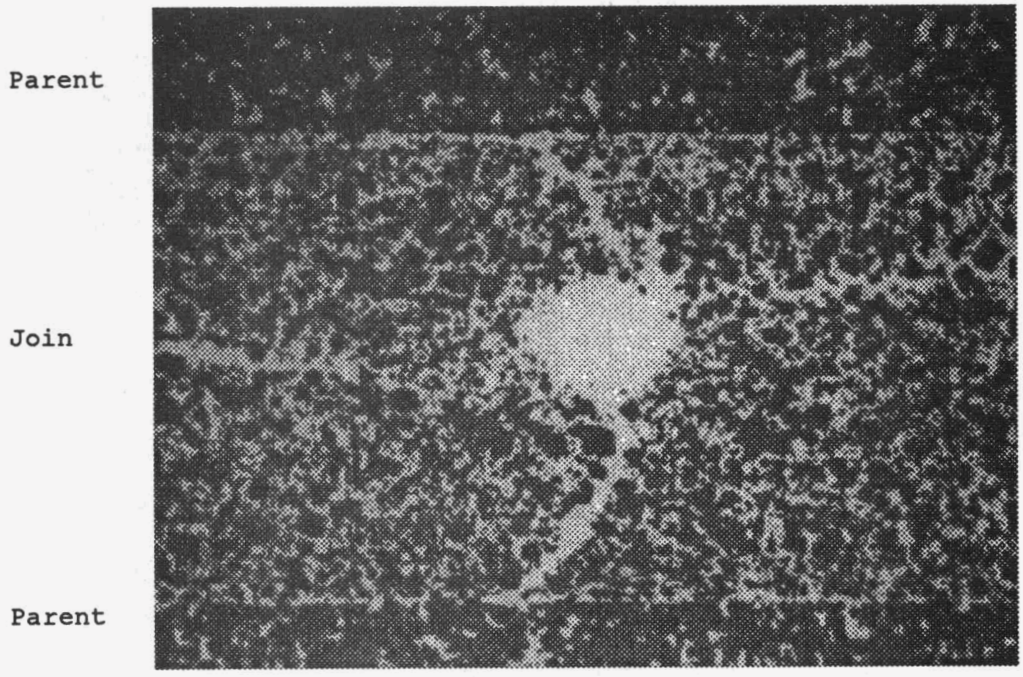

B) 500X

Figure 18: Optical Micrograph Of Join Interlayer B Made With Initially Siliconized Parent Material

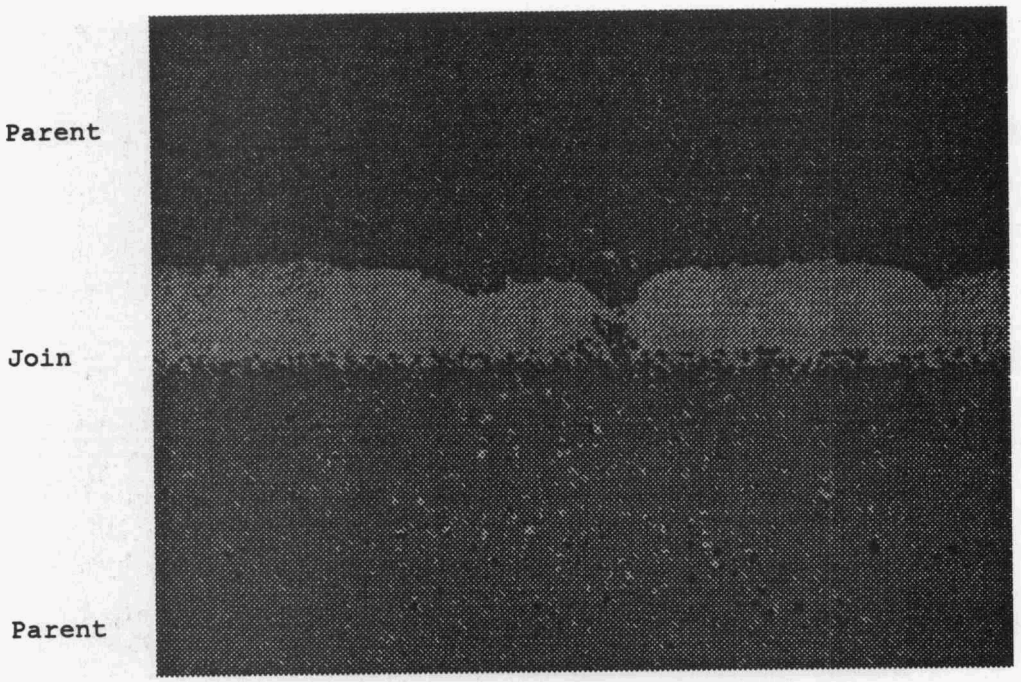

A) 200X

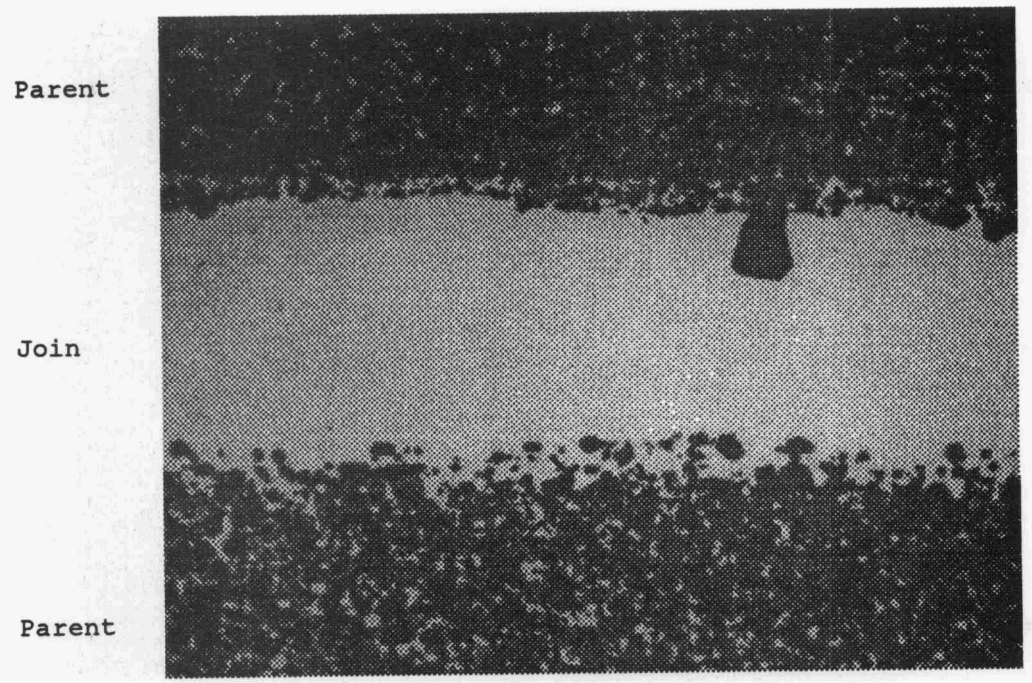

B) 500X

Figure 19: Optical Micrograph Of Join Interlayer C Made With Initially Siliconized Parent Material

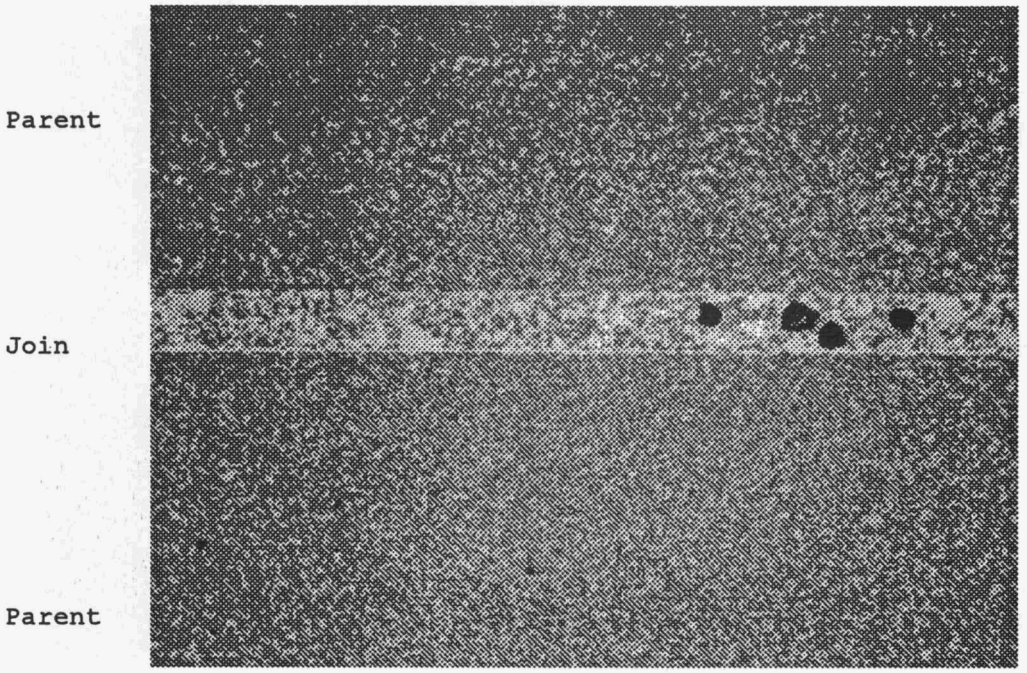

A) 200X

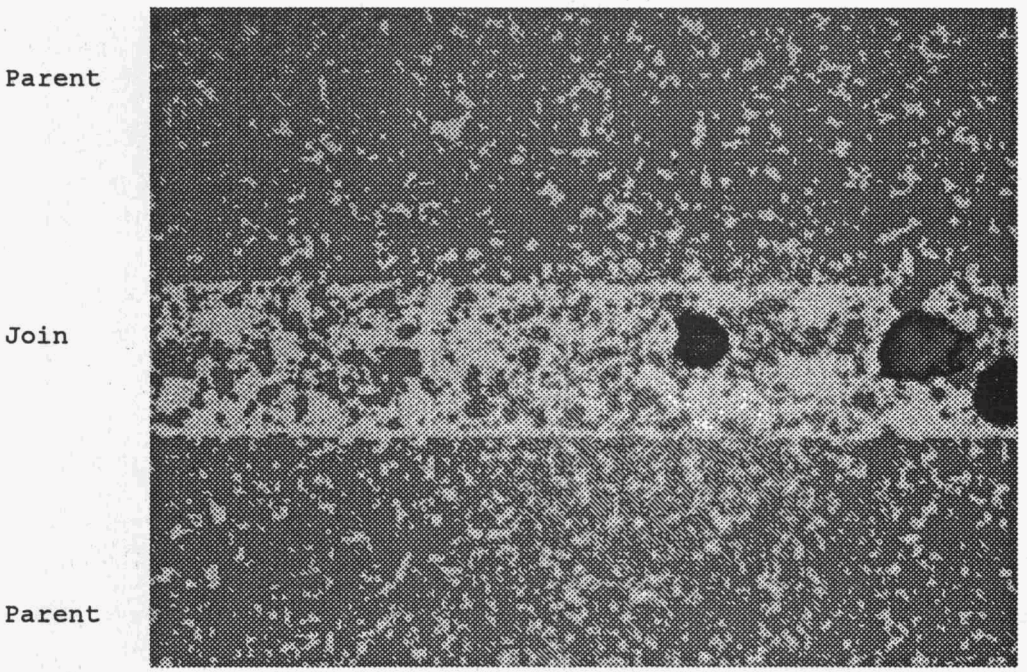

B) 500X

Figure 20: Optical Micrograph Of Join Interlayer D Made With Initially Siliconized Parent Material

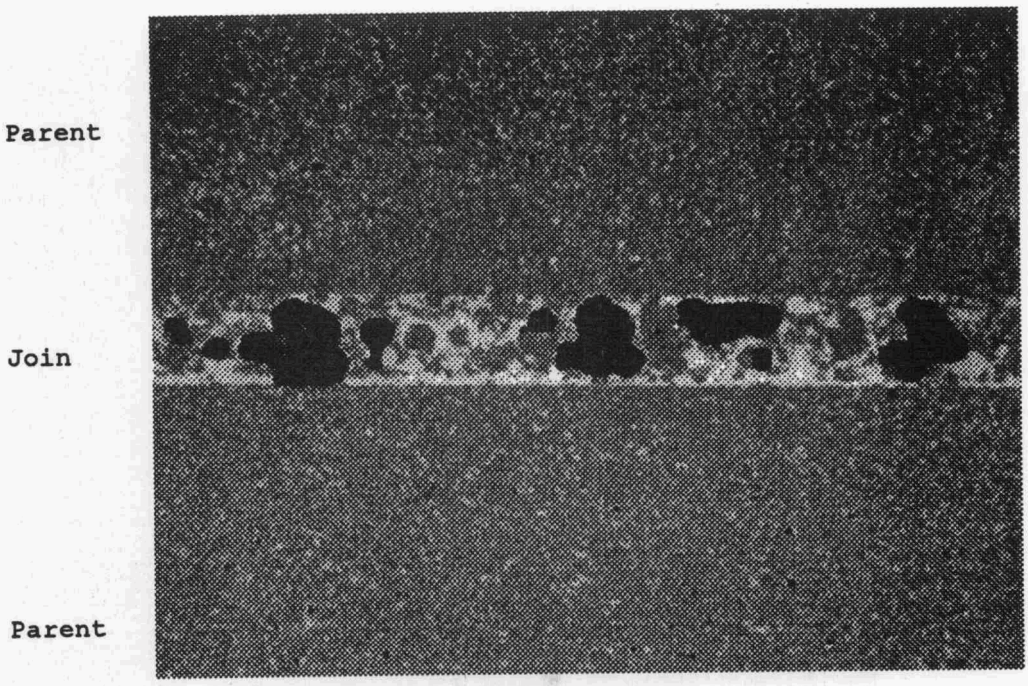

A) 200X

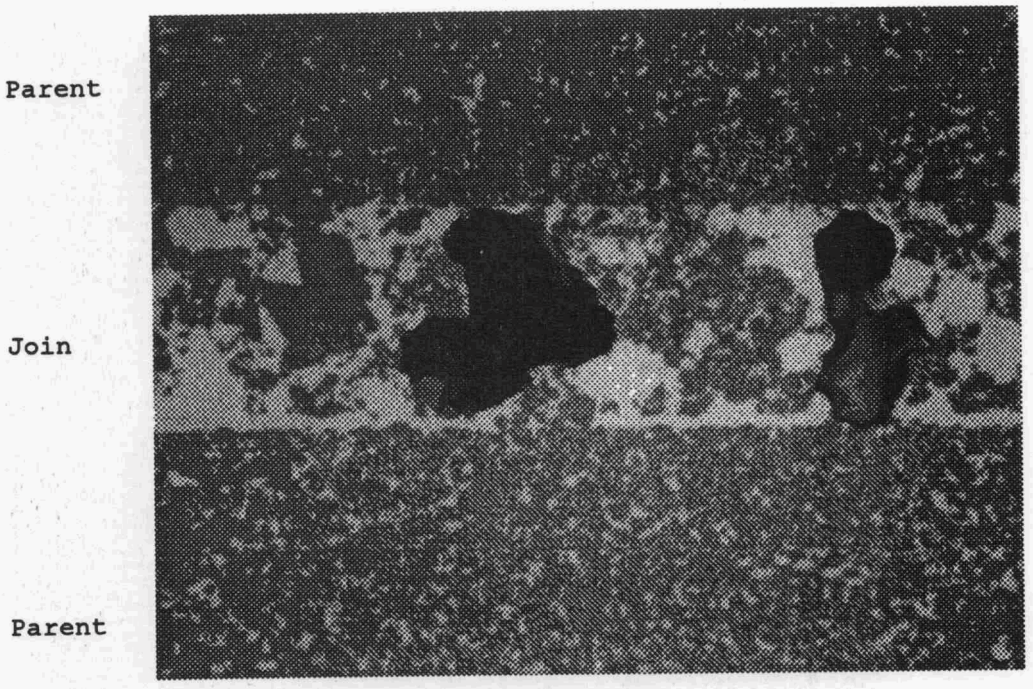

B) 500X

Figure 21: Optical Micrograph Of Join Interlayer E Made With Initially Siliconized Parent Material

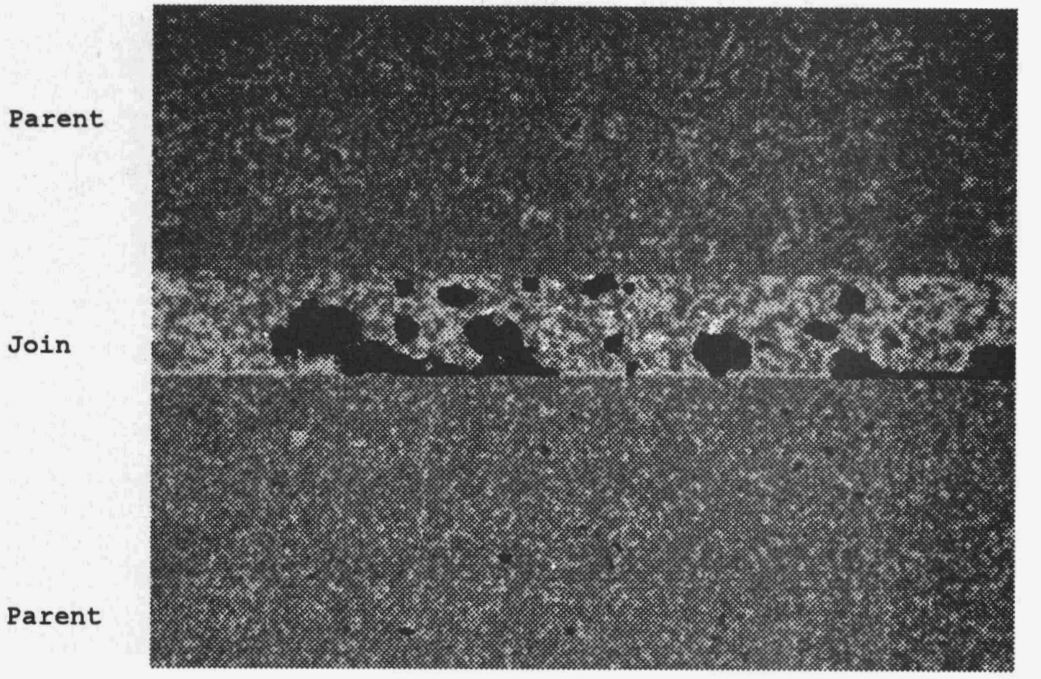

A) 500X

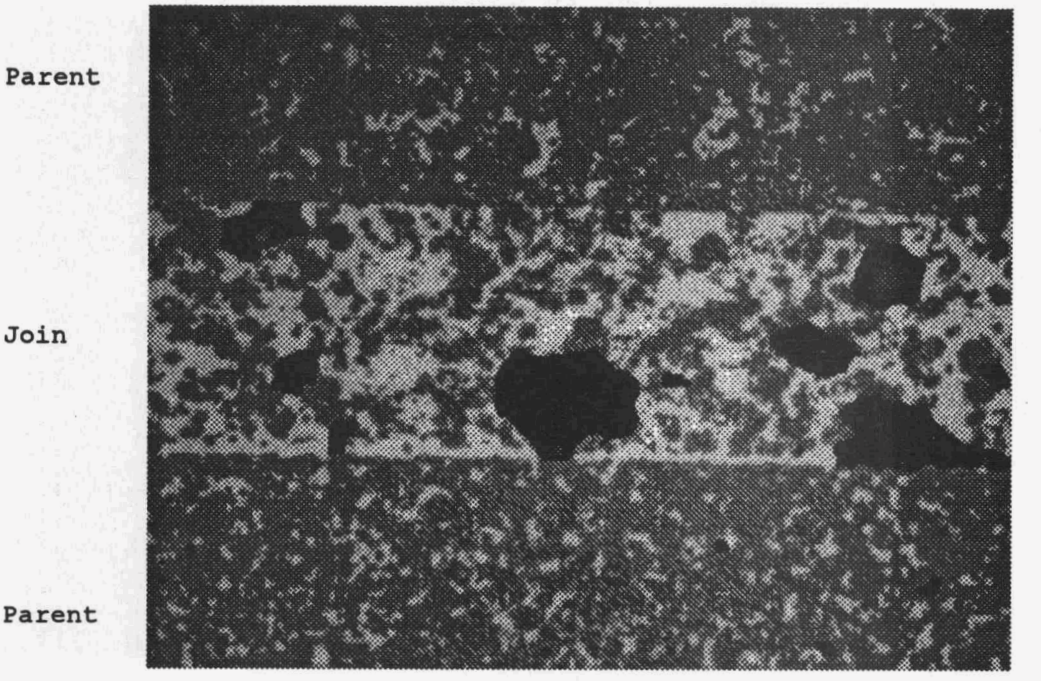

B) 500X

Figure 22: Optical Micrograph Of Join Interlayer F Made With Initially Siliconized Parent Material

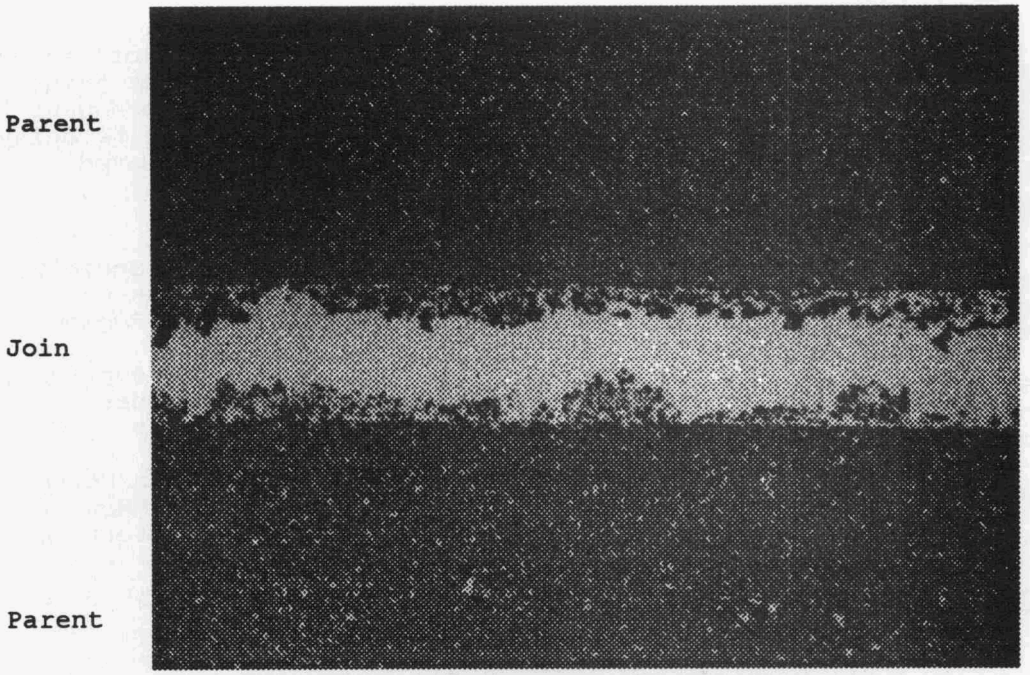

A) 200X

B) 500X

Figure 23: Optical Micrograph Of Join Interlayer D Made With Initially Unsiliconized Parent Material

STATUS OF MILESTONES

Milestones are on schedule with the exception of Tasks 2.1A through 2.4B. The development of silicon carbide butt joins (Task 2.1A) will be extended to improve join quality. Subsequent silicon carbide join development and characterization will be delayed until acceptable silicon carbide butt join quality is achieved.

COMMUNICATIONS/VISITS/TRAVEL

GJSundberg and JAWade attended the American Ceramic Society Third International Ceramic Science and Technology Congress & Exposition in conjunction with the 45th Pacific Coast and Regional Meeting, November 1-4, 1992.

J.A. Wade presented a paper titled "Prediction of Creep Behavior of Silicon Nitride Components Using Finite Element Techniques" at the 16th Annual Conference on Composites and Advanced Materials at Cocoa Beach, Florida, January 1993.

LABroderick, JNPanzarino and GJSundberg of St. Gobain/Norton Industrial Ceramics Corporation have had discussions with MHoulihan and BRabin of INEL concerning a potential collaborative effort on SiC joining.

PROBLEMS ENCOUNTERED

See STATUS OF MILESTONES section.

PUBLICATIONS

None.

ACKNOWLEDGEMENTS

The authors would like to acknowledge the continued contributions of J.G. Gillam, M.J. Mangaudis, L.D. Ton, T.M. Trostel and A.M. Vartabedian.

REFERENCES

1. M.R. Foley, G.A. Rossi, G.J. Sundberg, J.A. Wade, F.J. Wu, *Analytical and Experimental Evaluation of Joining Silicon Carbide to Silicon Carbide and Silicon Nitride For Advanced Heat Engine Applications, Final Report, Subcontract 86X-SB045C*, Norton Company, September 30, 1991, 56-86.

2. G.J. Sundberg, J.A. Wade, C.S.White, *Analytical and Experimental Evaluation of Joining Silicon Carbide to Silicon Carbide and Silicon Nitride to Silicon Nitride for Advanced Heat Engine Applications, Phase II, Bi-Monthly Report, Subcontract 86X-SB045C*, August 1992 to September 1992, Norton Company, Northboro, MA.

3. Ding, J.L., Liu, K.C., and Brinkman, C.R., *Development of a Creep Deformation and Life Prediction Model for a HIPed Silicon Nitride Ceramic*, presented at the Annual Automotive Technology Development Contractors' Coordination Meeting, Dearborn, Michigan, Nov. 2-4, 1992.

4. Brown, S.B., Kim, K.H., and Anand L., *An Internal Variable Constitutive Model for Hot Working of Metals*, International Journal of Plasticity, Vol. 5, pp. 95-13 (1985).

5. T.R. Wilshaw, *Measurement of Tensile Strength of Ceramics*, Journal of The American Ceramic Society, February 1968, page 111.

Cost-Effective Ceramic Machining

P. J. Blau and S. R. Srinivasan (Oak Ridge National Laboratory)

Objective/scope

The objective of this task is to investigate the effects of machining practices on the durability of ceramics for valve and valve seat applications and to assess the surface and subsurface machining damage. The scope of the program includes: (1) developing a repetitive impact testing machine to simulate operation of a valve and valve seats in combustion engines with respect to mechanical, chemical, and thermal factors, (2) studying the effect of machining methods on the repetitive impact behavior of machined ceramics, and (3) characterizing the detailed nature of machining-induced surface and subsurface damage and their evolution in advanced ceramic materials.

Technical highlights

Relative humidity (RH) in the test environment has been determined to have a significant effect on the impact wear behavior of silicon nitride (Kyocera SN220M). A series of tests in three different RH ranges, 50 to 60%, 20 to 30% and <3%, have been completed. Each test series consisted of impacting the flat machined specimen, a standard flexure bar, with an NBD200 silicon nitride ball 2000, 5000, 10000, and 20000 times. The ball impacts the specimen at an angle of 45° to simulate the valve seating configuration during engine operation. The inclined impact configuration adds a component of slip to the impact. The impact wear was quantified by measuring the cross-sectional areas of the impact craters from stylus traces through the widest portion of the impacts in two mutually perpendicular directions. The plot in Fig. 1 shows the dependence of the average crater cross-sectional areas on the number of impacts. A large decrease (by almost an order of magnitude) in crater areas occurs when the RH in the test environment increases, i.e., the environment goes from dry to humid conditions.

Having established the effect of RH on impact wear behavior of silicon nitride, baseline data are being generated under "dry" (<3% RH) conditions for three different silicon nitrides: Kyocera SN220M, Eaton/Ceradyne sintered reaction bonded silicon nitride (SRBSN), and Norton/Saint Gobain NCX-5102. Two sets of baseline tests are being done: (1) tests where the slip component of the impact is along the lay direction of the machining and (2) tests where the slip component of the impact is normal to the lay direction of the machining. Test configuration (2) is expected to be more pertinent to valves. Baseline impact wear data are also being established for the SRBSNs machined under six different conditions. Preliminary correlations of machining parameters with impact wear show significant effects.

The test system has been modified to admit hot gases into the test environment. A humidifier assembly is also being developed to introduce known amounts of water vapor into the gas. These modifications are expected to more closely simulate the valve environment.

Important findings and observations

An increase in RH of the test atmosphere results in a significant decrease in the impact wear of silicon nitride. This apparent increase in impact resistance of silicon nitride

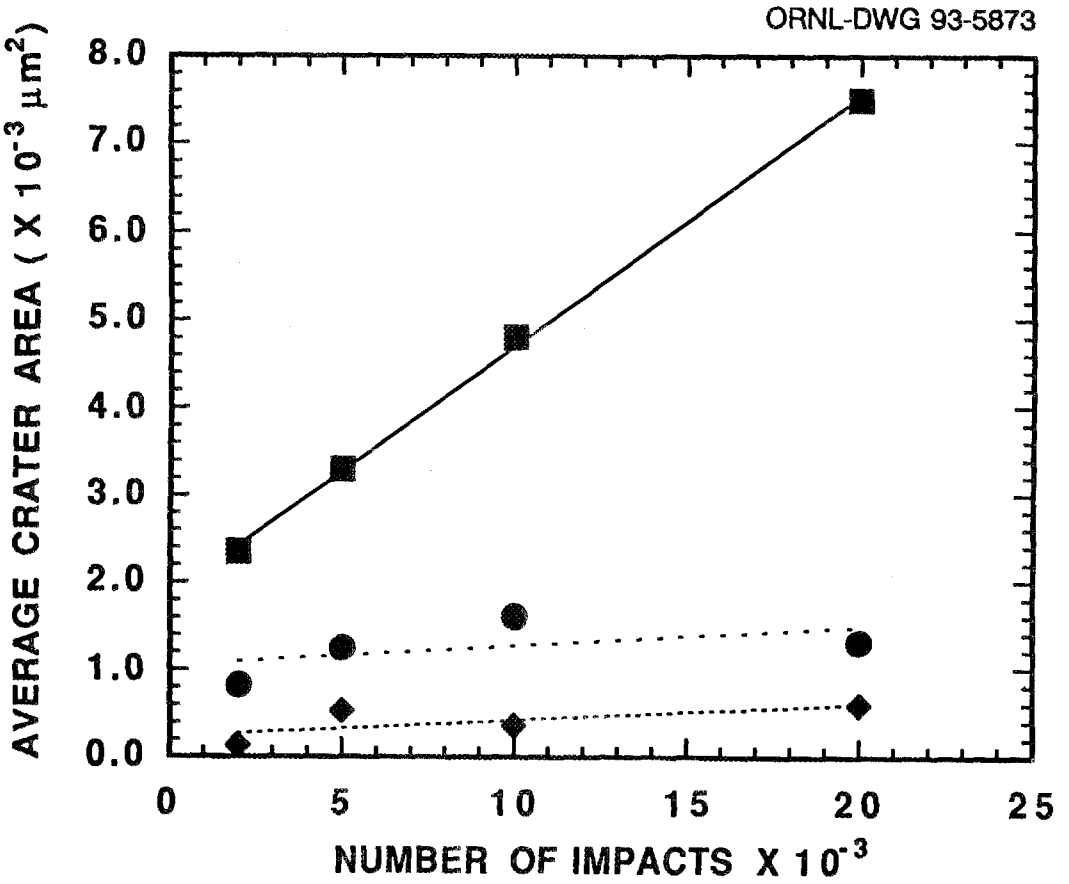

Fig. 1. Plot shows crater area dependence on the number of impacts for room-temperature repetitive impact tests on SN220M silicon nitride impacted by NBD200 silicon nitride ball under various relative humidity conditions. Circles correspond to tests at a humidity range between 50 and 60% (lab air), diamonds correspond to tests at a humidity range between 20 and 30% (lab air), and squares correspond to tests at a humidity of <3% under dry nitrogen atmosphere. The lines through the data points represent linear fits through the data. The slopes of these lines are 0.02, 0.04, and 0.30 for the 50 to 60% humidity lab air test data, 20 to 30% humidity lab air test data, and dry nitrogen test data, respectively.

under humid conditions is expected to be beneficial for valve materials since the engine atmosphere contains as much as 7% water vapor from the combustion products.

Impact wear data on the SRBSNs indicate a significant effect of machining methods. A possible relationship to the subsurface residual stresses caused by machining is being investigated.

Impact wear data also show a dependence on the specimen grinding orientation and the direction of slip during the impact. This behavior is in the process of being quantified as is the possible relation to surface roughness.

Status of milestones

1. Design, fabrication, and installation of hot-gas delivery system is complete. A temperature of 120°C on the sample surface has been achieved, and the first set of repetitive impact tests has been completed at 120°C on SN220M.
2. Baseline tests under "dry" conditions are complete for the three silicon nitrides and for the SRBSNs machined under six different conditions.
3. Installation of the humidifier assembly is complete.

Communications/visitors/travels

Visitors:
Dr. Harold Kanost, Crestel Ltd., Australia, October 20, 1992, for a product exhibition/ demonstration and presentation on DIASIL grinding wheels.

Dr. Chander Bhateja, Contemporary Technologies, Inc., Farmington, Conn., January 26, 1993, for a product exhibition/demonstration and presentation on sensor systems for monitoring grinding operations.

Dr. Bishu Bandyopadhyay, University of North Dakota, March 4, 1993, to discuss/debrief on the status of ceramic machining technology in Japan (subcontract).

Dr. Joe Kovach, Eaton Corporation, and Prof. Steve Malkin, University of Massachusetts, March 3-4, 1993, to discuss Low-Damage, High-Speed Machining subcontract.

Mr. Mike Hazelkorn, Caterpillar, Inc., April 22, 1993, to discuss valve simulation/repetitive impact test results.

Dr. Ron Chand, Chand-Kare Inc., Worcester, Mass., May 18, 1993, to discuss providing test specimens (machined silicon nitride) for repetitive impact tests.

Travel/visits:
S. Srinivasan, two-day workshop on "Fundamentals of Ceramic Grinding," Charlotte, N.C., February 16-17, 1993.

P. J. Blau and S. Srinivasan, Coors Technical Ceramics, Oak Ridge, Tenn., March 26, 1993, to discuss collaboration between Coors and ORNL for development of optimum grinding wheel for grinding advanced ceramics.

Problems encountered

None.

Publications/presentations

P. J. Blau and T. Hanft, "Quantitative Measurements of Repetitive Impact Damage on Ground Silicon Nitride and Alumina Surfaces," submitted to *Tribol. Int.*, 1993.

S. R. Srinivasan and P. J. Blau, "Effect of Relative Humidity on Repetitive Impact Behavior of Silicon Nitride," to be submitted to *J. Am. Ceram. Soc.*, June 1993.

Grinding Optimization for Advanced Ceramics

Said Jahanmir (National Institute of Standards and Technology)

Objective/Scope

The overall objective of this project is to develop guidelines and recommendations for grinding optimization of advanced structural ceramics to achieve minimum cost and maximum reliability. The following steps are being taken to achieve the objective: conduct grinding experiments jointly with industrial participants, determine effect of grinding parameters on machining damage and strength, elucidate mechanisms of material removal and damage formation, evaluate several damage detection techniques, and transfer data and information to industry in computerized database format.

Technical Progress

a) Background

Advanced structural ceramics, such as silicon nitride, are attractive for many advanced engine applications due to their high strength at elevated temperatures, resistance to chemical degradation, abrasive wear resistance, and low density. Despite these advantages, there are considerable impediments to the introduction of ceramics. Recent comprehensive studies have indicated that with current technology, fabrication costs are high and component reliability is uncertain. Machining was identified as a major contributor to both high cost and low reliability. The cost of machining can be as high as 90% of the total cost of some high precision components. Damage produced during machining can be detrimental to the performance, and can produce premature failure. Many industrial laboratories and companies have indicated that machining data and guidelines are badly needed for optimization of grinding, in order to produce cost-effective ceramic components.

The NIST Ceramic Machining Consortium has been established to provide measurement methods, data, and mechanistic information needed by industry to develop innovative cost-effective methods for machining advanced structural ceramics. Currently, the consortium has seventeen members - Ceradyne, Cincinnati Milacron, Corning, Dow Chemical Company, Eaton Corporation, Ford Motor Company, GE Superabrasives, General Motors, Norton, SAC International, Sonoscan, Stevens Institute of Technology, Texas A&M University, Therm Advanced Ceramics, Tower Oil and Technology, University of Maryland, and W. R. Grace & Company. In addition to the project on Grinding Optimization for Advanced Ceramics, which is described herein, research is performed on Characterization of Machining Damage, Nano-precision Grinding of Silicon Nitride Bearing Materials, Chemomechanical Effects in Drilling and Grinding of Ceramics, and Polishing of Silicon Carbide Ceramics. Consortium members participate in these projects by providing materials, testing, advice, and other in-kind contributions. Funding for the projects is provided by DOE - Ceramics Technology Project, DARPA - Ceramic Bearing Technology Program, U.S. Navy - Manufacturing Technology Program, NIST - Ceramics Division, NIST -

Office of Intelligent Processing of Materials, and NIST - Standard Reference Data Program.

b) Introduction

Grinding with diamond wheels is the most prevalent method of machining advanced ceramics. This machining method is highly complex and its optimization requires detailed knowledge of many interdependent factors. The major elements of a grinding system are the grinding wheel, the grinding fluid, the machine tool, and the workpiece. Each of these is associated with several parameters that can influence the grinding process. For example, the type of diamond grit, its size and concentration, as well as the bonding material control the behavior of the grinding wheel. The chemical and physical properties of the grinding fluid, and method of delivery to the grinding zone contribute to the grinding rate and the quality of finished surface. The variables used in grinding such as feed rate and wheel surface speed, and the machine tool characteristics such as stiffness and vibration are major factors in grinding. The workpiece material and its properties are important factors in the selection of the grinding parameters, since each material responds differently to the grinding action.

Optimization of the grinding process consists of finding the most appropriate set (or sets) of parameters to be used for each material such that a maximum machining rate is obtained and at the same time relevant performance parameters such as strength and/or surface roughness are maintained at the required level. This objective requires data and information on the effect of grinding parameters on material removal rate, strength, surface roughness, surface integrity, residual stress and others. In addition to these data, detailed information on the mechanisms of material removal processes, and reliable methods for damage detection are required.

c) Experimental Procedure

This project has been planned in three phases. In Phase I, the participating consortium members were asked to use their experience in selecting grinding conditions to be used in the study. Each participant machined one set of flexure test bars (28 to 30), which were then tested and characterized at NIST for surface integrity and fracture strength. All grinding was performed along the length of the samples, i.e., parallel to the major tensile axis in four-point bending. The surface roughness was determined by a 3-D stylus surface profilometer; and the surfaces were examined by scanning electron microscopy to evaluate the surface condition. The test bars were subjected to four-point bend tests according to the ASTM Standard C 1161. The fracture strength data were analyzed using Weibull statistics. Two types of silicon nitride materials were selected for this study: reaction-bonded (RBSN) and sintered-reaction-bonded (SRBSN). The grinding conditions used to prepare the flexure bars are summarized in Table 1. The major difference between the grinding conditions is in the volumetric material removal rate, which varies from 30 to 1737 mm^3/min. This is achieved by using different combinations of

down feed, cross feed, and table speed. Grinding conditions A and B represent the conventional practice and are recommended for use in the ASTM Standard. Grinding conditions E through H represent creep feed grinding; whereas condition D represents conventional practice with additional spark-out passes.

Table 1. Grinding Conditions Used in the Study

Condition	A	B	C	D*	E	F	G	H
Grinding Wheel	320 grit 100 conc.	320 grit 75 conc.	120 grit 63 conc.	320 grit 150 conc.	150 grit 75 conc.	80 grit 100 conc.	150 grit 75 conc.	80 grit 100 conc.
Grinding Fluid	Synthetic 20:1	Emulsion 50:1	Emulsion 50:1	Emulsion+	Emulsion 20:1	Emulsion+ 20:1	Emulsion 20:1	Emulsion+ 20:1
Table Speed m/min	7.62	12.2	6.10	15.2	1.52	1.52	1.52	1.52
Cross Feed mm/pass	1.58	0.381	0.381	4.00	1.91	4.50	1.91	4.50
Down Feed mm	0.0025	0.0127	0.2540	0.0051	0.1778	0.0508	0.2540	0.2540
Vol. Removal Rate mm^3/min	30	59	590	310	516	347	737	1737

* Condition D was completed with 2-3 spark-out passes.
\+ Grinding fluid used was Cimperial HD90.

d) Results

The results of fracture tests are summarized in Weibull plots in Figures 1 to 4. These figures also list the characteristic strength (probability of failure = 0.63) and Weibull modulus (slope of line drawn through the data points, a measure of data distribution). The data in the figures show a clear distinction between the two materials. Although, the surface roughness was somewhat influenced by the grinding condition, the characteristic fracture strength and Weibull modulus are unaffected by the choice of grinding parameters, with the possible exception of grinding condition D. In this case spark-out appears to have decreased the Weibull modulus, especially for RBSN. Following the fracture tests, fractography was performed to identify the location of fracture initiation. The results showed that, as expected, most fractures initiated from surface and near surface flaws. Further examination by SEM showed only a few indications for fracture initiation from machining damage. Although this data is limited, no correlations could be established between strength, Weibull modulus, surface roughness, and grinding conditions (except for condition D). Nevertheless, these results suggest that an increase in the removal rate by a factor of 60 is possible without a reduction in

strength. This will undoubtedly lower the cost of machining for ceramic components.

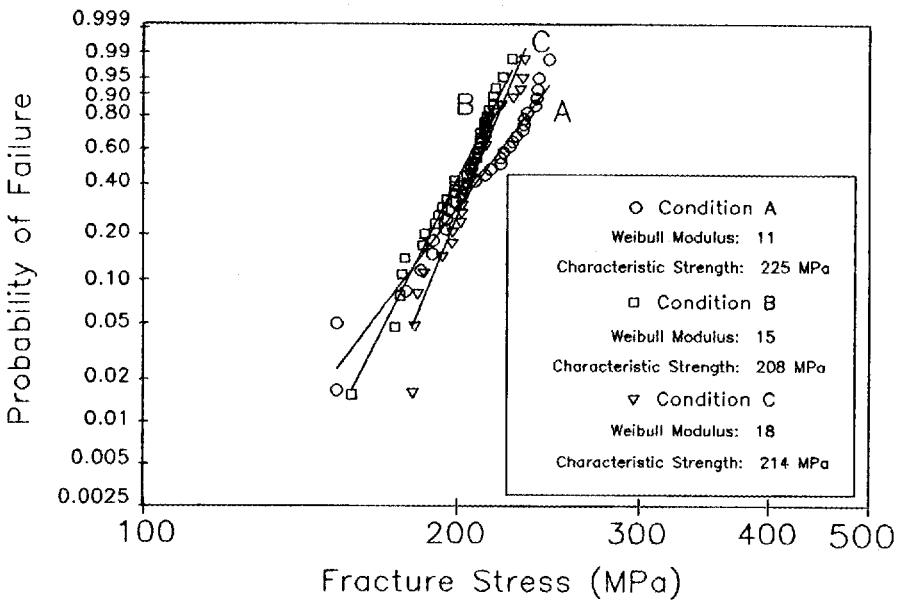

Figure 1. Weibull plot for RBSN samples ground under conditions A, B, and C.

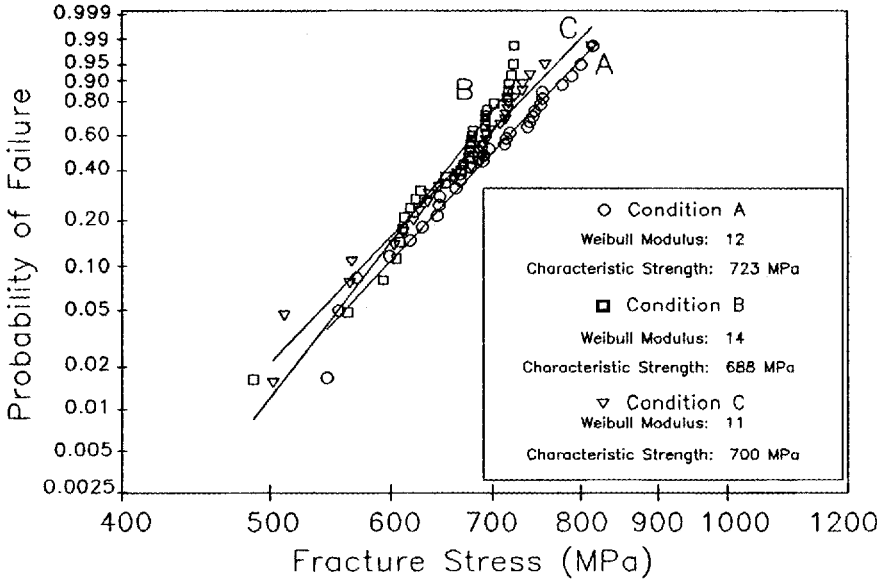

Figure 2. Weibul plot for SRBSN samples ground under conditions A, B, and C.

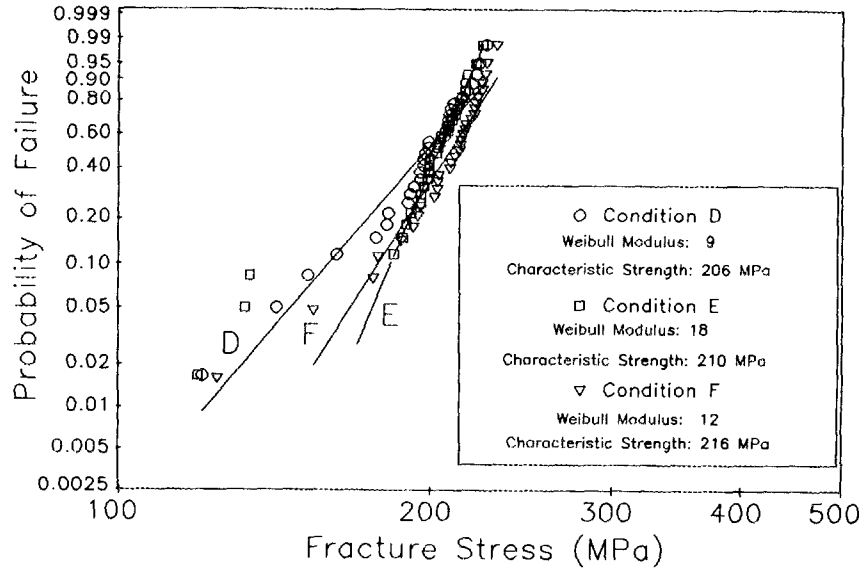

Figure 3. Weibull plot for RBSN samples ground under conditions D, E, and F.

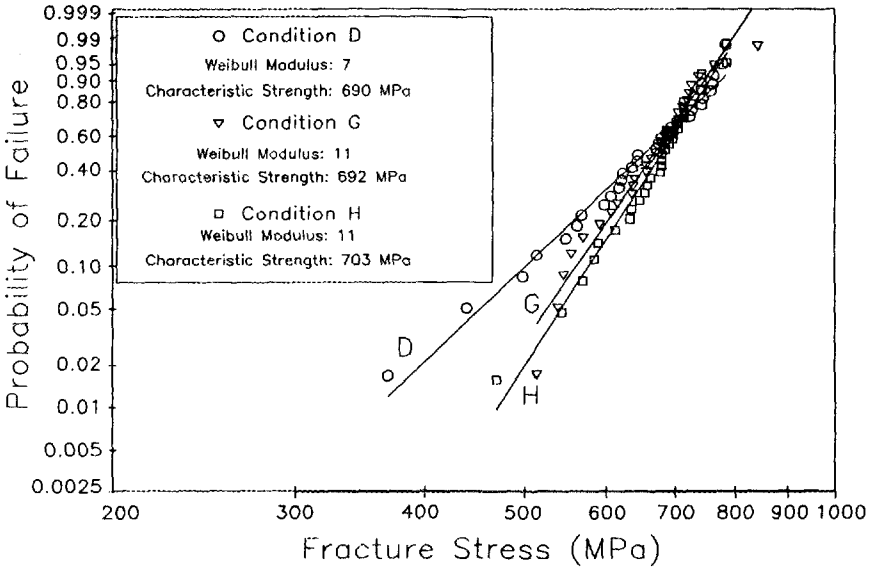

Figure 4. Weibul plot for SRBSN samples ground under conditions D, G, and H.

Thermal wave imaging was evaluated as a nondestructive technique for detection of machining damage. This technique responds to changes in thermal diffusivity of a thin layer at the surface. Machining damage that has an effect on thermal diffusivity at the surface can be detected. Recent results at NIST obtained on surfaces abraded with different size diamond particles show that there is a correlation between thermal

diffusivity of silicon nitride and the abrasive particle size. This effect can be attributed to the larger amount of damage produced by the larger particles. Selected SRBSN flexure bars were examined with the thermal wave measurement technique to assess the machining damage in these specimens. The results indicated that a surface layer with a thickness of about 30 to 45 μm exists on most of the samples. However, the layer thickness on the sample ground under condition D (with spark-out passes) was approximately 11 μm, which is much thinner than the layer found on the other samples . This finding is encouraging, since the same grinding condition resulted in a wider distribution of strength values. This experiment will be repeated and confirmed by acoustic evaluations and taper sectioning. Although these result are preliminary, they are encouraging in confirming the feasibility of using thermal wave measurement method for the detection of machining damage.

e) Future Plans

The information obtained during the first phase of this projects will be used to develop an extended test matrix based on statistical design of experiments using Taguchi method. This method is particularly powerful for minimizing the number of tests, and maximizing the amount of information that can be obtained from the experimental data. The statistical design of experiments is also useful for determining interactions between different variables. Grinding wheel type, grinding fluid, wheel surface speed, table speed, and down feed will be specified. The outputs that will be measured and reported include: removal rate, grinding ratio, cutting forces, power consumption, and surface roughness.

The machining data will be assembled in a spread sheet format, and will be statistically analyzed to determine trends and effects of variables. The complete set of data will be available to the participants for their use in a database format. These data may be complemented with evaluated data from literature and from consortium members. The database structure and search strategy will be designed to allow users find an optimum set of parameters for grinding specific ceramic materials. The *CERAMIC MACHINABILITY DATABASE* will be published and become available through NIST.

Status of Milestones

1. Prepare 300 specimens ground under "best in-house" conditions to establish bounds for a more extensive data program (Sep-1-1992 Completed).

2. Complete fracture testing, characterization, and preliminary statistical analysis of data (Dec-1-1992 Completed).

3. Evaluate feasibility of thermal wave measurement on selected flexure specimens ground under different conditions (Apr-1-1993 Completed).

4. Select grinding conditions based on statistical design of experiments, and distribute additional 2000 flexure bars for grinding (Jun-1-1993 On Schedule).

5. Develop a preliminary database structure to be used for data collected in this study and those collected from literature (Sep-1-1993 On Schedule).

Publications

1. S. Jahanmir, T. Strakna, G. Quinn, H. Liang, R. Allor, and R. West, "Effect of Grinding on Strength and Surface Integrity of Silicon Nitride, Part 1," International Conference on Machining of Advanced Materials, NIST, Gaithersburg, MD, July 20-22, 1993.

2. S. Jahanmir, T. Strakna, G. Quinn, R. Kopp, S. C. Yoon, and K. Kumar, "Effect of Grinding on Strength and Surface Integrity of Silicon Nitride, Part 2," International Conference on Machining of Advanced Materials, NIST, Gaithersburg, MD, July 20-22, 1993.

Chemically Assisted Machining of Ceramics

S. M. Hsu, T. N. Ying, J. Gu, Y. S. Wang, R. S. Gates
(National Institute of Standards and Technology)

Objective/Scope

The ceramics industry has identified the lack of a rapid low cost ceramic machining technology as one of the major barriers for widespread use of ceramics. Current machining technology is slow and labor intensive. Residual surface damage is a primary concern. This project aims to increase the machining rate of ceramics using chemical reactions at the interface. The chemical reactions could produce a softer reaction layer hence reduces the contact stresses and damage. Si_3N_4 is the main material of focus, even though other materials such as SiAlON, SiC may be examined if it appears that these materials may be suitable for engine applications.

The project involves several subtasks including:

1. Development of a bench test simulation to allow screening of chemistries under well-controlled conditions.

2. Identify new chemistries that can significantly improve the machining rate of ceramics, especially for silicon nitrides.

3. Provide understanding on the working mechanisms of the chemistries identified and develop correlations with the surface quality of the machined surface.

4. Establish limits of performance and applicability of the chemistry on different material compositions and processes. Establish optimum machining conditions for each chemistry, material combinations.

5. Validate the concepts and methodology in industrial applications.

Technical Progress

SCREENING OF CHEMISTRIES

A simple cutting device (VC-50 diamond saw made by Leco Corp.) was used as the screening tool for various chemistries. The cutter has a maximum linear speed of 3.3 m/sec. with a diamond cutting wheel of 12.7 cm diameter, 0.35 mm thick. The average diamond grain size is 50 μm and the diamond is bonded by copper. Before each test, the diamond wheel is dressed by a dressing stone for consistent initial cutting condition. The loading mechanism was modified to accommodate a dead weight loading system. A displacement transducer was attached on the loading arm to measured the cutting rate. The transducer was linked with a data acquisition system and a computer. The cooling fluid container was replaced by a plastic zipper bag. For each test, a new bag is used to avoid cross contamination of chemicals from test to test. The apparatus is shown in Fig. 1.

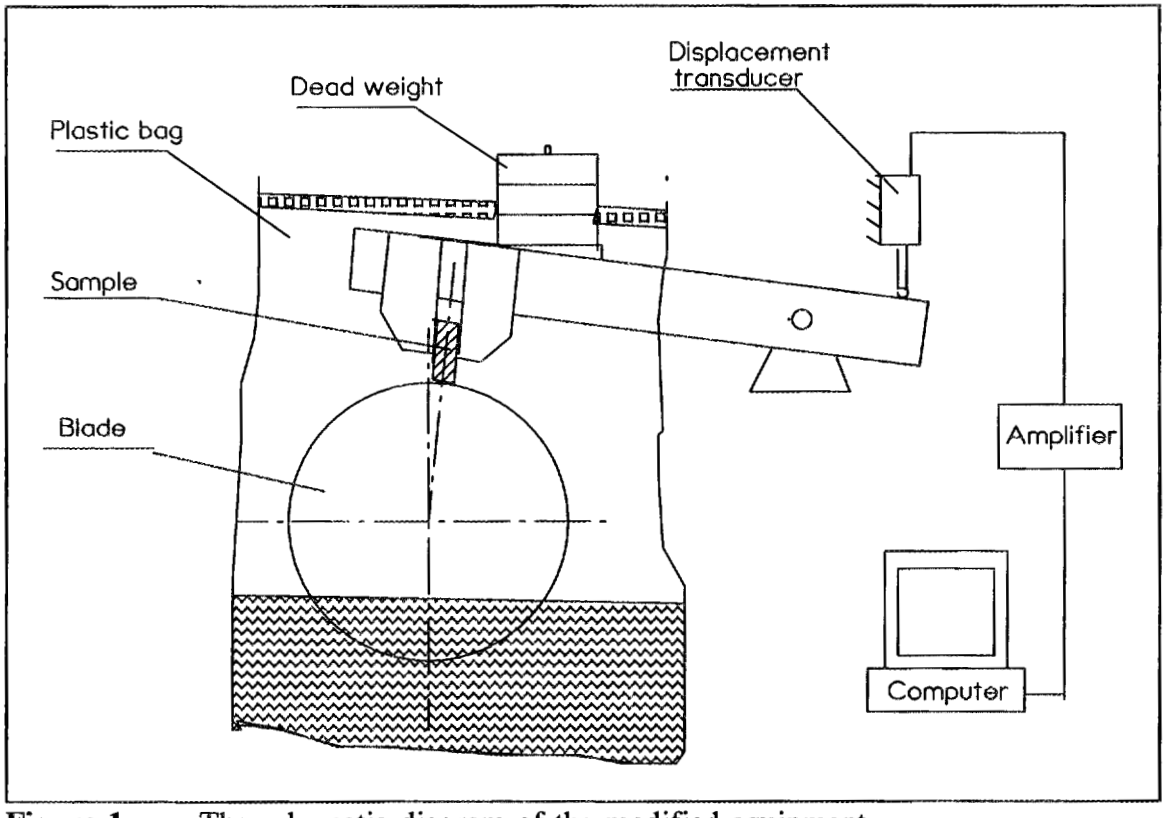

Figure 1 The schematic diagram of the modified equipment.

Baseline data on a silicon nitride supplied by Kennametal Corp. were obtained using current commercial cutting fluids used in NIST machine shop. For a rectangular bar of 4.6 x 16.5 mm, the time it takes to cut through the bar under a constant load of 7 N is from 248 sec. to 700 sec. depending on the fluid. For deionized water, the cut-through time is 1800 sec.

Over 100 chemical compounds have been screened during the past six months. Many compounds show dramatic increase in cutting rate. Some selected results are shown in Table 1. Several parameters are presented. One is the intial cutting rate. This represents the maximum cutting rate when the diamond grains are sharp. As the cutting proceeds, the cutting rate decreases due to several possible factors: polishing of the diamond edges, adhesion of ceramic fine particles onto the wheel, and increased friction from the two side surfaces. This produces a steady state cutting rate. We define the loss of efficiency in cutting as the difference between the intial rate and the steady state rate divided by the initial rate. The time it takes to change from the initial rate to the steady state rate has also been determined by using the slope intersect method. Generally, the larger the transition time, the more effective the chemical is at maintaining the initial cutting rate. The names of the chemicals tested are shown in codes because of potential patent applications.

As one can see from Table 1, the range of intial rates is relatively small, 0.083 to 0.158 mm^2/sec. The difference in the steady state cutting rate is larger, from 0.01 to 0.096. The best fluid in the organic-based fluids is CM011 with 188 sec. cut-through time, which is 24% decrease from the commercial baseline. The best fluid in the water-based group is CM004 which has a cut-through time of 309 sec. which is 60% reduction from the commercial fluid.

MECHANISTIC PERSPECTIVE

In machining silicon nitride, diamond impregnated cutting wheels are generally used. The diamond grains penetrate the silicon nitride surface and remove the material by plowing. The rate of material removal depends on the sharpness of the diamond particle. Dressing of the wheel using abrasive is usually done to maintain the sharpness of the diamond particles. Fig. 2 shows a typical diamond grain morphology just after dressing. During the machining process, the diamond particles themselves may be damaged, worn, or suffer grain pull-out. Under the chemically assisted machining process, the diamond particles are usually polished to form small plateau on the top, as shown in Fig. 3. This dulls the diamond and the machining rate drops. This polishing process, we have found, can be influenced by the chemistry of the fluid. Fig. 4 shows the comparison of two fluids, one currently commercially available for ceramic machining, the other developed under this project. One can observe that initially, the two fluids provide the same machining efficiency. After ten seconds, the cutting rate for the commercial fluid drops rapidly while the best candidate maintains a high cutting rate through out the process.

SURFACE QUALITY

The quality of the as machined surface is an important issue with respect to the

Table 1. Selected data of silicon nitride cutting rate

NO	CACM#	CHEMICAL CODE	CUTTING TIME (sec)	CUTTING RATE *10², (mm³/sec)			
				initial	steady state	loss of efficiency (%)	T_t (sec)
		Organic Base					
1	151	CM010 (commercial)	248	11.5	5.7	50	158
2	149	2%CM005 in CM011	162	15.8	12.1	23	93
3	147	CM011	188	15.6	9.6	38	110
4	96	CM014	210	12.4	8.7	30	159
5	95	CM015	232	12.9	5.8	55	123
6	130	CM018	364	13.7	3.3	76	135
7	121	20%CM012 80%CM022	510	10.7	2.1	80	144
8	79	CM009	>700	10.4	1.3	88	131
		Aqueous Base					
9	120	3%CM001 (commercial)	780	9.1	1.7	81	156
10	62	4%CM002 (commercial)	>700	8.3	1.5	82	87
11	135	2%CM004	309	13.1	4.9	63	95
12	128	1%CM006	>700	9.5	1.9	80	136
13	80	0.5MCM008	>700	9.5	1.0	89	139

Loss of efficiency = (initial rate - steady state rate) / initial rate * 100%

T_t = transition time at which the initial rate slope intersects the steady state slope.

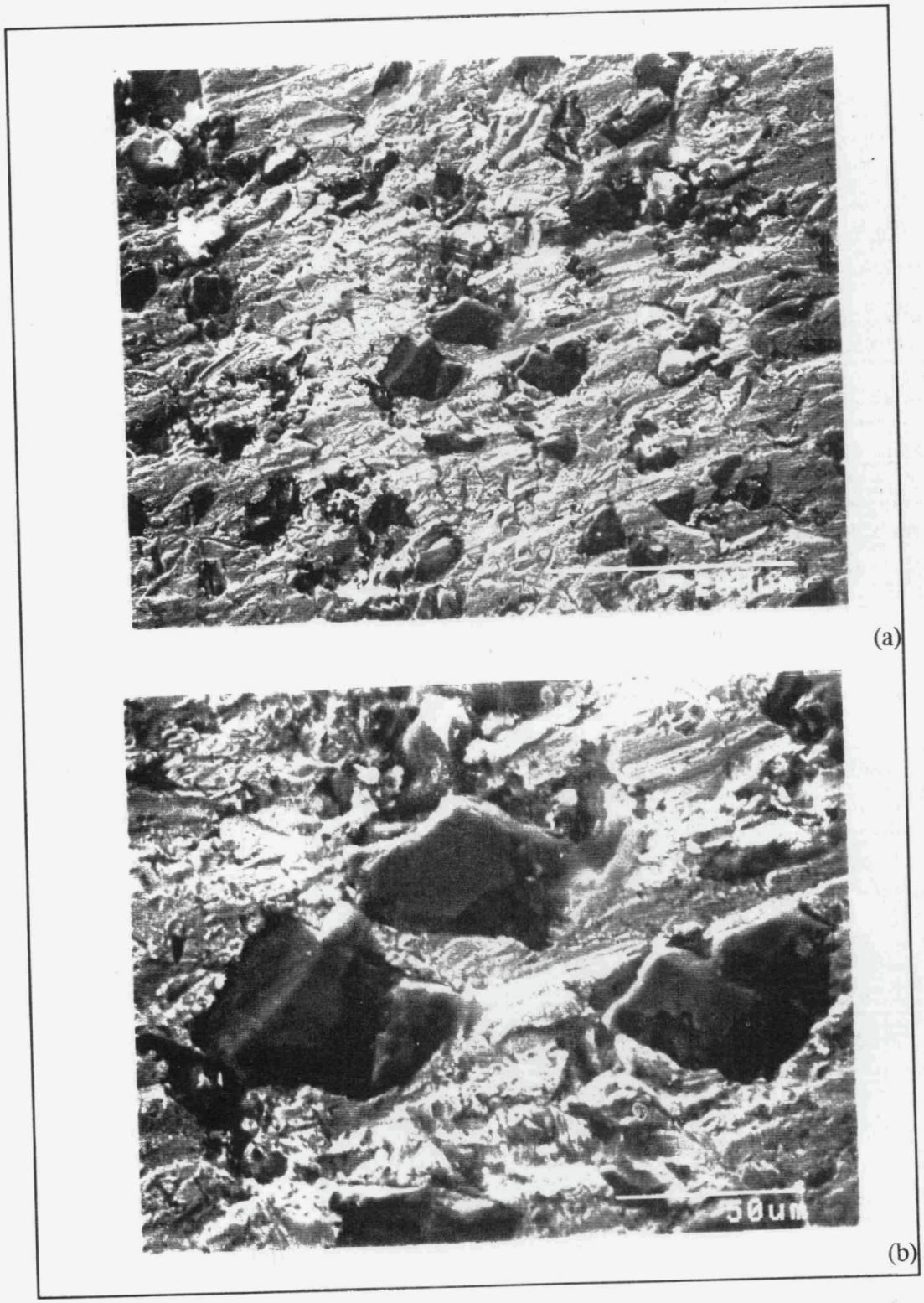

Fig. 2 Morphology of the diamond particles after dressing.

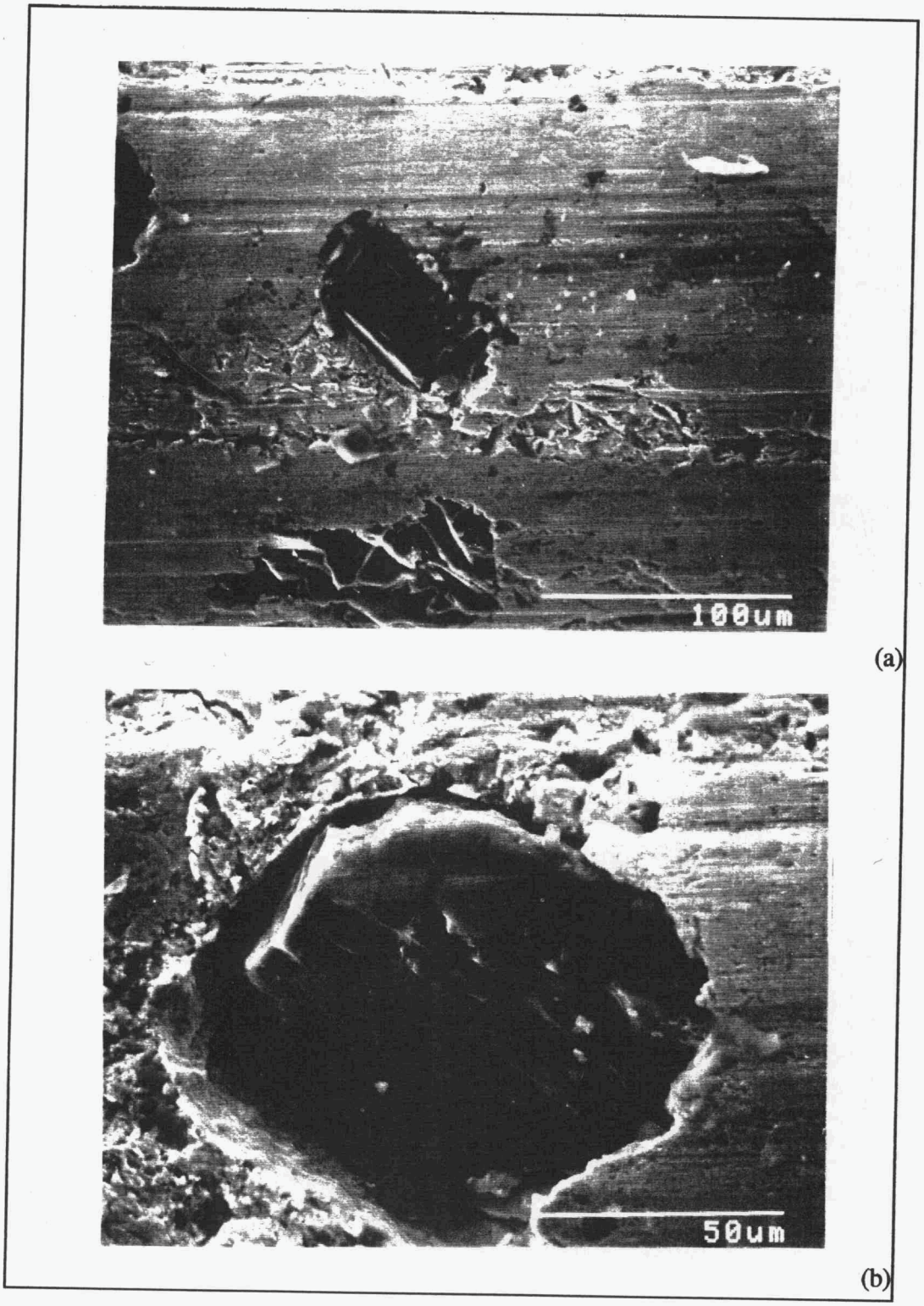

Fig. 3 Morphology of the diamond particles after cutting.

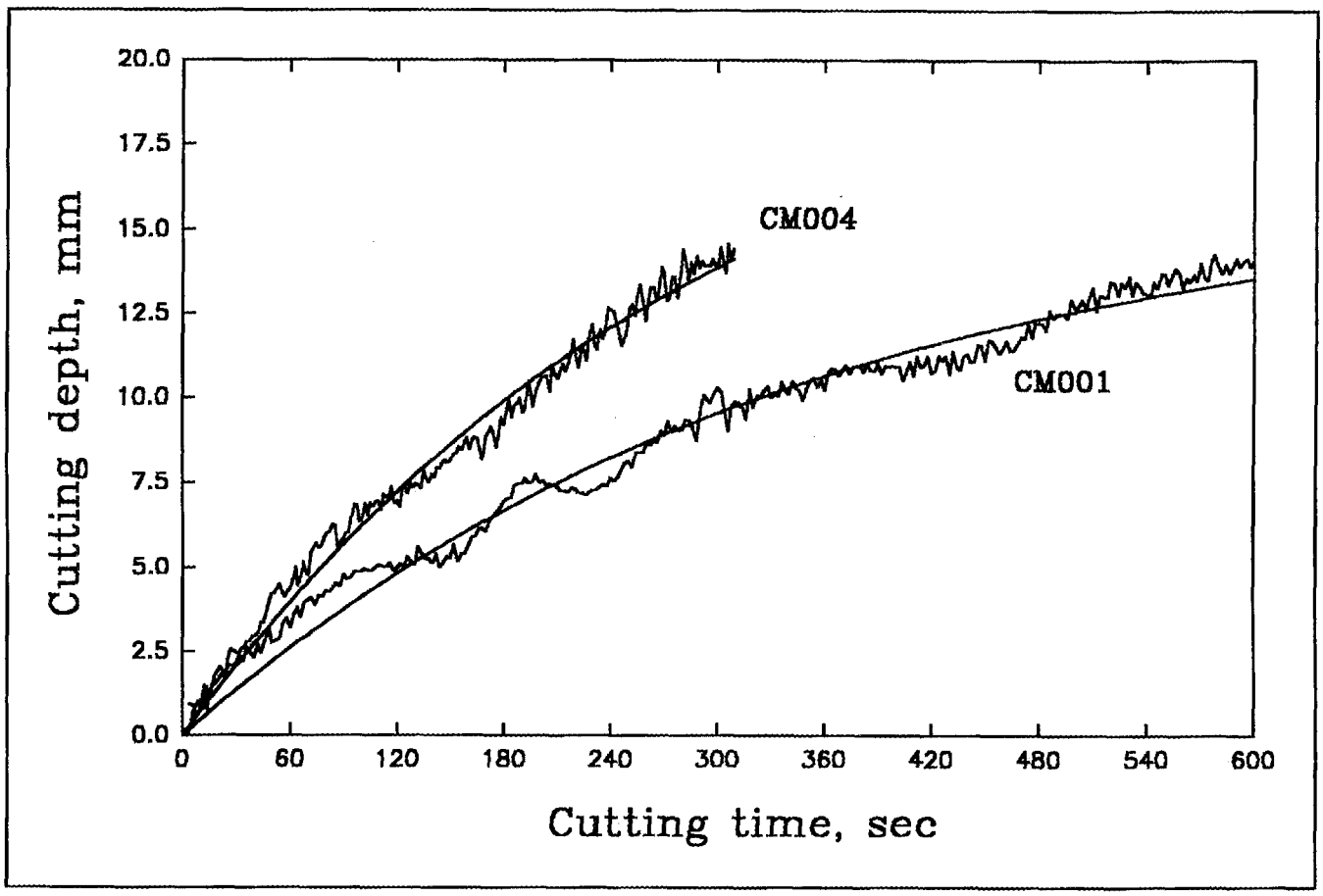

Fig. 4. Comparison of the two cutting curves of a commercial fluid with the best candidate chemistry.

strength and durability of ceramics. The issue is complex and commonly used bend-bar tests and tensile tests are expensive and require relatively large number of samples for statistical significant correlation.

Initially, we measured the surface roughness of the machined surface as an indicator of surface quality. In order to obtain realistic surfaces, a surface grinder was used to generate the surfaces under different chemistries. The surface grinder has a 220 diamond grit grinding wheel with a diameter of 25.4 cm diameter and 0.64 cm thick. The grinding was done under a linear speed of 30.8 m/sec. with a constant feed rate of 0.01 mm. The grinding wheel was dressed before each test. The surface roughness of the ground surfaces under three different chemistries is shown in Fig. 5. Fluid A is a commercial reference fluid, and fluids B and C are examples of candidate chemistries. As can be observed, the candidate fluids exhibit smoother surfaces. The SEM micrographs of the as-ground surfaces shown in Figures 6-8 reveal additional surface features. Fig. 6 shows the surface features obtained for the commercial fluid. There are considerable amount of surface damage and the presence of many wear particles on the surface. Under fluids B and C, the surfaces appear clean without wear debris. There are indications of a reacted layer on the surface. This suggests that chemistry can influence the surface damage. At the same time, surface roughness may not an effective indicator of the surface quality.

EVALUATION OF SURFACE DAMAGE

Eventhough the chemically assisted machining appears to be able to increase the machining rate and also able to improve the surface roughness, precise measurement of the quality of the surface as related to the strength is difficult. Towards this end, effort to develop such a measurement has been made, especially for the relatively smooth surfaces generated under the chemically assisted conditions. A single diamond indentor scratching on an inclined plane technique is being developed to assess the quality of the surface.

The experimental set-up of this apparatus is schematically shown in Figure 9. The specimen surface is inclined with an angle Θ (which is adjustable) with respect to the horizontal plane, as shown in Figure 10. A spherical diamond indentor (with 0.2 mm radius) is used. The horizontal force (F_x) and vertical force (F_z) are measured by force transducers.

The whole concept is to introduce well-controlled defects such as micro-indentation marks on the surface systematically before the sliding. When the indentor begins to slide on the surface, due to the increasing angle, the force increases with sliding distance. When the force reaches a certain level, the cracks at the tips of the preexisting indentor marks will propagate. The location can be identified and the stresses can be calculated.

For a sphere sliding on a plane, the maximum tensile stress (σ_{max}) during the sliding which has been derived by Hamilton is given by:

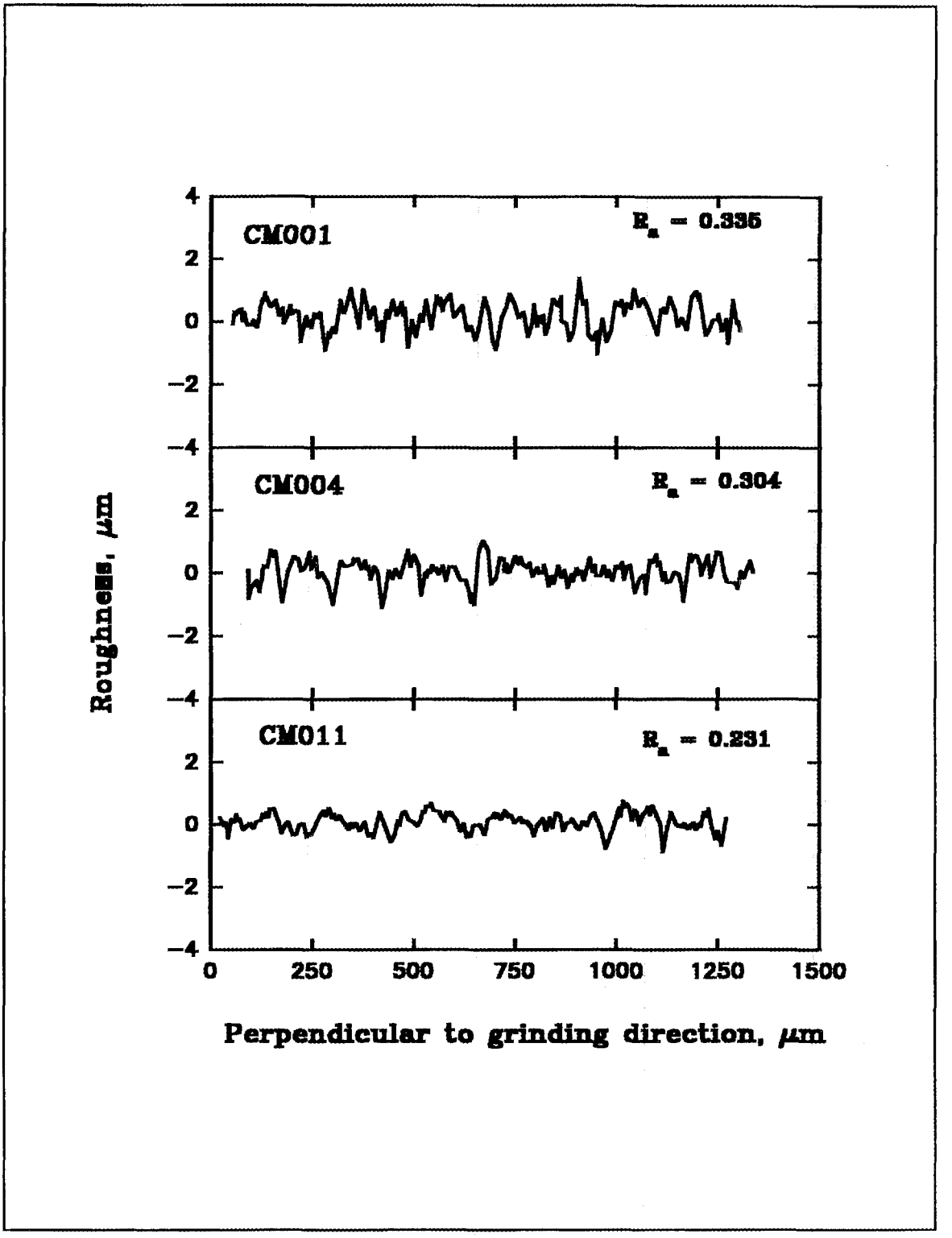

Fig. 5 The surface roughness of the ground surfaces under different chemicals.

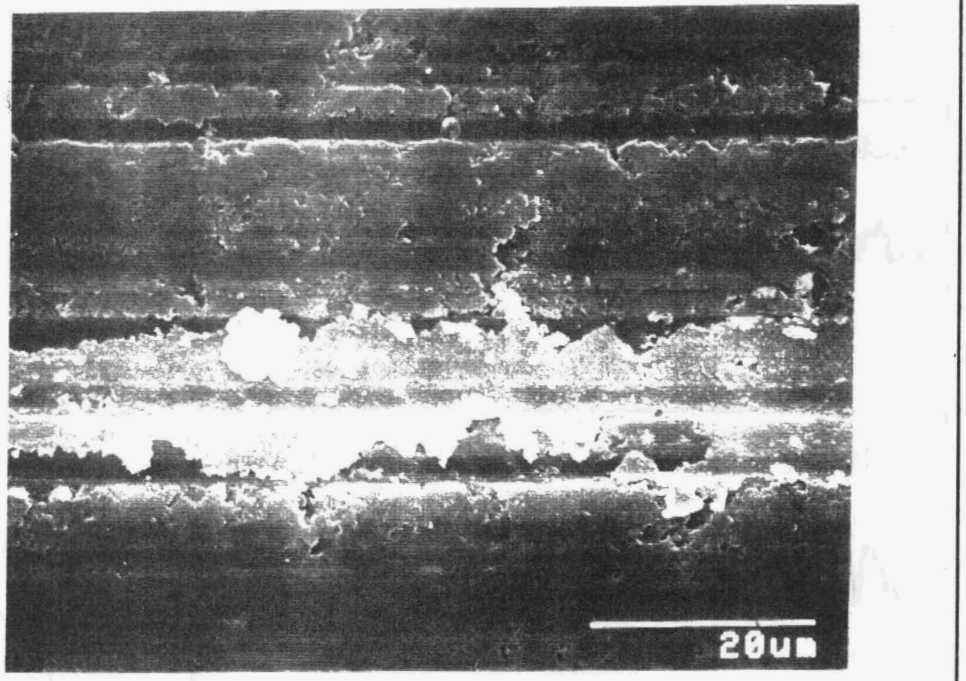

(a)

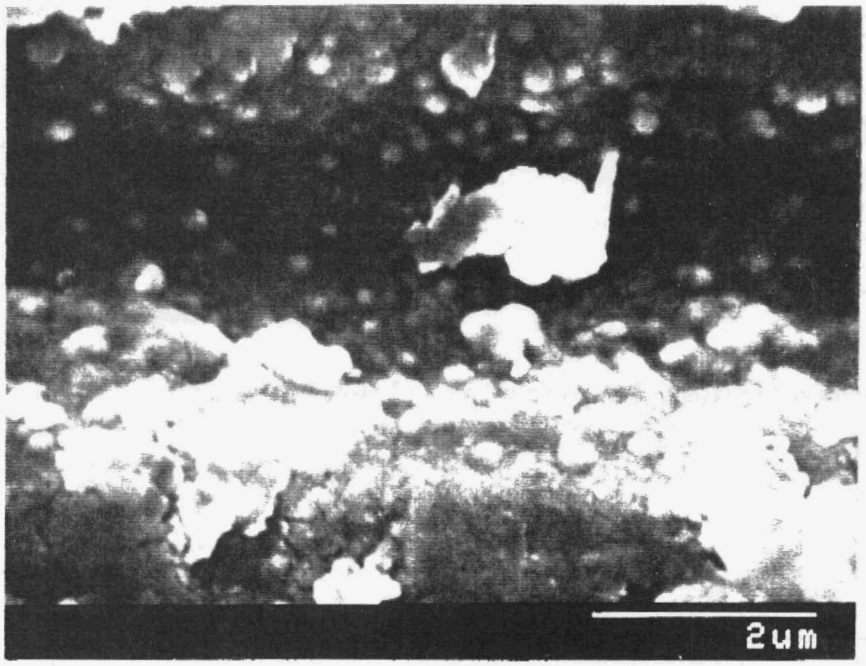

(b)

Fig. 6 The morphology of the ground surface with fluid CM001

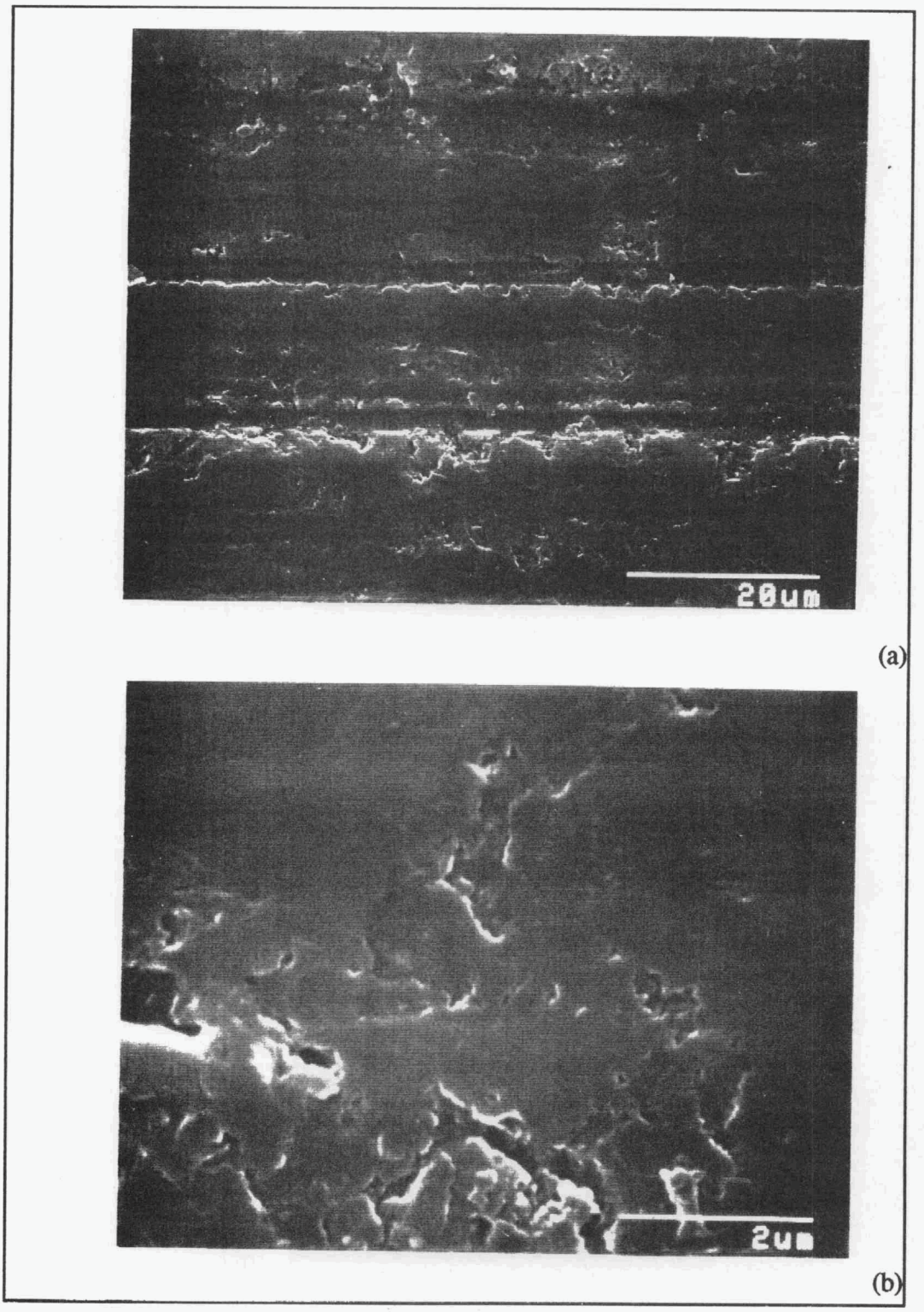

Fig. 7 The morphology of the ground surface with fluid CM004

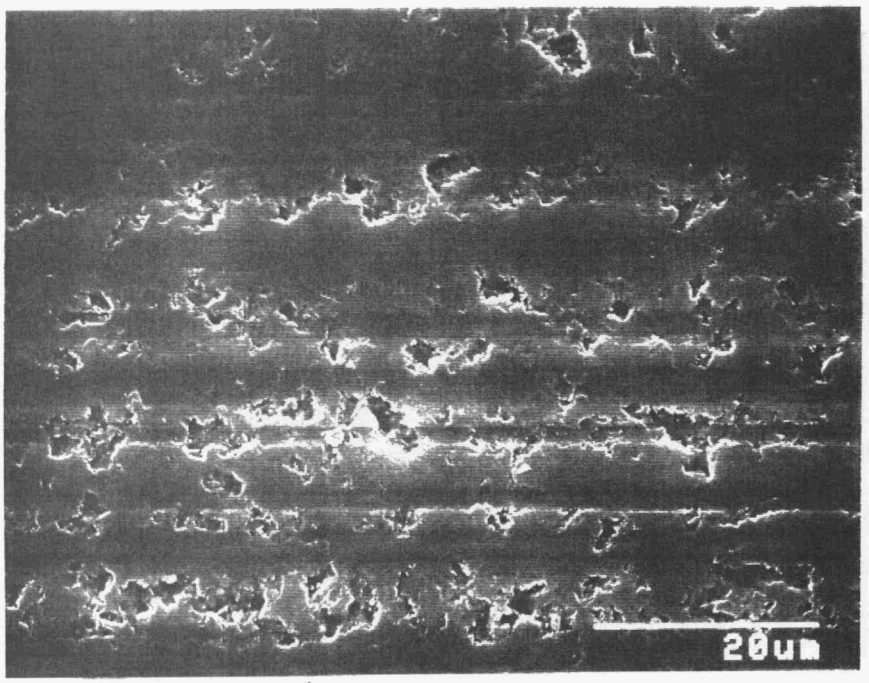

(a)

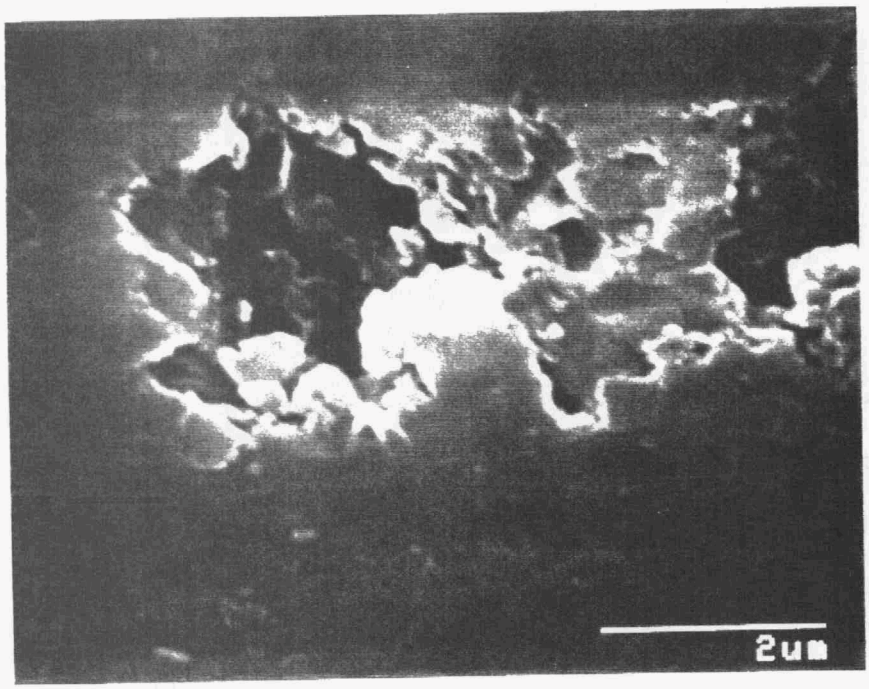

(b)

Fig. 8 The morphology of the ground surface with fluid CM011

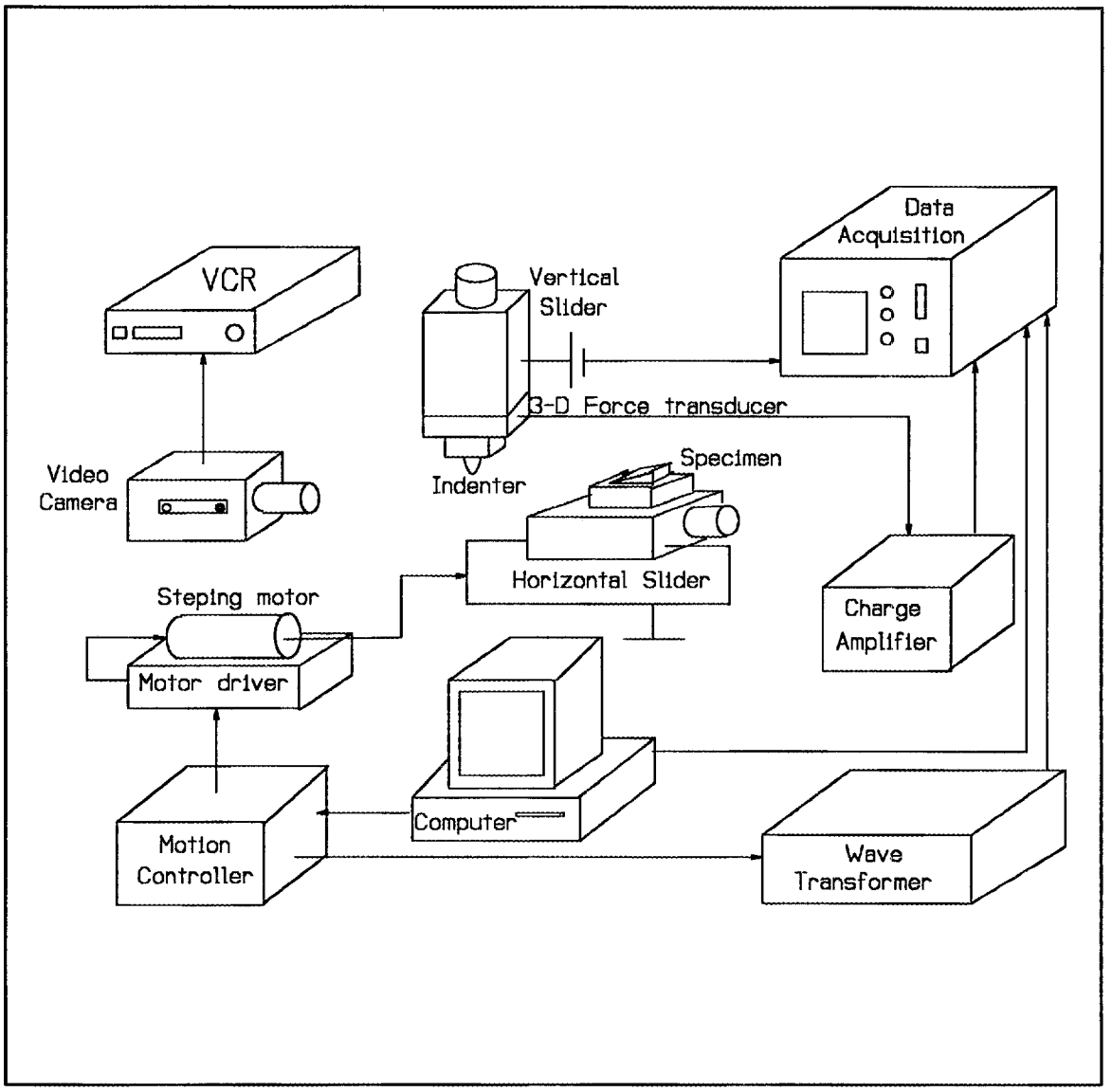

Fig. 9 A schematic diagram of micro-scratch test apparatus.

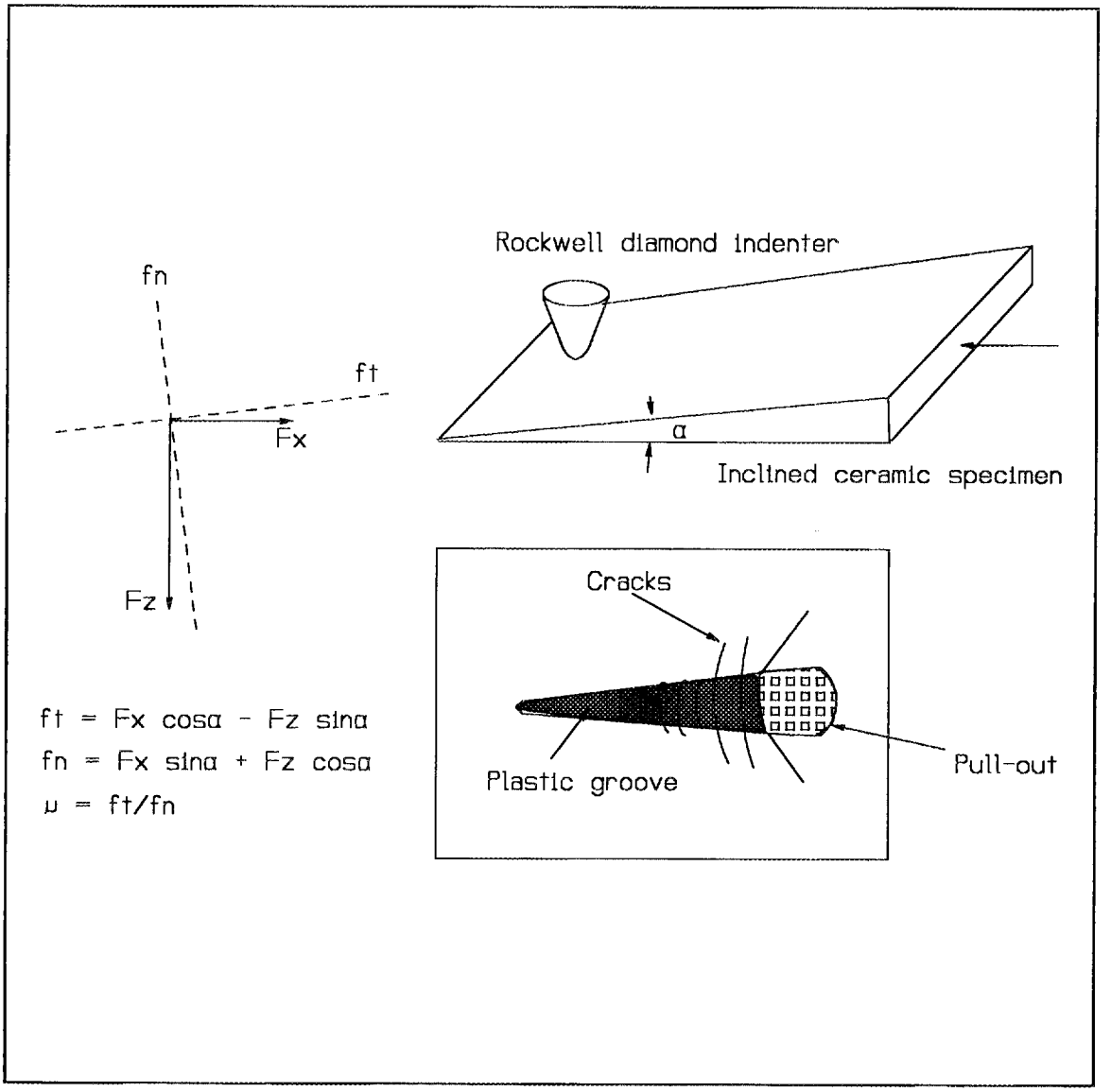

Fig. 10 A schematic diagram of the micro-scratch test apparatus showing the inclined surface and the damage pattern of the scratch.

$$\sigma_{max} = p_0\left[\frac{(1-2\nu)}{3} + \frac{(4+\nu)}{8}\pi\mu\right] \quad (1)$$

where: p_0 is the maximum Hertzian contact pressure, μ is friction coefficient, and ν is the Poisson ratio of the specimen. The calculation of the external critical tensile stress at which crack propagates is based on the linear elastic fracture mechanic. We also consider the effects of internal residual stress on the propagation of preexisted cracks and arrived at the following expression for the net stress intensity factor for an equilibrium crack:

$$\sum_i K_{Ii} + K_D = T_0 \quad (2)$$

where K_D is the stress intensity factor due to the applied loading. The term K_{Ii} represents contributions of "internal" forces on the crack, such as those associated with microstructure and machining. T_0 is taken to be the intrinsic material toughness (i.e., the effective K_{IC} for bulk cleavage or grain boundary fracture) and is strictly independent of crack size. Neglecting gradients in the stress distributions over the flaw dimensions, the equilibrium requirement may be expanded in the form:

$$\psi\sigma_I c^{1/2} + \psi\sigma_D c^{1/2} = T_0 \quad (3)$$

where ψ is a crack-geometry coefficient, $\Sigma\sigma_I$ are the summary of internal stresses retained from the thermal process, with compressive stresses are represented a negative sign, c is the preexisted crack size and σ_D is the critical tensile stress induced by external sliding required for microfracture. Equation (3) can be rewritten as follow:

$$\sigma_D = \frac{T_0}{\psi}c^{-\frac{1}{2}} - \sigma_I \quad c \neq 0 \quad (4)$$

Equation (4) shows that the critical external stress to propagate the cracks on the ceramic surface inversely proportional to the square root of the crack length and is proportional to the residual tensile stress on the surface. When micro cracks and/or residual tensile cracks exist on the surface due to machining, the external stress necessary to propagate these cracks will be lower. By using the diamond scratching on an inclined plane, the critical stress at which cracks will propagate can be determined. This critical stress can be used as the criterion to evaluate the effect of the machining process on the property of ceramic materials.

Figure 11 shows the results of an experiment where Vickers indentations are introduced on a silicon nitride surface. There are no cracks on the surface except radial cracks on the corners of the Vicker's indent. Then, after scratching with the a spherical silicon nitride ball (3.2 mm diameter) close to the indentation marks on an inclined plane, some cracks are generated near the edges of indents. No such crack was observed at other places. This observation suggests that the residual stress near the indentation marks are high,

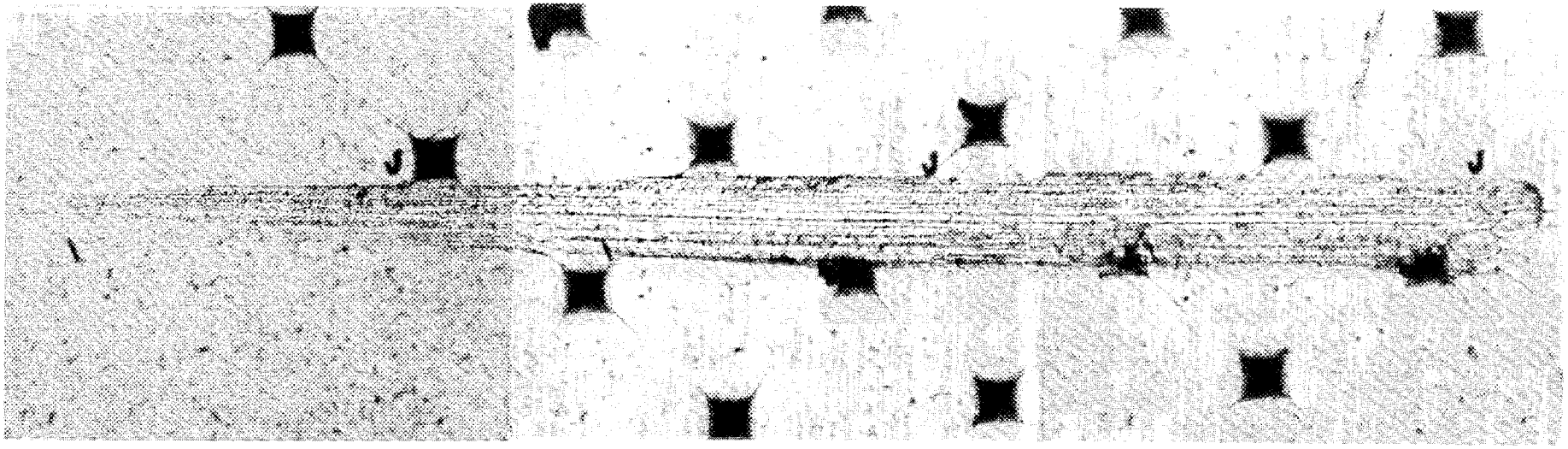

Fig. 11 SEM of scratching test on previously indented surface. The cracks between the scracthing track and the indent are generated during the scratching test.

when the external stress induced by scratching superimposes on the residual stress and exceed the strength of the material, cracks are then observed.

Initial results of this technique are promising and we are currently conducting experiments on as machined surfaces. Further development of this technique is required to evaluate the quality of the as machined surfaces.

Status of Milestones

On schedule

Communications and Visits

S. M. Hsu visited Benz Oil at Milwaukee on Oct. 7, 1992 to discuss possible cooperation in ceramic machining.

S. M. Hsu presented a talk to the ACerS Chicago Section on Chemically Assisted Machining of Ceramics on Oct. 6, 1992 in Chicago, IL.

Douglas Placek of FMC Corp. visited NIST on Dec. 11, 1992 to discuss chemistry in lubrication and machining.

Kennametal Inc. has furnished a variety of ceramic samples including SiAlON for evaluation of developed fluids. They have also provided a corrosion test procedure they use to qualify grinding fluids for their operations. This procedure will be used to ensure that developed grinding fluids are not too corrosive for commercial use.

Publications:

The paper "Chemical Assisted Machining of Ceramics," by S. Hsu and J. Wang has been accepted for publication in the ASME Journal of Tribology.

High-Speed, Low-Damage Grinding of Advanced Ceramics

Dr. Joseph A. Kovach (Eaton Manufacturing Technologies Center)
and Dr. Stephen Malkin (University of Massachusetts)

Objective/Scope

The fundamental objective of this project is to conduct a feasibility investigation of High Speed Low Damage (HSLD) grinding relative to the development of a single step, roughing/finishing process suitable for producing high quality silicon nitride ceramic parts. Current industrial grinding approaches sacrifice productivity and costs in order to achieve good surface finishes. However, by using high wheel speeds and fine grits to achieve the small grain depths of cut necessary for low damage grinding, it is anticipated that a process can be identified to finish grind silicon nitride at high material removal rates while producing acceptable surface integrity at substantially lower costs than traditional, multi-stage grinding processes.

Technical Highlights

It is important to realize that grinding with small grain depths of cut (necessary for low damage) and high wheel speeds (generally proven to increase G-Ratios) will generate higher specific energies which, in turn, may lead to higher grinding zone temperatures. It has been suggested by some Japanese researchers that these elevated grinding zone temperatures tend to inhibit fracture and promote the non-detrimental ductile mode of grinding. Conversely, excessive heating can drastically reduce the useful life of the grinding wheel.

With this in mind, the critical HSLD process success factors require a delicate balance between the potentially beneficial heat flow into the workpiece and the resulting detrimental grinding wheel (diamond) heating. Since improved thermal conductivity in the grinding wheel bond may reduce diamond heating, the majority of the grinding wheels selected for this study will be shipped with accompanying "thermal test coupons" for subsequent determination of thermal conductivity, specific heat, and thermal diffusivity of the composite grinding wheel bond.

However, in order to calculate the complete grinding zone temperature profile, an experimental investigation is being conducted to determine the fraction of the grinding energy entering the workpiece as heat. The initial approach will utilize measurement of sub-surface temperatures as given by thermocouples embedded in the workpiece. From the measured temperature response, an inverse heat transfer analysis can be used to obtain the heat input to the workpiece in the grinding zone. This is then compared with the total measured energy input, obtained from the measured grinding force and power, to determine the fraction of the grinding energy conducted as heat to the workpiece. Subsequent efforts will utilize infra-red pyrometry and an optical fiber system (rather than embedded thermocouples) to enhance system response.

To date, over 200 Eaton S/RBSN cylindrical rollers have been received for test purposes. In addition, over 300 Eaton S/RBSN MOR bars were fabricated and have been prepared for use in the laboratory grinding studies. SN-220 silicon nitride test specimens (rollers, MOR bars, and creep feed test blocks) have also been recently received from Kyocera. Coors Ceramics is currently in the process of fabricating additional S/RBSN test blanks. Grinding wheels and dressing tools have been received from Norton, Universal/Beck Supercut, and Abrasive Technology.

Several MOR bar type S/RBSN specimens have been drilled using a 0.050" diamond drill at the University of Massachusetts for thermocouple installation. The holes were drilled from the underside to within 0.050" of the workpiece surface. Type K thermocouples (5TC-TT-K-36-36) were then installed and held in place with a special cement. A fixture for holding the workpiece was also designed and built. Data acquisition systems at both the Eaton MRC (Machining Research Center) and the U. Mass. Grinding Lab have been tested. The U. Mass. system has been modified for temperature measurement.

Test machine setup efforts are also well underway at Eaton and U. Mass. The MRC "Eagle" is being modified for high speed O.D. cylindrical grinding studies. A custom wheel adapter hub has been designed and fabricated to adapt standard wheel hub sizes to the high speed GMN motorized spindle. Workholding fixtures are being designed to allow for O.D. creep feed grinding studies as well as conventional O.D. grinding.

A high speed surface grinding simulation has also been developed on the Weldon Universal ID/OD machine which will permit surface workpiece velocities up to 400 ft./min. In addition, standard baseline grinding load studies have been conducted to calibrate the internal Weldon piezoelectric load cells with a Kistler 3-axis force dynamometer.

It must be noted, however, that before any ceramic grinding can begin, the diamond grinding wheel must be accurately dressed. Typical industrial practice involves the use of a brake controlled dressing device. After considerable testing at the University of Massachusetts, a Norton 38A 80 M VBE aluminum oxide brake dressing wheel was found to successfully true a coarse grit resin bonded grinding wheel (Norton SD150-R100-BX619C) to within 0.0005" out-of-roundness. Subsequently, the wheel surface was conditioned using a 37C 220 KV silicon carbide abrasive stick.

In testing at Eaton's Machining Research Center, similar brake dressing results were also noted. In these tests, however, a finer grit resinoid wheel (D-400-R-B) was initially employed. After evaluating five different brake dressing wheels (grit sizes ranging from 80 to 220, hardness between H & M, with 38A aluminum oxide and 37C & 39C silicon carbide) it was found that the 38A 220 K 9VBE provided the most reasonable brake dressing results.

Nevertheless, brake dressing is extremely slow and may not provide a uniform profile across the wheel surface. Non-uniform wheel bonds (hardness, density) may lead to non-uniform breakdown under brake dressing conditions. Up to 0.002" of wheel taper was formed in one resin wheel under both traverse and plunge type brake dressing conditions. Additionally, after five minutes of brake dressing, only

0.0003" was removed from the wheel radius. Although pre-conditioning the wheel with a 38A 220H stick increased the removal rate by approximately 30%, these rates are still unattractive for high volume cost effective ceramic finishing. Unfortunately, as industry moves toward vitrified and metal bonded diamond wheels for higher G-ratios and higher wheel speeds, the brake dressing rates will become even slower.

With this in mind, additional dressing experiments were conducted to improve wheel profile while increasing dressing rates. Both resin and vitrified diamond wheels are under evaluation using hydraulically powered dressing devices. Tests were conducted using uni & counter-directional O.D. dressing, as well as 90° traverse cup dressing techniques. Dressing wheels ranged from aluminum oxide, to silicon carbide, to metal bonded diamond wheels. To date, the best results were obtained by pre-conditioning the wheel (rotating at 2000 SFM) with a 37C 220 I silicon carbide stick fed in at 2"/minute for 0.25", followed by 90° traverse cup dressing at 15"/minute with 0.001" dress depth per pass. Using a 38A 60 K5 cup wheel operating at 3500 SFM, up to 0.0009" was removed from the resin wheel in less than 2 minutes.

After having dressed the wheel, an initial series of grinding studies was performed to provide baseline grindability characterization. Building upon data developed at the University of Massachusetts grinding laboratory, the forces and corresponding specific energy (i.e. energy per unit volume of material removed) for the sintered reaction bonded silicon nitride appear to be approximately 20% less than what has been obtained for hot pressed silicon nitride. Under conventional surface grinding conditions (i.e. wheel speed V_S = 30 m/sec (6000 SFM), workpiece velocity V_W = 173 mm/sec (34 ft/min.), wheel depth of cut a = 25 microns (0.001")), the specific energy with the S/RBSN was 35 J/mm^3 (5.07 * 10^6 in-lbs/in^3) as compared to about 42 J/mm^3 (6.08 * 10^6 in-lbs/in^3) for the HPSN. This suggests that, while providing improved grindability, the S/RBSN material may not be as tough as the HPSN.

Grinding tests are continuing over a wide range of conditions. Conventional, as well as abusive tests at elevated speeds are being performed such that contrasting surface damage conditions can be characterized. Of particular interest is the identification of a straightforward surface analysis technique capable of readily distinguishing between ductile flow, brittle fracture, and mixed mode grinding under HSLD conditions.

Initial temperature measurement tests will also be conducted using the embedded thermocouple technique. Subsequently, the tests will utilize an infrared pyrometric measuring system currently under development at the University of Massachusetts. The first design employs a sheathed fluoride glass fiber and a lead selenide detector. Although this approach should prove successful at elevated temperatures (500 °C), it is unclear how accurate the sensor will be at lower temperature regimes (200 - 300 °C). As such, several other infrared detector systems are also being investigated.

Status of Milestones

Based on the milestone/gantt chart given in the February, 1993 bi-monthly report, the project is essentially on schedule. Specimen preparation (153201) is nearly completed. The experimental development (153202) is well underway. Moreover, some of the laboratory grinding studies have already begun (153203).

Publications

None

2.0 MATERIALS DESIGN METHODOLOGY

INTRODUCTION

This portion of the project is identified as project element 2 within the work breakdown structure (WBS). It contains two subelements: (1) Modeling, (2) Contact Interfaces, and (3) New Concepts. The subelements include macromodeling and micromodeling of ceramic microstructures, properties of static and dynamic interfaces between ceramics and between ceramics and alloys, and advanced statistical and design approaches for describing mechanical behavior and for employing ceramics in structural design.

The major objectives of research in Materials Design Methodology elements include determining analytical techniques for predicting structural ceramic mechanical behavior from mechanical properties and microstructure, tribological behavior at high temperatures, and improved methods for describing the fracture statistics of structural ceramics. Success in meeting these objectives will provide U.S. companies with methods for optimizing mechanical properties through microstructural control, for predicting and controlling interfacial bonding and minimizing interfacial friction, and for developing a properly descriptive statistical data base for their structural ceramics.

2.2 CONTACT INTERFACES

2.2.2 Dynamic Interfaces

Development of Standard Test Methods for Evaluating the Wear Performance of Ceramics

P. J. Blau (Oak Ridge National Laboratory)

Objective/scope

The goal of this effort is to improve consistency in reporting ceramic wear data by helping to develop one or more standard test methods for quantitatively determining the wear resistance of structural ceramics in reciprocating sliding, a type of motion that is experienced by several types of automotive and truck engine wear parts. ORNL is working with the American Society for Testing and Materials (ASTM) in meeting this objective. Wear-test development normally falls within the scope of ASTM's G-2 Committee on "Wear and Erosion," and in 1990, P. J. Blau was appointed chairman of a newly established Task Group G02.40.07, "Reciprocating Sliding Wear Testing," within the G-2 Committee. This report describes activities within the Task Group.

Technical highlights

Progress of the draft: During the last period, we submitted a draft reciprocating wear test standard to ASTM subcommittee G-2.40 on "Non-abrasive Wear" for comment and review and led a round-robin testing program of unlubricated wear tests using tool steel and silicon nitride materials as test specimens. The draft standard, entitled "Reciprocating Sliding Wear of Ceramic and Metallic Materials," was written in the prescribed ASTM standards format and presented to the subcommittee chairman for "Non-Abrasive Wear." After preliminary balloting at the subcommittee level and discussion at the December 1992 meeting, the draft was returned for revision. Based on these comments, the initial draft is currently being revised for consideration at the next committee meeting, May 20-21, 1993. One required section on "Precision and Accuracy" remains to be completed based on the results of the interlaboratory ("round-robin") test program, which is still in progress.

Progress of the round-robin program: The first round was completed by Fall 1992. Two combinations of materials were included: a tool steel wear couple and a silicon nitride wear couple. The following seven participants, in addition to ORNL, completed the tests and returned the specimens: Howard Hawthorne, National Research Council of Canada; Glenn Elliott, Caterpillar Tech Center; Peter Vernia, General Motors Research Staff; Ken Budinsky, Eastman Kodak Company; Alex Alliston-Greiner, Cameron-Plint (United Kingdom); Carlton Rowe, Mobil Research; and Malcolm Naylor, Cummins Engine Company. Except for Kodak, which used a custom-made testing machine, all participants had reciprocating test machines made by Cameron-Plint. An ASTM software package, specifically designed to analyze round-robin test data (per ASTM E 691), was used to compute the statistics of seven quantities recorded for each test. Repeatability of results within each laboratory was good, but reproducibility of results between laboratories was unacceptable. The following causes were identified:

1. testing machines were in the proximity of lubricant testers whose vapors may have contaminated the initially unlubricated test specimen surfaces,

2. most participants had not calibrated the normal force application system or their friction force sensors since the machines were installed, and

3. humidity in the participants' laboratories varied widely.

The above results, coupled with the responses from automotive industry, suggested the need for a second round-robin program. This second round will use only silicon nitride specimens and involve elevated-temperature, lubricated tests.

Future plans

The revised draft (without the precision and accuracy section) will be completed. A second round robin will be conducted. Preliminary discussions indicate the following participants (pending final confirmation): General Motors (two participants), Mobil Research, Cummins Engine Company, Caterpillar, Cameron-Flint, National Physical Laboratory (United Kingdom), National Research Council (Canada), and ORNL.

References

None.

Status of milestones

222204, Submit first draft of wear test standard to ASTM. June 30, 1992 - completed.

222205, Complete round-robin wear tests. December 31, 1993 - completed.

222206, Make revisions to the first ballot and resubmit. June 30, 1993 - on schedule.

Communications/visits/travel

P. J. Blau attended the ASTM G-2 Committee meeting in Miami, Florida, on December 10-11, 1992. A workshop on the subject of "Wear Test Selection for Design and Application" was held in conjunction with the meeting.

Problems encountered

Results of the first round-robin test series had unacceptable scatter. A second round will be conducted. The draft standard is being revised but cannot be completed until round-robin results from the second round are available.

Publications/presentations

None.

2.3 NEW CONCEPTS

Advanced Statistical Concepts of Fracture in Brittle Materials

C. A. Johnson and W. T. Tucker (General Electric Corporate Research and Development)

Objective/Scope

The design and application of reliable load-bearing structural components from ceramic materials requires a detailed understanding of the statistical nature of fracture in brittle materials. The overall objective of this program is to advance the current understanding of fracture statistics, especially in the following four areas:

- Optimum testing plans and data analysis techniques.
- Consequences of time-dependent crack growth on the evolution of initial flaw distributions.
- Confidence and tolerance bounds on predictions that use the Weibull distribution function.
- Strength distributions in multiaxial stress fields.

The studies are being carried out largely by analytical and computer simulation techniques. Actual fracture data are then used as appropriate to confirm and demonstrate the resulting data analysis techniques.

Technical Highlights

Work during this reporting period concentrated in two areas: generalized goodness-of-fit tests for the size-scaled Weibull distribution; and refinement of approaches for probabilistic strength analysis in multiaxial stress fields.

I. Goodness-Of-Fit

Quantitative tests of goodness-of-fit are helpful in judging applicability of the distribution and validity of resulting estimates of strength and probability of failure. As shown in recent bimonthly and semi-annual reports, Monte Carlo simulations are very useful in generating tables of critical values for goodness-of-fit tests in the two-parameter size-scaled Weibull distribution.

Goodness-of-fit tests are contained within a larger class of distribution hypothesis tests that are used to make statements of statistical significance concerning the consistency of data with an assumed model of probabilistic material behavior. The broader class includes:

- Tests to determine if one subgroup of specimens is consistent with the remainder of available strength data. As an example, one might ask if a group of 10 tensile specimens are consistent with a group of 100 bend specimens of the same material.
- Tests to determine if several subgroups of strength measurements are consistent with a common underlying strength distribution. For instance, if 10 laboratories

each measure the bend strength of 20 specimens of the same material, one could determine if the observed variability in apparent distributions is likely to be due to random sampling error.

- Goodness-of-fit tests to determine if a set of strength data is consistent with an assumed distribution such as the two-parameter Weibull.

The statistical literature includes approaches for performing tests of statistical significance in many of the above types of problems when the underlying distribution is expected to be Gaussian (normal). In general, however, similar tests are not available when the underlying distribution is expected to be Weibull. Work to date on goodness-of-fit tests has demonstrated that even when a specific test is described in the literature, it typically has only limited applicability to the wide range of size-scaled problems encountered in ceramic strength testing. Monte Carlo simulations techniques are expected to be valuable in creating tables of critical values for customized hypothesis tests in a manner similar to that demonstrated previously in goodness-of-fit tests.

During this reporting period, work continued on generalized goodness-of-fit tests for problems involving the size-scaled Weibull distribution function. In addition, initial consideration was given to extensions of the logic used in the goodness-of-fit simulations to cover the broader class of distribution hypothesis tests.

II. Probabilistic Strength Analysis in Multiaxial Stress Fields

During this reporting period, a detailed study of the possible difference between the Batdorf-Heinisch (B-H), Ref. 1, and Lamon-Evans (L-E), Ref. 2, approaches to multiaxial failure has been carried out. The equivalence of the B-H and L-E approaches has been challenged by Lamon, Ref. 3, who further claims that the L-E approach is superior to the B-H approach. Lamon, Ref. 3, compared results of Shetty et al., Ref. 4, employing the B-H approach to results of analyzing the same data via the L-E approach. In both Ref.'s 3 and 4 the analysis of 4-point bending data was employed to predict the results of 3-point bending and pressurized disk tests. The L-E approach successfully extrapolated to both the 3-point bending and pressurized disk results, whereas the B-H approach only extrapolated to the 3-point bending results; thus Lamon's conclusion. Given the equivalence of the two methods (reported in earlier bimonthly reports and shown in completeness in Ref. 5), they should have given comparable results--not exact since the L-E approach as applied employed a different failure criterion than the shear sensitive criterion employed by Shetty et al. (Shetty et al. also studied the normal stress criterion.) But the shear sensitive fracture criteria employed in each study are comparable in their shear sensitivity, so that the end results should have been more comparable. The more detailed studies reported herein are in response to a request for clarification on this issue by a referee in the review process of Ref. 5. While the study of the difference between the L-E and B-H approaches could seem to be minor--they are equivalent--Ref. 3 is the only citation known to the authors in which a difference between the approaches is reported. Thus the apparent difference needs to be resolved. The further new results given herein aim to do this.

Perusal of Lamon, Ref. 3, indicates that he employed "initial" data of Shetty et al., Ref. 6, for the shear sensitive failure mode studied. He then compared to results of Shetty et al., Ref. 6, for the Weibull approach and to Shetty et al., Ref. 4, for the B-H approach.

(Apparently Lamon did not carry out any analyses in the B-H manner but just employed published results of Shetty et al. Moreover, the pressurized disk results of Ref. 6 were only employed for comparison to the prediction from the 4-point bending results.) The 3- and 4-point data appear to be the same in both the Shetty et al. papers. However, the shear sensitive data are distinctly different and this difference favors Lamon's conclusion. Unfortunately (and apparently resolving the discrepancy) it had been reported in earlier reports that by employing the stress distribution equations for the pressure disk loading from Shetty et al., Ref. 6, the coplanar strain energy release rate failure criterion from Shetty et al., Ref. 4, and numerically integrating, in essentially the L-E manner, a Weibull failure probability plot nearly equal to that obtained by Lamon, Ref. 3, for the L-E approach (and the L-E failure criterion) was obtained. The more careful study carried out during this reporting period indicates that this is not the case. As an aside, all of the combinations of failure criteria and loading geometries given in Ref. 4 have been analytically integrated in the L-E manner under the Shetty et al. assumptions and duplicated exactly the Shetty et al. results. Thus, there is a discrepancy between the two analyses of the pressure disk fracture data. Our further studies indicate how this could have come about.

The further analyses begin by developing bounds for the subject failure criteria. The development of the bounds is based on the use of

$$P_f = 1 - \exp\left[-IV\sigma_M^m/\sigma_0^m\right], \tag{1}$$

where

$$I = I(m) = \frac{1}{2\pi V}\int_0^{\pi/2}\int_0^{2\pi}\left(\int_V(\sigma_e/\sigma_M)^m dv\right)\cos\phi d\phi d\psi, \tag{2}$$

σ_e expresses the failure criterion as a function of the local principal stresses, σ_M denotes the maximum value of σ_e, m is the Weibull modulus, and σ_0 is the inherent strength or second Weibull parameter. Eq.'s 1 and 2 follow from the equivalence of the B-H and L-E approaches as shown in Ref. 5. As pointed out in Ref. 5, use of σ_M is natural from a mathematical viewpoint. However, use of any other value that is in a one-to-one and onto relationship to σ_M can be made. The key is to employ a consistent usage of a failure stress, e.g., one that is measured at the same place and conditions for the test specimen. In the developments that follow (cf. (10)) the observed failure stresses, or a multiple that is not a function of any of the variables of integration, will be employed. Indeed in most cases it will be simplest to employ the observed failure stress as the factor. With this background, it is clear that bounds only need be developed for the σ_e employed by Lamon and Shetty et al.

The normal stress criterion plays a central role in the development of bounds. While the normal stress criterion is not a function of the shear stress, τ, in the plane of the possible failure producing crack, it is sensitive to the shear stresses within the structure. For a given location and orientation, since σ_1, σ_2, and σ_3 (the three principal stresses) are invariant, it follows that the value of σ (the normal stress to the plane) varies as τ varies through the relationship

$$\sigma^2 + \tau^2 = (\sigma_1 l_1)^2 + (\sigma_2 l_2)^2 + (\sigma_3 l_3)^2, \tag{3}$$

where the l_i denote the direction cosines of the given orientation as measured from the principal axes of the σ_i, $i = 1,2,3$. Thus, if (3) is held constant, i.e., only values of the σ_i that produce the same value for the sum, $\sigma^2 + \tau^2$, are considered, and the failure criterion is only a function of σ, then the event of failure occurs as τ varies. There can be combinations of σ_1, σ_2, and σ_3 for which (3) is constant and failure occurs and combinations for which it does not. Clearly, the normal stress failure criterion could be expressed as a function of τ and the left hand side of (3), as well. Put another way, the normal stress criterion is just a function of l_i and σ_i, with $i = 1,2,3$. However, of those criteria that are direct functions of σ and τ, and are based on energy or ultimate strength considerations, the normal stress criterion is the least shear sensitive. In this sense it serves as an upper bound on the probability of failure for these types of shear sensitive failure criteria. For example, the coplanar strain energy release rate criterion is greater than or equal to the normal stress criterion or $\sqrt{\sigma^2 + \tau^2} \geq \sigma$. Moreover, the maximum strain energy release rate criterion employed by Lamon is given by

$$\begin{aligned} \sigma_e &= (\sigma^4 + 6\sigma^2\tau^2 + \tau^4)^{1/4} \\ &= \sqrt{\sigma^2 + \tau^2}\left[1 + \frac{4\sigma^2\tau^2}{(\sigma^2 + \tau^2)^2}\right]^{1/4}. \end{aligned} \tag{4}$$

Now it is straightforward to show that $(\sigma^2 + \tau^2)^2 \geq 4\sigma^2\tau^2$, so that

$$(\sigma_e)_{\text{Max. } Strain} \leq [2]^{1/4}(\sigma_e)_{\text{Cop. } Strain}. \tag{5}$$

Finally, we have

$$[2]^{1/4}(\sigma_e)_{\text{Cop. } Strain} \geq (\sigma_e)_{\text{Max. } Strain} \geq (\sigma_e)_{\text{Cop. } Strain} \geq (\sigma_e)_{\text{Nor. } Stress} \tag{6}$$

since $[1 + 4\sigma^2\tau^2/(\sigma^2 + \tau^2)^2]^{1/4} \geq 1$. In hindsight (4), (5), and (6) are obvious; earlier they were not. (Along these lines see Figure 2. of Ref. 1.)

Eq. 6 implies that if Lamon, Ref. 3, had employed the coplanar strain energy release rate criterion in the L-E method, then the probability plot for this failure criterion would have plotted to the right of that for the maximum strain energy release rate criterion in his Figure 7 and would have, possibly, plotted on or near the pressure disk data from Shetty et al., Ref 4. Moreover, the normal stress criterion would have plotted even further to the right. Also if Shetty et al., Ref. 4, had employed the maximum strain energy release rate criterion, it would have produced a plot to the left of the lower bound given by Eq. 20 (cf. (11) ff.) in their Figure 4, which is just to the left of the curve for the 4-point bending data. This shows clearly that the treatments of Lamon and Shetty et al. differ in some way.

In order to more completely address the difference between the Lamon and Shetty et al. methods, bounds for the coplanar strain energy release rate criterion were then developed. The coplanar strain energy release rate criterion applied to the pressure disk loading is given by

$$(\sigma_e)_{\text{Cop. Strain}} = \sqrt{(\sigma_t l_1)^2 + (\sigma_r l_2)^2}\,, \tag{7}$$

where $l_1 = \cos\phi\cos\psi$ and $l_2 = \cos\phi\sin\psi$ are the direction cosines from the local principal axes. Also

$$\sigma_r = \sigma_u[1 - \alpha(r/r_1)^2] \tag{8}$$

and

$$\sigma_t = \sigma_u[1 - \beta(r/r_1)^2], \tag{9}$$

where σ_u is the observed failure stress produced at the center of the disk, and α, β, r, and r_1 are defined in Ref.'s 4 and 6. The definitions, setup, and numerical values given in Ref. 6 are employed herein. (There are some typographical errors in Ref. 4 coupled with a rounding of certain physical dimensions that exacerbate the difference between the Lamon and Shetty et al. results.) Also σ_r will be taken to be zero when (8) would give a negative value for certain $r \le r_1$. With this setup

$$(\sigma_e)_{\text{Cop. Strain}} = \sigma_u \cos\phi \sqrt{\tilde{\sigma}_t^2 \cos^2\psi + \tilde{\sigma}_r^2 \sin^2\psi}\,, \tag{10}$$

where $\tilde{\sigma}_r = [1 - \alpha(r/r_1)^2]$ and $\tilde{\sigma}_t = [1 - \beta(r/r_1)^2]$, follows from (7)-(9). From the fact that $\tilde{\sigma}_t \ge \tilde{\sigma}_r \ge 0$, bounds on the portion of (10) involving the square root are given by

$$\tilde{\sigma}_t \ge \sqrt{\tilde{\sigma}_t^2 \cos^2\psi + \tilde{\sigma}_r^2 \sin^2\psi} \ge \tilde{\sigma}_r. \tag{11}$$

In view of (10), and since $\tilde{\sigma}_t$ and $\tilde{\sigma}_r$ are only functions of r and this corresponds to a size integration, it follows that the bounds given by (11) can be evaluated in closed form by use of (2). Also note in view of (10) that σ_u factors out of the integrations. It replaces σ_M in (1): The term $\cos\phi\sqrt{\tilde{\sigma}_t^2 \cos^2\psi + \tilde{\sigma}_r^2 \sin^2\psi}$ is analogous to the term F in the L-E formulation. The result of carrying out the closed form integrations associated with (10) and (11) yields a lower bound for the product IV equal to the lower bound given by Eq. 20 of Ref. 4 and is given by

$$\frac{\sqrt{\pi}\,\Gamma(m/2+1)}{\Gamma(m/2+1+1/2)} \pi r_1^2 \left[\frac{1}{\alpha 2(m+1)}\right]. \tag{12}$$

The upper bound obtained by the same method is

$$\frac{\sqrt{\pi}\,\Gamma(m/2+1)}{\Gamma(m/2+1+1/2)}\pi r_1^2\left(\frac{1}{\beta 2(m+1)}\right)[1-(1-\beta)^{m+1}], \tag{13}$$

and differs from that given by Eq. 20 of Ref. 4 by the term $[1-(1-\beta)^{m+1}]$. Therefore the upper bound given by this method is less than or equal to the upper bound given by Eq. 20 (Ref. 4) and is thus a tighter bound than that given by Eq. 20. However, in many cases the two upper bounds are numerically close. All in all, the bounds given by Eq. 20 of Ref. 4 are quite good. Similarly bounds for the normal stress criterion applied to the pressure disk loading can be obtained. The relationship to Eq. 15 of Ref. 4 is analogous to the relationship of the bounds developed herein to Eq. 20 just discussed.

As a final step in studying the discrepancy between the Lamon and Shetty et al. evaluations, two dimensional integrations of the normal stress and coplanar strain energy release rate failure criteria and numerical evaluation of the various bounds were carried out. A two dimensional integration will suffice in view of (10) and its counterpart for the normal stress failure criterion. As an aside, it will require a triple integration to evaluate the failure criterion employed by Lamon. Programming to carry out the required triple integration is under development. The double integration is based on a double application of a Gaussian type numerical integration rule (see Chapter 25 of Ref. 7) with 28 points employed for each individual integration. Also all computations were done in double precision on a VAX 6000. The earlier integrations that were in error were based on use of a trapezoidal rule and Simpson's rule. (It is not clear how the erroneous results were obtained, but it was probably not due to the integration rules employed.)

To begin the numerical evaluations and to compare with the results of Shetty et al., the physical constants of Ref. 4 were employed to evaluate the various bounds and actual solutions for the product IV for the normal stress and coplanar strain energy release rate criteria. These results were then used to make probability plots as shown in Figure 4 of Ref. 4. In doing this the intercept of the line for 4-point bending data was estimated from Figure 4. This intercept changes for the various plots and is given by $(m\ln\sigma_0 - \ln IV)$--the $\ln IV$ term is what actually changes for the various cases. The line that was estimated in this way is given by

$$y = 23.8x - 140.3816, \text{ for 4-point bending}, \tag{14}$$

where x denotes the abscissa and y denotes the ordinate of Figure 4 of Ref. 4. With the exception of the line denoting Eq. 15 in Figure 4 all of the Shetty et al. results were duplicated. Also in view of (6) the location of the line for Eq. 15 (Ref. 4) is questionable. The upper bound from Eq. 15 (Ref. 4) computed by the method just described falls about half way between the upper and lower bounds from Eq. 20 (Ref. 4). Similarly, the lower bound from Eq. 15 (Ref. 4) falls about half way between the lower bound from Eq. 20 (Ref. 4) and the line from the 4-point bending data (Ref. 4). The actual solution for the coplanar strain energy release rate failure criterion produces a line essentially equal to that from the upper bound of Eq. 15 (Ref. 4). The actual solution for the normal stress criterion produces a line near to that from the lower bound of Eq. 20 (Ref. 4). (See Table 1 to follow.) These results are self consistent. Thus the plotting of Eq. 15 in Figure 4 of Ref. 4 appears to be incorrect. However, the overall implications of Figure 4 are correct.

The values of IV that produced these results (from the constants of Ref. 4) are shown in Table 1, along with solutions for the constants given in Ref. 6 and solutions for the constants of Ref. 6, but with the value of r_1 taken as 23.0/2 mm.

Table 1

IV Values (mm^3) for the Two Failure Criteria with Various Loads and Bounds

Weibull Modulus	Normal Stress Criterion						Coplanar Strain Criterion			
	3-Pt. Bend	4-Pt. Bend	Pressurized Disk				Pressurized Disk			
			Lower Bound	Actual	Upper Bound		Lower Bound	Actual	Upper Bound	
					(11)	Eq. 15			(11)	Eq. 20
Constants: Ref. 4										
1.00	50.0000	79.6875	231.728	289.725	347.731	449.496	272.998	349.006	409.661	529.551
23.8	.265391	4.01569	5.01367	6.98280	9.72532	9.72532	6.98402	9.75159	13.5473	13.5473
33.3	.137980	2.86611	3.07812	4.28706	5.97082	5.97082	4.30580	6.00757	8.35221	8.35221
Constants: Ref. 6										
1.00	49.7865	79.3750	134.226	181.256	228.236	260.367	158.132	222.276	268.885	306.737
23.8	.263732	4.01403	2.90413	4.04473	5.63330	5.63330	4.04543	5.64852	7.84716	7.84716
33.3	.137118	2.86525	1.78298	2.48324	3.45854	3.45854	2.49409	3.47983	4.83794	4.83794
Constants: Ref. 6--r_1 = 23.0/2										
1.00	49.7865	79.3750	79.7950	116.481	153.068	154.783	94.0062	145.178	180.329	182.349
23.8	.263732	4.01403	1.72645	2.40451	3.34889	3.34889	2.40493	3.35794	4.66498	4.66498
33.3	.137118	2.86525	1.05994	1.47624	2.05604	2.05604	1.48269	2.06869	2.87606	2.87606

The value of 23.0 mm comes about by subtracting the diameter (2.4 mm) of the ball bearings used in the support ring of the pressure apparatus from the diameter of the circle (25.4 mm) on which the ball bearings rested in the supporting ring (cf. Ref. 6 for details). This is a crude attempt to correct for any possible residual stresses that may have been produced by the loading of the pressure disk by the ring of ball bearings and, thus, are not accounted for by (8) and (9). Clearly, this latter solution set will have a stress pattern that is generally below those shown for each of σ_t and σ_r in Figure 2 of Ref. 6 and is employed only for illustrative purposes to indicate the sensitiveness of the solutions to the stress state. The maximum value of 33.3 for the Weibull modulus was the largest that the subroutines which were employed to evaluate the gamma function could accommodate. Once the value of the Weibull modulus takes on values of 20 or so or larger the sensitiveness to changes in its value is greatly lessened. Also there are somewhat significant changes between the constants of Ref. 4 and those of Ref. 6. However, with the constants of Ref. 6 (but letting r_1 vary) and the Weibull modulus in an acceptable range, IV seems to be most sensitive to changes in the stresses, σ_t and σ_r. The normal stress solution with the constants of Ref. 6 with r_1 = 23.0/2 mm gives a value of 2.40451 mm^3 for IV for the pressurized disk loading. This solution would plot close to the solution that Lamon obtained in Ref. 3 but would still be to the left of Lamon's curve. Thus it may well be that the manner in which the principal stress field was determined by Lamon has produced the difference between his results and those of Shetty et al.; Ref. 3 does not indicate how the principal stress field is computed. Also the numerical integration must be carried out carefully. In this vein evaluation of the failure criterion appears to be crucial (and this may be the source of our earlier erroneous results). Moreover, the solution that Lamon should have obtained even with the constants of Ref. 6 and r_1 = 23.0/2 mm would be greater than the coplanar strain solution of 3.35794 mm^3 for the pressurized disk loading. In this situation in view of (6) the maximum strain energy release rate failure criterion should not produce a line about half way between those for the 4-point and 3-point bending case.

In summary Lamon's solution appears questionable unless the stress solutions given by (8) and (9) are in large error. However, this could be the case due to the effect of residual stresses that these equations do not take into account. Further study of this issue seems warranted.

References

1. S.B. Batdorf and H.L. Heinisch, "Weakest Link Theory Reformulated for Arbitrary Fracture Criterion," *J. Am. Ceram. Soc.*, 61, 7-8, 355-358, 1978.
2. J. Lamon and A.G. Evans, "Statistical Analysis of Bending Strengths for Brittle Solids: A Multiaxial Fracture Problem," *J. Am. Ceram. Soc.*, 66, 3, 177-182, 1983.
3. J. Lamon, "Statistical Approaches to Failure for Ceramic Reliability Assessment," *J. Am. Ceram. Soc.*, 71, 2, 106-12, 1988.
4. D.K. Shetty, A.R. Rosenfield, and W.H. Duckworth, "Statistical Analysis of Size and Stress State Effects on the Strength of an Alumina Ceramic," *Methods for Assessing the Structural Reliability of Brittle Materials,* ASTM STP 844, S.W. Freiman and C.M. Hudson, Eds., American Society for Testing Materials, Philadelphia, 57-80, 1984.
5. W.T. Tucker and C.A. Johnson, "The Multiaxial Equivalent of Stressed Volume," *Life Prediction Methodologies and Data for Ceramic Materials,* ASTM STP 1201, C.R. Brinkman and S.F. Duffy, Eds., American Society for Testing Materials, Philadelphia, 1993, in review.
6. D.K. Shetty, A.R. Rosenfield, W.H. Duckworth, and P.R. Held, "A Biaxial-Flexure Test for Evaluating Ceramic Strengths," *J. Am. Ceram. Soc.*, 66, 1, 36-42, 1983.
7. M. Abramowitz and I.A. Stegun, Eds., *Handbook of Mathematical Functions with Formulas, Graphs, and Mathematical Tables,* National Bureau of Standards, Applied Mathematics Series, 55, Washington, D.C., 1964.

Status of Milestones

All milestones are on schedule.

Publications

W.T. Tucker and C.A. Johnson, "The Multiaxial Equivalent of Stressed Volume," Submitted to ASTM for publication in "Life Prediction Methodologies and Data for Ceramic Materials", ASTM STP 1201, 1993.

C.A. Johnson and W.T. Tucker, "Weibull Estimators for Pooled Fracture Data," Submitted to ASTM for publication in "Life Prediction Methodologies and Data for Ceramic Materials", ASTM STP 1201, 1993.

3.0 DATA BASE AND LIFE PREDICTION

INTRODUCTION

This portion of the project is identified as project element 3 within the work breakdown structure (WBS). It contains five subelements, including (1) Structural Qualification, (2) Time-Dependent Behavior, (3) Environmental Effects, (4) Fracture Mechanics, and (5) Nondestructive Evaluation (NDE) Development. Work in the Structural Qualification subelement includes proof testing, correlations with NDE results and microstructure, and application to components. Work in the Time-Dependent Behavior subelement includes studies of fatigue and creep in structural ceramics at high temperatures. Research in the Environmental Effects subelement includes study of the long-term effects of oxidation, corrosion, and erosion on the mechanical properties and microstructures of structural ceramics. Work in the Fracture Mechanics subelement includes development of techniques for measuring the tensile strength and creep resistance of ceramic materials at high temperatures, and testing ceramic materials at high temperatures under uniaxial tension. Work in the NDE Development subelement is directed at identifying approaches for quantitative determination of conditions in ceramics that affect their structural performance.

Major objectives of research in the Data Base and Life Prediction project element are understanding and application of predictive models for structural ceramic mechanical reliability, measurement techniques for long-term mechanical property behavior in structural ceramics, and physical understanding of time-dependent mechanical failure. Success in meeting these objectives will provide U.S. companies with the tools needed for accurately predicting the mechanical reliability of ceramic heat engine components, including the effects of applied stress, time, temperature, and atmosphere on the critical ceramic properties.

3.1 STRUCTURAL QUALIFICATION

Microstructural Analysis of Structural Ceramics

B. J. Hockey and S. M. Wiederhorn
(National Institute of Standards and Technology)

Objective/Scope

The objective of this part of the program is to identify mechanisms of failure in structural ceramics subjected to mechanical loads at elevated test temperatures. Of particular interest is the damage that accumulates in structural ceramics as a consequence of high temperature exposure to stresses normally present in heat engines.

Design criteria for the use of ceramics at low temperature differ from those at high temperature. At low temperature ceramics are elastic and brittle; failure is controlled by a distribution of flaws arising from processing or machining operations, and the largest flaw determines the strength or lifetime of a component. By contrast, at high temperature where ceramics are viscoelastic, failure occurs as a consequence of accumulated, or distributed damage in the form of small cavities or cracks that are generated by the creep process. This damage effectively reduces the cross-section of the component and increases the stress that must be supported. Such increases in stress are autocatalytic, since they increase the rate of damage and eventually lead to failure as a consequence of loss in cross section. When this happens, the individual flaw loses its importance as a determinant of component lifetime. Lifetime now depends on the total amount of damage that has occurred as a consequence of the creep process. The total damage is now the important factor controlling lifetime.

Recent studies of high temperature failure of the non-oxide ceramics intended for use for heat engines indicates that for long term usage, damage accumulation will be the primary cause of specimen failure. Mechanical defects, if present in these materials, are healed or removed by high temperature exposure so that they have little influence on long term lifetime at elevated temperature. In this situation, lifetime can be determined by characterizing the damage and the rate of damage accumulation in the material at elevated temperatures. In ceramic materials such as silicon nitride and SiAlON, such characterization required high resolution analyses because of the fine grain size of these materials: hence the need for transmission electron microscopy as an adjunct to the mechanical testing of ceramics for high temperature applications is apparent.

In this project, the creep and creep-rupture behavior of several ceramic materials will be correlated with microstructural damage that occurs as a function of creep strain and rupture time. Materials to be studied include: SiAlON; hot-pressed silicon nitride; sintered silicon carbide. This project will be coordinated with WBS 3.4.1.3, Tensile Creep Testing, with the ultimate goal of developing a test methodology for assuring the reliability of structural ceramics for high temperature applications.

Technical Highlights

A study of the effect of microstructure on the tensile creep of GTE PY-6 silicon nitride was initiated. Analytical transmission electron microscopy (ATEM) was used to characterize both the microstructure of this material and the cavity damage produced during tensile creep. Examination of PY-6 reaved a variable interface structure, which appears related to a relatively high volume fraction of second phase material of nominally yttrium disilicate composition. Both the nature and width of the interphase separating silicon nitride grains varied, not only from interface to interface but along the same interface. Roughly categorized, interfaces separating adjacent silicon nitride grains were either narrow (1-2 nm) and glassy or were much wider (>10 nm) and largely crystalline (due to devitrification). As a consequence of this variation in interface widths, two different interfacial cavity morphologies are produced during tensile creep depending on temperature and stress. At 1400 C. tensile creep can result in both crack-like cavities of micron size lengths and discrete, ellipsoidal-shaped cavities of 100 to 300 nm dimensions. With increasing stress, crack-like cavity formation is favored and can be related to rapid cavity growth within the largely crystalline second phase contained within the wide interfaces. With decreasing stress, and at lower temperatures (1350 C.), the formation of discrete, ellipsoidal-shaped cavities within narrow, glassy interfaces is favored. As in other grades of silicon nitride examined in the course of this project, creep also results in cavitation of the second phase normally present within multi-grain junctions. These cavities, which resemble inherent porosity, range in size from roughly 200 to over 600 nm and appear to increase in density with increasing strain.

Experimental Technique

The results of this study were obtained by analytical transmission electron microscopy (ATEM). ATEM was used to examine samples of PY-6 silicon nitride (GTE) which had been subjected to tensile creep at 1350 and 1400 C., under the tensile testing portion of this project (WBS 3.4.1.3). At 1400 C., creep lifetimes ranged from 3.5 to over 2500 hours.

Results and Discussion

During the past six months, microstructural analysis of crept PY-6 has shown that this material contains a matrix structure of silicon nitride grains which are largely "blocky" in shape and which range in size from a few tenths of a micron to several microns. The smaller grains tend to be found in clusters interstitial to the larger grains along with second phase crystallites of similar size. As with other grades of silicon nitride much of the retained glass phase devitrifies at the test temperatures. Both direct observation and EDS analysis indicate the presence of a narrow (1 to 2nm) glassy interphase separating most adjacent grains. More generally however, the interface structure in PY-6 was variable, ranging from narrow (1 - 2

nm) and glassy to wide (>10 nm) and largely crystalline (due to devitrification). As illustrated in Figure 1, such variations in interface structure occur even along the same interface. Although incomplete, analyses of the second phases in this material indicate yttrium/silicon oxide or yttrium/silicon oxynitride compositions, consistent with yttria being the sole sintering additive. In this regard, hexagonal nitrogen apatite (H-phase) and orthorhombic delta-phase yttrium disilicate appear to be the primary crystalline products of devitrification of the original "sintering glass".

Tensile creep of PY-6 results in various forms of cavitation depending on temperature and applied stress. At 1400 C. and stresses above 75 mPa, creep rupture occurs at relatively low strains due to interfacial cavitation. Two forms of cavities are observed at interfaces aligned normal to the stress axis. At narrow, glassy interfaces, cavitation results in high densities of discrete, ellipsoidal cavities of 100 to 300 nm dimensions, Figure 2. Similar interfacial cavities form in NT-154, and their nucleation and growth has been described previously. In addition, crack-like cavities of grain size lengths also form, apparently by rapid diffusive growth within the largely crystalline second phase originally present within wider (>10 nm) interfaces, Figure 3. In contrast, samples tested at lower stresses at 1400 C. or at comparable stresses at 1350 C. exhibit only discrete cavities at narrow, glassy interfaces; crack-like cavity growth was not evident. In addition to interfacial cavitation, large scale (>300 nm) cavities at multi-grain junctions were also found in PY-6, Figure 4. As in NT-154, the growth of these large cavities results in the removal of the second phase (which is largely crystalline) from multi-grain junctions and the density of these cavities increases with strain.

Status of Milestones

Milestone 311109 has been delayed from January 30, 1993 to August 30, 1993 to include results from PY-6 in paper comparing cavity formation in different grades of silicon nitride. Other milestones are completed or on schedule.

Publications/Communications

1. W. Luecke, S. M. Wiederhorn, B. Hockey and G. G. Long, "Cavity Evolution During Tensile Creep of Silicon Nitride", Mat. Res. Soc. Symp. Proc. 287, 467-472 (1993).

2. S. M. Wiederhorn, B. J. Hockey, D. C. Cranmer and R. Yeckley, "Transient Creep Behavior of Hot Isostatically Pressed Silicon Nitride", J. Mater. Sci., 28, 445-53 (1993).

References

None

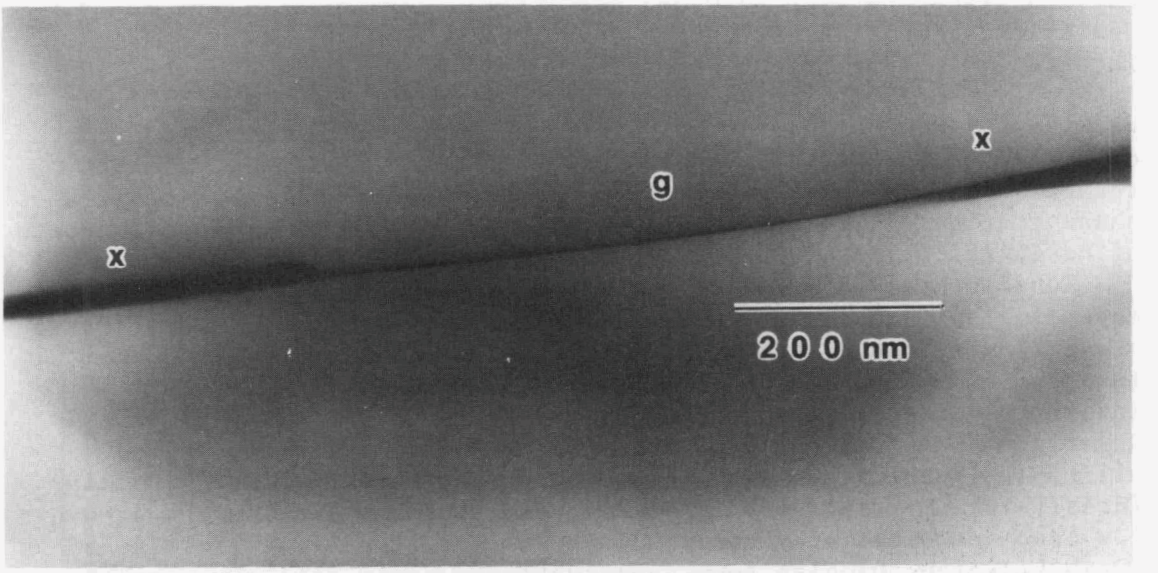

Figure 1. Interface separating silicon nitride grains in PY-6. Within central region (G) interphase is glassy and, typically, 1-2 nm thick; within outer regions (X) interphase is thicker (>10 nm) and contains crystalline second phase.

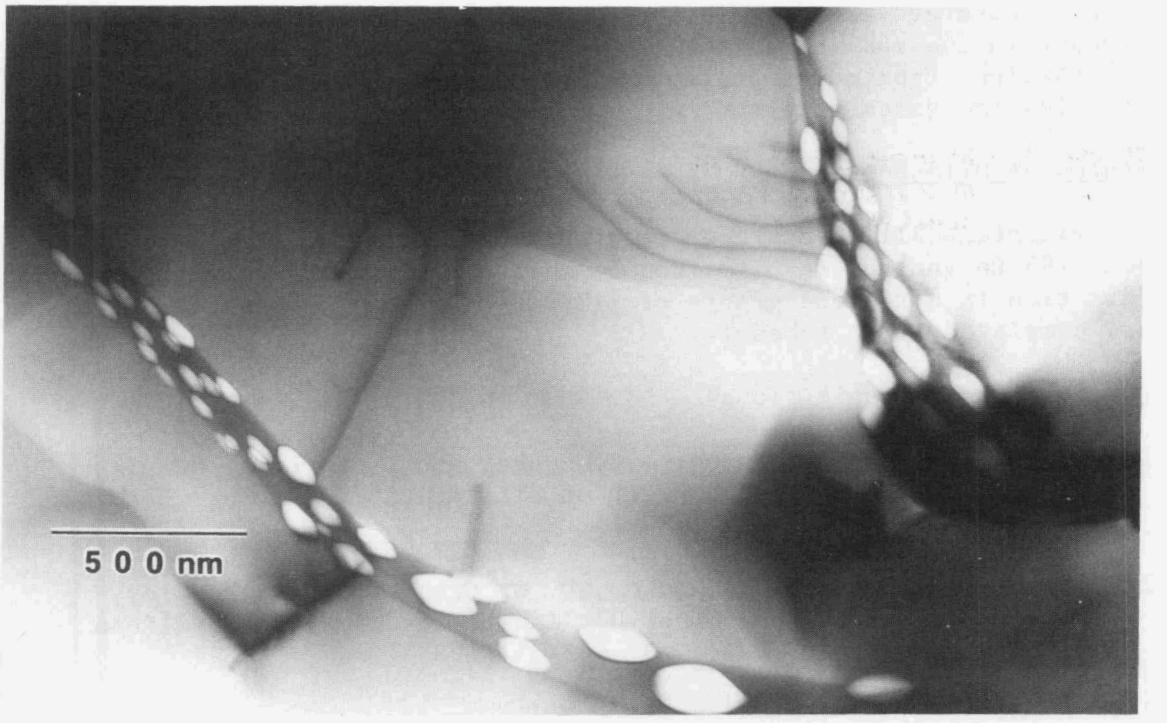

Figure 2. Crack-like interfacial cavity produced in PY-6 during creep at 1400 C. With reference to Fig. 1, rapid cavity growth within wider portions of the interface results in crack-like morphology.

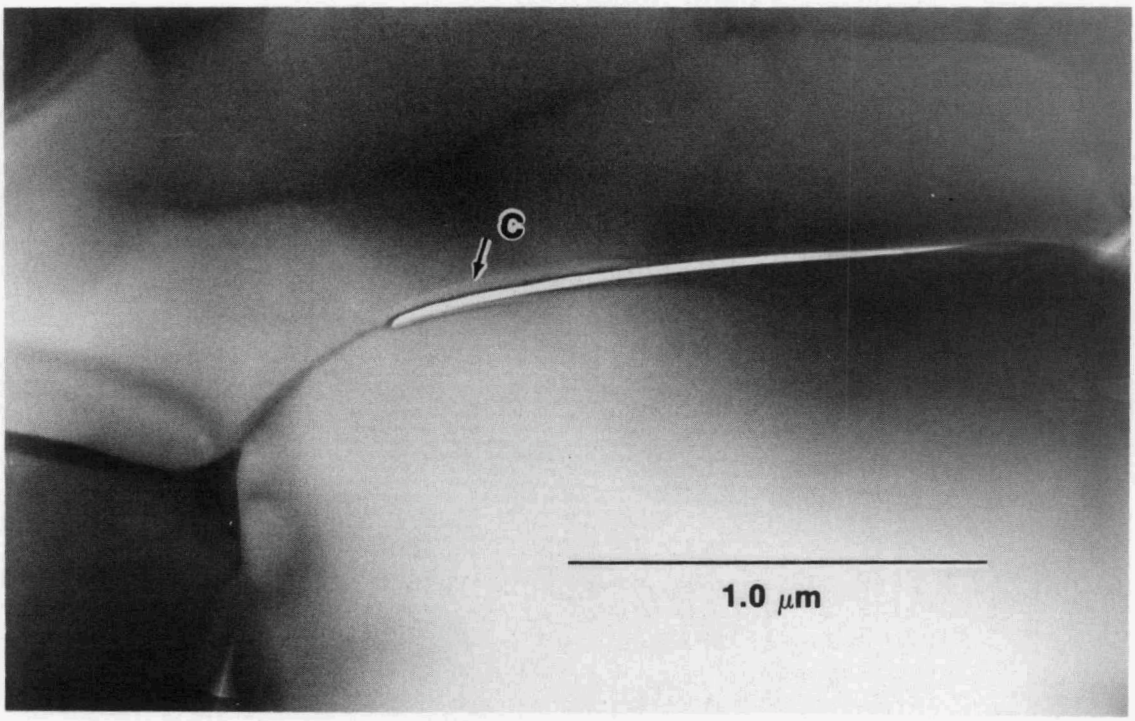

Figure 3. Discrete, ellipsoidal shaped cavities typically produced at narrow (1-2 nm), glassy interfaces in PY-6 during tensile creep.

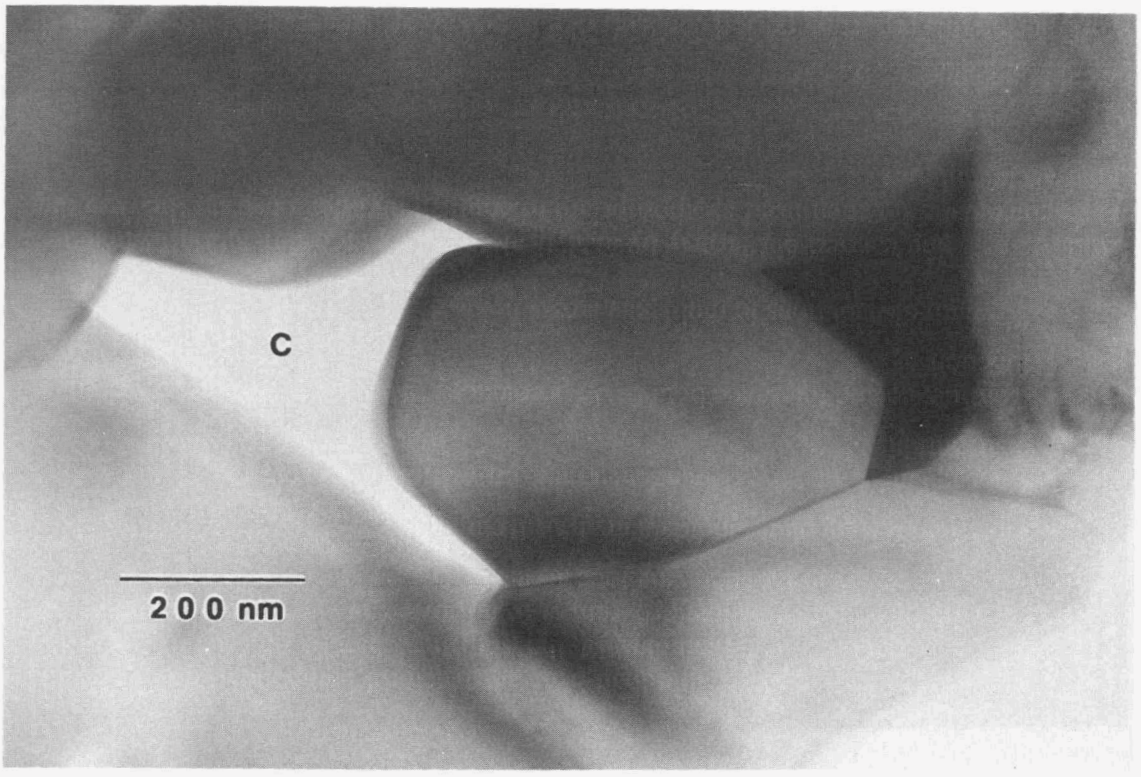

Figure 4. Large-scale multi-grain junction cavity in PY-6. Diffusive transport of second phase from triple and multi-grain junctions during creep results in cavities of varied size and shape.

Mechanical Properties and Microstructural Characterization of Si_3N_4 Ceramics

K. L. More, T. A. Nolan, and L. F. Allard (Oak Ridge National Laboratory)

Objective/scope

The objective of the research is to use analytical and high-resolution electron microscopy to characterize the microstructure of a microwave-annealed GTE SNW-1000 Si_3N_4 ceramic material following mechanical strength (tensile) testing at elevated temperatures in air. This work represents a collaboration with K. Liu of Oak Ridge National Laboratory.

Technical highlights

The material under investigation is a hot-pressed Si_3N_4 supplied by GTE and designated SNW-1000. The Si_3N_4 contains both Y_2O_3 and Al_2O_3, added as densification aids. SNW-1000 specimens for microstructural characterization were initially microwave annealed at either 1400°C for 20 h or 1500°C for 20 h and subsequently creep tested in tension at 1200°C. The processing and creep history for all samples is summarized in Table 1. The mechanical properties of the Si_3N_4 were improved following the microwave annealing. This investigation is being conducted to determine the effects of the microwave annealing on the microstructure of the SNW-1000 and the reason for the subsequent improvement in mechanical properties.

Table 1. SNW-1000 creep specimens supplied for microstructural characterization

Sample designation	Microwave anneal	Creep conditions	Rupture time
SNW-1000-1	1400°C, 20 h	1200°C, 140 MPa	2977 h
SNW-1000-2	1400°C, 20 h	1200°C, 160/180/200	2257 h
SNW-1000-3	1400°C, 20 h	1200°C, 180 MPa	17 h
SNW-1000-4	1400°C, 20 h	1200°C, 160 MPa	12 h
SNW-1000-5	1400°C, 20 h	1200°C, 160 MPa	7 h
SNW-1000-6	1400°C, 20 h	1200°C, 140 MPa	369 h
SNW-1000-7	1500°C, 20 h	1200°C, 160 MPa	3 h
SNW-1000-8	1500°C, 20 h	1200°C, 140 MPa	72 h
SNW-1000-9	1500°C, 20 h	1200°C, 120 MPa	933 h
SNW-1000-10	1500°C, 20 h	1200°C, 130 MPa	427 h

The tensile creep curves for the specimens microwave annealed at 1400°C for 20 h (% strain versus time) are compared to unannealed SNW-1000 in Fig. 1 (creep experiments performed by K. Liu). Note that the creep behavior is enhanced following microwave annealing in some cases (SNW-1000-1 and -2) but not in others (SNW-1000-3 and -5). Similar inconsistencies were observed in the microstructural analysis. X-ray diffraction, the results of which are summarized in Tables 2 and 3, has been conducted on specimens SNW-1000-1, -2, and -3. It is interesting to note that the crystalline second phase was transformed as a result of microwave annealing alone from $Y_{10}Al_2Si_3O_{18}N_4$ (JCPDS #32-1426) as the only phase in the original as-hot-pressed material (see Standard - Table 3) to several different phases (summarized in Table 2). However, the new phases found in the three buttonhead specimens were not the same from one specimen to the next, indicating that the microwave-annealing process is not very reproducible or consistent within the billet from which the specimens were machined. Following high-temperature tensile experiments, additional phases were also found in the specimens, as shown in Table 3. Note that the same phases were found in the gage sections for specimens SNW-1000-1 and -2 but that SNW-1000-3 showed different phases.

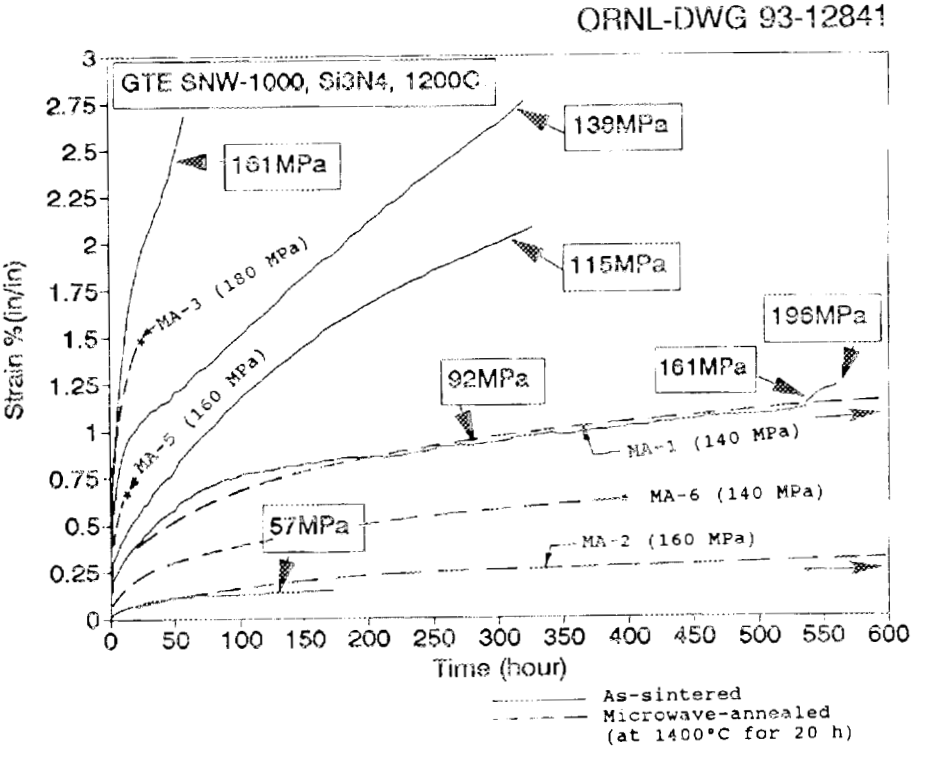

Fig. 1. Creep curves comparing microwave-annealed (1400°C for 20 h) to as-hot-pressed SNW-1000.

Table 2. Summary of X-ray diffraction results for microwave-annealed SNW-1000

Sample	Major Phases	Minor Phases	2θ For I	I/Iβ
SNW-1000-1 NRT0016	β Si_3N_4 33-1160	Y_2SiO_5 36-1476 (I*/a)	28.352	0.094
		$YSiO_2N$ 31-1462, Wollastonite	19.532	0.021
		$Y_{4.67}(SiO_4)_3O$ 30-1457, O-Apatite	32.560	0.009
SNW-1000-2 NRT0017	β Si_3N_4 33-1160	Y_2SiO_5 36-1476 (I*/a)	28.338	0.100
		$YSiO_2N$ 31-1462, Wollastonite	19.446	0.017
		$Al_5Y_3O_{12}$ 33-40 ,YAG	27.368	0.002
SNW-1000-3 NRT0018	β Si_3N_4 33-1160	Y_2SiO_5 36-1476 (I*/a)	28.351	0.126
		$YSiO_2N$ 31-1462, Wollastonite	19.568	0.018

There is probably also some O-apatite present in NRT0017 and NRT0018 but in much smaller quantities than in NRT0016.
No alpha - Si_3N_4 was detected in any of the samples.
A slight trace(100% peak = 1% Imax) of Al2SiO3 was possibly detected in all 3 samples in equal quantities (single peak at 26°

Table 3. Summary of X-ray diffraction results for the gage sections of SNW-1000 tensile tested at 1200 ° C

Sample	Major Phases	Minor Phases	2Q for I	I/I_β
SNW-1000-1 NRT0012	β – Si_3N_4 33-1160	Y_2SiO_5 36-1476 (I*/a)	30.691	0.160
		$Y_2Si_3N_4O_3$ 28-1457 Melilite	18.172	0.016
		$YSiO_2N$ 31-1462 Wollastonite	31.933	0.106
		$Y_{4.67}(SiO_4)_3O$ 30-1457 O-Apatite	32.623	0.030
SNW-1000-2 NRT0013	β - Si_3N_4 33-1160	Y_2SiO_5 36-1476 (I*/a)	30.691	0.122
		$Y_2Si_3N_4O_3$ 28-1457 Melilite	18.172	0.010
		$YSiO_2N$ 31-1462 Wollastonite	31.933	0.056
		$Y_{4.67}(SiO_4)_3O$ 30-1457 O-Apatite	32.623	0.018
SNW-1000-3 NRT0014	β – Si_3N_4 33-1160	$YSiO_2N$ 31-1462 Wollastonite	31.933	0.107
		Y_2SiO_5 41-4 (P21/c)	31.125	0.041
Standard NRT0015	β – Si_3N_4 33-1160	$Y_{10}Al_2Si_3O_{18}N_4$ 32-1426	29.403	0.166

Relative intensity ratios based on β–Si_3N_4 100% peak at 27.1503 ° 2Θ.
α-Si_3N_4 was not detected in any of the samples.

Polished samples for scanning electron microscopy (SEM) and specimens for transmission electron microscopy (TEM) have been prepared. Thus far, the original fracture surfaces and polished longitudinal gage sections have been examined by SEM. The general microstructure of the SNW-1000 can be observed in the original fracture surface of SNW–1000-1. The fracture origin in this specimen was not on the surface, as is often the case in these materials, but was on the specimen interior, as shown in Fig. 2. A typical defect in SNW-1000 is shown in Fig. 3. These large pores are much greater than the grain size of the silicon nitride and are usually greater than several microns in diameter (arrowed black areas in Figs. 2 and 3). These features can also be observed on the longitudinally cut and polished gage sections, but there are differences between the SNW-1000-1, -2, and -3 samples. Figures 4, 5, and 6 are representative low–magnification SEM images from the gage sections in SNW-1000-1, -2, and –3, respectively. The arrowed areas in these images are the large, open areas characteristic of SNW-1000, features normally associated with poor overall mechanical properties in silicon nitride. Note that microwave annealing does not create these areas; these defects are present in large numbers in the starting

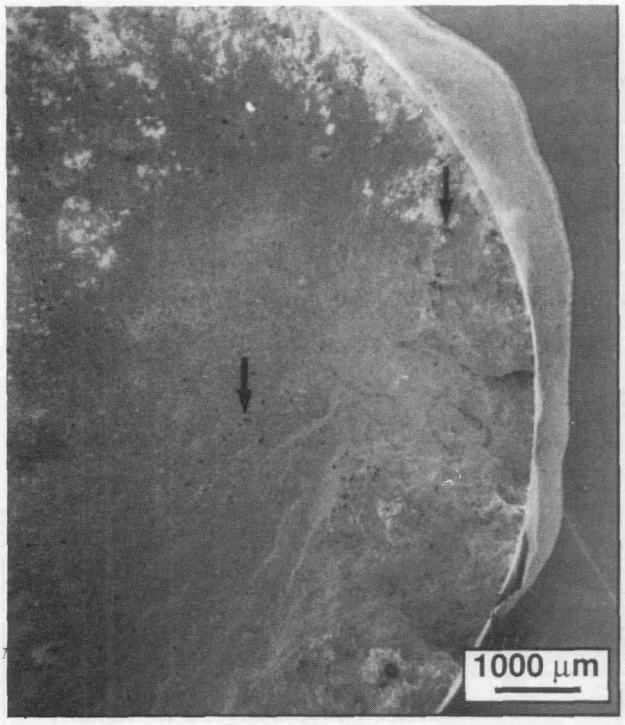

Fig. 2. Fracture surface of SNW-1000-1.

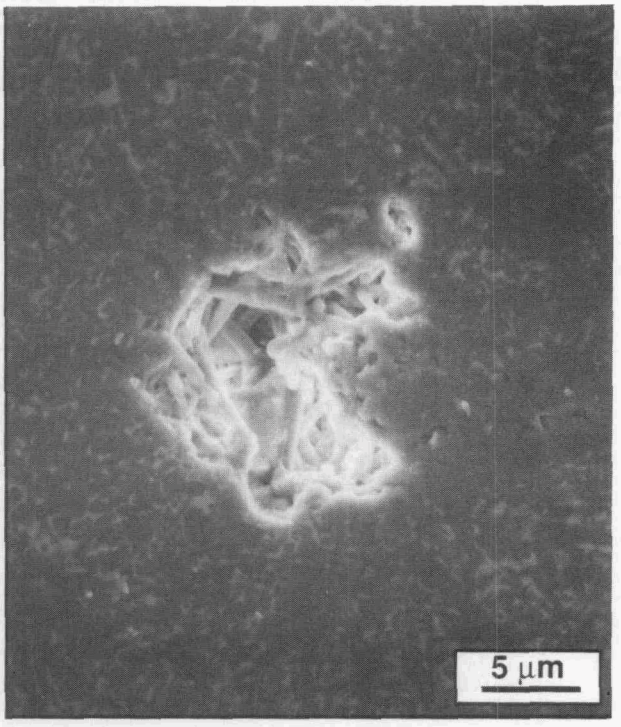

Fig. 3. Large, porous defect found in SNW-1000-1.

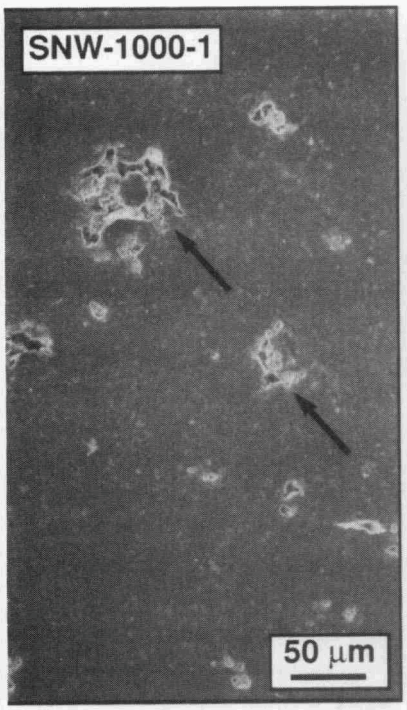

Figure 4.

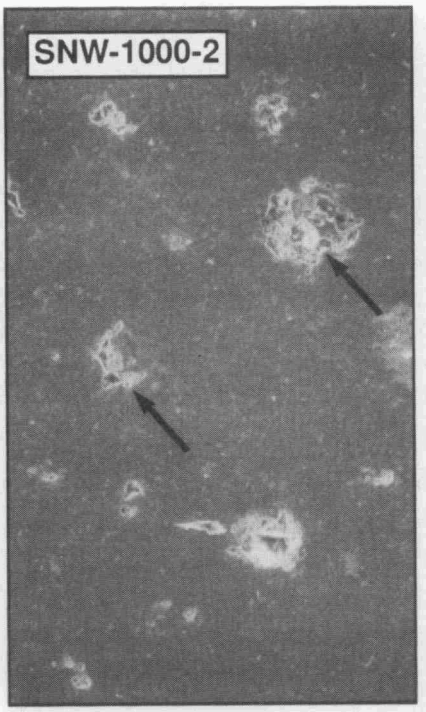

Figure 5.

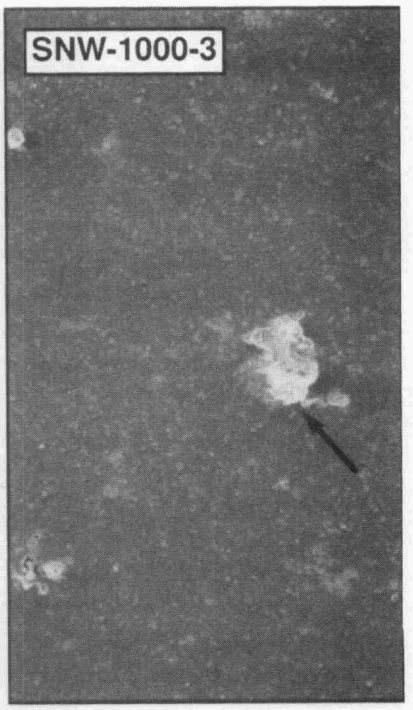

Figure 6.

Figs. 4, 5, and 6. Low-magnification scanning electron microscopy images of polished longitudinal sections from SNW-1000-1, SNW-1000-2, and SNW-1000-3, respectively, following creep.

material. However, it is significant that microwave annealing does not reduce the number of such areas either. Two features that were observed in the microwave-annealed and crept gage sections, but were not observed in the as-hot-pressed specimen, are shown in Figs. 7 and 8. Figure 9 shows a similar image of the as-hot-pressed SNW-1000 for comparison. It appeared that there were quite a few small voids or cavities between silicon nitride grains in the microwave-annealed and crept specimen (see arrowed in Fig. 7), SNW-1000-1. Another feature in the microwave-annealed and crept material was the formation of large "agglomerated" secondary-phase regions (see Fig. 8). It is yet unclear the role that these additional defects played with regard to the creep behavior. In fact, it will be important to look at the TEM specimens, as well as similarly prepared samples of the unannealed and crept material (similar creep conditions), in order to determine the role of the defects.

Status of milestones

Program on schedule.

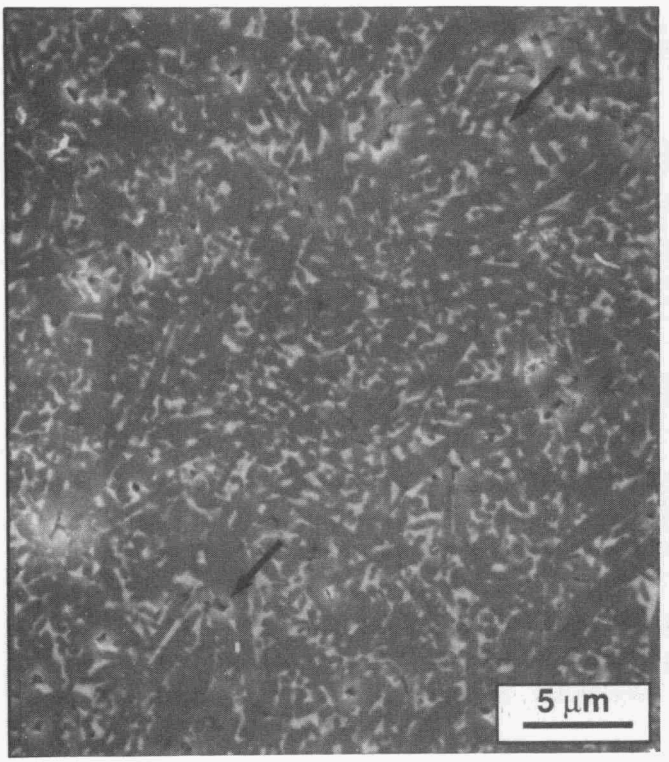

Fig. 7. Scanning electron microscopy image of possible cavitation in SNW-1000-1 following creep.

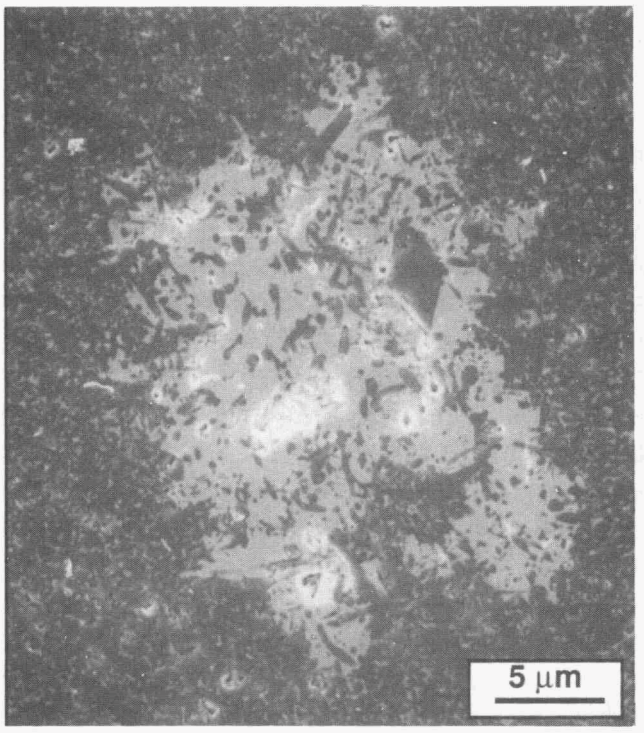

Fig. 8. Scanning electron microscopy image of "agglomeration" of secondary-phase particles in microwave-annealed SNW-1000 following creep.

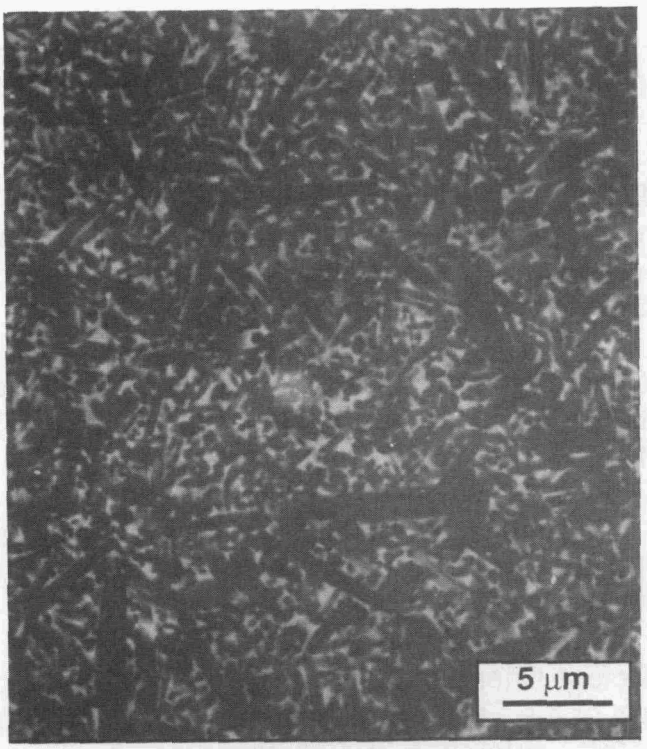

Figure 9. Scanning electron microscopy image of overall microstructure of as-hot-pressed SNW-1000.

Communications/visits/travel

1. K. L. More, D. A. Koester, and R. F. Davis, "Microstructural Characterization of a Creep-Deformed SiC Whisker-Reinforced Si_3N_4 Composite," presented at the Frontiers of Electron Microscopy in Materials Science Meeting, May 21, 1990, Oak Brook, Ill. Published in *Ultramicroscopy*.

2. K. L. More, D. A. Koester, and R. F. Davis, "The Role of Interfaces in the Creep-Deformation of a SiC Whisker-Reinforced Si_3N_4 Composite," presented at the International Congress for Electron Microscopy, August 17-22, 1990, Seattle, Wash. Published in conference proceedings.

3. D. A. Koester, K. L. More, and R. F. Davis, "Steady-State Creep of Hot-Pressed SiC Whisker-Reinforced Silicon Nitride," presented at the U.S.-Japan Seminar on Processing, Microstructure, Development, and Properties of Advanced Ceramics and Their Composites, Tokyo, Japan, August 20-22, 1990.

4. K. L. More, D. A. Koester, and R. F. Davis, "Creep Behavior of a SiC Whisker-Reinforced Si_3N_4 Composite in Air and Nitrogen," presented at the 2nd International Ceramic Science and Technology Congress, Orlando, Fla., November 12-15, 1990.

5. K. L. More, D. A. Koester, and R. F. Davis, "Creep of a SiC Whisker-Reinforced Silicon Nitride in Compression and Bending," presented at the 15th Annual Conference on Composites and Advanced Ceramics, Cocoa Beach, Fla., January 13-16, 1991.

6. K. L. More, "Defect Characterization in a CVD α-Si_3N_4," presented at the 93rd Annual Meeting of the American Ceramic Society, Cincinnati, Ohio, April 28 - May 2, 1991.

7. T. A. Nolan, L. F. Allan, D. W. Coffey, M. K. Ferber, and K. L. More, "Microstructural Characterization of Tensile and Flexural Creep Deformation and Fatigue in a Si_3N_4 Ceramic," ibid.

8. K. L. More, "Defect Characterization in a CVD α-Si_3N_4," presented at the 49th Annual Meeting of the Electron Microscopy Society of America, San Jose, Calif., August 5-9, 1991. Published in conference proceedings.

9. D. A. Koester, K. L. More, and R. F. Davis, "Steady-State Creep of Hot-Pressed SiC Whisker-Reinforced Silicon Nitride," presented at the 1st Canadian International Composites Conference and Exhibition, Montreal, Canada, September 4-6, 1991. To be published in conference proceedings.

10. K. L. More, D. A. Koester, and R. F. Davis, "Microstructural Analysis and Mechanisms of Deformation of Hot-Pressed SiC Whisker-Reinforced Silicon Nitride," presented at the 1st International Symposium on the Science of Engineering Ceramics, Osaka, Japan, October 14-18, 1991. To be published in conference proceedings.

11. K. L. More, "Defect Characterization in a CVD α-Si_3N_4," invited presentation at ASM/TMS Materials Week '92, Chicago, Ill., November 2-5, 1992.

Problems encountered

None

Publications

1. K. L. More, D. A. Koester, and R. F. Davis, "Microstructural Characterization of a Creep-Deformed SiC Whisker-Reinforced Si_3N_4 Composite," *Ultramicroscopy* **37**, 263 (1991).

2. K. L. More, D. A. Koester, and R. F. Davis, "The Role of Interfaces in the Creep-Deformation of a SiC Whisker-Reinforced Si_3N_4 Composite," p. 382 in *Electron Microscopy 1990*, Vol. 4, ed. L. D. Peachey and D. B. Williams, San Francisco Press, San Francisco, 1990.

3. D. A. Koester, K. L. More, and R. F. Davis, "Deformation and Microstructural Changes in SiC Whisker-Reinforced Si_3N_4 Composites," *J. Mater. Res.* **6**[12], 2735 (1991).

4. K. L. More, "Defect Characterization in a CVD α-Si_3N_4," p. 936 in *Proceedings of the 49th Annual Meeting of the Electron Microscopy Society of America*, ed. G. W. Bailey, San Francisco Press, San Francisco, 1991.

5. D. A. Koester, K. L. More, and R. F. Davis, "The High Temperature Creep of a SiC Whisker-Reinforced Si_3N_4 in an Air Ambient," submitted to *J. Mater. Res.*

6. T. A. Nolan, L. F. Allard, D. W. Coffey, C. R. Hubbard, and R. A. Padgett, "Microstructure and Crystallography of Titanium Nitride Whiskers Grown by a VLS Process," *J. Am. Ceram. Soc.* **74**[11], 2769 (1991).

Project Data Base

B. L. Keyes (Oak Ridge National Laboratory)

Objective/scope

The objective of this task is to develop a comprehensive computer data base containing the experimental data on properties of ceramic materials generated in the total effort. This computer system should provide a convenient and efficient mechanism for the compilation and distribution of the large amounts of data involved. The data base will be available in electronic form to all project participants. In addition, periodic hard-copy summaries of the data, including graphical representation and tabulation of raw data, will be issued to provide convenient information sources for project participants.

Technical highlights

Data collection and input began again during this period. Information is being taken from the latest Ceramic Technology Project semiannual and bimonthly progress reports and from data supplied by individual contributors. Silicon nitrides (NT-154, GTE PY6, NT-164, and various other Si3N4-based compositions) comprise the main class of ceramic now under investigation in this project, so most of the data input has been on silicon nitride-based materials. Test results for monolithics and composites, as joins and solids, are currently in the input process.

The data base was sent to six requestors during this semiannual period. A few minor errors were found and corrected during the data preparation and reformatting process. Upgrading and updating the data base also continued during this period.

New terms and field descriptions were added to the GLOSSRY file in the data base. Several fields from the PROCESS data base were included, and the fracture test definitions were transferred from the TESTBKGD file. Test specification information, including the specification number, date of last revision, specification organization, and a brief description of the specification, will be added to the data base as time permits.

Work resumed on the computerized user interface during this period. The main search modules were revised, tested, and debugged in March 1993; more modules will be added to this core to expand the capabilities of the interface. Improved printer output and increased search criteria are goals for the next reporting period. The estimate of a September 1993 completion-through-draft date is still on schedule.

Revisions based on reviews were made on the September 1992 data base summary report. This document is now in the process of being published.

Data base personnel are involved in developing an American Society for Testing and Materials (ASTM) guideline document (for the E-49 Committee on Computerized Materials Data Bases) on ceramic material designations for computer data base storage. The main obstacle has been a lack of an accepted general nomenclature and classification system for ceramics. A VAMAS document on classification of ceramics has been chosen as a basis for the ASTM guideline and, after extensive revisions, appears to be the most likely candidate for adoption by the international community. Future interactions with the C-28 Committee on Advanced Ceramics should speed up progress on the E-49 guideline.

Communications/visits/travel

B. L. Keyes travelled to Miami, Florida, in November 1992 to attend the semiannual ASTM E49 committee meetings. Work is continuing on developing standards for computerizing ceramic materials property data. Travel is being restricted this year to conserve funding and to allow time for other ASTM committees to make progress on ceramic-related problems that are impacting the E49 guideline document.

Problems encountered

None.

Status of milestones

The September 1992 data base summary report is now in publication.

Publications

The Ceramic Technology for Advanced Heat Engines Project Data Base: September 1992 Summary Report is in publication.

3.2 TIME-DEPENDENT BEHAVIOR

Fracture Behavior of Toughened Ceramics

H. T. Lin, P. F. Becher, and W. H. Warwick (Oak Ridge National Laboratory)

Objective/scope

Ceramic composites, such as fiber- and whisker-reinforced ceramics, particulate phase composites, and ceramics with similar grain structures, offer important advantages for heat engine applications. Chief among these is the improved fracture toughness which can be achieved by appropriate design of microstructural and material parameters. Previous studies show that these materials often exhibit substantial improvements in damage, thermal shock, and slow crack growth resistances. However, design of such systems must also consider those factors influencing their performance at elevated temperatures.

In response to these needs, studies are conducted to determine the mechanical properties (e.g., creep, delayed failure, strength, and toughness) at elevated temperatures for these toughened ceramics. Particular emphasis is placed on understanding how microstructure and composition influence the mechanical performance at elevated temperatures and the stability of these properties for extended periods at these temperatures. The knowledge gained from these studies provides input on how to modify materials to optimize their mechanical properties for the temperature ranges of interest.

Technical highlights

The research efforts during this 6-month period were devoted to evaluating: (1) the flexural and tensile creep behavior of *in situ* reinforced silicon nitride ceramics containing elongated grain structure and (2) tensile creep response of Al_2O_3 composite reinforced with SiC whiskers. These are part of a large effort to understand the effect of microstructure and composition on the creep response of silicon nitride ceramics.

1. Creep Behavior of In Situ Reinforced Si_3N_4 Ceramics

Flexural creep behavior. The flexural creep properties of silicon nitride ceramics hot-pressed with 11.5% La_2O_3 (11La) and 4% Y_2O_3-6% La_2O_3 (4Y6La) were evaluated at temperatures of 1300 and 1370°C under selected stress levels in air. The silicon nitride ceramics were fabricated under the work breakdown structure (WBS) Element 1.2.3.1. (Dispersion-Toughened Ceramic Composite). Figure 1 shows the creep data of silicon nitride material containing 11La additive at temperatures of 1300 and 1370°C and at stresses from 100 to 460 MPa in air. The creep results[1] of material with 2Sr6Y are also shown for comparison. The results indicate that the 11La material exhibits similar creep behavior, e.g., creep rate and stress exponent, to the material with 2Sr6Y additive under the same test conditions. The linear regression analysis of the creep rate versus stress curves yields a stress exponent of one. For ceramics containing a low-viscosity secondary phase, a stress exponent of one is generally attributed to a viscous creep mechanism. The creep data for 4Y6La material at 1300°C is shown in Fig. 2 with the creep results of materials containing additives of 2Sr6Y and 11La. The results indicate

ORNL-DWG 93-12786

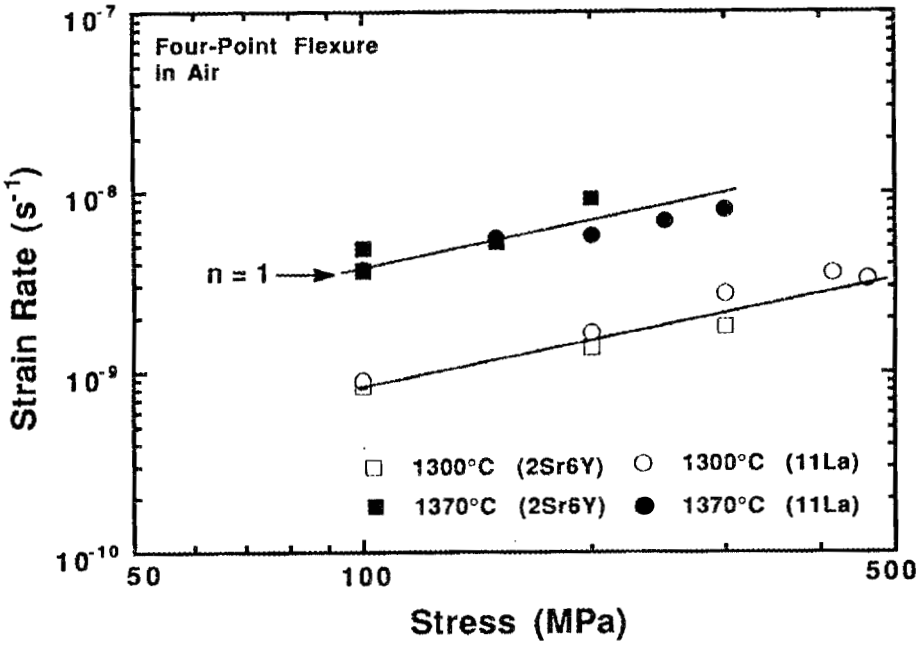

Fig. 1. Strain rate versus stress curves for Si_3N_4 ceramics with 11La and 2Sr6Y additives.

ORNL-DWG 93-12787

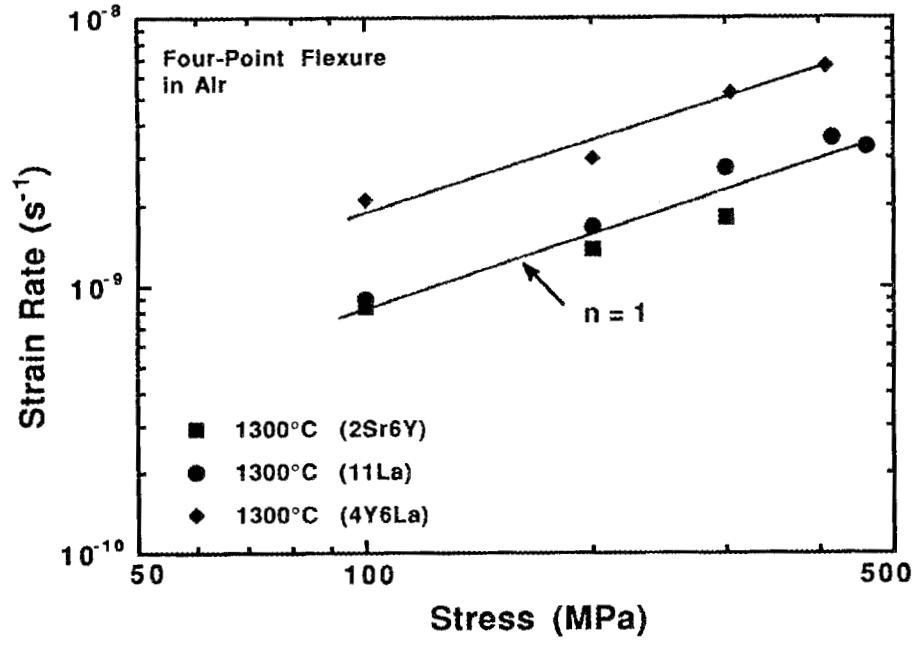

Fig. 2. Strain rate versus stress curves for Si_3N_4 ceramics with additives of 4Y6La, 11La, and 2Sr6Y.

that the 4Y6La material exhibits creep rates which are about two times higher than silicon nitride materials hot pressed with 11La and 2Sr6Y additives under the applied stress levels. The stress exponent of 4Y6La at 1300°C is also one.

The similarity in creep behavior for materials containing 2Sr6Y and 11La additives could be attributed to their relatively high eutectic temperature with respect to the temperature range investigated in this study. The eutectic temperature for La-Si-O-N is estimated to be about 1450°C and that of Sr-Y-Si-O-N is between 1350 and 1400°C.[2,3] In addition, X-ray and transmission electron microscopy results indicated that both materials have apatite phases present at grain boundary which lead to an increase in viscosity of grain boundary phase consistent with enhanced creep resistance. On the other hand, the eutectic temperature of grain boundary phase in 4Y6La material[3] is estimated to be between 1500 to 1550°C, which is higher than materials containing additives of 11La and 2Sr6Y. The high eutectic temperature of 4Y6La material is reflected by its good strength retention (77%) up to 1400°C.[4] However, the creep results at 1300°C show that the 4Y6La material is less creep resistant as compared with 11La- and 2Sr6Y-containing materials. Scanning electron microscopy examinations indicate that the creep degradation in 4Y6La material was due to its lower oxidation resistance as compared to 11La and 2Sr6Y materials at 1300°C. In addition, the variation in the distribution of size and aspect ratio of elongated grains and amount of refractory crystalline phases in the grain boundary glasses could also lead to the difference in creep resistance.

Tensile creep behavior. Tensile creep tests were performed on *in situ* reinforced silicon nitride ceramics containing the compositions of 5 vol % Yb_2O_3 (SN5Yb) and 10 vol % Yb_2O_3 plus 0.5 wt % Al_2O_3 (SN10YbAl). The materials were sintered to greater than 99% of theoretical density by a gas-pressure sintering process and were subsequently annealed for 12 h at 1250°C to crystallize the grain boundary phase(s). The X-ray analysis following the post-heat treatment indicates that the secondary phase in the SN5Yb material is $Yb_2Si_2O_7$ and in the SN10YbAl is Yb_2SiO_5 plus $Yb_2Si_2O_7$ as a minor phase. Note that the secondary phase at the two-grain junction remains amorphous after the post-heat treatment.[5]

Figure 3 shows the tensile creep results for SN5Yb and SN10YbAl materials at 1200°C and at stresses ranging from 50 to 150 MPa in air. The results indicate that the SN10YbAl material exhibits creep rates that are five times higher than the SN5Yb composition under the stress range employed. This may be due to the presence of alumina (SN10YbAl) in the remaining glassy phase that lowers the eutectic temperature. Regression analysis of the creep rate versus stress curves yields a creep stress exponent (n) of four. The creep-controlling mechanism for ceramics containing viscous secondary phase(s) is generally attributed to diffusional or viscous flow processes with a stress exponent of one. The high stress exponent, also obtained for other silicon nitride ceramics tested in tension,[6,7] is due to extensive creep cavitation damage.

2. Stress State Effect on Creep Behavior of Al_2O_3-SiCw Composites

As a model for understanding the influence of reinforcing phases such as the elongated grain structures in Si_3N_4 ceramics, the creep behavior of whisker-reinforced ceramics is being characterized. In this case, the whiskers not only have the same shape but also the same function as the larger elongated grains in silicon nitride ceramics. In

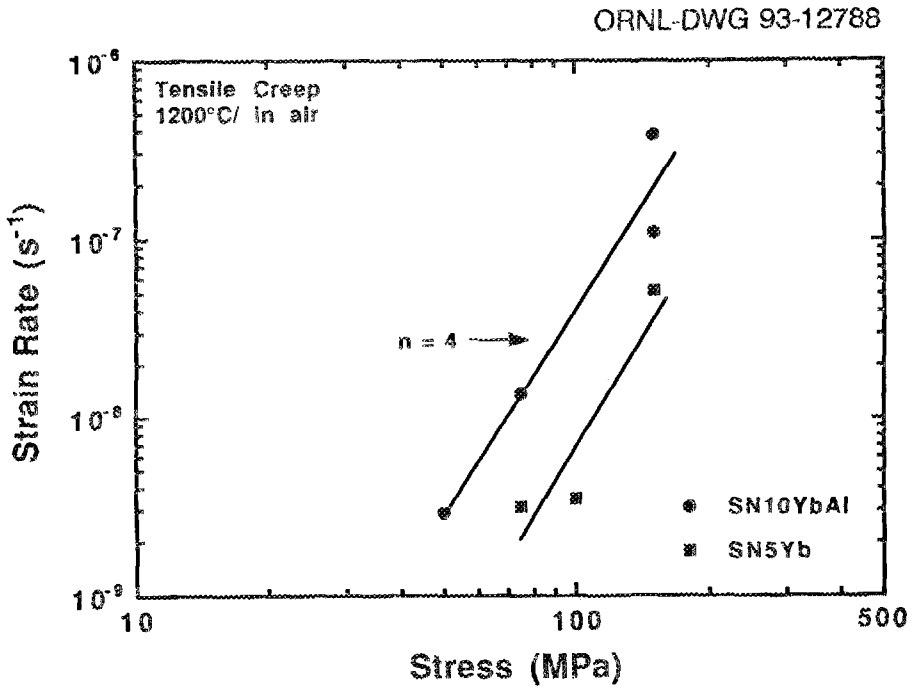

Fig. 3. Strain rate versus tensile stress curves of Si_3N_4 ceramics with additives of 5Yb and 10YbAl.

addition, the whisker-reinforced ceramics are of interest themselves for elevated-temperature applications. Using the whisker-reinforced ceramics in these initial studies also allows us to systematically alter the microstructure and characterize the resulting creep response. In addition, a data base is being developed for the creep response under tensile versus flexure versus compressive loading in order to fully characterize the creep and cavitation behaviors. The tensile and flexural creep response of alumina composites reinforced with 20 vol % SiC whiskers at 1300° C under selected stress levels in air was determined in this reporting period and is compared to earlier flexure and compressive creep results.

Two slightly different alumina-20 vol % SiC whisker composites using the F-9 SiC whiskers from Advanced Composite Materials Corporation (ACMC) were tested. The composite designated ORNL-1 was made of a mixture of alumina (Baikowski CR10) and whiskers blended in a high-speed shear mill at ORNL. The sample designated as ORNL-2 was prepared from a blend of alumina powder and whiskers provided by ACMC. Neither contained densification additives, and each composite was hot pressed at ORNL under identical conditions to produce a dense composite with a fine-grained (1- to 2-μm) matrix.

Figure 4 shows the creep results as a function of applied stress state for two alumina composites reinforced with 20 vol % SiC whiskers at 1300° C at stress levels from 50 to 230 MPa in air. Creep data for the ORNL-1 composite in compression and flexure reported previously[6] are also included. The results indicate that the creep rates of both ORNL-1 and -2 composites are not sensitive to the applied stress state under the test conditions employed. The insensitivity of creep rate to stress state has been observed for

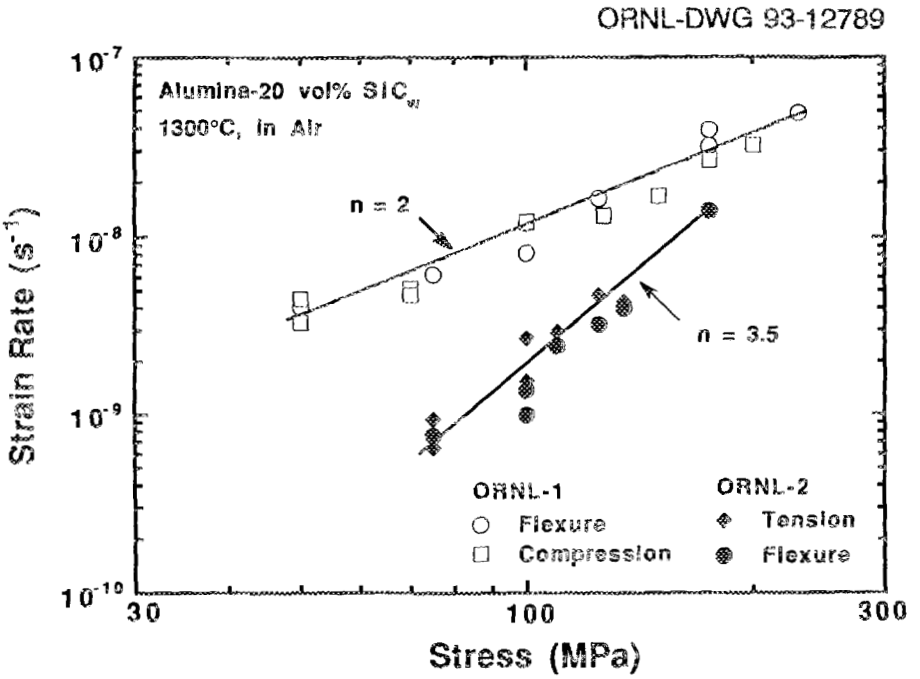

Fig. 4. The strain rate versus applied stress behavior for two SiC_w-reinforced aluminas for tensile, flexural, and compressive loading at 1300°C.

polycrystalline alumina without amorphous grain boundary phases.[8-10] On the other hand, the results show that the creep rates of ORNL-2 composite are three to eight times lower than the ORNL-1 composite. In addition, the stress dependence of ORNL-2 composite is ~ 3.5 and that of ORNL-1 is ~ 2, indicative of different creep-governing mechanisms. The higher stress exponent (3.5) in ORNL-2 composite is an indication of creep cavitation. The differences in processing method, alumina powder, and batch of whiskers led to the observed differences in creep behavior between ORNL-1 and -2 composites. However, the results of these tests indicate that different stress states will yield the same creep rates in SiC whisker-reinforced aluminas as long as the dominant creep mechanism remains the same.

Status of milestones

On schedule.

Publications

None

References

1. H. T. Lin, P. F. Becher, and W. H. Warwick, "Fracture Behavior of Toughened Ceramics," pp. 33-35 in *Ceramic Technology Project Bimonthly Technical Progress Report*, ORNL/CF-92/86, May 1, 1992.

2. D. P. Thompson, "Alternative Grain-Boundary Phases for Heat-Treated Si_3N_4 and β'-Sialon Ceramics," *Proc. Br. Ceram. Soc.* **45**, 1-13 (1990).

3. "Phase Diagram for Ceramics," 1969 Supplement, The American Ceramic Society, Inc., Columbus, Ohio, 1969.

4. H. T. Lin, P. F. Becher, and W. H. Warwick, "Fracture Behavior of Toughened Ceramics," pp. 265-70 in *Ceramic Technology Project Semiannual Progress Report*, ORNL/TM-11984, Martin Marietta Energy Systems, Inc., Oak Ridge Natl. Lab., March 1992.

5. J. S. Vetrano, H.-J. Kleebe, E. Hampp, M. J. Hoffmann, R. M. Cannon, and M. Rühle, "Yb2O3-Fluxed Sintered Silicon Nitride: Part 1: Microstructure Characterization," submitted to *J. Mater. Sci.*

6. M. K. Ferber and M. G. Jenkins, "Evaluation of the Strength and Creep-Fatigue Behavior of Hot Isostatically Pressed Silicon Nitride," *J. Am. Ceram. Soc.* 75[9], 2453-62 (1992).

7. M. K. Ferber and M. G. Jenkins, "Rotor Data Base Generation," pp. 332-40 in *Ceramic Technology for Advanced Heat Engines Project Semiannual Progress Report for April 1990 to September 1990*, ORNL/TM-11719, Martin Marietta Energy Systems, Inc., Oak Ridge Natl. Lab.

8. H. T. Lin, W. H. Warwick, and P. F. Becher, "Fracture Behavior of Toughened Ceramics," pp. 265-70, in *Ceramic Technology Project Semiannual Progress Report*, ORNL/TM-11984, Martin Marietta Energy Systems, Inc., Oak Ridge Natl. Lab. March 1992.

9. A. G. Robertson, D. S. Wilkinson, and C. H. Cáceres, "Creep and Creep Fracture in Hot-Pressed Alumina," *J. Am. Ceram. Soc.* 74[5], 915-21 (1991).

10. S. M. Wiederhorn of the National Institute of Standards and Technology, personal communication.

Cyclic Fatigue and Static Fatigue of Toughened Ceramics

K. C. Liu, C. O. Stevens, and C. R. Brinkman (Oak Ridge National Laboratory)

Objective/scope

The objective of this task is multifold:

1. To develop, design, fabricate, and demonstrate the capabilities of performing cyclic fatigue in tension-tension/compression and static fatigue testing in uniaxial tension/compression on candidate structural ceramics at elevated temperatures. While significant progress has been made in several areas of the experimental front (such as specimen/grip alignment, specimen heating, and high-temperature extensometry), testing capabilities in fully reversed tension-compression cyclic fatigue and compression creep in uniaxial direction remain to be developed and demonstrated.
2. To develop the baseline information on cyclic fatigue behavior of candidate ceramics and, in turn, to establish a design data base.
3. To develop creep and creep-rupture data bases for advanced heat-engines design applications in the range of 1150 to 1370°C.
4. To evaluate and refine existing constitutive models based on the information generated above.
5. To develop new constitutive models to facilitate design analyses of high-temperature structural components and improve their reliability.

Technical highlights

Cyclic Fatigue of SiC_w/Al_2O_3 (CERCOM PAD-AS34W)

It has been shown that addition of SiC whiskers in Al_2O_3 can raise the room-temperature tensile strength by 50% and fatigue strength in the high-cycle range by a factor of two. However, the strengthening effects diminish as temperature increases to 1200°C, as shown by a comparison of fatigue data obtained previously for both monolithic Al_2O_3 and Sic_w/Al_2O_3 ceramic composite tested at 1200°C (see Fig. 1). The degenerative temperature at which the strengthening effects starts to diminish is not known.

To fill the information gap, cyclic fatigue behavior of the composite material was investigated at 1000°C. All testing was performed in cyclic tension-tension using a constant-amplitude, triangular waveform with a stressing rate of 21,000 MPa/min, as shown in Fig. 2(*a*). The cyclic load may be increased intermittently in small steps after completing a large block of cycles at each peak stress, as shown in Fig. 2(*b*). Since neither the tensile strength nor fatigue strength of the composite material at 1000°C is known, a first specimen was cycled to the peak stress of 250 MPa as a starting point, which was roughly equal to the average of room-temperature and 1200°C fatigue strengths. The peak stress was raised to 275 MPa after completing a first block of $\sim 10^6$ cycles. The specimen failed after completing an additional block of 194,000 cycles, bringing to a total of 1.256×10^6 cycles to failure.

A second specimen was cycled to the peak stress of 275 MPa from the beginning to the end with a fatigue rupture life of 529,161 cycles. A third specimen was cycled to 285 MPa with a fatigue life of 191,265 cycles. More testing is to follow.

ORNL-DWG 92-15418R1

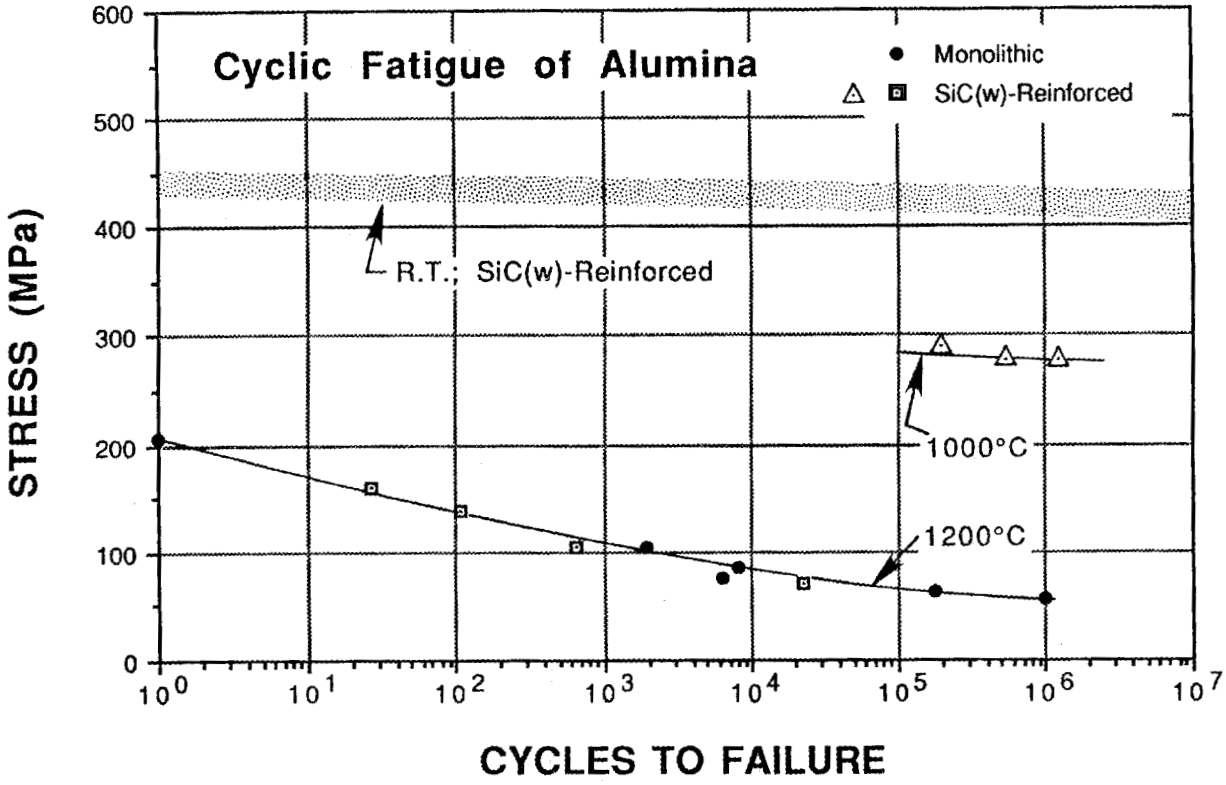

Fig. 1. Cyclic fatigue behavior of monolithic Al_2O_3 and SiC whisker-reinforced Al_2O_3 matrix composite materials tested at 1200°C.

ORNL-DWG 93-12790

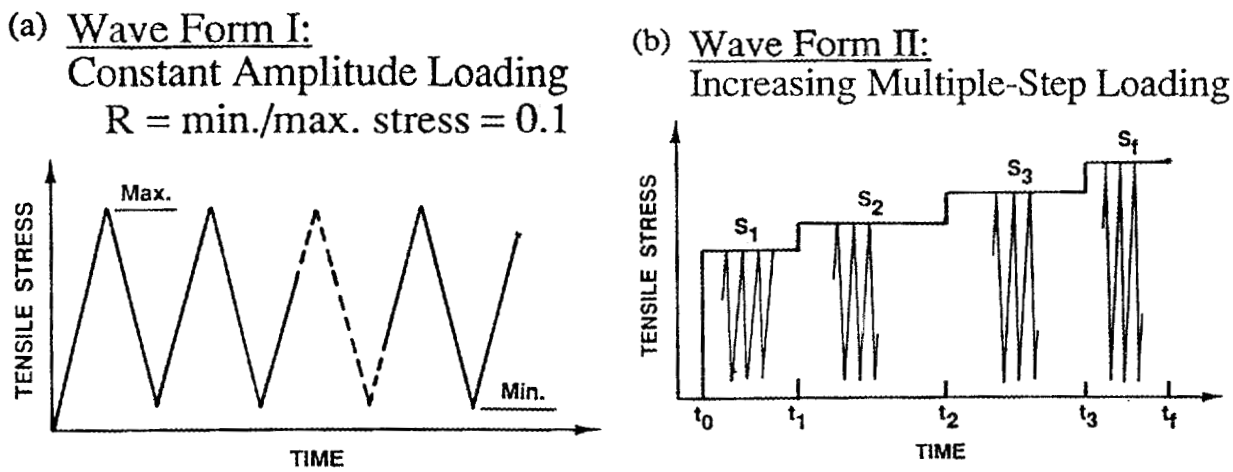

Fig. 2. Wave forms used in cyclic fatigue tests.

The limited information obtained to date indicates that the composite material at 1000° C retains about 60 to 70% of the room-temperature fatigue strength. No fatigue data for monolithic alumina at 1000° C are available for comparison at this time.

Cyclic Fatigue of SiC (Hexoloy-SA) at 1400° C.

It has been shown that fatigue strength of SiC at 1400° C can be enhanced dramatically by means of coaxing, i.e., applying cyclic loading in steps intermittently from low to high stresses. Coaxing with a starting stress below 75% of the tensile strength (σ_t) has successfully raised the fatigue strength in excess of the tensile strength by 25%. Cycling with a starting stress above 80% of the tensile strength can raise the fatigue strength but failed to extend the high-cycle life beyond 10^6 cycle.

To confirm the above stated findings, two fatigue tests were performed at 1400° C, but, none of the tests were successfully carried out to the conclusion due to an inadvertent power outage. The first specimen was cycled with a starting stress of 190 MPa (75% of σ_t). After it completed a block of megacycles (10^6 cycles), the test was shut down by a power outage. Restarting of the test was unsuccessful because the specimen fractured at the specimen shank.

The second specimen was cycled with a starting stress of 205 MPa (82% of σ_t). The cyclic stress amplitude was then increased in a step of 15 MPa after completing a block of about 1 megacycle at each stress level. The heating system was shut down again due to an open thermocouple after the test completed a third block of megacycles at 235 MPa. The specimen was also damaged during the inadvertent shutdown. The speci-men could have been saved if the shutdown had not occurred unattended in the night. However, some useful information was obtained although the tests were incomplete in both cases. Power outage (unplanned) has been a serious problem to the high-cycle fatigue testing.

Creep testing of NT-154 Si_3N_4

Three long-term creep tests at 1250° C continued since the last reporting period. The status of the three ongoing tests is as follows:

Specimen 20-56: The test is continuing at 1250° C under a constant stress of 175 MPa. The specimen has accumulated a total of about 0.83% strain after 15,760 h (~1.8 years) of testing to date, as shown in Fig. 3. Creep deformation rate was once thought to have reached the steadystate after completing the first 5000 h of testing. However, the creep rate continued to decrease subsequently after 7000 h of testing. Although the creep rate was reasonably steady at a rate of about 3.3E-11 s^{-1} during the last 3500 h of testing, there was a hint of continuing deceleration of creep rate.

Specimen 20-00: The test is continuing at 1250° C under a constant stress of 150 MPa. The specimen has accumulated a total of about 0.45% strain after about 12,000 h (~16.5 months) of testing, as shown in Fig. 4. The creep rate was reasonably steady after completing the first 2000 h of testing until the most recent power outage at t = 10,500 h. Subsequent restarting of the test yielded the same creep rate for a duration of about 400 h as if no test interruption had occurred. However, the creep rate decreased rather sharply thereafter. This observation is inconclusive at this time, since the last segment of the creep curve is too short to be extrapolated reliably.

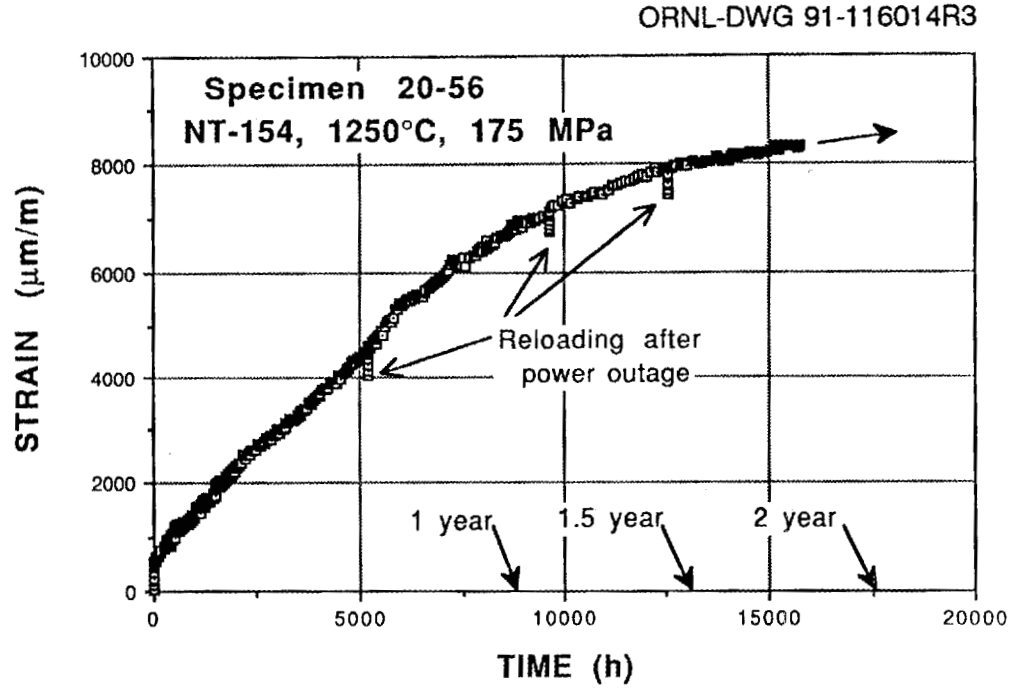

Fig. 3. Creep curve of NT-154 Si_3N_4 (specimen 20-56) tested at 1250°C under an applied stress of 175 MPa.

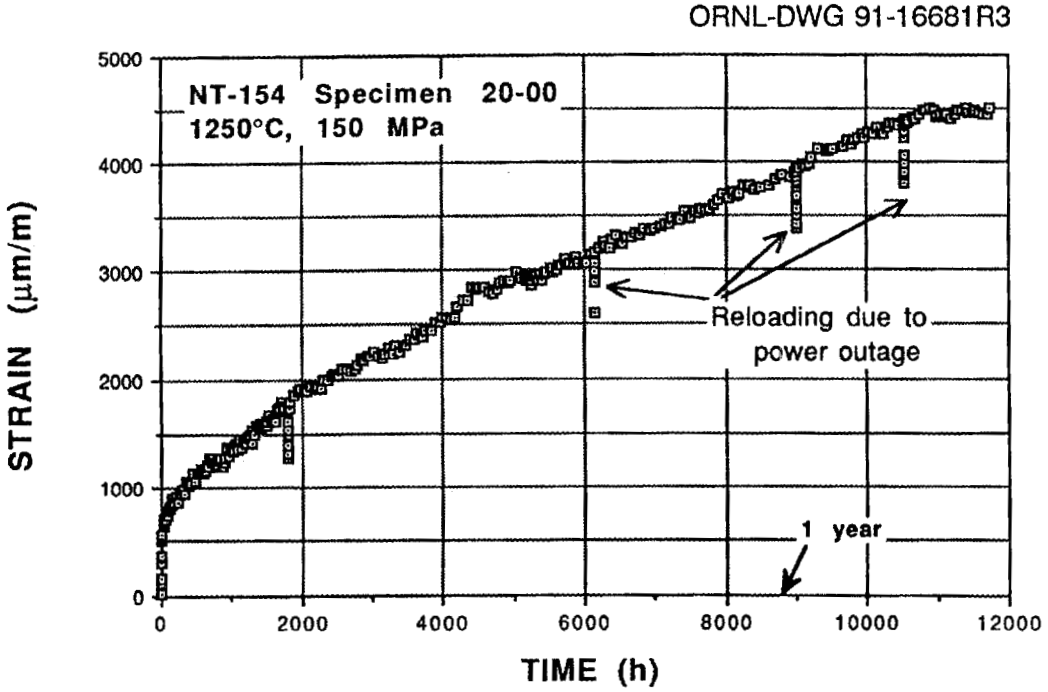

Fig. 4. Creep curve of NT-154 Si_3N_4 (specimen 20-00) tested at 1250°C under an applied stress of 150 MPa.

Specimen 20-32: The specimen has been tested at 1250°C under a constant stress of 150 MPa for about 5500 h since the stress was reduced from the earlier testing condition at 175 MPa, as shown in Fig. 5. The total test time to date is 8460 h (300 h short of 1 year). This specimen is currently deforming at a strain rate of about 4.17E-11 s^{-1}, and the test is continuing.

Creep testing of GN-10 Si_3N_4

The status of three ongoing creep tests on GN-10 Si_3N_4 at the low-stress end of the creep rupture range (long-term tests) is as follows:

Specimen 89367-1-2: The specimen has been tested at 1200°C and 125 MPa for 1650 h with a total creep strain of 0.243%, as shown in Fig. 6, and the test is continuing. Strain recovery was observed to have occurred thrice between the period of t = 650 and 1450 h. Interestingly, each strain recovery consumed less time to complete its cycle compared to the immediate preceding recovery period, as in the order of approximately 400, 200, and 100 h for each of the three recovery periods. Careful examination indicates the behavior was apparently the result of internal changes in the material and was not caused by external changes such as fluctuations of ambient temperature. This phenomenon appeared to be further accentuated in the following test.

Specimen 89367-1-3: This specimen has been tested at 1150°C and 150 MPa for 1500 h with a total creep strain of about 0.1% to date, as shown in Fig. 7. The creep behavior was more erratic compared to the situation observed in the preceding case. Perhaps low applied stresses facilitated internal redistribution of strain energy. The sporadic occurrences of strain recovery appear to be a common feature of low creep-rate tests in the range of 10^{-7} to 10^{-8} h^{-1}. If the results of the above test are the guide, the specimen is currently undergoing a strain recovery period, as indicated by the upper curve. However, from a different perspective, a creep curve can be drawn contiguously, as indicated by the lower curve, if the strain riser occurring between t = 750 to 950 h is an aberration. The uncertainty will be clarified when more test data become available.

Specimen 89367-1-1: This specimen has been tested for about 6700 h at 1300°C under a constant stress of 50 MPa, as shown in Fig. 8, and the test is continuing. It appears that the creep rate will continue to decrease as testing continues.

Creep Behavior of Microwave-Annealed (MA) SNW-1000 Si_3N_4

Testing of ten MA specimens, six annealed at 1400°C for 20 h and four at 1500°C for 20 h, has been completed. Test results are summarized in Table 1 and compared with unannealed data in Figs. 9 and 10. The unannealed data were obtained by North Carolina A & T State University.[2] Note that all the above tests were done at 1200°C.

Examinations of Figs. 9 and 10 indicate that microwave annealing was, generally speaking, effective for enhancement of creep resistance in terms of lowering creep rate and, hence, extending creep rupture life. However, some annealed specimens showed inferior creep rupture lives, which fell even below those for the unannealed specimens tested under the same applied stresses.

Further examinations indicate that creep resistance was enhanced more effectively by the low-temperature (1400°C) annealing compared to the high-temperature (1500°C)

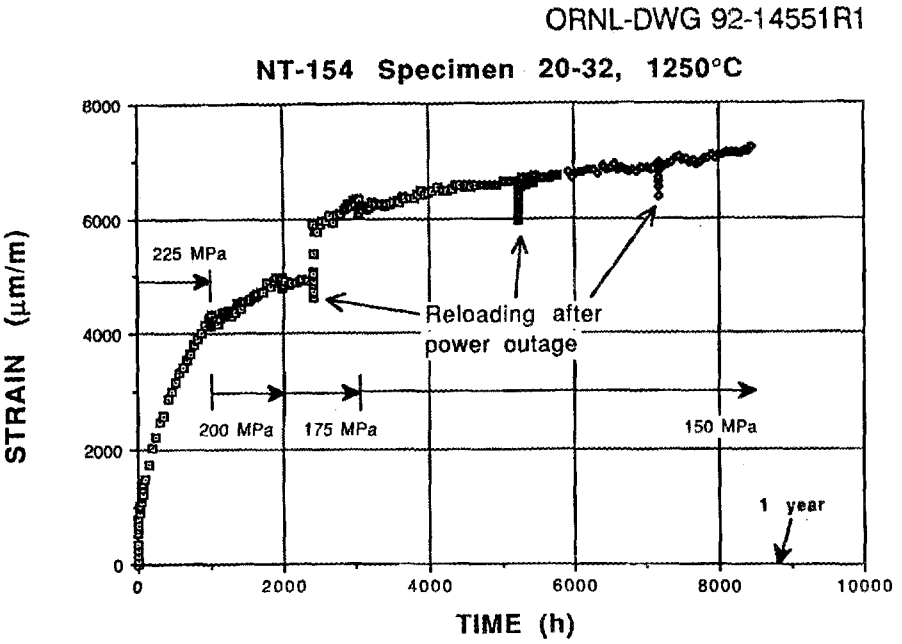

Fig. 5. Creep curve of NT-154 Si_3N_4 (specimen 20-32) tested at 1250°C under step-down loading conditions. The specimen was tested initially at 225 MPa followed by partial unloading in steps of 25 MPa at the end of each 1000 h of testing until the applied stress decreased to 150 MPa.

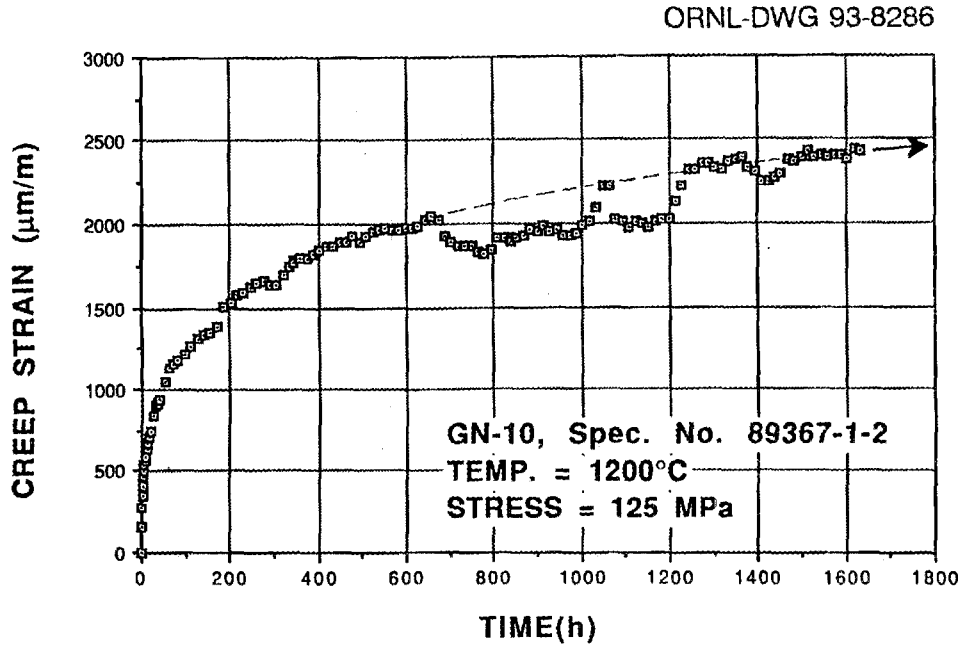

Fig. 6. Creep curve of GN-10 Si_3N_4 (specimen 89367-1-2) tested at 1200°C with an applied stress of 125 MPa. The strain recovery behavior was believed to be results of internal changes in the material and was not caused by external factors such as fluctuations of ambient temperature.

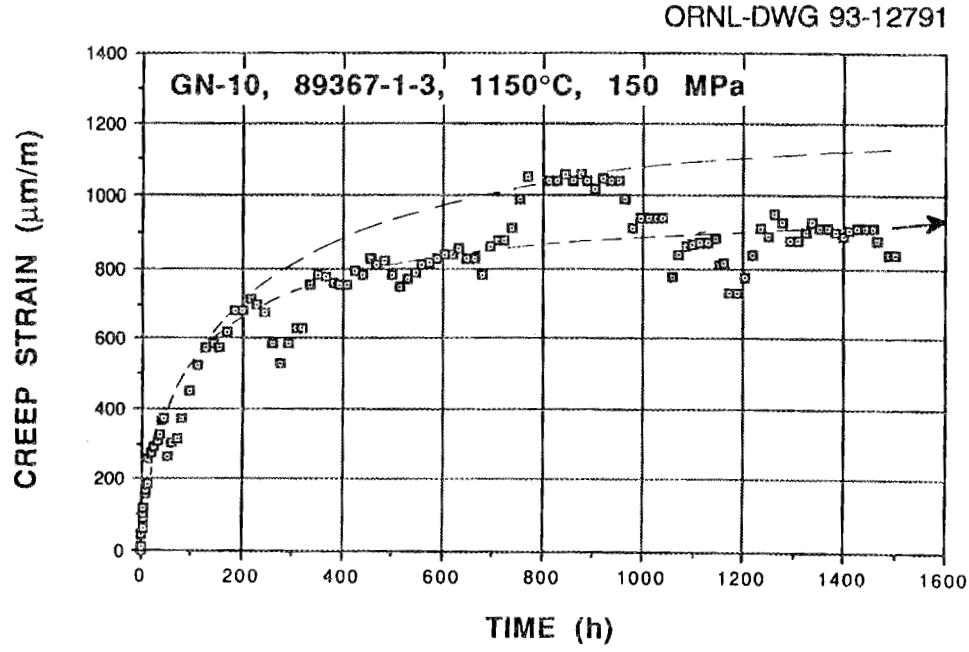

Fig. 7. Creep curve of GN-10 Si_3N_4 (specimen 89367-1-3) tested at 1150°C with an applied stress of 150 MPa. Two creep curves were drawn to approximate the creep behavior due to uncertainty in the limited data obtained to date.

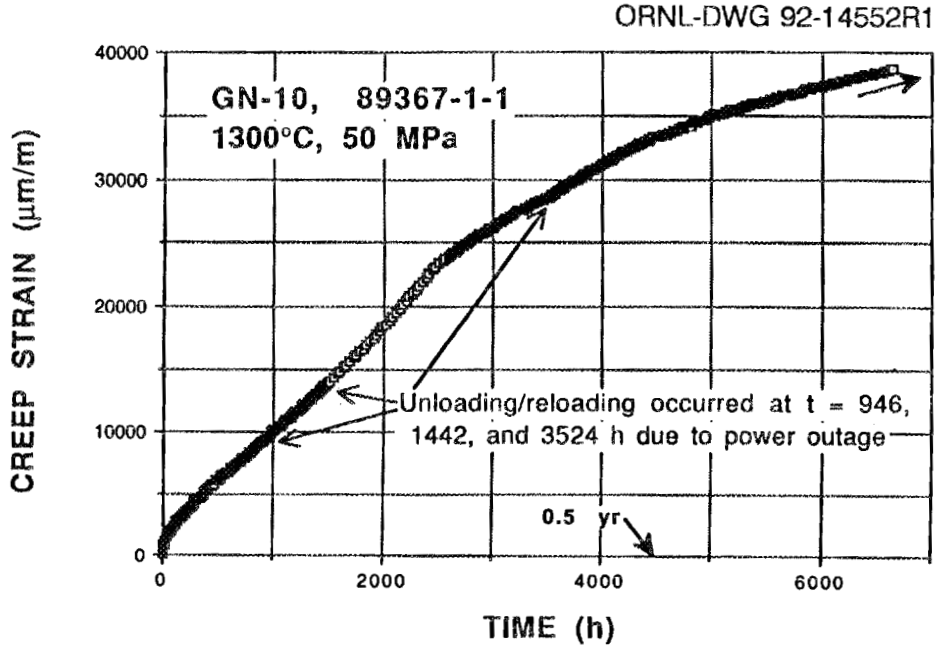

Fig. 8. Creep curve of GN-10 Si_3N_4 (specimen 89367-1-1) tested at 1300°C with an applied stress of 50 MPa.

Table 1. Results of creep tests on microwave-annealed SNW-1000 Si_3N_4 at 1200°C

Group (annealing temp/time)	Specimen No.	Stress (MPa)	Rupture time (h)	Creep strain (%)
No. 1 1400°C/20 h	MA-1	140	2976.9	2.645
	MA-2	160/180/200	2256.88	0.744
	MA-3	180	16.65	1.382
No. 2 1400°C/20 h	MA-4	160	12.1	--
	MA-5	160	7.42	0.609
	MA-6	140	368.65	0.59
No. 3 1500°C/20 h	MA-7	160	3.42	0.127
	MA-8	140	71.51	0.664
	MA-9	120	933.3	1.290
	MA-10	130	427.1	1.736

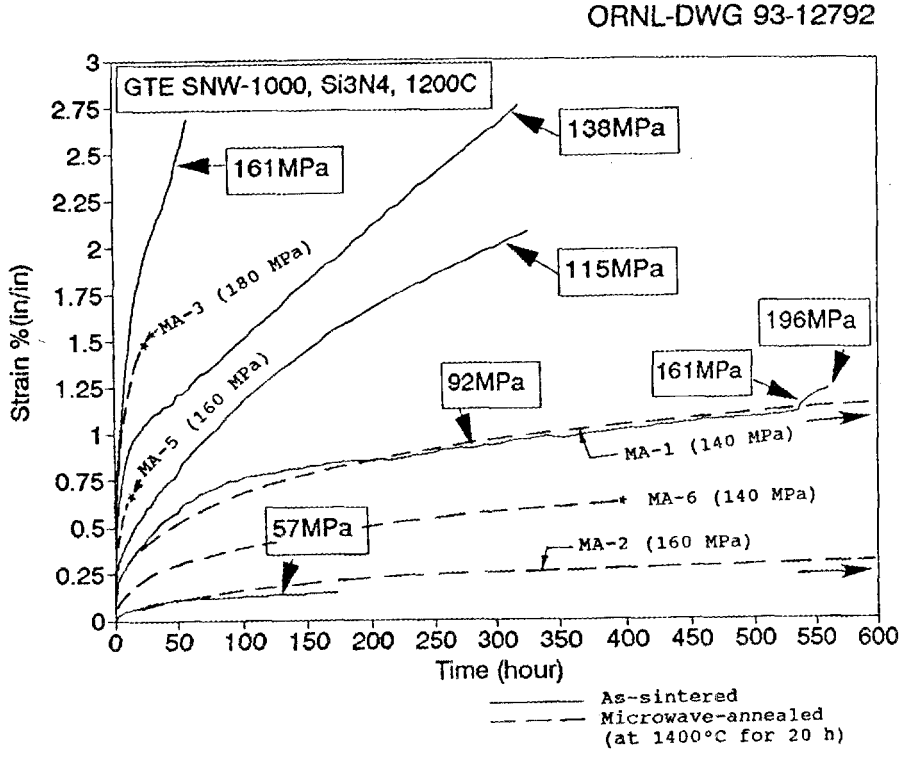

Fig. 9. Comparisons of creep curves for unannealed and microwave-annealed specimens (at 1400°C for 20 h) tested at 1200°C under applied stresses as indicated. Annealing at 1400°C appeared to enhance creep resistance of this material. However, the inconsistency in creep performance exhibited by specimens MA-2 and MA-5, which also showed inferior creep rupture life, remains to be resolved.

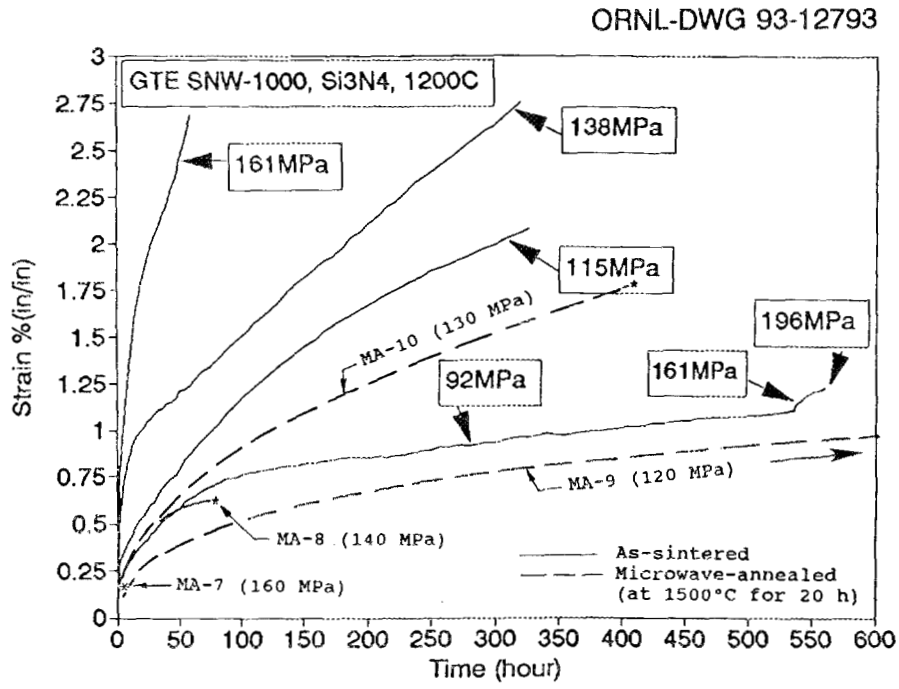

Fig. 10. Comparisons of creep curves for unannealed and microwave-annealed specimens (at 1500°C for 20 h) tested at 1200°C under applied stresses as indicated. Annealing at 1500°C somewhat enhanced the creep resistance but was much less effective compared to that at 1400°C. However, inferior creep rupture lives exhibited by specimens MA-8 and MA-10 showed otherwise.

annealing treatment. However, inconsistencies in creep behavior within the group are clearly discernable in two situations where severely contrasting creep behavior was illustrated by specimens MA-2 and MA-5 (both annealed at 1400°C for 20 h) and that specimen MA-2 under 160 MPa showed lower creep rate compared to that for specimens MA-1 and MA-6 under a lower stress of 140 MPa. Some plausible reasons for the inconsistencies can be cited. Since these specimens were annealed at an earlier date, while the developing technology was still in its infancy, some degree of nonuniformity in annealing was not entirely unexpected. Furthermore, the annealing was done in three separate batches with numbers of specimens grouped in three, three, and four, as indicated in Table 1; batch-to-batch variations in annealing can not be ruled out. It was also learned that heating may bias toward one or two specimens when more than two specimens were heated together in a bundle, due to the nature of microwave heating. To avoid the heating bias, specimen blanks must be annealed individually. True reasons for the inconsistencies will not be known until detailed microstructural analyses are completed.

ATTAP Tensile Rupture/Creep Testing

Tensile rupture characterization tests for GN-10 specimens were completed. Test parameters and test results are summarized in Table 2, and data are shown in Fig. 11.

Table 2. ATTAP stress-rupture test matrix for GN-10 Si_3N_4

Stress (ksi)	Specimen No.	Minimum creep rate (m/m s^{-1})	Time to rupture (h)	Creep strain at failure (%)
1204° C (2200° F)				
30	E-2	1.54 E-8	57.35	0.633
	F-2	3.5 E-8	41.16	0.871
	G-4	3.13 E-9	>307.5	0.613
32.5	F-3	1.34 E-7	9.92	0.513
	F-4	1.24 E-7	13.55	0.662
35	G-2	4.37 E-8	23.48	0.493
	C-4	5.11 E-8	16.93	0.386
	H-1	1.91 E-7	5.23	0.361
	D-1	1.79 E-8	51.54	0.346
40	H-2	2.66 E-7	2.87	0.274
	B-1	3.85 E-7	4.26	0.46
	B-2	4.26 E-8	26.63	0.421
1260° C (2300° F)				
22.5	E-3	6.51 E-8	20.76	0.879
	F-1	1.65 E-7	12.65	1.191
	I-3	5.77 E-8	20.15	0.796
25	G-3	1.05 E-7	13.78	0.74
	D-3	1.14 E-8	78.98	0.658
	D-4	5.61 E-7	114.5	0.608
	I-2	6.82 E-7	2.11	0.567
27.5	H-3	5.60 E-7	2.47	0.532
	I-1	8.81 E-7	1.73	0.567
	B-4	2.74 E-7	4.99	0.497
30	C-1	5.52 E-7	2.88	0.561
1315° C (2400° F)				
10	D-5	3.72 E-9	>150	0.334
15	E-1	9.69 E-8	18.4	1.101
20	C-2	2.87 E-7	6.85	0.984
	C-3	6.40 E-7	2.73	0.870

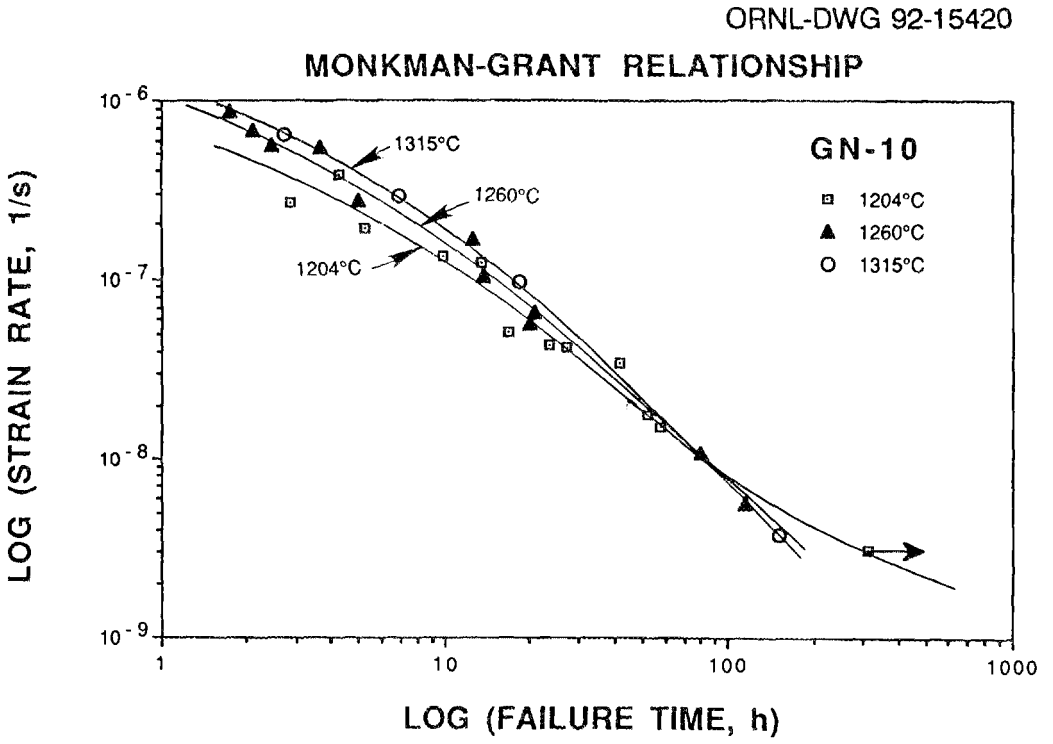

Fig. 11. Creep rupture data for GN-10 Si_3N_4 showing that the Monkman-Grant Curves are nonlinear and temperature dependent.

The distribution of the final rupture data shown in Fig. 11 indicates that a straight-line Monkman-Grant relationship can not appropriately represent the data collectively. The curves, which were drawn visually in Fig. 11, for GN-10 are not only nonlinear but also weakly dependent on temperature, contrary to the earlier cursory observations that the Monkman-Grant relationship was approximately linear and independent of temperature.

The above information has been transmitted to GAPD for a review and inclusion in their final report.

Important Findings and Observations

Examinations indicate that creep resistance of SNW-1000 Si_3N_4 can be enhanced by microwave annealing but more effectively by the low-temperature (1400°C) annealing compared to the high-temperature (1500°C) annealing. However, the optimum annealing temperature is not known at this time.

Status of milestones

1. Completed stress-rupture tests on both GN-10 and NT-154 Si_3N_4 ceramics at elevated temperatures by November 30, 1992 (Milestone 321510).

2. Milestone 321416 (to complete tensile and fatigue tests on MA Si_3N_4 ceramics by March 31, 1993) will be deferred due to the delay and cancellation of the purchase order to acquire SNW-1000 Si_3N_4.

Publications

1. K. C. Liu and J. L. Ding, "A Mechanical Extensometer for High Temperature Tensile Testing of Ceramics," will appear in the *ASTM Journal of Testing and Evaluation*, American Society for Testing and Materials, Philadelphia, September 1993 (in press).

2. J. L. Ding, K. C. Liu, and C. R. Brinkman, " A Comparative study of Existing and Newly Proposed Models for Creep Deformation and Life Prediction of Si_3N_4," will appear in Life Prediction Methodologies and Data for Ceramic Materials, ASTM Special Technical Publication (STP) No. 1201, ed C. R. Brinkman and S. F. Duffy, American Society for Testing and Materials, Philadelphia, 1993 (in press).

3. J. L. Ding, K. C. Liu, and C. R. Brinkman, "Development of a Constitutive Model for Creep and Life Prediction of Advanced Silicon Nitride Ceramics," in *Proceedings of the Annual Automotive Technology Development Contractors' Coordination Meeting, Dearborn, Michigan, November 2-5, 1992*, Society of Automotive Engineers, Warrendale, Pa., 1993.

4. O. M. Jaadan, K. C. Liu, and H. Pih, "Studies of Fatigue in Ceramic Materials by Acoustic Emission," submitted to *J. of Mater. Sci.* for publication, April 1993.

References

1. K. C. Liu, C. O. Stevens, and C. R. Brinkman, "Cyclic Fatigue of Toughened Ceramics," in *Ceramic Technology Project Semiannual Progress Report for April 1992 through September 1992*, ORNL/TM 12363, Martin Marietta Energy Systems, Inc., Oak Ridge Natl. Lab., July 1993.

2. J. Sankar, A. D. Kelkar, R. Vaidyanathan, and J. Gao, "Creep Testing of SNW-1000 Sintered Silicon Nitride," pp. 293-305, in *Proceedings of the Annual Automotive Technology Development Contractors' Coordination Meeting, Dearborn, Michigan, October 28-31, 1991*, P-256, Society of Automotive Engineers, Inc., Warrendale, Pa., June 1992.

Rotor Data Base Generation

C.-K. J. Lin, A. Wereszczak, and M. K. Ferber (Oak Ridge National Laboratory)

Objective/scope

The goal of the proposed research program is to systematically study the tensile strength of a silicon nitride ceramic as a function of temperature and time in an air environment. Initial tests will be aimed at measuring the statistical parameters characterizing the strength distribution of three sample types (two tensile specimens and one flexure specimen). The resulting data will be used to examine the applicability of current statistical models, as well as sample geometries, for determining the strength distribution.

In the second phase of testing, stress-rupture data will be generated by measuring fatigue life at a constant stress. The time-dependent deformation will also be monitored during testing so that the extent of high-temperature creep may be ascertained. Tested samples will be thoroughly characterized using established ceramographic, scanning electron microscopy (SEM), and transmission electron microscopy (TEM) techniques. A major goal of this effort will be to better understand the microstructural aspects of high-temperature failure including:

1. extent of slow crack growth (SCG),
2. evolution of cavitation-induced damage and fracture,
3. transition between brittle crack extension and cavitation-induced growth, and
4. crack blunting.

The resulting stress-rupture data will be used to examine the applicability of a generalized fatigue-life (SCG) model. If necessary, model refinements will be implemented to account for both crack blunting and creep damage effects. Insights obtained from the characterization studies will be crucial for this modification process. Once a satisfactory model is developed, separate stress-rupture (confirmatory) experiments will be performed to examine the model's predictive capability. Consequently, the data generated in this program will not only provide a critically needed base for component utilization in automotive gas turbines but also facilitate the development of a design methodology for high-temperature structural ceramics.

Technical progress

Studies of the high-temperature mechanical properties of a high-performance silicon nitride (PY6)* were continued this reporting period. The PY6 material is fabricated by hot isostatic pressing (HIP) using 6 wt % yttria as the densification aid. The microstructure typically consists of 1 to 6-μm-long acicular grains surrounded by equiaxed grains 0.1 to 1.0 μm in diameter. This morphology leads to a relatively dense microstructure. The silicon nitride grains, which are generally in the form of β-Si_3N_4, are separated by relatively thin layers of an amorphous yttrium silicate. The intergranular phase is also present in the triple points as a crystalline yttrium silicate. The exact phase composition of these intergranular com-pounds depends upon the HIP conditions.

*PY6 silicon nitride, GTE Laboratories, Inc., Waltham, Massachusetts.

A comprehensive study of the cyclic fatigue behavior in this HIPed silicon nitride at elevated temperatures was completed during this reporting period. Data were generated using button-head tensile specimens (6.35-mm gage diameter and 35-mm gage length), which were machined from isopressed and HIPed rods 160 mm long and 22 mm in diameter. Three wave forms were used (trapezoidal at 0.1 Hz with 0.5-s ramp and 4.5-s dwell, triangular at 0.1 Hz, and sinusoidal at 10 Hz) at consistent stress ratio R = 0.1 over the temperature range of 1150 to 1370° C.

In conventional ceramic fatigue analysis, an SCG model (with a power law relationship between crack growth rate and stress-intensity factor) is widely used for estimating fatigue life. With the assumption that all fatigue failures occur from growth of the initial flaws to final, critical sizes, the following relations can be obtained for uniform stress tests:

$$t_{sf} = \beta \sigma_s^{-N} , \tag{1}$$

and

$$t_{cf} = \beta \sigma_{max}^{-N} \tau \left(\int_0^{\tau} [f(t)]^N dt \right)^{-1} . \tag{2}$$

In Eq. (1), t_{sf} is the time to failure for static fatigue under a constant stress, σ_s; β is a constant related to initial flaw size and geometry; and N is the crack growth exponent. Time to failure in cyclic fatigue, t_{cf}, is given in Eq. (2) where σ_{max} is the maximum stress, τ is the cycle period, and f(t) is a function of time associated with the cyclic wave form such that the applied stress in a cycle can be described as $\sigma(t) = \sigma_{max} f(t)$. Details of the derivation of Eqs. (1) and (2) are given in ref. 1. The effective time to failure for cyclic fatigue can be defined as follows:

$$t_{cf,eff} = t_{cf} \tau^{-1} \left(\int_0^{\tau} [f(t)]^N dt \right) . \tag{3}$$

Thus, for equivalent values of σ_{max} and σ_s, the effective time to failure in cyclic fatigue is equal to the failure time in static fatigue, provided that SCG similar initial flaws is the primary mechanism for all the failures. Therefore, making comparison among the effective times to failure in static and cyclic fatigue under similar maximum stresses will aid in assessing whether all fatigue failures are dominated by the same SCG mechanism. With the results of such comparison, one can obtain the first approximation whether there exists any cyclic loading effect on the failure mechanism.

Results of static fatigue tests[2] provided estimates of N as 22 at 1150°C and 6.4 at 1260 and 1370°C. These N values were then applied to Eq. (3) to convert the actual failure time to effective time to failure in cyclic fatigue. Cyclic and static fatigue results are compared in log-log plots of maximum stress versus effective time to failure (see Fig. 1). The comparison indicates that the levels of maximum applied stress required to generate failures within 1 to 1000 h were greater in cyclic fatigue tests (both low and high frequency) than those in static fatigue tests. In this region, the effective failure times under cyclic loading were longer than those under static loading with the same maximum applied stresses. This difference in failure times becomes greater when the comparison is made by using the actual cyclic fatigue failure times.

As shown in Figs. 1(a)—(c), the difference between static and cyclic fatigue life decreases with increasing stress level. Although a direct comparison could not be made at high applied stresses (failure time less than 1 h) due to the absence of static fatigue data, both static and cyclic fatigue failures, at stress levels near the fast fracture strength, would result from SCG of a dominant inherent flaw. Such a transition of dominant failure mechanism from creep rupture to SCG in static fatigue at elevated temperatures has been shown in other silicon nitrides (e.g., ref. 3). Consequently, the cyclic effective life would be closer to the static fatigue life at higher stresses, which is somewhat consistent with the SCG model approach. However, for stresses well below the fast fracture strength, the static and cyclic fatigue life could not be well correlated by the SCG model, suggesting a true cyclic loading effect. More importantly, the evolution of damage under cyclic loading was much less than for static loading.

Figure 1 also indicates that under the same maximum applied stress, the effective cyclic fatigue life for specimens tested at 1260 and 1370°C takes the following order: sinusoidal > trapezoidal > triangular wave form. This difference in effective cyclic fatigue life between low- and high-frequency tests could be as large as an order of magnitude or more, depending on the applied stress levels. This result implies that cyclic fatigue life for this PY6 silicon nitride at 1260 and 1370°C is cycle-shape or stress-rate dependent. Note that the maximum stress rates are at the orders of 10^1, 10^2, and 10^3 MPa/s for triangular, trapezoidal, and sinusoidal loading, respectively. Such dependence of cyclic fatigue life on cycle shape or stress rate might be related to the rate sensitivity of the viscous characteristics of the secondary phase. Apparently, higher frequency or higher stress rate would cause less strength degradation.

The influence of stress rate on the elevated-temperature damage mechanisms for the PY6 material has been discussed previously.[4] The static fatigue failure mechanisms agree with the dynamic fatigue failure mechanisms if the stress rates in static fatigue tests are considered extremely low. At 1150°C, SCG has been reported as the dominant failure mechanism for static fatigue[2], which agrees with the fact that SCG was responsible for all the dynamic fatigue failures regardless of the levels of stress rate. At 1260 and 1370°C, static fatigue failures were found to be dominated by creep rupture[2] which also controlled the dynamic fatigue failures at low stress rates ($\leq 10^{-2}$ MPa/s). The absence of extensive creep damage at 1150°C in both static and dynamic fatigue was a consequence of the increased viscosity of the intergranular phase.[2,4] The stress rates in cyclic fatigue tests

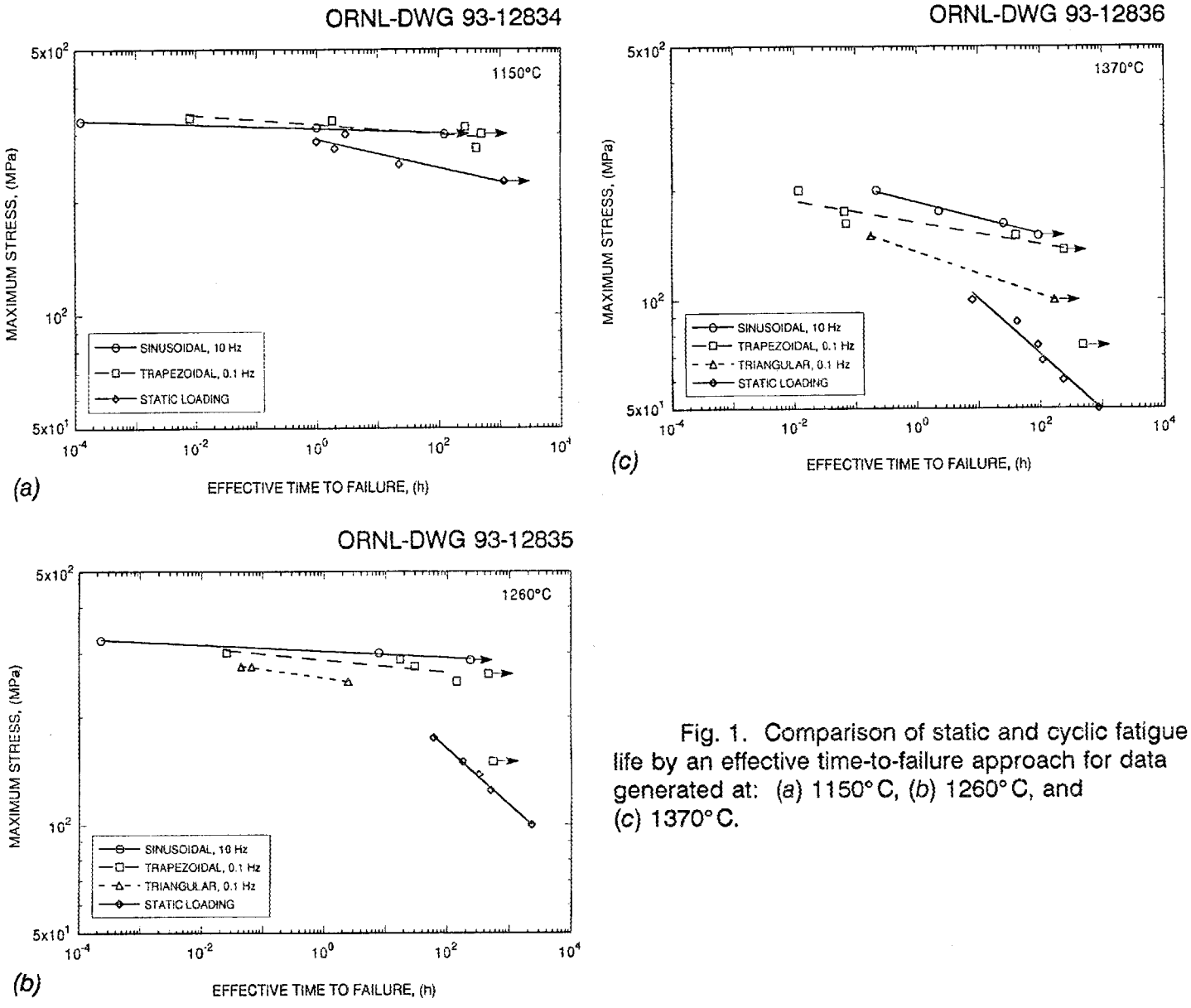

Fig. 1. Comparison of static and cyclic fatigue life by an effective time-to-failure approach for data generated at: (*a*) 1150°C, (*b*) 1260°C, and (*c*) 1370°C.

were so high that their failure mechanisms were different from those in static fatigue, particularly at 1260 and 1370°C, as supported by the dynamic fatigue results.

The apparent N values (>80 at 1150°C, >40 at 1260°C, and >23 at 1370°C) in cyclic fatigue are much greater than those in static fatigue, suggesting the failure mechanisms are different between static and cyclic fatigue. The N values estimated from dynamic fatigue data[4] were 98 for all applied stress rates at 1150°C, 24 and 7.1 for stress rates $>10^{-2}$ MPa/s at 1260 and 1370°C, respectively, and 18 and 3.9 for stress rates $\leq 10^{-2}$ MPa/s at 1260 and 1370°C, respectively. Except at 1150°C, where the N values of cyclic and dynamic fatigue are comparable, the N values of cyclic fatigue at 1260 and 1370°C are also greater than those in the SCG regime (stress rates $>10^{-2}$ MPa/s) of dynamic fatigue at 1260 and 1370°C. The differences in N values imply that the failure mechanisms and/or crack growth mechanisms for cyclic loading and monotonic loading (including static loading and constant stress rate loading) are not identical.

The loading/unloading in the cyclic fatigue tests appeared to inhibit the creep damage nucleation and accumulation process, in particular at 1260 and 1370°C, and decrease the crack growth rates thus allowing greater stresses to be sustained for similar failure times. This is supported by the cyclic stress-strain and strain-time behavior, which will be discussed next.

Cyclic fatigue tests under 0.1-Hz trapezoidal loading were conducted with measurements of cyclic stress-strain relations at discrete intervals. The typical cyclic stress-strain behavior is shown in Fig. 2. For all applied stress levels at 1150 to 1370°C, the cyclic stress-strain behavior remained linear to the final few cycles prior to the failure of specimens. Moreover, the Young's modulus, slopes of the cyclic stress-strain curves, did not change significantly during cyclic fatigue testing. Previous studies[5,6] have indicated that damage accumulation by formation and growth of creep cavities and microcracks could cause a progressive decrease in Young's modulus and lead to an apparent nonlinear stress-strain relation. Therefore, the absence of measurable hysteresis in the cyclic stress-strain response implies that little, if any, creep cavitation or microcracking occurred during cyclic fatigue testing.

As creep rupture was the controlling failure mechanism for static fatigue at 1260 and 1370°C, a limited number of cyclic fatigue tests were conducted under 0.1-Hz triangular loading at 1260 and 1370°C, with the extensometers in continuous contact with the specimens for the entire tests. In these tests, not only the cyclic stress-strain response but also the strain-time history was obtained. Similar to the results generated at 0.1-Hz trapezoidal loading, the cyclic stress-strain behavior obtained under 0.1-Hz triangular loading was also free of hysteresis and remained linear to the final few cycles before failure. Such similarity in cyclic stress-strain response between trapezoidal and triangular loading suggests that loading/unloading procedures in cyclic fatigue tests appear to inhibit the nucleation and/or growth of creep cavities and microcracks, no matter what wave form is applied.

Fig. 3 shows the typical strain-time plot for a cyclic fatigue test (0.1-Hz triangular loading with a maximum stress of 100 MPa) compared to strain-time histories of static fatigue tests at 1370°C. The strain-time curve plotted in Fig. 3 for cyclic fatigue test was

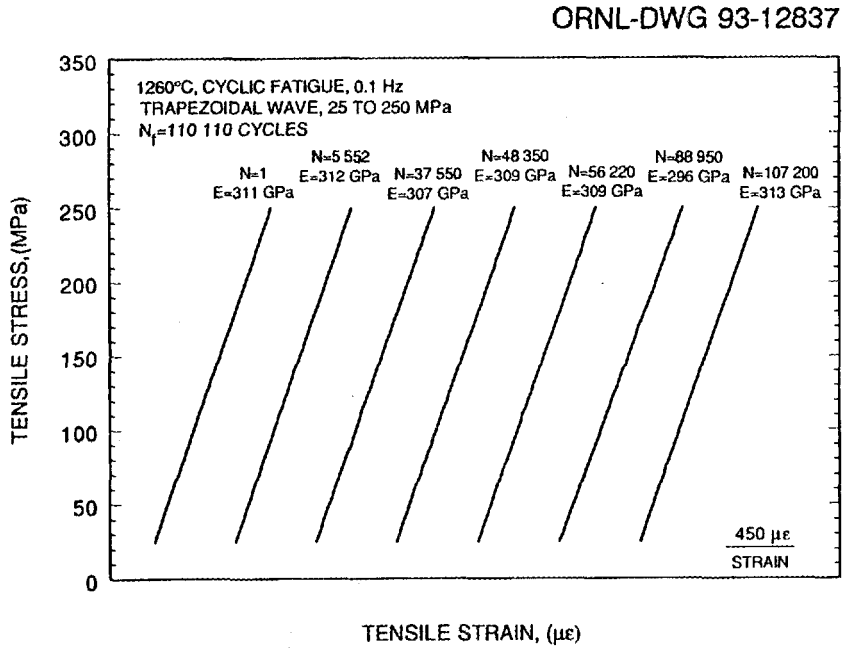

Fig. 2. Cyclic stress-strain behavior of PY6 silicon nitride tested under 0.1-Hz trapezoidal loading at 1260° C with a maximum stress of 250 MPa. Note these cyclic stress-strain curves were discretely recorded without monitoring the strain-time relation for the entire test such that only relative scale instead of absolute scale was used for the abscissa.

taken at the minimum stress level with additional short, discrete "vertical" segments which represent the cyclic stress-strain response at that particular time. The upper peak of each segment is the corresponding strain at the maximum stress. Since the cyclic stress-strain behavior was linear throughout almost the entire cyclic fatigue test, using other strain values (e.g., that corresponding to the mean or maximum stress level) as the reference strain in strain-time history would simply translate the strain-time curve along the strain axis but would not alter its slope. In Fig. 3, the cyclic fatigue strain-time curve shows a pronounced steady-state regime (or minimum strain rate regime) and absence of tertiary regime as compared to the short steady-state regime and dominant tertiary regime in the static fatigue tests. The absence of the tertiary regime provides more evidence for the conclusion that the normal damage accumulation process in static fatigue was interrupted by the loading/unloading steps in cyclic fatigue.

Although stress-strain hysteresis was not observed during cyclic fatigue testing, an extensive amount of strain ratchetting was found (see Fig. 3). Note that strain ratchetting here refers to the time-dependent progression of the cyclic stress-strain curves along the strain axis. Creep deformation under a tensile mean stress was the first speculation as the mechanism responsible for this strain ratchetting. As shown in Fig. 3, at the early stage of the strain-time history, the cyclic fatigue curve (mean stress = 55 MPa) fell

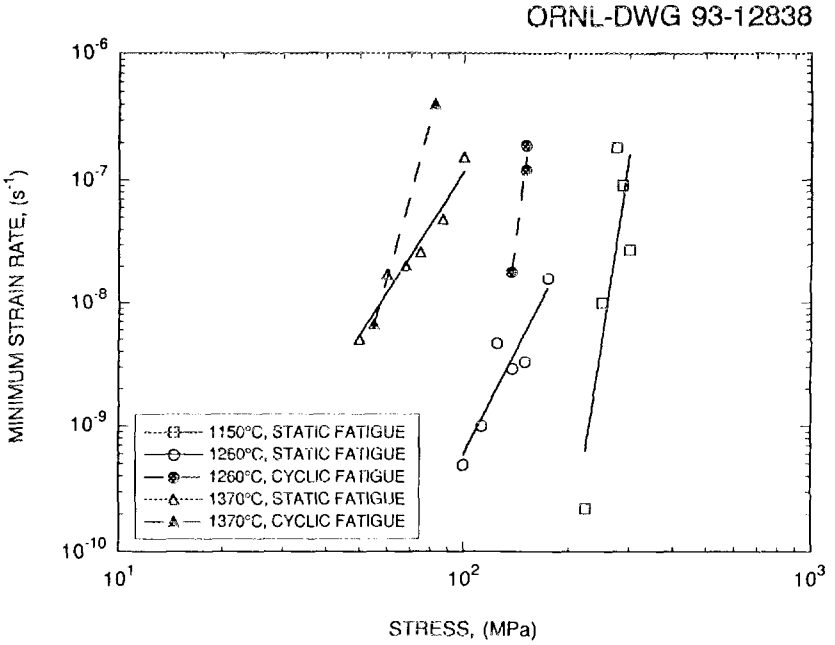

Fig. 3. Comparison of strain-time relations for static and cyclic fatigue of PY6 silicon nitride at 1370°C. The label for each curve includes the applied maximum stress, failure time, and minimum strain rate. Each of the "vertical" segments on the cyclic fatigue curve represents the corresponding cyclic stress-strain response at that particular time.

between the two static fatigue curves (applied stresses = 50 and 60 MPa, respectively). This seems to agree with the postulation. However, as no tertiary regime occurred under cyclic loading, the cyclic fatigue curve eventually fell below the static fatigue curve with an applied stress of 50 MPa, suggesting the mechanisms controlling the process of damage accumulation for static and cyclic fatigue were different.

More evidence supporting this conclusion is presented in Fig. 4 where minimum strain rate was plotted against applied stress in log-log base for both static and cyclic fatigue (0.1-Hz triangular loading) tests. The minimum strain rate for cyclic fatigue was defined as the minimum degree of increase in the strain corresponding to the minimum stress level throughout the test. The mean stress was used as the abscissa for the cyclic fatigue tests in Fig. 4. Fitting the data given in Fig. 4 to a simple power-law relation between minimum strain rate and applied stress ($\dot{\varepsilon}_{min} = A\sigma^n$, A is a constant) yields the following n values: n = 19, 5.6, and 4.4 for static fatigue at 1150, 1260, and 1370°C, respectively, while n = 22 and 10 for cyclic fatigue tests at 1260 and 1370°C, respectively. The significant difference in the corresponding stress exponent values between static fatigue (n = 5.6 and 4.4) and cyclic fatigue (n = 22 and 10) at 1260 and 1370°C indicates the damage mechanisms are different for these two loading histories. Therefore, creep might not be the primary damage mechanism leading to the final failures in cyclic fatigue

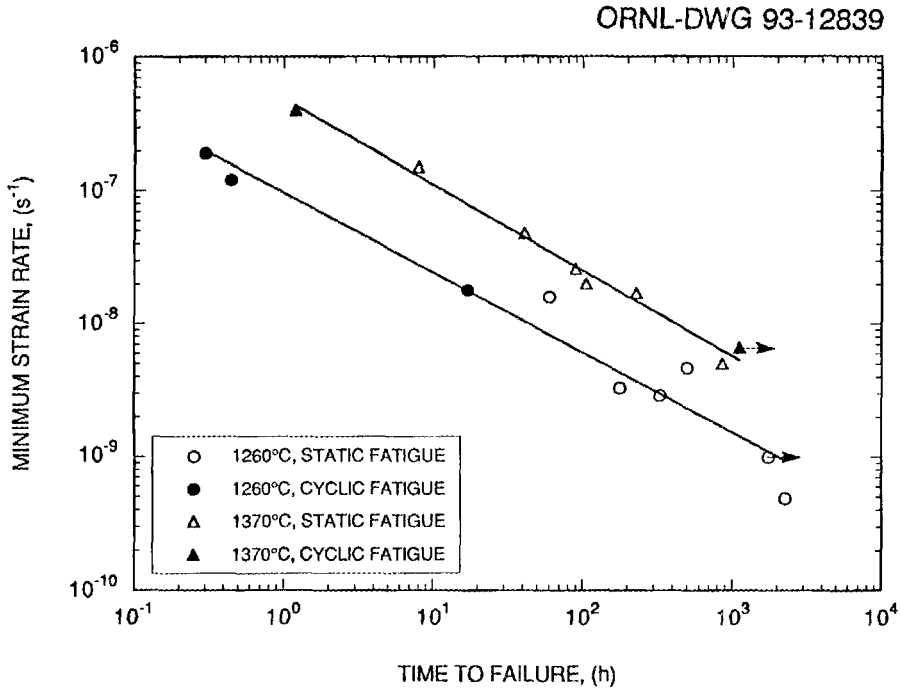

Fig. 4. Comparison of minimum strain rate for static and cyclic fatigue of PY6 silicon nitride at 1150 to 1370°C as a function of static or mean stress.

specimens. The similarity of high n values between static fatigue at 1150°C (n = 19) and cyclic fatigue at 1260 and 1370°C (n = 22 and 10, respec-tively) suggests a damage accumulation process analogous to SCG might be the primary failure mechanism for cyclic fatigue. Note that the strain-time curves for static fatigue at 1150°C also had a dominant steady-state regime.[2] In this sense, the observed strain ratchetting for cyclic fatigue at 1260 and 1370°C might actually reflect compliance changes resulting from the subcritical extension of a localized damage zone in a way similar to SCG.

In Fig. 5, a Monkman-Grant plot ($t_f = C(\dot{\varepsilon}_{min})^{-m}$, C is a constant) of the minimum strain rate versus time to failure indicates distinct curves for each test temperature of 1260 and 1370°C regardless of loading history. The values of m estimated from the data in Fig. 5 are approximately 1.5 and relatively independent of temperature. The agreement of cyclic and static fatigue data fitted in the Monkman-Grant relationship implies that stress may not be an appropriate controlling parameter for correlating static and cyclic fatigue life at elevated temperatures. However, this agreement inevitably puzzles the fact that the failure mechanisms in static and cyclic fatigue are different as described above. More microstructural evidence for the different failure mechanisms in cyclic and static fatigue is given next.

Typical fracture surfaces of cyclic fatigue specimens tested at 1150, 1260, and 1370°C are shown in Figs. 6(*a*), (*b*), and (*c*), respectively. At 1150°C, the fracture

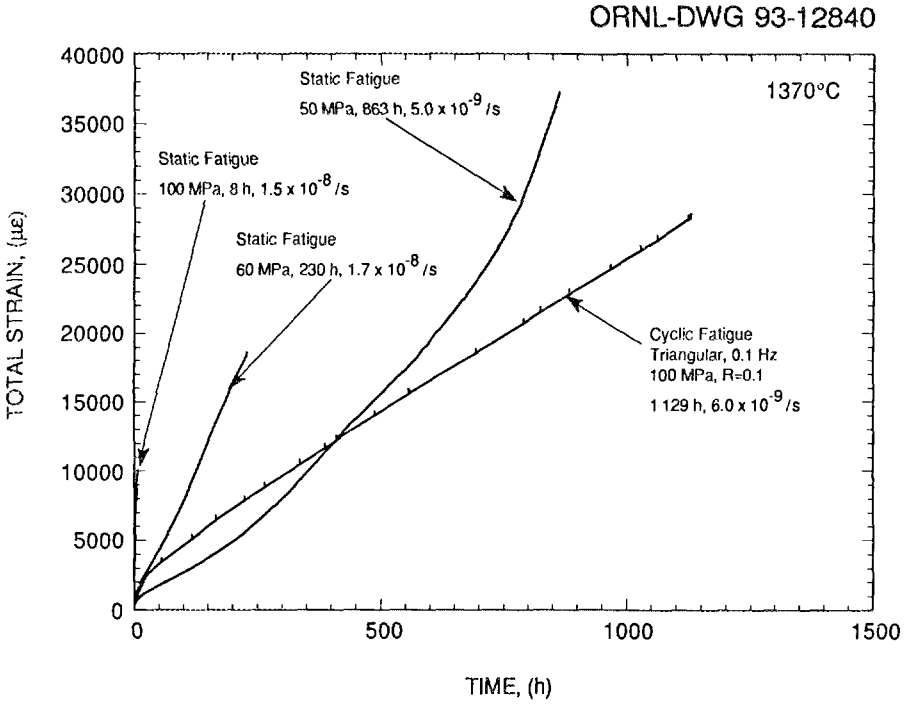

Fig. 5. Comparison of Monkman-Grant-type relations for static and cyclic fatigue of PY6 silicon nitride at 1260 and 1370°C.

surfaces contained well-defined mirror, mist, and hackle regions [see Fig. 6(*a*)]. A region of apparent SCG (label s) from a preexistent defect was also identified within the mirror region. All of the cyclic fatigue failures at 1150°C were related to preexistent flaws located in the volume or at the surface. Even though both static and cyclic fatigue failures at 1150°C were due to subcritical crack extension of preexistent flaws, the comparison of stress-life relations implies that crack propagation rates were less in cyclic loading than in static loading. The lesser damage caused by cyclic fatigue relative to static fatigue in ceramics at elevated temperatures might be related to the viscous intergranular phase.[7-9] For example, the effect of bridging the crack surfaces by the viscous intergranular phases could be more pronounced in cyclic loading than in static loading under certain conditions.[9] Because of the inability of the viscous ligaments behind the crack tip to relax during the high-frequency cycling, the effective stress-intensity factor at the crack tip is larger under static loading than for cyclic loading with a high frequency or a short hold time at maximum applied stress. In this sense, the crack growth rate is lower in cyclic loading than in static loading. Lower crack growth rates in cyclic loading over static loading with the same maximum applied stress-intensity factor at elevated temperatures have been reported in other ceramics.[8]

For cyclic fatigue specimens tested at 1260°C, the fracture surfaces still showed the mirror-mist-hackle feature with failure originating from the surface. Only a couple of specimens tested at the highest applied stresses clearly showed the internal preexistent flaws as the fracture origins. The majority of the specimens had surface-initiated failures,

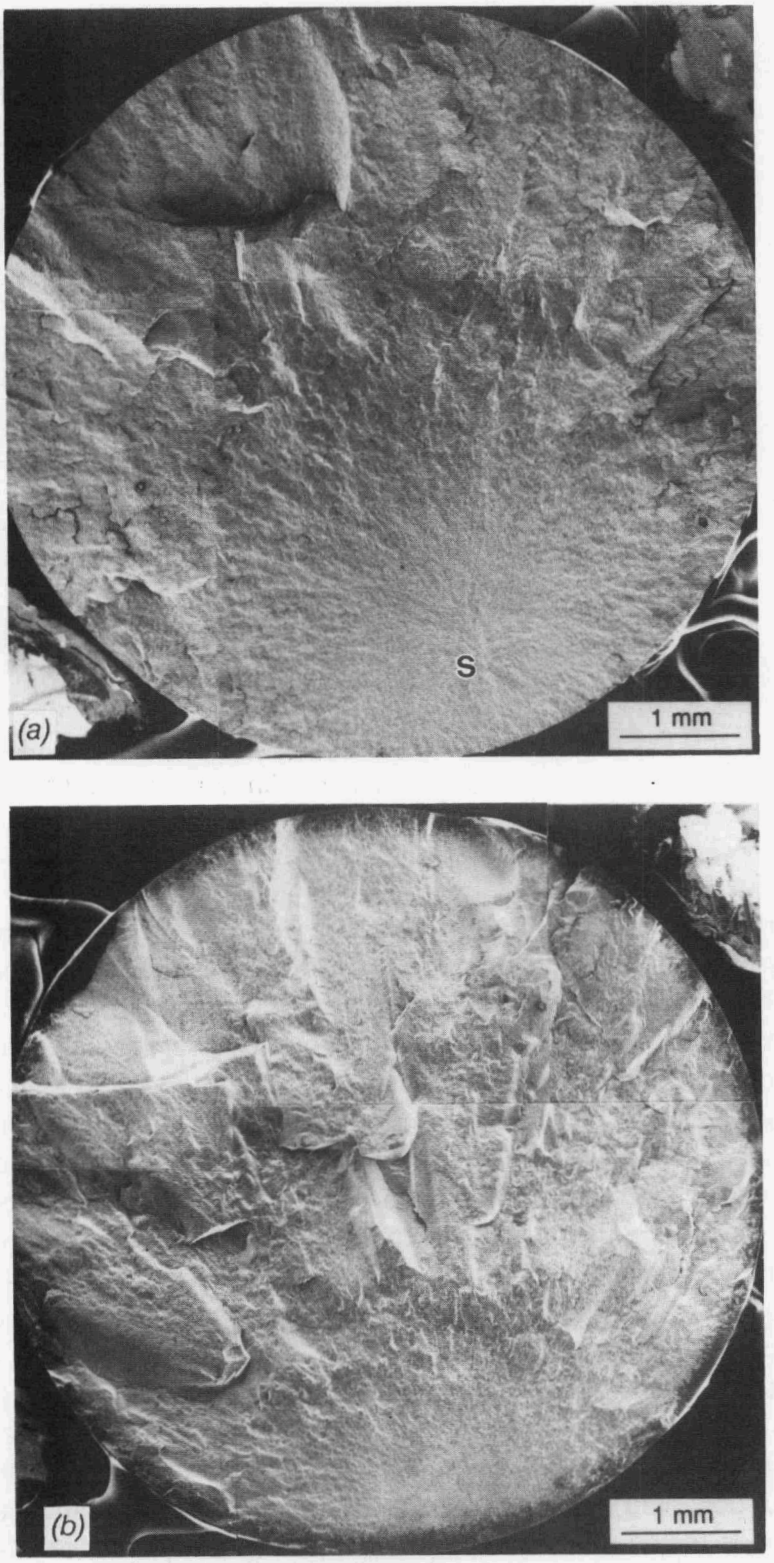

Fig. 6. Typical fracture surfaces for cyclic fatigue (0.1-Hz trapezoidal wave form) specimens of PY6 silicon nitride tested at: (*a*) 1150° C (σ_{max} = 275 MPa, t_{cf} = 916 h), label s: slow crack growth region; (*b*) 1260° C (σ_{max} = 250 MPa, t_{cf} = 306 h); and (*c*) 1370° C (σ_{max} = 150 MPa, t_{cf} = 86 h).

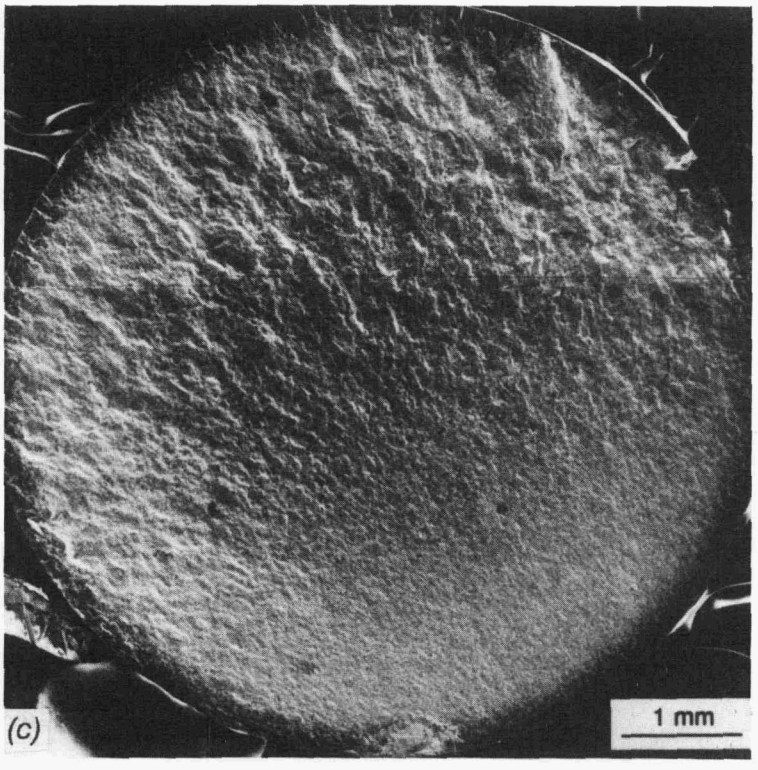

Fig. 6 (Continued)

but no clear fracture origins, such as preexistent defects, could be identified [see Fig. 6(*b*)]. A possible explanation for this phenomenon is that at temperatures ≥1260° C, the oxidation rate increased as evidenced by the outer, darker rings on the fracture surfaces shown in Figs. 6(*b*) and (*c*), thereby providing preferred sites for fracture initiation. As observed in other silicon nitrides,[10,11] oxidation could increase the strength by rounding or blunting preexistent flaws or decrease the strength by producing new flaws such as bubbles, pits, and microcracks in the oxide scale. The effects of oxidation process and products on the mechanical properties are related to the complex factors such as impurities and sintering aids, temperature, duration of oxidation, loading conditions during oxidation, and others.[10,11] It is likely due to the oxidation that most of the cyclic fatigue failures at 1260° C were initiated at or near the surfaces, and their origins could not be clearly identified.

The features for the fracture surfaces of cyclic fatigue specimens tested at 1370° C look similar to those generated at 1260° C, except the mirror regions are larger due to the lower applied stresses [Fig. 6(*c*)]. In addition, a small damage zone with greater roughness was observed within the mirror region on the fracture surfaces of a few cyclic fatigue specimens tested at 1370° C. Macroscopically, the feature of this small damage zone does not look like that of the SCG region at 1150° C but is similar to the larger creep damage zone previously identified for the static fatigue specimens tested at 1260 and 1370° C.[2] However, microscopically, no extensive creep cavities were detected throughout

the gage sections of cyclic fatigue specimens tested at 1150 to 1370°C. This is one of the major differences in the microstructure between the failed static and cyclic fatigue specimens, in particular at 1260 and 1370°C [see Figs. 7(*a*) and (*b*)]. The origination of this small damage zone from the surface once again implies that surface oxidation might make some contributions to the fatigue failures at 1260 and 1370°C.

Based on these observed features of fracture surfaces and microstructure, it is likely that a damage accumulation process analogous to SCG might be the primary failure mechanism for cyclic fatigue at 1260 and 1370°C. This damage accumulation process might involve the subcritical extension of a localized damage zone originating from surface where oxidation-assisted damage or oxidation-modified preexistent flaws would provide the favorable sites for crack nucleation. The difference of microstructural observations in cyclic and static fatigue is consistent with the macroscopic observations that cyclic fatigue data generated at 1260 and 1370°C demonstrated significantly higher values of crack growth exponent, N, and stress exponent, n, over those generated by static fatigue loading at the same temperatures.

The fact that cyclic fatigue specimens did not display such extensive creep cavities as observed in the static fatigue specimens tested at 1260 and 1370°C agrees with the characteristics of stress-life and strain-time results. Although the exact cyclic fatigue mechanisms at 1260 and 1370°C are not clear at present, unloading in each cycle may play an important role in either suppressing development of creep damage or retarding the accumulation of creep deformation. Solution-precipitation of the silicon nitride in the intergranular phase was suggested as the mechanism for the development of cavities with lenticular shape along two-grain boundaries in PY6 silicon nitride crept at 1260 and 1370°C.[2] The driving force for a typical solution-precipitation mechanism is related to the deviatoric stress (which is the applied stress in uniaxial loading condition).[12,13] It is possible that the endurance of such a driving force in each loading period was not long enough for nucleation and/or growth of cavities for selected cyclic loading conditions in the present study. This might result from relaxation of local stress concentration at potential sites for cavity development and recovery of viscoelastic deformation during unloading.

Status of milestones

1. Apply phenomenological model creep rate/creep rupture model to PY6 tensile data (completed).

2. Complete cyclic fatigue studies and submit open literature publication on results (completed).

Communications/visitors/travel

1. M. K. Ferber presented talks entitled, "Fracture of a HIPed Silicon Nitride Under Tensile Static and Dynamic Loading at High Temperatures" and "Creep and Fatigue

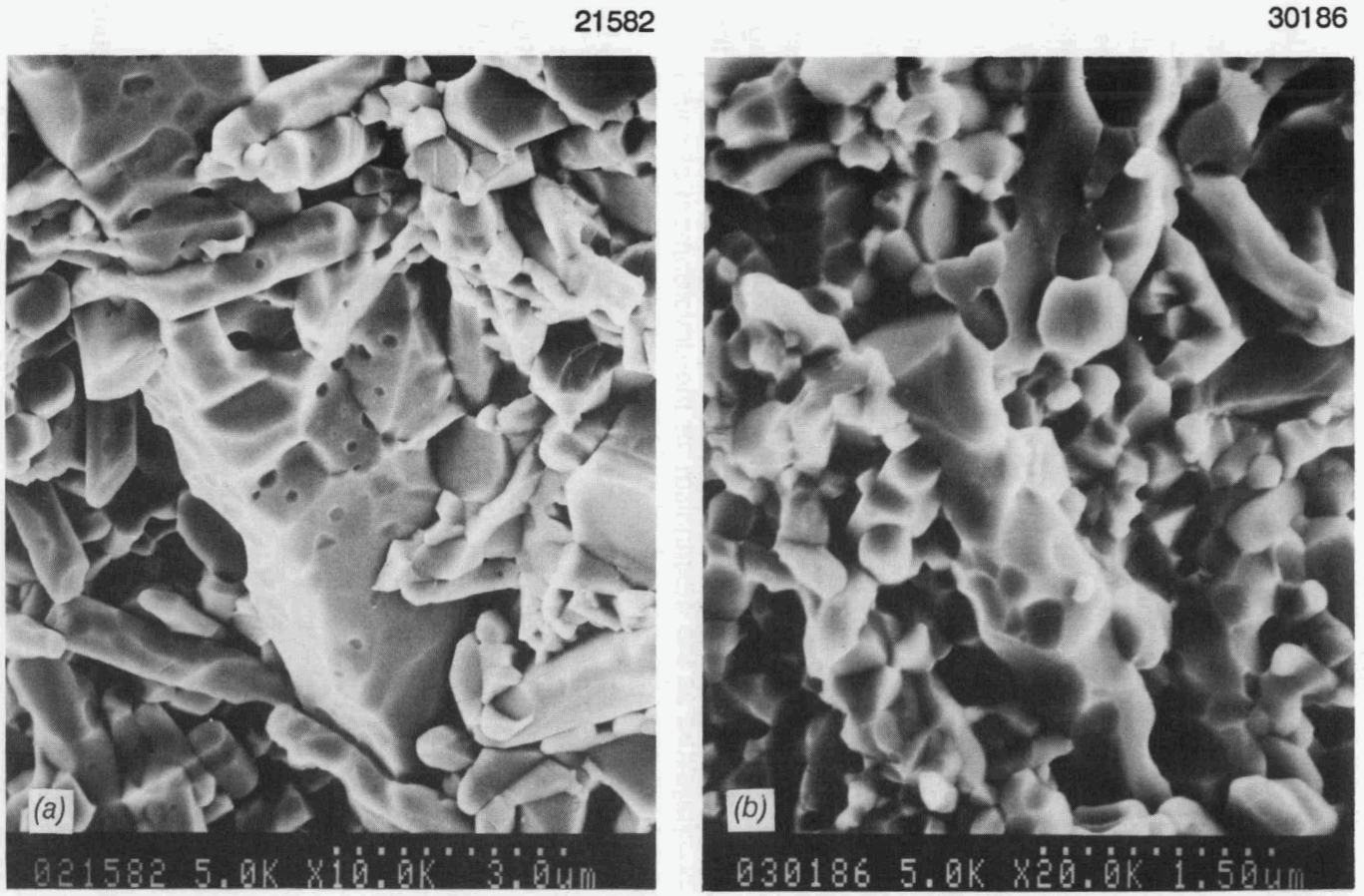

Fig. 7. Scanning electron microscopy micrographs for static and cyclic fatigue specimens of PY6 silicon nitride tested at 1370° C: (*a*) static fatigue, σ_s = 75 MPa, t_{sf} = 90 h (with cavities along two-grain boundaries) and (*b*) cyclic fatigue, 0.1-Hz trapezoidal loading, σ_{mean} = 75 MPa (σ_{max} = 137 MPa), t_{cf} = 516 h (without cavities).

Behavior of a HIPed Silicon Nitride," at the Third International Ceramic Science and Technology Congress, San Francisco, Calif., November 1-4, 1992.

2. C.-K. J. Lin presented a talk entitled, "Evaluation of Tensile Static, Dynamic, and Cyclic Fatigue Behavior for a HIPed Silicon Nitride at Elevated Temperatures," at the 1992 Fall Meeting of the Materials Research Society, Boston, Mass., November 30 - December 4, 1992.

Problems encountered

None.

Publications

1. C.-K. J. Lin, M. G. Jenkins, and M. K. Ferber, "Evaluation of Tensile Static, Dynamic, and Cyclic Fatigue Behavior for a HIPed Silicon Nitride at Elevated Temperatures," pp. 455-60 in *Silicon Nitride Ceramics – Scientific and Technological Advances*, Vol. 287, ed. by I-W. Chen, P. F. Becher, M. Mitomo, G. Petzow, and T.-S. Yen. Materials Research Society, Pittsburgh, 1993.

2. M. G. Jenkins, M. K. Ferber, and C.-K. J. Lin, "Apparent Enhanced Fatigue Resistance Under Cyclic Tensile Loading for a HIPed Silicon Nitride," *J. Am. Ceram. Soc.* **76**[3], 788-92 (1993).

3. C.-K. J. Lin, M. G. Jenkins, and M. K. Ferber, "Tensile Dynamic and Static Fatigue Relations for a HIPed Silicon Nitride at Elevated Temperatures," *J. Eur. Ceram. Soc.*, in press, 1993.

4. C.-K. J. Lin, M. G. Jenkins, and M. K. Ferber, "Cyclic Fatigue of Hot Isostatically Pressed Silicon Nitride at Elevated Temperatures," submitted to *J. Mater. Sci.*, February 1993.

References

1. A. G. Evans and E. R. Fuller, "Crack Propagation in Ceramic Materials under Cyclic Loading Conditions," *Metall. Trans. A* **5**[1], 27-33 (1974).

2. M. K. Ferber and M. G. Jenkins, "Evaluation of the Strength and Creep-Fatigue Behavior of Hot Isostatically Pressed Silicon Nitride," *J. Am. Ceram. Soc.* **75**[9], 2453-62 (1992).

3. G. D. Quinn, "Fracture Mechanism Maps for Advanced Structural Ceramics, Part 1: Methodology and Hot-Pressed Silicon Nitride Results," *J. Mater. Sci.* **25**, 4361-76 (1990).

4. C.-K. J. Lin, M. G. Jenkins, and M. K. Ferber, "Tensile Dynamic and Static Fatigue Relations for a HIPed Silicon Nitride at Elevated Temperatures," *J. Eur. Ceram. Soc.*, in press, 1993.

5. A. Venkateswaran, K. Y. Donaldson, and D. P. H. Hasselman, "Role of Intergranular Damage-Induced Decrease in Young's Modulus in the Nonlinear Deformation and Fracture of an Alumina at Elevated Temperatures," *J. Am. Ceram. Soc.* **71**[7], 565-76 (1988).

6. S. Suresh and J. R. Brockenbrough, "A Theory for Creep by Interfacial Flaw Growth in Ceramics and Ceramic Composites," *Acta Metall. Mater.* **38**[1], 55-68 (1990).

7. T. Fett, G. Himsolt, and D. Munz, "Cyclic Fatigue of Hot-Pressed Si_3N_4 at High Temperatures," *Adv. Ceram. Mater.* **1**[2], 179-84 (1986).

8. L. Ewart and S. Suresh, "Elevated-Temperature Crack Growth in Polycrystalline Alumina under Static and Cyclic Loads," *J. Mater. Sci.* **27**, 5181-91 (1992).

9. C.-K. J. Lin, D. F. Socie, Y. Xu, and A. Zangvil, "Static and Cyclic Fatigue of Alumina at High Temperatures: II, Failure Analysis" *J. Am. Ceram. Soc.* **75**[3], 637-48 (1992).

10. R. W. Davidge, A. G. Evans, D. Gilling, and P. R. Wilyman, "Oxidation of Reaction-Sintered Silicon Nitride and Effects on Strength"; pp. 329-43 in *Special Ceramics 5*, ed. P. Popper, British Ceramic Research Association, Stoke-on-Trent, England, 1972.

11. T. E. Easler, R. C. Bradt, and R. E. Tressler, "Effects of Oxidation and Oxidation under Load on Strength Distributions of Si_3N_4," *J. Am. Ceram. Soc.* **65**[6], 317-20 (1982).

12. R. Raj and C. K. Chyung, "Solution-Precipitation Creep in Glass Ceramics," *Acta Metall.* **29**[1], 159-66 (1981).

13. R. L. Tsai and R. Raj, "A Theoretical Estimate of Solution-Precipitation Creep in MgO-Fluxed Si_3N_4," *J. Am. Ceram. Soc.* **65**[6], C88-C90 (1982).

TOUGHENED CERAMICS LIFE PREDICTION

Jonathan A. Salem, Sung R. Choi and Lynn M. Powers
(NASA Lewis Research Center)

Objective/Scope

The purpose of this research is to understand the room temperature and high temperature [≤ 1370°C (2500°F)] behavior of toughened ceramics as the basis for developing a life prediction methodology. A major objective is to understand the relationship between microstructure and mechanical behavior within the bounds of a limited number of materials. A second major objective is to determine the behavior as a function of time and temperature. Specifically, the room temperature and elevated strength and reliability, the fracture toughness, slow crack growth and the creep behavior will be determined for the as-manufactured material. The same properties will also be evaluated after long-time exposure to various high temperature isothermal and cyclic environments. These results will provide input for parallel materials development and design methodology programs. Resultant design codes will be verified.

Technical Highlights

The objective of this work is to demonstrate validity of the integrated design program CARES (Ceramics Analysis and Reliability Evaluation of Structures [1]), to predict the fast-fracture reliability of monolithic ceramic components. Thus far, the fast-fracture strength of sintered alpha silicon carbide tested in three- and four-point bending has been used to predict the failure strength distribution of ring-on-ring (biaxial strength) tests, and thereby check validity of the code. Testing of other volumes and stress states, such as wide MOR bars and torsion specimens are in progress. Also, testing of specimens with machining damage is in progress.

The material was chosen because it exhibits very low fracture toughness, no crack growth resistance, high elastic modulus and a very low susceptibility to slow crack growth (fatigue). Such properties make this an ideal ceramic for the verification of fast fracture reliability models and codes.

EXPERIMENTAL METHOD

Material and Specimen Preparation

The material used in this study was a commercially available sintered alpha silicon carbide processed in the form of 25 by 25 by 42 mm billets. The biaxial plate specimens were ground from the billets and finished by 320 grit diamond uniaxial grinding on one face of the specimen. The nominal dimensions of the biaxial plate specimens were 25 mm on edge by 2 mm in thickness. Bend test specimens were ground from randomly selected plates in order to have the same flaw population

(surface finish and orientation) in both the plates and bend beams. The bend bars were oriented in the longitudinal direction of grinding and the edges on the tensile surface were beveled by hand sanding to eliminate spurious edge failures. Bend specimens nominally measured 2 by 3 by 25 mm. In order to minimize any remnant machining damage, all the specimens were annealed at 1200°C for 2 hours in air.

Young's Modulus and Poisson's Ratio

Reliability analysis of structural components is sensitive to both Young's Modulus and Poisson's ratio. Therefore, measurements of these specific material constants were taken statically via (90°) biaxial strain gages and by the impulse excitation method. Both disk (25 mm diameter by 2 mm thick) and beam configurations were used in the impulse excitation tests.

Bend Testing

Fast-fracture bend tests were conducted at room temperature with a stroke rate of 0.05 mm/min. The outer span of the three- and four-point fixtures was 20 mm and the inner span of the four-point fixture was 8 mm. The rollers of the test fixture were free to roll and the upper span to articulate relative to the lower span. A minimum of 33 specimens were tested per condition.

Biaxial Testing and Rig Verification

The biaxial fixture consisted of two concentric half-hard cold rolled copper rings with diameters of 5.75 and 11.54 mm, and contact curvatures of 1.50 and 2.82 mm, respectively. The rings were allowed to articulate relative to each other, insuring a uniform contact area. Although the procedures for four-point bend testing are well established [2], those for biaxial testing are not. Further, the availability and accuracy of stress solutions for a wide variety of ring loaded square plates is limited [3]. In order to assess the degree of biaxiality produced by the test rig and its conformance to plate theory (or FEM modeling), as-machined and polished plate specimens were strain gaged with rosettes at several radial positions. The specimens were loaded to 150 MPa, about 50% of the average plate strength, both with and without a lubricant. The radial and tangential stresses at each gage were resolved and the maximum stress was compared to that calculated from the equation of Vitman and Pukh [4]

$$\sigma_f = \frac{3\,P}{4\,\pi\,h^2}\left[2\,(1+\nu)\,\ell n\left(\frac{r_o}{r_i}\right) + \frac{(1-\nu)\,(r_o^2 - r_i^2)}{R_s^2}\right] \qquad (1)$$

where σ_f is the maximum stress, P is the applied load, R_s is one-half

the average of the diagonal and edge lengths, r_i is the inner radius, r_o is the outer radius, h is the thickness, and ν is Poisson's ratio. The stresses measured in the test rig were within 1 % of equation (1) for the polished and lubricated specimen, as tabulated in Table 1. The as-machined specimen exhibited stresses that were 5% less than those calculated with equation (1). Evidently the friction generated between the copper load rings and the silicon carbide specimens is sufficient to lower the stresses in the as-machined specimens by 4 %.

With reasonable agreement between the test ring and equation (1) established, specimens were tested at a stroke rate of 0.05 mm/min in room temperature air. A total of 36 specimens were tested.

Table 1. Stresses Generated by the Biaxial Test Fixture

Test Condition	Measured Stress (MPa)	Difference with Eq. (1) (%)
As-machined	144	-5
As-machined and lubricated	149	-2
Polished	142	-7
Polished and Lubricated	150	-1

Note: Young's modulus and Poisson's ratio of 367 GPa and 0.17, respectively, were used in stress calculations.

Fractography

Fracture surface analysis (fractography) was performed on the bars and plates after testing to determine the type of flaws causing failure. Fractographic analysis is a necessary component of reliability analysis, in order to determine whether surface, volume, or combined (surface and volume) flaw reliability analysis should be performed, and if flaws of different processing sources are present. Fractography was done in accordance with military handbook procedure [5].

RESULTS AND DISCUSSION

Young's Modulus and Poisson's Ratio

Young's modulus and Poisson's ratio are summarized in Table 2. All methods resulted in a Poisson's ratio of 0.17, however, the impulse excitation method resulted in slightly higher modulus values than those

measured via stain gages.

Table 2. Young's Modulus and Poisson's Ratio

	Impulse Excitation Disk	Impulse Excitation Bar	Strain Gaged Bar
Young's Modulus (GPa)	396 (6)	385 (6)	367
Poisson's Ratio	0.17	-----	0.17

Notes: numbers in parenthesis are one standard deviation.

Fractography

All of the silicon carbide bars and plates failed from processing agglomerates at or near the surface, with the exception of one specimen which could not be identified. For this analysis, near surface flaws were defined a being within two flaw diameters of the free surface. All of the failure origins, except six, were within the inner ring and orientation of the fracture mirrors was totally random. This indicates that the machining damage was totally eliminated via annealing. Fig. 1 shows a typical fracture surface of a biaxially loaded plate. Fig. 1(a) shows the plate after failure, (b) shows the fracture mirror, and (c) shows the flaw from which failure was initiated. Fig. 2 is a plot of the crack branching length C_L as a function fracture strength σ_f obtained from the plate specimens. The relationship between C_L and σ_f for ceramics and glasses is given [6] as

$$\sigma_f C_L = A_b \qquad (2)$$

where A_b is the branching constant. The branching for this material based on equation (2) was found to be $A_b = 6.30 \pm 0.54$ MPam$^{0.5}$. For glass the branching constant is about three times the fracture toughness, however, for many ceramics the constant is slightly lower ($A_b \approx 2.5 \times K_{Ic}$). The toughness of alpha silicon carbide is between 2.5 and 3 MPa$^{0.5}$ [7], indicating the measured branching constant to agree with those for many ceramics.

Strength Measurements

The material parameters describing the variability in strength were obtained from the fracture strength measurements. Surface flaw analysis was carried out on the bars and plates. Fig. 3 shows the

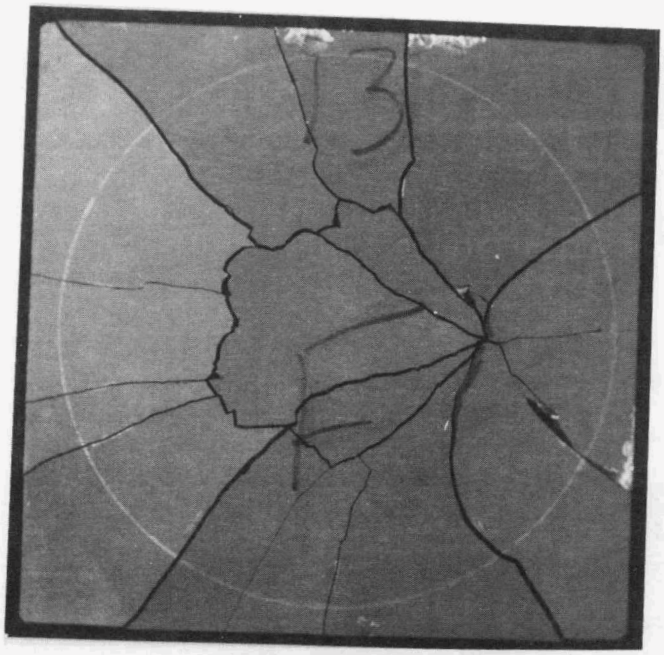

(A)

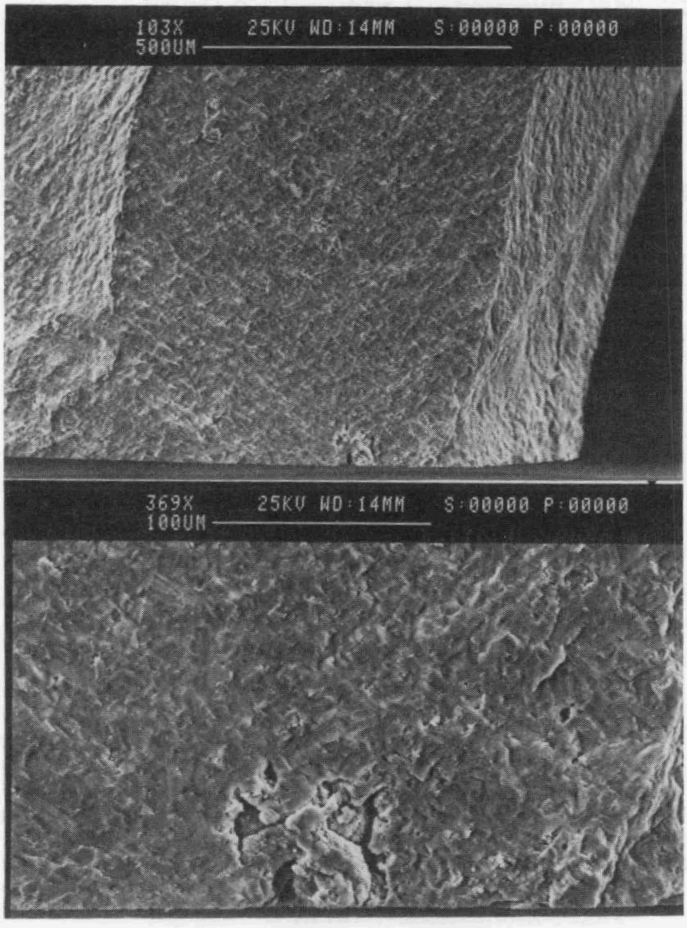

(B)

(C)

Figure 1. - (A) Fracture pattern; (B) Fracture surface in the vicinity of the fracture origin; (C) Fracture origin in the silicon carbide plate.

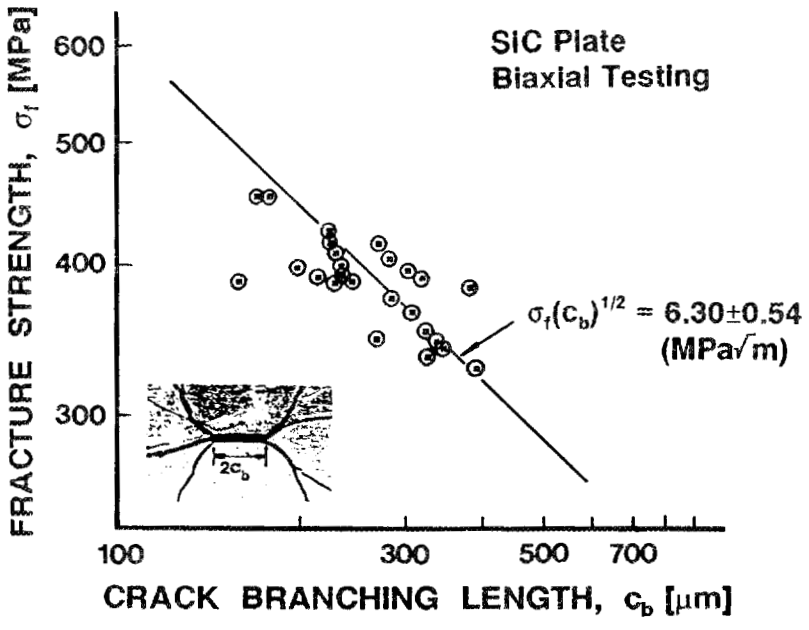

Figure 2. - Crack branching length as a function of fracture strength for the silicon carbide plates subjected to biaxial loading.

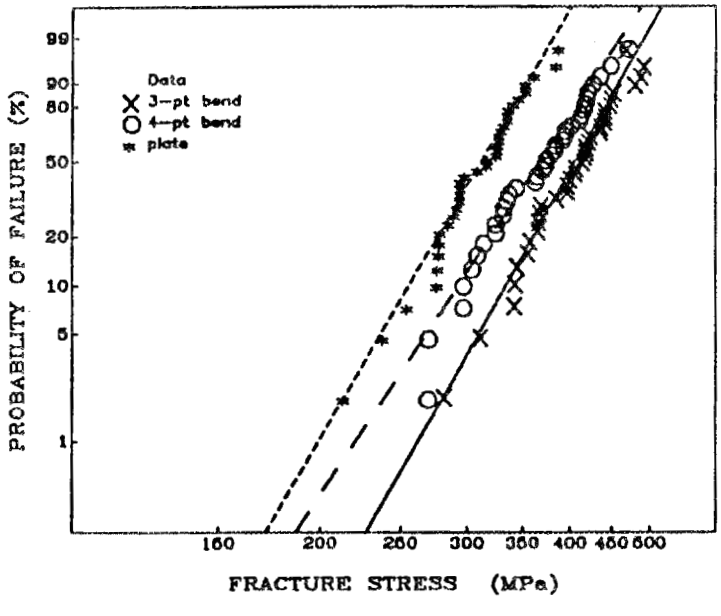

Figure 3. - Weibull plot of the fracture stresses for the bend and ring-on-ring tests.

Weibull plot of the failure strengths of the plates, three-point bars and four-point bars, and the results of the statistical analysis are presented in Table 3. Maximum likelihood estimates (MLE) and least squares best fit estimates (LS) of the Weibull modulus, characteristic strength, and scale parameter are provided.

Table 3 - ESTIMATES OF THE SURFACE WEIBULL PARAMETERS FOR SILICON CARBIDE.

Test	Weibull Modulus m_s	Characteristic Strength $\sigma_{\theta s}$ (MPa)	Scale Parameter σ_{0s} (Mpa $\times$ mm$^{2/m}$)
3-pt bend			
MLE	9.72	420.9	508.3
LS	9.40	421.1	510.4
4-pt bend			
MLE	8.31	384.0	577.7
LS	8.30	384.0	577.7
ring-on-ring			
MLE	9.40	324.7	578.7
LS	9.43	324.9	577.0

Reliability Prediction

Since the plates failed in a consistent, unimodal and isotropic manner, a conventional reliability analysis could be performed. The statistical material properties chosen were obtained from the three-point bend test analyzed with the maximum likelihood technique (Table 3). CARES was used to predict the fast-fracture reliability of the plates as a function of the fracture stress. The finite element mesh used for the silicon carbide plate and the copper supports is shown in Fig. 4. One-quarter of the assembly is meshed, taking advantage of symmetry conditions. Figure 5 is a Weibull plot showing the experimental data for the three-point bend and plate tests, and the superimposed reliability prediction for the plates.

The probability of failure for a ceramic component using the Batdorf model for surface flaws is

$$P_{fs} = 1 - \exp\left\{-\int_A \left[\int_0^{\sigma_{max}} \frac{\omega}{\pi} \frac{dn_s(\sigma_{cr})}{d\sigma_{cr}} d\sigma_{cr}\right] dA\right\} \qquad (3)$$

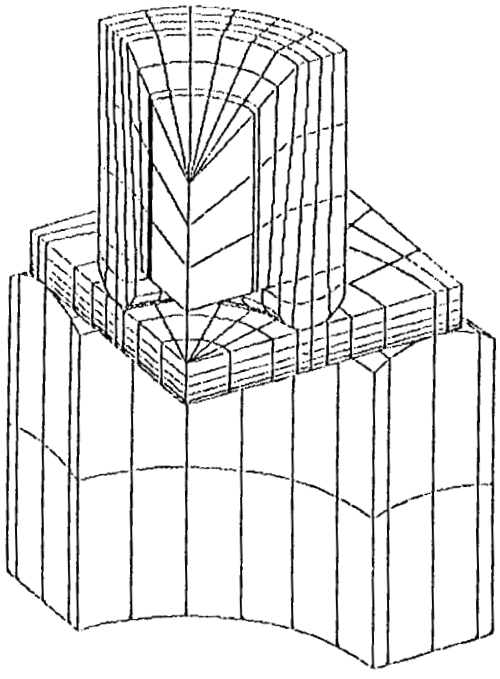

Figure 4. - Finite element mesh of the ring-on-ring assembly.

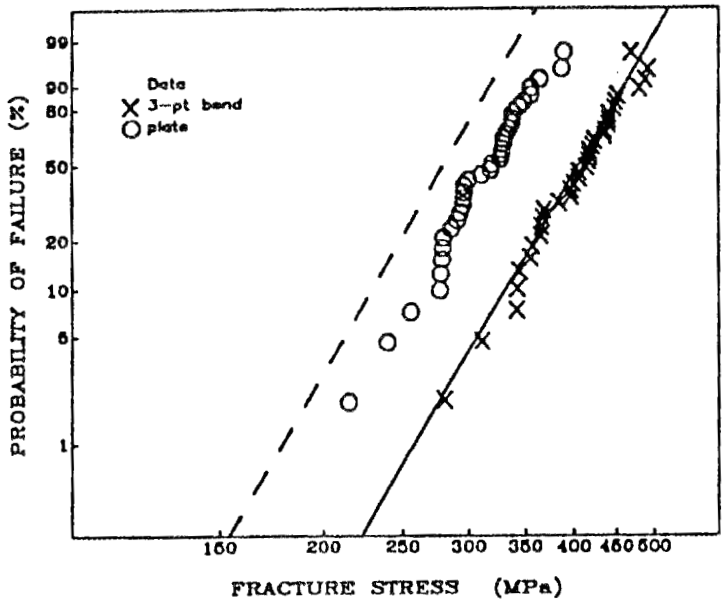

Figure 5. - Experimental and predicted failure probabilities for the plates as a function of fracture stress.

where A is the surface area, n_s is the crack density function, σ_{emax} is the maximum value of the mode I equivalent stress on the crack, and ω is the length of an angle α projected onto a unit radius semi-circle in principal stress space containing all of the crack orientations for which the effective stress is greater than or equal to the critical stress, σ_{cr}. A number crack shapes and fracture criteria are available, such as the Weibull normal stress averaging (a shear-insensitive case of the Batdorf theory), total coplanar strain energy release rate, and the noncoplanar criterion.

The finite element method enables discretization of the surface of the component into incremental area elements. CARES evaluates the failure probability at the Gaussian integration points of shell elements or optionally at the element centroids. The area of each subelement (corresponding to a Gaussian integration point) is calculated using the shape functions inherent to the element type [8].

The reliability prediction for the plates, is based on the Batdorf model, a semicircular crack, and noncoplanar crack extension with a shear sensitivity constant of $\overline{C}$=0.82 (dashed line). The shear sensitivity constant corresponds to an approximation of the maximum principal stress criterion. However, it should be mentioned that the shear sensitivity constant should be determined from mixed mode (modes I and II) fracture testing for a given materials. In consideration of the confidence intervals on the strength data, the prediction shown in Fig. 5 is in reasonable agreement with the experimental result.

It is usually recommended that penny-shaped and semicircular cracks be used in the volume and surface reliability analyses, respectively, as they are more representative of small embedded flaws. One complication with reliability prediction of processing flaws is that ceramic materials fail from a variety of sources: semi-spherical pores, large equiaxed grains, large acicular grains, porous regions and inclusions of complex and variable three dimension shapes. A further complication is that these flaws are ground open or further damaged in specimen or component preparation, and some manufactures heat treat specimens and components to "heal" the grinding induced damage, which is particularly severe if stresses are applied normal to the grinding direction, as occurs in biaxially stressed specimens. The effects of these complications on reliability analysis are unclear.

Continuing Verification Efforts

The effects of finite element mesh refinement on the reliability prediction is being pursued. Also, additional tests are being performed to determine the effects of grinding orientation, annealing, and volume (independent of stress state) on reliability predictions with the CARES code. Grinding effects can be of importance as the flaw population becomes anisotropic, thereby introducing a preferred failure orientation. Further, the shear sensitivity constant will be determined for this material and used in future verification work.

CONCLUSIONS

(1). The prediction of the reliability of a biaxial stress state with a larger surface area from uniaxial stress state data with CARES is reasonable, but conservative.

(2). Increasing stressed area and/or the addition of a second principal stress decreases the measured strength, as expected.

(3). Further testing to determine the independent effects of surface area and stress state, and effects of grinding orientation on reliability predictions are needed.

REFERENCES

[1] J. P. Gyekenyesi, "SCARE: A Postprocessor Program to MSC/NASTRAN for Reliability Analysis of Structural Ceramic Components," J. Eng. Gas Turbine Power Vol 108, 540-546 (1986).

[2] ASTM C 1161-90 "Standard Test Method for Flexural Strength of Advanced Ceramics at Ambient Temperature," Annual book of ASTM Standards, Vol. 15.01, 333-339, (1990).

[3] W. F. Adler and D. J. Mihora, "Biaxial Flexure Testing: Analysis and Experimental Results," pp. 227-246 in *Fracture Mechanics of Ceramics*. R. C. Bradt et al., eds., Plenum, New York (1992).

[4] F. F. Vitman and V. P. Pukh, "A method for Determining the Strength of Sheet Glass, Aavodskaya Laborayoriya, 29 pp. 863-867, (1963).

[5] "Fractography and Characterization of Fracture Origins in Advanced Structural Ceramics," MIL-HDBK-790, (July, 1992).

[6] J. A. Salem, J. L. Shannon, Jr., and M. G. Jenkins, "Some Observations in Fracture Toughness and Fatigue Testing with Chevron-Notched Specimens,", *Chevron-Notch Test Experience: Metals and Non-Metals, ASTM STP 1172*, K. R. Brown and F. I. Baratta, Eds., ASTM, pp. 9-25, (1992).

[7] J. J. Mecholsky, S. D. Freiman and R. W. Rice, "Fracture Surface Analysis of Ceramics," J. Mater. Sci., 11, 1310-19 (1976).

[8] L. M. Powers, A. Starlinger, J. P. Gyekenyesi, "Ceramic Component Reliability With the Restructured NASA/CARES Computer Program", NASA TM-105856, (1992).

Status of Milestones

Milestone are on time.

Publications

None

Life Prediction Methodology

P. K. Khandelwal (Allison Gas Turbine Division, General Motors Corporation)

Objective/Scope

The objective of this project is to develop and demonstrate the necessary nondestructive examination (NDE) technology, materials data base, and design methodology for predicting the useful life of structural ceramic components of advanced heat engines. The analytical methodology will be demonstrated through confirmatory testing of ceramic components subject to thermal-mechanical loading conditions similar to those anticipated to occur in actual vehicular service. The project addresses fast fracture, slow crack growth (SCG), creep, and oxidation failure modes.

Technical Highlights

Data Base Development

Uniaxial Tensile Testing (Button-Head)

Monotonic tensile testing of 262 PY6 injection molded and hot isostatic pressed (HIP'ed) silicon nitride was completed during this reporting period at Southern Research Institute (SoRI) from room temperature to 1400°C at 4137 MPa/min (600 KSI/min). Table I summarizes the average strength and the flaw characteristics (location, type, and number) at the failure origin for each temperature. Optical micrography and failure analysis of all the specimens have been completed. A limited number of specimens have been examined by scanning electron microscopy (SEM) including X-ray energy dispersive analysis (XEDA). The vast majority of the specimens failed inside the gage section of the specimen. At room temperature about 80% of the specimens failed from inclusions of iron based compounds. At higher temperatures, the failures were evenly mixed between surface and volume flaws, except at 1200°C where about 70% of the specimens failed from surface defects and 30% from volume flaws. The completed data base is being analyzed using the NASA CARES program to estimate the Weibull modulus and characteristic strength at each temperature. The two parameter Weibull analysis will utilize the maximum likelihood estimator (MLE) with suspended items.

Nondestructive Evaluation Development

During this reporting period reference standards with volume holes were designed and fabricated to assess both the detectability and spatial resolution for various types of PY6 material specimens. Both pilot and laser drilled holes varying between 10 to 500 microns in diameter and at various depths were machined in Type-B modulus-of-rupture (MOR) bars, rectangular 15 mm thick billets, and cylindrical button-head specimens. The pilot holes were machined by Bullen Ultrasonics, Eaton, Ohio, and the laser holes were fabricated by Resonatics, Inc., Nashua, New Hampshire, using an Excimer laser. The laser drilled holes in the MOR bars varied from 10 to 100 microns in diameter of varying depths with an aspect ratio ranging from 1 to 290. Two type of holes, namely a combination of pilot/laser holes and laser holes only from 25 to 500 micron diameter and 3 mm deep, were machined in tensile and rectangular billets.

Table I.
Average monotonic tensile strength and analysis of failure origins of button-head specimens.

Temperature – °C	Number of specimens	Average strength – MPa	Standard deviation – MPa	Failure origin: Surface failures: Machining defect	Surface failures: Inclusion	Volume failures: Inclusion	Volume failures: Pore	Other
RT	70	414.40	69.40	5	2	45	6	2 II (O) 10 BHF
1000	20	379.40	115.00	9	1	7	3	
1100	20	313.70	64.80	12	2	2	4	
1200	75	311.20	61.00	50	3	16	6	
1300	20	383.90	53.70	4	0	10	6	
1400	57	301.50	71.80	18	7	20	9	3 SF (O)

BHF = button head failures
II = internal inclusion
SF = surface failure from machining defects
(O) = outside gage in the transition region

A rectangular billet (50 mm x 60 mm x 15 mm with an 88 mm diagonal length) was evaluated using computed tomography (CT). The diagonal length is also called "chord length" in the CT industry, and in general, flaw detection and resolution sensitivity decreases as the chord length increases. In addition, X-ray beam hardening effects also start to play a significant role in defect detection sensitivity. The aforementioned specimen was evaluated with X-ray CT using the Tomoscope Microscopic CT System (TOMO) at ARACOR, Dayton, Ohio. The Tomoscope system had insufficient power (95 kV) to penetrate the 88 mm chord test block length. The reference holes could not be detected with a reasonable signal-to-noise ratio (SNR). The specimen was machined to effectively decrease the chord length to 55 mm. The modified phantom was evaluated using 195 kV tube voltage, 1.0 mm slice thickness, and pixel size of 0.038 mm. Imagery of the new phantom showed considerably more detail; the 500 micron diameter holes were readily detected and resolved, and the 250 micron and 125 micron diameter holes were detected but not resolved. Smaller 25 micron and 50 micron holes were not detected. The specimen will be machined to further decrease the chord length and to determine the detection limit and resolution capability of the Tomoscope.

Chalk River Laboratories, Chalk River, Canada, is assessing the effect of pixel size, system noise, SNR, and the type of defect (air bubbles, iron, iron oxide, iron silicide) on defect detection capability. Analysis for both 2-D and 3-D defects is being conducted. Table II shows a typical example of the detectability limits calculated for a 2-D air (void) cylindrical defect at two rectangular voxel sizes and varying image noise levels. At 0.125 x 0.125 x 1 mm^3 voxel size, 50% smaller flaws could be detected compared to 0.250 x 0.25 x 1 mm^3 voxel size. Figure 1 compares the experimental measurements with the calculated results. It is evident that 50 micron 2-D voids were readily detected at a SNR of 3 and image noise of about 1.5%. The 100 micron cylindrical holes were detected up to almost 5% noise levels. Detectability can be further improved by decreasing the voxel size and increasing the data collection time, which lowers the statistical image noise. Chalk River is continuing the theoretical assessment and experimental verification of the detection capability for the CT technique.

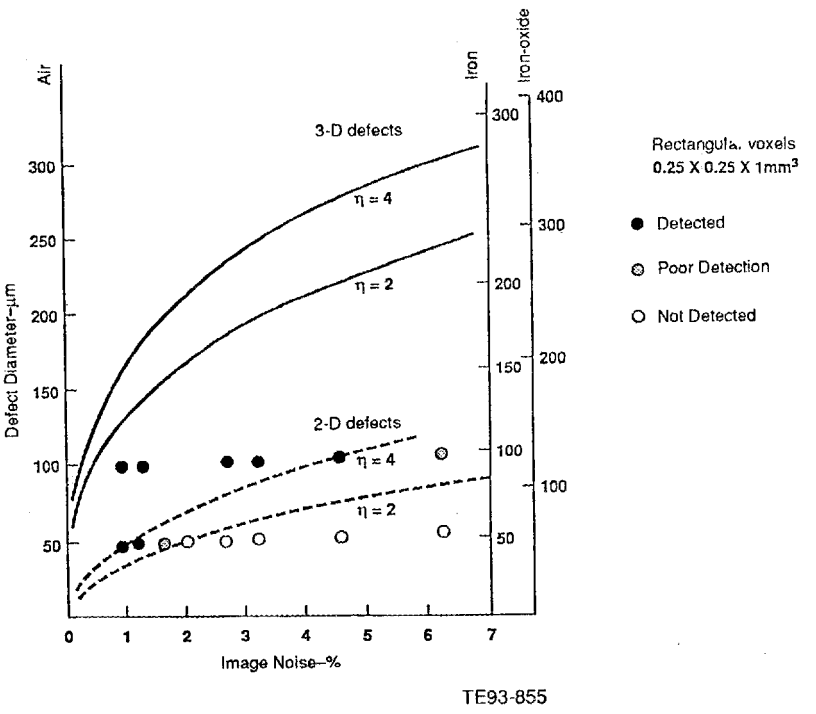

Figure 1. Comparison of calculated and measured flaw detection capability of computed tomography for 2-D cylindrical voids in PY6 silicon nitride.

Table II.
Minimum detectability limits of 2-D cylindrical voids in silicon nitride material using computed tomography.

Image noise – %	Void diameter – mm Voxel size $0.125 \times 0.125 \times 1\ mm^3$	$0.250 \times 0.250 \times 1\ mm^3$
10.0	0.068	0.137
5.0	0.048	0.097
3.0	0.038	0.075
2.0	0.031	0.061
1.0	0.022	0.043
0.5	0.015	0.031
0.2	0.010	0.019
0.1	0.007	0.014

Signal-to-noise ratio (SNR) = 3

Acoustic microscopy (AM) detected 100 micron nominal diameter laser drilled subsurface holes at a depth of 12 mm using a 25 MHz flat transducer and 3.75 mm water path (Figure 2). One Type-B MOR bar 3 mm x 4 mm x 50 mm reference standard with laser drilled holes of 10 to 100 microns in diameter was acoustically examined at various water paths using a 50 MHz, 12.7 mm focal length focused transducer. It was observed that 25 micron diameter holes 0.75 mm below the surface were readily detected at a water path of 1 mm. The same specimen was examined after rotating 90 deg to ascertain the quality of the drilled holes. Figure 3 shows that the 25 and 50 micron holes were tapered. The 10 micron holes were not properly drilled which indicated that small diameter and high aspect ratio defects are difficult to produce. Further ultrasonic analysis of the reference standards is continuing.

Analytical Methodology

During this reporting period Allison received fast fracture data for cold isostatically pressed and HIP'ed NT154 silicon nitride from Garrett Auxiliary Power Division (GAPD). The data included Type-B MOR bars, Type-E MOR bars, and button-head tensile specimens. Failure origins for the room temperature specimens were also transferred. The data was statistically analyzed using the NASA CARES program. In addition, time dependent behavior models were developed and improved. Analysis was conducted on (i) PY6 creep rupture data generated under the current program and the Garrett data on NT154 and (ii) dynamic fatigue data obtained at Allison and HTML/ORNL on MOR bars and at SoRI on button-head tensile specimens.

Fast Fracture Analysis

The NT154 data was normalized to tensile specimen surface area and volume, and analyzed using the CARES probabilistic maximum liklihood method. Type-B MOR bars only had 4 volume failures. No meaningful comparison was possible with either the Type-E bars or the tensile specimen. The volume properties of the Type-E bars and tensile specimens showed excellent correlation (Figure 4). This is expected because the Type-E bars were machined from the same cylindrical specimen used to fabricate button-head tensile specimens. The chamfers of the Type-E bars were polished to minimize corner/chamfer failures as per information provided by Garrett. It is worth noting that the tensile surface finish was different than the chamfer polished surface.

Correlation between both types of the MOR bars and the tensile specimens for surface properties was conducted. Initially, all the MOR data including the chamfer failure was used. Figure 5 shows poor correlation. Subsequently, the chamfer failures were removed from the data set and reanalysed. Figures 6 and 7 show some improvement in comparison between the MOR bars and tensile specimens. However, the difference is still large, which may be due to differing surface flaw populations caused by surface machining variations between the three type of specimens. The Type-E bars were machined from cylindrical rods which have been shown to have large numbers of inclusions.

Analysis of the GAPD elevated temperature data will begin as soon as the fractography data is available. This will determine if the fast fracture data can be consolidated for all temperature levels.

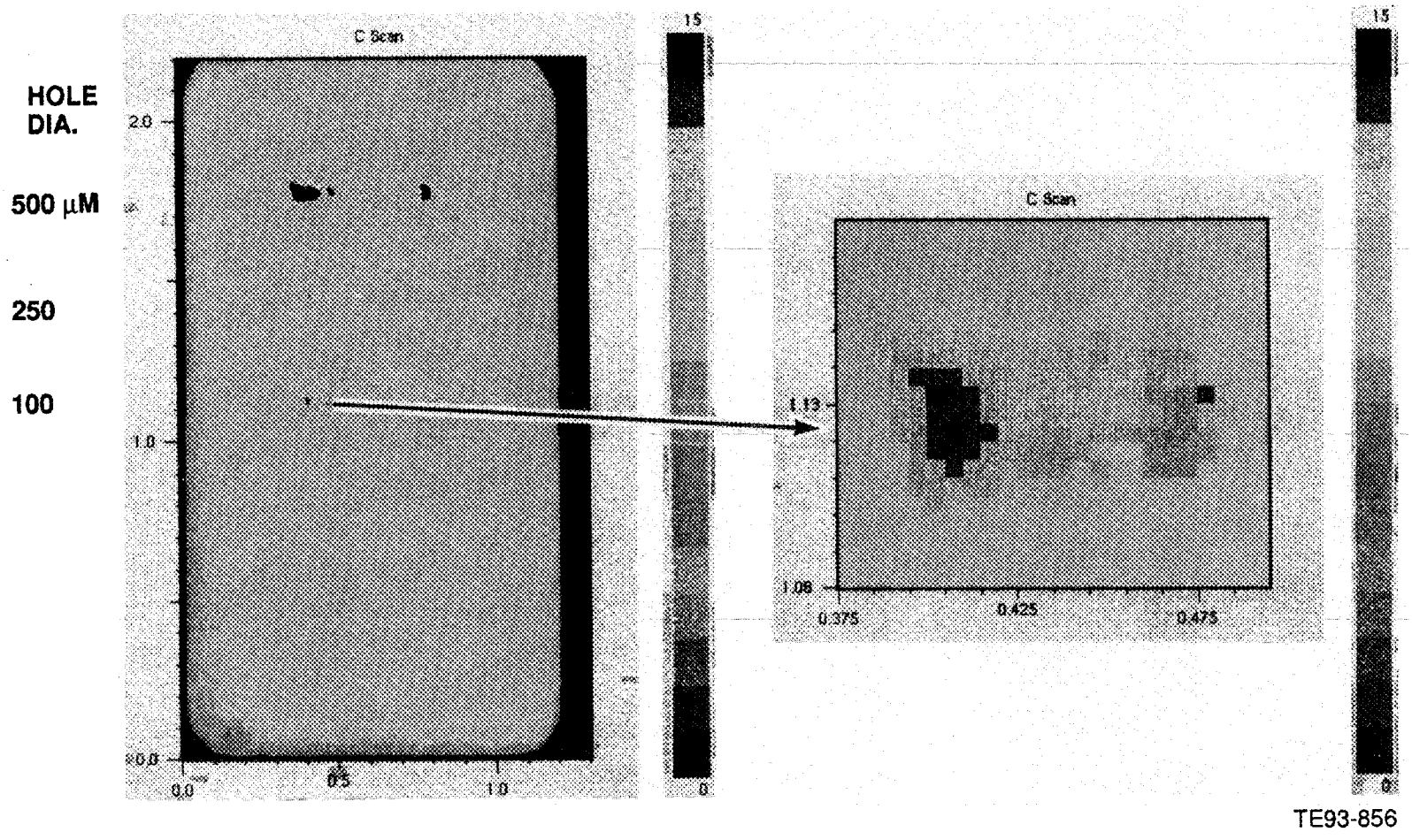

Figure 2. Detection of 100 micron diameter subsurface laser drilled holes at 12 mm depth using ultrasonic imaging.

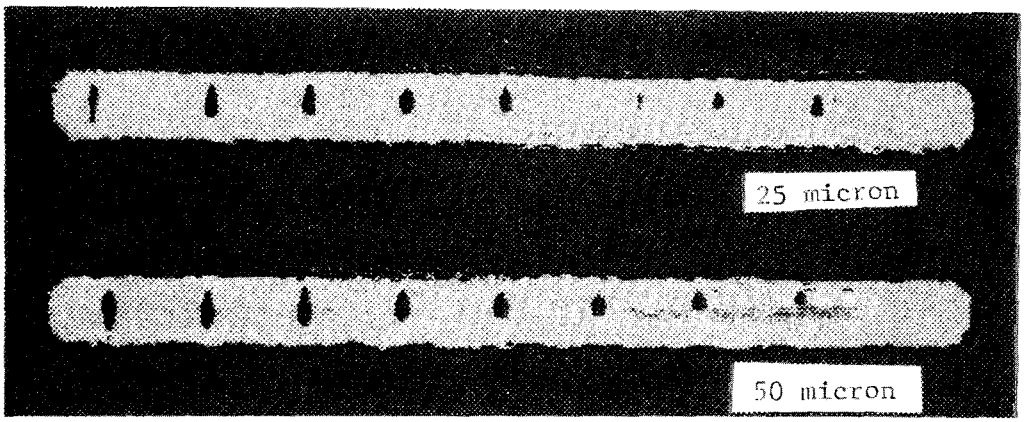

TE93-857

Figure 3. Detection and quality of subsurface holes in Type-B MOR bars.

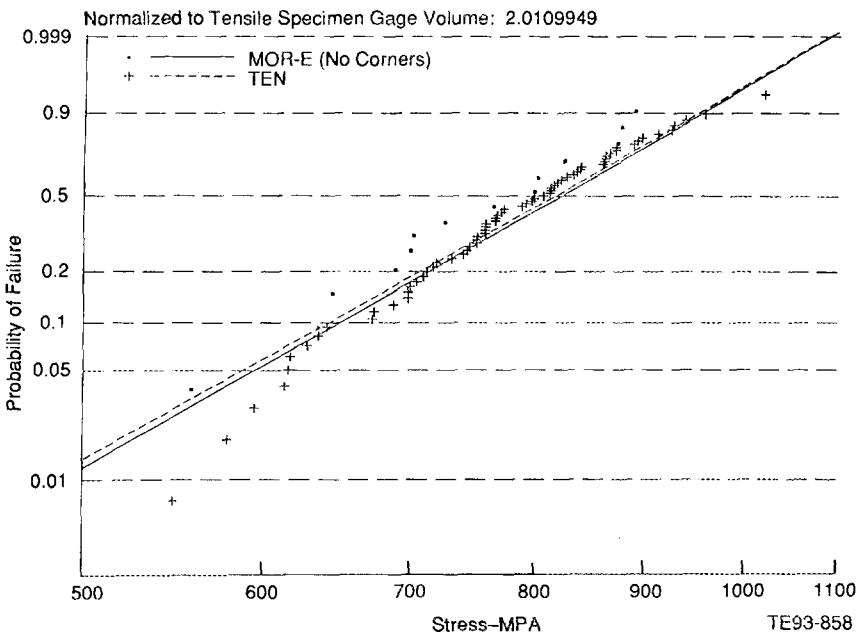

Figure 4. Analysis and correlation of Type-E MOR volume failures normalized to tensile specimen volume for NT154 silicon nitride. The specimens were tested at room temperature by GAPD.

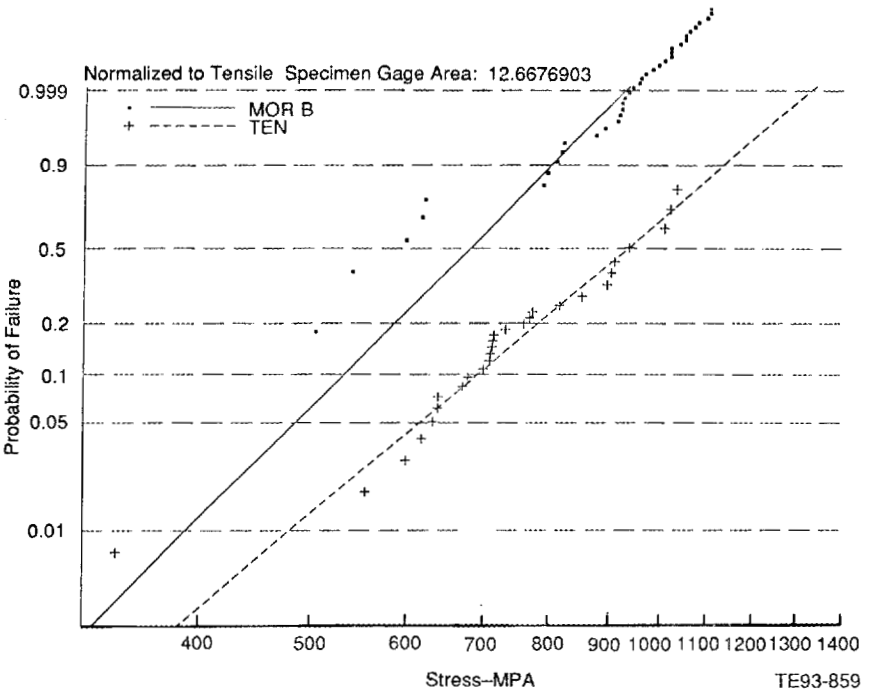

Figure 5. Analysis and correlation of Type-B bar surface failures including chamfer data normalized to tensile specimens of NT154 silicon nitride. The specimens were tested at room temperature by GAPD.

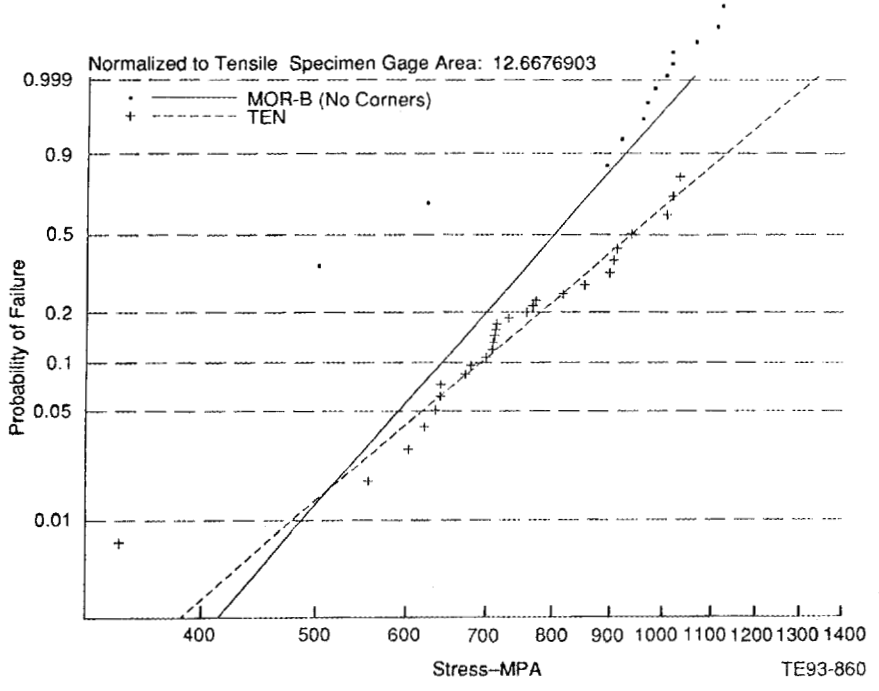

Figure 6. Analysis and correlation of the NT154 Type-B MOR bar surface failures without chamfer failures normalized to tensile specimen surface area. The specimens were tested at room temperature by GAPD.

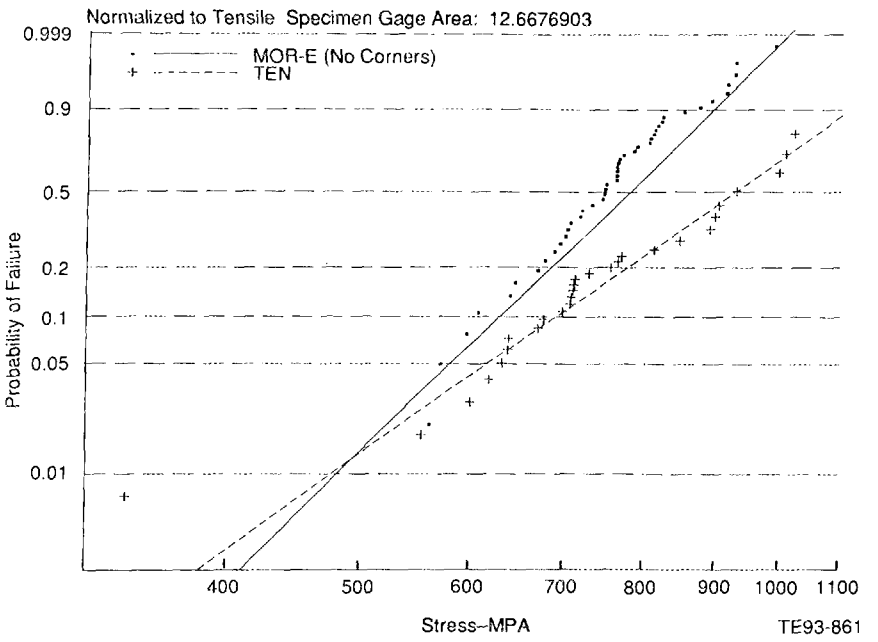

Figure 7. Analysis and correlation of NT154 Type-E bar surface failures without chamfer failures normalized to tensile specimen surface area. Data generated at room temperature by GAPD.

Time Dependent Behavior

When a ceramic specimen is subjected to a constant load at elevated temperatures, both SCG and creep deformation occur, which ultimately result in the failure of the material. In general, at low applied stresses and high temperatures, creep has been microscopically observed to be the dominant failure mode in structural ceramic materials. At higher stresses and lower temperatures, subcritical crack growth has been identified as the primary failure mechanism. There are two methods, namely constant load or stress rupture testing and constant stress rate or dynamic fatigue testing, respectively, which are commonly employed to study the SCG behavior of the ceramic materials. Since either or both of these mechanisms may be present in a constant stress or creep rupture test, analytical models must be structured to account for both of these effects.

Unified Slow Crack Growth/Creep Model

Two general approaches currently exist to develop life prediction analytical models to account for both the SCG and creep failure modes. The first approach utilizes fractographic analysis of each specimen to ascertain the specimen failure mode; then individual models are applied. In the second approach, a somewhat unified model is applied to all of the data; the final result is a data regression and curve fit methodology which characterizes in a continuous manner both the effects of SCG and creep. Such a model has been used by Garrett to characterize the creep rupture data generated on NT154 cold isostatically pressed and HIP'ed silicon nitride material. This work has been conducted under Garrett's Life Prediction program. Allison, during this reporting period, has also explored and developed such a general alternate methodolgy.

The rational and development of the time to failure (T_F) model is as follows:

Under SCG $\quad T_F = B*S_I^{N-2}*S^{-N}*EXP\ (Q_{SCG}/RT)$

If the initial strength is assumed to be independent of temperature, the above equation simplifies to

$$T_F = A*S^{-N}*EXP(Q_{SCG}/RT) \tag{1}$$

The steady-state creep behavior of ceramics is generally represented by a power law function

$$\dot{\varepsilon} = Const.*\ S^{N1}*EXP(-Q_{CR}/RT)$$

and Monkman-Grant relationship

$$T_F = Const.\ \dot{\varepsilon}^{-M}$$

Combining the above two equations and assuming M=1, the equations reduce to

Under Creep $\quad T_F = C*\ S^{-N1}*\ EXP(Q_{CR}/RT)$ (2)

Where:
- T_F = time to failure
- S = applied stress
- S_I = initial fast fracture strength
- T = temperature (absolute)
- Q_{SCG} = activation energy for SCG regime
- Q_{CR} = activation energy for creep regime
- A,B,C,N,N1 = material constants

If the activation energy in SCG is assumed to be the same as that in creep and if $\log(T_F*EXP(-Q/RT))$ is plotted versus log(S), both the SCG and the creep equations require that a least squares regression technique be applied to obtain the optimum bi-log linear curve fit of all the data. Furthermore, the optimum lines are obtained when the standard deviation between the two regressed lines is minimized. For this model, the low stress line segment defines the creep domain and the high stress line defines the SCG domain.

The model described above was applied to both the Allison PY6 and the Garrett NT154 published data bases to assess the differences and similarities in the time-to-rupture behavior of the two materials.

Allison test PY6 data were obtained from 1200°C to 1400°C while Garrett NT154 data were obtained from 1149°C to 1400°C. Table III shows that the Norton rupture exponents (N1) were quite close for both the materials, while the SCG exponent (N) was much higher for the Garrett NT154 material. The effective activation energy for the NT154 material was much higher than that of PY6 material, possibly indicating that the material is less susceptible to high temperature deformation by SCG and creep compared to the PY6 silicon nitride. Additionally, the standard deviation of 2.65 in the LN(failure time) for the PY6 was much higher than that of 1.88 for the NT154. This may be due to the cumulative effect of material composition, varying process controls, and

Table III.
Comparison of PY6 and NT154 rupture time behavior.

Material	Norton creep exponent (N1)	SCG exponent (N)	Activiation energy J/GM-mole	Std. dev. LN(T_F)
PY6	6.8	11.4	498	2.65
NT154	6.7	18.7	1013	1.88

presence of impurities during the manufacture of the test specimens of the two materials. It is known that both the NT154 and PY6 had iron based inclusions which modified the intrinsic behavior of the materials and added to the complexity of analyzing the data. Furthermore, the temperature variation in the gage area including the gradient and strain measurement methods may add to some uncertainity in the overall assessment of the deformation behavior of the materials.

A similar model applicable to regressing creep or SCG deformation rate data was also developed.

Under SCG $$\dot{\varepsilon} = A1*S^{N2}*EXP(-Q_{SCG}/RT) \quad (3)$$

Under Creep $$\dot{\varepsilon} = C1*S^{N3}*EXP(-Q_{CR}/RT) \quad (4)$$

where $\dot{\varepsilon}$ = creep rate
S = applied stress
T = temperature (absolute)
Q_{SCG}, Q_{CR} = activation energy
A1,C1,N3,N2 = material constants

Table IV shows that the Norton creep rate and SCG exponents were similar for both materials. The effective activation energy of the NT154 found from creep data changed little from that found from stress rupture, while the value for PY6 increased about 30%, presumably a small change. Again, the standard deviation of 1.97 in the LN (creep rate) for the PY6 material was much higher than the corresponding 1.06 value for NT154.

Table IV.
Comparison of PY6 and NT154 creep behavior.

Material	Norton creep exponent (N3)	SCG exponent (N2)	Activiation energy J/GM-mole	Std. dev. LN
PY6	5.1	10.2	664	1.97
NT154	5.3	11.7	996	1.06

While this model has appeal as a result of its relative simplicity, the number of assumptions used in this model may compromise the accuracy more than is acceptable when compared with a more rigorous and separate development of both creep and SCG methodologies. The assumptions inherent in the above models are as follows:

- The activation energy in SCG and creep is assumed to be identical.
- The scatter in both the SCG and creep domain is constant.
- The effect of initial fast fracture strength on the SCG behavior of the material is ignored.

Further modeling is in progress to address some of the inadequacies which have been observed in the current models.

Dynamic Fatigue Testing/Modeling

In the constant load or stress rupture testing, time to rupture of the specimens is determined for various applied stress levels. In constant rate or dynamic fatigue characteriztion of a material, the specimen failure strength is measured at various stressing rates. Both the approaches were used during this reporting period to analytically model the experimental data to assess the SCG parameters using the button-head tensile and Type-B MOR specimens of PY6 HIP'ed silicon nitride material. The governing equations for the two type of tests were derived and simplified as follows:

Constant load $$T_F = B^*S_i^{N-2}*S^{-N}*EXP\ (Q/RT) \quad (5)$$

Constant rate $$S_F = (B^*(N+1)^*S_i^{N-2}*\dot{S})^{1/(N+1)}*EXP(Q/RT^*(1+N)) \quad (6)$$

where
- T_F = time to failure (constant load test)
- S_F = fracture strength (constant rate test)
- S_i = initial, fast fracture, strength
- S = applied stress
- $\dot{S}$ = applied stress rate
- T = temperature (absolute)
- Q = activation energy (material constant)
- B, N = material constants

In these equations, the activation energy allows the consolidation of test data obtained at various temperatures. In theory the material constants Q, B, and N obtained from constant rate (dynamic fatigue) testing should be identical to those obtained from constant load or stress rupture testing. Also, it can be shown that a standard deviation on the $LN(T_F)$ is related to a standard deviation of $LN(S_F)$ by the equation:

$$std(LN(T_F)) = (1+N) * std(LN(S_F)) \quad (7)$$

Constant rate or dynamic fatigue behavior of three groups of PY6 hip'ed silicon nitride specimens was measured and analyzed using equation (6). The most comprehensive data set was developed at Allison on 117 Type-B MOR bars tested from 1200 to 1400°C characterized at various stress

rates. A second set of 29 Type-B MOR bars were tested from 1000 to 1400°C under a user agreement at Oak Ridge National Laboratories under the direction of Dr. M.K.Ferber. Finally, 28 button-head tensile specimens were tested by SoRI at various temperatures and stress rates. Table V summarizes the the calculated results. As can be seen, all three data sets yielded similar results for values of N, B, and activation energy (Q). The major difference was in the much smaller value of B for tensile specimens. Excellent agreement was observed in the values of the constant obtained from the Allison and ORNL data on MOR bars indicating that the activation energy term worked well in consolidating the data. Further modeling effort is continuing.

Table V.
Comparison of slow crack growth constants for differing specimens and laboratories.

Source	Temperature °C	SCG exponent (N)	Coefficient 'B' MPa^2-sec	Activation energy (Q) J/gm-mole	Scatter LN (T_F)
Allison	1200-1400	17.2	3.44E-4	277	1.66
ORNL	1000-1400	20.2	4.43E-4	206	3.71
SoRI	1000-1400	17.8	2.74E-6	283	2.36

Status of Milestones

322201: Computer Implementation of Initial Failure Models — complete
322202: Initiation of MOR Testing — complete
322203: Initiation of Tensile Testing — complete
322204: Initiation of Biaxial Testing — complete
322205: Confirmatory Testing — discontinued because of the poor quality spin disks received from GTE
322206: Completion of All Specimen Testing — on schedule
322207: Finalization/Verification of Computer Code — on schedule
322208: Draft Final Report — on schedule
322209: Final Report — on schedule

Presentations and Publications

1. Pramod Khandelwal presented a paper "Life Prediction Methodology for Engine Components" at the ASTM Symposium *Life Prediction Methodologies and Data for Ceramic Materials in Advanced Applications - A Basis for Standards*, January 11-13, 1993, Cocoa Beach, FL.
2. A paper entitled "Fracture Toughness of a HIPed Silicon Nitride at Elevated Temperatures," A. A. Wereszczak, M. K. Ferber, and R. R. Sanders, Oak Ridge National Laboratories, M. G. Jenkins, University of Washington, Seattle, and P. Khandelwal, Allison Gas Turbine Division of General Motors Corporation, was presented at the 17th Annual Conference and Exposition on Composites and Advanced Ceramics, January 10-15, 1993, Cocoa Beach, FL.
3. Pramod Khandelwal presented a paper "Development of NDE Techniques for Ceramic Components" at the ASNT 2nd Annual Research Symposium, March 30-April 1, 1993, Nashville, TN.

3.3 ENVIRONMENTAL EFFECTS

Environmental Effects in Toughened Ceramics

Norman L. Hecht (University of Dayton)

Objective/scope

Since December 1984, the University of Dayton has been involved in a five-phase project to investigate the effects of environment on the mechanical behavior of commercially available ceramics being considered for heat engine applications. In the first phase of this project, the effects of environment on the mechanical behavior of transformation-toughened ZrO_2 ceramics were investigated. In the second phase, two Si_3N_4 ceramics (GTE PY6 and Norton/TRW XL144) and one SiC ceramic (Hexoloy SA) were evaluated. In the third phase, the tensile, flexural, and fatigue strength of three SiC and six Si_3N_4 ceramics were evaluated at temperatures ranging from 20 to 1400°C. Microstructure, chemistry, and physical properties were also investigated. In the fourth phase, the flexural strength and fatigue behavior of two additional Si_3N_4 ceramics (Kyocera SN-260 and Garrett GN-10) were investigated. In addition, the fatigue behavior of one Si_3N_4 ceramic (Norton/TRW NT-154) was investigated. In phase five, five newly developed SiC and three newly developed Si_3N_4 ceramics are being investigated. In addition, the effects of different machining processes on the mechanical behavior of selected SiC/Si_3N_4 ceramics will be studied.

During the past six months (October 1992 through March 1993) analysis of the mechanical behavior of candidate SiC and Si_3N_4 ceramics was continued. Evaluation of Kyocera's SN-253, Si_3N_4, Dow Corning's β-SiC, Carborundum's Hexoloy SX-G1, SiC, and Garrett's GS-44, Si_3N_4 was conducted.

Technical progress

Flexural strength, elastic modulus, hardness, density, coefficient of thermal expansion, and fracture toughness were evaluated for β-SiC and SN-253. In addition, the flexural strengths of GS-44 and SX-G1 were also measured. The flexural strength test matrix for these four ceramics is presented in Table 1.

The flexural strength measurements were made using Instron Universal Testing Machines (Model 1123) following MIL-STD-1942(MR). Elevated temperature measurements were conducted in ATS model #3320 high-temperature furnaces. Flexural strengths were measured on test specimens with nominal dimensions of 3 x 4 x 50 mm with all surfaces ground to a 16-microinch finish [MIL-STD-1942(MR) specimen size B]. The long edges of the tensile surface were beveled to minimize edge failures. Flexural strength was measured using four-point bend test fixtures, and the test specimens were loaded at machine crosshead speeds of 0.004, 0.0004, and 0.00004 cm/sec (0.1, 0.01, 0.001 in/min). The bend fixtures for all measurements were made of SiC. The four-point bend fixtures have an outer span of 40 mm and an inner span of 20 mm.

*Research sponsored by the U.S. Department of Energy, Assistant Secretary for Energy Efficiency and Renewable Energy, Office of Transportation Technologies, as part of the Ceramic Technology Project of the Materials Development Program under contract DE-AC05-840R21400 with Martin Marietta Energy Systems, Inc.

Table 1. Flexural Strength Test Matrix for SN-253, β-SiC, GS-44, and SX-G1

Temperature (°C)	Crosshead Speed (cm/s)	Number of Specimens SN-253	β-SiC	GS-44	SX-G1
20	0.004	10	10	10	5
20	0.00004	10	5	5	5
1000/1050	0.004	-	-	10	5
1000/1050	0.00004	-	-	5	5
1250	0.004	10	5	-	-
1250	0.00004	5	5	-	-
1350	0.004	10	5	-	-
1350	0.0004	5	-	-	-
1350	0.00004	5	5	-	-
20/1000+	0.004	-	-	5	-

+After 200 hours aging at 1100°C in air.

Physical property measurements were made using the following methods.

- Fracture origins were determined by optical microscopy (Nikon Epiphot) and SEM (JEOL/SM-80 with EG&G Ortec System 5000 Microanalysis System).
- The microstructure and chemistry of the candidate materials were also studied. Polished specimens were plasma etched and viewed by optical microscopy and scanning electron microscopy.
- Thermal expansion was measured from 20°C to 1370°C using a Theta Industries Dilatronic II (Model 6024).
- The elastic modulus was measured from 20°C to 1350°C using a Grindo-Sonic (Model MR35T) Transient Impulse/Elastic Modulus apparatus.
- The hardness of the candidate materials was measured by a Vickers micro-indent hardness tester. Fracture toughness was measured by the controlled flaw method using an indent load of 500g.

The results of the flexural strength measurements are summarized in Tables 2, 3, 4, and 5, respectively, and are shown graphically in Figures 1, 2, 3, and 4. The Weibull statistics obtained for these flexural strength measurements are presented in Table 6. Photomicrographs of typical fracture surfaces for β-SiC, SX-G1, and GS-44 are presented in Figures 5, 6, and 7. The inclusion observed in the Hexoloy SX-G1 were found to be metal impurities containing Al, Fe, and Ni (see Figure 8). For β-SiC and SN-253 hardness, density, Young's modulus , coefficient of thermal expansion, and fracture toughness were measured. The results of these measurements are compiled in Tables 7 and 8, respectively. The GS-44 flexure specimens were aged in air for 200 hours at 1100°C. The flexural strength of these air aged specimens was measured at 20°C and the results are included in Table 4. In addition, the change in weight and surface roughness was measured after 200 hours of aging. The results of these aging measurements for GS-44 are presented in Table 9. In addition, five SN-253 specimens were aged for 500 hours in air at 1300°C. Weight changes were measured every 100 hours. The results of these measurements are presented in Table 10.

Table 2. Flexural Strength Measured for SN-253

Temperature (°C)	Crosshead Speed (cm/s)	Strength (MPa)	Fracture Origin
21	0.004	859 (±99)	9 surface/1 edge
21	0.00004	819 (±63)	7 surface/2 edge/1 inclusion
1250	0.004	732 (±38)	7 surface/1 edge/2 inclusion
1250	0.00004	618 (±33)	5 surface
1350	0.004	617 (±43)	8 surface/1 edge/1 inclusion
1350	0.0004	572 (±32)	5 surface
1350	0.00004	505 (±42)	5 surface*

*Appearance of slow crack growth.

Table 3. Flexural Strength Measured for β-SiC

Temperature (°C)	Crosshead Speed (cm/s)	Strength (MPa)	Fracture Origin+
21	0.004	463 (±22)	3 surf/2 edge/4 vol pits/2 surf pits
21	0.00004	421 (±33)	5 surf
1250	0.004	442 (±73)	2 vol incl/1 edge, 1 surf pit/1 surf
1250	0.00004	464 (±19)	2 surf/1 pit, 1 incl surf/edge incl
1350	0.004	460 (±62)	2 vol incl/2 edge incl/surf pit
1350	0.00004	475 (±52)	2 surf/1 pit, 1 incl vol/edge incl

+surf - surface, vol - volume, incl - inclusion

Table 4. Flexural Strength Measured for GS-44

Temperature (°C)	Crosshead Speed (cm/s)	Strength (MPa)	Fracture Origin
21	0.004	1160 (±162)	*
21	0.00004	1139 (±42)	1 surface/1 edge/remainder *
1050	0.004	759 (±80)	*
1050	0.00004	635 (±66)	5 surface
21+	0.004	984 (±24)	3 surface/1 volume inclusion/1*
1000+	0.004	902 (±192)	4 surface/1 edge

+Tested after aging 200 hrs @ 1100°C.
*Could not be determined because of the high fracture energy

Table 5. Flexural Strength Measured for Hexoloy SX-G1

Temperature (°C)	Crosshead Speed (cm/s)	Strength MPa)	Fracture Origin
21	0.004	898 (±150)	3 surface/1 volume/1 inclusion
21	0.00004	864 (±99)	4 volume inclusion
1000	0.004	581 (±91)	4 surface/1 edge
1000	0.00004	625 (±92)	3 surface/1 volume/1 inclusion

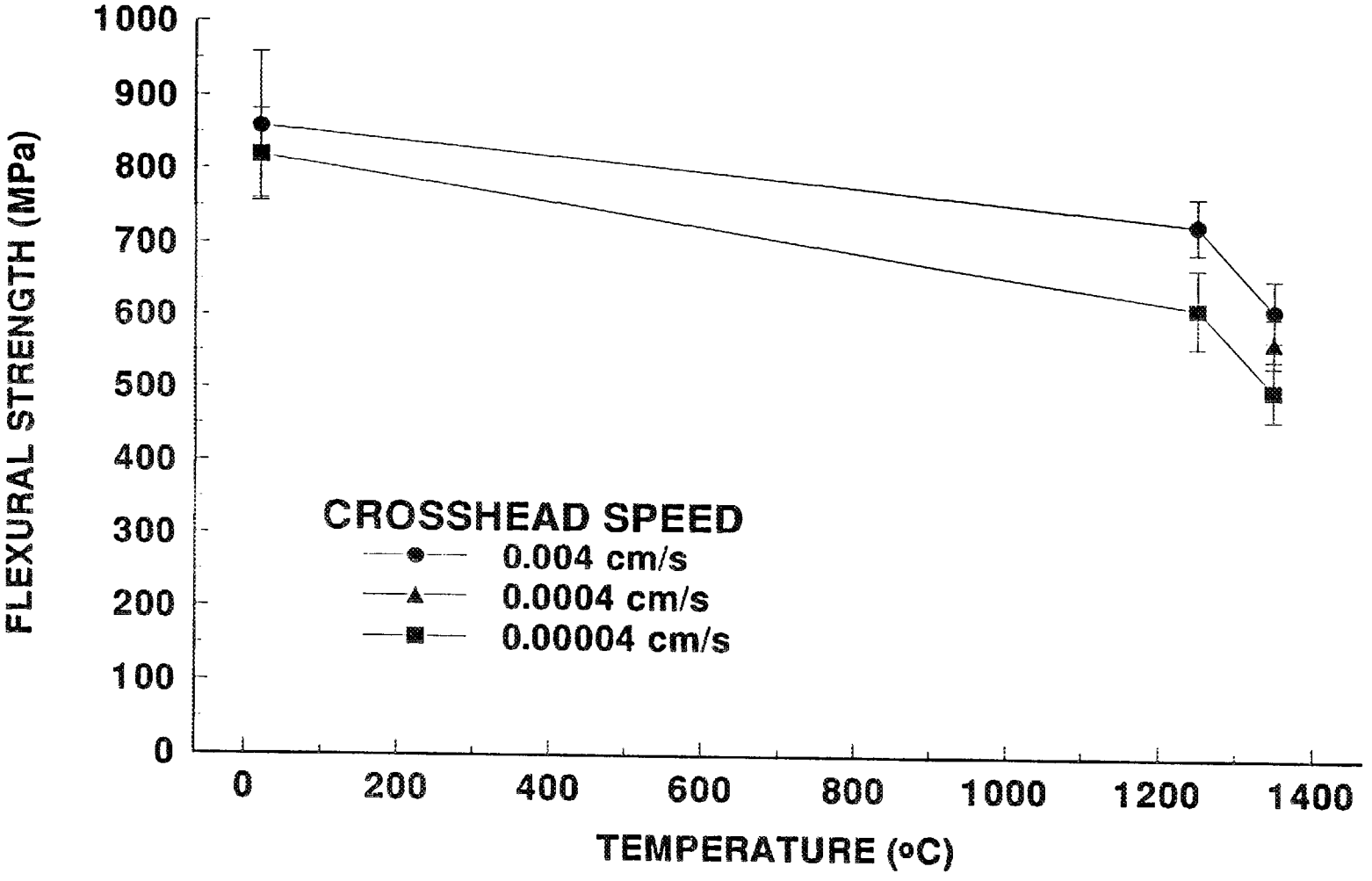

Figure 1. Flexural Strength of Kyocera SN-253

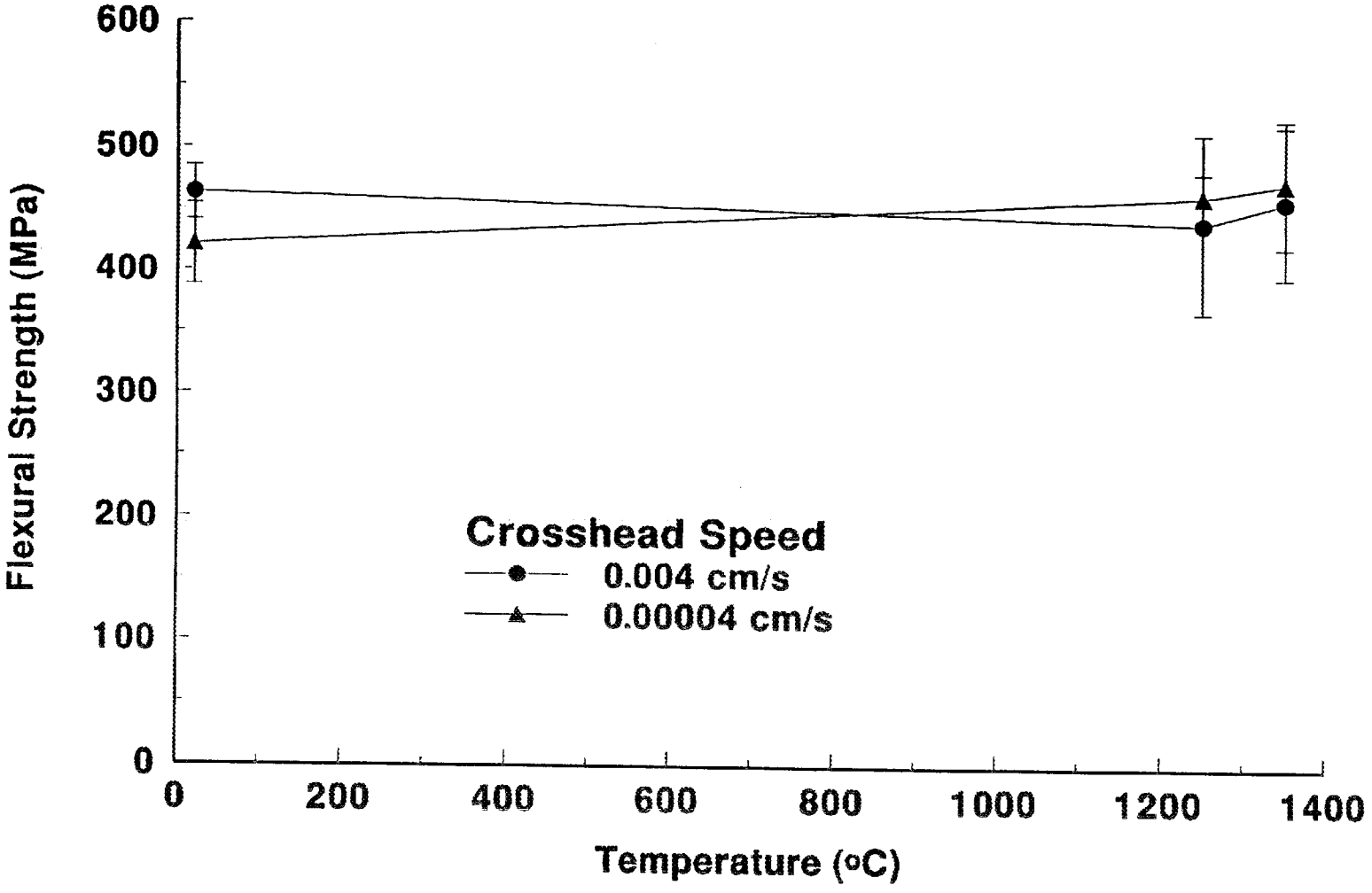

Figure 2. Flexural Strength of Dow Corning β-SiC.

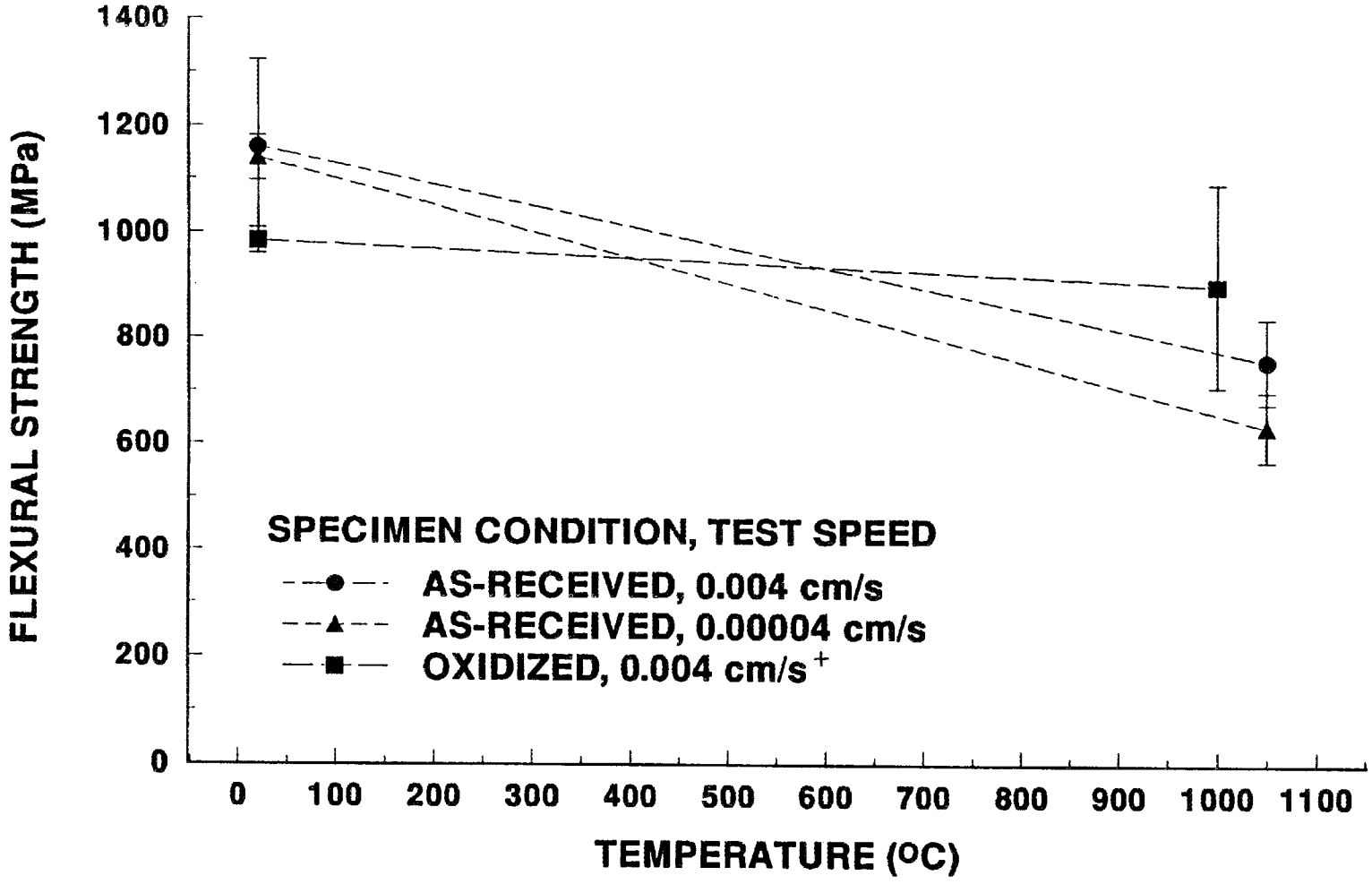

Figure 3. Flexural Strength of Garrett GS-44

+Specimens were oxidized for 200 hours at 1100°C.

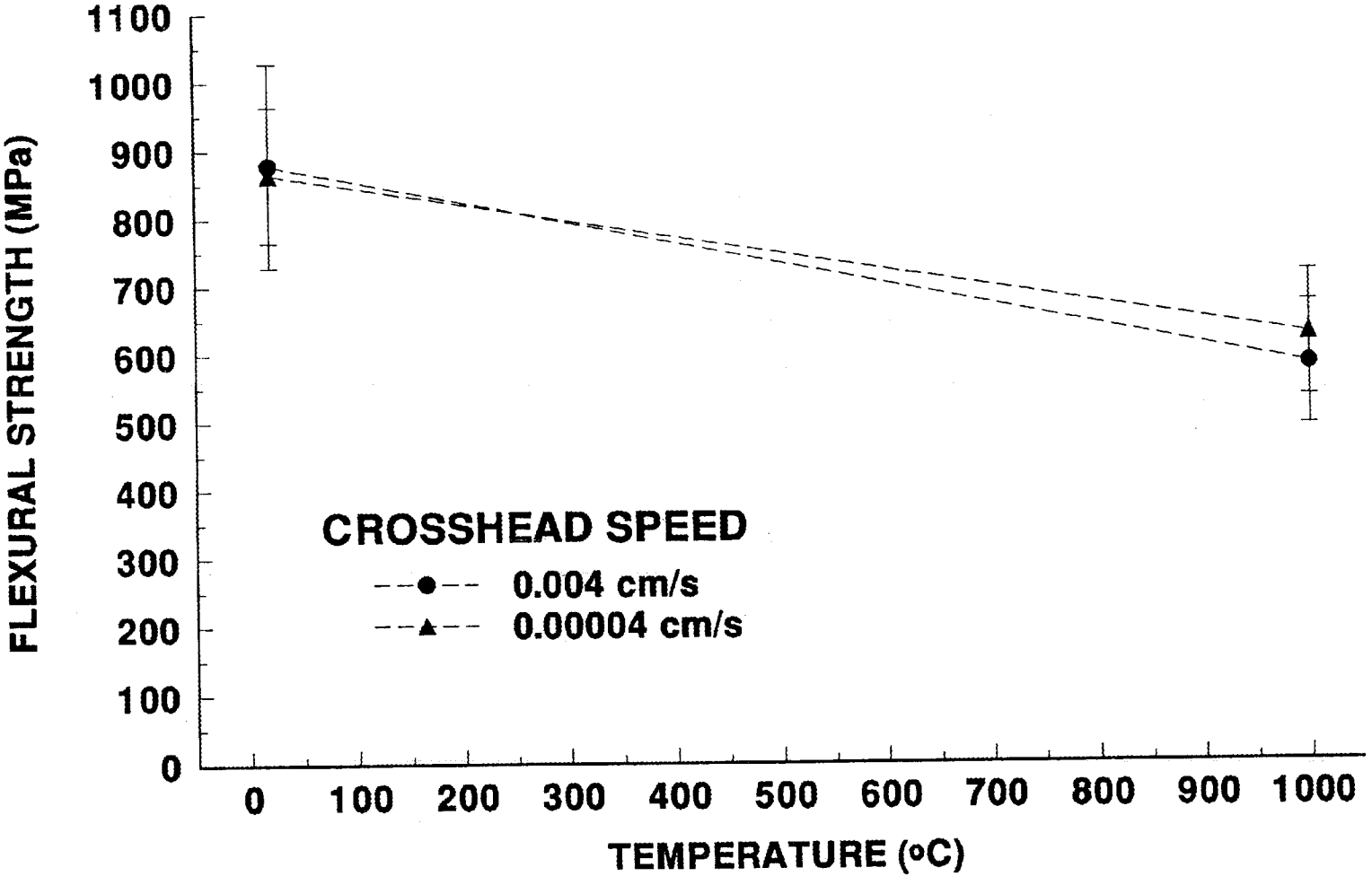

Figure 4. Flexural Strength of Carborundum SX-G1.

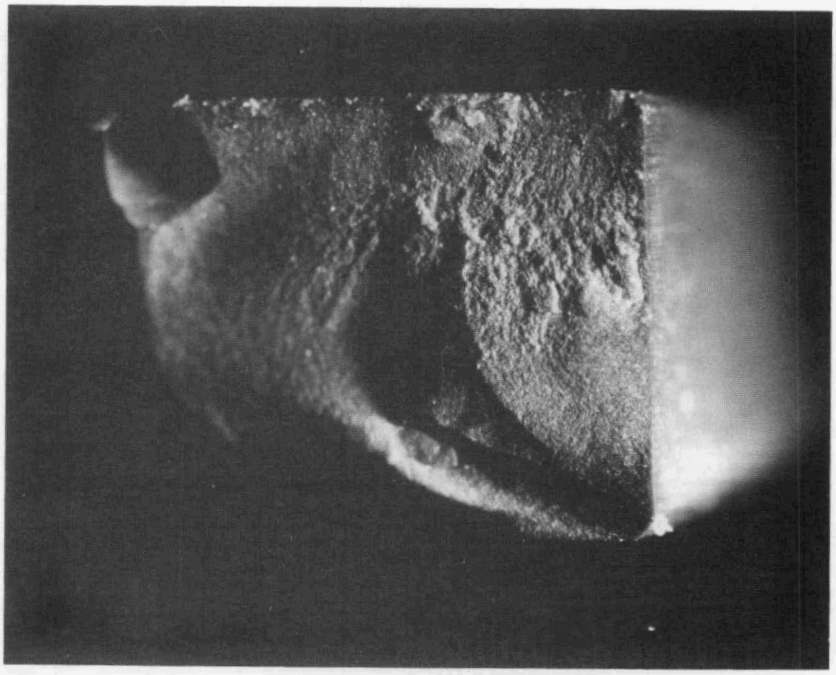

(a) 20X

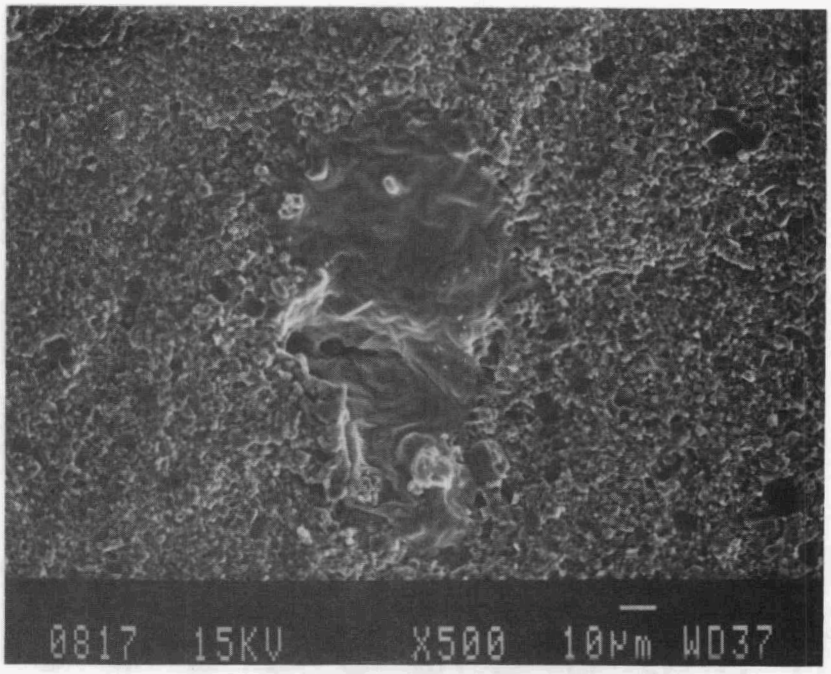

(b) 500X

Figure 5. Photomicrographs of the Fracture Surface of an SX-G1 Flexure Specimen.

(a) 20X

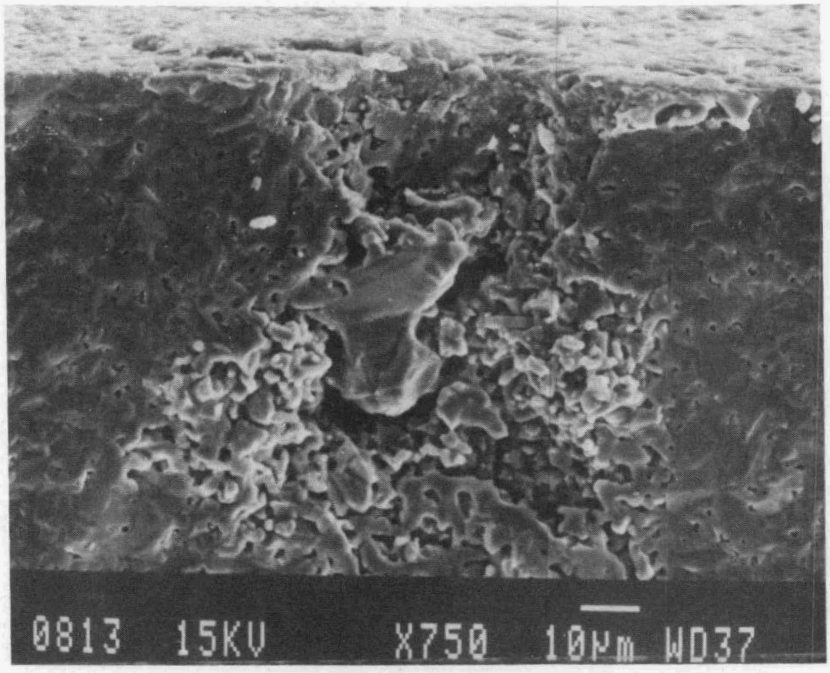

(b) 750X

Figure 6. Photomicrographs of the Fracture Surface of a β-SiC specimen..

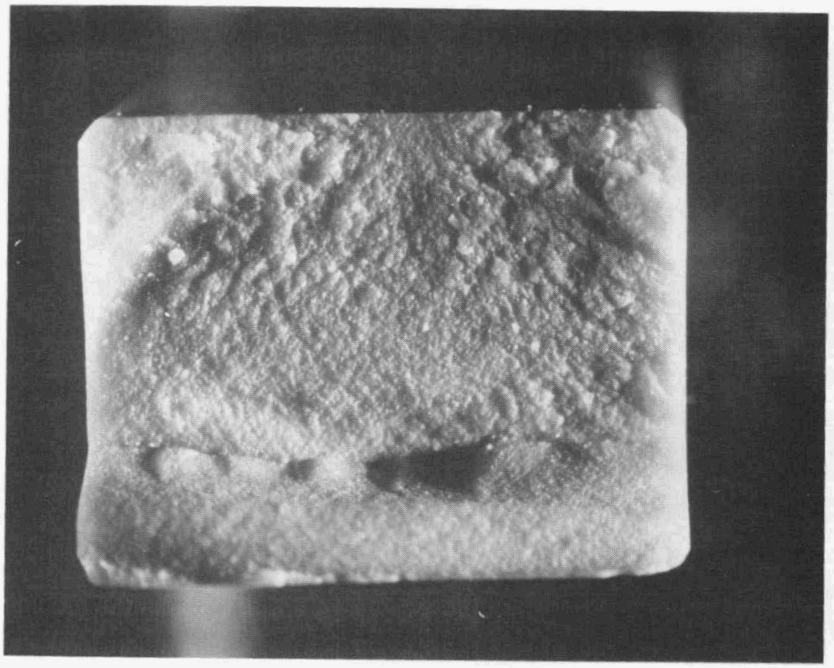

(a) 20X

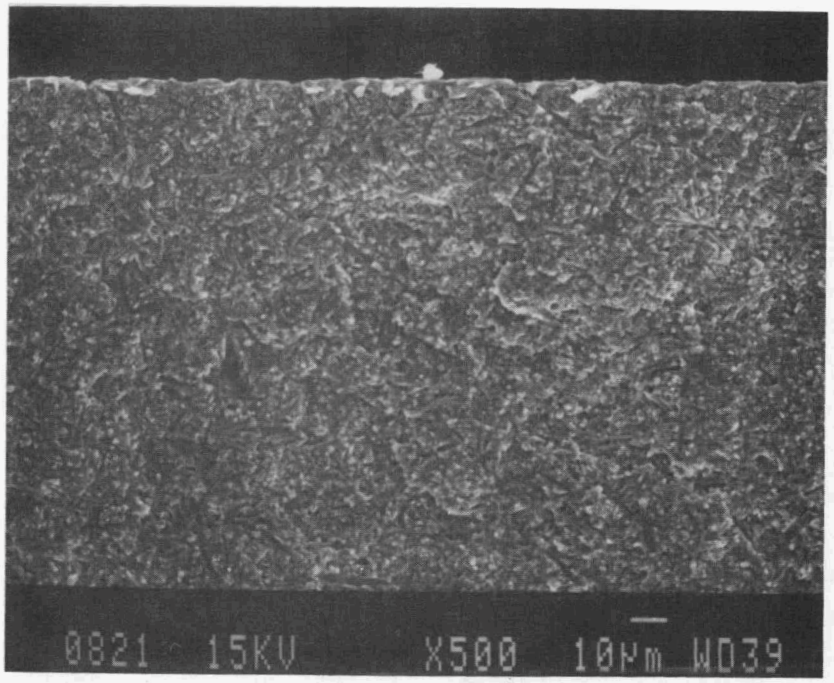

(b) 500X

Figure 7. Photomicrographs of the Fracture Surface of a GS-44 Specimen.

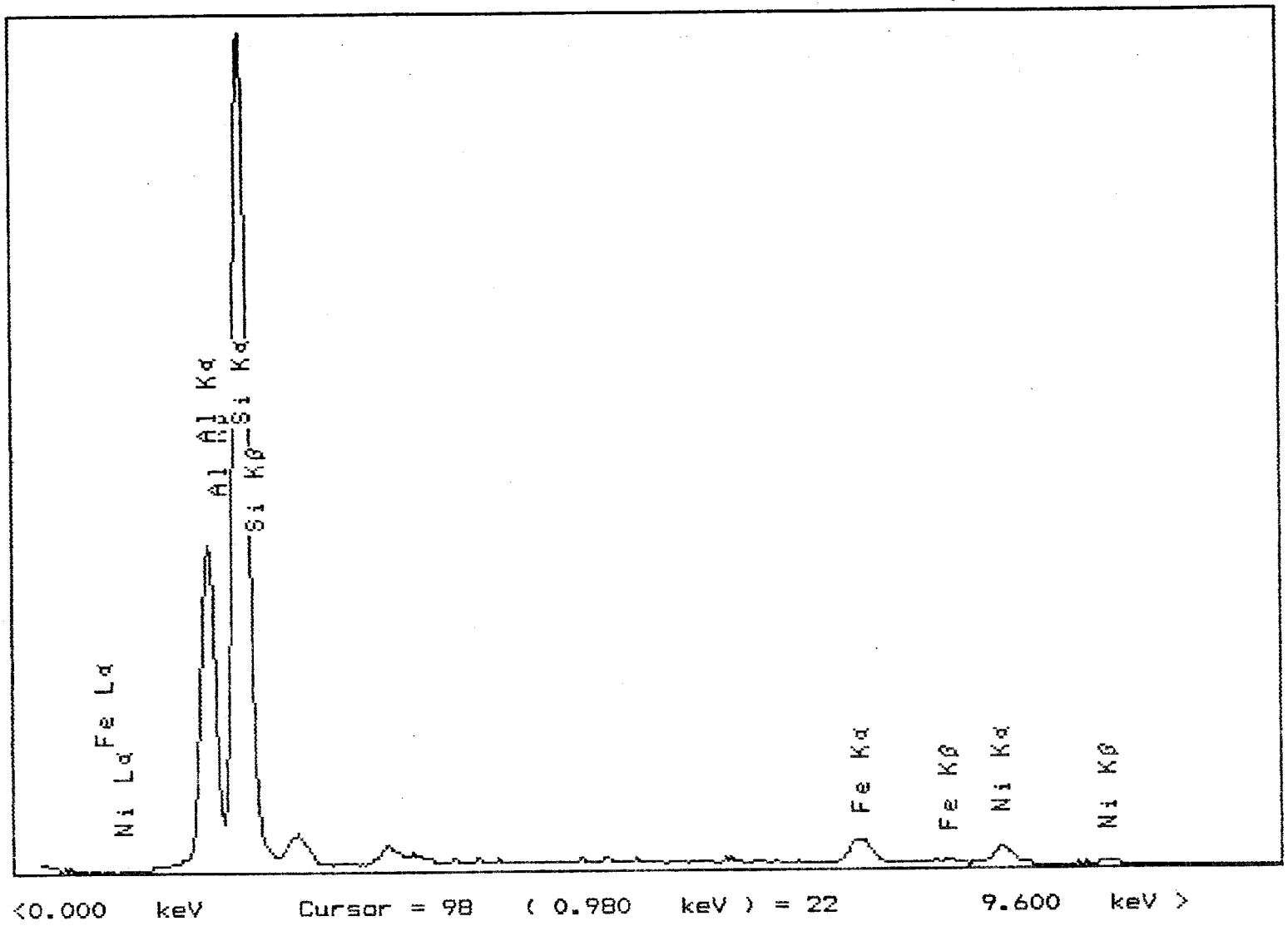

Figure 8. EG&G Ortec System 500 Spectra for Specimen 2-5 Hexoloy SX-G1.

Table 6. Weibull Statistics - Flexure Tests, 10 Specimens per Test Set

Material	Temp. (°C)	Loading Rate (MPa/s)	Weibull Modulus (m)	Weibull Scale (Data) S_o(MPa)	Weibull Scale (Area) S_o(MPa)	95% Confidence Limits on Scale (Data) S_o(MPa)
β-SiC	20	190	22.9	473	314	(457,490)
NT-164	20	143	14.3	1134	588	(1072,1199)
	1250	118	12.0	787	359	(736,841)
	1350	116	38.5	798	625	(782,815)
SN-253	20	143	10.7	901	375	(836,971)
	20	1.43	16.9	846	485	(807,887)
	1250	118	22.0	749	489	(722,777)
	1350	116	17.0	636	366	(607,667)
GS-44	20	143	11.6	1221	542	(1139,1309)

Table 7. Some Physical and Thermal Properties of SN-253

1. Young's modulus 20° 316 GPa 1000° 301 GPa 1250° 299 GPa 1350° 294 GPa
2. Density 3.45 g/cc
3. Fracture toughness 6.2 MPa $\sqrt{m}$
4. Hardness 1599 (±86) kg/mm^2
5. Coefficient of thermal expansion (20-1400°C) 4.55 $^{mm}/_{mm}$/°C

Table 8. Some Physical and Thermal Properties of β-SiC

1. Young's modulus 20° 412 GPa 1000° 412 GPa 1250° 385 GPa 1350° 379 GPa
2. Density 3.15 g/cc
3. Fracture toughness 2 MPa $\sqrt{m}$
4. Hardness 2769 (±619) kg/mm^2
5. Coefficient of thermal expansion (20-1400°C) 6.78 $^{mm}/_{mm}$/°C

Table 9. Oxidation Results for GS-44

1. Change in surface roughness
As-received 7μ inch
Post-oxidation 9 μ inch
2. Change in weight
As-received 1.92796
Post oxidation 1.92822
0.00026 = 0.0135% change

Table 10. Oxidation Results for Kyocera SN-253*

Specimen Number	Percent Weight Change					
	100 hrs	200 hrs	300 hrs	400 hrs	500 hrs	Total
1	0.046	-0.015	0.031	0.015	0.015	0.093
6	0.061	-0.010	0.020	0.020	0.010	0.102
9	0.049	0.016	0.000	0.049	0.000	0.115
18	0.030	0.000	0.020	0.030	0.010	0.090
20	0.031	0.016	0.000	0.047	0.000	0.093
Average	0.044	0.001	0.014	0.032	0.007	0.099

*Oxidation temperature: 2372°F (1300°C) in air.

The evaluation of Kyocera SN-253, Dow Corning, β-SiC, and Carborundum Hexoloy SXG-1 is part of our project to characterize new generation SiC and Si_3N_4 ceramics. As part of this project, Norton/TRW's NT-230 and NT-164 were also evaluated and the results are reported in earlier reports. Garrett's GS-44 is being used to investigate the effects of selected machining treatments. The base line characterization of GS-44 machined according to MIL STD-1942 were reported during this reporting period. The GS-44 Si_3N_4 had very high room temperature flexure strengths and high fracture energies. After aging in air for 200 hours at 1100°C the room temperature strength dropped 15%. Flexure strength of GS-44 at 1050°C decreased 35% from the strength measured at 20°C.

Based on the results obtained, it was found that SN-253 has flexural strengths greater than SN-252 and its mechanical behavior is similar to that observed for NT-154. The SN253 was not effected by exposure to aging in air. The SX G-1 has flexural strength values at 20°C and 1000°C considerably higher than Hexoloy SA. However, the flexural strength of SX G-1 dropped about 25% from 20°C to 1000°C, and relatively large standard deviations at both measuring temperatures (~16% variation from the mean) were observed.

The β-SiC had an average flexural strength of ~450 MPa from 20-1350°C. The β-SiC exhibit similar behavior as was observed for Hexoloy SA but with an average flexural strength that was 10% higher. About half the strength failures originated at pits or inclusions.

Status of milestones

Milestones 331415, 331416, and 331417 are in progress.

3.4 FRACTURE MECHANICS

Testing and Evaluation of Advanced Ceramics at High Temperature in Uniaxial Tension — J. Sankar, A. D. Kelkar, and J. Neogi (Department of Mechanical Engineering, North Carolina A & T State University, Greensboro, NC 27406)

Objective/Scope

The purpose of this effort will be to test and evaluate the mechanical behavior of a Si_3N_4 in uniaxial tension at temperatures up to 1300 °C. Testing include tensile strength and creep strength. This effort will comprise of the following tasks:

Task 1. Specifications for testing machine and controls + (procurement) for creep testing.
Task 2. Identification of test material(s) for the present year + (procurement of specimens).
Task 3. Identification of test specimen configuration.
Task 4. Identification and procurement of test grips, high temperature extensometer and furnace for the creep machine.
Task 5. High temperature fatigue-creep interaction study and tensile testing.
Task 6. Reporting (periodic).
Task 7. Final report.

It is anticipated that this program will help in understanding the behavior of ceramic materials at very high temperature in uniaxial tension.

Technical Progress

During the semiannual reporting period Nov. '92 to April '93, the following were accomplished:

Detailed creep tests were performed on Si_3N_4 GTE-PY6 specimens in uniaxial tension under different loading conditions. Two typical test data obtained are shown in figure 1 and 2.

Figure 1 is for specimen #2, constant load of 175.7 MPa (70% tensile strength (σ_{ts}) of GTE-PY6 at 1300 °C) at 1300 °C and figure 2 is for specimen #6, constant load of 186 MPa (60% tensile strength (σ_{ts}) of GTE-PY6 at 1200 °C) at 1200 °C. Analysis of all data in terms of strain rate vs. stress, calculation of stress exponents and Monkman-Grant relation are being carried out at present.

Four GTE-PY6 specimens were also pulled in pure tension at room and elevated temperatures to determine their tensile strength. Comparisons (Table 1, Fig. 3) were made between the tensile strength data obtained at A&T, UDRI (University of Dayton Research Institute, OH) and ORNL (Oak Ridge National Laboratory, TN). The results obtained at 1200 °C fall within the curves of UDRI and ORNL. As can be seen from the plot, the strength drops significantly after 1000 °C. The strength dropped by 59.72% from room temperature to 1300 °C. Comparison of tensile strength values of GTE-PY6

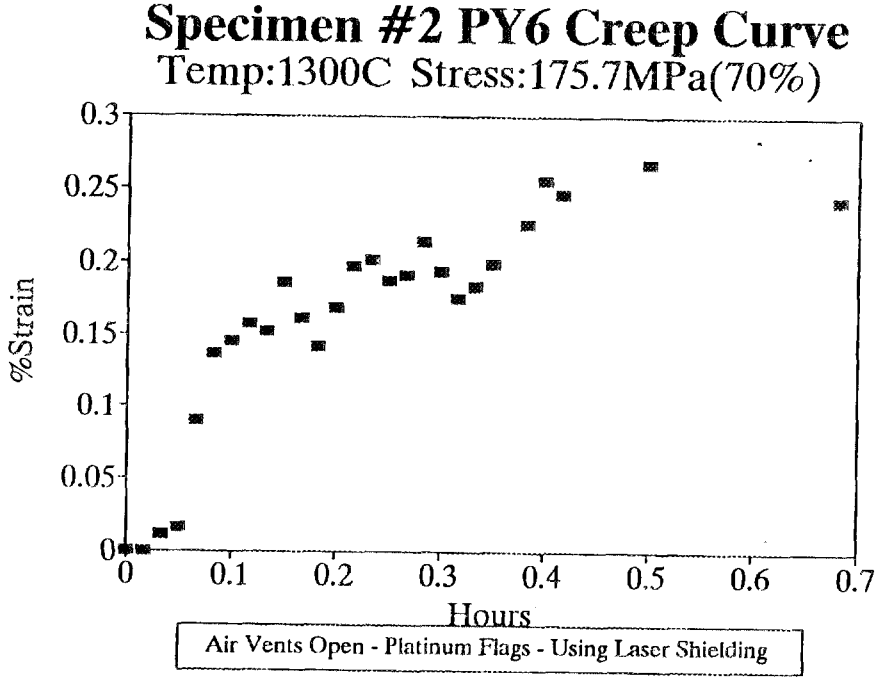

Figure 1

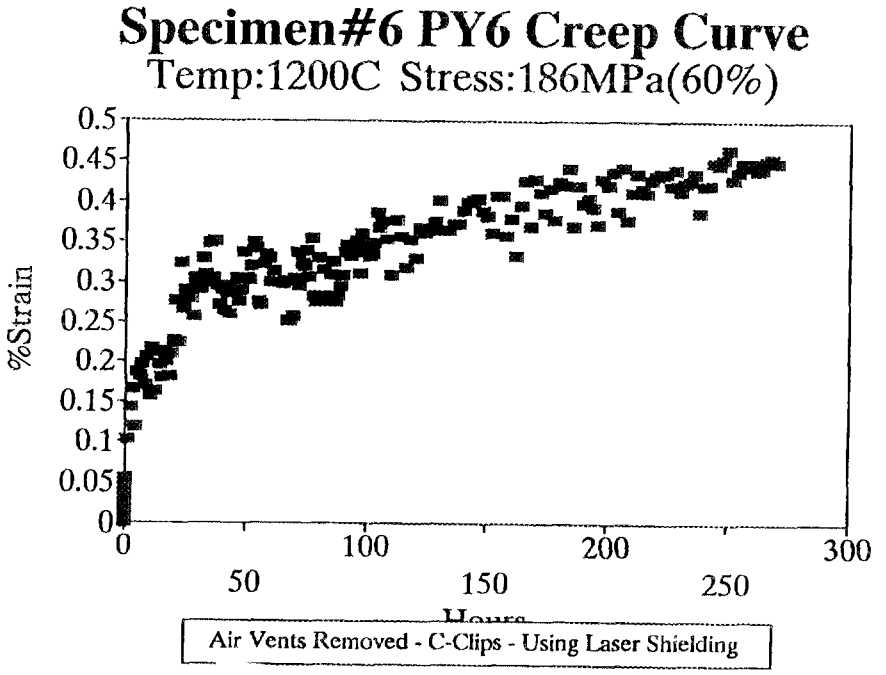

Figure 2

Table 1: Tensile Strength obtained at different temperatures for GTE-PY6

Temperature (°C)	Residual Tensile Strength (MPa)		
	NC A&T SU	UDRI	ORNL
RT	621	619	650
1000	451	447	400
1200	370	310	-
1260	-	-	370
1300	250	-	-
1370	-	-	310
1400	-	153	-

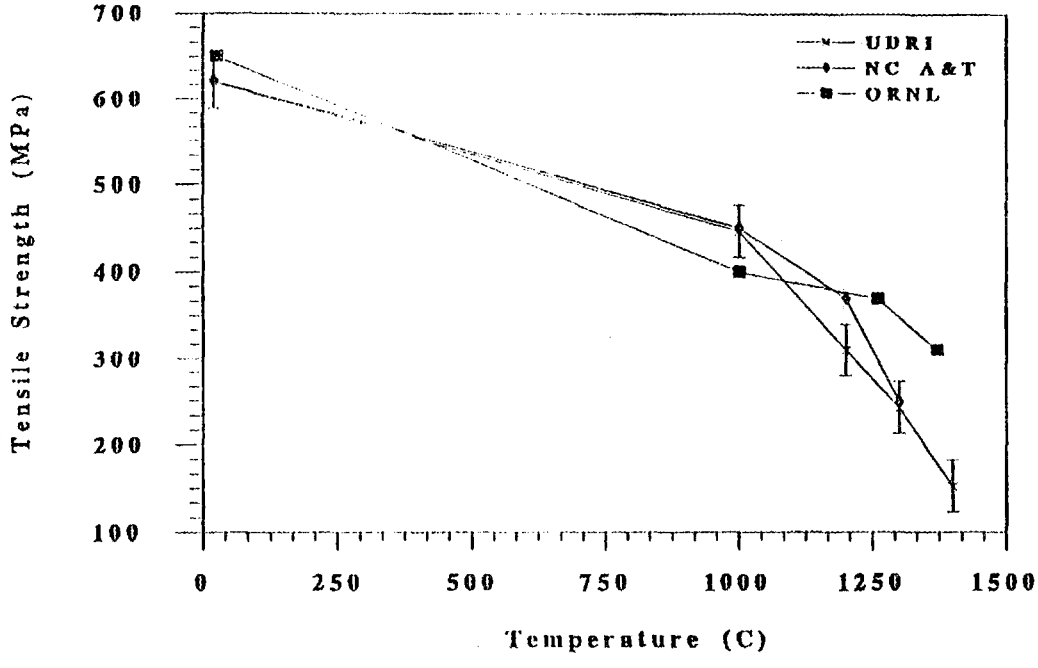

Figure 3: Tensile strength vs. Temperature for GTE-PY6

with GTE SNW-1000 (Table 2, Fig. 4) were also done. From the tests it can be observed that the strength drop from room temperature to 1000 °C is rather low, after which the drop is significant in both materials.

The specimens used for microstructural investigations included transverse and longitudinal TEM specimens which were prepared from close to the center of the gage length, as illustrated in figure 5. The steps for preparing the TEM specimens are shown in figure 5(a-e) and are as follows: (a) cut the 2 mm x 2 mm square samples from the specimen after the test using a low speed diamond (Buehler ISOMET Low speed saw, Buehler Ltd., Lake Bluff, IL), (b) mechanically grind and polish the specimen using coarse (6 μm) and fine (1 μm) grade diamond, respectively, to a final thickness ~ 75 μm (Buehler MINIMET grinder/polisher, Buehler Ltd., Lake Bluff, IL), (c) dimple the specimen to a center thickness of ~ 25 μm (Gatan Model 656 Dimple grinder, Gatan Inc., Warrendale, PA), (d) mount on a 3 mm carbon support ring having a 1.5 mm hole using M-Bond 610 adhesive (Measurements Group Inc., Raleigh, NC), and (e) ion mill from both sides of the specimen at 6 kV, 15^0 incident angle, and 1 A total current till perforation (Gatan DuoMill, Model 600, Gatan Inc., Warrendale, PA). A short time (10 minutes), low voltage (3 kV), shallow angle (10^0) bombardment was performed before removing the specimen from the ion mill to remove surface damage if any. Samples were prepared from both GTE-PY6 and GTE SNW-1000.

Status of Milestones
On schedule

Communications/Visitors/Travel
None

Problems Encountered
None

Publications and Presentations
None

Research sponsored by the Ceramic Technology Project, DOE Office of Transportation Technologies, under contract DE-AC05-84OR21400 with Martin Marietta Energy Systems, Inc.

Table 2: Comparison of Tensile Strength at different temperatures for GTE-PY6 and GTE SNW-1000

Temperature (°C)	Residual Tensile Strength (MPa)	
	GTE-PY6	SNW-1000
RT	621	492
900	-	489
1000	451	-
1100	-	448
1200	370	230
1300	250	-

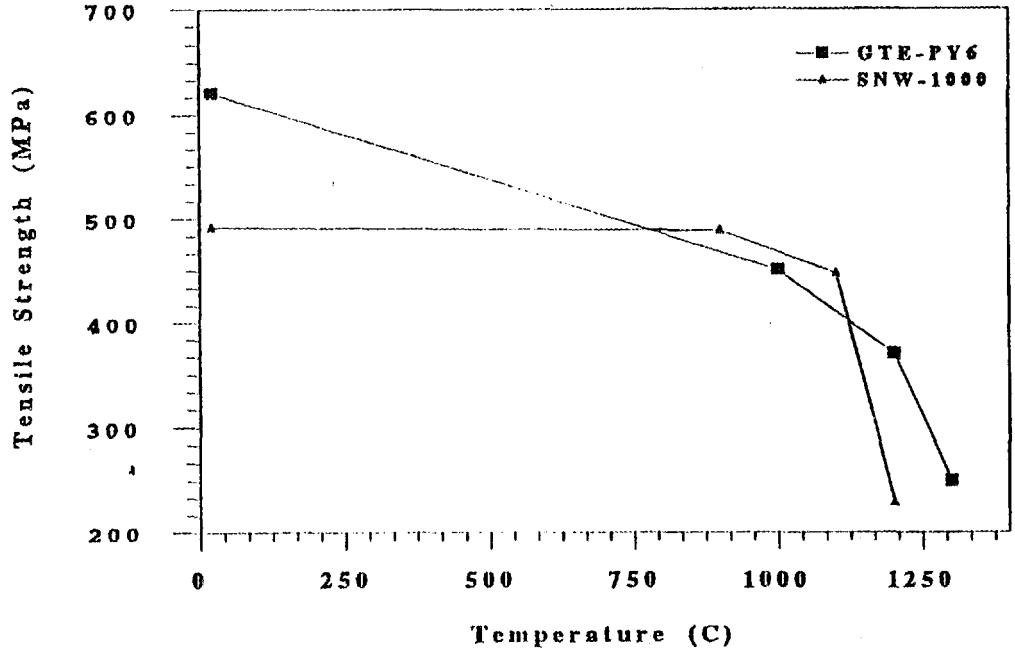

Figure 4: Comparison of Tensile Strength vs. Temperature for GTE-PY6 and SNW-1000

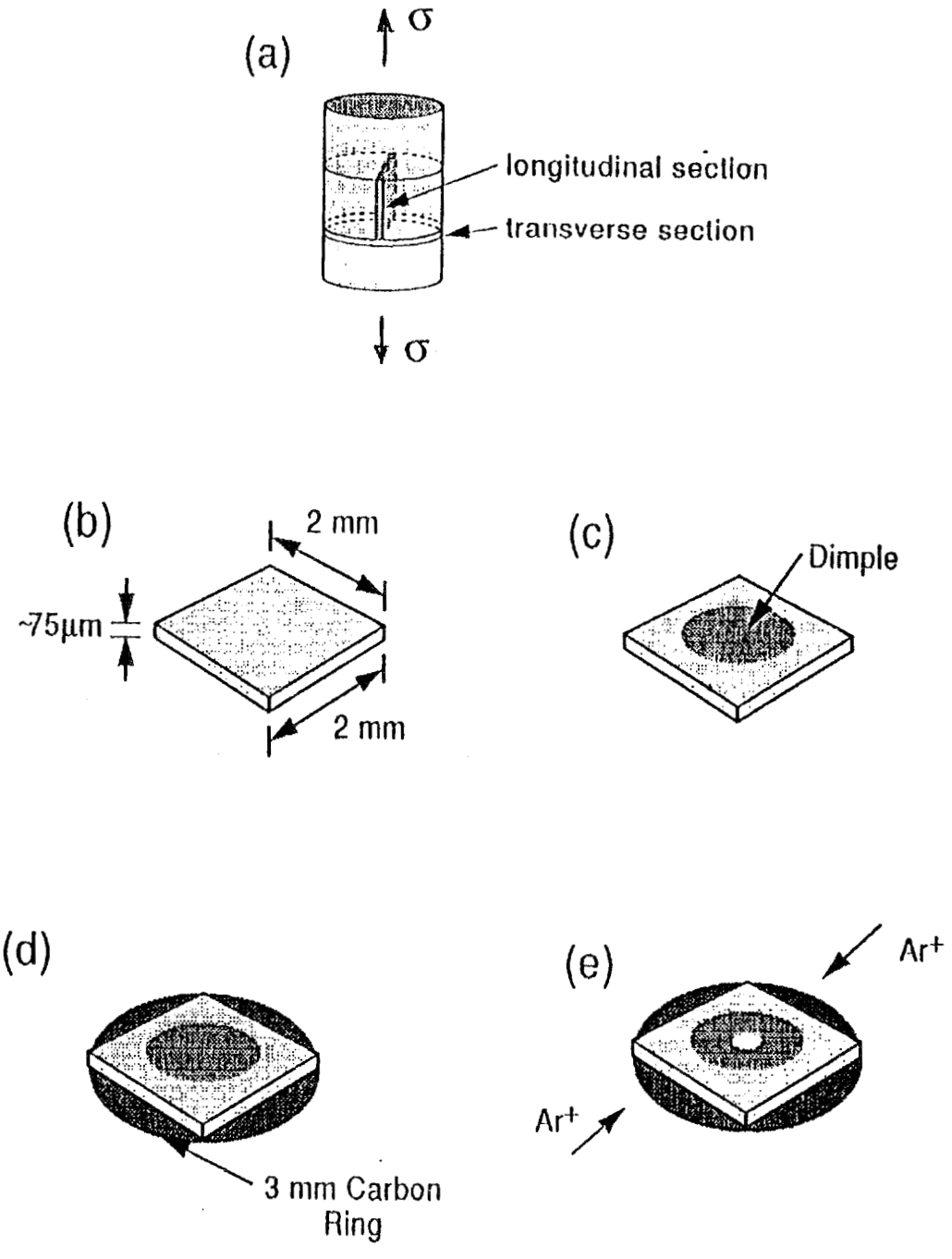

Figure 5. Schematic illustrating the steps for making a TEM specimen from the Si_3N_4 cylinders following testing: a) cut the specimen, b) grind and polish, c) dimple, d) mount on a carbon ring, and e) ion mill.

Standard Tensile Test Development

S. M. Wiederhorn, R. F. Krause, Jr., W.E. Luecke and G.D. Quinn
(National Institute of Standards and Technology)

Objective/Scope:

This project is concerned with the development of test equipment and procedures to determine the tensile strength and creep resistance of ceramic materials at elevated temperatures. Inexpensive techniques for measuring the creep behavior and strength of structural ceramics have been developed and are being used to characterize the mechanical behavior of these materials. The ultimate goal of the project is to help develop a data base and a test methodology for the structural design of heat engines for vehicular applications.

Technical Highlights:

During the past six months, studies on the creep and creep rupture of PY6, a commercial (GTE) grade of silicon nitride containing ≈6 wght. % Y_2O_3 were completed. This work was performed in collaboration with Pramod Khandelwal of Allison Gas Turbine. In total, 39 specimens were tested in creep; 21 of these were tested to failure yielding creep rupture data. In addition, tensile strengths were measured on 26 specimens in the temperature range 1100 to 1400°C. These data were compared with data collected at Oak Ridge National Laboratories (ORNL) and Southern Research Institute (SoRI) on the same material. Finally, strength and creep rupture data collected at the National Institute of Standards and Technology (NIST) were combined with dynamic fatigue data from ORNL to create a fracture map for PY6. In this report, we suggest that fracture maps may be used as a method of predicting component lifetime at elevated temperature.

Experimental Techniques:

Creep data on high temperature structural ceramics are currently being collected by two methods. In one, the entire specimen is immersed in the hot zone of the test furnace so that the grips used to hold the specimen are at the same temperature as the specimen. In the other method, specimens penetrate into the cooler portions of the furnace, so that the loading points on the specimen are much cooler than the gauge section. Consequently, the grips that hold the ends of the specimen are also relatively cool, and high temperature alloys can be used for this purpose.

At NIST and a number of other laboratories, "hot grip" techniques were developed because of the relatively low cost of specimens [1-3]. Flat dogbone shaped specimens were developed at NIST, figure 1, for this purpose [1]. Pin loading reduces flexural strains during testing to less than 2% of the total creep strain. Specimens are relatively small, ≈50 mm overall length, are made by simple machining techniques, and are relatively inexpensive, ≈$65 per specimen. Because of the simple geometry, the size of the specimen is easily reduced for testing small experimental batches of material. The specimen gauge length is measured by attaching flags to the specimens, and using a laser transducer to detect the position of the flags. With this technique, gauge length measurements at temperatures as high as 1500°C were accurate to ±2 μm.

When grips are cooled, specimens must be long enough to span the hot zone of the test furnace and, therefore, are larger and more expensive than hot grip specimens. Specimen costs for warm grip specimens can be as much as 10 times those for hot grip specimens. However, because the grips are made of high temperature alloys, larger

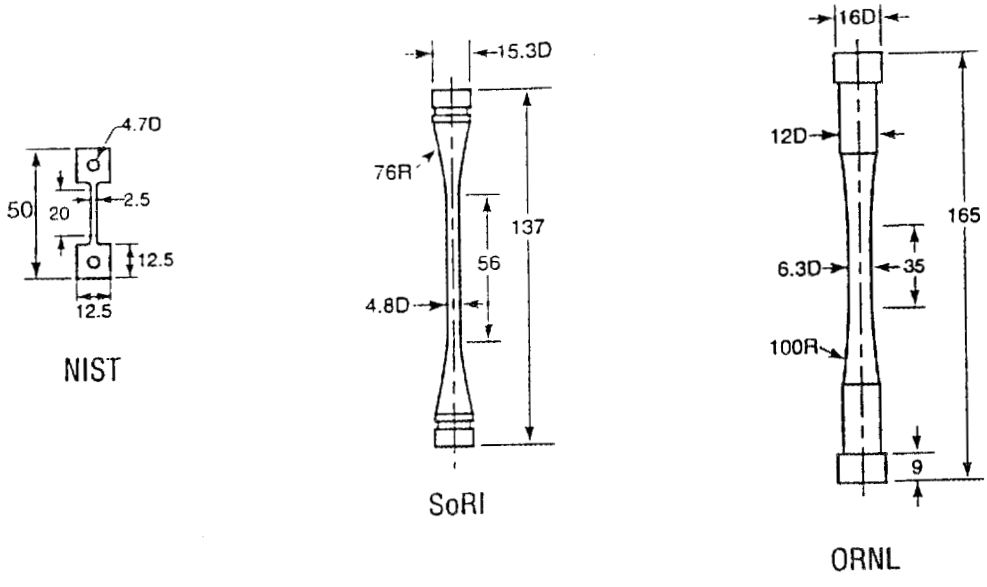

1. Examples of specimens used to study the creep behavior of silicon nitride.

forces can be applied to the specimens. Hence, larger volumes of material can be tested. Specimen cross sections of warm grip specimens are typically ≈6 times those of the hot grip specimens. Warm grip specimens most commonly used today were designed by Liu et al. [4] of ORNL. They are made from rods of material ≈160 mm long and 20 mm in diameter. They are cylindrical and are gripped by a button head in the cooler parts of the furnace, figure 1. Alignment accomplished via a room temperature fixture is excellent with less than 1% strain in bending. A slightly different cylindrical specimen was developed earlier by Pears and Digesu [5] at SoRI, figure 1. This geometry is being used by SoRI for high temperature testing of silicon nitride.

In the present study, creep and creep rupture data collected at NIST are compared with data collected at SoRI[1] and ORNL. All studies were conducted on PY6 which contained 6 w/o as a sintering aid. Material for the NIST and SoRI specimens was made by injecting molding and HIP-ing, whereas material for the ORNL was made by cold isostatically pressing and HIP-ing. This difference in processing procedure resulted in a difference in creep resistance.

Results:

An example of creep behavior of PY6 is shown in figure 2. For the run lasting ≈2511 hr, figure 2a, transient creep was observed for almost 1000 hr. Transient creep was observed during the entire creep test for the run lasting 23.5 hr, figure 2b. These data are representative of much of the data presented in the literature. Tensile creep tests on silicon nitride suggest that most grades of this material exhibit a long primary creep stage, which may take up more than half the total creep life. In some grades of silicon nitride, the entire creep life may consist of primary creep [6-9]; in others, steady state creep may be apparent after about one-half the specimen lifetime [6, 10, 11]. Devitrification of the grain boundary phase in these materials, caused by long term annealing, tends to reduce, but not eliminate the primary creep [6]. In all cases, silicon nitride exhibits little if any tertiary creep. Strains to failure range from about 0.5 to 2 percent depending on the test conditions and the grade of silicon nitride.

Data of the type shown in figure 2 can be represented graphically by plotting the minimum creep rate (usually the creep rate just prior to failure) as a function of stress and temperature. When plotted in this manner, experimental data is usually found to fit an Arrhenius modified Norton equation:

$$\dot{\epsilon}_{min} = D \cdot \sigma_a^n \cdot \exp(-Q_c/RT) \qquad (1)$$

Where $\dot{\epsilon}_{min}$ is the minimum creep rate and n is the stress exponent and Q_c is the apparent activation energy for creep. In figure 3, the solid straight lines represent a fit of the experimental data over a temperature range 1250°C to 1400°C. The apparent activation energy, Q_c, for the fit was 1349 kJ/mol; the stress exponent, n, was 8.7; and the logarithm of the coefficient, $\log_{10}D$, was 17.67 (for stress given in MPa and creep rate given in s^{-1}).

---

[1] Data were collected at SoRI for the Allison Division of General Motors as part of a DoE program on component reliability.

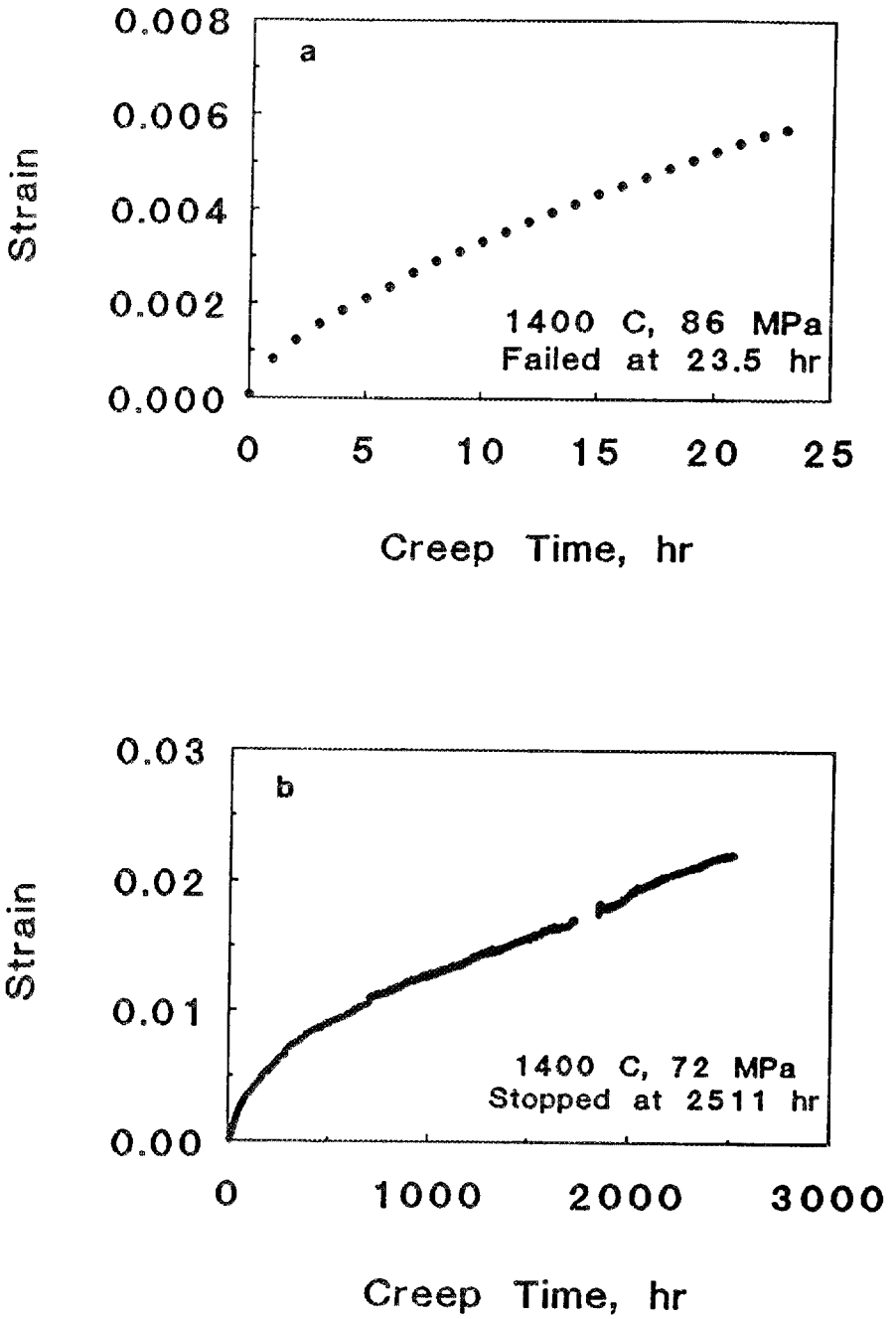

2. Typical creep data obtained on NIST specimens. Very long primary transient creep and the absence of tertiary creep before failure is characteristic of silicon nitride.

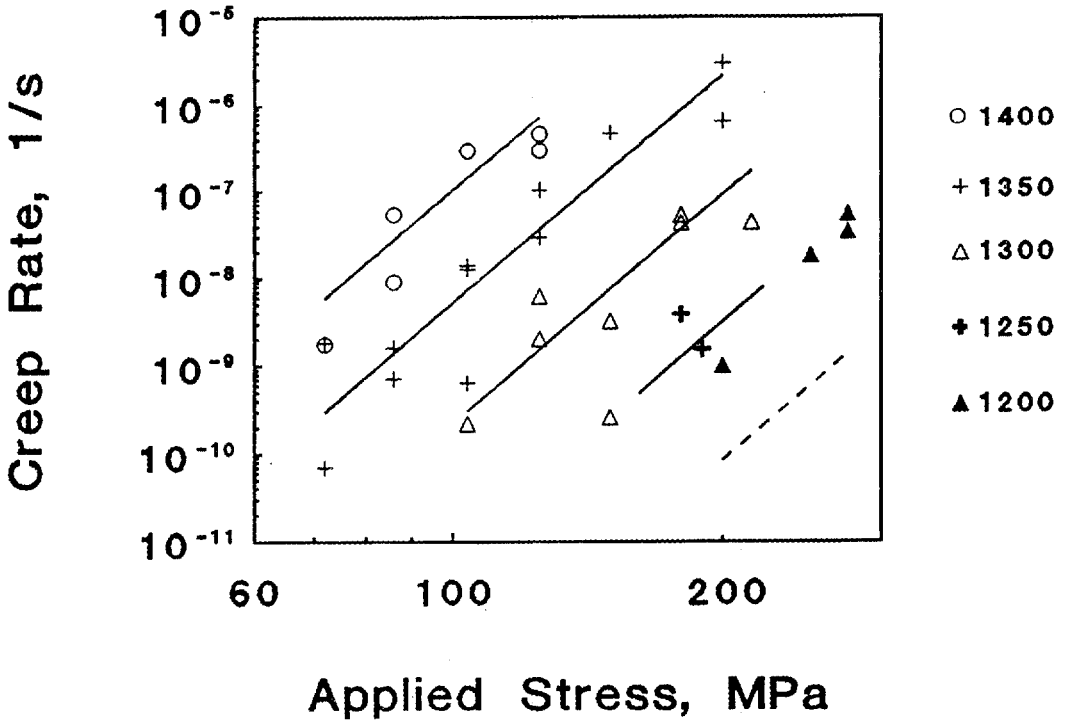

3. Minimum creep rate of PY6 as a function of applied stress. Data from 1250°C to 1400°C fit a Norton type of equation.

The high values of the apparent activation energy and the stress exponent are typical of what is observed for PY6 [10]. The high value of the stress exponent is attributed to cavitation during the creep process. High values of the apparent activation energy are probably a consequence of high activation energies for the diffusivity of glass at the grain boundaries and the temperature dependence of the solubility of silicon nitride in the glass [12]. Most of the data points in figure 3 lie within one order of magnitude of the least square fit lines. An exception to this observation occurs for data collected at 1200°C. For these data, the least squares fit line for 1200°C (the dotted line in the figure) lies far from the data. This deviation of the fit from the data is similar to that observed by Ferber and Jenkins on PY6 [10], and has been attributed [10] to a change in mechanism from creep cavitation to crack growth.

The data shown in figure 3 were compared with data collected on the same material by Ferber and Jenkins [10] at ORNL and by Khandelwal at The Allison Gas Turbine Division of The General Motors Corporation (GM) [13], figure 4 (This work was carried out at SoRI for GM). The lines in these figures were calculated from NIST data. For each temperature, the data from ORNL systematically plot at a higher creep rate than the data from NIST. Depending on stress, the creep rate determined at ORNL plot from one to two orders of magnitude higher. By contrast, the data from GM tend to plot close to the lines predicted from the NIST data. These results suggest that the material tested at ORNL was more susceptible to creep than that tested at NIST. Agreement between the GM and NIST data is consistent with the fact that specimens in both studies were obtained from the same powder lot, and were made by the same technique. Furthermore, as the SoRI specimen is substantially larger than the NIST specimen, these results suggest that specimen size does not have a strong effect on the creep rate.

Creep Rupture Data

The rupture data for all three laboratories are plotted in figure 5 in the form of a Monkman-Grant curve, equation 2:

$$t_f = C \cdot \dot{\epsilon}_{min}^{-m} \qquad (2)$$

where C and m are constants. Only the data from the creep fracture region are included in figure 5. All three sets of data plot along the same curve; most of the data fall well within one order of magnitude of the median failure time for a given creep rate. For the NIST data, the constants for equation 2 are m=1.14 and $\log_{10}C = -7.2$, where time is expressed in hours, and strain rate is expressed in s^{-1}. As with most Monkman-Grant plots for ceramics, the Monkman-Grant exponent, m, is slightly greater than 1. In metals by contrast, the exponent, m, is often slightly less than 1 [14].

Based on equation 2 it is concluded that lifetime for PY6 depends only on the creep rate. The faster the creep rate, the shorter the lifetime, regardless of temperature or applied stress. The time to failure for a given temperature and applied stress is obtained by combining equations 1 and 2:

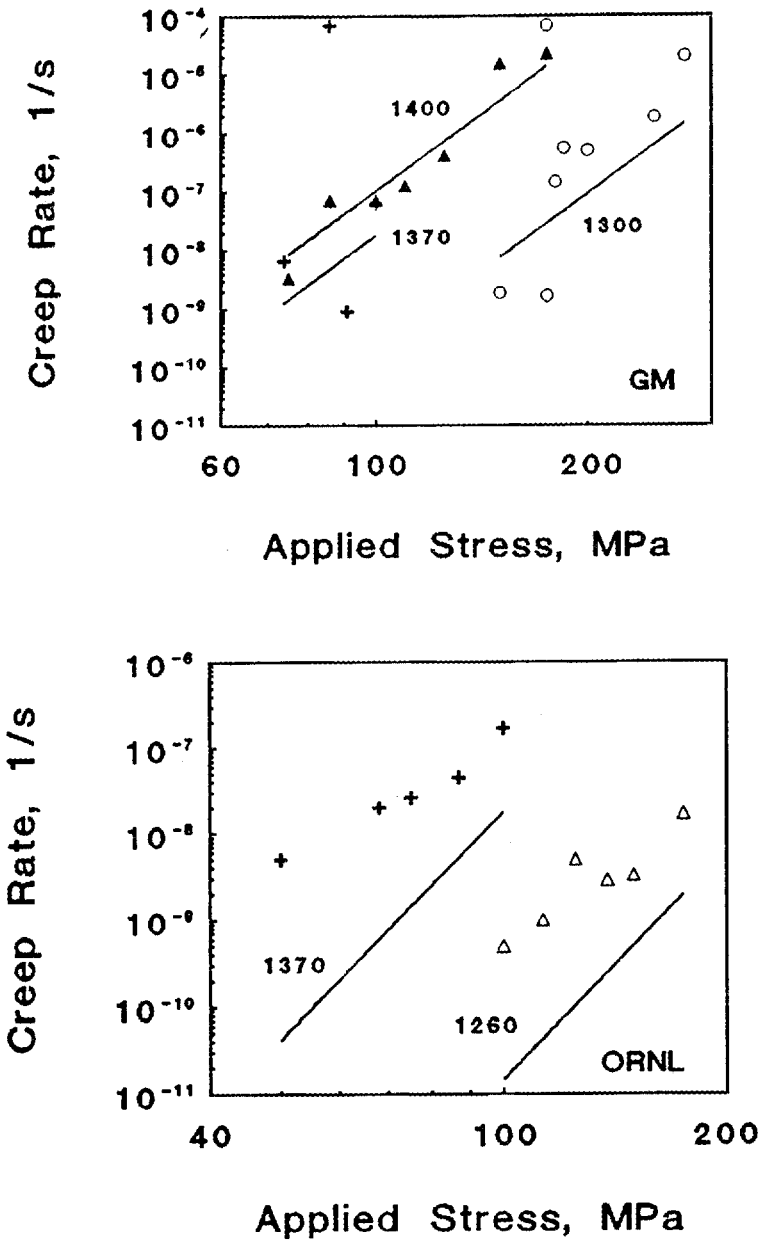

4. Comparison of data collected at NIST, solid lines, with data collected at GM (a) and at ORNL (b).

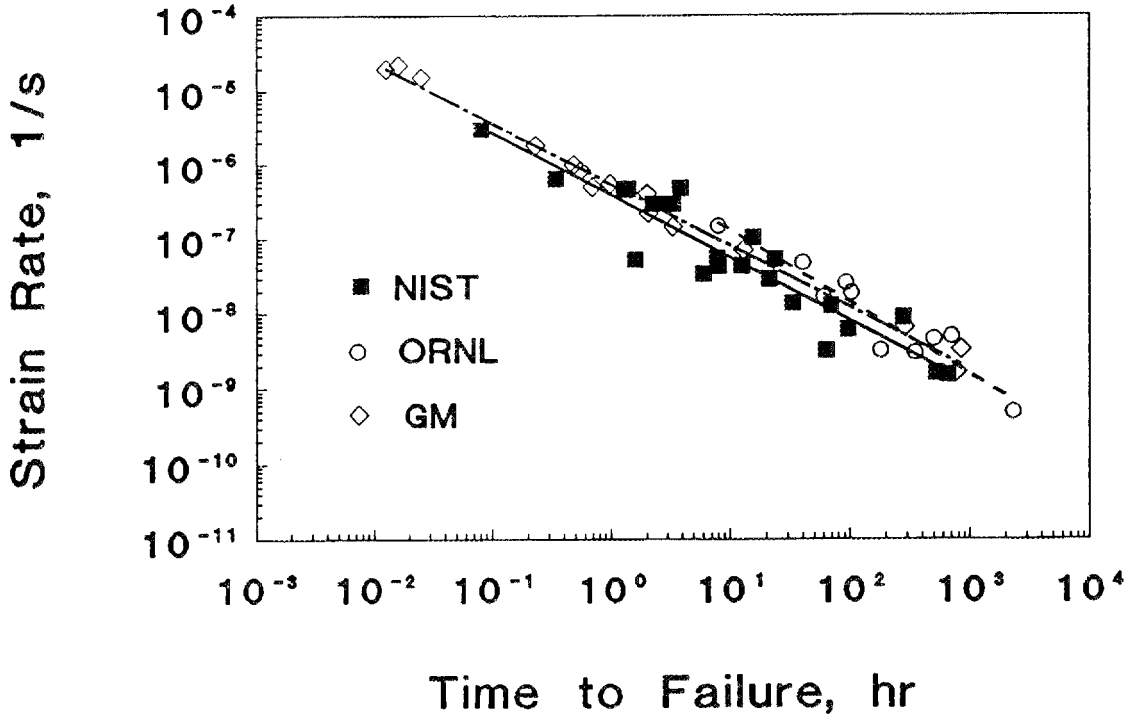

5. Monkman-Grant curve for PY6. Data from NIST, GM and ORNL fall close to one another.

$$t_f = C \cdot D^{-m} \cdot \sigma_a^{-mn} \exp(m \cdot Q_c / RT) \quad (3)$$

where C and D are empirical constants.

Strength Data

Data on the tensile strength of PY6 were collected at Oak Ridge National Laboratories, Southern Research Institute (for GM) and at the National Institute of Standards and Technology. Large button head tensile specimens were used at ORNL; a slightly different specimen was used at SoRI; small flat dogbone specimens were used at NIST, figure 1. Despite these differences in test geometry, general agreement was obtained between strengths determined at test temperatures above 1000°C. A comparison of the data collected at high loading rates, >16 MPa/s, are shown in figure 6. Within the temperature range 900°C to 1400°C, the strength of PY6 ranged from about 400 MPa to about 300 MPa. Although there was considerable scatter of the data, most fell within 50 MPa of the mean curve. Studies at lower rates of loading, ≈0.06 MPa/s, showed that as the temperature increased from 1000°C to 1400°C, strength depended on the loading rate during the test. Creep damage accumulation and subcritical crack growth reduce the strength at lower rates of loading.

Crack Growth Data

Data in the crack growth region for PY6 were collected only at Oak Ridge National Laboratory [15]. Below temperatures of ≈1200°C, crack growth dominates the failure process in PY6. The change in mechanism is indicated by an increase in the stress dependence of the creep rate, and a shift in the position of the data from the positions predicted from creep data taken at higher temperatures, as shown for example in figure 7. In addition a change in mechanism of fracture is observed [15]. At temperatures above 1260°C, fracture is intergranular and cavitation is observed on the fracture surface. At 1150°C this mode of fracture changes to transgranular fracture. Based on these observations and a set of data collected by dynamic fatigue techniques[2], a set of curves representing the crack growth region of the fracture mechanism map was obtained. These are represented by the following equation:

$$t_f = B \cdot \sigma_a^{-N} \cdot S_i^{N-2} \cdot \exp(Q_{scg} / RT) \quad (4)$$

---

[2] In static fatigue, the time to failure is measured as a function of stress for a constant applied stress. In dynamic fatigue, the breaking stress is measured as a function of the stressing rate. Both techniques can be used to obtain the constants in equation 4. The relationship between failure time in dynamic fatigue and failure time in static fatigue developed first by Davidge et al. [16]: $t_s = t_d/(N+1)$, where N is the stress exponent in the crack growth equation.

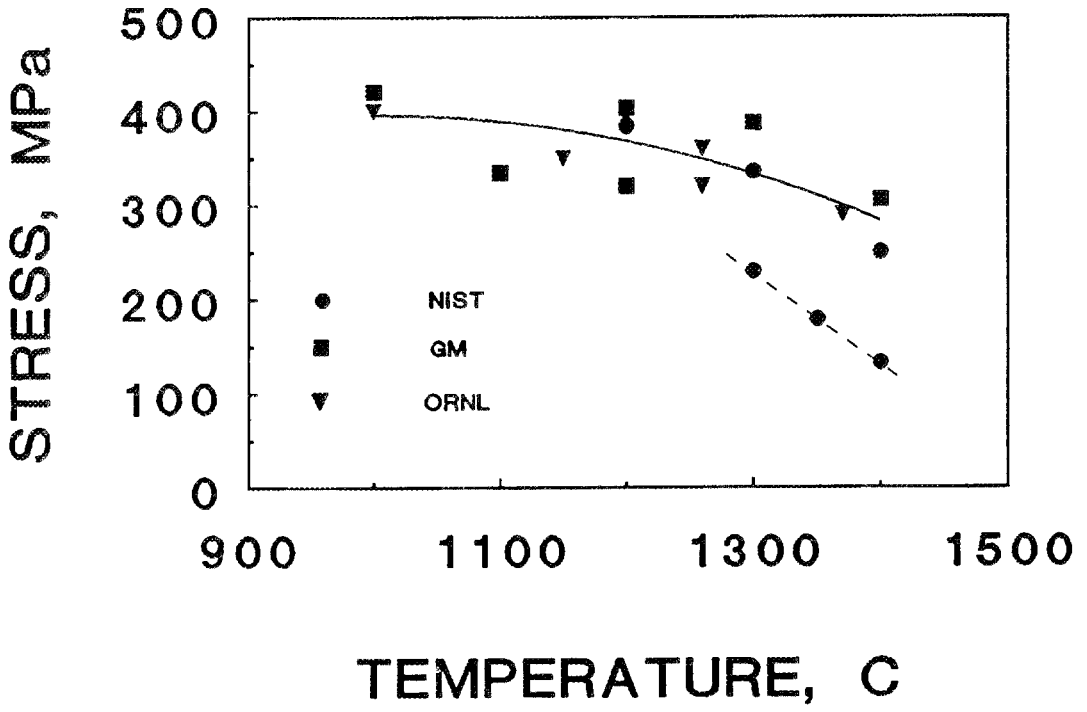

6. Strength data collected on PY6 at four laboratories. Strength is found to depend on rate of loading. High rates of loading, >16 MPa/s, are given by the solid curve; low rates, <0.06 MPa/s are given by the dashed line.

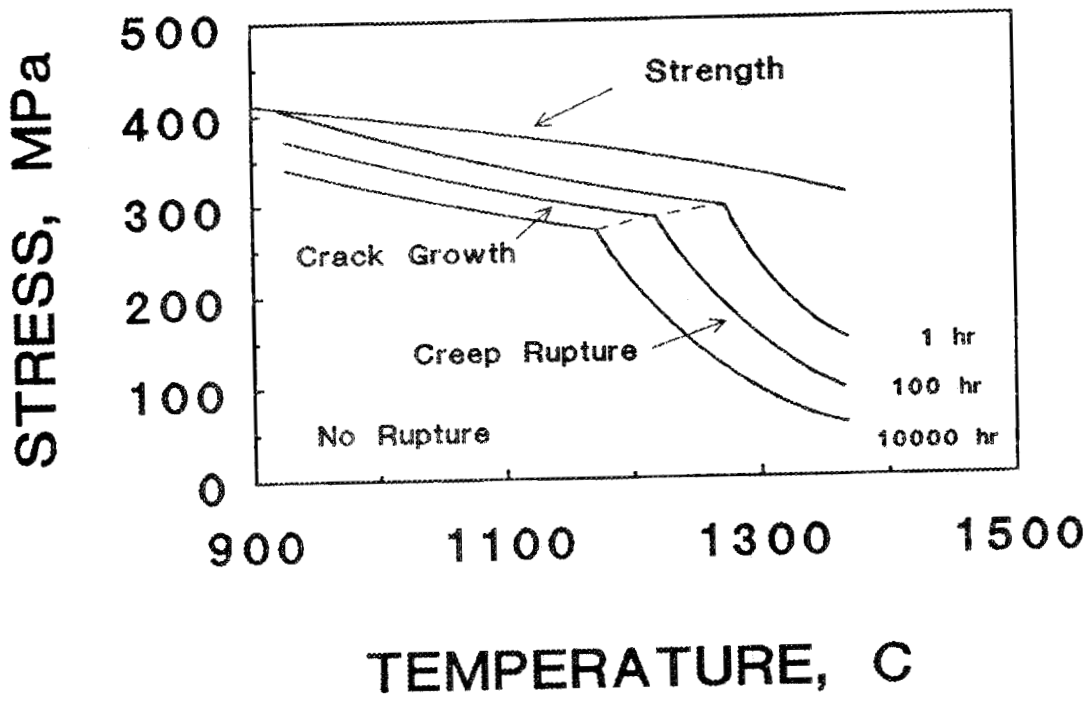

7. Fracture mechanism map for PY6 in air in tension.

where $B = 2/[AY^N(N-2)K_{Ic}^{N-2}]$, N is the stress exponent for crack growth and Q_{scg} is the apparent activation energy for crack growth[3]. Fitting the experimental data to equation 3, the constants for equation 4 were determined: $Q_{scg} \approx 760$ kJ/mol; $N \approx 55$; $\log_{10}(B \cdot Si_i^{N-2}) = 110.38$.

Fracture Mechanism Map for PY6

The fracture mechanism map for PY6, figure 8, was developed from the data discussed above. Four regions of behavior are indicated on the figure: no failure, fast fracture, slow crack growth and creep rupture. Lines of constant failure time are indicated on the figure as solid lines. The boundary for regions of slow crack growth and creep rupture, dotted line, are obtained by solving equations 3 and 4 for the given failure times. The map differs somewhat from the earlier one developed by Quinn for NC132 [17], figure 9. Because of the higher stress dependence of the crack growth data for PY6, distinct breaks are observed in the time contours. The time contours in NC132 are continuous from the creep fracture to the crack growth regions, suggesting similar stress dependencies for both mechanisms. Also, the creep fracture region in PY6 goes to very much higher stresses, ≈250 MPa. Reasons for this difference in behavior are not understood at the present time.

Maps such at that shown in figure 8 can be used either for materials selection, as a guide for improving the microstructure of materials, or for purposes of design. For a given application, materials selection requires the comparison of two or more such maps. Thus, one might select a line of constant time to failure and compare it for two grades of silicon nitride, or for a grade of silicon nitride and another material to determine the best one for a given application. A comparison of this sort is given in figure 9 for PY6, MAR-R246 and NC132 for a total expected lifetime of 100 hr[4]. The MAR-R246 is a high temperature alloy used in turbine engines; the NC132 is an older grade of silicon nitride; the PY6 is one of the newer grades of silicon nitride. At an applied stress of 200 MPa, the PY6 has an advantage of ≈290°C over the MAR-M246 and ≈200°C over the NC132. The temperature advantage over the NC132 represents a considerable improvement in high temperature mechanical behavior for silicon nitride as a consequence of processing research over the past 10 years.

Designing with Fracture Mechanism Maps

Fracture mechanism maps were originally intended as a qualitative means of comparing the relative fracture behavior of materials, and were not intended for the final design of components. Matsui et al. [19], however, showed that if confidence levels are put on the different regions of the fracture mechanism map then an allowable stress-temperature envelope could be defined, within which failure would not be expected. It is possible to place such error bands on the lines of constant failure shown in figure 8. In both the crack growth region and the creep rupture region, these bands can be determined empirically from the actual scatter in time to failure.

---

[3] These constants comp from the following crack growth equation: $v = A \cdot K_c^N \cdot \exp(-Q_{scg}/RT)$. Where A is an empirical constant, K_c is the applied stress intensity factor.

[4] A 100 hour lifetime was selected because data on the alloy was easily obtained in this range [18].

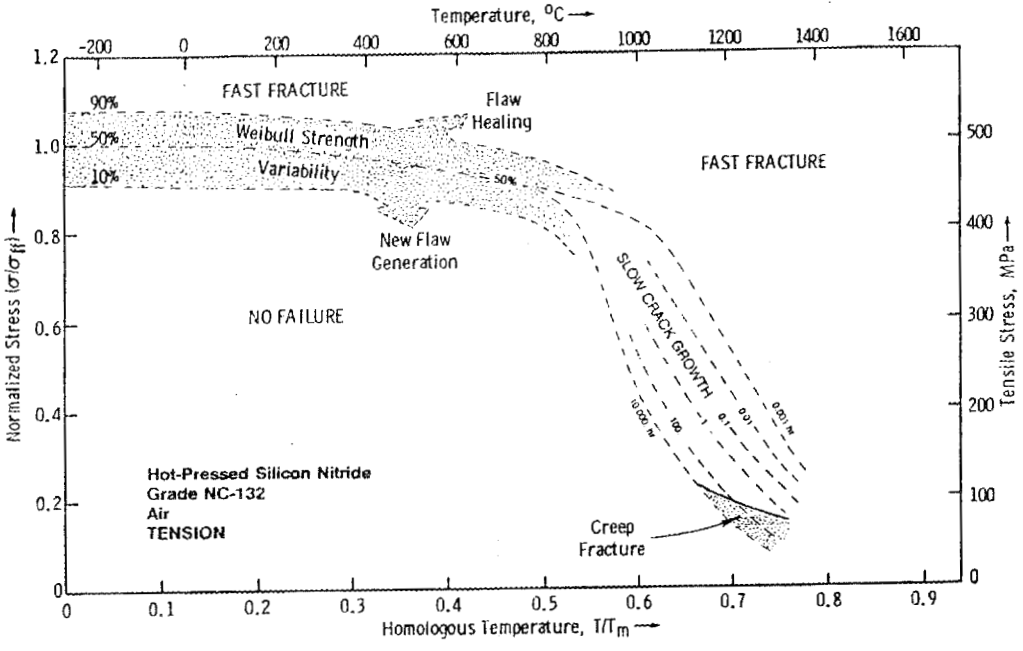

8. Fracture mechanism map for magnesia-doped hot-pressed silicon nitride in air in direct tension. The left ordinate axis is the tensile stress normalized by the mean room-temperature fast fracture strength (σ_{ff}). From ref. 17.

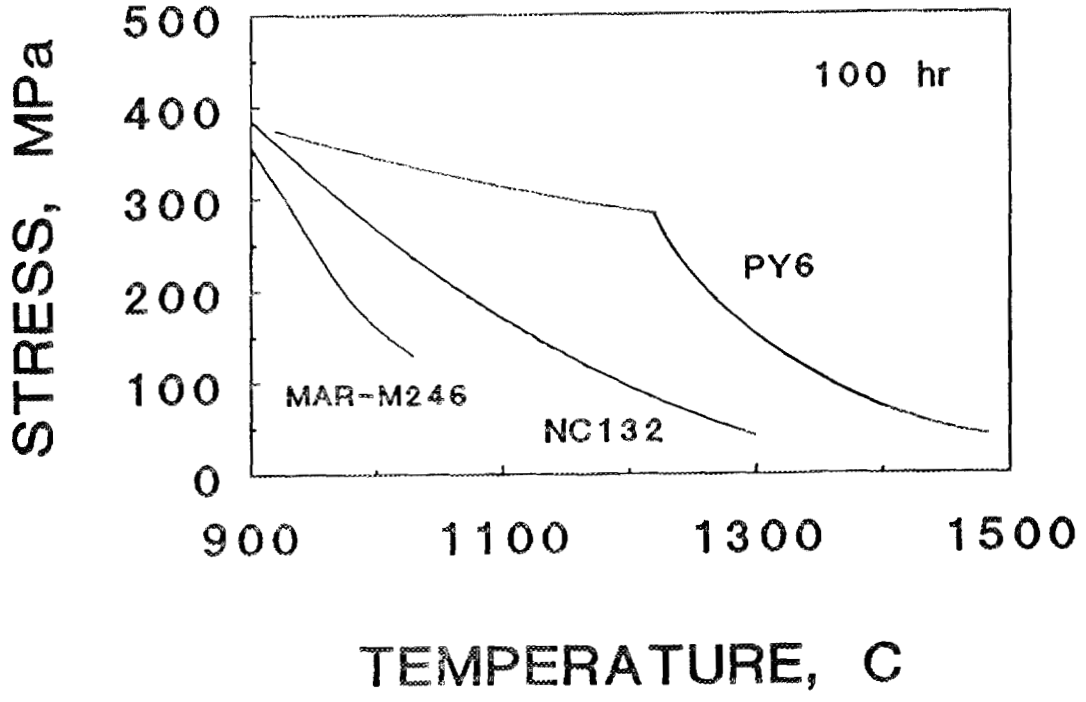

9. A comparison of the high temperature behavior of PY6 with an older grade of silicon nitride, NC132 and a high temperature alloy, MAR-M246.

This procedure is illustrated for the NIST creep rupture data of figure 10. First, the differences between the expected and measured times to failure are determined. The logarithmic mean and standard deviation of these differences are then evaluated. Since the scatter of the data about the line in figure 10 does not depend on the logarithm of the failure time, the standard deviation is also assumed to be independent of the logarithm of the time to failure. The standard deviation, σ, of the data in figure 10 was approximately 0.46. As the data is expressed in terms of $\log_{10}t$, this means that approximately 95% of the data lies between $\log_{10}t-2\sigma$ and $\log_{10}+2\sigma$, for any given value of $\log_{10}t$. If 2σ is selected as the lower confidence limit of $\log_{10}t_f$, only 2.5% of the components will fail in times shorter than this value[5]. In figure 11, a curve of constant failure time for 1000 hr is plotted on a fracture mechanism map along with a curve indicating the lower confidence bound for two standard deviations. This curve is congruent with the curve given by $\log_{10}(1000)+.92$, which equals 3.92, or ≈8318 hr.

The same procedure was followed in the crack growth regime using data collected by Jenkins, Ferber and Lin [15]. In this case, dynamic fatigue data collected at 1150°C and 1260° were used. The pooled standard deviation of $\log_{10}t$ from both sets of data was 2.82. This very large standard deviation is typical of the type of scatter observed in times to failure for materials that fail by crack growth. The scatter reflects the scatter in severity of the life limiting flaw that is present in the specimen and therefore is responsible for failure. The lower confidence bound for the crack growth region is thus $\log_{10}(1000)+5.64$, or 4.37×10^8 hr. This curve is plotted in figure 11 as a dashed line.[6]

The effect of the confidence band is to limit the conditions under which the material can be used. The crack growth band effectively lowers the allowable stress by about 50 MPa over the temperature range ≈950°C to ≈1200°C. This reduction in allowed stress is consistent with the scatter in the strength reported for this material at elevated temperatures. The lower confidence band for the creep rupture region has a much smaller effect on the allowable operating conditions. Here, the reduction in strength ranges from ≈30 MPa at 1200°C to ≈10 MPa at 1400°C. This reduction in strength is consistent with the smaller scatter in the rupture time usually observed in the creep rupture region. In the creep rupture region lifetimes usually lie within an order of magnitude of one another, whereas, in the crack growth region lifetime typically scatters over two or more orders of magnitude.

---

[5] As only 19 specimens were tested to failure, a confidence level of greater than 2σ was not justified.

[6] As the scatter in failure time for crack growth data is a consequence of the scatter in initial flaw size, Weibull statistics is more appropriate for describing the lower confidence bounds for the crack growth region. It can be shown [29] that the time to failure is related to cumulative failure probability, P, through the following equation: $t=t_o\cdot\{\ln(1-P)^{-1}\}^{1/\alpha'}$, where $t_o=B\cdot\sigma^{-N}\cdot S_o^{N-2}$ and $\alpha'=\alpha/(N-2)$. The treatment given in this paper for the crack growth region is an approximation of
the correct procedure.

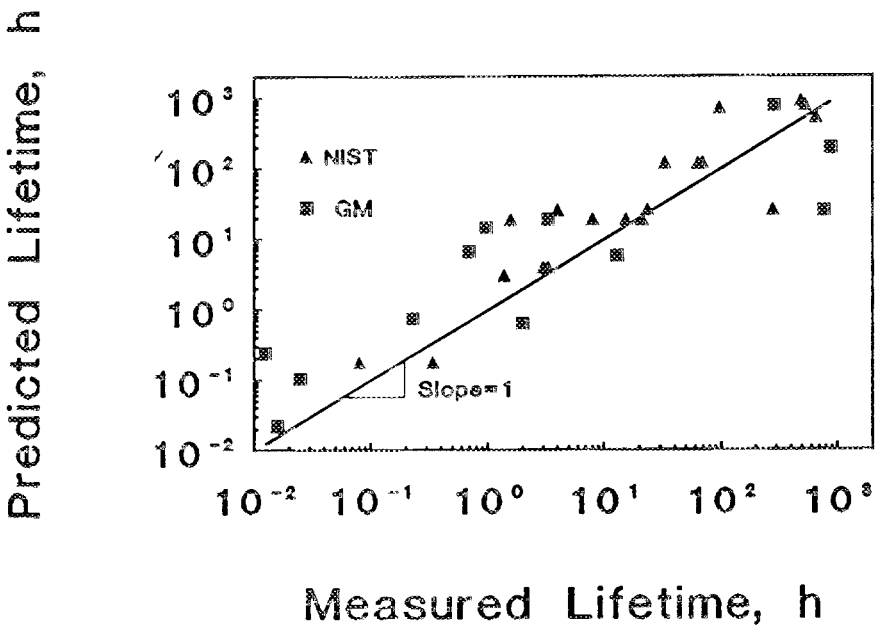

10. Comparison of failure times measured at SoRI for GM with those measured at NIST.

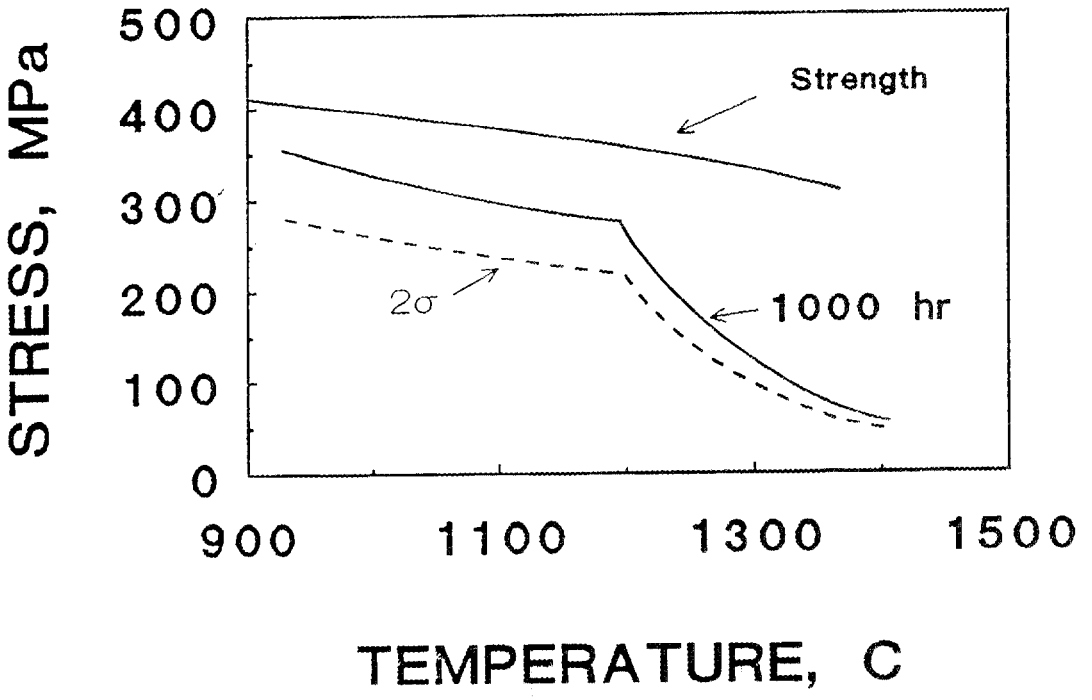

11. Effect of measurement scatter on the design envelope.

Status of Milestones:

All milestones are on schedule.

Publications:

1. W.E. Luecke, S.M. Wiederhorn, B.J. Hockey and G.G. Long, "Cavity Evolution During Tensile Creep of Si_3N_4," Mat. Res. Soc. Symp. Proc. 287 467-472 (1993).

2. S.M. Wiederhorn, G.D. Quinn and R. Krause, "Fracture Mechanism Maps: Their Applicability to Silicon Nitride," to be published in *Life Prediction Methodologies and Data for Ceramic Material, ASTM STP 1201*, C.R. Brinkman and S.F. Duffy, Eds., American Society for Testing and Materials, Philadelphia, 1993.

3. B.A. Fields and S.M. Wiederhorn, "Variation of Creep Damage with Depth Below the Surface in a Siliconized Silicon Carbide." Scripta Metallurgica, Submitted.

References:

1. D.F. Carroll, S.M. Wiederhorn and D.E. Roberts, "Technique for Tensile Creep Testing of Ceramics," J. Am. Ceram. Soc., 72, 1610-14 (1989).

2. Tatstuki Ohji, "Long-Term Tensile Creep Testing for Advanced Ceramics," J. Am. Ceram. Soc. 75[8] 2304-307 (1992).

3. M. Gürtler, A. Weddigen and G. Grathwohl, "Werkstoffprüfung von Hochleistungskeramik mit Zugproben," Mat.-wiss. u. Werkstofftech. 20 291-299 (1989).

4. K.C. Liu, H. Pih, and D.W. Voorhes, "Uniaxial Tensile Strain Measurement for Ceramic Testing at Elevated Temperatures: Requirements, Problems, and Solutions," Int. J. High Tech. Ceramics, 4 161-171 (1988).

5. C.D. Pears, and F.J. Digesu, "Gas-Bearing Facilities for Determining Axial Stress-Strain and Lateral Strain of Brittle Materials to 5500 F," Proc. ASTM, 65 855-73 (1965).

6. M. Gürtler and G. Grathwohl, "Tensile Creep Testing of Sintered Silicon Nitride," pp. 399-408 in Proceedings of the Fourth International Conference on Creep and Fracture of Engineering Materials and Structures, Institute of Metals, 1 Carlton House Terrace, London SW1Y 5DB (1990).

7. R.M. Arons and J.K. Tien, "Creep and Strain Recovery in Hot-Pressed Silicon Nitride," J. Mat. Sci. 15 2046-2058 (1980).

8. B.J. Hockey, S.M. Wiederhorn, W. Liu, J.G. Baldoni and S.-T. Buljan, "Tensile Creep of Whisker-Reinforced Silicon Nitride," 26, 1991, pp 3931-3930.

9. S.M. Wiederhorn, B.J. Hockey, D.C. Cranmer and R. Yeckley, "Transient Creep Behavior of Hot Isostatically Pressed Silicon Nitride," J. Mat. Sci. 28 445-453 (1993).

10. M.K. Ferber, and M.G. Jenkins, "Evaluation of the Elevated-Temperature Mechanical Reliability of a HIP-ed Silicon Nitride," J. Am. Ceram. Soc. 75[9], 2453-62 (1992).

11. Ohji, T. and Yamauchi, Y., "Tensile Creep and Creep Rupture Behavior of Silicon Nitride," J. Am. Ceram. Soc. to be published.

12. R. Raj and P.E.D. Morgan, "Activation Energies for Densification, Creep and Grain-Boundary Sliding in Nitrogen Ceramics," J. Am. Ceram. Soc. 64 C143-C145 1981.

13. P.K. Khandelwal, "Life Prediction Methodology for Ceramic Components of Advanced Vehicular Heat Engines," pp. 176-179 in Ceramic Technology Project Bimonthly Technical Progress Report to DOE Office of Transportation Technologies, April to May 1992, D.R. Johnson, Project Manager, Ceramic Technology Project.

14. F.C. Monkman, and N.J. Grant, "An Empirical Relationship between Rupture Life and Minimum Creep Rate in Creep-Rupture Tests," Proc. ASTM 56 593-620 (1956).

15. M.G. Jenkins, M.K. Ferber, and C.-K. J. Lin, "Apparent Enhanced Fatigue Resistance under Cyclic Tensile Loading for a HIPed Silicon Nitride," J. Am. Ceram. Soc. in press.

16. R.W. Davidge, J.R. McLaren, and G. Tappin, "Strength Probability Time (SPT) Relationships in Ceramics," J. Mat. Sci. 8 1699-1709 (1973).

17. G.D. Quinn, "Fracture Mechanism Maps for Advanced Structural Ceramics, Part 1, Methodology and Hot Pressed Silicon Nitride Results," J. Mat. Sci. 25 4361-4376 (1990).

18. R.W. Hertzberg, Deformation and Fracture Mechanics of Engineering Materials, John Wiley and Sons, New York (1976).

19. M. Matsui, M. Ishida, T. Soma, and I. Oda, "Ceramic Turbocharger Rotor Design Considering Long Term Durability," pp. 1043-50 in Ceramic Materials and Components for Engines, W. Bunk and H. Hausner eds., Verlag Deutsche Keramische Gesellschaft, D-5340 Bad Honnef, Germany (1986).

3.5 NONDESTRUCTIVE EVALUATION DEVELOPMENT

Nondestructive Characterization
D. J. McGuire (Oak Ridge National Laboratory)

Objective/scope

The purpose of this program is to conduct nondestructive evaluation (NDE) development directed at identifying approaches for quantitative determination of conditions (including both properties and flaws) in ceramics that affect the structural performance. Those materials that have been seriously considered for application in advanced heat engines are all-brittle materials whose fracture is affected by structural features whose dimensions are on the order of the dimensions of their microstructure. This work seeks to characterize those features using high-frequency ultrasonics and radiography to detect, size, and locate critical flaws and to measure nondestructively the elastic properties of the host material.

Technical progress

Ultrasonics - W. A. Simpson, Jr., and K. V. Cook

We completed moving our ceramics evaluation system into new quarters. The hardware has been reconnected and tested, and most of the equipment seems to have survived the transition. However, the stepless gate function on the high-frequency pulser/receiver was no longer operational. For most purposes this loss is inconsequential, but it did have ramifications for our synthetic aperture work, where the stepless gate allowed us to suppress the long electronic recovery time caused by the saturated front-surface signal resulting when the system gain is very high. This overload was evidenced by an amplitude bias in the acquired data, which varied with flaw depth. In particular, flaws lying relatively near the entry surface were masked by the bias. The gate function has now been repaired.

In spite of the temporary loss of our high-frequency stepless gate function, we succeeded in testing our three-dimensional (3-D) synthetic aperture data acquisition system and the software that we wrote to implement synthetic aperture processing. We had previously demonstrated the capabilities of the synthetic aperture approach on two-dimensional (2-D) data, showing that it was possible to obtain from a single scan diffraction-limited imaging at all depths covered by the data record. In the 2-D case, a single linear scan of the sample is made with the transducer focused on or just below the surface. The second dimension of the data record is represented by the digitized echo information originating from scattering centers within the sample. In synthetic aperture processing, the full analytic signal, i.e., the entire radio frequency (rf) waveform, rather than just the peak amplitude required by a more conventional test such as the C-scan, is acquired. The resulting 2-D record is then processed to yield a cross-sectional image of the flaw locations as a function of depth. One advantage of this approach is that information from all depths is obtained from a single scan, whereas conventional testing requires that the transducer be refocused for each new depth to be interrogated.

In 3-D synthetic aperture testing, a 2-D scan of the sample is made with the transducer focused on or just below the surface. The digitized echo data then form the

third dimension of the resulting data set. After processing, the data can be plotted as a 3-D image of all detected flaws within the material volume covered by the original data set or as a series of cross-sectional "slices" analogous to those produced by computed tomography (CT). As in the case of 2-D implementation, the sample is scanned but once; the synthetic aperture is "focused" in software at each depth.

The first test of the 3-D algorithm was performed not on test data but on actual data obtained on a modulus of rupture (MOR) bar containing an artificial void. For the 2-D cases previously tested, the raw data set was sufficiently small to permit processing in system (high-speed) memory. For the 3-D case, however, the maximum data record size permitted by our software is 64 MB, which greatly exceeded the available system memory. Consequently, the software was written to use the hard disk as virtual memory. This slows the execution speed of the algorithm enormously and was found unacceptable. Several corrective approaches were considered, but we ultimately chose the simplest: we purchased additional high-speed memory. This allows data sets that approach the maximum size permitted by our commercial B-scan software to be processed entirely in high-speed random access memory (RAM).

For our test case, a zirconia MOR bar containing a 250-μm artificial flaw was used. The flaw was approximately 3 mm deep, and the bar was known to contain several natural flaws, as determined by conventional ultrasonic inspection. An area centered on the artificial flaw and approximately 6 mm square was scanned. Because of the small aperture for this test, the resulting data set was so small that, even using disk virtual memory, the data could be processed very rapidly. The aperture was limited to this small size because the bar is only 6 mm wide and because this aperture is more than adequate for a flaw 3 mm deep using the selected transducer.

Figure 1 shows the partially contrast-enhanced raw data obtained on the MOR bar. The figure is composed of 48 scans numbered 0 to 47. The scans are numbered from left to right and from bottom to top. The lower leftmost scan is thus scan 0, and the top rightmost scan is No. 47. For each of these scans, the vertical direction corresponds to distance along the surface of the MOR bar, and the horizontal direction represents time, or depth. Forty-eight data samples were taken along each scan line at intervals of approximately one-half wavelength (in the ceramic), and the stepsize between scan lines was also one-half wavelength. Each scan contains information from approximately 1 mm to more than 3 mm deep in the sample; the first 1 mm was excluded because of the highly saturated front-surface signal, and the back-surface response was also eliminated by the electronic gate. The response from any internal scattering center is encoded into an 8-bit grey scale.

Several scan characteristics may be noted in Fig. 1. The first two scans, 0 and 1, are featureless because the transducer was actually just off the edge of the sample. Beginning about scan line 4, valid data were obtained. For each of scans 4 through 47, the leftmost 50% of the scan is saturated (bright). This is because of the slow recovery of the electronics from the overload imposed by the very large front-surface signal; this overload is usually eliminated by the stepless gate, which, as was mentioned earlier, was not functioning at the time. Beginning in scan 19 and continuing until scan 35, the characteristic parabolic response from the 250-μm flaw can be seen near the right end of each scan. This indicates that the flaw was detected over a length of about 1.5 mm. In addition, the response from a natural flaw can be seen in scans 5 through 12 in the lower half of each scan and at about the same depth as the artificial flaw. In scans 22 through 30, one-half of the characteristic flaw parabolic arc can be seen at the extreme bottom of

YP16107

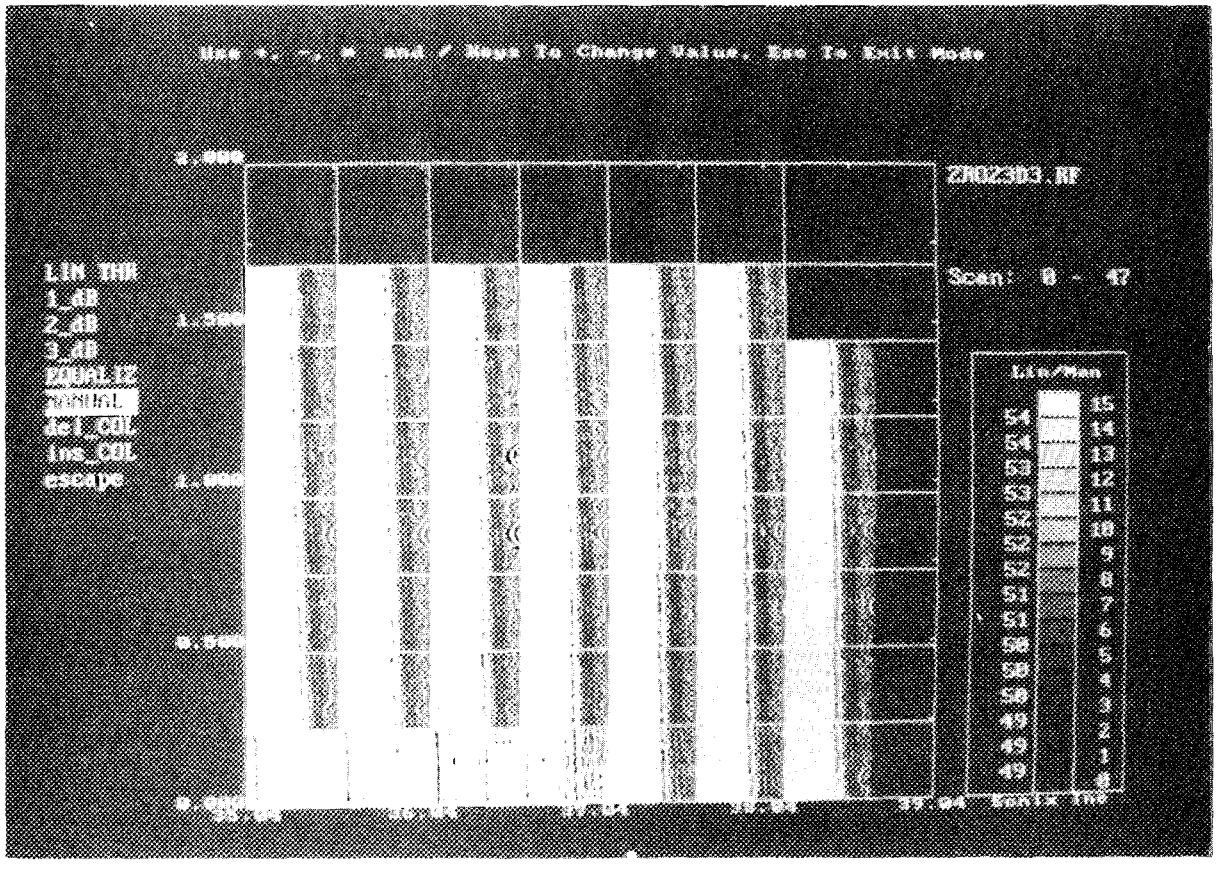

Fig. 1. Contrast-enhanced raw synthetic aperture data showing response (parabolic arcs) from a 250-μm flaw in zirconia.

each scan, indicating a natural flaw located just at the beginning of the scan line. A few additional, smaller flaw indications can be seen in many of the scans.

Figure 2 shows a partially contrast-enhanced image of the data after processing by our synthetic aperture algorithm. The arrow indicates the artificial flaw, which is now imaged as a line segment of alternating light and dark portions corresponding to alternations of the rf waveform of the transducer. The algorithm has sharpened the response laterally to within the resolution of the aperture, and the flaw can be seen for about 4 scan lines, which is slightly larger than the 250-μm diam of the flaw. One of the two natural flaws mentioned earlier can be seen clearly in scans 7 through 9 and the other in scans 27 through 28. Other flaws can be seen scattered around the image.

Figure 3 shows a fully contrast-enhanced enlargement of scan 26. The arrow indicates the artificial flaw. Use of the commercial software's cross-hair measurement function indicated that the flaw image in the lateral direction was again slightly larger than the actual 250-μm-diam of the flaw.

The preceding results indicate that our synthetic aperture software appears to be working very well. Flaws at each depth were correctly imaged and at an apparent resolution commensurate with that of the aperture. The results also suggest the following

YP16102

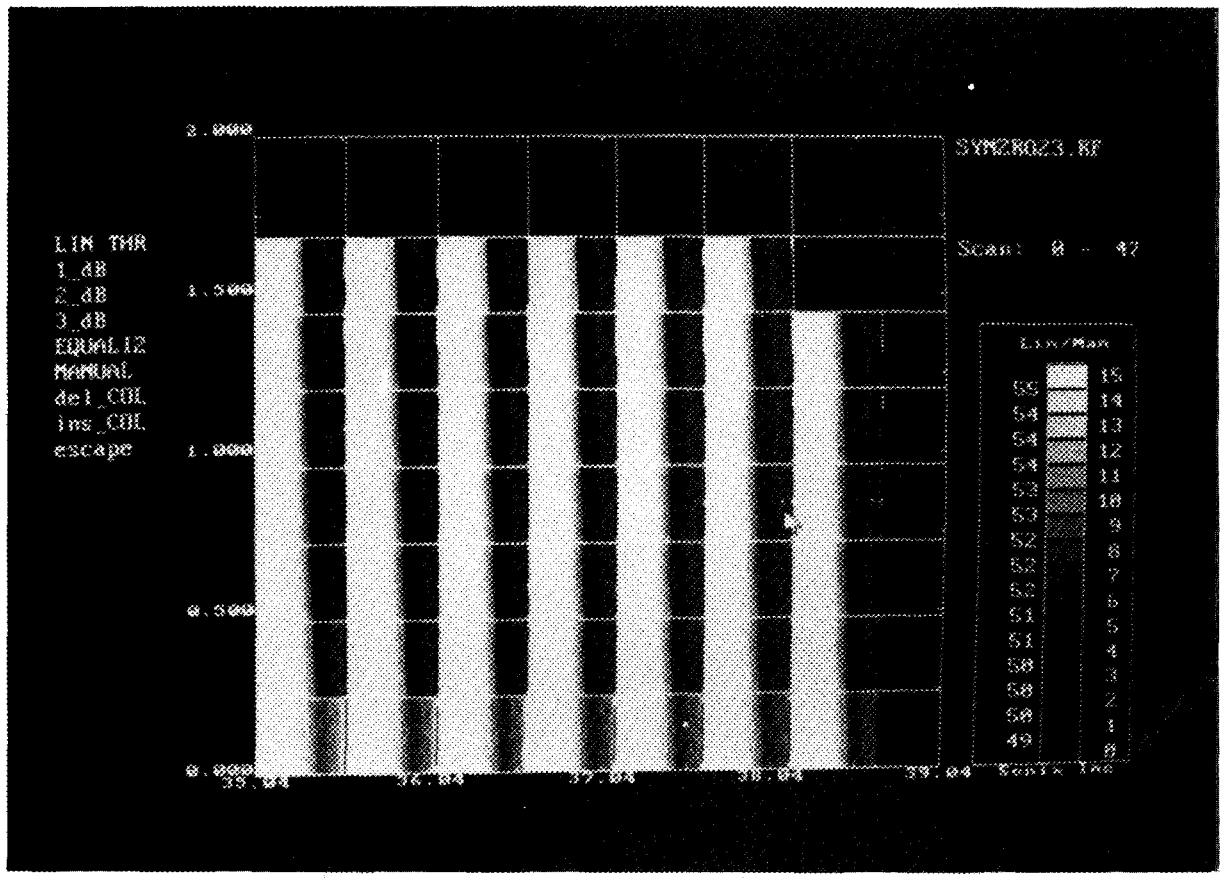

Fig. 2. Partially contrast-enhanced processed synthetic aperture data showing detection of 250-μm flaw (arrow) in zirconia.

improvements: (1) repair of the stepless gate function to help eliminate electronic saturation effects caused by the front-surface signal (completed), (2) addition of more gain (we have up to 40 dB additional gain available in an external amplifier, but this approach would require temporal signal averaging to reduce the electronic noise), and (3) inclusion of a 3-D plotting routine for proper display of the processed data. The data of Figs. 2 and 3 are drawn from a volume of the MOR bar, and the proper spatial relationship of the flaws can best be seen in a 3-D display. We will be making these improve-ments in the future.

The actual flaw results just described were highly encouraging, but the sample contained only a single flaw, which did not test the ability of the code to process different depths. In a reversal of standard procedure, we also conducted a synthetic aperture analysis on artificial data generated by computer. Such a data set allows us to evaluate our software in the absence of noise, transducer diffraction and aberration effects, and interference from the highly saturated front-surface signal present in actual data. The artificial data were assumed to originate from three flaws at different positions and depths in zirconia. The transducer impulse response was modeled as a cosine-modulated

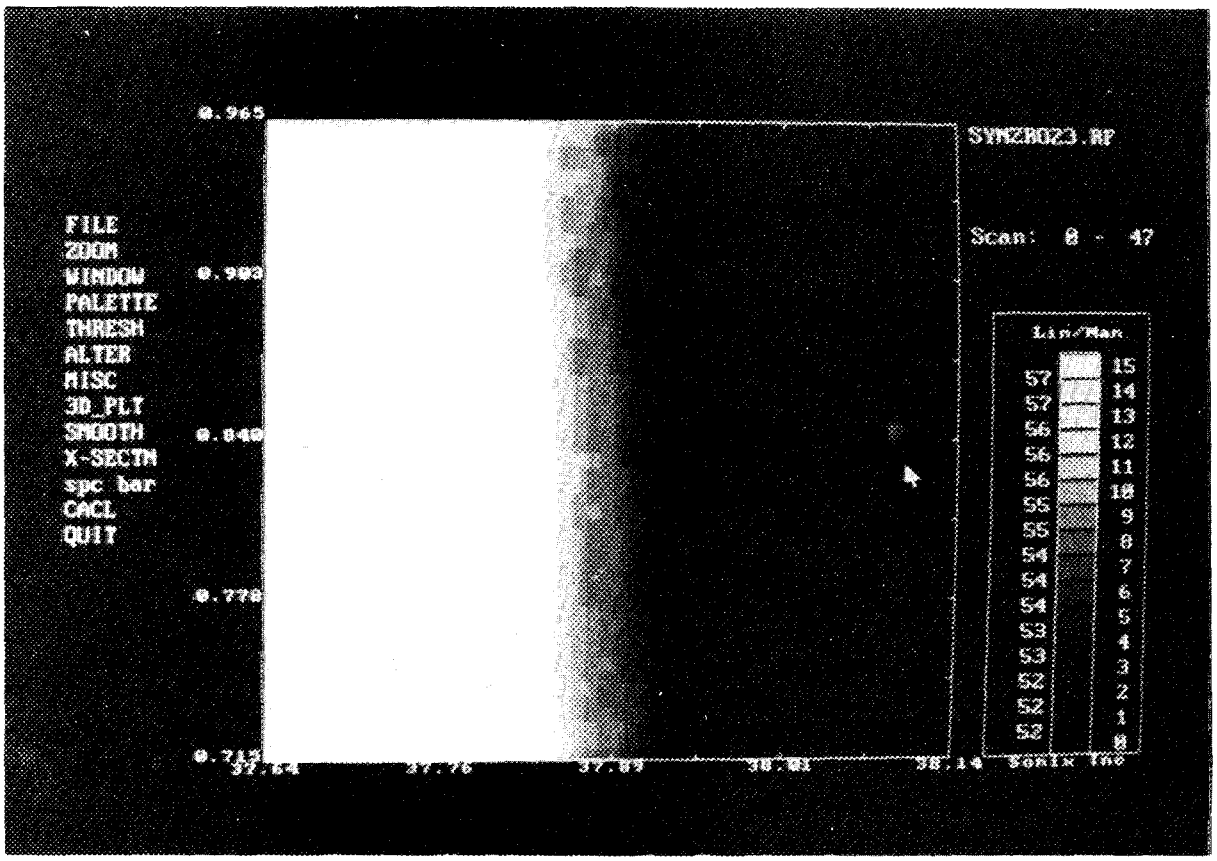

Fig. 3. Contrast-enhanced and magnified image (arrow) of 250-μm flaw in zirconia.

Gaussian having a bandwidth of about 100% and the focal properties as those of an f/4, spherically focused transducer. Although the size of the data set (about 400 Kb) was far from the largest (20 Mb), which our system can now hold in high-speed (RAM) memory, it represents about one-fourth of the volume of a standard MOR bar and was adequate to assess the ability of the software to provide stigmatic imaging over all depths present in the data set.

The test data set consisted of 80 scan lines separated by about one-half wavelength. Each scan line was, in turn, composed of 80 records, each of which contained the time-domain response obtained at a single aperture point. The aperture points along a scan line were also separated by about one-half wavelength.

Figure 4 shows the second 30 scans (scans 30 through 59, as shown at the upper right of the figure), which are centered on the midplane flaw and that have been contrast-enhanced to make the flaw response (the parabolic arcs) more evident. The full data set, including the results before contrast enhancement, has been shown previously.[1] Within each scan, depth increases to the right, and position along a scan line increases upward. The midplane flaw can be seen for all of these 30 scan lines, with the maximum response occurring in line 40, when the transducer passes directly over the flaw. The response from the shallowest flaw begins to appear in scan 55 (second from the left in the top row).

YP16476

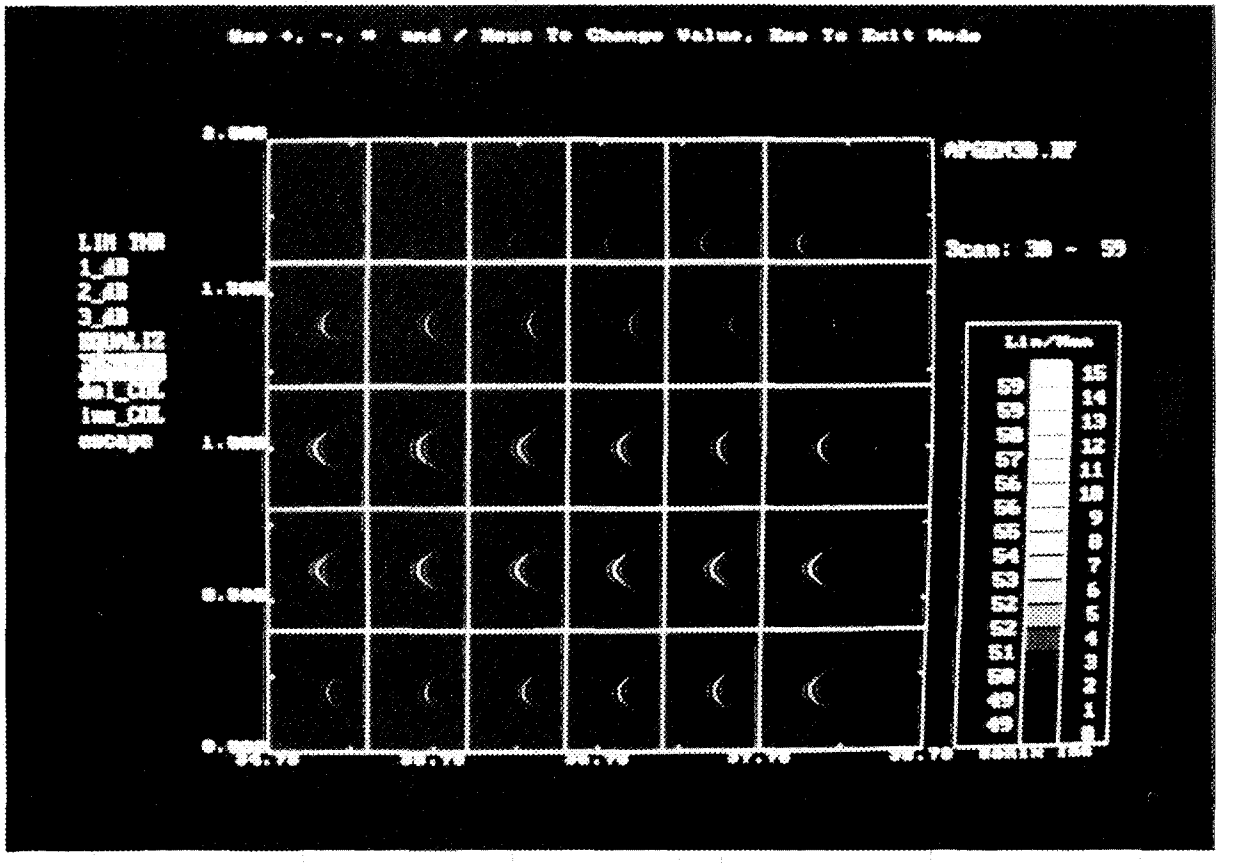

Fig. 4. Scans 30 through 59 of an unprocessed synthetic aperture data set showing response (parabolic arcs) of midplane flaw.

Figure 5 shows the contrast-enhanced results after processing by our 3-D synthetic aperture algorithm. The midplane flaw is indicated by the arrow in scan line 40. Note that the flaw "image" has now been sharpened to a pointlike indication that is visible only for the two adjacent scan lines; i.e., the apparent diameter of the flaw is about one wavelength, a value commensurate with the resolution expected from the size of the synthetic aperture (which is considerably less than the total scan aperture) and the flaw depth.

The images of the deepest and the shallowest flaws were also shown previously[1] and will not be repeated here. The results are essentially identical to those shown in Fig. 5 with the respective flaw appearing at the proper location within the scan aperture. Each flaw image thus appears stigmatic and correctly located, both with respect to position and depth.

These results and those obtained on actual ceramic samples suggest that our synthetic aperture software is working extremely well. Flaws at different positions and depths seem to be handled correctly, and the results, while requiring more time than for a single scan of the same area by conventional techniques, are obtained for all depths simultaneously. To cover the same depth range using conventional techniques, multiple scans must be made with the transducer focused at different depths. Thus, the inspection

YP16473

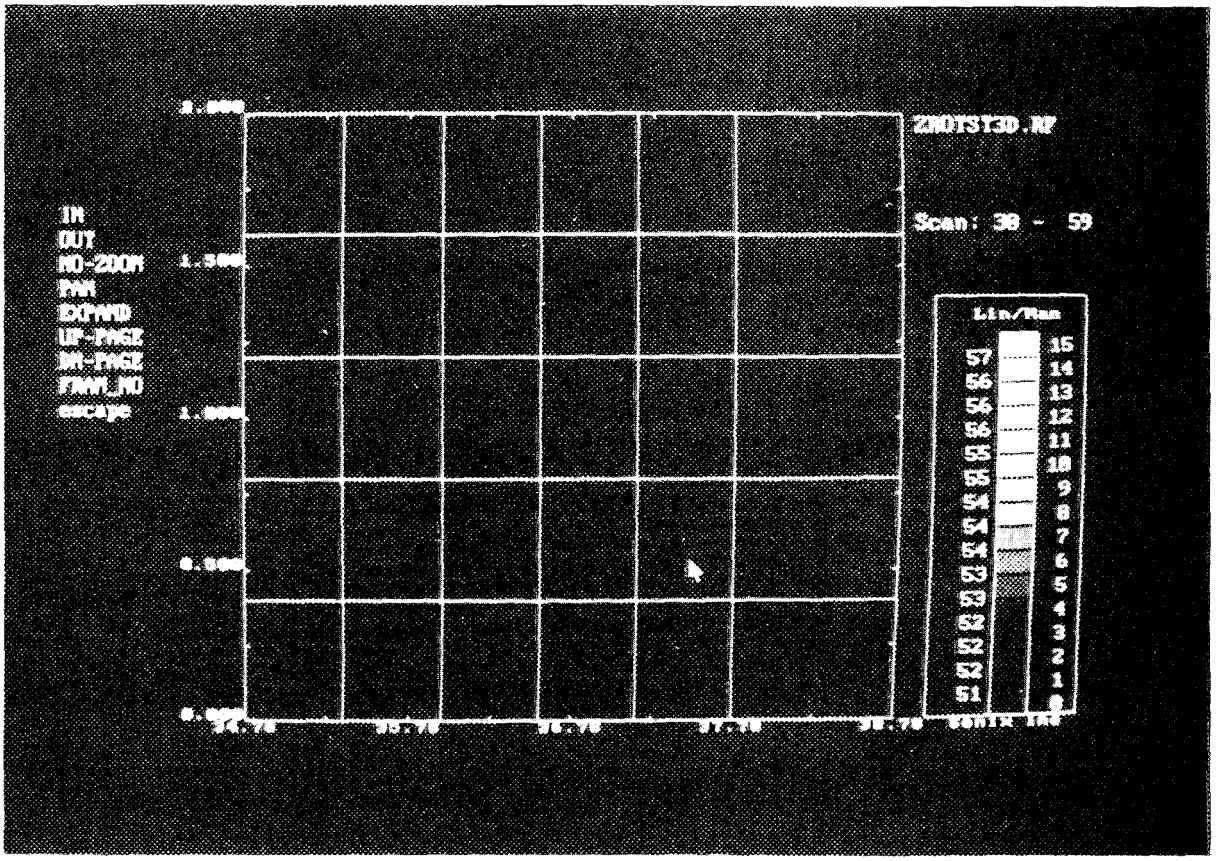

Fig. 5. Scans 30 through 59 of processed synthetic aperture data set showing image (arrow) of midplane flaw.

time for the conventional approach is that required for a single scan multiplied by the number of different depths at which the transducer must be focused. For the zirconia inspection simulated by our test data, the synthetic aperture approach was definitely faster than for a conventional inspection covering the same depth range. We now need to increase the system gain to permit a greater depth range to be inspected and to implement temporal averaging at each aperture point to improve the signal-to-noise ratio necessitated by a gain increase.

As mentioned earlier, we have acquired and installed additional high-speed memory for our 50-MHz, 486-based computer. This system is the primary one for synthetic aperture processing and now contains a total of 20 Mb of extended memory. Assuming a temporal record having a maximum length of 256 bytes at each pulse-echo synthetic aperture point (corresponding to a depth interval of almost 14 mm in alumina, silicon carbide, or silicon nitride), the area inspected would be about 112 mm square (assuming a step size of one wavelength). Proportionately larger areas could be inspected at reduced depth intervals. This means that more than 175,000 mm^3 of these materials could, in principle, be inspected with synthetic aperture techniques using high-speed memory for processing. We cannot yet detect critical flaws at such depths because of

limited system gain and available signal-to-noise ratios, but we no longer require excessive processing times for practical data set sizes because of the necessity of using virtual (hard-disk) memory.

One of the requirements driving our development of synthetic aperture technology for ceramic inspection is the need to detect critical flaws at depths exceeding those available to focused high-frequency transducers. A second and no less important reason is the high degree of aberration, specifically astigmatism, suffered by a focused ultrasonic beam upon propagating through the surface of small-diameter (~6 mm) cylindrical specimens. It is not uncommon for flaws as large as 100 to 200 μm to be undetectable by conventional techniques at depths exceeding 0.5 mm because of severe defocusing of the beam. Using synthetic aperture techniques, however, the beam is focused on, rather than below, the surface of the sample, with the result that the entry surface may be considered planar over the small focal spot diameter. The curvature of the surface is not negligible over the area of the synthetic aperture, of course, but the beam entry conditions may be assumed to approximate those for planar geometries.

We showed previously[2] that the phase delay of a flaw signal over a planar synthetic aperture is given by:

$$\Phi(x,y) = \exp[ik(x^2+y^2)/2d], \tag{1}$$

where x and y denote position within the aperture relative to the point directly over the flaw, k is the wave vector of the incident ultrasonic wave, and d is the flaw depth. For a cylindrical specimen, the phase relationship must be altered to reflect the change in geometry. Figure 6 shows the coordinate system appropriate to a cylinder. The point O lies on the axis of the cylinder, and points A and B are two points on the surface, where OA and OB are radii of the cylinder and are equal to a. These three points define a plane perpendicular to the cylinder axis. Point C also lies on the surface, with the line segment BC directed along the axis. Primary displacements in this coordinate system are thus $d\phi$ (circumferential) and dz (axial). Assume a flaw at position P on the line joining A and O. The depth of the flaw is thus d. The arc of the chord joining A and B is denoted by x and is equal to:

$$x = 2a\sin(d\phi/2). \tag{2}$$

The distance PB is:

$$\rho^2 = x^2+d^2-2xd\sin(d\phi/2). \tag{3}$$

Substituting for x above and collecting terms:

$$\rho^2 = 4a\sin^2(d\phi/2)(a-d)+d^2. \tag{4}$$

ORNL-DWG 93-12794

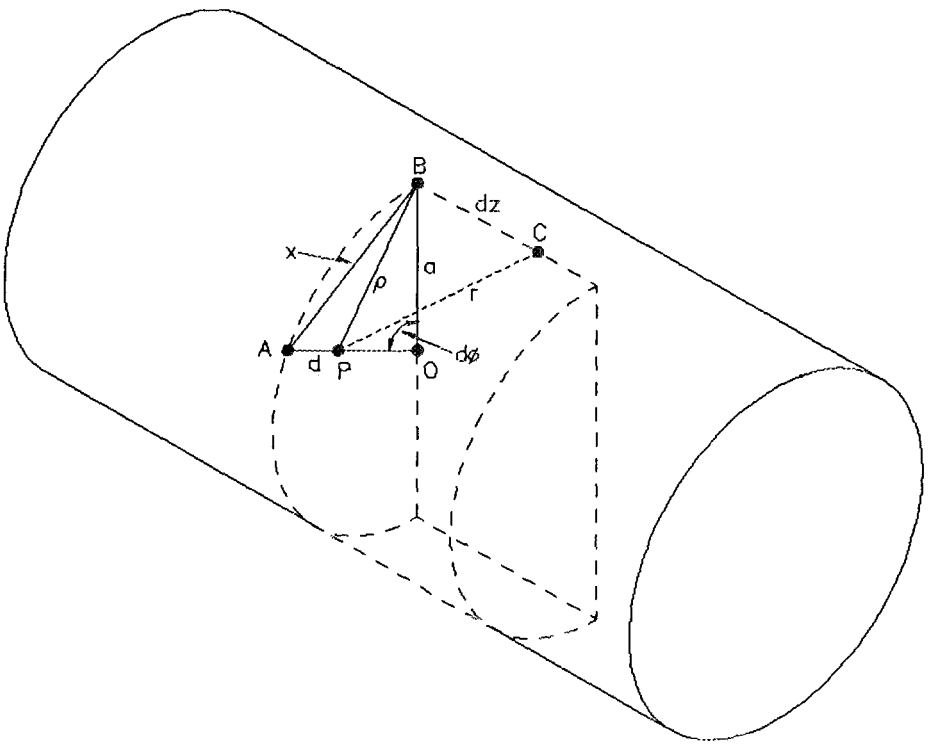

Fig. 6. Coordinate system for calculation of phase shift for synthetic aperture implementation in a cylindrical geometry.

Finally, the distance PC is denoted by r, where r is given by:

$$r^2 = \rho^2 + dz^2 = 4a\sin^2(d\phi/2)\,(a-d) + d^2 + dz^2. \qquad (5)$$

The phase of the flaw signal at C referenced to that at A is thus:

$$\Phi(\phi, z) = \exp[ik(r-d)], \qquad (6)$$

or twice this value in pulse-echo.

It is easy to show that these results reduce to the planar case in the limit of large cylinders and for displacements small compared to the flaw depth. If the displacement $d\phi$ is sufficiently small, the sines can be replaced by their arguments. If dz is also small compared to flaw depth, and the latter is small compared to the cylinder radius, the expression for $\Phi(\phi,z)$ reduces to that for a planar surface, with $ad\phi$ playing the role of x and dz that of y. In this approximation, which is <u>not</u> valid for ceramic tensile specimens and is not assumed in our programming, the cylinder is so large that it may be regarded as flat. If the flaw lies at the center of the cylinder (d = a), however, then ρ = d, and the

last equation above reduces to that of a one-dimensional synthetic aperture, which is expected since the phase of the flaw signal is then independent of ϕ.

We have written software to perform the necessary phase-coherent summation in cylindrical geometries. This programming makes no assumptions regarding the magnitudes of $d\phi$, d, or dz; i.e., the code assumes a true cylinder rather than a plane.

We also completed construction of a modification to our scan hardware that permits evaluation of cylindrical ceramic specimens. Both conventional focused-transducer inspection and synthetic aperture techniques can be used on specimens up to about 3 in. in diameter and 7 in. long with this modification. Perhaps more importantly, however, the new system will allow automated inspection of small-diameter ceramic parts such as tensile specimens, heretofore one of the more difficult geometries to inspect.

Figure 7 shows the scan system with the cylindrical geometry modification installed. A silicon nitride tensile specimen can be seen mounted in the horizontal position. The specimen is held in position by stainless steel self-centering cones at either end of a precision dovetail slide. One of the centering cones is driven by a toothed belt and stepping motor, and the other is spring loaded to place the specimen under the appropriate compression. The dovetail slide will adjust to accommodate specimen lengths from 0 to about 7 in. The centering cones shown can be used with specimens up to about 1 in. diam, while additional cones can be made to accommodate larger specimens. A silicon nitride piston wrist pin is also shown in the figure.

The stepping motor shown in Fig. 7 is that which normally drives the y-axis of the scan system. This motor will be replaced with an identical type and a connector placed in the y-axis drive cable so that the system can be converted quickly from planar to cylindrical geometries.

The stepping motor can be run in either the full- or half-step mode. In the former mode, the motor requires 200 steps per revolution. For a 6-mm-diam gauge region tensile specimen, this means that the azimuthal step size is 100 μm. This is less than a wavelength for volumetric inspections up to about 100 MHz or surface-wave inspection at frequencies up to 50 MHz. If finer intervals are required, the stepping motor may be operated in the half-step mode, which reduces the azimuthal step size to 50 μm. Changing the number of teeth on the centering guides (gear ratio) could also be used to control the step size.

After alignment, the system was checked for specimen wobble and miscentering. Using a 50-MHz, f/0.2 transducer focused on the sample surface, the observed wobble appears to be dominated by sample surface finish rather than bearing wobble. Most ceramic tensile specimens have visible irregularities in diameter in the gauge length. The ceramic wrist pin, which has a highly polished surface, proved to be a much better indicator of bearing irregularities, which appear to be acceptable.

One of the first specimens to be inspected with the new system was the ceramic wrist pin. We had previously examined this sample visually and ultrasonically using very crude manual rotation and knew that it contained at least three surface pits about 75 μm in diameter and about 50 μm deep. The new inspection was performed at 50 MHz using our surface-wave transducer. Figure 8 shows the results. In this figure, the abscissa is along the axis of the pin, while the ordinate is along the azimuthal direction. The y-axis stepping motor was operated in the half-step mode, which means that 400 data points were taken in the azimuthal direction. The three dark, pointlike indications are the previously detected surface pits. Several other indications were noted, however, one of which was a 25-μm-diam pit about 20 μm deep. The other indications were not detected visually and are presumably caused by subsurface voids.

YP16645

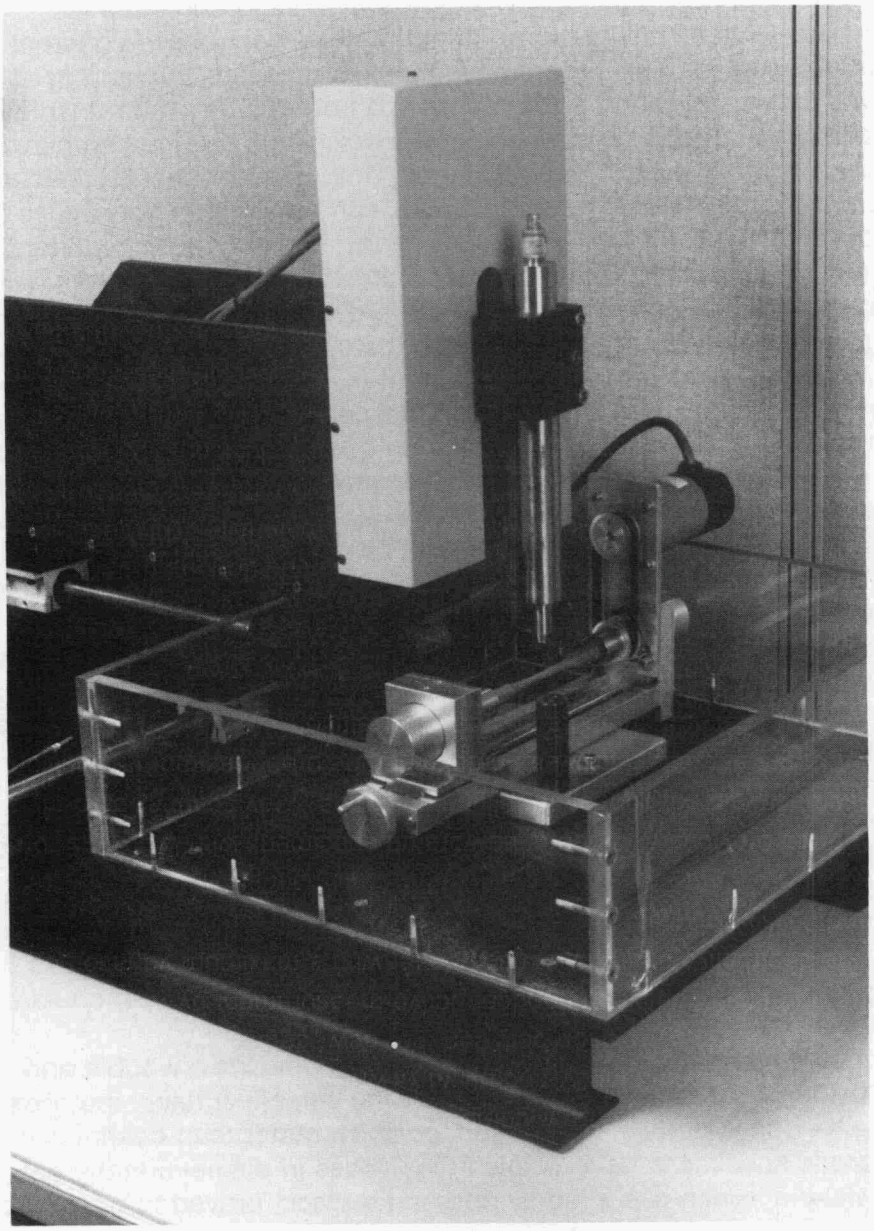

Fig. 7. Photograph of cylindrical geometry inspection modification made to our ultrasonic scan system.

YP16792

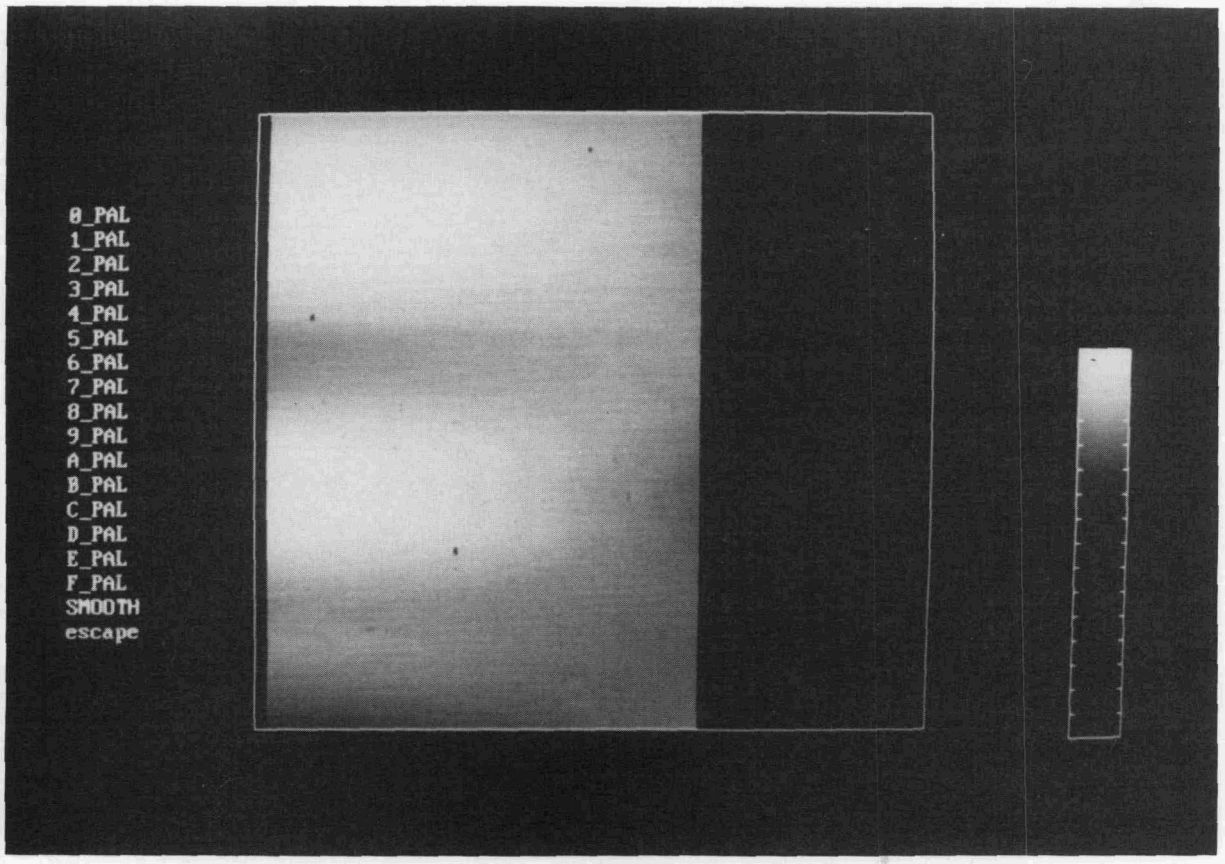

Fig. 8. Ultrasonic surface-wave image of a ceramic wrist pin showing detection of surface and near-surface voids (dark, pointlike indications).

The periodic brightness variations evident in the figure are caused by specimen wobble. However, the f/0.2 surface-wave transducer is extremely sensitive to changes in the transducer-specimen distance, and the wobble appears to be less than 75 μm. This is completely negligible for both surface-wave and volumetric flaw inspection, but it may have to be taken into account in our synthetic aperture work.

We continue to receive requests from commercial vendors for help in evaluating new products or processes. One such recent request concerned a proprietary silicon carbide whisker-toughened ceramic. Of particular concern to the vendor was the effectiveness of whisker dispersal in the ceramic matrix of two samples. Since we have developed several effective techniques for detecting whisker clumping in composite ceramics, we agreed to examine the new materials. The vendor was interested in actual images of whisker inhomogeneity, so we simply subjected the samples to high-frequency C-scans. Both 25- and 75-MHz scans were made for volumetric flaws, and the samples were also examined with a 50-MHz surface-wave transducer. Figure 9 shows the volumetric flaw results obtained at 25 MHz on the more inhomogeneous of the two samples. The bright, pointlike indications are voids or whisker clumps located mostly near the middle one-third of the sample, which was about 1.5 cm thick. These are quite large flaws (~1 mm).

YP16777

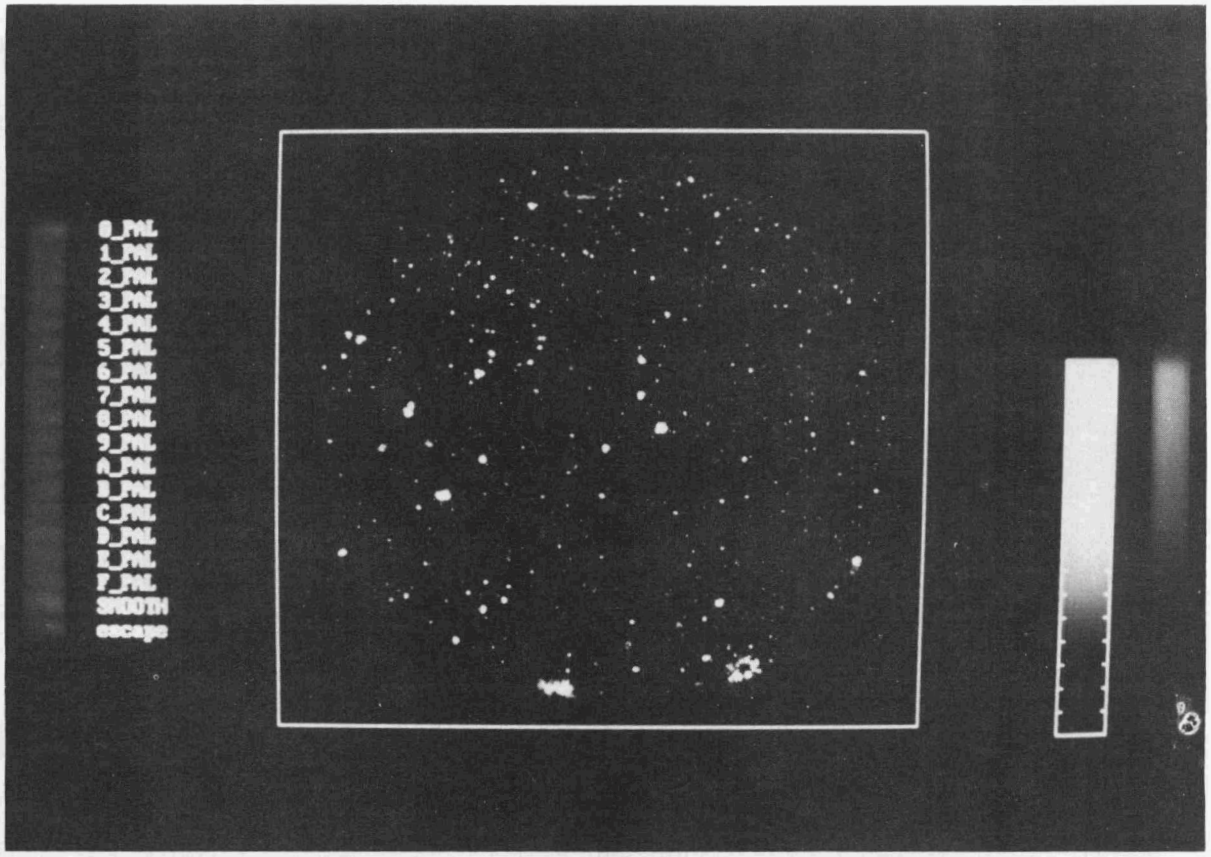

Fig. 9. Ultrasonic image at 25 MHz of large flaws (voids or whisker clumps) in a whisker-toughened ceramic.

Figure 10 shows the results obtained at 75 MHz on the same sample. Again, the pointlike indications are voids or clumps, but the apparent size of most of these indications is only about 100 to 200 μm. These flaws are located about 3 mm deep in the sample and are typical of those found in whisker-toughened ceramics with inadequate whisker dispersal.

Figure 11 shows the surface-wave results obtained on one of the samples. This sample, which was considerably more homogeneous than the other, nevertheless exhibited severe surface cracking (dark, circular features). Examined by visible microscopy, faint indications of cracks could be found in the regions delineated by the ultrasonic results. These cracks must extend at least a wavelength (~150 μm) into the sample, however, because of the intensity of the ultrasonic indications. One sample thus appeared to exhibit severe whisker clumping and the other matrix cracking.

A contract has been awarded for a very high-frequency (2-GHz) acoustic microscope for surface and near-surface characterization of structural ceramics. At this frequency, the acoustic wavelength (in water) is only about 0.75 μm. As the instrument is designed to be used primarily for exciting surface waves, the resolution expected in

YP16776

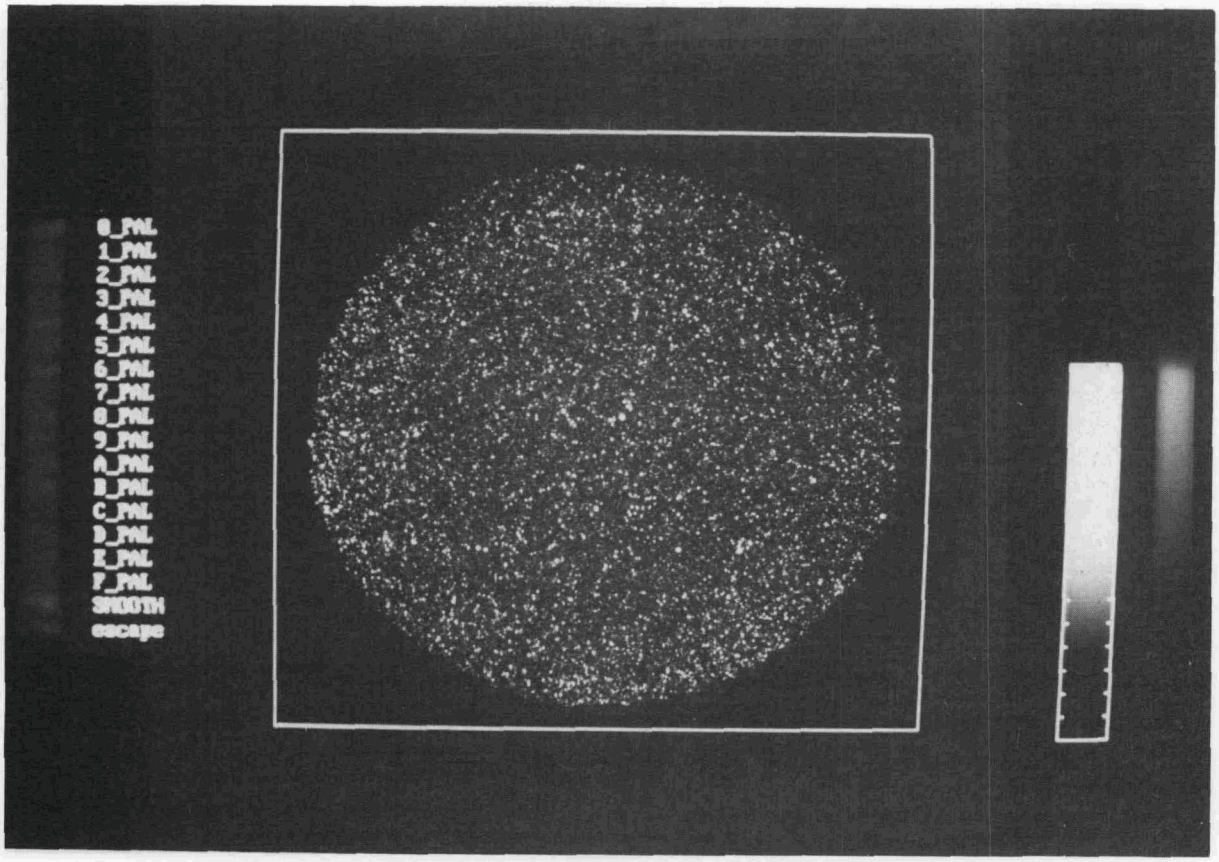

Fig. 10. Ultrasonic image at 75 MHz of voids or whisker clumps in a whisker-toughened ceramic.

structural ceramics is about 2 to 3 μm. Features much smaller than this should be detectable, of course. For such short wavelengths, individual material grains, which are anisotropic and randomly oriented, modulate the surface-wave velocity to produce contrast differences in the resulting image. We expect the hardware to be installed in 3 to 4 months.

CT - B. E. Foster

Specifications have been completed, approved, and submitted to the Purchasing Department for procurement of the Sun workstation and software upgrade for the CT system. This upgrade with four array processors will allow data manipulation and image processing about ten times faster than the present system. In addition, the memory of the new array processors is increased by a factor of about 100, which will eliminate the need for using time-consuming "mosaic" processes to build high-resolution images. The capability will be provided for direct interface to an existing digital film recorder for high-quality hard-copy printouts.

YP16779

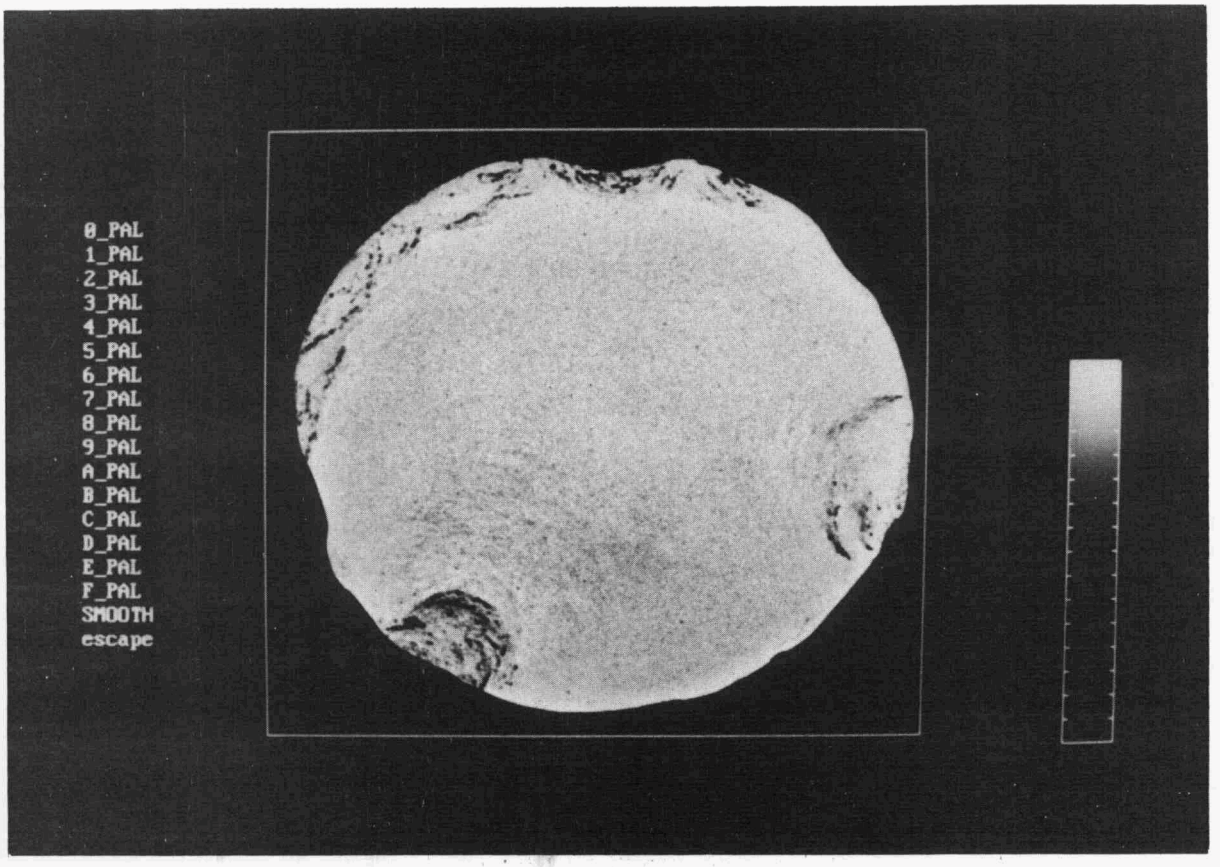

Fig. 11. Ultrasonic surface-wave image of matrix cracking (dark, circular features) in a whisker-toughened ceramic.

Three Si_3N_4 disks were received from Southern Illinois University for evaluation using both CT and high-resolution film radiographic techniques. The disks were identified as S4-3, S4-11, and CEP 513 with diameters ranging from 55 to 65 mm and thicknesses of 10 to 12 mm. The two S4 disks contained 4% alumina, 13% yttria, 5 wt % Si_3N_4 seeds. In addition, S4-11 contained UBE-E10 powder. Both disks were pressure cast and isopressed. S4-3 was fired to 1625° C for 90 min, but S4-11 was unfired. Sample CEP-513, also unfired, did not contain any seeds but contained ASN-34 powder from Performance Ceramics instead of UBE-E10.

Most of the CT scanning and all of the high-resolution film radiography has been completed on these disks. The CT scanning was slowed because of bugs found in the new versions of software.

A CT slice (0.25 mm thick) was made through the approximate midpoint of the thickness of each sample. Figure 12 shows the slice of S4-3 after the application of beam-hardening corrections. Density variations of approximately 9.8% can be be seen across the image. Similar slices of S4-11 and CEP- 513 are shown, respectively, in Figs. 13 and 14. The noted density variations are significantly less, only about 2% for S4-11 and 1% for CEP-513. In addition, digital radiography is being performed, but

YP16431

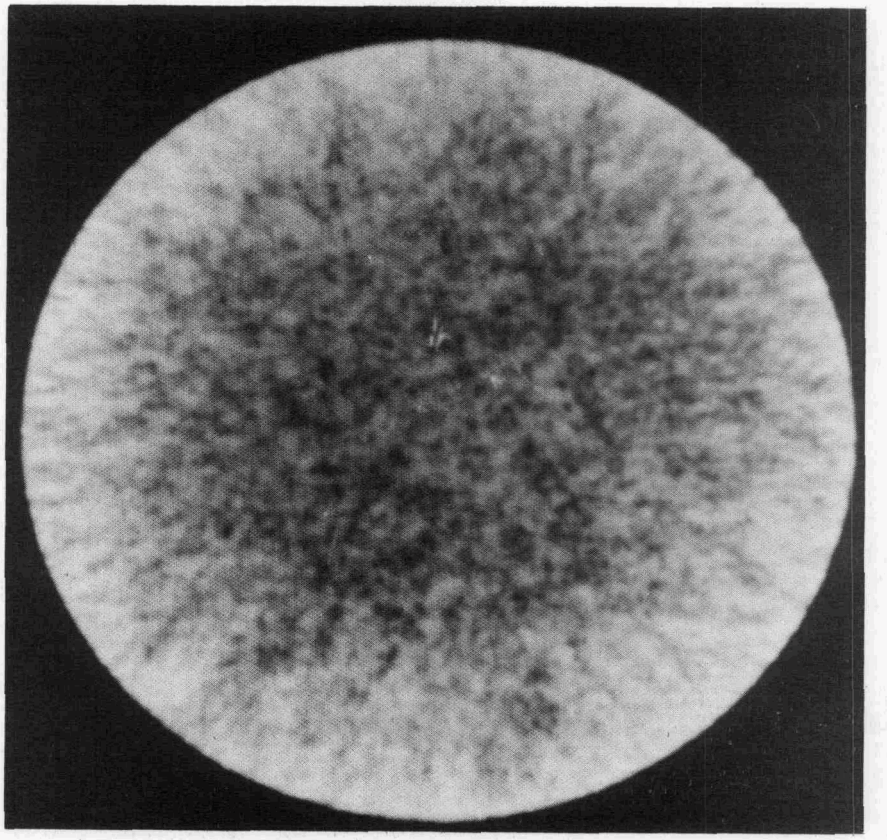

Fig. 12. CT slice (0.24 mm thick) of Si_3N_4 sample S4-3.

quantitative data are not yet available. However, it is evident from the early radiograms that the density variations noted in the thin CT slice are volumetric.

Visually, the film radiographs were very uniform for all three samples. However, densitometric analysis showed similar density variations noted with the CT scans. For a semiquantitative evaluation, we developed a radiographic equivalence curve between film densities of different thicknesses of aluminum and the film density variations in the radiographs of the three samples. Sample S4-3 showed density variations of 9.4%, S4-11 contained density variations of about 1%, and CEP-513 showed variations slightly less than 1%. The volumetric data from these film radiographs agreed quite well with what was determined with the CT scans.

During February 1993, personnel from Scientific Measurement Systems (SMS) [the CT vendor] performed the semiannual system alignment and maintenance operations as per our service and maintenance agreement. Everything seemed to be in order. Shortly thereafter, the 760-MB user disk drive failed to come up to speed, thus rendering the CT system inoperable. The drive was sent to SMS for repair or replacement and data recovery. The problem was found to be with the drive's "header blocks," which were successfully repaired with full recovery of the data. This was accomplished under our service agreement at no additional cost.

YP16432

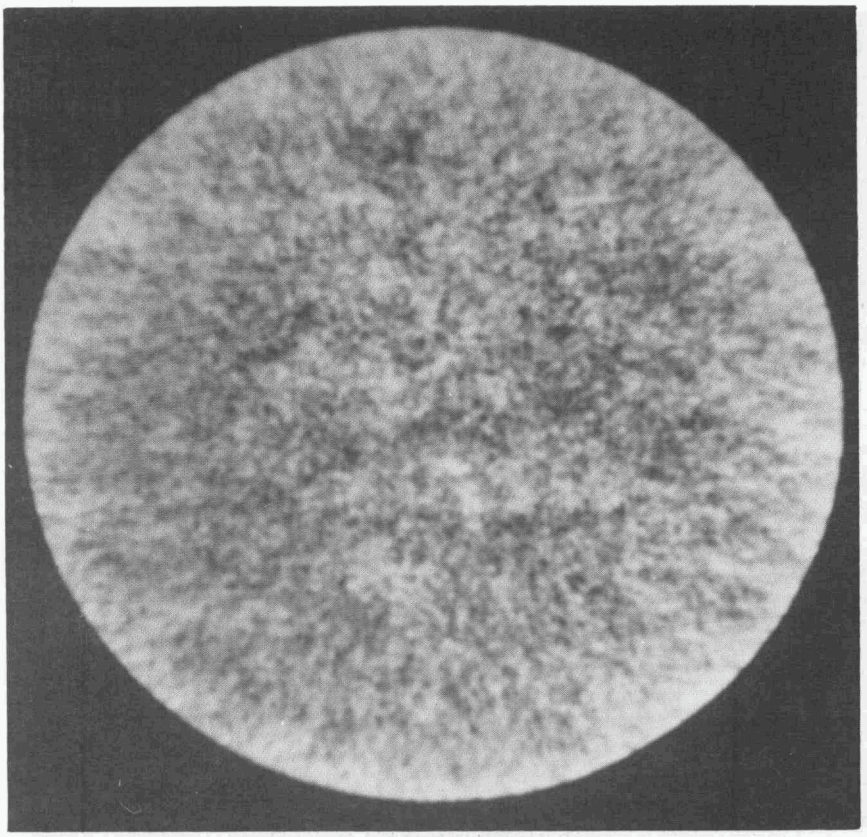

Fig. 13. CT slice (0.25 mm thick) of Si_3N_4 sample S4-11.

The drive has been reinstalled, and we are now back up to speed and operational. The scanning and analysis of the three Si_3N_4 disks from Southern Illinois University is continuing. Four tensile test samples of Si_3N_4 have been received for evaluation following completion of the ceramic disk analysis.

Milestones

Milestone 351106 was completed on schedule.

Publications

W. A. Simpson, Jr., and R. W. McClung, "An Ultrasonic Evaluation of Silicon Carbide Whisker-Reinforced Ceramic Composites," *Mater. Eval.* **51**(3), 391-95.

References

1. W. A. Simpson, Jr., "Nondestructive Evaluation Development," p. 57 in *Ceramic Technology Project Bimonthly Progress Report*, December 1992 - January 1993.

2. W. A. Simpson, Jr., "Nondestructive Evaluation Development," p. 56 in *Ceramic Technology Project Bimonthly Progress Report*, December 1991 - January 1992.

YP16433

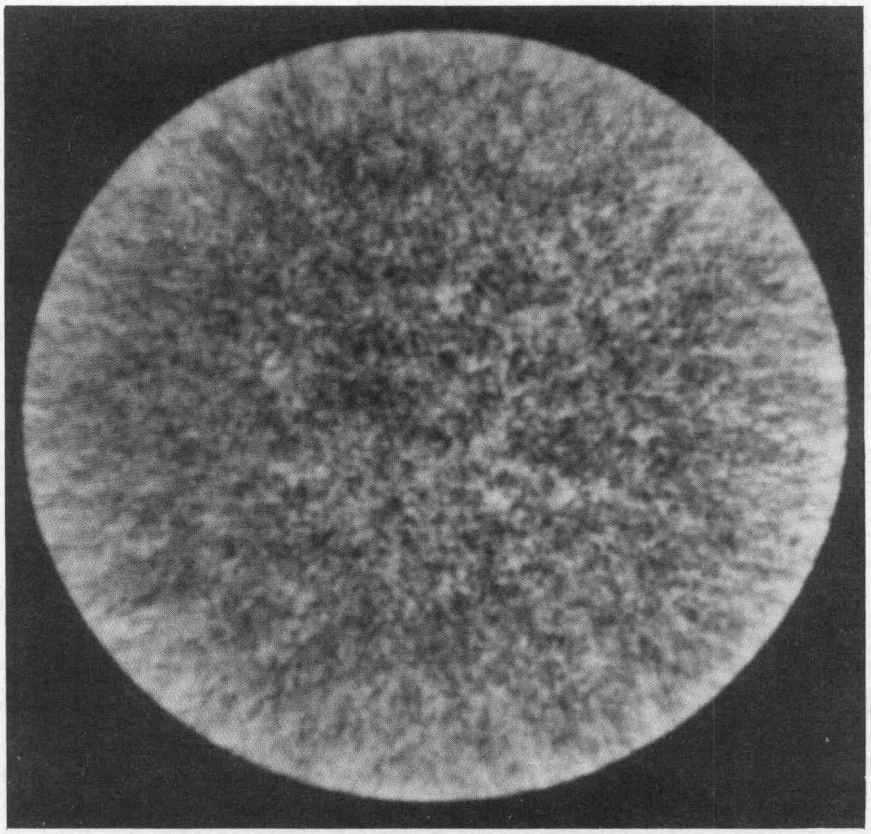

Fig. 14. CT slice (0.25 mm thick) of Si_3N_4 sample CEP-513.

NDE STANDARDS FOR ADVANCED CERAMICS

R. W. McClung (Oak Ridge National Laboratory)

The development of standards is important for the establishment of reliability and acceptance of advanced structural materials. Committee C-28, on Advanced Ceramics, is organized in the American Society for Testing and Materials (ASTM) to address this issue. One of the activities of the C-28 committee is nondestructive examination (NDE). The Task Group on NDE (TGNDE) is reviewing existing standards on NDE (primarily developed for metals) to determine potential applicability for ceramics as well as preparing original standards. Use of existing or modified standards is more efficient than generation of new documents and will ensure the input of a large body of NDE expertise. Close liaison is established with ASTM Committee E-7 on Nondestructive Testing, and documents are in various stages of review, recommendation for change modification, and balloting. R. W. McClung is a member of both committees and the official liaison.

Liaison and technical support have been continued between ASTM Committees C-28 and E-7. To date, 31 NDE standards have been reviewed in detail with recommendations made to E-7 for modifications to identified documents. Successful action is complete on 27 documents; the others require action by C-28.

A newly approved ASTM standard C-1212 on "Fabrication of Seeded Voids in Pressureless Sintered Ceramics" was used as a guide for preparation of a new draft standard for ceramic reference specimens containing seeded inclusions. The latter document will be distributed by mail for comments by the TGNDE. A revision of C-1175, the guide for use of relevant E-7 standards [adding a new standard on NDE terminology (replacing three older documents) and five new standards on liquid penetrant examination] was balloted successfully in a concurrent subcommittee and committee letter ballot. It has now been approved by Society ballot. In the meeting of the C-28 TGNDE in January 1993, a new draft standard on "Ceramic Reference Specimens Containing Seeded Inclusions" was discussed and additional input identified with plans for an early subcommittee ballot. A draft standard was presented for making precise measurements of ultrasonic velocity in advanced ceramics. One application is determination of porosity in ceramics. The draft will be circulated for an advisory ballot within the TGNDE. A letter and questionnaire have been drafted to request data for "radiographic equivalence factors" from members of the TGNDE and other potential sources of data. Other work in progress is an amplified outline for a draft standard for reference specimens containing laser-drilled holes. In the meetings of Committee E-7 (January 25-28, 1993), several documents are in progress on radiography, computer tomography, and ultrasonics with relevance for application to advanced ceramics.

X-ray Computed Tomographic Imaging – W. A. Ellingson, D. L. Holloway, E. A. Sivers (Argonne National Laboratory) J. Ling, (Ceramic Research Institute, Shanghai, China) J. P. Pollinger (Garrett Ceramic Components of Allied-Signal Aerospace Corporation)

Objective/scope

The objective of this program is to develop X–ray computed tomographic (CT) imaging technology for application to structural ceramic materials. This technique has the potential to map short–range (<5-mm) and long–range (>5-mm) density variations (to perhaps 0.5–1%), detect and size high– and low–density inclusions, and detect and size (within limits) cracks in green–state and densified ceramics. Use of three dimensional (3-D) CT (volume CT) imaging allows interrogation of the full volume of a component and is noncontacting. It is also relatively insensitive to specimen shape and thus can be used to inspect components with complex shapes, such as turbocharger rotors, rotor shrouds, and large individual turbine blades.

Technical progress

The work accomplished during this reporting period covered two areas: (1) finalizing the report on reliability of X-ray CT to detect density distributions in as-cast pressure-slip-cast SiC(w)/Si_3N_4 and (2) conduct of initial work on Phase III relative to density measurements in pressure slip-cast ATTAP rotors. This continues to be a joint project with Ceramic Components of Allied-Signal Aerospace Corporation of Torrance, California.

Part 1

All of the specimens of SiC(w)/Si_3N_4 billets (length/diameter ratio = 1.5 and 2.67) made by pressure slip-casting have now been examined and questionable data on the L/D = 1.5 specimens re-evaluated.

This period we re-evaluated the data reported earlier for L/D = 1.5 for specimens containing 27 and 30 wt.% whiskers. A comparison between the "old" data and the "new" data are shown in Figs. 1 and 2 for 27 and 30 wt.% whiskers respectively. To be noted is the significant difference in correlation between the "new" data and the "old" data. In the "new" data, the agreement between nondestructive measurement by X-ray computed tomography and destructive analysis is much better with a maximum variation of < 2% for both the 27 and 30% whiskers.

As we reported previously, in our initial work on specimens with L/D = 1.5 for 20 and 23 wt.% whiskers, we did not control our alignment in the X-ray scanner properly and as a result, the destructive analysis data was not taken at the proper azimuthal position. The result if a significant scatter in the data and poor correlation.

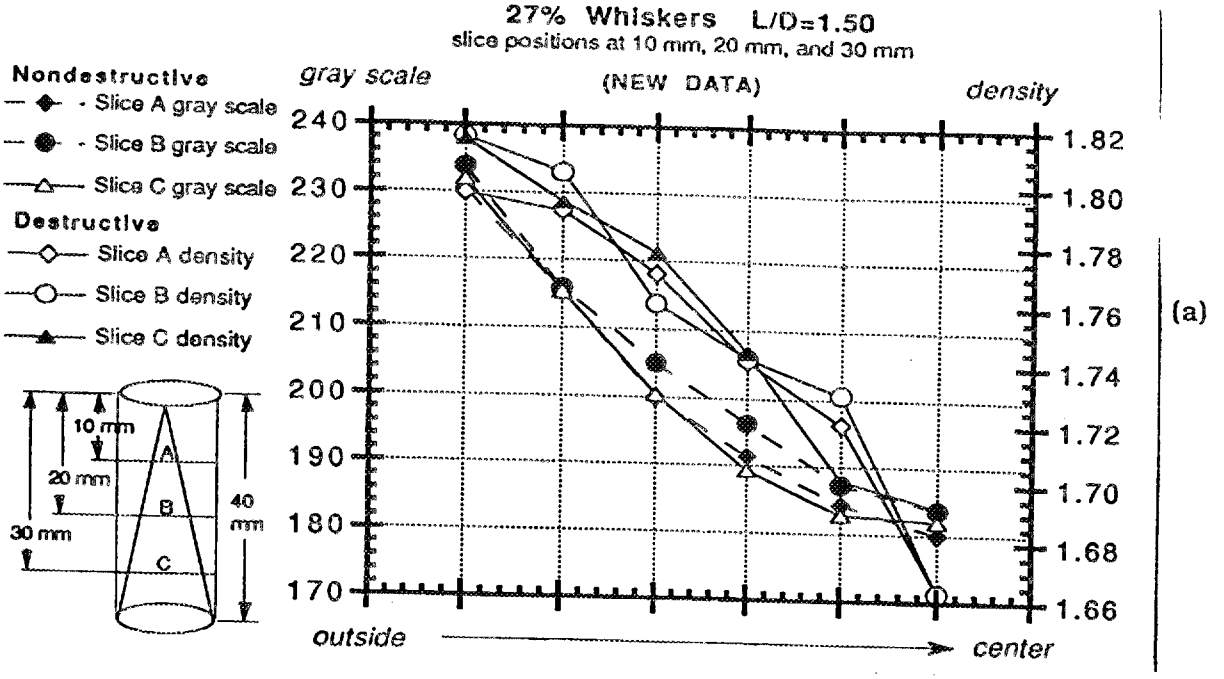

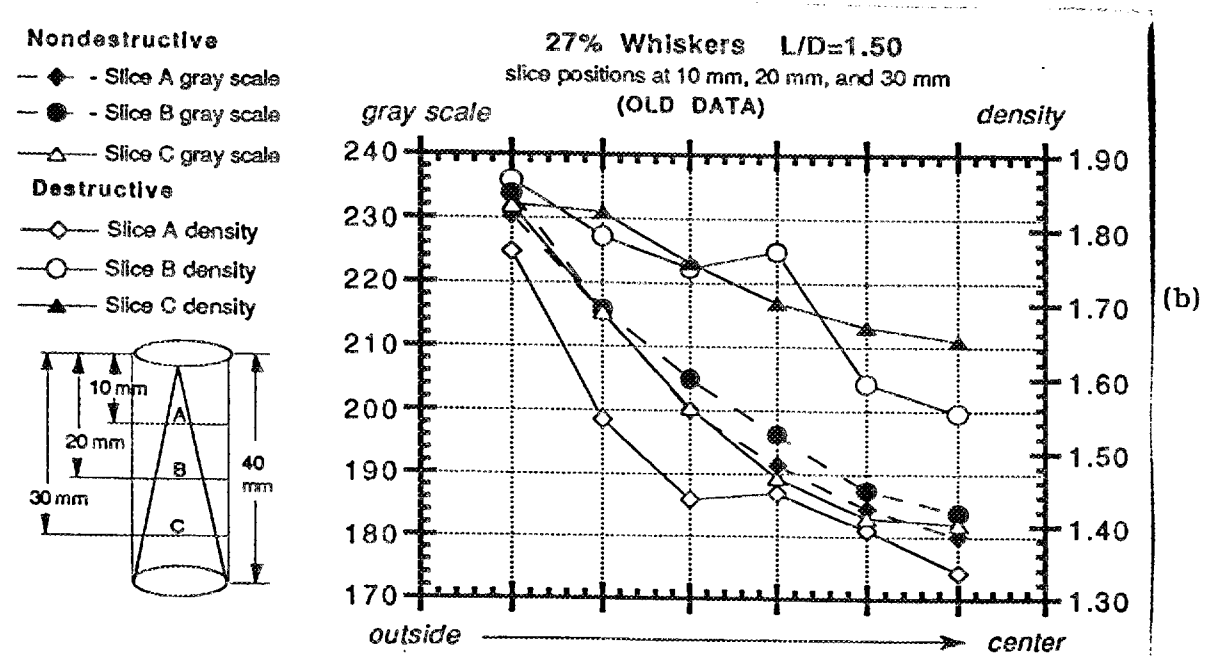

Fig. 1. Comparison between destructive density measurements and nondestructive density measurements on pressure slip-cast Si_3N_4. The ceramic was air-dried after slip casting. (a) new data, (b) old data

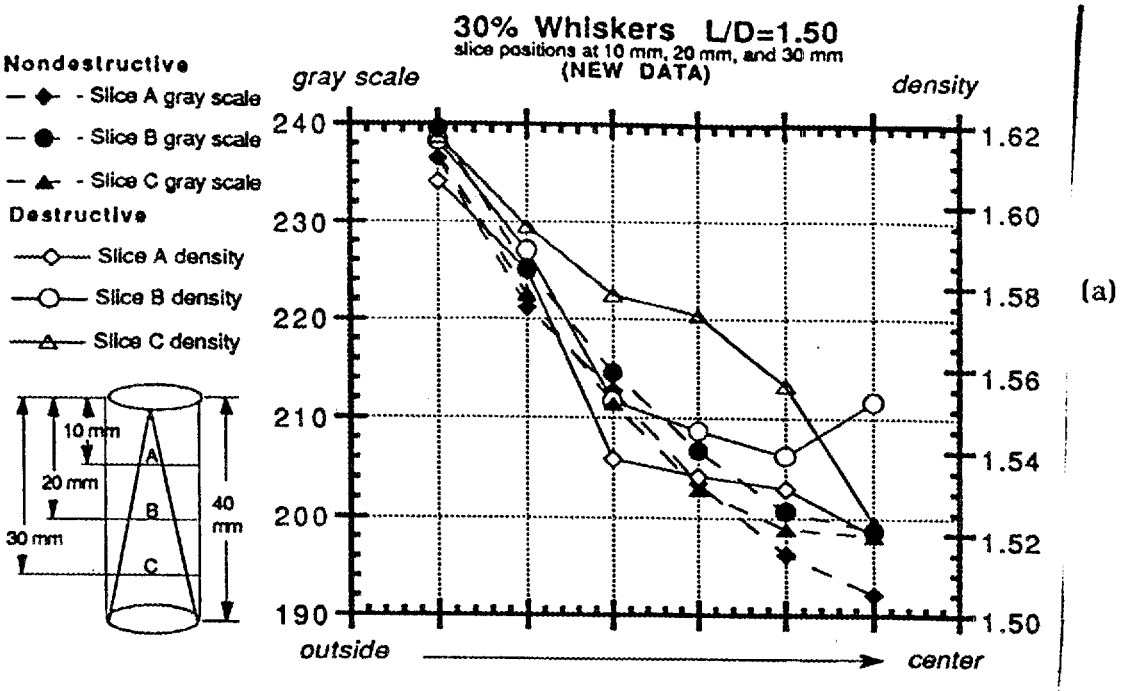

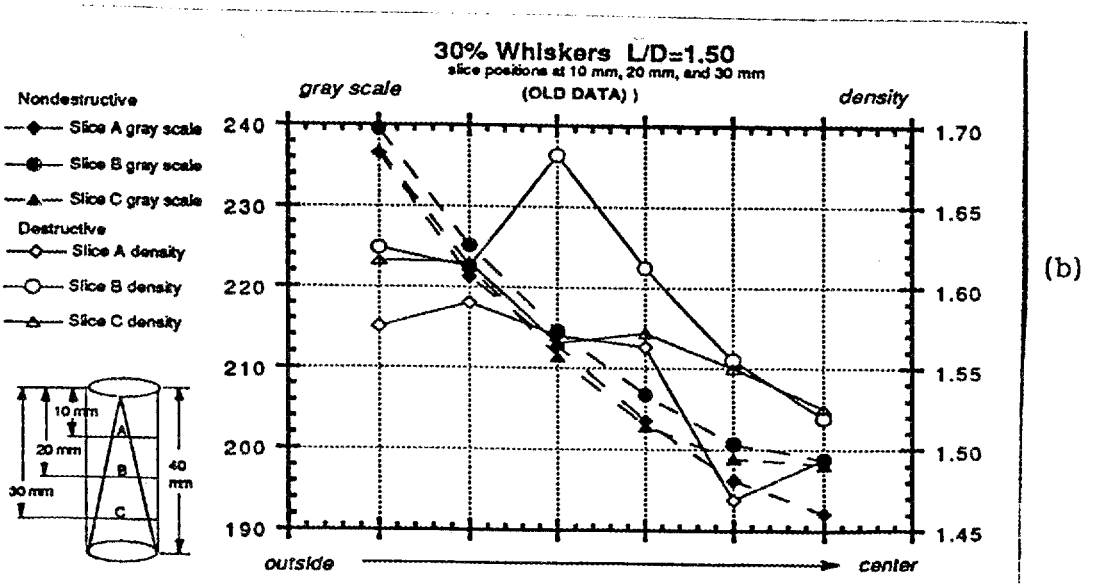

Fig. 2. Comparison between destructive density measurements and nondestructive density measurements on pressure slip-cast Si_3N_4. The ceramic was air-dried after slip casting. (a) new data, (b) old data

This can be seen by looking at Figs. 3 and 4 which show respectively, the 20 and 23 wt.% whisker-density data. You will also note that these specimens were cut in half so that NMR imaging data could be obtained to try to establish the potential of NMR imaging to measure open, connected porosity. Thus, the 20 wt.% whisker specimen was studied for density on the upper half of the specimen, and the 23 wt.% specimen was studied for density distribution in the lower half of the specimen. Upper and lower referred to the orientation of the specimen in the pressure casting position. The data for 20 wt.% whiskers is surprisingly good even though the data were not taken at the same locations. The correlation of data for the 23 wt.% whiskers is very poor however (see Fig. 4), especially for the data obtained at the mid section, Section A. By omitting this particular plane, the data again shows reasonable correlation.

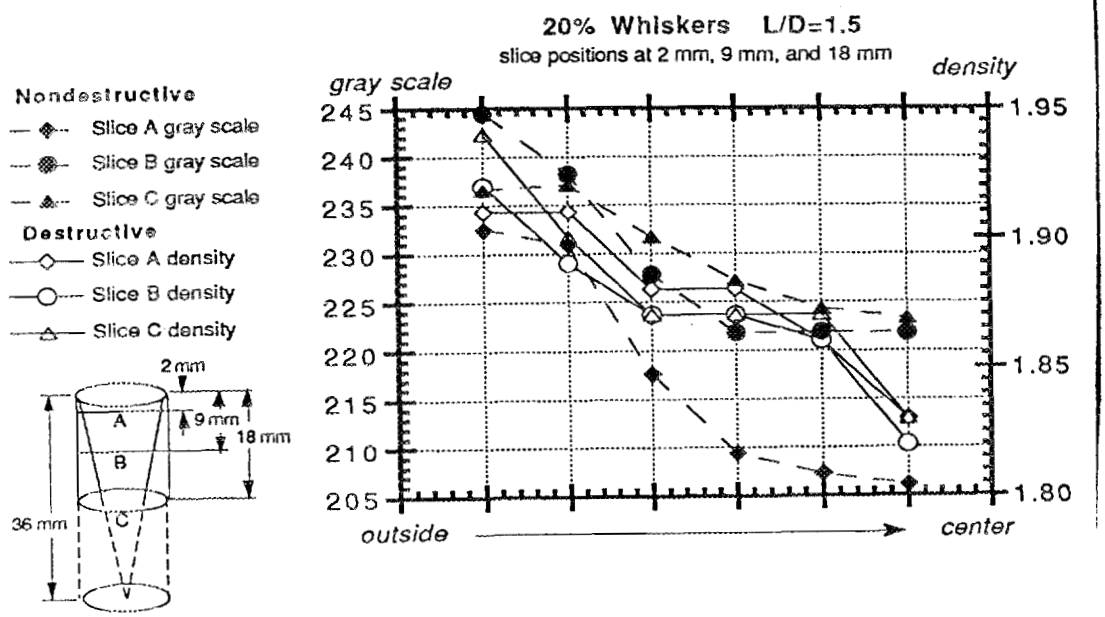

Fig. 3. Comparison between destructive density measurements and nondestructive density measurements on pressure slip-cast SiC/Si_3N_4. The ceramic was air-dried after slip-casting. [X-ray CT data not taken at exact location of destructive analysis].

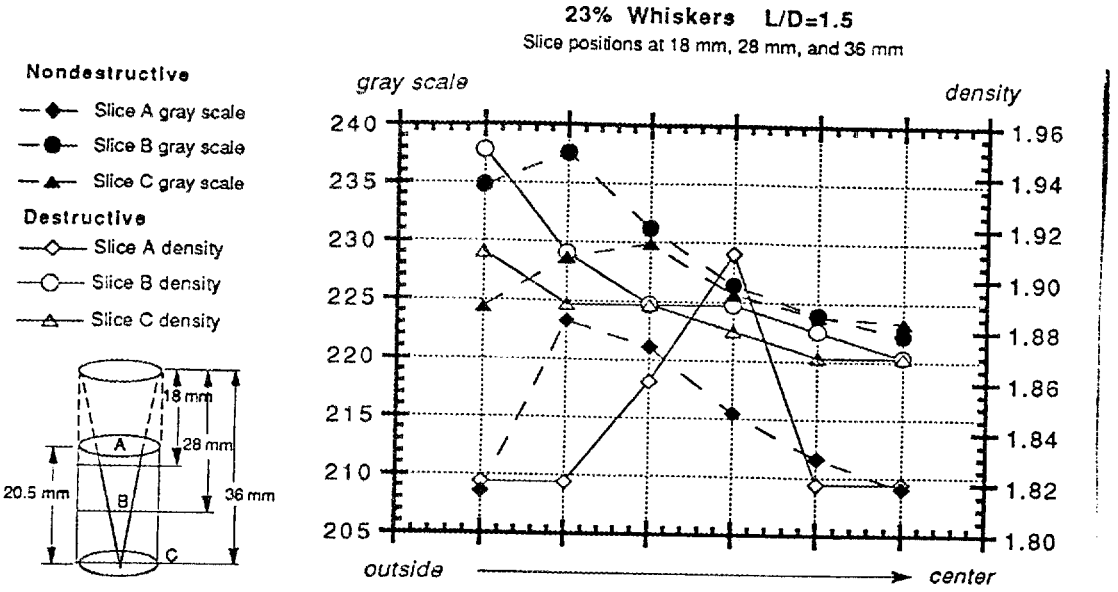

Fig. 4. Comparison between destructive density measurements and nondestructive density measurements on pressure slip-cast SiC/Si_3N_4. The ceramic was air-dried after slip-casting. [X-ray CT data not taken at exact location of destructive analysis].

Part 2

ATTAP Rotor Density Studies

One pressure slip cast ATTAP rotor has been received. This has allowed us to verify X-ray penetration studies and complete the initial region of interest reconstruction study. The rotor as received is shown below in Fig. 5.

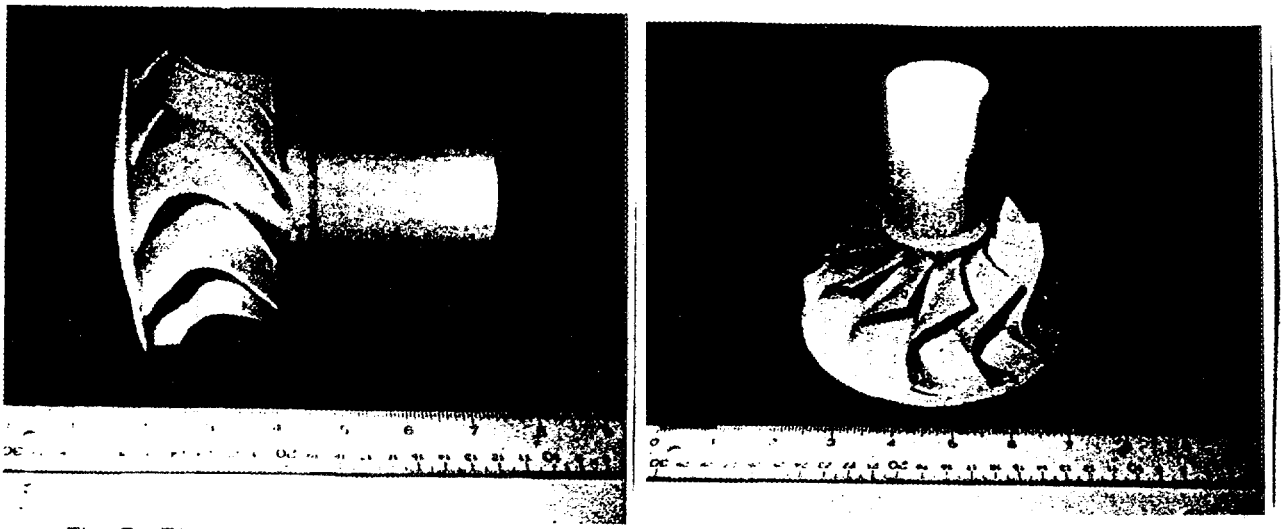

Fig. 5. Photos of Allied-Signal/Ceramic Components pressure slip cast ATTAP rotor used in X-ray computed tomographic imaging study.

In Phase III of this work, we will make density measurements on these rotors corrected for X-ray beam hardening. In order to do this correction, we will use a calibration step wedge as shown in Fig. 6.

We will obtain X-ray CT density data on the rotors at the locations shown in Fig. 7. Further, at these locations, 2x2x2 mm cubes will be cut at one azimuthal position for destructive weigh and measure data. As in the Phase II research work on pressure slip cast billets, these destructive data will then be compared to the X-ray CT density data but in this study we will have added a beam hardening correction.

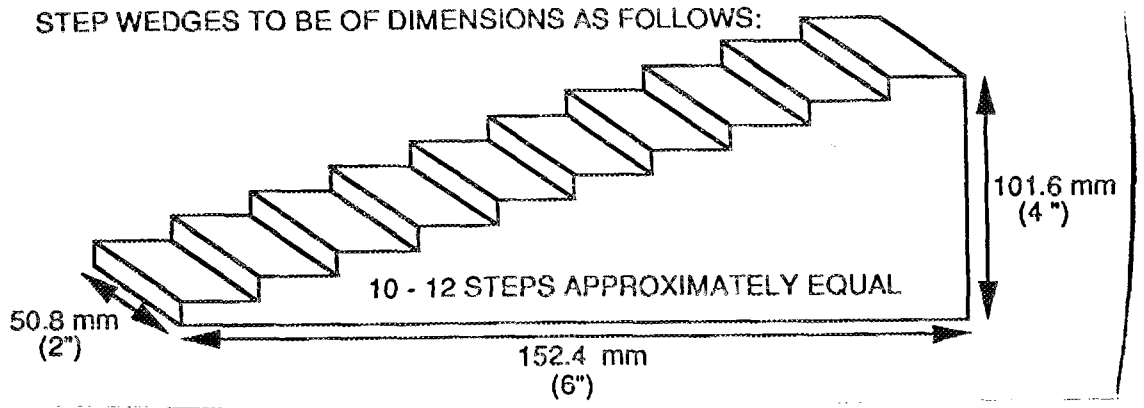

Fig. 6. Schematic diagram of calibration step wedges to be used for Phase III density studies of ATTAP rotors.

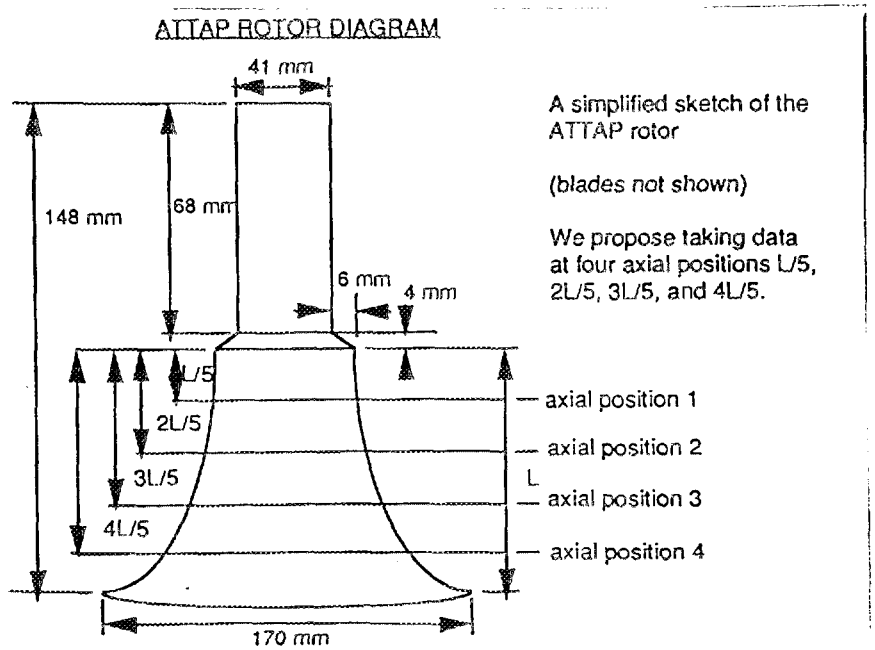

Fig. 7. Schematic diagram of pressure slip-cast ATTAP rotor showing locations of planned X-ray CT and destructive analysis to be used for correlation study.

Nuclear Magnetic Resonance Imaging – S. L. Dieckman, A. C. Raptis, W. A. Ellingson (Argonne National Laboratory), and H. Yeh and J. P. Pollinger (Garrett Ceramic Components of Allied-Signal Aerospace Corporation)

Objective/Scope

The objectives of this task are to (1) utilize NMR imaging techniques to study the distribution of whiskers and other possible variations in composite pressure-slip-cast green-state (as-cast) billets, (2) conduct destructive analysis of the same billets (to be performed by Garrett Ceramic Components a Division of Allied Signal Corp.), and (3) correlate the results obtained from the NMR imaging techniques with those obtained from both three dimensional (3-D) X-ray and optical microscopy.

Technical Highlights

The purpose of this work is to evaluate the potential of NMR imaging to impact the development and process control of near-net-shape gel-cast ceramic composites. The specific objectives of this work are to determine the utility of NMR imaging for: (1) 3D mapping of polymerization homogeneity; (2) real-time imaging of the polymerization process; (3) nondestructive evaluation of voids and flaws in the resultant components; and (4) measurement of physical properties such as as degree of polymerization, viscosity, and specimen strength via correlation of these properties with measureable NMR parameters (T_1, T_{1r}, and T_2). This work will be performed in conjunction with Dr. Ogbemi O. Omatete from the Materials and Ceramics Division at Oak Ridge National Laboratory.

In this reporting period, funding for this proposal was not in place. However in preparation for the initiation of this program, a meeting was held at ORNL with Dr. Ogbemi O. Omatete. The discussions centered upon the choice of two appropriate gel cast polymeric systems for the NMR experiments, and a discussion of the NMR technique. Additionally, Dr. Omatete conducted detailed laboratory demonstrations of the gel cast technique. Work in this project will begin in the upcoming reporting period.

Status of Milestones

Milestones have been completed for Phase II.

Trips/Communications/Visits

None

Problems Encountered

None.

MILESTONE SCHEDULE (3.5.1.6)

3.5.1.6.08	Complete NMR Imaging of two slip-cast billets	8/15/91
3.5.1.6.09	Submit initial report on correlation between NDE data and destructive testing.	6/15/92
3.5.1.6.10	Complete NMR imaging of remaining billets	Deleted

4.0 TECHNOLOGY TRANSFER

4.1 TECHNOLOGY TRANSFER

4.1.1 Technology Transfer

Technology Transfer
D. R. Johnson (Oak Ridge National Laboratory)

Technology transfer in the Ceramic Technology Project is accomplished by a number of mechanisms including the following:

Trade Shows - A portable display describing the program has been built and has been used at numerous national and international trade shows and technical meetings.

Newsletter - A Ceramic Technology Newsletter is published regularly and sent to a large distribution.

Reports - Semiannual technical reports, which include contributions by all participants in the program, are published and sent to a large distribution. Informal bimonthly management and technical reports are distributed to the participants in the program. Open-literature reports are required of all research and development participants.

Direct Assistance - Direct assistance is provided to subcontractors in the program via access to unique characterization and testing facilities at the Oak Ridge National Laboratory.

Workshops - Topical workshops are held on subjects of vital concern to the ceramics community.

International Cooperation - This program is actively involved in and supportive of the cooperative work being done by researchers in West Germany, Sweden, the United States, and, most recently, Japan under an agreement with the International Energy Agency. This effort is ultimately aimed at development of international standards and includes physical, morphological, and micro-structural characterization of ceramic powders and dense ceramic bodies, and mechanical characterization of dense ceramics.

IEA ANNEX II Management

V. J. Tennery (Oak Ridge National Laboratory)

Objective/scope

The purpose of this task is to organize, assist, and facilitate international research cooperation on the characterization of advanced structural ceramic materials. A major objective of this research is the evolution of ceramic property measurement standards. This task, which is managed in the United States by ORNL, now includes a formal International Energy Agency (IEA) Annex agreement identified as Annex II between the United States, Germany, Sweden, and Japan. The original annex included four subtasks: (1) information exchange, (2) ceramic powder characterization, (3) ceramic chemical and physical characterization, and (4) ceramic mechanical property measurements. In the United States, a total of 13 industrial and government laboratories have participated and contributed their resources to this research. The research in Subtasks 2, 3, and 4 is now complete. During CY 1990, agreements were reached for Japan to join the annex, and for research in two new subtasks to be initiated. These include, Subtask 5, Tensile and Flexural Properties of Ceramics, and Subtask 6, Advanced Ceramic Powder Characterization. The next IEA Annex II Executive Committee Meeting will be held on October 6, 1993, in conjunction with the conference "Silicon Nitride 93" at the Max-Planck Institute for Metals Research, Stuttgart, Germany, October 4-6, 1993.

A letter was received from Mr. Erauw of the Mol Laboratory, Belgium, inquiring about participation in at least powder characterization work, which may be done in later subtasks. A letter was sent requesting clarification regarding whether his organization would be representing Belgium or the European Community and also informing him that, in order to be a participant, each organization had to participate in both Subtasks 7 and 8 (January 4, 1993). No answer was received.

Ms. Foust, Recording Secretary, Annex II, received a letter and attachments (March 2, 1993) regarding the Implementing Agreement on High Temperature Materials for Automotive Engines from Eiji Yamada, IEA Representative for Annex II in Paris, for distribution to the Executive Committee for discussion at the next Executive Committee meeting. The first item concerns involvement of the CEN and other new members; the second concerns the maximum term of the implementing agreement.

Proposed future research

Subtask 7

The proposal for future (Subtask 7) research interest in mechanical properties of structural ceramics, which had been provided to the Executive Committee, was discussed in detail at the IEA Executive Committee Meeting held at the Contractor's Coordination Meeting (CCM) in Dearborn, Michigan, November 5, 1992. The economic situation in all of these countries and the European Economic Community (EEC) situation for Germany, and the EEC uncertainty in Sweden, makes rapid decisions regarding future commitments difficult. Germany outlined a program including (1) preparing silicon nitride specimens using two sets of machining parameters, one imparting high damage and one imparting low damage, and (2) measuring subcritical crack extensions under static, dynamic, and cyclic loading at room temperature to evaluate fatigue behavior and lifetimes. The latter

would include flexure and tensile strength measurements, S-N curves with 4-point flexure specimens, followed by calculation of the Weibull parameters, and prediction of Weibull parameters for tensile specimens from flexure results. Japan proposed a research plan in which the Japan Fine Ceramics Center and Government Industrial Research Institute Nagoya laboratories would conduct, in the first year, machining research on a selected silicon nitride and a silicon carbide using a two-step grinding process for flexure bars, followed by flexure strength measurement and analysis. The machining condition example given included three sets of machining conditions, including a variation in the diamond grit size for "rough" grinding followed by a constant condition of 800-grit fine grinding. Starting in the Japanese FY 1995, Japan would then join an international effort in which six of their laboratories participated in addition to an international exchange of specimens, etc. Sweden proposed high-temperature creep work. After this meeting, the Swedish representative stated that Sweden would very probably participate in work involving studies of machining of a selected structural ceramic, similar to what is outlined above in the Japanese proposal. In regard to the U.S. proposal, which includes all of the elements in the German and Japanese proposals except for the slow crack growth measurements, etc., in the German proposal, the consensus was that the U.S. proposal from ORNL of September 1992 was too expensive. The committee asked V. J. Tennery to redraft the proposal so that the number of specimens was greatly reduced. The original proposal involved approximately 120 flexure specimens and perhaps 20+ tensile specimens being prepared for each participating domestic laboratory. A reformulated proposal (Version 3 - a smaller number of specimens) was drafted and sent to the candidate U.S. industries (10 laboratories, including ORNL plus NASA Lewis Research Center, and eight industrial companies) [December 9, 1992]. The reformulated proposal includes only 30 flexure specimens for each U.S. participant, an aggregate total of 60 tensile specimens for the entire effort, and exchange of 30 flexure specimens and billets for an additional 30 specimens for each international participant. U.S. comments on this plan were requested for mid-December 1992. After receiving confirmation from the U.S. participants that they were still in agreement with the reformulated proposal, the international participants were solicited as to whether their countries were willing to participate in the ceramic machining research as described in Version 3 (December 17, 1992). An additional U.S. participant was added to Subtask 7 (December 23, 1992). Clarification of Sect. 6.0 of the research proposal for Subtask 7, regarding work proposed to be done in each country with each particular strength specimen, was sent to the international representatives (March 16, 1993).

A planning session to discuss the proposed Subtask 7 research for the U.S. participants and representatives from the participating countries will be held in conjunction with the American Ceramic Society Meeting on April 19, 1993.

Dr. Hollstein's (Germany) letter of March 25, 1993, said that a project on cyclic fatigue of silicon nitride using two different machining procedures for the specimen preparation was being proposed (Subtask 7). Dr. Hollstein also stated that Dr. Seitz would be discussing the situation with the German government. A letter to Mr. Schulz from Dr. Seitz and Mr. Faul (March 26, 1993) reported that German participants from industry and science in Subtasks 5 and 6 met March 15 and 16, 1993, to discuss the German participation in the proposals for Subtasks 7 and 8. Due to economic conditions in Germany and other factors, it now appears unlikely that there will be German participation in Subtask 7.

Dr. Frykfors (February 2, 1993) confirmed that Sweden was ready to participate in Subtask 7 as outlined in Dr. Tennery's revised proposal of December 17, 1992.

Mr. Ogiyama sent notification on January 20, 1993, for Mr. Terasawa, Japanese Executive Committee Member, that Japan is ready to participate in the latest proposal (Version 3).

Subtask 8

A proposal for a new Subtask 8 on ceramic powder characterization was discussed at the IEA Annex II Executive Committee Meeting in Dearborn, Michigan, on November 5, 1992. The proposed future work constituted a review of current status of follow-on activity to Subtask 6. All four participating countries have agreed to this proposal, however, but the degree of involvement is different, and some of these details remain to be resolved. The United States, Germany, and Sweden want to pursue the development of secondary properties of powders, whereas Japan's participants want to participate on a limited scale. A number of German participants in Subtask 6 may not continue in any follow-on work. The major emphasis of participants in Japan is to improve precision and accuracy of primary properties of powders studied in Subtask 6. The plan, as proposed, was approved by the Executive Committee. Further, the technical leaders were asked to refine and develop a consensus-based program.

Significant progress has been made toward the development of the proposed final technical plan on Subtask 8. Responses from the participants show that the current level of participation should be accepted to proceed with the plan. The tabulation of these data shows that the participants in all four countries are interested in Group II secondary properties. The level of participation in Group I, though not very large, is sufficient to accomplish the stated goal, i.e., to improve procedures so as to increase the precision of measurements. Currently, we are discussing with powder producers and participants to select four new batches of powders for Group II properties. These powders are silicon nitride, silicon carbide, alumina, and zirconia. The selection will be solely based on the powder's availability in 100-kg quantity, technical factors such as the use of powders for energy conservation applications, and participant needs.

Technical progress

Subtask 5, Flexural and Tensile Properties of Ceramics

Presentations on the status of Subtask 5 were given at the IEA Executive Committee meeting in Dearborn, Michigan, on November 5, 1993, by the international participants.

United States

Analysis of the flexural strength data and tensile strength data has been completed. The draft report of the Subtask 5 data is being drafted.

Germany

Status of German research in Subtask 5: (1) all tests have been performed except the Brazilian Disk Tests and Compression Tests; (2) fractographic investigations are nearly finalized; (3) the first statistical evaluation has been performed; (4) an evaluation of volume effects and failure criteria is being done; (5) a joint meeting on fractographic assessment was held on January 20, 1993, in Karlsruhe, Germany; and (6) the final report is expected: Spring 1993.

Currently, Germany is working on the final report for Subtask 5.

Sweden

Status of Swedish research in Subtask 5:

(1) Two labs, the Swedish Ceramic Institute (SCI) and Swedish National Testing and Research Institute (SP), have completed flexure testing at room temperature of ABB, ESK, GN10, and Kyocera material. Fractography analysis of their data sets is complete. (2) SCI has tested ABB and ESK material according to the ball-on-disc method. Fractography is ongoing. (3) SCI has tested ABB and ESK material at room temperature in tension according to the Ascera method. Fractography is completed. (4) Volvo performed tensile testing according to Instron's method during October 1992. (5) United Turbine performed spin tests during October 1992. (6) Linköping Technical University (LiTH) has completed the residual stress measurements. (7) The radiography equipment will be delivered to LiTH in 1994.

Dr. Carlsson (Sweden) has sent the strength results of the tensile tests completed at Volvo Flygmotor (March 11, 1993). The fractography on the tensile specimens is being performed at the SCI and will be ready soon. Dr. Carlsson has sent the results from the strength testing and fractography of 50 Kyocera flexure bars that were completed by the SP, which included results of the Weibull analysis performed at the SCI (March 4, 1993).

Sweden is currently working on their final report for Subtask 5.

Japan

Status of Japanese research in Subtask 5:

(1) The research in Japan is nearly complete; final reporting remains to be done. (2) Flexure testing at room temperature and 1250°C using the JIS specimens (30/10) of the Kyocera material has been completed at all six participating labs. Fractography on these sets is also complete. (3) JFCC has tested 30 specimens each of Kyocera, ABB, ESK, and GN10 material at room temperature with the American Society for Testing and Materials specimen (40/20). Fractography on these is complete. (4) GIRIN has tested 20 specimens of the Kyocera material in tension at room temperature according to the GIRIN method. Fractography is complete. (5) JFCC has tested 20 specimens each of the Kyocera material in tension at RT according to their method and Instron's method. Fractography is complete. (6) JFCC has tested in tension at room temperature, according to the Instron method, five specimens each of ABB, ESK, and GN10 materials. Fractography is complete.

Japan is currently preparing the Subtask 5 report.

Subtask 6, Advanced Ceramic Powder Characterization

Major responsibility for this subtask in the United States is at the National Institute of Standards and Technology (NIST), and a detailed report of progress on this subtask is provided in the section of this report submitted by NIST.

During this period, the major activities were on data analysis, preparation of preliminary conclusions and recommendations, and future program planning.

In order to prepare the preliminary conclusions and recommendations, additional data analysis, beyond the statistical parameters estimation, was carried out by technical leaders. Based on their analysis, draft statements were developed. These statements were compiled, edited, and a draft of preliminary conclusions and recommendations was developed. This draft has been circulated to the technical leaders for their input. The revised draft was sent to participants for their comments. The final approved version of the original interim report, "Procedures on Ceramic Powder Characterization," was prepared for publication and distribution at ORNL. It was sent to the representatives of Japan, Germany, Sweden, and the United States for distribution to the standard-setting representatives in their countries (January 25, 1993). Thirty-nine copies of the interim report, "Procedures on Ceramic Powders Characterization," were sent to one representative from each laboratory of Subtask 6 participants and contributors to the report (March 26, 1993). This limited release will only be to the standard-setting bodies in Germany, Japan, Sweden, and the United States and to the participants. The report contained disclaimers restricting distribution outside of these organizations at this time.

A presentation was made at the IEA Annex II Executive Committee Meeting in Dearborn, Michigan, on November 5, 1992. A brief review of the results of Subtask 6 was presented. The accomplishments of this program in the development of a number of procedures and supporting data were summarized.

The draft report on Subtask 6 is being prepared. The detailed table of contents has been developed and sent to the technical leaders for their review. The first two chapters of the report, including the executive summary and introduction, have been drafted. The introduction chapter contains details of the objectives of Subtask 6 and technical details of the project such as powders, procedures development, and analysis protocol. The drafts of all chapters that include procedures and data (statistical analysis, tabulated data, and precision statements) will be sent to the technical leaders for incorporating their inputs. In addition, a chapter on summary and conclusion has been drafted and is ready for distribution to the participants for their review and comments.

References

None

Status of milestones

Milestone 411511 (Complete data analysis of research results on Mechanical Properties of Ceramics, Subtask 5) has been completed (November 30, 1992).

Milestones 411513 and 411514 are on schedule.

Communications/visits/travel

V. J. Tennery, F. M. Foust, and K. Breder attended the Annual Automotive CCM Meeting in Dearborn, Michigan, November 1-5, 1992, and the IEA Executive Committee Meeting in Dearborn, Michigan, November 5, 1992.

Mr. Andreas Wagemann and Mr. Edgar Verlemann of the Fraunhofer Institut für Produktionstechnologie, Aachen, Germany, visited ORNL on March 26, 1993, to discuss ceramic machining technology.

Publications and presentations

V. J. Tennery made two presentations in Dearborn, Michigan, on November 5, 1992, entitled "IEA Subtask 5, Annex II Flexure and Tensile Strength Results - United States, German, Swedish, and Japanese Specimens" and "IEA Annex II Proposed U.S. Subtask 7 Research."

Characterization of Ceramic Powders

S. G. Malghan, L.-S. Lum, J. F. Kelly, E. Begley and S. M. Hsu
(National Institute of Standards and Technology)

Objective/Scope

Ceramics have been successfully employed in engines on a demonstration basis. The successful manufacture and use of ceramics in advanced engines depends on the development of reliable materials that will withstand high, rapidly varying thermal stress loads. Improvement in the characterization of ceramic starting powders is a critical factor in achieving reliable ceramic materials for engine applications. The production and utilization of such powders require characterization methods and property standards for quality assurance.

The objectives of the NIST program are: (1) to assist with the division and distribution of ceramic starting powders for an international round-robin on powder characterization; (2) to provide reliable data on physical (dimensional), chemical and phase characteristics of powders; and (3) to conduct statistical assessment, analysis and modeling of round-robin data. This program is directed toward a critical assessment of powder characterization methodology and toward establishment of a basis for the evaluation of fine powder precursors for ceramic processing. This work will examine and compare by a variety of statistical means the various measurement methodologies employed in the round-robin and the correlations among the various parameters and characteristics evaluated. The results of the round-robin are expected to provide the basis for identifying measurements for which Standard Reference Materials are needed and to provide property and statistical data which will serve the development of internationally accepted standards.

Technical Progress

During this period, we have pursued the following activities: data analysis of Subtask 6 project, development of a technical plan for follow-up Subtask 8 project, preparation of final draft report, and continuation of ASTM C-28.05 activities.

Data Analysis: The data analysis activities at NIST have been directed to inter-method comparison and analysis of data from standard reference powders. Some of the data obtained from more than two methods constitute the following: particle size distribution by gravity sedimentation, light scattering and scanning electron microscopy; specific surface area by multi-point and single-point BET; chemical impurities by acid dissolution and fusion followed by digestion; and interface chemistry by electrokinetic and electroacoustic methods. Preliminary analysis has been completed by comparing data from these methods. In most cases, data comparison is not entirely correct, in the sense that the measurement principle of each method is different which should result in a different value. For example, in particle size distribution measurement by light scattering and gravity sedimentation

principles mentioned above, one of the major assumptions is that primary particles have a spherical shape. Any deviation from this idealized shape will result in a different particle size distribution data from either method. There is sufficient evidence that all powders in this program contain particles that are non-spherical and, in some cases, cylindrical or needle shape particles are found. To add to this complexity, none of the commercial equipment provides data on deviation resulting from particle non-sphericity. Therefore, for commercial powders, an agreement between the data from two different types of equipment is unlikely to be obtained. However, if there is an agreement, one can only assume that all basic assumptions of the measurement principles have been fulfilled. To obtain a true measure of particle size distribution, scanning electron microscopy was included. Only a small number of participants had the equipment to carry out this procedure. In reviewing the comments and data of participants, it is clear that the recommended procedure is acceptable, but requires additional effort in the preparation of samples for SEM examination. One of the steps in this procedure is to filter dilute, dispersed suspension over a 0.1 μm filter and place it over a stub. Subsequently, particles on the stub are analyzed using automated image analysis system on SEM. Two technical issues affecting variability in the data from SEM are agglomeration of particles on the filter, and potential loss of finer than 0.2 μm particles through 0.2 μm openings of the filter cloth. Hence, improvements to this procedure are being studied.

While recognizing these drawbacks of the procedures used for particle size measurement, we have compared data from the three methods. These data reveal that repeatability and reproducibility are higher for light scattering data than for gravity sedimentation or SEM. In addition, the data from light scattering show a slightly finer size distribution than those from gravity sedimentation. Similar data analysis has been conducted for other procedures.

Subtask 8 Planning: The plan for continuation of Subtask 6 was developed by technical leaders, and was presented at the IEA Executive Committee Meeting in November 1992 at Dearborn, Michigan. The committee approved the plan pending more detailed discussion between the technical leaders. These discussions were primarily on equitable distribution of data contribution by the participants. Each participant is expected to put in the same effort to be eligible for receiving all the data and results of the program. In addition, the participants are encouraged to put approximately the same effort on primary and secondary properties. The technical leaders have been promoting these goals.

Subsequent to the approval of a draft plan for Subtask 8 at the IEA Executive Committee meeting in Dearborn, MI, on November 5, 1992, we prepared a detailed technical plan. A review of inputs provided by prospective participants showed that the level of participation, as measured by estimates of number of hours spent for analysis of powders, varied over a wide range. The total number of hours required for analysis were calculated as follows: (total number of powders selected) x (number of hours per method x number of methods selected for analysis). One of our goals has been to achieve approximately equal participation by all participants to be eligible to receive all the data

and results of the program. To accomplish this goal, a questionnaire was developed and sent to participants to seek their input on an appropriate level of participation. The responses received so far show that the existing level of participation is acceptable to those who have lower than average level of participation. Some participants are requesting that the overall level of participation should be increased in secondary properties. Since the majority wanted to accept the current level of participation, the technical leaders have decided to proceed with it.

Significant progress has been made towards the development of the proposed final technical plan on Subtask 8. Responses from the participants show that the current level of participation should be taken to proceed with the plan. The tabulation of these data show that the participants in all four countries are very much interested in Group II secondary properties. The level of participation in Group I, though not very large, is sufficient to accomplish the stated goal, i.e., to improve procedures so as to increase precision of measurements. Currently, we are discussing with powder producers and participants to select four new batches of powders for Group II properties. These powders are silicon nitride, silicon carbide, alumina and zirconia. The selection will be solely based on the powders availability in 100 kg quantity, technical factors such the use of powders for energy conservation applications, and participants needs. The draft of Subtask 8 technical plan including the powder properties and powders to be studied, and request for procedures will be submitted to the participants for their review.

Subtask 6 Report: At the Dearborn meeting, the technical leaders met to develop a plan for the draft report. The report will consist of tabulated data, data analysis, figures and procedures. At this stage, one single volume of the report is planned.

Following extensive discussions with technical leaders, an improved outline of the final draft report was developed. We plan to include procedures followed by the data developed by using the specific procedure. In the main body of the report, only summarized data and graphical analysis of the data will be presented. In addition, suggested modifications and improvements to the procedures will be incorporated based on data analysis.

The detailed table of contents has been developed and sent to the technical leaders for their review. Since the table of content is in sufficient detail, the rest of the activities should proceed more smoothly. The first two chapters of the report on executive summary and introduction have been drafted. The chapter on introduction contains details of the objectives of Subtask 6, technical details of the project such as powders, procedures development and analysis protocol. The drafts of all chapters that include procedures and data (statistical analysis, tabulated data, and precision statements) will be sent to the technical leaders for their review and detailed analysis.

In addition, a chapter on summary and conclusion has been drafted and is ready for distribution to the participants for their review and comments.

Subtask 6 Procedure Report: The Subtask 6 participants and standards setting bodies in Japan, Germany and the U.S. have received a report containing procedures compilation. The IEA Executive Committee was instrumental in taking this decision on release of the Subtask 6 procedures well before the final report. These procedures will be highly useful to the standards setting bodies to begin their work on the development of standards for powders characterization.

ASTM Activities: In the C-28.05 activity, the following three procedures were submitted for subcommittee ballot: (1) particle size distribution by gravity sedimentation; (2) particle size distribution by centrifugal sedimentation; (3) methods for specific surface area. Due to lack of participation, less than 60% voting was obtained. There were two negative votes on two procedures. These negative votes have been addressed and the modified procedures have been returned to ASTM for concurrent main and sub-committee ballots. In addition, a fourth procedure on specific surface area determination by BET method has been submitted for ballot. A meeting of the subcommittee on powders characterization has been scheduled for April 18 in Cincinnati at the ACerS annual meeting.

Status of Milestones

On target.

Publications/Presentations

Malghan, S. G., Lum, L., Kelly, J., Lagergren, E., and Kacker, R. N., "Statistical Analysis of Parameters Affecting the Measurement of Particle Size Distribution of Silicon Nitride Powders by Sedigraph,®" Powder Technology, 73 (1992) 275-284.

Malghan, S. G., Wang, P. S., and Hackley, V. A., "Techniques for Characterization of Advanced Ceramic Powders," accepted for publ. in Chemical Processing of Ceramics, B. Lee editor, Marcel Dekker, October 1992.

Technical Leaders, "Procedures on Ceramic Powders Characterization-Interim Report," DOE-ORNL to IEA participants and standards setting bodies in Japan, Germany, Sweden and U.S., January 1993.

Communications/Visits

S. G. Malghan and S. M. Hsu attended Contractors Coordination meeting in Dearborn, MI to present technical papers and participate in IEA meetings.

S. G. Malghan visited Coors Ceramic Company/Golden Technologies to discuss powders characterization activities.

Ceramic Mechanical Property Test Method Development
George D. Quinn (National Institute of Standards and Technology)

Objective/Scope

This task is to develop mechanical test method standards in support of the Ceramic Technology for Advanced Heat Engines and Advanced Turbine Technology Applications Programs. The prime DOE contractors and subcontractors will be surveyed to assess their needs and capabilities. Test method development should also consider the general USA structural ceramics community as well as foreign laboratories and companies, but emphasis will be placed on the needs on the DOE community.

Draft recommendations for practices or procedures shall be developed based upon the needs identified above and circulated within the DOE ceramics heat engine community for review and modification. Round robins will be conducted as necessary, but shall be well-focussed, limited in scope and not interfere with ongoing IEA round robins. Procedures developed in this program shall be presented as ATTAP or CTAHE "standard procedures." Alternatively, (and eventually) these will be advanced for final standardization by ASTM or by the U.S. Army as possible MIL STD's.

Technical Highlights and Results

Previous work in this project has contributed to the following completed standards:

1. ASTM C-1198-91 "Dynamic Young's Modulus, Shear Modulus, and Poisson's Ratio for Advanced Ceramics by Sonic Resonance," by S. Gonczy, G. Quinn and J. Helfinstine.
2. ASTM C-1161-90 "Standard Test Method for Flexural Strength of Advanced Ceramics at Ambient Temperature,"
3. ASTM C-1211-92 "Standard Test Method for Flexural Strength of Advanced Ceramic at Elevated Temperature," by G. Quinn in cooperation with Mr. M. Foley, Norton; Mr. T. Richerson, Allied-Signal; and Dr. M. Ferber, ORNL.
4. MIL HDBK 790 "Fractography and Characterization of Fracture Origins in Advanced Structural Ceramics," with J. Swab and M. Slavin, U. S. Army, MTL.

The draft standard: "Reporting Uniaxial Strength Data and Estimating Weibull Distribution Parameters for Advanced Ceramics," by S. Duffy, G. Quinn and C. Johnson was submitted for an ASTM Society ballot. A number of comments were received during the main C 28 main committee ballot. Editorial revisions were made to the draft standard, but a number of substantive changes will have to wait until the document is up for renewal or if a "revision to" ballot process is commenced.

Standardization of fracture toughness testing continues. Mr. Jonathan Salem of NASA-Lewis has been appointed overall leader of this activity. Prof. Isa Bar-on of Worcester Polytechnic Institute is acting as the C 28 - E 9 committee liaison. This is a contentious topic since very strong preferences and opinions have developed over the years. Much of the work in recent years has focussed on fracture toughness of composites or R-curve phenomena.

During this six month period, a comprehensive final report and a condensed summary report on a VAMAS (Versailles Advanced Materials and Standards) round-robin exercise was published. Very successful results for the IS and SEPB methods have spurred new initiatives to standardize these methods in ASTM.

Work in the present task has concentrated on refinement of the controlled surface flaw method (Fig. 1) This is one of the five candidates for an ASTM fracture toughness standard (Fig. 2). Extensive testing has indicated that a slight tilt (1/2 degree) to the indenter orientation can be extremely beneficial in causing the initial precrack to stand out clearly on a fracture surface. Superb results have been obtained on a sintered alumina, hot pressed silicon nitride, sintered silicon nitride, and sintered silicon carbide. Work in October and November 1992 resulted in a number of refinements to technique in the method.

A VAMAS round robin based on this method was set up and commenced in Nov. 1992. The round robin is a joint program by NIST and by EMPA, the Swiss Federal Research Laboratory. Twenty four laboratories in Europe and the United States are participating. In the USA the participants are St. Gobain-Norton, NASA-Lewis, Carborundum, NIST, and Alfred University. The round robin will involve three materials: Norton hot pressed silicon nitride, grade NC 132; ESK hipped silicon nitride; and EMPA (Swiss) sintered yttria partially stabilized zirconia. The latter two materials were donated by EMPA. Each participant received ten specimens of each material with detailed instructions on procedure. It is hoped that the exercise will require no more than 1-2 man weeks of effort per lab and that results will be returned to NIST by May 1993. This round robin will interface nicely with an ongoing round robin in Europe conducted under the auspices of the European Structural Integrity Society. The latter exercise includes chevron notch, single edge precracked beam, indentation strength and single edge notched beam methods on similar materials.

Work continues at NIST on developing hardness standards for advanced ceramics. An internally funded program is attempting to develop two "standard reference materials" for which the hardness is certified by NIST. Parallel to this is an intensive review of the world standards for Vickers and Knoop hardness and laboratory work on examining the techniques and errors in measurements. At the moment, there is widespread confusion and lack of consistency in hardness results and procedures. A review of the world literature shows that Knoop and Vickers hardnesses are predominant. Some groups use Rockwell C or Superficial Rockwell indentations (usually the carbide tool makers) or even the Moh's scale (scratch two materials against each other)!

The Vickers indenter is widely used in research studies and by some manufacturers. The Knoop indenter is preferred by many industrial concerns, probably due to the existence of two related ASTM standards: C-730 Knoop Microhardness of Glass, and C-849, Knoop Hardness of Ceramic Whitewares. The Knoop indentation creates a longer indent for the same load (see Fig. 3) and is much less susceptible to cracking. Preliminary observations and findings were presented at the C 28 meeting in Cocoa Beach in January 1993.

Hardness testing is in principal very simple, but in practice it is very sensitive to technique. Our original intent was to simply modify current techniques and write a simple standard for advanced ceramics. Unfortunately, it will require a little more work, but the problem should be solvable in the near term. Figure 4 shows some of the difficulties in the method. Figure 5 illustrates some of the problems in the specifications of Vickers diamond indenters. The problem with measuring the hardness of advanced ceramics is that the materials are themselves hard, and the indentations are very small. It is difficult to get a precise or accurate reading of the diagonal length with an ordinary microscope. Operator bias and technique is critical. Furthermore,

Figure 1. Schematic of the Controlled Surface Flaw (CSF) method.

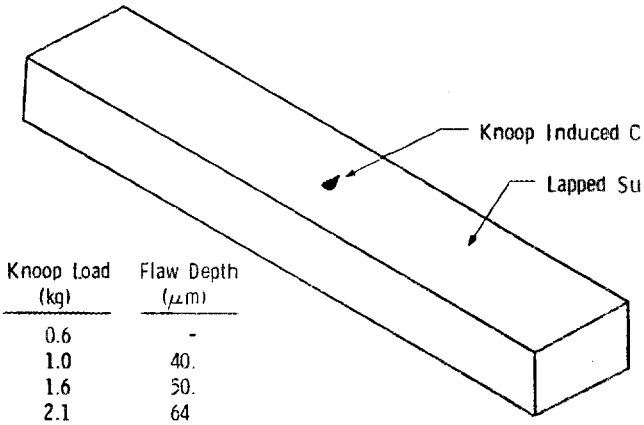

Knoop Load (kg)	Flaw Depth (μm)
0.6	-
1.0	40.
1.6	50.
2.1	64
2.6	70.
3.5	85.

FLEXURAL SAMPLE WITH KNOOP INDENTATION INDUCED FLAW

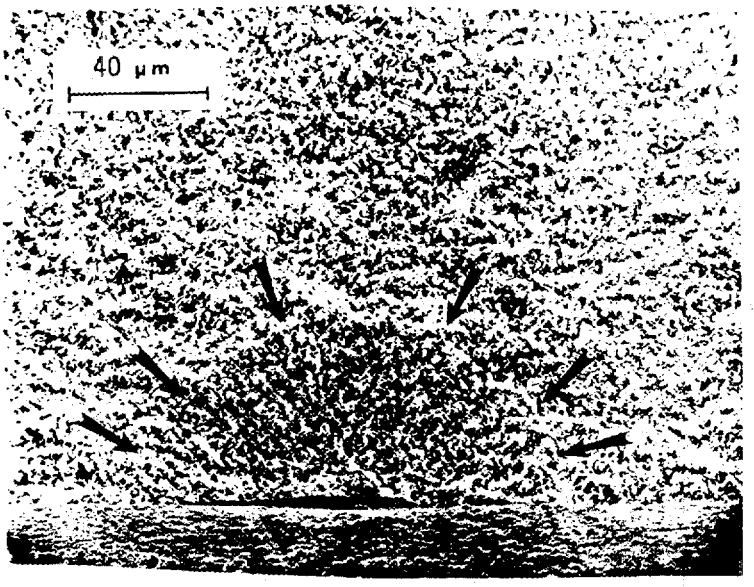

Knoop induced surface flaw

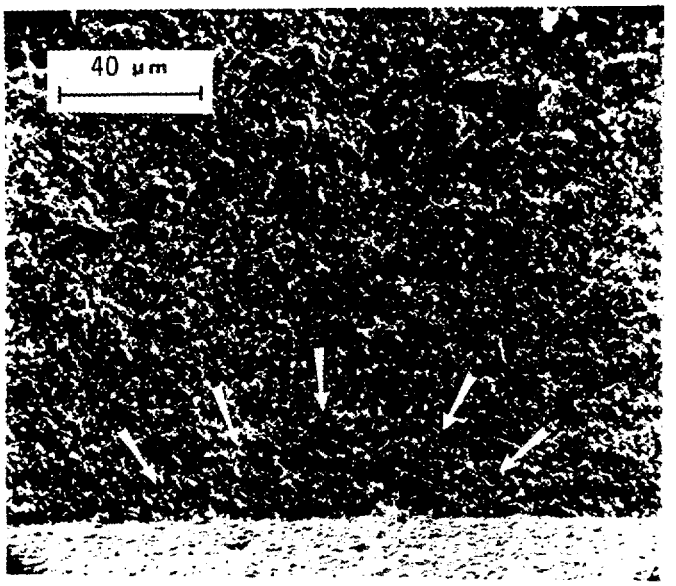

machining damage

Figure 2. The candidate test methods for an ASTM fracture toughness standard as of May 1993. The DCB or CM-DCB specimen may be prepared as a separate standard. The other four methods will be combined in one comprehensive standard.

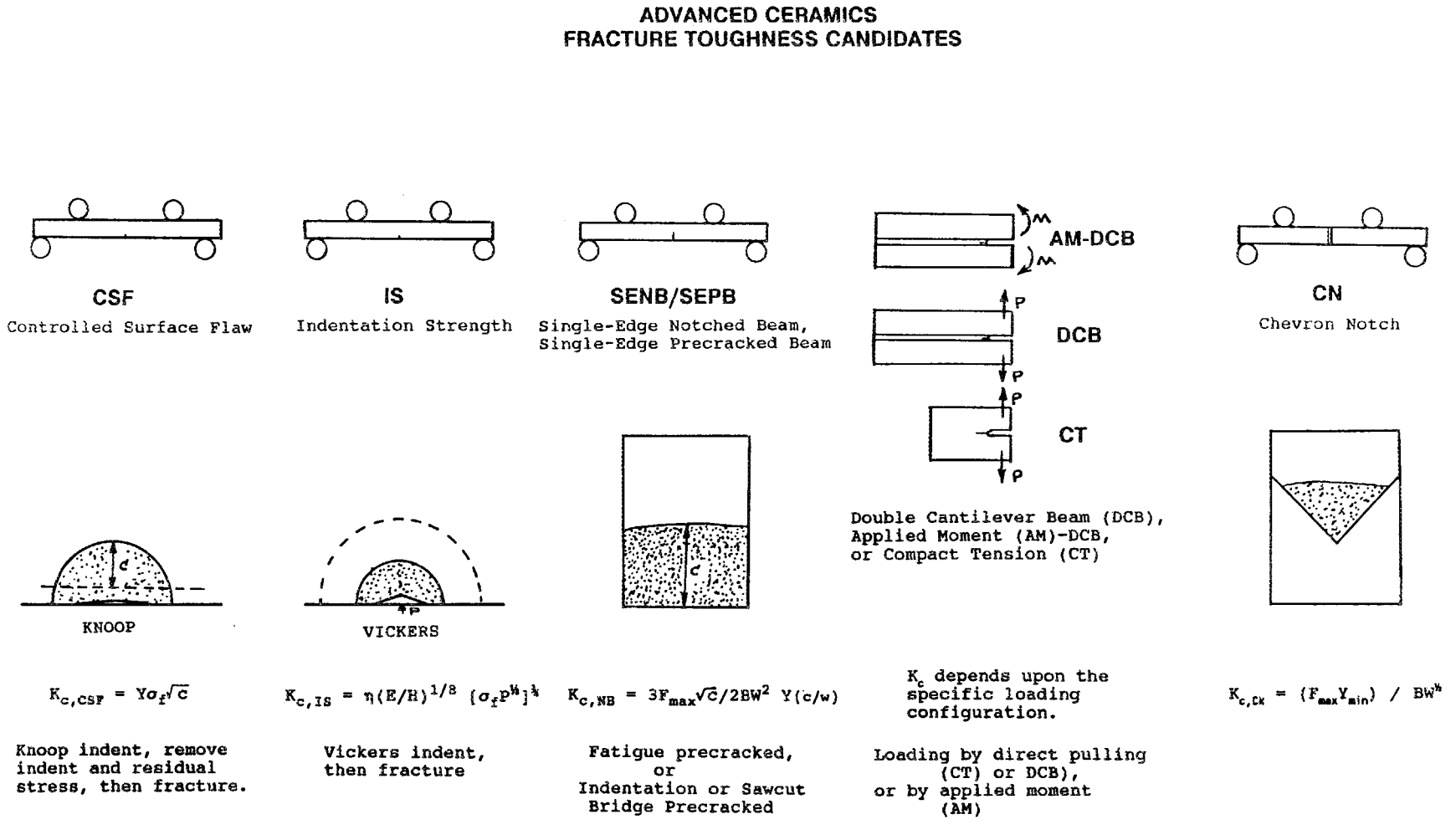

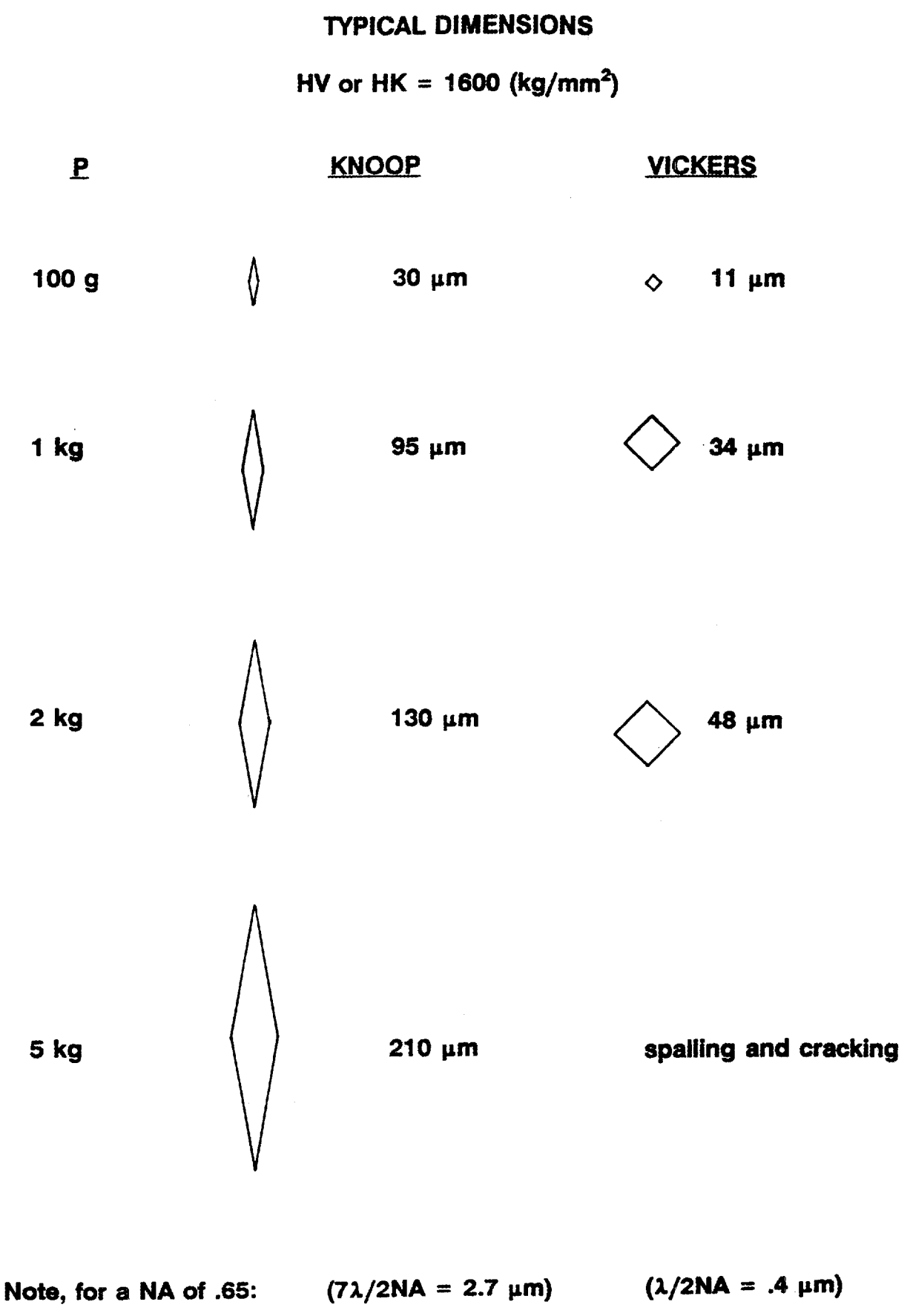

Figure 3. A comparison of the relative sizes of Knoop and Vickers indentations at the same load in a ceramic with hardness of 1600 kg/mm^2.

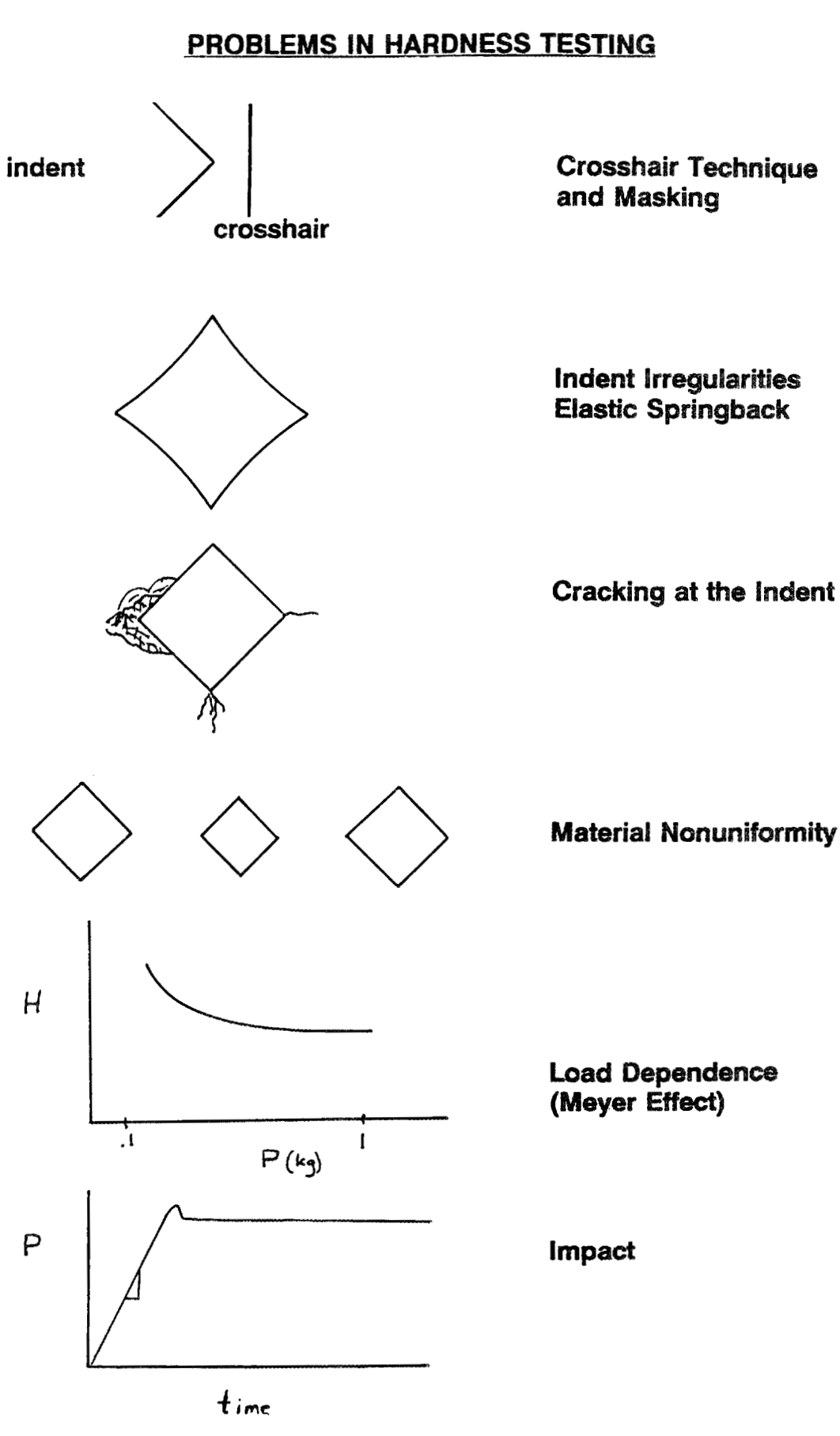

Figure 4. Problems in hardness testing.

INDENTER DETAILS

CHISEL TIP "Offset"

ASTM E 384
Knoop, 1. μm max.
Vickers, .5 μm max.

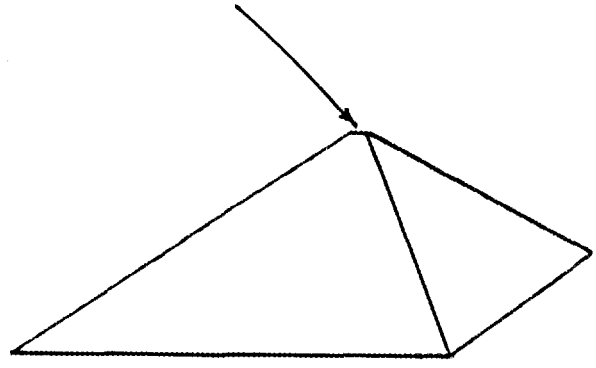

ISO 640
Vickers, 1. μm max.

DIN 51-225
Vickers, 2. μm max.!!!

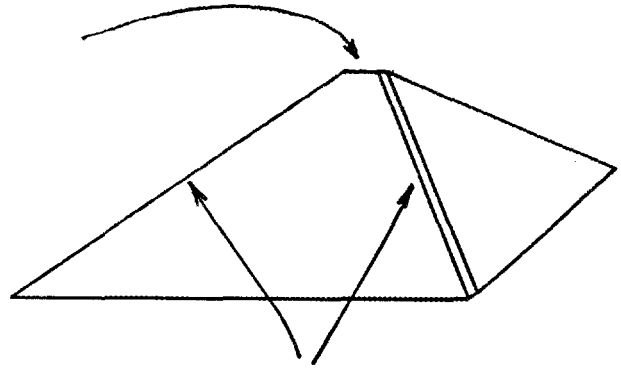

DIN 51-225 allows chamfered edges up to 1 μm wide!!!

Figure 5. Specifications of the shape of Vickers diamond indenters vary around the world. One DIN (German) standard even permits flats on the four long edges. This is bound to affect the shape of the tips in an impression.

the uncertainty in measuring the diagonal size is magnified when computing hardness since the hardness depend upon the length squared. An earlier VAMAS round robin revealed there is very wide scatter in results.

It has been decided that work will initially focus on a Knoop standard since there are already two related ASTM standards as noted above. We are carefully studying the matter of the apparent shortening of the diagonal lengths due to the limits of resolution of optical microscopes as illustrated in Figure 6. The $7\lambda/2NA$ correction factor is mandated in the two ASTM standards C 730 and C 8459, but is not used by standards in the rest of the world. The difference in hardness with or without the correction factor is about 100-150 units of most glasses! This has led to wild confusion in the literature with respect to whether the correction factor has or has not been applied. For example, older versions of the Schott Glass catalog list hardnesses both with and without the factor. The original work which suggested the correction factor was necessary was done in the 1950's, before the advent of scanning electron microscopy. We therefore are measuring indentations with several optical microscopes and with a calibrated scanning electron microscope in order to verify the effect.

During this six month period, elements of MIL HDBK 790, "Standard Practice for Characterizing Fracture Origins Limiting Defects in Advanced Structural Ceramics" were brought into the ASTM C-28 forum. This work is a collaborative undertaking with NIST and with M. Slavin and J. Swab of U. S. Army Research Laboratory (ARL). A list of flaw definitions will be introduced into the Characterization Subcommittee, C 28.05. The definition for "fracture origin" was submitted for a subcommittee C 28.91 ballot. Two negative ballots were received and a revised definitions was prepared at the January 1993 Cocoa Beach meeting of ASTM C28.

In the meantime, a fractography round robin has been organized under the auspices of the VAMAS collaboration. The framework for the exercise was developed by the US ARL in cooperation with NIST. Emphasis will be on several topics including: the detection and characterization of machining damage, the detection and characterization of material processing related flaws, and fractographic techniques and analysis. The round robin will include the examination of photos and specimens. The US (ARL) has prepared photos and specimens for distribution in May.

A chapter on Standardization of Mechanical Properties Tests for Advanced Ceramics was prepared by C. Brinkman and G. Quinn for a book on mechanical properties of ceramics being published by Marcel Dekker. A similar paper for an ASME conference May 1993 was written. An overview article on the status of ASTM committee C28 was written by G. Quinn and published in the November issue of the Ceramic Bulletin.

Status of Milestones

All milestones are on schedule.

Communications/Visits/Travel

1. G. Quinn attended the ASTM C 28 meeting in Cocoa Beach in Jan. 1993.
2. Mr. Jakob Kübler of the Swiss Federal Research Laboratory collaborated

OPTICAL RESOLUTION LIMITS

The least distance separable by a given objective is:

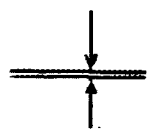

λ/(2NA)

VICKERS

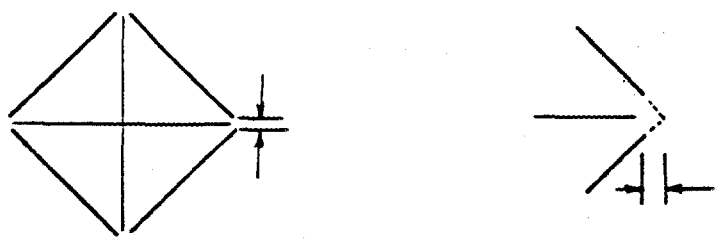

λ/(2NA) **λ/(4NA)**

both ends: λ/(2NA) = .55 μm/(2•.65) = 0.4 μm

KNOOP

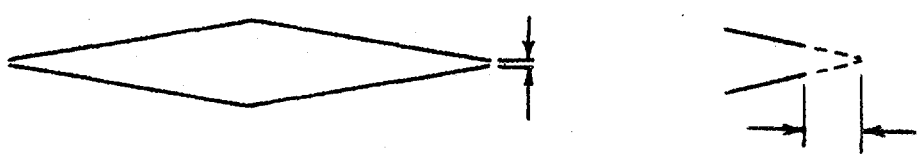

λ/(2NA) **7λ/(4NA)**

both ends: 7λ/(2NA) = 7•.55 μm/(2•.65) = 3.0 μm!

(After Mott, 1955; Brown and Ineson, 1951; and ASTM C 730 and C 849.)

Figure 6. The limits of resolution of an optical microscope can lead to an underestimate of the length of diagonals in all materials. The problem is more pronounced in the Knoop configuration. A 3 micron error in a 30 micron diagonal can occur with a normal 40X objective with a 0.65 numerical aperture. This 10% underestimate in length will lead to a 20% error in hardness! As an example, for silicon nitride this means a difference in apparent hardness of 320 out of 1600!

Figure 7. The draft Knoop standard for advanced ceramics will be a clone of standards C 730 and C 849.

COMPARATIVE INDENTATION SIZES
FOR THE THREE ASTM KNOOP STANDARDS

ASTM C-730
Knoop Hardness of Glasses
100 g

HKN 470-540

55 - 51 µm

ASTM C-849
Knoop Hardness of Ceramic Whitewares
1000 g (or less if cracking)

HKN 500-800

168 - 133 µm

C-XXXX
Knoop Hardness of Advanced Ceramics
Load Options:

HKN 1000 - 2000

2 kg **169 - 119 µm**

e.g.: S_3N_4 with HKN = 1450,

d = 140 µm

1 kg **119 - 84 µm**

e.g.: S_3N_4 with HKN = 1450,

d = 99 µm

extensively in order to help set up a fracture toughness round robin project.

3. G. Quinn collaborated with Drs. C. Brinkman and R. McClung to prepare an ASME manuscript summarizing progress on mechanical property standardization in ASTM committee C 28.

Problems encountered

None.

Publications/Presentations

1. ASTM Standard C-1211, "Standard Test Method for Flexural Strength of Advanced Ceramics at Elevated Temperature," ASTM Annual Book of Standards, Vol. 15.01, March 1992.
2. G. Quinn, "Twisting and Friction Errors in Flexure Testing," Ceramic Engineering and Science Proceedings," July/August, (1992) pp. 319-330.
3. MIL HDBK 790, "Fractography and Characterization of Fracture Origins in Advanced Structural Ceramics," 1 July, 1992. (With M. Slavin and J. Swab)
4. G. D. Quinn, "High Temperature Flexure Fixture for Advanced Ceramics," NIST Internal Report 4864, June 1992.
5. G. D. Quinn, "Room Temperature Flexure Fixture for Advanced Ceramics," NIST Internal Report 4877, August 1992.
6. G. D. Quinn, J. Salem, I. Bar-on, K. Cho, M. Foley, and H. Fang, "Fracture Toughness of Advanced Ceramics at Room Temperature," J. Res. NIST, 97, (1992) pp. 579-607.
7. G. Quinn, "Fracture Toughness of Advanced Ceramics at Room Temperature: A VAMAS Round Robin," to be publ. Ceram. Eng. and Sci. Proc. 1993.
8. G. Quinn, "ASTM Committee C-28, Advanced Ceramics: A Progress Report," Bul. Amer. Ceram., Soc., 71 [10] (1992) pp. 1508-1510.

ORNL/TM-12428

INTERNAL DISTRIBUTION

Central Research Library (2)
Document Reference Section
Laboratory Records Department (2)
Laboratory Records, ORNL RC
ORNL Patent Section
M&C Records Office (3)
L. F. Allard, Jr.
L. D. Armstrong
D. L. Balltrip
R. L. Beatty
P. F. Becher
T. M. Besmann
P. J. Blau
A. Bleier
E. E. Bloom
K. W. Boling
R. A. Bradley
C. R. Brinkman
V. R. Bullington
R. S. Carlsmith
P. T. Carlson
G. M. Caton
S. J. Chang
R. H. Cooper, Jr.
S. A. David
J. H. DeVan
J. L. Ding
M. K. Ferber
F. M. Foust
W. Fulkerson
R. L. Graves
D. L. Greene
M. H. Harris
H. W. Hayden, Jr.
E. E. Hoffman
C. R. Hubbard
M. A. Janney
D. R. Johnson (5)
F. W. Jones
D. Joslin
R. R. Judkins
M. A. Karnitz
B. L. Keyes
H. D. Kimrey, Jr.
T. G. Kollie
K. C. Liu
E. L. Long, Jr.
W. D. Manly
R. W. McClung
D. J. McGuire
J. R. Merriman
T. A. Nolan
A. E. Pasto
J. L. Rich
C. R. Richmond
J M Robbins
G. V. Rogers, Jr.
M. L. Santella
A. C. Schaffhauser
S. Scott
E. J. Soderstrom
D. P. Stinton
R. W. Swindeman
V. J. Tennery
T. N. Tiegs
J. R. Weir, Jr.
B. H. West
S. G. Winslow
J. M. Wyrick
C. S. Yust

Pioneering Research Info. Ctr.
E.I. Dupont de Nemours & Co. Inc.
Experimental Station
P.O. Box 80302
Wilmington DE 19880-0302

James H. Adair
University of Florida
Materials Science & Engineering
317 MAE Bldg.
Gainesville FL 32611-2066

Donald F. Adams
University of Wyoming
Mechanical Engineering Department
P.O. Box 3295
Laramie WY 82071

Jalees Ahmad
AdTech Systems Research Inc.
Solid Mechanics
1342 N. Fairfield Road
Dayton OH 45432-2698

Yoshio Akimune
NISSAN Motor Co., Ltd.
Materials Research Laboratory
1 Natsushima-Cho
Yokosuka 237
JAPAN

Mufit Akinc
Iowa State University
322 Spedding Hall
Ames IA 50011

Ilhan A. Aksay
Princeton University
A313 Engineering Quadrangle
Princeton NJ 08544-5263

R. G. Alexander
BASE
26 Malvern Close
Kettering Northants NN16 AJP
UNITED KINGDOM

Richard L. Allor
Ford Motor Company
Materials Systems Reliability
P.O. Box 2053, Room S-2031
Dearborn MI 48121-2053

Joseph E. Amaral
Instron Corporation
Corporate Engineering Office
100 Royale Street
Canton MA 02021

Edward M. Anderson
Aluminum Company of America
N. American Industrial Chemical
P.O. Box 300
Bauxite AR 72011

Norman C. Anderson
Ceradyne, Inc.
Ceramic-to-Metal Division
3169 Redhill Avenue
Costa Mesa CA 92626

Don Anson
BCL
Thermal Power Systems
505 King Avenue
Columbus OH 43201-2693

Thomas Arbanas
G.B.C. Materials Corporation
580 Monastery Drive
Latrobe PA 15650-2698

Frank Armatis
3M Company
Building 60-1N-01
St. Paul MN 55144-1000

Everett B. Arnold
Detroit Diesel Corporation
Mechanical Systems Technology
13400 Outer Drive West
Detroit MI 48239-4001

Bertil Aronsson
Sandvik AB
S-12680
Stockholm Lerkrogsvagen 19
SWEDEN

Dennis Assanis
University of Illinois
Dept. of Mechanical Engineering
1206 W. Green Street
Urbana IL 61801

V. S. Avva
North Carolina A&T State Univ.
Dept. of Mechanical Engineering
Greensboro NC 27411

Patrick Badgley
Adiabatics, Inc.
3385 Commerce Drive
Columbus IN 47201

Sunggi Baik
Pohang Institute of Sci. & Tech.
P.O. Box 125
Pohang 790-600
KOREA

John M. Bailey
Consultant
Caterpillar, Inc.
P.O. Box 1875
Peoria IL 61656-1875

Bob Baker
Ceradyne, Inc.
3169 Redhill Avenue
Costa Mesa CA 92626

Frank Baker
Aluminum Company of America
Alcoa Technical Center
Alcoa Center PA 15069

J. G. Baldoni
GTE Laboratories, Inc.
40 Sylvan Road
Waltham MA 02254

Clifford P. Ballard
AlliedSignal Aerospace Company
Ceramics Program
P.O. Box 1021
Morristown NJ 07962-1021

B. P. Bandyopadhyay
University of North Dakota
Mechanical Engineering Department
Grand Forks ND 58202-8359

P. M. Barnard
Ruston Gas Turbines Limited
P.O. Box 1
Lincoln LN2 5DJ
ENGLAND

Harold N. Barr
Hittman Corporation
9190 Red Branch Road
Columbia MD 21045

Renald D. Bartoe
Vesuvius McDanel
510 Ninth Avenue
Box 560
Beaver Falls PA 15010-0560

David L. Baty
Babcock & Wilcox - LRC
P.O. Box 11165
Lynchburg VA 24506-1165

Donald F. Baxter, Jr.
ASM International
Advanced Materials & Processes
Materials Park OH 44073-0002

M. Brad Beardsley
Caterpillar Inc.
Technical Center Bldg. E
P.O. Box 1875
Peoria IL 61656-1875

John C. Bell
Shell Research Limited
Thornton Research Centre
P.O. Box 1
Chester CH1 3SH
ENGLAND

M. Bentele
Xamag, Inc.
259 Melville Avenue
Fairfield CT 06430

Larry D. Bentsen
BFGoodrich Company
R&D Center
9921 Brecksville Road
Brecksville OH 44141

Joseph C. Bentz
ENCERATEC
2525 Sandcrest Drive
Columbus IN 47203

Louis Beregszazi
Defiance Precision Products
P.O. Drawer 428
Defiance OH 43512

Tom Bernecki
Northwestern University
1801 Maple Avenue
Evanston IL 60201-3135

Charles F. Bersch
Institute for Defense Analyses
1801 N. Beauregard Street
Alexandria VA 22311

Ram Bhatt
NASA Lewis Research Center
21000 Brookpark Road
Cleveland OH 44135

Deane I. Biehler
Caterpillar Inc.
Engineering Research Materials
P.O. Box 1875, Bldg. E
Peoria IL 61656-1875

John W. Bjerklie
Consolidated Natural Gas Service Co. Inc.
Research Department
Pittsburgh PA 15222-3199

William D. Bjorndahl
TRW, Inc.
One Space Park, MS:R6-2188
Building 01, Room 2040
Redondo Beach CA 90278

Keith A. Blakely
Advanced Refractory Technologies, Inc.
699 Hertel Avenue
Buffalo NY 14207

Edward G. Blanchard
Netzsch Inc.
119 Pickering Way
Exton PA 19341

Bruce Boardman
Deere and Company Technical Ctr.
3300 River Drive
Moline IL 61265

Russell Bockstedt
Hoechst Celanese Corporation
150 JFK Parkway
Short Hills NJ 07078

M. Boehmer
DLR German Aerospace Research Estab.
Postfach 90 60 58
D-5000 Koln 90
GERMANY

Lawrence P. Boesch
EER Systems Corp.
1593 Spring Hill Road
Vienna VA 22182-2239

Donald H. Boone
Boone & Associates
2412 Cascade Drive
Walnut Creek CA 94598-4313

Tom Booth
AlliedSignal, Inc.
AiResearch Los Angeles Division
2525 West 190th Street
Torrance CA 90509-2960

Tibor Bornemisza
Sundstrand Power Systems
4400 Ruffin Road
San Diego CA 92186-5757

J.A.M. Boulet
University of Tennessee
Engineering Science and Mechanics
Knoxville TN 37996-2030

H. Kent Bowen
Massachusetts Institute of Technology
77 Massachusetts Ave., Rm E40-434
Cambridge MA 02139

Leslie J. Bowen
Materials Systems
53 Hillcrest Road
Concord MA 01742

Steven C. Boyce
Air Force Office of Scientific Research
AFOSR/NA Bldg. 410
Bolling AFB DC 20332-6448

Gary L. Boyd
Ceramic Engineering Consulting
328 Sneath Way
Alpine CA 91901

Steve Bradley
UOP Research Center
50 E. Algonquin Road
Des Plaines IL 60017-6187

Michael C. Brands
Cummins Engine Company, Inc.
P.O. Box 3005, Mail Code 50179
Columbus IN 47201

Raymond J. Bratton
Westinghouse Science & Technology
1310 Beulah Road
Pittsburgh PA 15235

John J. Brennan
United Technologies Corporation
Silver Lane, MS:24
East Hartford CT 06108

Jeff D. Bright
Ceramatec, Inc.
2425 South 900 West
Salt Lake City UT 84108

Terrence K. Brog
Golden Technologies Company
4545 McIntyre Street
Golden CO 80403

Gunnar Broman
317 Fairlane Drive
Spartanburg SC 29302

Al Brown
High-Tech Materials Alert
P.O. Box 882
Dayton NJ 08810

Jesse J. Brown
VPI & SU
Ctr. for Advanced Ceram Materials
Blacksburg VA 24061-0256

Sherman D. Brown
University of Illinois
Materials Science and Engineering
105 South Goodwin Avenue
Urbana IL 61801

S. L. Bruner
Ceramatec, Inc.
2425 South 900 West
Salt Lake City UT 84119

Walter Bryzik
U.S. Army Tank Automotive Command
R&D Center, Propulsion Systems
Warren MI 48397-5000

S. J. Burden
2572 Devonwood
Troy MI 48098

Curt V. Burkland
AMERCOM, Inc.
8928 Fullbright Avenue
Chatsworth CA 91311

Bill Bustamante
AMERCOM, Inc.
8928 Fullbright Avenue
Chatsworth CA 91311

Oral Buyukozturk
Massachusetts Institute of Technology
77 Massachusetts Ave., Room 1-280
Cambridge MA 02139

David A. Caillet
Ethyl Corporation
451 Florida Street
Baton Rouge La 70801

Frederick J. Calnan
Heany Industries, Inc.
249 Briarwood Lane
Scottsville NY 14546

Roger Cannon
Rutgers University
P.O. Box 909
Piscataway NJ 08855-0909

Scott Cannon
P.O. Box 567254
Atlanta GA 30356

Harry W. Carpenter
1844 Fuerte Street
Fallbrook CA 92028

David Carruthers
Kyocera Industrial Ceramics Company
P.O. Box 2279
Vancouver WA 98668-2279

Calvin H. Carter, Jr.
Cree Research, Inc.
2810 Meridian Parkway
Durham NC 27713

J. David Casey
35 Atlantis Street
West Roxbury MA 02132

Jere G. Castor
J. C. Enterprise
5078 N. 83rd Street
Scottsdale AZ 85250

James D. Cawley
Case Western Reserve University
Materials Science & Engineering
Cleveland OH 44106

Thomas C. Chadwick
Den-Mat Corporation
P.O. Box 1729
Santa Maria CA 93456

Ronald H. Chand
Chand Kare Technical Ceramics
2 Coppage Drive
Worcester MA 01603

Robert E. Chaney
EG&G Idaho, Inc.
Idaho National Engineering Lab
P.O. Box 1625
Idaho Falls ID 83415-3525

Frank C. Chang
U.S. Army Materials Technology
AMTL-EMM
405 Arsenal Street
Watertown MA 02172

Robert M. Chapman
AlliedSignal Aerospace Company
1001 Pennsylvania Avenue, N.W.
Suite 700 South
Washington DC 20004

William Chapman
Williams International Corp.
2280 W. Maple Road
Walled Lake MI 48390-0200

Charlie Chen
LECO Corporation
P.O. Box 211688
Augusta GA 30917

Frank Childs
EG&G Idaho, Inc.
Idaho National Engineering Lab
P.O. Box 1625
Idaho Falls ID 83415-3527

William J. Chmura
Torrington Company
59 Field Street
Torrington CT 06790-4942

Tsu-Wei Chou
University of Delaware
201 Spencer Laboratory
Newark DE 19716

R. J. Christopher
Ricardo Consulting Engineers
Bridge Works
Shoreham-By-Sea W. Sussex BN435FG
ENGLAND

Joel P. Clark
Massachusetts Institute of
Technology
Room 8-409
Cambridge MA 02139

Giorgio Clarotti
Commission of the European Comm
DGXII-C3, MO75, 1-53;
200 Rue de la Loi
B-1049 Brussels
BELGIUM

W. J. Clegg
ICI Advanced Materials
P.O. Box 11, The Heath
Runcorn Cheshire WA7 4QE
ENGLAND

Joseph Cleveland
GTE Products Corporation
Hawes Street
Towanda PA 18848-0504

Gloria M. Collins
ASTM
1916 Race Street
Philadelphia PA 19103

William C. Connors
Sundstrand Aviation Operations
Materials Science & Engineering
4747 Harrison Avenue
Rockford IL 61125-7002

John A. Coppola
Carborundum Company
Niagara Falls R&D Center
P.O. Box 832
Niagara Falls NY 14302

Normand D. Corbin
Norton Company
Advanced Ceramics
Goddard Road
Northboro MA 01532-1545

Douglas Corey
AlliedSignal, Inc.
2525 West 190th Street, MS:T52
Torrance CA 90504-6099

Keith P. Costello
Chand/Kare Technical Ceramics
2 Coppage Drive
Worcester MA 01603-1252

Ed L. Courtright
Pacific Northwest Laboratory
MS:K3-59
Richland WA 99352

Anna Cox
Mitchell Market Reports
P.O. Box 23
Monmouth Gwent NP5 4YG
UNITED KINGDOM

J. Wesley Cox
BIRL
1801 Maple Avenue
Evanston IL 60201-3135

Art Cozens
Instron Corporation
3414 Snowden Avenue
Long Beach CA 90808

Mark Crawford
New Technology Week
4604 Monterey Drive
Annandale VA 22003

Richard A. Cree
Markets & Products, Inc.
P.O. Box 14328
Columbus OH 43214-0328

Les Crittenden
Vesuvius McDanel
Box 560
Beaver Falls PA 15010

William J. Croft
U.S. Army Materials Technology
405 Arsenal Street
Watertown MA 02172

M. J. Cronin
Mechanical Technology, Inc.
968 Albany-Shaker Road
Latham NY 12110

Gary M. Crosbie
Ford Motor Company
1430 Culver Avenue
S-2079, SRL Building
Dearborn MI 48121-4036

Floyd W. Crouse, Jr.
U.S. Department of Energy
Morgantown Energy Technology Ctr
P.O. Box 880
Morgantown WV 26505

John Cuccio
AlliedSignal, Inc.
Auxiliary Power
P.O. Box 52180, MS:1302-2Q
Phoenix AZ 85072-2180

Raymond A. Cutler
Ceramatec, Inc.
2425 South 900 West
Salt Lake City UT 84119

Stephen C. Danforth
Rutgers University
P.O. Box 909
Piscataway NJ 08855-0909

Sankar Das Gupta
Electrofuel Manufacturing Co.
9 Hanna Avenue
Toronto Ontario MGK-1W8
CANADA

Frank Davis
AlliedSignal Aerospace Company
7550 Lucerne Drive, #203
Middleburg Heights OH 44130

Robert F. Davis
North Carolina State University
Materials Engineering Department
P.O. Box 7907
Raleigh NC 27695

Thomas DeAngelis
Carborundum Company
Niagara Falls R&D Center
P.O. Box 832
Niagara Falls NY 14302

George DeBell
Ford Motor Company
Material Systems Reliability
P.O. Box 2053, Room S-2023
Dearborn, MI 48121-2053

Michael DeLuca
RSA Research Group
1534 Claas Ave.
Holbrook NY 11741

Gerald L. DePoorter
Colorado School of Mines
Metallurgical & Materials Engr
Golden CO 80401

J. F. DeRidder
Omni Electro Motive, Inc.
12 Seely Hill Road
Newfield NY 14867

Nick C. Dellow
Materials Technology Publications
40 Sotheron Road
Watford Herts WD1 2QA
UNITED KINGDOM

L. R. Dharani
University of Missouri-Rolla
224 M.E.
Rolla MO 65401

Douglas A. Dickerson
Union Carbide Specialty Powders
1555 Main Street
Indianapolis IN 46224

John Dodsworth
Vesuvius Research & Development
Technical Ceramics Group
Box 560
Beaver Falls PA 15010

B. Dogan
Institut fur Werkstofforschung
GKSS-Forschungszentrum Geesthacht
Max-Planck-Strasse
D-2054 Geesthacht
GERMANY

Jean-Marie Drapier
FN Moteurs S.A.
Material and Processing
B-4041 Milmort (Herstal)
BELGIUM

Kenneth C. Dreitlein
United Technologies Research Ctr
Silver Lane
East Hartford CT 06108

Robin A.L. Drew
McGill University
3450 University Street
Montreal Quebec H3A 2A7
CANADA

Winston H. Duckworth
BCL
Columbus Division
505 King Avenue
Columbus OH 43201-2693

Bill Durako
Sundstrand Aviation Operations
P.O. Box 7002
Rockford IL 61125-7002

Ernest J. Duwell
3M Abrasive Systems Division
3M Center
St. Paul MN 55144-1000

Chuck J. Dziedzic
Coors Ceramics Company
17750 West 32nd Avenue
Golden CO 80401

Robert J. Eagan
Sandia National Laboratories
Engineered Materials & Processes
P.O. Box 5800
Albuquerque NM 87185-5800

Jeffrey Eagleson
Lanxide Corporation
1001 Connecticut Avenue, N.W.
Washington DC 20036

Harry E. Eaton
United Technologies Corporation
Silver Lane
East Hartford CT 06108

Harvill C. Eaton
Louisiana State University
240 Thomas Boyd Hall
Baton Rouge LA 70803

Christopher A. Ebel
Carborundum Company
Technology Division
P.O. Box 337
Niagara Falls NY 14302

J. J. Eberhardt
U.S. Department of Energy
Office of Transportation Matrl's
CE-34, Forrestal Building
Washington DC 20585

Jim Edler
Eaton Corporation
26201 Northwestern Highway
P.O. Box 766
Southfield MI 48037

G. A. Eisman
Dow Chemical Company
Ceramics and Advanced Materials
52 Building
Midland MI 48667

William A. Ellingson
Argonne National Laboratory
Materials Science & Technology
9700 S. Cass Avenue
Argonne IL 60439

William S. Ellis
Machined Ceramics
629 N. Graham Street
Bowling Green KY 42101

Glen B. Engle
Nuclear & Aerospace Materials
16716 Martincoit Road
Poway CA 92064

Jeff Epstein
Ceramic Technologies, Inc.
12739 Ashford Knoll
Houston TX 77082

Kenneth A. Epstein
Dow Chemical USA
800 Building
Midland MI 48667

Art Erdemir
Argonne National Laboratory
9700 S. Cass Avenue
Argonne IL 60439

E. M. Erwin
Lubrizol Corporation
1819 East 225th Street
Euclid OH 44117

John N. Eustis
U.S. Department of Energy
Industrial Energy Efficiency Div
CE-221, Forrestal Building
Washington DC 20585

W. L. Everitt
Kyocera International, Inc.
8611 Balboa Avenue
San Diego CA 92123

Gordon Q. Evison
332 S. Michigan Avenue
Suite 1730
Chicago IL 60604

John W. Fairbanks
U.S. Department of Energy
Office of Propulsion Systems
CE-322, Forrestal Building
Washington DC 20585

Tim Fawcett
Dow Chemical Company
Advanced Ceramics Laboratory
1776 Building
Midland MI 48674

Robert W. Fawley
Sundstrand Power Systems
Div. of Sundstrand Corporation
P.O. Box 85757
San Diego CA 92186-5757

John J. Fedorchak
GTE Products Corporation
Hawes Street
Towanda PA 18848-0504

Jeff T. Fenton
Vista Chemical Company
900 Threadneedle
Houston TX 77079

Larry Ferrell
Babcock & Wilcox
Old Forest Road
Lynchburg VA 24505

Raymond R. Fessler
BIRL
1801 Maple Avenue
Evanston IL 60201

Ross F. Firestone
Ross Firestone Company
188 Mary Street
Winnetka IL 60093-1520

Sharon L. Fletcher
Arthur D. Little, Inc.
15 Acorn Park
Cambridge MA 02140-2390

Thomas F. Foltz
Textron Specialty Materials
2 Industrial Avenue
Lowell MA 01851

Renee G. Ford
Materials and Processing Report
P.O. Box 72
Harrison NY 10528

John Formica
Supermaterials
2020 Lakeside Avenue
Cleveland OH 44114

Edwin Frame
Southwest Research Institute
P.O. Drawer 28510
San Antonio TX 78284

Armanet Francois
French Scientific Mission
4101 Reservoir Road, N.W.
Washington DC 20007-2176

R. G. Frank
Technology Assessment Group
10793 Bentley Pass Lane
Loveland OH 45140

David J. Franus
Forecast International
22 Commerce Road
Newtown CT 06470

Marc R. Freedman
NASA Lewis Research Center
21000 Brookpark Road, MS:49-3
Cleveland OH 44135

Douglas Freitag
LTV Missiles Division
P.O. Box 650003, MS:WT-21
Dallas TX 75265

Brian R.T. Frost
Argonne National Laboratory
9700 S. Cass Avenue, Bldg. 900
Argonne IL 60439

Lawrence R. Frost
Instron Corporation
100 Royall Street
Canton MA 02021

George A. Fryburg
Norton/TRW Ceramics
7A-4 Raymond Avenue
Salem NH 03079

Xiren Fu
Shanghai Institute of Ceramics
1295 Ding-xi Road
Shanghai 200050
CHINA

John Gahimer
P.O. Box 1302
Dublin OH 43017

J. P. Gallagher
University of Dayton Research Institute
300 College Park, JPC-250
Dayton OH 45469-0120

Garry Garvey
Golden Technologies Company Inc.
4545 McIntyre Street
Golden CO 80403

Joy A. Garwood
Norton Company
Advanced Ceramics
Goddard Road
Northboro MA 01532-1545

Richard Gates
NIST
Materials Bldg., A-256
Gaithersburg MD 20899

H. Maury Gatewood
Reynolds Metals Company
P.O. Box 27003
Richmond VA 23261

L. J. Gauckler
ETH-Zurich
Sonneggstrasse 5
CH-8092 Zurich 8092
SWITZERLAND

George E. Gazza
U.S. Army Materials Technology
Ceramics Research Division
405 Arsenal Street
Watertown MA 02172-0001

D. Gerster
CEA-DCOM
33 Rue De La Federation
Paris 75015
FRANCE

John Ghinazzi
Coors Technical Ceramics Company
1100 Commerce Park Drive
Oak Ridge TN 37830

Robert Giddings
General Electric Company
P.O. Box 8
Schenectady NY 12301

A. M. Glaeser
University of California
Lawrence Berkeley Laboratory
Hearst Mining Building
Berkeley CA 94720

Joseph W. Glatz
Naval Air Propulsion Center
Systems Engineering Division
P.O. Box 7176, PE24
Trenton NJ 08628

W. M. Goldberger
Superior Graphite Company
R&D
2175 E. Broad Street
Columbus OH 43209

Allan E. Goldman
U.S. Graphite, Inc.
907 W. Outer Drive
Oak Ridge TN 37830

Stephen T. Gonczy
Allied Signal Research
P.O. Box 5016
Des Plaines IL 60017

Jeffrey M. Gonzales
GTE Products Corporation
Hawes Street
Towanda PA 18848-0504

Robert J. Gottschall
U.S. Department of Energy
ER-131, MS:G-236
Washington DC 20545

Earl Graham
Cleveland State University
Dept. of Chemical Engineering
Euclid Avenue at East 24th Street
Cleveland OH 44115

John W. Graham
Astro Met, Inc.
9974 Springfield Pike
Cincinnati OH 45215

Robert E. Green, Jr.
Johns Hopkins University
Materials Science and Engineering
Baltimore MD 21218

Lance Groseclose
General Motors Corporation
Allison Gas Turbine Division
P.O. Box 420, MS:W-5
Indianapolis IN 46206

Thomas J. Gross
U.S. Department of Energy
Transportation Technologies
CE-30, Forrestal Building
Washington DC 20585

Mark F. Gruninger
Union Carbide Corporation
Specialty Powder Business
1555 Main Street
Indianapolis IN 46224

Ernst Gugel
Cremer Forschungsinstitut
GmbH&Co.KG
Oeslauer Strasse 35
D-8633 Roedental 8633
GERMANY

Donald L. Guile
Corning Glass Works
SP-DV-1-9
Corning NY 14831

John P. Gyekenyesi
NASA Lewis Research Center
21000 Brookpark Road, MS:6-1
Cleveland OH 44135

Nabil S. Hakim
Detroit Diesel Corporation
13400 Outer Drive West
Detroit MI 48239

Philip J. Haley
General Motors Corporation
P.O. Box 420, MS:T12A
Indianapolis IN 46236

Judith Hall
Fiber Materials, Inc.
Biddeford Industrial Park
5 Morin Street
Biddeford ME 04005

Y. Hamano
Kyocera Industrial Ceramics Corp.
5713 E. Fourth Plain Blvd.
Vancouver WA 98661-6857

Y. Harada
IIT Research Institute
10 West 35th Street
Chicago IL 60616

R. A. Harmon
25 Schalren Drive
Latham NY 12110

Norman H. Harris
Hughes Aircraft Company
P.O. Box 800520
Saugus CA 91380-0520

Alan M. Hart
Dow Chemical Company
1776 Building
Midland MI 48674

Pat E. Hart
Battelle Pacific Northwest Labs
Ceramics and Polymers Development
P.O. Box 999
Richland WA 99352

Stephen D. Hartline
Norton Company
Advanced Ceramics
Goddard Road
Northboro MA 01532-1545

Michael H. Haselkorn
Caterpillar In.
Technical Center, Building E
P.O. Box 1875
Peoria IL 61656-1875

N. B. Havewala
Corning Inc.
SP-PR-11
Corning NY 14831

John Haygarth
Teledyne WAA Chang Albany
P.O. Box 460
Albany OR 97321

Norman L. Hecht
U. of Dayton Research Institute
300 College Park
Dayton OH 45469-0172

Peter W. Heitman
General Motors Corporation
P.O. Box 420, MS:W-5
Indianapolis IN 46206-0420

Robert W. Hendricks
VPI & SU
210 Holden Hall
Blacksburg VA 24061-0237

Wynne Henley
Hertel Cutting Technologies Inc.
1000 Clearview Court
Oak Ridge TN 37830

Thomas L. Henson
GTE Products Corporation
Chemical & Metallurgical Division
Hawes Street
Towanda PA 18848

Thomas P. Herbell
NASA Lewis Research Center
21000 Brookpark Road, MS:49-3
Cleveland OH 44135

Marlene Heroux
Rolls-Royce, Inc.
2849 Paces Ferry Road, Suite 450
Atlanta GA 30339-3769

Robert L. Hershey
Science Management Corporation
1255 New Hampshire Ave., N.W.
Suite 1033
Washington DC 20036

Hendrik Heystek
Bureau of Mines
Tuscaloosa Research Center
P.O. Box L
University AL 35486

Robert V. Hillery
GE Aircraft Engines
One Neumann Way, M.D. H85
Cincinnati OH 45215

Arthur Hindman
Instron Corporation
100 Royall Street
Canton MA 02021

Hans Erich Hintermann
CSEM
Rue Breguet 2
Neuchatel 2000
SWITZERLAND

Shinichi Hirano
Mazda R&D of North America, Inc.
1203 Woodridge Avenue
Ann Arbor MI 48105

Tommy Hiraoka
NGK Locke, Inc.
1000 Town Center
Southfield MI 48075

John M. Hobday
U.S. Department of Energy
Morgantown Energy Technology Ctr
P.O. Box 880
Morgantown WV 26507

Clarence Hoenig
Lawrence Livermore National Lab
P.O. Box 808, Mail Code L-369
Livermore CA 94550

Thomas Hollstein
Fraunhofer-Institut fur
Werkstoffmechanik
Wohlerstrabe 11
D-7800 Freiburg
GERMANY

Richard Holt
National Research Council Canada
Structures and Materials Lab
Ottawa Ontario K1A OR6
CANADA

Michael Horgan
Materials Engineering Magazine
1100 Superior Avenue
Cleveland OH 44114

Woodie Howe
Coors Technical Ceramics Company
1100 Commerce Park Drive
Oak Ridge TN 37830

Stephen M. Hsu
NIST
Gaithersburg MD 20899

Hann S. Huang
Argonne National Laboratory
9700 S. Cass Avenue
Argonne IL 60439-4815

Gene Huber
Precision Ferrites & Ceramics
5576 Corporate Drive
Cypress CA 90630

Harold A. Huckins
Princeton Advanced Technology
4 Bertram Place
Hilton Head SC 29928

Fred R. Huettic
Advanced Magnetics Inc.
45 Corey Lane
Mendham NJ 07945

Brian K. Humphrey
Lubrizol Petroleum Chemicals Co.
3000 Town Center, Suite 1340
Southfield MI 48075-1201

Robert M. Humrick
Dylon Ceramic Technologies
3100 Edgehill Road
Cleveland Heights OH 44118

Lorretta Inglehart
National Science Foundation
Division of Materials Research
1800 "G" Street, N.W., Room 408
Washington DC 20550

Michael S. Inoue
Kyocera International, Inc.
8611 Balboa Avenue
San Diego CA 92123-1580

Osama Jadaan
U. of Wisconsin-Platteville
1 University Plaza
Platteville WI 53818

Said Jahanmir
NIST
Materials Science & Engineering
Gaithersburg MD 20899

Curtis A. Johnson
General Electric Company
P.O. Box 8
Schenectady NY 12301

Sylvia Johnson
SRI International
333 Ravenswood Avenue
Menlo Park CA 94025

Thomas A. Johnson
Lanxide Corporation
P.O. Box 6077
Newark DE 19714-6077

W. S. Johnson
Indiana University
One City Centre, Suite 200
Bloomington IN 47405

Walter F. Jones
Air Force Office of Scientific Research
Bolling Air Force Base
Washington DC 20332-6448

Jill E. Jonkouski
U.S. Department of Energy
9800 S. Cass Avenue
Argonne IL 60439-4899

L. A. Joo
Great Lakes Research Corporation
P.O. Box 1031
Elizabethton TN 37643

A. David Joseph
SPX Corporation
700 Terrace Point
Muskegon MI 49443

Adam Jostsons
Australian Nuclear Science & Technology
New Illawarra Road
Lucas Heightss New South Wales
AUSTRALIA

Matthew K. Juneau
Ethyl Corporation
451 Florida Street
Baton Rouge LA 70801

Hartmut Kainer
Didier-Werke AG
Anlagentechnik Wiesbaden
D-62 Wiesbaden
GERMANY

Tom Kalamasz
Norton/TRW Ceramics
7A-4 Raymond Avenue
Salem NH 03079

Lyle R. Kallenbach
Phillips Petroleum
Mail Drop:123AL
Bartlesville OK 74004

Nick Kamiya
Kyocera Industrial Ceramics Corp.
25 Northwest Point Blvd., #450
Elk Grove Village IL 60007

Roy Kamo
Adiabatics, Inc.
3385 Commerce Park Drive
Columbus IN 47201

Chih-Chun Kao
Industrial Technology Research Institute
195 Chung-Hsing Road, Sec. 4
Chutung Hsinchu 31015 R.O.C.
TAIWAN

Keith R. Karasek
AlliedSignal Aerospace Company
50 E. Algonquin Road
Des Plaines IL 60017-5016

Martha R. Kass
U.S. Department of Energy
Oak Ridge Operations
Building 4500N, MS:6269
Oak Ridge TN 37831-6269

Robert E. Kassel
Ceradyne, Inc.
3169 Redhill Avenue
Costa Mesa CA 92626

Allan Katz
Wright Laboratory
Metals and Ceramics Division
Wright-Patterson AFB OH 45433

R. Nathan Katz
Worcester Polytechnic Institute
100 Institute Road
Worcester MA 01609

Tony Kaushal
Detroit Diesel Corporation
13400 Outer Drive, West
Detroit MI 48239-4001

Ted Kawaguchi
Tokai Carbon America, Inc.
375 Park Avenue, Suite 3802
New York NY 10152

Noritsugu Kawashima
TOSHIBA Corporation
4-1 Ukishima-Cho
Kawasaki-Ku Kawasaki 210
JAPAN

Lisa Kempfer
Penton Publishing
1100 Superior Avenue
Cleveland OH 44114-2543

Frederick L. Kennard, III
General Motors Corporation
AC Rochester, Dept. 32-24, EB
1300 N. Dort Highway
Flint MI 48556

David O. Kennedy
Lester B. Knight Cast Metals Inc.
549 W. Randolph Street
Chicago IL 60661

George Keros
Photon Physics
3175 Penobscot Building
Detroit MI 48226

Pramod K. Khandelwal
General Motors Corporation
Allison Gas Turbine Division
P.O. Box 420, MS:W05
Indianapolis IN 46206

Jim R. Kidwell
AlliedSignal, Inc.
Auxiliary Power
P.O. Box 52180
Phoenix AZ 85072-2180

Shin Kim
Korea Institute of Machinery & Metals
66 Sangnam-dong, Changwon
Kyungnam 641-010
KOREA

W. C. King
Mack Truck, Z-41
1999 Pennsylvania Avneue
Hagerstown MD 21740

Carol Kirkpatrick
MSE, Inc.
P.O. Box 3767
Butte MT 59702

Tony Kirn
Caterpillar Inc.
Defense Products Department, JB7
Peoria IL 61629

James D. Kiser
NASA Lewis Research Center
21000 Brookpark Road, MS:49-3
Cleveland OH 44135

Max Klein
900 24th Street, N.W., Unit G
Washington DC 20037

Richard N. Kleiner
Golden Technologies Company
4545 McIntyre Street
Golden CO 80403

Stanley J. Klima
NASA Lewis Research Center
21000 Brookpark Road, MS:6-1
Cleveland OH 44135

Chris E. Knapp
Norton Advanced Ceramics of
Canada Ltd.
8001 Daly Street
Niagara Falls Ontario L2G 6S2
CANADA

Albert S. Kobayashi
University of Washington
Mechanical Engineering Department
Mail Stop:FU10
Seattle WA 98195

Shigeki Kobayashi
Toyota Central Research Labs
Nagakute Aichi 480-11
JAPAN

Richard A. Kole
Z-Tech Corporation
8 Dow Road
Bow NH 03304

E. Kostiner
University of Connecticut
Chemistry Department, U-60
Storrs CT 06269-3060

Joseph A. Kovach
Eaton Corporation
32500 Chardon Road
Willoughby Hills OH 44094

Kenneth A. Kovaly
Technical Insights Inc.
P.O. Box 1304
Fort Lee NJ 07024-9967

Ralph G. Kraft
Spraying Systems Company
North Avenue at Schmale Road
Wheaton IL 60189-7900

Arthur Kranish
Trends Publishing Inc.
1079 National Press Building
Washington DC 20045

A. S. Krieger
Radiation Science, Inc.
P.O. Box 293
Belmont MA 02178

Pieter Krijgsman
Ceramic Design International
Holding B.V.
P.O. Box 68
Hattem 8050-AB
THE NETHERLANDS

Waltraud M. Kriven
University of Illinois
105 S. Goodwin Avenue
Urbana IL 61801

Edward J. Kubel, Jr.
ASM International
Advanced Materials & Processes
Materials Park OH 44073

Dave Kupperman
Argonne National Laboratory
9700 S. Cass Avenue
Argonne IL 60439

Oh-Hun Kwon
North Company
Advanced Ceramics
Goddard Road
Northboro MA 01532-1545

W. J. Lackey
GTRI
Materials Science and Tech. Lab
Atlanta GA 30332

Jai Lala
Tenmat Ltd.
40 Somers Road
Rugby Warwickshire CV22 7DH
ENGLAND

Hari S. Lamba
General Motors Corporation
9301 West 55th Street
LaGrange IL 60525

Richard L. Landingham
Lawrence Livermore National Lab
P.O. Box 808, L-369
Livermore CA 94550

James Lankford
Southwest Research Institute
6220 Culebra Road
San Antonio TX 78228-0510

Stanley B. Lasday
Business News Publishing Co.
1910 Cochran Road, Suite 630
Pittsburgh PA 15220

Mark S. Laser
Solar Turbines, Inc
2211 Erie Street
San Diego CA 92110

S. K. Lau
Carborundum Company
Technology Division
P.O. Box 832, B-100
Niagara Falls NY 14302

Edward A. Lauder
Advanced Composite Materials Corp
1525 S. Buncombe Road
Greer SC 29651-9208

J. Lawrence Lauderdale
Babcock & Wilcox
1850 "K" Street, Suite 950
Washington DC 20006

Jean F. LeCostaouec
Textron Specialty Materials
2 Industrial Avenue
Lowell MA 01851

Benson P. Lee
Interscience, Inc.
9718 Lake Shore Boulevard
Cleveland OH 44108

Burtrand I. Lee
Clemson University
Olin Hall
Clemson SC 29634-0907

June-Gunn Lee
KIST
P.O. Box 131, Cheong-Ryang
Seoul 130-650
KOREA

Ran-Rong Lee
Ceramics Process Systems
Corporation
155 Fortune Boulevard
Mildford MA 01757

Stan Levine
NASA Lewis Research Center
21000 Brookpark Road, MS:49-3
Cleveland OH 44135

Alan V. Levy
Lawrence Berkeley Laboratory
One Cyclotron Road, MS:62-203
Berkeley CA 94720

Ai-Kang Li
Materials Research Labs., ITRI
195-5 Chung-Hsing Road, Sec. 4
Chutung Hsinchu 31015 R.O.C.
TAIWAN

Winston W. Liang
Hong Kong Industrial Technology
Centre
78 Tat Chee Avenue
4/F, HKPC Building -- Kowloon
HONG KONG

Robert Licht
Norton Company
Advanced Ceramics
Goddard Road
Northboro MA 01532-1545

E. Lilley
Norton Company
Advanced Ceramics
Goddard Road
Northboro MA 01532-1545

Chih-Kuang Lin
National Central University
Dept. of Mechanical Engineering
Chung-Li 32054
TAIWAN

Laura J. Lindberg
AlliedSignal Aerospace Company
Garrett Fluid Systems Division
P.O. Box 22200
Tempe AZ 85284-2200

Hans A. Lindner
Cremer Forschungsinstitut
GmbH&Co.KG
Oeslauer Strasse 35
D-8633 Rodental 8866
GERMANY

Ronald E. Loehman
Sandia National Laboratories
Chemistry & Ceramics Dept. 1840
P.O. Box 5800
Albuquerque NM 87185

Jeffrey C. Logas
Winona State University
115 Pasteur Hall
Winona MN 55987

Bill Long
Babcock & Wilcox
P.O. Box 11165
Lynchburg VA 24506

William D. Long
Wacker Chemicals (USA), Inc.
ESK Engineered Ceramics
50 Locust Avenue
New Canaan CT 06840

L. A. Lott
EG&G Idaho, Inc.
Idaho National Engineering Lab
P.O. Box 1625
Idaho Falls ID 83415-2209

Raouf O. Loutfy
MER Corporation
7960 S. Kolb Road
Tucson AZ 85706

Gordon R. Love
Aluminum Company of America
Alcoa Technical Center
Alcoa Center PA 15960

Lydia Luckevich
Ortech International
2395 Speakman Drive
Mississauga Ontario L5K 1B3
CANADA

James W. MacBeth
Carborundum Company
Structural Ceramics Division
P.O. Box 1054
Niagara Falls NY 14302

H. MacLaren
General Electric Company
1000 Western Avenue
Lynn MA 01910

George Maczura
Aluminum Company of America
3450 Park Lane Drive
Pittsburgh PA 15275-1119

David Maginnis
Tinker AFB
OC-ALC/LIIRE
Tinker AFB OK 73145-5989

Frank Maginnis
Aspen Research, Inc.
220 Industrial Boulevard
Moore OK 73160

Tai-il Mah
Universal Energy Systems, Inc.
4401 Dayton-Xenia Road
Dayton OH 45432

Kenneth M. Maillar
Barbour Stockwell Company
83 Linskey Way
Cambridge MA 02142

S. G. Malghan
NIST
I-270 & Clopper Road
Gaithersburg MD 20899

Lars Malmrup
United Turbine AB
Box 13027
Malmo S-200 44
SWEDEN

John Mangels
Ceradyne, Inc.
3169 Redhill Avenue
Costa Mesa CA 92626

Murli Manghnani
University of Hawaii
2525 Correa Road
Honolulu HI 96822

Russell V. Mann
Matec Applied Sciences, Inc.
75 South Street
Hopkinton MA 01748

William R. Manning
Champion Aviation Products Div
P.O. Box 686
Liberty SC 29657

Ken Marnoch
Amercom, Inc.
8928 Fullbright Avenue
Chatsworth CA 91311

Robert A. Marra
Aluminum Company of America
Alcoa Technical Center
Alcoa Center PA 15069

Chauncey L. Martin
3M Company
3M Center, Building 60-1N-01
St. Paul MN 55144

Steve C. Martin
Advanced Refractory Technologies
699 Hertel Avenue
Buffalo NY 14207

Kelly J. Mather
William International Corporation
2280 W. Maple Road
Walled Lake MI 48088

James P. Mathers
3M Company
3M Center, Bldg. 201-3N-06
St. Paul MN 55144

Ron Mayville
Arthur D. Little, Inc.
15-163 Acorn Park
Cambridge MA 02140

F. N. Mazadarany
General Electric Company
Bldg. K-1, Room MB-159
P.O. Box 8
Schenectady NY 12301

James W. McCauley
Alfred University
Binns-Merrill Hall
Alfred NY 14802

Louis R. McCreight
2763 San Ramon Drive
Rancho Palos Verdes CA 90274

Colin F. McDonald
McDonald Thermal Engineering
1730 Castellana Road
La Jolla CA 92037

B. J. McEntire
Norton Company
TRW Ceramics
Goddard Road
Northboro MA 01532-1545

Chuck McFadden
Coors Ceramics Company
600 9th Street
Golden CO 80401

Thomas D. McGee
Iowa State University
110 Engineering Annex
Ames IA 50011

Carol McGill
Corning Inc.
Sullivan Park, FR-02-08
Corning NY 14831

James McLaughlin
Sundstrand Power Systems
4400 Ruffin Road
P.O. Box 85757
San Diego CA 92186-5757

Matt McMonigle
U.S. Department of Energy
Improved Energy Productivity
CE-231, Forrestal Building
Washington DC 20585

J. C. McVickers
AlliedSignal, Inc.
Auxiliary Power, Bldg. 1303-206
P.O. Box 52180, MS:9317-2
Phoenix AZ 85072-2180

D. B. Meadowcroft
"Jura," The Ridgeway
Oxshott
Leatherhead Surrey KT22 OLG
UNITED KINGDOM

Joseph J. Meindl
Reynolds International, Inc.
6603 W. Broad Street
P.O. Box 27002
Richmond VA 23261-7003

Michael D. Meiser
AlliedSignal, Inc.
Ceramic Components
P.O. Box 2960, MS:T21
Torrance CA 90509-2960

George Messenger
National Research Council of
Canada
Building M-7
Ottawa Ontario K1A OR6
CANADA

D. Messier
U.S. Army Materials Technology
SLCMT-EMC
405 Arsenal Street
Watertown MA 02172-0001

Arthur G. Metcalfe
Arthur G. Metcalfe and
Associates, Inc.
2108 East 24th Street
National City CA 91950

R. Metselaar
Eindhoven University
P.O. Box 513
Endhoven 5600 MB
THE NETHERLANDS

David J. Michael
Harbison-Walker Refractories Co.
P.O. Box 98037
Pittsburgh PA 15227

Ken Michaels
Chrysler Motors Corporation
P.O. Box 1118, CIMS:418-17-09
Detroit MI 48288

Bernd Michel
Institute of Mechanics
P.O. Box 408
D-9010 Chemnitz
GERMANY

David E. Miles
Commission of the European Comm.
rue de la Loi, 200
B-1049 Brussels
BELGIUM

Carl E. Miller
AC Rochester
1300 N. Dort Highway, MS:32-31
Flint MI 48556

Charles W. Miller, Jr.
Centorr Furnaces/Vacuum
Industries
542 Amherst Street
Nashua NH 03063

R. Minimmi
Enichem America
2000 Cornwall Road
Monmouth Junction NJ 08852

Michele V. Mitchell
AlliedSignal, Inc.
Ceramic Components
P.O. Box 2960, MS:T21
Torrance CA 90509-2960

Howard Mizuhara
WESGO
477 Harbor Boulevard
Belmont CA 94002

Helen Moeller
Babcock & Wilcox
P.O. Box 11165
Lynchburg VA 24506-1165

Francois R. Mollard
Concurrent Technologies Corp.
1450 Scalp Avenue
Johnstown PA 15904-3374

Phil Mooney
Panametrics
221 Crescent Street
Waltham MA 02254

Geoffrey P. Morris
3M Company
3M Traffic Control Materials
Bldg. 209-BW-10, 3M Center
St. Paul MN 55144-1000

Jay A. Morrison
Rolls-Royce, Inc.
2849 Paces Ferry Road, Suite 450
Atlanta GA 30339-3769

Joel P. Moskowitz
Ceradyne, Inc.
3169 Redhill Avenue
Costa Mesa CA 92626

Brij Moudgil
University of Florida
Material Science & Engineering
Gainesville FL 32611

Christoph J. Mueller
Sprechsaal Publishing Group
P.O. Box 2962, Mauer 2
D-8630 Coburg
GERMANY

Thomas W. Mullan
Vapor Technologies Inc.
345 Route 17 South
Upper Saddle River NJ 07458

M. K. Murthy
MkM Consultants International
10 Avoca Avenue, Unit 1906
Toronto Onntario M4T 2B7
CANADA

David L. Mustoe
Custom Technical Ceramics
8041 West I-70 Service Rd. Unit 6
Arvada CO 80002

Curtis V. Nakaishi
U.S. Department of Energy
Morgantown Energy Technology Ctr.
P.O. Box 880
Morgantown WV 26507-0880

Yoshio Nakamura
Faicera Research Institute
3-11-12 Misono
Sagamihara, Tokyo
JAPAN

Stefan Nann
Roland Berger & Partner GmbH
Georg-Glock-Str. 3
40474 Dusseldorf
GERMANY

K. S. Narasimhan
Hoeganaes Corporation
River Road
Riverton NJ 08077

Robert Naum
Applied Resources, Inc.
P.O. Box 241
Pittsford NY 14534

Malcolm Naylor
Cummins Engine Company, Inc.
P.O. Box 3005, Mail Code 50183
Columbus IN 47202-3005

Fred A. Nichols
Argonne National Laboratory
9700 S. Cass Avenue
Argonne IL 60439

H. Nickel
Forschungszentrum Juelich (KFA)
P.O. Box 1913
Juelich 1-5170 BRD NRW
GERMANY

Dale E. Niesz
Rutgers University
Center for Ceramic Research
P.O. Box 909
Piscataway NJ 08855-0909

Paul W. Niskanen
Lanxide Corporation
P.O. Box 6077
Newark DE 19714-6077

David M. Nissley
United Technologies Corporation
Pratt & Whitney Aircraft
400 Main Street, MS:163-10
East Hartford CT 06108

Bruce E. Novich
Ceramics Process Systems Corp.
155 Fortune Boulevard
Milford MA 01757

Daniel Oblas
50 Meadowbrook Drive
Bedford MA 01730

Don Ohanehi
Magnetic Bearings, Inc.
1908 Sussex Road
Blacksburg VA 24060

Robert Orenstein
General Electric Company
55-112, River Road
Schenectady NY 12345

Norb Osborn
Aerodyne Dallas
151 Regal Row, Suite 120
Dallas TX 75247

Richard Palicka
Cercom, Inc.
1960 Watson Way
Vista CA 92083

Muktesh Paliwal
GTE Products Corporation
Hawes Street
Towanda PA 18848

Joseph E. Palko
General Electric Company
55-113, River Road
Schenectady NY 12345

Joseph N. Panzarino
Saint-Gobain/Norton Industrial Ceramics
Northboro Research Center
Goddard Road
Northboro MA 01532-1545

Pellegrino Papa
Corning Inc.
MP-WX-02-1
Corning NY 14831

Terry Paquet
Boride Products Inc.
2879 Aero Park Drive
Traverse City MI 49684

E. Beth Pardue
MPC
8297 Williams Ferry Road
Lenior City TN 37771

Soon C. Park
3M Company
Building 142-4N-02
P.O. Box 2963
St. Paul MN 55144

Harmut Paschke
Schott Glaswerke
Christoph-Dorner-Strasse 29
D-8300 Landshut
GERMANY

James W. Patten
Cummins Engine Company, Inc.
P.O. Box 3005, Mail Code 50183
Columbus IN 47202-3005

Robert A. Penty
Eastman Kodak Company
1669 Lake Avenue
Rochester NY 14652-5150

Robert W. Pepper
Textron Specialty Materials
2 Industrial Avenue
Lowell MA 01851

Peter Perdue
Detroit Diesel Corporation
13400 Outer Drive West,
Speed Code L-04
Detroit MI 48239-4001

Bruce Peters
Dow Chemical Company
Building 52
Midland MI 48667

John J. Petrovic
Los Alamos National Laboratory
Group MST-4, MS:G771
Los Alamos NM 87545

Frederick S. Pettit
University of Pittsburgh
Pittsburgh PA 15261

Ben A. Phillips
Phillips Engineering Company
721 Pleasant Street
St. Joseph MI 49085

Richard C. Phoenix
Ohmtek, Inc.
2160 Liberty Drive
Niagara Falls NY 14302

Bruce J. Pletka
Michigan Technological University
Metallurgical & Materials Engr.
Houghton MI 49931

John P. Pollinger
AlliedSignal, Inc.
Ceramic Components
P.O. Box 2960, MS:T21
Torrance CA 90509-2960

P. Popper
High Tech Ceramics International
Journal
22 Pembroke Drive - Westlands
Newcastle-under-Lyme
Staffs ST5 2JN
ENGLAND

F. Porz
Universitat Karlsruhe
Institut fur Keramik Im
Maschinendau
Postfach 6980
D-7500 Karlsruhe
GERMANY

Harry L. Potma
Royal Netherlands Embassy
Science and Technology
4200 Linnean Avenue, N.W.
Washington DC 20008

Bob R. Powell
General Motors Technical Center
Metallurgy Department
Box 9055
Warren MI 48090-9055

Stephen C. Pred
ICD Group, Inc.
1100 Valley Brook Avenue
Lyndhurst NJ 07071

Karl M. Prewo
United Technologies Research Ctr.
411 Silver Lane, MS:24
East Hartford CT 06108

Peter E. Price
Industrial Materials Technology
P.O. Box 9565
Andover MA 01810

Vimal K. Pujari
Norton Company
Advanced Ceramics
Goddard Road
Northboro MA 01532-1545

George Quinn
NIST
Ceramics Division, Bldg. 223
Gaithersburg MD 20899

Ramas V. Raman
Ceracon, Inc.
1101 N. Market Boulevard, Suite 9
Sacramento CA 95834

Charles F. Rapp
Owens Corning Fiberglass
2790 Columbus Road
Granville OH 43023-1200

Dennis W. Readey
Colorado School of Mines
Metallurgy and Materials Engr.
Golden CO 80401

Wilfred J. Rebello
PAR Enterprises, Inc.
12601 Clifton Hunt Lane
Clifton VA 22024

Harold Rechter
Chicago Fire Brick Company
7531 S. Ashland Avenue
Chicago IL 60620

Robert R. Reeber
U.S. Army Research Office
P.O. Box 12211
Research Triangle Park NC 27709

K. L. Reifsnider
VPI & SU
Engineering Science and Mechanics
Blacksburg VA 24061

Paul E. Rempes
McDonnell Douglass Aircraft Co.
P.O. Box 516, Mail Code:0642263
St. Louis MO 63166-0516

Gopal S. Revankar
John Deere Company
3300 River Drive
Moline IL 61265

K. Y. Rhee
Rutgers University
P.O. Box 909
Piscataway NJ 08854

James Rhodes
Advanced Composite Materials Corp
1525 S. Buncombe Road
Greer SC 29651

Roy W. Rice
W. R. Grace and Company
7379 Route 32
Columbia MD 21044

David W. Richerson
2093 E. Delmont Drive
Salt Lake City UT 84117

Tomas Richter
J. H. France Refractories
1944 Clarence Road
Snow Shoe PA 16874

Michel Rigaud
Ecole Polytechnique
Campus Universite De Montreal
P.O. Box 6079, Station A
Montreal, P.Q. Quebec H3C 3A7
CANADA

Barry Ringstrom
Superior Graphite Company
P.O. Box 2373
Smyrna GA 30081

John E. Ritter
University of Massachusetts
Mechanical Engineering Department
Amherst MA 01003

Frank L. Roberge
AlliedSignal, Inc.
Auxiliary Power
P.O. Box 52180
Phoenix AZ 85072-2180

W. Eric Roberts
Advanced Ceramic Technology, Inc.
990 "F" Enterprise Street
Orange CA 92667

Y. G. Roman
TNO TPD Keramick
P.O. Box 595
Einhoven 5600 AN
HOLLAND

Michael Rossetti
Arthur D. Little, Inc.
15 Acorn Park
Cambridge MA 01240

Barry Rossing
Lanxide Corporation
P.O. Box 6077
Newark DE 19714-6077

Steven L. Rotz
Lubrizol Corporation
29400 Lakeland Boulevard
Wickliffe OH 44092

Bruce Rubinger
Global Competitiveness, Inc.
One Devonshire Place, Suite 1011
Boston MA 02109

Robert Ruh
Wright Laboratory
WL/MLLM
Wright-Patterson AFB OH 45433

Robert J. Russell
17 Highgate Road
Framingham MA 01701

L. William Sahley
Supermaterials Company
24400 Highland Road
Richmond Heights OH 44143

Jon A. Salem
NASA Lewis Research Center
21000 Brookpark Road
Cleveland OH 44135

W. A. Sanders
NASA Lewis Research Center
21000 Brookpark Road, MS:49-3
Cleveland OH 44135

J. Sankar
North Carolina A&T State Univ.
Dept. of Mechanical Engineering
Greensboro NC 27406

Yasushi Sato
NGK Spark Plugs (U.S.A.), Inc.
1200 Business Center Drive, #300
Mt. Prospect IL 60056

Maxine L. Savitz
AlliedSignal, Inc.
Ceramic Components
P.O. Box 2960, MS:T21
Torrance CA 90509-2960

Ashok Saxena
GTRI
Materials Engineering
Atlanta GA 30332-0245

David W. Scanlon
Instron Corporation
100 Royall Street
Canton MA 02021

Charles A. Schacht
Schacht Consulting Services
12 Holland Road
Pittsburgh PA 15235

Robert E. Schafrik
National Materials Advisory Board
2101 Constitution Ave., NW
Washington DC 20418

James Schienle
AlliedSignal, Inc.
Auxiliary Power
P.O. Box 52180, MS:1302-2P
Phoenix AZ 85072-2180

John C. Schneider
San Juan Technologies
P.O. Box 49326
Colorado Springs CO 80949-9326

Gary Schnittgrund
Rocketdyne, BA05
6633 Canoga Avenue
Canoga Park CA 91303

Mark Schomp
Lonza, Inc.
17-17 Route 208
Fair Lann NJ 07410

Joop Schoonman
Delft University of Technology
P.O. Box 5045
2600 GA Delft
THE NETHERLANDS

John Schuldies
Industrial Ceramic Technology
30 Orchard Way, North
Potomac MD 20854

Robert B. Schulz
U.S. Department of Energy
Office of Transportation Matrls.
CE-34, Forrestal Building
Washington DC 20585

Murray A. Schwartz
Materials Technology Consulting
30 Orchard Way, North
Potomac MD 20854

Peter Schwarzkopf
SRI International
333 Ravenswood Avenue
Menlo Park CA 94025

William T. Schwessinger
Multi-Arc Scientific Coatings
1064 Chicago Road
Troy MI 48083-4297

W. D. Scott
University of Washington
Materials Science Department
Mail Stop:FB10
Seattle WA 98195

Nancy Scoville
Thermo Electron Technologies
P.O. Box 9046
Waltham MA 02254-9046

Thomas M. Sebestyen
U.S. Department of Energy
Advanced Propulsion Division
CE-322, Forrestal Building
Washington DC 20585

Brian Seegmiller
Coors Ceramics Company
600 9th Street
Golden CO 80401

T. B. Selover
AICRE/DIPPR
3575 Traver Road
Shaker Heights OH 44122

J. H.. Selverian
GTE Laboratories, Inc.
40 Sylvan Road
Waltham MA 02254

Charles E. Semler
Semler Materials Services
4160 Mumford Court
Columbus OH 43220

Thomas Service
Service Engineering Laboratory
324 Wells Street
Greenfield MA 01301

Kish Seth
Ethyl Corporation
P.O. Box 341
Baton Rouge LA 70821

Karleen Seybold
AlliedSignal, Inc.
Auxiliary Power
P.O. Box 52180
Phoenix AZ 85072-2180

William J. Shack
Argonne National Laboratory
9700 S. Cass Avenue, Bldg. 212
Argonne IL 60439

Peter T.B. Shaffer
Technical Ceramics Laboratories,
4045 Nine/McFarland Drive
Alpharetta GA 30201

Richard K. Shaltens
NASA Lewis Research Center
21000 Brookpark Road, MS:302-2
Cleveland OH 44135

Robert S. Shane
1904 NW 22nd Street
Stuart FL 34994-9270

Ravi Shankar
Chromalloy
Research and Technology Division
Blaisdell Road
Orangeburg NY 10962

Terence Sheehan
Alpex Wheel Company
727 Berkley Street
New Milford NJ 07646

Dinesh K. Shetty
University of Utah
Materials Science and Engineering
Salt Lake City UT 84112

Masahide Shimizu
Ceramic Society of Japan
2-2-503 Takiyama 6-chome
Higashikurume-Shi Tokyo 203
JAPAN

Thomas Shreves
American Ceramic Society, Inc.
735 Ceramic Place
Westerville OH 43081-8720

Jack D. Sibold
Coors Ceramics Company
4545 McIntyre Street
Golden CO 80403

Johann Siebels
Volkswagen AG
Werkstofftechnologie
3180 Wolfsburg 1
GERMANY

George H. Siegel
Point North Associates, Inc.
P.O. Box 907
Madison NJ 07940

Richard Silberglitt
FM Technologies, Inc.
10529-B Braddock Road
Fairfax VA 22032

Mary Silverberg
Norton Company
Goddard Road
Northboro MA 01532-1545

Gurpreet Singh
Department of the Navy
Code 56X31
Washington DC 20362-5101

Maurice J. Sinnott
University of Michigan
5106 IST Building
Ann Arbor MI 48109-2099

John Skildum
3M Company
3M Center
Building 224-2S-25
St. Paul MN 55144

Richard H. Smoak
Smoak & Associates
3554 Hollyslope Road
Altadena CA 91001-3923

Jay R. Smyth
AlliedSignal, Inc.
Auxiliary Power
P.O. Box 52180
MS:93-173/1303-207
Phoenix AZ 85072-2180

Rafal A. Sobotowski
British Petroleum Company
Technical Center, Broadway
3092 Broadway Avenue
Cleveland OH 44115

A. G. Solomah
SAC International Ltd.
1445 Bonhill Road, #13
Mississauga Ontario L5T 1V3
CANADA

S. Somiya
Nishi Tokyo University
3-7-19 Seijo, Setagaya
Tokyo 157
JAPAN

Boyd W. Sorenson
DuPont Lanxide Composites
1300 Marrows Road
Newark DE 19711

Charles A. Sorrell
U.S. Department of Energy
Advanced Industrial Concepts
CE-232, Forrestal Building
Washington DC 20585

C. Spencer
EA Technology
Capenhurst Chester CH1 6ES
UNITED KINGDOM

Allen Spizzo
Hercules Inc.
Hercules Plaza
Wilmington DE 19894

Richard M. Spriggs
Alfred University
Center for Advanced Ceramic
Technology
Alfred NY 14802

Charles Spuckler
NASA Lewis Research Center
21000 Brookpark Road, MS:5-11
Cleveland OH 44135-3191

M. Srinivasan
Material Solutions
P.O. Box 663
Grand Island NY 14702-0663

Gordon L. Starr
Cummins Engine Company, Inc.
P.O. Box 3005, Mail Code:50182
Columbus IN 47202-3005

Tom Stillwagon
AlliedSignal, Inc.
Ceramic Components
P.O. Box 2960, MS:T21
Torrance CA 90509-2960

H. M. Stoller
TPL Inc.
3754 Hawkins, N.E.
Albuquerque NM 87109

Paul D. Stone
Dow Chemical USA
1776 "Eye" Street, N.W., #575
Washington DC 20006

Roger S. Storm
Carborundum Company
Technology Division
P.O. Box 337
Niagara Falls NY 14302-0337

F. W. Stringer
Aero & Industrial Technology Ltd.
P.O. Box 46, Wood Top
Burnley Lancashire BB11 4BX
UNITED KINGDOM

Thomas N. Strom
NASA Lewis Research Center
21000 Brookpark Road, MS:86-6
Cleveland OH 44135

M. F. Stroosnijder
Institute for Advanced Materials
Joint Research Centre
21020 Ispra (VA)
ITALY

Karsten Styhr
30604 Ganado Drive
Rancho Palos Verdes CA 90274

T. S. Sudarshan
Materials Modification, Inc.
2929-P1 Eskridge Center
Fairfax VA 22031

M. J. Sundaresan
University of Miami
P.O. Box 248294
Coral Gables FL 33124

Patrick L. Sutton
U.S. Department of Energy
Office of Propulsion Systems
CE-322, Forrestal Building
Washington DC 20585

Willard H. Sutton
United Technologies Corporation
Silver Lane, MS:24
East Hartford CT 06108

J. J. Swab
U.S. Army Materials Technology
Ceramics Research Division,
SLCMT-EMC
405 Arsenal Street
Watertown MA 02172

Robert E. Swanson
Metalworking Technology, Inc.
1450 Scalp Avenue
Johnstown PA 15904

Steve Szaruga
Air Force Wright Aeronautical Lab
WL/MLBC
Wright-Patterson AFB OH
45433-6533

Yo Tajima
NGK Spark Plug Company
2808 Iwasaki
Komaki-shi Aichi-ken 485
JAPAN

Fred Teeter
5 Tralee Terrace
East Amherst NY 14051

Monika O. Ten Eyck
Carborundum Company
Technology Division
P.O. Box 832
Niagara Falls NY 14302

David F. Thompson
Corning Glass Works
SP-DV-02-1
Corning NY 14831

Merle L. Thorpe
Hobart Tafa Technologies, Inc.
146 Pembroke Road
Concord NH 03301

T. Y. Tien
University of Michigan
Materials Science and Engineering
Dow Building
Ann Arbor MI 48103

D. M. Tracey
Norton Company
Advanced Ceramics
Goddard Road
Northboro MA 01532-1545

L. J. Trostel, Jr.
Box 199
Princeton MA 01541

W. T. Tucker
General Electric Company
P.O. Box 8, Bldg. K1-4C35
Schenectady NY 12301

Masanori Ueki
Nippon Steel Corporation
1618 Ida
Nakahara-Ku Kawasaki 211
JAPAN

Filippo M. Ugolini
ATA Studio
Via Degli Scipioni, 268A
ROMA, 00192
ITALY

Donald L. Vaccari
General Motors Corporation
Allison Gas Turbines
P.O. Box 420, Speed Code S49
Indianapolis IN 46206-0420

Carl F. Van Conant
Boride Products, Inc.
2879 Aero Park Drive
Traverse City MI 49684

Marcel H. Van De Voorde
Commission of the European Comm.
P.O. Box 2
1755 ZG Petten
THE NETHERLANDS

O. Van Der Biest
Katholieke Universiteit Leuven
Dept. Metaalkunde en Toegepaste
de Croylaan 2
B-3030 Leuven
BELGIUM

Michael Vannier
Washington University, St. Louis
510 S. Kings Highway
St. Louis MO 63110

Stan Venkatesan
Southern Coke & Coal Corporation
P.O. Box 52383
Knoxville TN 37950

V. Venkateswaran
Carborundum Company
Niagara Falls R&D Center
P.O. Box 832
Niagara Falls NY 14302

Dennis Viechnicki
U.S. Army Materials Technology
405 Arsenal Street
Watertown MA 02172-0001

Ted Vojnovich
U.S. Department of Energy, ST-311
Office of Energy Research, 3F077P
Washington DC 20585

John D. Volt
E.I. Dupont de Nemours & Co. Inc.
P.O. Box 80262
Wilmington DE 19880

John B. Wachtman
Rutgers University
P.O. Box 909
Piscataway NJ 08855

Shigetaka Wada
Toyota Central Research Labs
Nagakute Aichi 480-11
JAPAN

Janet Wade
AlliedSignal, Inc.
Auxiliary Power
P.O. Box 52180, MS:1303-2
Phoenix AZ 85072-2180

Richard L. Wagner
Ceramic Technologies, Inc.
537 Turtle Creek South Dr., #24D
Indianapolis IN 46227

J. Bruce Wagner, Jr.
Arizona State University
Center for Solid State Science
Tempe AZ 85287-1704

Daniel J. Wahlen
Kohler, Co.
444 Highland Drive
Kohler WI 53044

Ingrid Wahlgren
Royal Institute of Technology
Studsvik Library
S-611 82 Nykoping
SWEDEN

Ron H. Walecki
AlliedSignal, Inc.
Ceramic Components
P.O. Box 2960, MS:T21
Torrance CA 90509-2960

Michael S. Walsh
Vapor Technologies Inc.
2100 Central Avenue
Boulder CO 80301

Chien-Min Wang
Industrial Technology Research Institute
195 Chung-Hsing Road, Sec. 4
Chutung Hsinchu 31015 R.O.C.
TAIWAN

Robert M. Washburn
ASMT
11203 Colima Road
Whittier CA 90604

Gerald Q. Weaver
Carborundum Specialty Products
42 Linus Allain Avenue
Gardner MA 01440-2478

Kevin Webber
Toyota Technical Center, U.S.A.
1410 Woodridge, RR7
Ann Arbor MI 48105

Karen E. Weber
Detroit Diesel Corporation
13400 Outer Drive West
Detroit MI 48239-4001

J. K. Weddell
DuPont Fibers
Experimental Station, E302
Wilmington DE 19880-0302

R. W. Weeks
Argonne National Laboratory
MCT-212
9700 S. Cass Avenue
Argonne IL 60439

Ludwig Weiler
ASEA Brown Boveri AG
Eppelheimer Str. 82
D-6900 Heidelberg
GERMANY

James Wessel
Dow Corning Corporation
1800 "M" Street, N.W., #325 South
Washington DC 20036

Robert D. West
Therm Advanced Ceramics
P.O. Box 220
Ithaca NY 14851

Thomas J. Whalen
Ford Motor Company
26362 Harriet
Dearborn Heights MI 48127

Ian A. White
Hoeganaes Corporation
River Road
Riverton NJ 08077

Sheldon M. Wiederhorn
NIST
Building 223, Room A329
Gaithersburg MD 20899

John F. Wight
Alfred University
McMahon Building
Alfred NY 14802

D. S. Wilkinson
McMaster University
1280 Main Street, West
Hamilton Ontario L8S 4L7
CANADA

James C. Williams
General Electric Company
Engineering Materials Technology
One Neumann Way, Mail Drop:H85
Cincinnati OH 45215-6301

Steve J. Williams
RCG Hagler Bailly, Inc.
1530 Wilson Boulevard, Suite 900
Arlington VA 22209-2406

Thomas A. Williams
National Renewable Energy Lab
1617 Cole Boulevard
Golden CO 80401

Craig A. Willkens
Norton Company
Advanced Ceramics
Goddard Road
Northboro MA 01532-1545

Roger R. Wills
TRW, Inc.
Valve Division
1455 East 185th Street
Cleveland OH 44110

David Gordon Wilson
Massachusetts Institute of
Technology
77 Massachusetts Ave., Room 3-455
Cambridge MA 02139

Matthew F. Winkler
Seaworthy Systems, Inc.
P.O. Box 965
Essex CT 06426

Gerhard Winter
Hermann C. Starck Berlin GmbH
P.O. Box 25 40
D-3380 Goslar 3380
GERMANY

W. L. Winterbottom
Ford Motor Company
20000 Rotunda Drive
SRL, Room E-3182
Dearborn MI 48121

William T. Wintucky
NASA Lewis Research Center
Terrestrial Propulsion Office
21000 Brookpark Road, MS:86-6
Cleveland OH 44135

Thomas J. Wissing
Eaton Corporation
Engineering and Research Center
P.O. Box 766
Southfield MI 48037

James C. Withers
MER Corporation
7960 S. Kolb Road
Building F
Tucson AZ 85706

Dale E. Wittmer
Southern Illinois University
Mechanical Engineering Department
Carbondale IL 62901

Warren W. Wolf
Owens Corning Fiberglass
2790 Columbus Road, Route 16
Granville OH 43023

Egon E. Wolff
Caterpillar Inc.
Technical Center
P.O. Box 1875
Peoria IL 61656-1875

George W. Wolter
Howmet Turbine Components Corp.
Technical Center
699 Benston Road
Whitehall MI 49461

James C. Wood
NASA Lewis Research Center
21000 Brookpark Road, MS:86-6
Cleveland OH 44135

Marrill Wood
LECO Corporation
P.O. Box 211688
Augusta GA 30917-1688

Wayne L. Worrell
University of Pennsylvania
3231 Walnut Street
Philadelphia PA 19104

John F. Wosinski
Corning Inc.
ME-2 E-5 H8
Corning NY 14830

Ian G. Wright
BCL
505 King Avenue
Columbus OH 43201

Ruth Wroe
ERDC
Capenhurst Chester CH1 6ES
ENGLAND

Bernard J. Wrona
Advanced Composite Materials Corp
1525 S. Buncombe Road
Greer SC 29651

Carl C. M. Wu
Naval Research Laboratory
Ceramic Branch, Code 6373
Washington DC 20375

John C. Wurst
U. of Dayton Research Institute
300 College Park
Dayton OH 45469-0101

Neil Wyant
ARCH Development Corp.
9700 S. Cass Avenue, Bldg. 202
Argonne IL 60439

Roy Yamamoto
Texaco Inc.
P.O. Box 509
Beacon NY 12508-0509

John Yamanis
AlliedSignal Aerospace Company
P.O. Box 1021
Morristown NJ 07962-1021

Harry C. Yeh
AlliedSignal, Inc.
Ceramic Components
P.O. Box 2960, MS:T21
Torrance CA 90509-2960

Hiroshi Yokoyama
Hitachi Research Lab
4026 Kuji-Cho
Hitachi-shi Ibaraki 319-12
JAPAN

Thomas M. Yonushonis
Cummins Engine Company, Inc.
P.O. Box 3005, Mail Code 50183
Columbus IN 47202-3005

Thomas J. Yost
Corning Inc.
Technical Products Div., 21-1-2
Corning NY 14831

Jong Yung
Sundstrand Aviation Operations
4747 Harrison Avenue
Rockford IL 61125

A. L. Zadoks
Caterpillar Inc.
Technical Center, Building L
P.O. Box 1875
Peoria IL 61656-1875

Avi Zangvil
University of Illinois
104 S. Goodwin Avenue
Urbana IL 61801

Charles H. Zenuk
Transtech
1340 N. Via Ronda Oeste
Tucson AZ 85715-4830

Carl Zweben
General Electric Company
P.O. Box 8555, VFSC/V4019
Philadelphia PA 19101

Department of Energy
Oak Ridge Operations Office
Assistant Manager for Energy
Research and Development
P.O. Box 2001
Oak Ridge, TN 37831-8600

Department of Energy (2)
Office of Scientific and
Technical
Information
Office of Information Services
P.O. Box 62
Oak Ridge, TN 37831

For distribution by microfiche
as shown in DOE/OSTI-4500,
Distribution Category UC-332
(Ceramics/Advanced Materials).

*U.S. GOVERNMENT PRINTING OFFICE: 1993-550-165/80013